MicroVention®
TERUMO

Leading the Way in Neuroendovascular Therapy

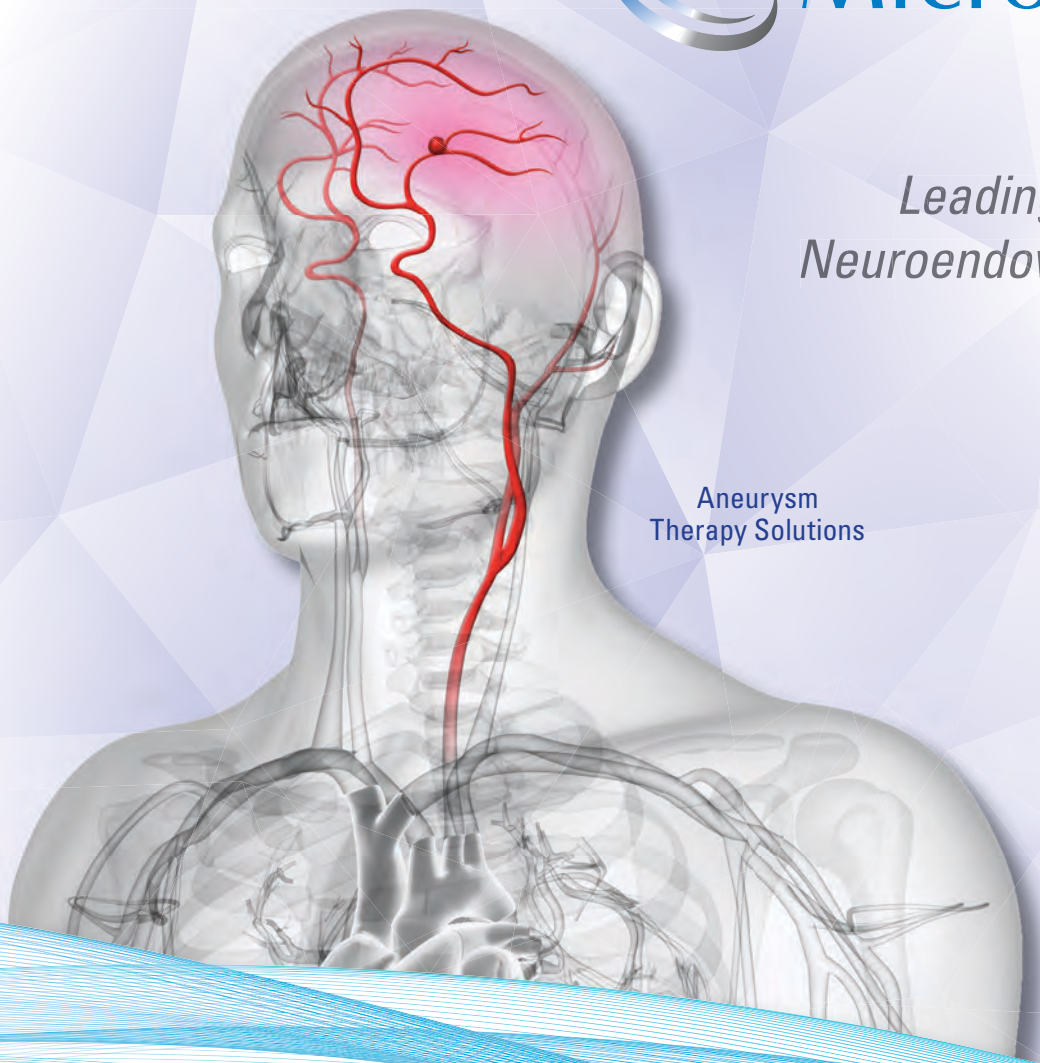

Aneurysm
Therapy Solutions

A 360-Degree Approach to Performance Based Solutions

microvention.com

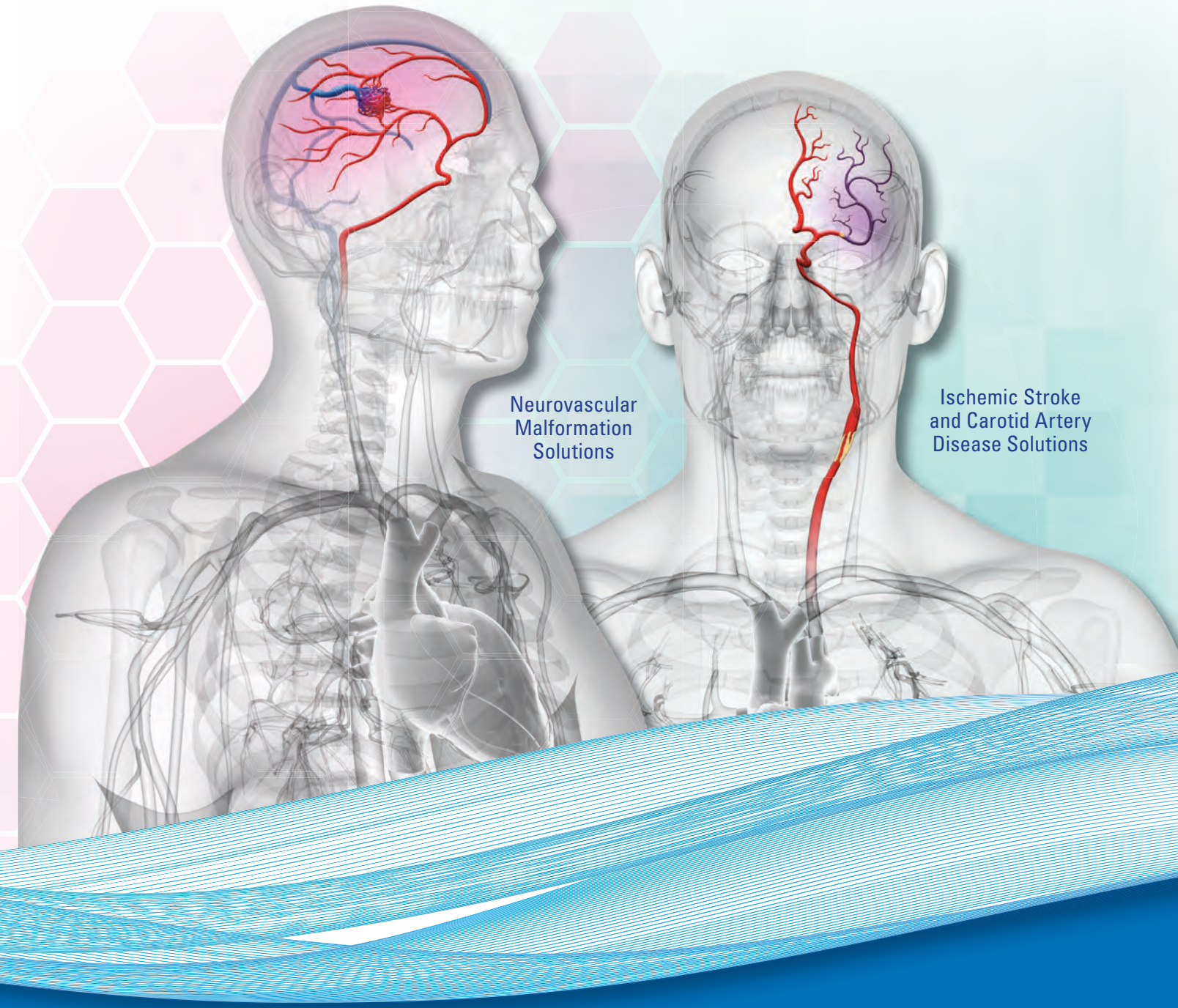

For more information or a product demonstration, contact your local MicroVention representative:

MicroVention®
TERUMO

MicroVention, Inc.
Worldwide Headquarters PH +1.714.247.8000
1311 Valencia Avenue
Tustin, CA 92780 USA
MicroVention UK Limited PH +44 (0) 191 258 6777
MicroVention Europe, S.A.R.L. PH +33 (1) 39 21 77 46
MicroVention Deutschland GmbH PH +49 211 210 798-0

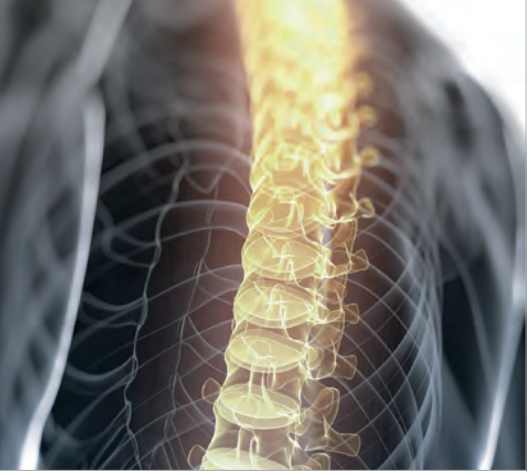

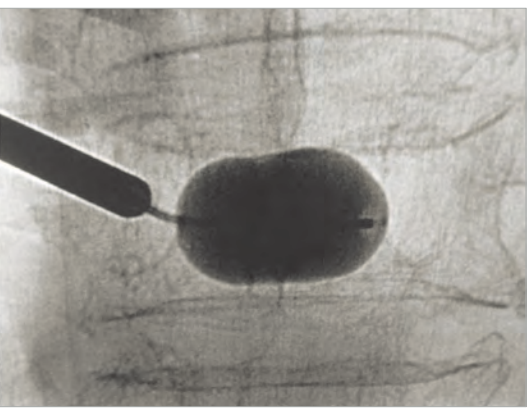

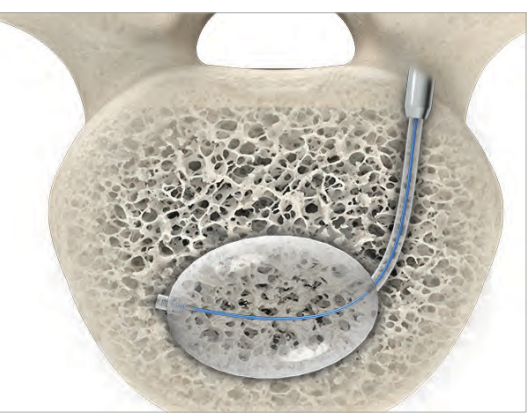

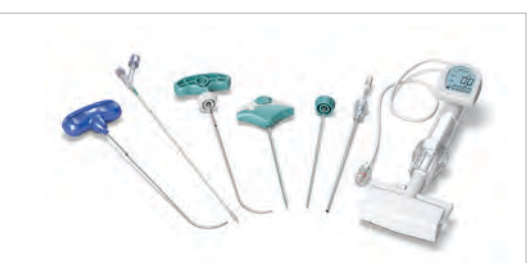

stryker

Unipedicular approach.

Bipedicular results.*

AVAflex® Balloon System

Simplify your approach in treating vertebral compression fractures (VCFs) and create larger voids with a single incision. The AVAflex system's flexible, curved balloon is available up to 30mm, the longest balloon on the market today.† Our curved, coaxial needle achieves targeted cement placement. It's more than a minimally invasive approach with the potential for less risk of patient trauma. It's a powerful reminder that we're in this together.

Achieve precision with a single incision.
strykerIVS.com/avaflex

* Based on fill volume
† As of February 2017

1000-025-577 Rev None

BARRICADE™ COIL SYSTEM

COILS THAT
PERFORM

Cost Analysis of Cerebral Aneurysms Treated with the Barricade Coil System, A Retrospective Review

22 Patients Treated ◆ 114 Total Barricade Coils Used ◆ 8.2mm Mean Aneurysm Size

RIGHT PERICALLOSAL ANEURYSM

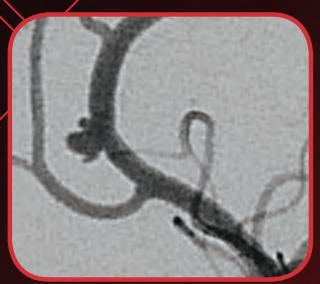

PRE-TREATMENT

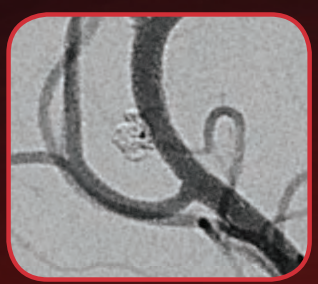

POST-TREATMENT

LEFT ICA TERMINUS ANEURYSM

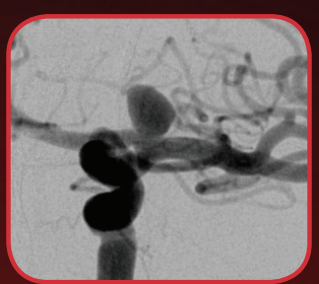

PRE-TREATMENT

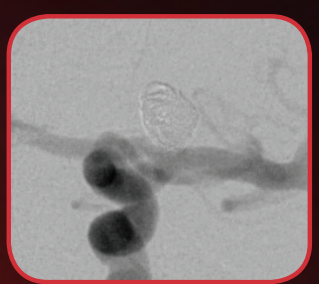

POST-TREATMENT

"I have successfully treated a wide range of aneurysms with the Barricade Coil System. I am impressed with the overall performance of the coils and the realized cost savings."

-Yince Loh, M.D.

COILS THAT
SAVE $

$110,000* SAVED

Images and data courtesy of Yince Loh, M.D., Seattle, WA

* Estimated savings in this case, data on file.

The Barricade Coil System is intended for the endovascular embolization of intracranial aneurysms and other neurovascular abnormalities such as arteriovenous malformations and arteriovenous fistulae. The System is also intended for vascular occlusion of blood vessels within the neurovascular system to permanently obstruct blood flow to an aneurysm or other vascular malformation and for arterial and venous embolizations in the peripheral vasculature. Refer to the instructions for use for complete product information.

18 TECHNOLOGY DRIVE #169, IRVINE CA 92618 | p: 949.788.1443 | f: 949.788.1444
WWW.BLOCKADEMEDICAL.COM

MKTG-050 Rev. A

BLOCKADE MEDICAL

The brain at your fingertips

Rapid Medical

www.rapid-medical.com > tigertriever

AJNR
AMERICAN JOURNAL OF NEURORADIOLOGY

2017 LUCIEN LEVY BEST RESEARCH ARTICLE

AWARD WINNER AND NOMINEES NAMED

This award is named for the late *AJNR* Senior Editor who championed its establishment and recognizes the best original research paper accepted in 2016. The winning paper, submitted by authors from the Texas Children's Hospital in Houston, was published electronically on October 13, 2016 and appeared in the February print issue. It was selected by a vote of the *Journal's* Editor-in-Chief and Senior Editors.


Brain Network Architecture and Global Intelligence in Children with Focal Epilepsy

The Editors of *AJNR* are pleased to announce the annual Lucien Levy Best Research Article Award has been presented to

"Brain Network Architecture and Global Intelligence in Children with Focal Epilepsy"

by M.J. Paldino, F. Golriz, M.L. Chapieski, W. Zhang, and Z.D. Chu

---

Other nominated papers were:

"Fate of Coiled Aneurysms with Minor Recanalization at 6 Months: Rate of Progression to Further Recanalization and Related Risk Factors" *by J.P. Jeon, Y.D. Cho, J.K. Rhim, D.H. Yoo, W.-S. Cho, H.-S. Kang, J.E. Kim, and M.H. Han*

"Diffusion-Weighted Imaging of Nasopharyngeal Carcinoma: Can Pretreatment DWI Predict Local Failure Based on Long-Term Outcome?" *by B.K.H. Law, A.D. King, K.S. Bhatia, A.T. Ahuja, M.K.M. Kam, B.B. Ma, Q.Y. Ai, F.K.F. Mo, J. Yuan, and D.K.W. Yeung*

"Porcine In Vivo Validation of a Virtual Contrast Model: The Influence of Contrast Agent Properties and Vessel Flow Rates" *by T.W. Peach, Y. Ventikos, J.V. Byrne, and Z. You*

"MR Imaging of Individual Perfusion Reorganization Using Superselective Pseudocontinuous Arterial Spin-Labeling in Patients with Complex Extracranial Steno-Occlusive Disease" *by V. Richter, M. Helle, M.J.P. van Osch, T. Lindner, A.S. Gersing, P. Tsantilas, H.-H. Eckstein, C. Preibisch, and C. Zimmer*

"A Semiautomatic Method for Multiple Sclerosis Lesion Segmentation on Dual-Echo MR Imaging: Application in a Multicenter Context" *by L. Storelli, E. Pagani, M.A. Rocca, M.A. Horsfield, A. Gallo, A. Bisecco, M. Battaglini, N. De Stefano, H. Vrenken, D.L. Thomas, L. Mancini, S. Ropele, C. Enzinger, P. Preziosa, and M. Filippi*

"Computer-Extracted Texture Features to Distinguish Cerebral Radionecrosis from Recurrent Brain Tumors on Multiparametric MRI: A Feasibility Study" *by P. Tiwari, P. Prasanna, L. Wolansky, M. Pinho, M. Cohen, A.P. Nayate, A. Gupta, G. Singh, K.J. Hatanpaa, A. Sloan, L. Rogers, and A. Madabhushi*

stryker

NEW

Indication for Trevo® Retrievers

A New Standard of Care in Stroke

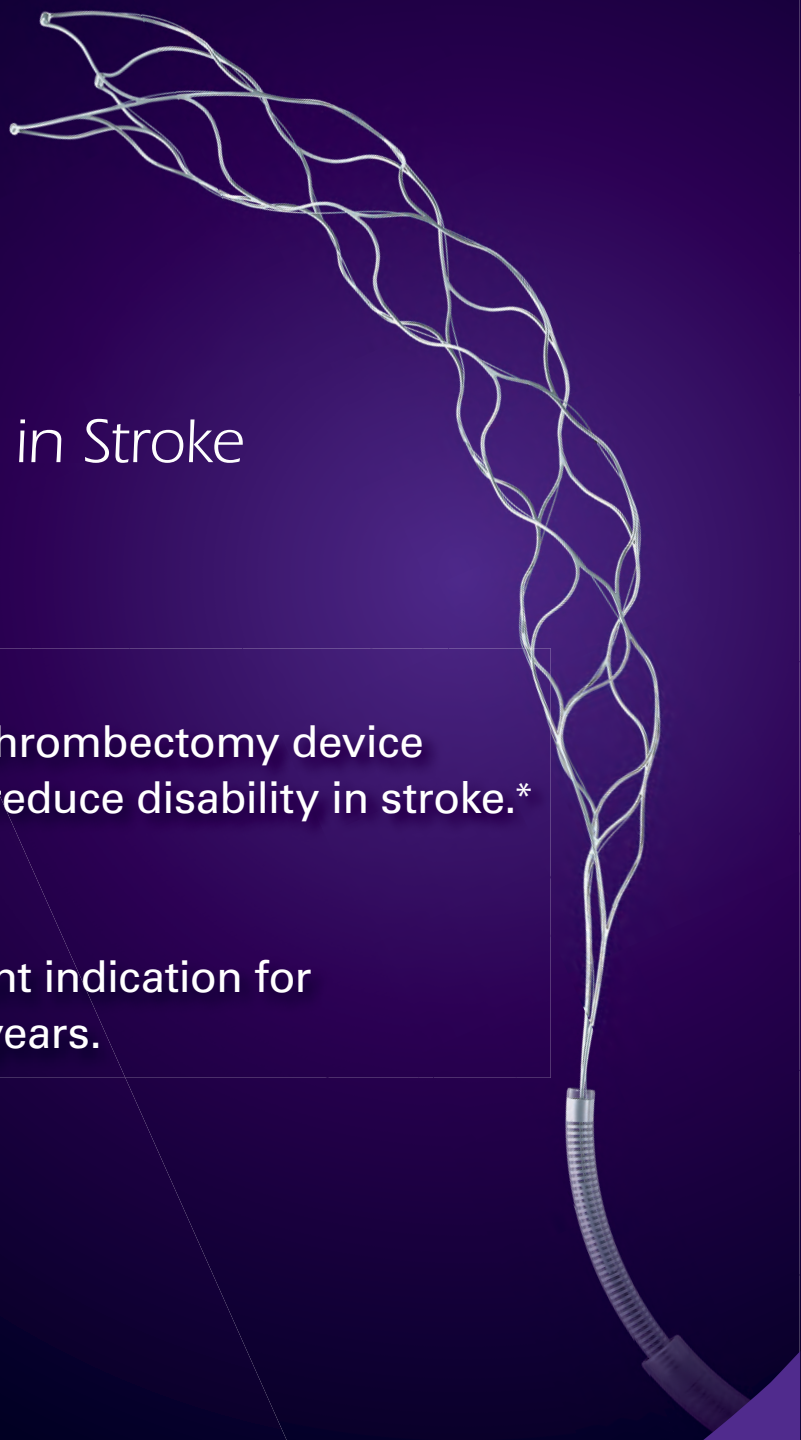

1st

FIRST
mechanical thrombectomy device indicated to reduce disability in stroke.*

FIRST
new treatment indication for stroke in 20 years.

Trevo XP
PROVUE RETRIEVER

Success accelerated.

*The Trevo Retriever is indicated for use to restore blood flow in the neurovasculature by removing thrombus for the treatment of acute ischemic stroke to reduce disability in patients with a persistent, proximal anterior circulation, large vessel occlusion, and smaller core infarcts who have first received intravenous tissue plasminogen activator (IV t-PA). Endovascular therapy with the device should start within 6 hours of symptom onset.

The Foundation of the ASNR Symposium 2017: *Discovery and Didactics* April 22-23, 2017

ASNR 55th Annual Meeting: *Diagnosis and Delivery* April 24-27, 2017

Register Now!
Visit 2017.asnr.org for more information.

Long Beach Convention & Entertainment Center

Jacqueline A. Bello, MD, FACR
ASNR 2017 Program Chair/President-Elect

Programming developed in cooperation with and appreciation of the…

American Society of Functional Neuroradiology (ASFNR)
Kirk M. Welker, MD

American Society of Head and Neck Radiology (ASHNR)
Rebecca S. Cornelius, MD, FACR

American Society of Pediatric Neuroradiology (ASPNR)
Susan Palasis, MD

American Society of Spine Radiology (ASSR)
Joshua A. Hirsch, MD, FACR, FSIR

Society of NeuroInterventional Surgery (SNIS)
Blaise W. Baxter, MD

American Society of Neuroradiology (ASNR) Health Policy Committee
Robert M. Barr, MD, FACR

Computer Sciences & Informatics (CSI) Committee
John L. Go, MD, FACR

Research Scientist Committee
Dikoma C. Shungu, PhD and Timothy, P.L. Roberts, PhD

The International Hydrocephalus Imaging Working Group (IHIWG)/CSF Flow Group
William G. Bradley, Jr., MD, PhD, Harold L. Rekate, MD and Bryn A. Martin, PhD

ASNR 55th Annual Meeting
c/o American Society of Neuroradiology
800 Enterprise Drive, Suite 205 • Oak Brook, Illinois 60523-4216
Phone: 630-574-0220 • Fax: 630 574-0661 • 2017.asnr.org

2017 ASNR Long Beach, California
Discovery Didactics Diagnosis Delivery

ASFNR ASHNR ASPNR ASSR SNIS
THE FOUNDATION OF THE ASNR

Come to the beach! Please join us in Long Beach, California, April 22-27, 2017, for the 55th Annual Meeting of the ASNR. Known for its 5.5 miles of Pacific Ocean waterfront, this southern California beach resort boasts a blend of city sophistication and seaside serenity. ASNR is delighted to provide a **"4D"** focus for this meeting, as depicted by our meeting logo: ***Discovery and Didactics*** for The Foundation of the ASNR Symposium 2017: ***Diagnosis and Delivery*** for the ensuing Annual Meeting Program.

Centered on Discovery and Didactics, the symposium will feature sessions on "What's New?" in the role neuroimaging plays defining CNS disease mechanisms and how to best prepare for "What's Next?" for our subspecialty in terms of training, teaching, and leading the process of lifelong learning. The annual meeting programming will address best practices in Diagnosis and Delivery, as we strive to provide value, promote quality in better health and care and consider cost. Our discussions will consider how to navigate the changing landscape of healthcare reform and reimbursement as subspecialists in a field that is changing at an equally "fast forward" pace!

Hyatt Regency Long Beach

Westin Long Beach

INTRODUCING
FULLY AUTOMATED
STROKE APPLICATIONS

Olea Sphere 3.0

ZERO CLICK
Calculation of infarct penumbra & mismatch

AUTOMATED STROKE REPORT
(MRI & CT) by email

VENDOR-NEUTRAL
& easy integration into IT systems

Ask for a free trial
www.olea-medical.com

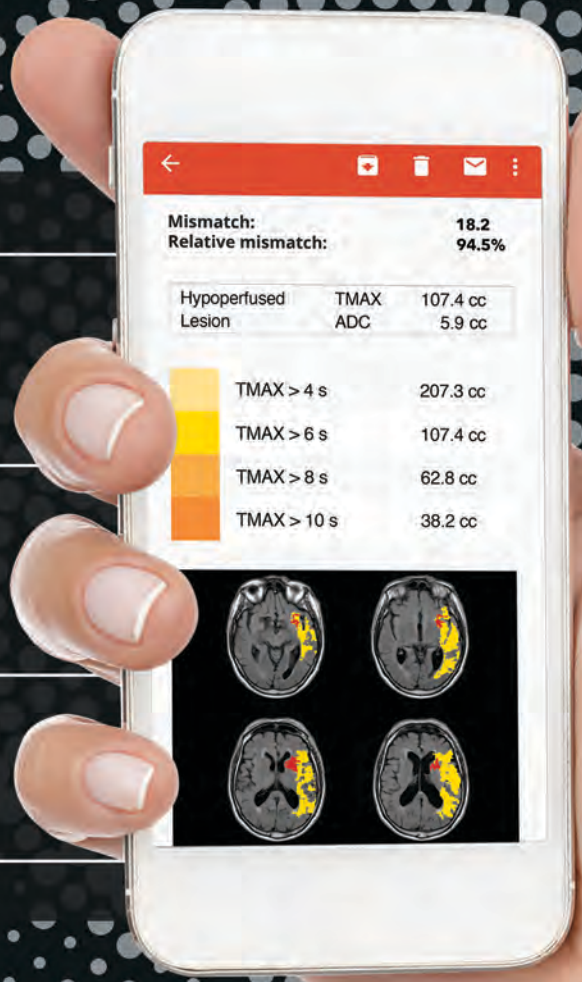

" **Innovation** is in our **DNA.** "

* FDA cleared

Olea MEDICAL

Improved diagnosis for life™

We're Inside Every Great Neuroradiologist!

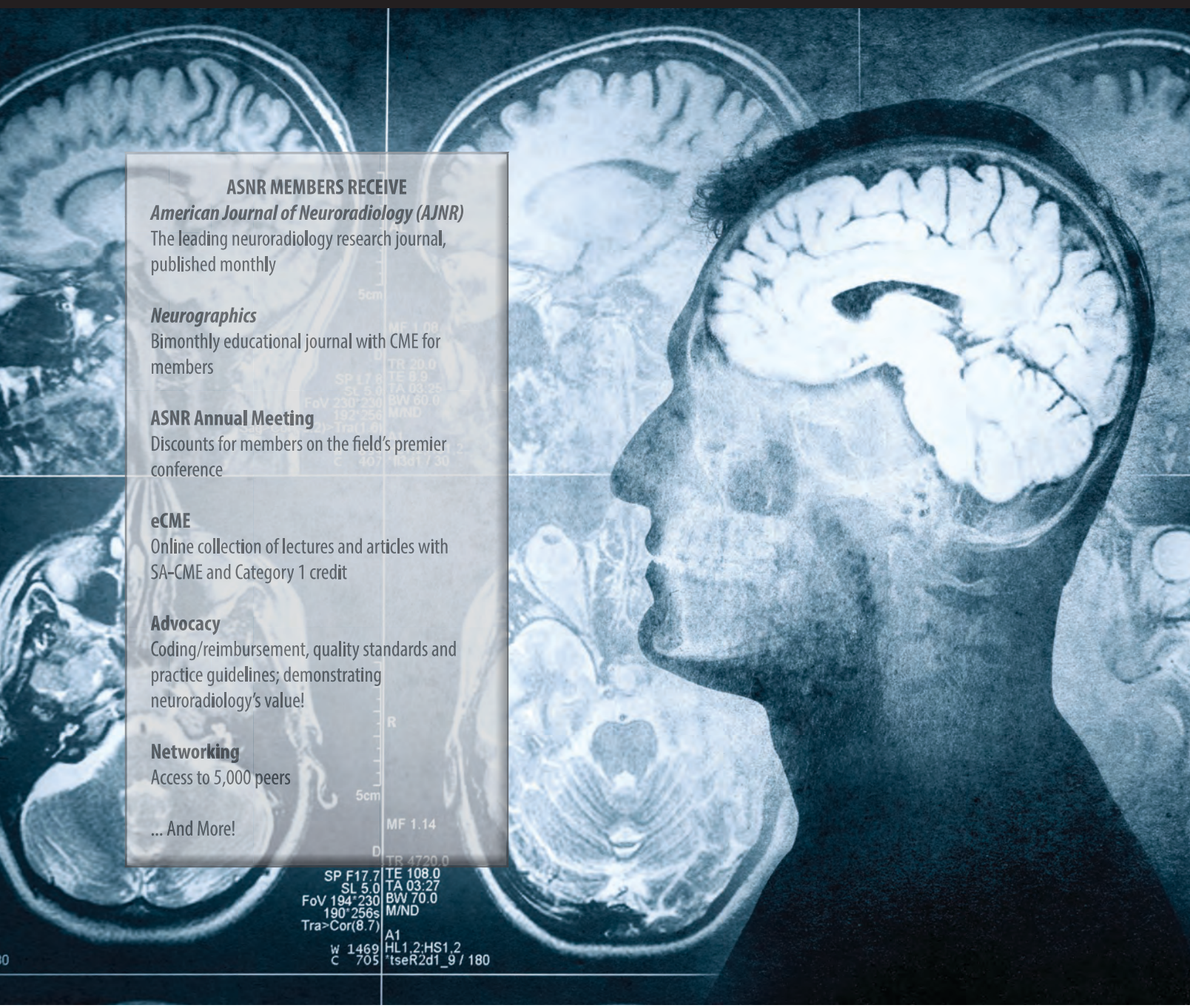

Join the leaders in neuroradiology today!
Learn more at www.asnr.org/join

ASNR
American Society of Neuroradiology

800 Enterprise Dr., Suite 205, Oak Brook, IL 60523 • (630)574-0220 • membership@asnr.org • www.asnr.org

ASHNR
American Society of
Head & Neck Radiology

51st Annual Meeting

American Society of

Head & Neck Radiology

Head and Neck Imaging in the City of Lights

Caesars Palace • Las Vegas, NV

September 16 – 20, 2017
(Saturday - Wednesday)

Please contact Educational Symposia at 813-806-1000 or ASHNR@edusymp.com or visit www.ASHNR.org for additional information.

Strengthen ASNR's representation at the national level.

Your membership in the American Medical Association strengthens ASNR's representation in the AMA House of Delegates—the policymaking body of the AMA that brings forth the views and interests of all physicians to establish national policy on health, medical, professional and governance matters.

Please activate your 2017 AMA membership, visit ama-assn.org or call AMA Member Relations at (800) 262-3211. If you are currently a member, thank you.

AMA member benefits and resources include:

- Unlimited access to **The JAMA Network®** which brings together *JAMA* and all 11 specialty journals with CME.
  jamanetwork.com
- **STEPS Forward™**, the AMA's new practice transformation series designed to help physicians achieve the Quadruple Aim: better patient experience, better population health and lower overall costs with improved professional satisfaction.
  stepsforward.org
- Free 18-month trial of ***DynaMed Plus®***, an evidence-based, clinical support tool that features thousands of images and provides immediate answers to clinical questions.
  offers.jamanetwork.com

AMA AMERICAN MEDICAL ASSOCIATION

ASNR American Society of Neuroradiology

AJNR

Go Green!

AJNR urges American Society of Neuroradiology members to reduce their environmental footprint by voluntarily suspending their print subscription.

The savings in paper, printing, transportation, and postage not only help members cut down on clutter, but go to fund new electronic enhancements and expanded content.

The digital edition of *AJNR* presents the print version in its entirety, along with extra features including:

- Publication Preview
- Case of the Week
- Podcasts
- Special Collections
- The *AJNR* Blog
- Weekly Poll

It also **reaches subscribers much faster than print**. An **electronic table of contents** will be sent directly to your mailbox to notify you as soon as it publishes.

Readers can **search, reference, and bookmark** current and archived content 24 hours a day on www.ajnr.org, rather than thumb through stacks of accumulated paper issues for articles and images they need.

http://www.ajnr.org/cgi/feedback

ASNR members who wish to opt out of print can do so by using the Feedback form on the *AJNR* Website (**http://www.ajnr.org/cgi/feedback**). Just type "Go Green" in the subject line to stop print and spare our ecosystem.

Trevo® XP ProVue Retrievers

See package insert for complete indications, complications, warnings, and instructions for use.

INDICATIONS FOR USE

1. The Trevo Retriever is indicated for use to restore blood flow in the neurovasculature by removing thrombus for the treatment of acute ischemic stroke to reduce disability in patients with a persistent, proximal anterior circulation, large vessel occlusion, and smaller core infarcts who have first received intravenous tissue plasminogen activator (IV t-PA). Endovascular therapy with the device should start within 6 hours of symptom onset.
2. The Trevo Retriever is intended to restore blood flow in the neurovasculature by removing thrombus in patients experiencing ischemic stroke within 8 hours of symptom onset. Patients who are ineligible for intravenous tissue plasminogen activator (IV t-PA) or who fail IV t-PA therapy are candidates for treatment.

COMPLICATIONS

Procedures requiring percutaneous catheter introduction should not be attempted by physicians unfamiliar with possible complications which may occur during or after the procedure. Possible complications include, but are not limited to, the following: air embolism; hematoma or hemorrhage at puncture site; infection; distal embolization; pain/headache; vessel spasm, thrombosis, dissection, or perforation; emboli; acute occlusion; ischemia; intracranial hemorrhage; false aneurysm formation; neurological deficits including stroke; and death.

COMPATIBILITY

3x20mm retrievers are compatible with Trevo® Pro 14 Microcatheters (REF 90231) and Trevo® Pro 18 Microcatheters (REF 90238). 4x20mm retrievers are compatible with Trevo® Pro 18 Microcatheters (REF 90238). 4x30mm retrievers are compatible with Excelsior® XT-27® Microcatheters (150cm x 6cm straight REF 275081) and Trevo® Pro 18 Microcatheters (REF 90238). 6x25mm Retrievers are compatible with Excelsior® XT-27® Microcatheters (150cm x 6cm straight REF 275081). Compatibility of the Retriever with other microcatheters has not been established. Performance of the Retriever device may be impacted if a different microcatheter is used.

Balloon Guide Catheters (such as Merci® Balloon Guide Catheter and FlowGate® Balloon Guide Catheter) are recommended for use during thrombus removal procedures.

Retrievers are compatible with the Abbott Vascular DOC® Guide Wire Extension (REF 22260).

Retrievers are compatible with Boston Scientific RHV (Ref 421242).

SPECIFIC WARNINGS FOR INDICATION 1

- The safety and effectiveness of the Trevo Retrievers in reducing disability has not been established in patients with large core infarcts (i.e., ASPECTS ≤ 7). There may be increased risks, such as intracerebral hemorrhage, in these patients.
- The safety and effectiveness of the Trevo Retrievers in reducing disability has not been established or evaluated in patients with occlusions in the posterior circulation (e.g., basilar or vertebral arteries) or for more distal occlusions in the anterior circulation.

WARNINGS APPLIED TO BOTH INDICATIONS

- Administration of IV t-PA should be within the FDA-approved window (within 3 hours of stroke symptom onset).
- Contents supplied STERILE, using an ethylene oxide (EO) process. Nonpyrogenic.
- To reduce risk of vessel damage, adhere to the following recommendations:
  - Take care to appropriately size Retriever to vessel diameter at intended site of deployment.
  - Do not perform more than six (6) retrieval attempts in same vessel using Retriever devices.
  - Maintain Retriever position in vessel when removing or exchanging Microcatheter.
- To reduce risk of kinking/fracture, adhere to the following recommendations:
  - Immediately after unsheathing Retriever, position Microcatheter tip marker just proximal to shaped section. Maintain Microcatheter tip marker just proximal to shaped section of Retriever during manipulation and withdrawal.
  - Do not rotate or torque Retriever.
  - Use caution when passing Retriever through stented arteries.
- Do not resterilize and reuse. Structural integrity and/or function may be impaired by reuse or cleaning.
- The Retriever is a delicate instrument and should be handled carefully. Before use and when possible during procedure, inspect device carefully for damage. Do not use a device that shows signs of damage. Damage may prevent device from functioning and may cause complications.
- Do not advance or withdraw Retriever against resistance or significant vasospasm. Moving or torquing device against resistance or significant vasospasm may result in damage to vessel or device. Assess cause of resistance using fluoroscopy and if needed resheath the device to withdraw.
- If Retriever is difficult to withdraw from the vessel, do not torque Retriever. Advance Microcatheter distally, gently pull Retriever back into Microcatheter, and remove Retriever and Microcatheter as a unit. If undue resistance is met when withdrawing the Retriever into the Microcatheter, consider extending the Retriever using the Abbott Vascular DOC guidewire extension (REF 22260) so that the Microcatheter can be exchanged for a larger diameter catheter such as a DAC® catheter. Gently withdraw the Retriever into the larger diameter catheter.
- Administer anti-coagulation and anti-platelet medications per standard institutional guidelines.

PRECAUTIONS

- Prescription only – device restricted to use by or on order of a physician.
- Store in cool, dry, dark place.
- Do not use open or damaged packages.
- Use by "Use By" date.
- Exposure to temperatures above 54°C (130°F) may damage device and accessories. Do not autoclave.
- Do not expose Retriever to solvents.
- Use Retriever in conjunction with fluoroscopic visualization and proper anti-coagulation agents.
- To prevent thrombus formation and contrast media crystal formation, maintain a constant infusion of appropriate flush solution between guide catheter and Microcatheter and between Microcatheter and Retriever or guidewire.
- Do not attach a torque device to the shaped proximal end of DOC® Compatible Retriever. Damage may occur, preventing ability to attach DOC® Guide Wire Extension.

Concentric Medical
301 East Evelyn Avenue
Mountain View, CA 94041

Stryker Neurovascular
47900 Bayside Parkway
Fremont, CA 94538

strykerneurovascular.com

Date of Release: SEP/2016

EX_EN_US

NV00018973.AB

Target® Detachable Coil

See package insert for complete indications, contraindications, warnings and instructions for use.

INTENDED USE / INDICATIONS FOR USE

Target Detachable Coils are intended to endovascularly obstruct or occlude blood flow in vascular abnormalities of the neurovascular and peripheral vessels.

Target Detachable Coils are indicated for endovascular embolization of:

- Intracranial aneurysms
- Other neurovascular abnormalities such as arteriovenous malformations and arteriovenous fistulae
- Arterial and venous embolizations in the peripheral vasculature

CONTRAINDICATIONS

None known.

POTENTIAL ADVERSE EVENTS

Potential complications include, but are not limited to: allergic reaction, aneurysm perforation and rupture, arrhythmia, death, edema, embolus, headache, hemorrhage, infection, ischemia, neurological/intracranial sequelae, post-embolization syndrome (fever, increased white blood cell count, discomfort), TIA/stroke, vasospasm, vessel occlusion or closure, vessel perforation, dissection, trauma or damage, vessel rupture, vessel thrombosis. Other procedural complications including but not limited to: anesthetic and contrast media risks, hypotension, hypertension, access site complications.

WARNINGS

- Contents supplied STERILE using an ethylene oxide (EO) process. Do not use if sterile barrier is damaged. If damage is found, call your Stryker Neurovascular representative.
- For single use only. Do not reuse, reprocess or resterilize. Reuse, reprocessing or resterilization may compromise the structural integrity of the device and/or lead to device failure which, in turn, may result in patient injury, illness or death. Reuse, reprocessing or resterilization may also create a risk of contamination of the device and/or cause patient infection or cross-infection, including, but not limited to, the transmission of infectious disease(s) from one patient to another. Contamination of the device may lead to injury, illness or death of the patient.
- After use, dispose of product and packaging in accordance with hospital, administrative and/or local government policy.
- **This device should only be used by physicians who have received appropriate training in interventional neuroradiology or interventional radiology and preclinical training on the use of this device as established by Stryker Neurovascular.**
- Patients with hypersensitivity to 316LVM stainless steel may suffer an allergic reaction to this implant.
- MR temperature testing was not conducted in peripheral vasculature, arteriovenous malformations or fistulae models.
- The safety and performance characteristics of the Target Detachable Coil System (Target Detachable Coils, InZone Detachment Systems, delivery systems and accessories) have not been demonstrated with other manufacturer's devices (whether coils, coil delivery devices, coil detachment systems, catheters, guidewires, and/or other accessories). Due to the potential incompatibility of non Stryker Neurovascular devices with the Target Detachable Coil System, the use of other manufacturer's device(s) with the Target Detachable Coil System is not recommended.
- To reduce risk of coil migration, the diameter of the first and second coil should never be less than the width of the ostium.
- In order to achieve optimal performance of the Target Detachable Coil System and to reduce the risk of thromboembolic complications, it is critical that a continuous infusion of appropriate flush solution be maintained between a) the femoral sheath and guiding catheter, b) the 2-tip microcatheter and guiding catheters, and c) the 2-tip microcatheter and Stryker Neurovascular guidewire and delivery wire. Continuous flush also reduces the potential for thrombus formation on, and crystallization of infusate around, the detachment zone of the Target Detachable Coil.
- Do not use the product after the "Use By" date specified on the package.
- Reuse of the flush port/dispenser coil or use with any coil other than the original coil may result in contamination of, or damage to, the coil.
- Utilization of damaged coils may affect coil delivery to, and stability inside, the vessel or aneurysm, possibly resulting in coil migration and/or stretching.
- The fluoro-saver marker is designed for use with a Rotating Hemostatic Valve (RHV). If used without an RHV, the distal end of the coil may be beyond the alignment marker when the fluoro-saver marker reaches the microcatheter hub.
- If the fluoro-saver marker is not visible, do not advance the coil without fluoroscopy.
- Do not rotate delivery wire during or after delivery of the coil. Rotating the Target Detachable Coil delivery wire may result in a stretched coil or premature detachment of the coil from the delivery wire, which could result in coil migration.
- Verify there is no coil loop protrusion into the parent vessel after coil placement and prior to coil detachment. Coil loop protrusion after coil placement may result in thromboembolic events if the coil is detached.
- Verify there is no movement of the coil after coil placement and prior to coil detachment. Movement of the coil after coil placement may indicate that the coil could migrate once it is detached.
- Failure to properly close the RHV compression fitting over the delivery wire before attaching the InZone® Detachment System could result in coil movement, aneurysm rupture or vessel perforation.
- Verify repeatedly that the distal shaft of the catheter is not under stress before detaching the Target Detachable Coil. Axial compression or tension forces could be stored in the 2-tip microcatheter causing the tip to move during coil delivery. Microcatheter tip movement could cause the aneurysm or vessel to rupture.
- Advancing the delivery wire beyond the microcatheter tip once the coil has been detached involves risk of aneurysm or vessel perforation.
- The long term effect of this product on extravascular tissues has not been established so care should be taken to retain this device in the intravascular space.

Damaged delivery wires may cause detachment failures, vessel injury or unpredictable distal tip response during coil deployment. If a delivery wire is damaged at any point during the procedure, do not attempt to straighten or otherwise repair it. Do not proceed with deployment or detachment. Remove the entire coil and replace with undamaged product.

- After use, dispose of product and packaging in accordance with hospital, administrative and/or local government policy.

CAUTIONS / PRECAUTIONS

- Federal Law (USA) restricts this device to sale by or on the order of a physician.
- Besides the number of InZone Detachment System units needed to complete the case, there must be an extra InZone Detachment System unit as back up.
- Removing the delivery wire without grasping the introducer sheath and delivery wire together may result in the detachable coil sliding out of the introducer sheath.
- Failure to remove the introducer sheath after inserting the delivery wire into the RHV of the microcatheter will interrupt normal infusion of flush solution and allow back flow of blood into the microcatheter.
- Some low level overhead light near or adjacent to the patient is required to visualize the fluoro-saver marker; monitor light alone will not allow sufficient visualization of the fluoro-saver marker.
- Advance and retract the Target Detachable Coil carefully and smoothly without excessive force. If unusual friction is noticed, slowly withdraw the Target Detachable Coil and examine for damage. If damage is present, remove and use a new Target Detachable Coil. If friction or resistance is still noted, carefully remove the Target Detachable Coil and microcatheter and examine the microcatheter for damage.
- If it is necessary to reposition the Target Detachable Coil, verify under fluoroscopy that the coil moves with a one-to-one motion. If the coil does not move with a one-to-one motion or movement is difficult, the coil may have stretched and could possibly migrate or break. Gently remove both the coil and microcatheter and replace with new devices.
- Increased detachment times may occur when:
  - Other embolic agents are present.
  - Delivery wire and microcatheter markers are not properly aligned.
  - Thrombus is present on the coil detachment zone.
- Do not use detachment systems other than the InZone Detachment System.
- Increased detachment times may occur when delivery wire and microcatheter markers are not properly aligned.
- Do not use detachment systems other than the InZone Detachment System.

Stryker Neurovascular
47900 Bayside Parkway
Fremont, CA 94538

strykerneurovascular.com

Date of Release: MAR/2016

EX_EN_US

NV00018669.AB

stryker®
Neurovascular

Purposeful innovation in mind.

Smooth and stable.

Target Detachable Coils deliver consistently smooth deployment and exceptional microcatheter stability. Designed to work seamlessly together for framing, filling and finishing. Target Coils deliver the high performance you demand.

For more information, please visit www.strykerneurovascular.com/Target or contact your local Stryker Neurovascular sales representative.

Target®
DETACHABLE COILS

NV00018669.AA

acandis®

ENGINEERING STROKE SOLUTIONS

FLEXIBLE ANEURYSM TREATMENT

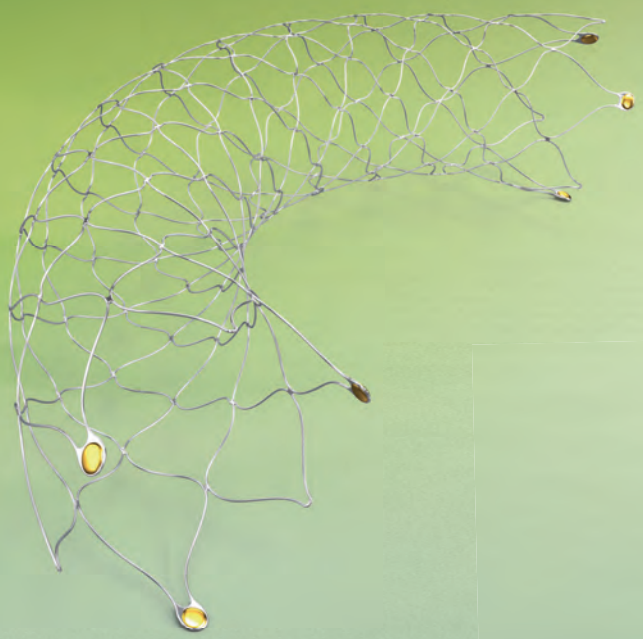

ACCLINO® flex Stent

- For microcatheters with 0.017" ID (Ø 3.5 and 4.5 mm) and 0.021" ID (Ø 6.5 mm)
- Repositionable up to 90 %

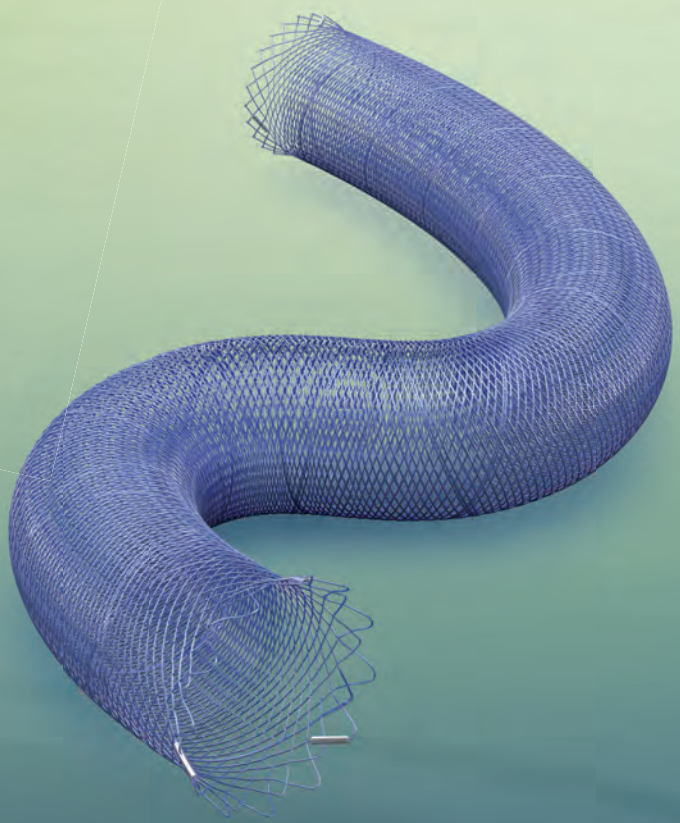

DERIVO® Embolisation Device

- Unique x-ray visibility
- BlueXide® surface
- Repositionable up to 70 – 90 %

AJNR

AMERICAN JOURNAL OF NEURORADIOLOGY

MARCH 2017
VOLUME 38
NUMBER 3
WWW.AJNR.ORG

THE JOURNAL OF DIAGNOSTIC AND INTERVENTIONAL NEURORADIOLOGY

Hydrogel vs bare platinum coils in recurrent aneurysms
MRI-guided focused ultrasound for intracranial applications
Transverse sinus stenosis in idiopathic intracranial hypotension

Official Journal ASNR • ASFNR • ASHNR • ASPNR • ASSR

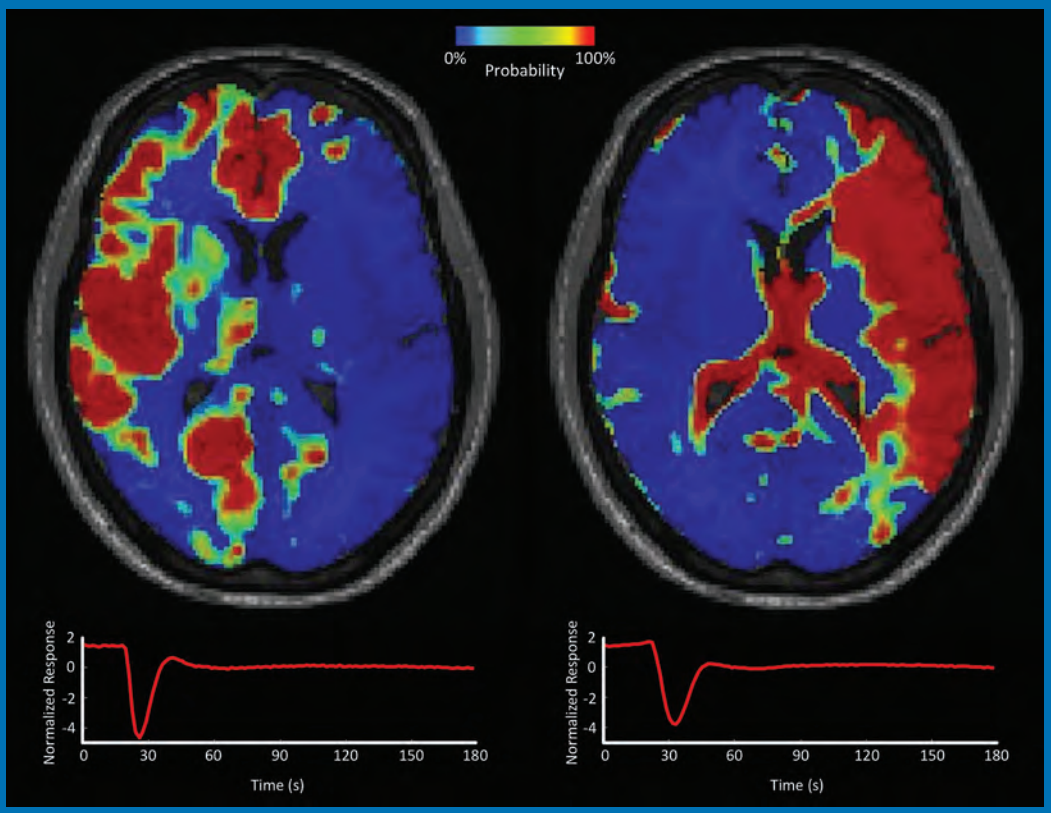

AJNR

AMERICAN JOURNAL OF NEURORADIOLOGY

MARCH 2017
VOLUME 38
NUMBER 3
WWW.AJNR.ORG

Publication Preview at www.ajnr.org features articles released in advance of print. Visit www.ajnrblog.org to comment on AJNR content and chat with colleagues and AJNR's News Digest at http://ajnrdigest.org to read the stories behind the latest research in neuroimaging.

AJNR (Am J Neuroradiol ISSN 0195–6108) is a journal published monthly, owned and published by the American Society of Neuroradiology (ASNR), 800 Enterprise Drive, Suite 205, Oak Brook, IL 60523. Annual dues for the ASNR include $170.00 for journal subscription. The journal is printed by Cadmus Journal Services, 5457 Twin Knolls Road, Suite 200, Columbia, MD 21045; Periodicals postage paid at Oak Brook, IL and additional mailing offices. Printed in the U.S.A. POSTMASTER: Please send address changes to American Journal of Neuroradiology, P.O. Box 3000, Denville, NJ 07834, U.S.A. Subscription rates: nonmember $390 ($460 foreign) print and online, $310 online only; institutions $450 ($520 foreign) print and basic online, $895 ($960 foreign) print and extended online, $370 online only (basic), extended online $805; single copies are $35 each ($40 foreign). Indexed by PubMed/Medline, BIOSIS Previews, Current Contents (Clinical Medicine and Life Sciences), EMBASE, Google Scholar, HighWire Press, Q-Sensei, RefSeek, Science Citation Index, and SCI Expanded.

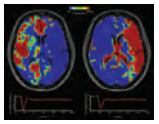

Presurgical DSC-MR probabilistic independent component analysis imaging (arterial, left; venous, right) of a patient undergoing EDAS. The respective time courses show delayed response in the venous component with a high probability for the venous component in the symptomatic left hemispheric cortex.

Indicates Editor's Choices selection

Indicates Fellows' Journal Club selection

Indicates open access to non-subscribers at www.ajnr.org

Indicates article with supplemental on-line table

Indicates article with supplemental on-line photo

Indicates article with supplemental on-line video

Evidence-Based Medicine Level 1

Evidence-Based Medicine Level 2

AJNR

AMERICAN JOURNAL OF NEURORADIOLOGY

Publication Preview at www.ajnr.org features articles released in advance of print. Visit www.ajnrblog.org to comment on AJNR content and chat with colleagues and AJNR's News Digest at http://ajnrdigest.org to read the stories behind the latest research in neuroimaging.

MARCH 2017 • VOLUME 38 • NUMBER 3 • WWW.AJNR.ORG

Official Journal:
American Society of Neuroradiology
American Society of Functional Neuroradiology
American Society of Head and Neck Radiology
American Society of Pediatric Neuroradiology
American Society of Spine Radiology

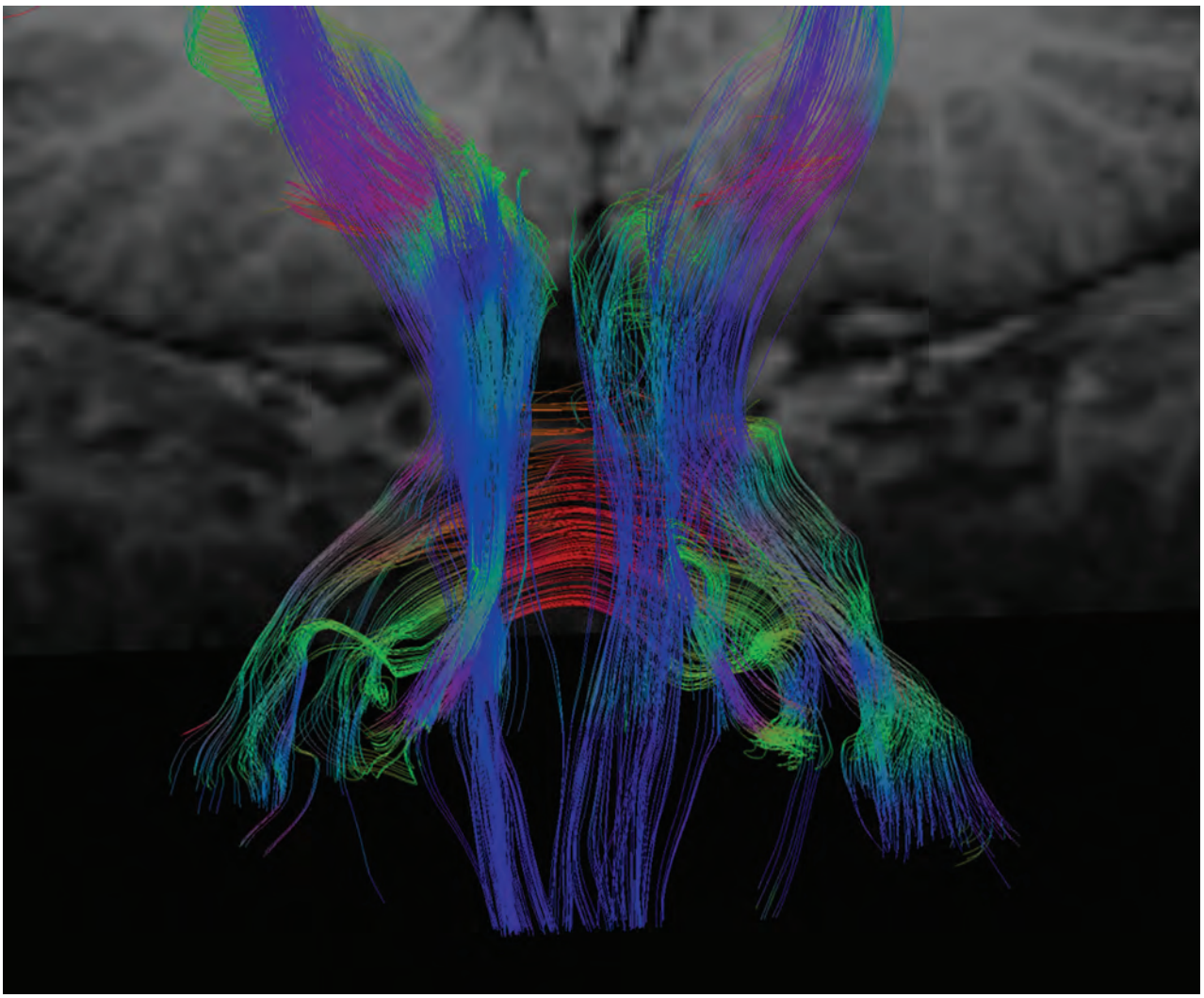

Title: The Brain Jellyfish. The brain is one of the most mysterious creatures that you'll ever encounter. 3D projection of brain stem tractography with 20 noncollinear diffusion-encoding directions shows the streamlines running longitudinally in the pontine tracts and some continuing into the middle cerebellar peduncles.

Saiz Ayala, Chief of Section of Neuroradiology, Asturias, Central University Hospital of Asturias, Oviedo, Asturias, Spain

The Need for Better Data on Patients with Acute Stroke Who Are Not Treated Because of Unfavorable Imaging

M. Goyal, B.K. Menon, M.A. Almekhlafi, A. Demchuk, and M.D. Hill

There are 2 "epochs" of time in acute ischemic stroke caused by large vessel occlusion: onset to imaging time, which is deterministic of the likelihood of favorable imaging (mild to moderate early ischemic changes [ASPECTS 6–10]), and imaging to reperfusion time, which is deterministic of the likelihood of a favorable outcome.[1] But what factors influence whether a particular patient with an acute stroke caused by large vessel occlusion will have favorable imaging? What is the rate at which the brain dies after stroke onset? What factors influence the velocity of irreversible infarction?

Ten minutes after stroke onset caused by large vessel occlusion, all patients will have a small core and sizeable penumbra. At the other extreme, in nearly all patients at 24 hours after stroke onset, the infarct will have expanded to its maximum volume and there is no penumbra. The decay curve for growth of infarct (expansion of core, reduction of penumbra) for an individual patient begins at 100% salvageable brain (zero core) at onset and follows a variable downward curve to reach 0% salvageable brain at a certain point (Figure).[2,3]

Some patients are likely "fast progressors" (with favorable imaging only very early) and others are "slow progressors" (with favorable imaging even at late time windows). The biologic infarct growth curve could also be linear, parabolic (steep initially and flattening out as time progresses), or even sigmoid shaped (slow infarct growth initially that increases as time progresses, then flattens out at later time points).[3,4] Recent analyses of workflow time relationships for both intravenous tPA and endovascular treatment attest to the variable nature of the infarct growth outcome relationships.[4-8] In particular, in a recent meta-analysis of all the endovascular trials, a nonlinear statistical exploration of the time-versus-outcome relationship showed a shallow slope very early, with a steep fall in good outcome rate from 190–390 minutes after stroke onset and a gradual decline later (see Fig 5 in Saver et al[4]). The nature of this time-versus-outcome relationship may likely be very different if patients with large infarcts at baseline (fast progressors) or those with minimal clinical deficits (very slow progressors) who were likely excluded from the recent intra-arterial therapy trials that were included in this analysis. Although "time is brain" is an established construct, we currently have very limited data on the time-versus-outcome relationship in all comers and how this relationship may be different in different groups of patients.

We also have little quality data on why some patients are fast progressors and some are slow progressors. All the recent trials (overtly or inadvertently) used imaging or clinical parameters that resulted in the inclusion of patients with a small core independent of time from onset.[9] So, by definition, nearly all patients in the later time windows had to be slow progressors. Fast progressors were excluded from these trials. A strong candidate as a pathophysiologic variable to explain the differences between slow and fast progressors is the status of leptomeningeal collaterals. The better the collaterals, the slower the progression of infarct. So what influences the presence of good collaterals, and what do we understand about it? It is likely that collaterals are influenced by genetic factors and coexisting conditions such as diabetes and hypertension. A second candidate variable is tissue susceptibility, which, to date, is impossible to measure in isolation and is poorly defined and understood. Another variable that likely comes into play in patient selection is tissue eloquence (nearly all patients who were enrolled in the recent trials had clinically major stroke symptoms; hence, it is possible that there are patients who have sizeable noneloquent tissue at risk, but were not included in the trials because of clinically mild symptoms).

Animal data suggest that there are significant genetic influences on the robustness of collaterals.[10] Other risk factors associated with poor collaterals include aging, hypertension, diabetes, or the presence of metabolic syndrome and hyperuricemia.[11] The use of statins and angiotensin converting–enzyme inhibitors may be associated with good collaterals.[12] Furthermore, the immediate physiology of collaterals may be acutely influenced by systemic blood pressure, locoregional factors such as carotid artery stenosis, or the degree of vessel occlusion caused by a large bore catheter and other modifiable factors.

Tissue susceptibility may be modifiable. Multiple compounds have been shown to be cytoprotective in ischemia-reperfusion models in rodents and other preclinical models. None have been proved in human stroke. Variables that are explanatory for tissue susceptibility include age and sex, premorbid brain health (perhaps measured crudely by functional status), comorbid conditions (such as diabetes mellitus, congestive heart failure, and cancer). Among these patients, the impact of a moderate stroke may be much worse. Both novel and well-known compounds such as NA-1,[13] minocycline,[14] and uric acid[15] may change tissue susceptibility, perhaps to a varying degree depending upon the patient.

So where do we go from here? The shape of the infarct growth curve is unknown. Variable rates of infarct growth likely exist because of variability in robustness of collaterals and tissue susceptibility to ischemia. We have limited understanding of the factors that influence these variables. Data to understand this issue in humans are limited by sampling biases stemming from current patient selection strategies in available studies. As a first step, we need better databases comprising *all* patients with acute ischemic stroke caused by large vessel occlusion. Such prospective databases should capture clinical information that includes time of onset, age, comorbidities, and information regarding vital signs (eg, "the patient was not hypotensive"). Imaging data should include modalities that assess the presence of a sizable penumbra indirectly "collateral information" or directly "perfusion imaging." Finally, laboratory investigations should be added for conditions that are known to impact the penumbra/collateral status, such as blood glucose, uric acid, or metabolic

http://dx.doi.org/10.3174/ajnr.A5094

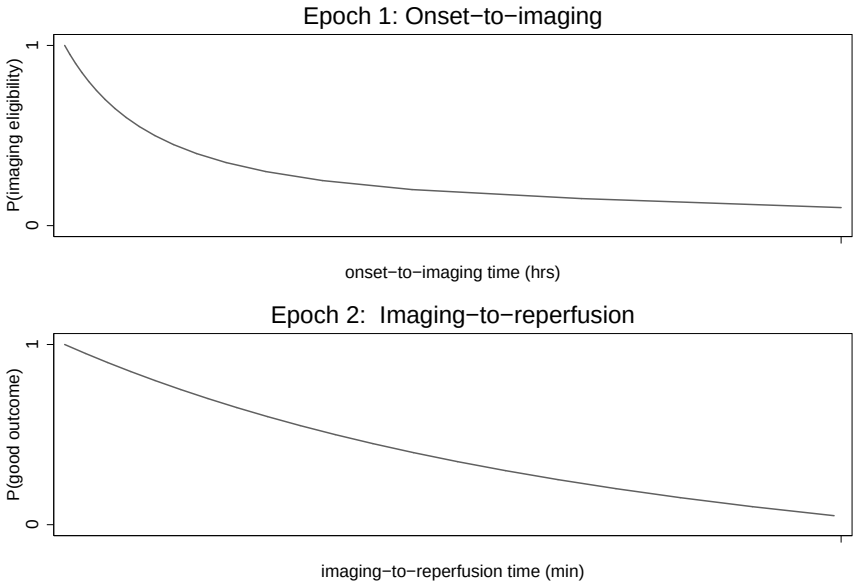

FIGURE. Interval times in acute stroke (modified from Hill et al[17]). With increasing data, we have a good understanding of the second curve (imaging to reperfusion). However, our understanding of the first curve remains limited because of a paucity of appropriate data.

syndrome work-up. Clinical follow-up and outcome data irrespective of how patients were treated are essential. Such data bases could be an expansion of existing stroke registries (eg, Austrian Stroke Unit Registry Collaboration[16]) or previous randomized trials that captured data on the patients who were screened for eligibility, but excluded because of unfavorable imaging. These will help advance our understanding of which factors are associated with the fast progressor state and, hopefully, could be modified to improve the stroke outcome of these patients.

Disclosures: Mayank Goyal—*UNRELATED: Research Grants*: Medtronic, *Comments*: partial funding of ESCAPE trial*; *Consultancy*: Medtronic, Stryker, Microvention, *Comments*: teaching and advice on acute stroke techniques and devices; *Grants/Grants Pending*: Medtronic, *Comments*: HERMES collaboration*; *Patents (Planned, Pending, or Issued)*: GE Healthcare, *Comments*: licensing agreement for development of systems of stroke diagnosis. Andrew Demchuk—*UNRELATED: Payment for Lectures (Including Service on Speakers Bureaus)*: Medtronic. Michael Hill—*UNRELATED*: *Board Membership*: Canadian Neuroscience Federation, *Comments*: not-for-profit board; *Consultancy*: Merck, *Comments*: adjudication panel for clinical trials outcomes panel (paid work); *Grants/Grants Pending*: Boehringer Ingelheim, Medtronic, *Comments*: grant to the University of Calgary for the TEMPO-two trial (Boehringer Ingelheim) and for the ESCAPE trial and the HERMES collaboration (Medtronic)*; *Stock/Stock Options*: Calgary Scientific Inc, *Comments*: private company stock ownership. *Money paid to the institution.

REFERENCES

1. Menon BK, Campbell BC, Levi C, et al. **Role of imaging in current acute ischemic stroke workflow for endovascular therapy.** *Stroke* 2015;46:1453–61 CrossRef Medline
2. Olivot JM, Mlynash M, Thijs VN, et al. **Relationships between cerebral perfusion and reversibility of acute diffusion lesions in DEFUSE: insights from RADAR.** *Stroke* 2009;40:1692–97 CrossRef Medline
3. Menon BK, Sajobi TT, Zhang Y, et al. **Analysis of workflow and time to treatment on thrombectomy outcome in the ESCAPE randomized controlled trial.** *Circulation* 2016:CIRCULATIONAHA. 115.019983
4. Saver JL, Goyal M, van der Lugt A, et al. **Time to treatment with endovascular thrombectomy and outcomes from ischemic stroke: a meta-analysis.** *JAMA* 2016;316:1279–88 CrossRef Medline
5. Goyal M, Almekhlafi MA, Fan L, et al. **Evaluation of interval times from onset to reperfusion in patients undergoing endovascular therapy in the Interventional Management of Stroke III trial.** *Circulation* 2014;130:265–72 CrossRef Medline
6. Khatri P, Abruzzo T, Yeatts SD, et al. **Good clinical outcome after ischemic stroke with successful revascularization is time-dependent.** *Neurology* 2009;73:1066–72 CrossRef Medline
7. Menon BK, Almekhlafi MA, Pereira VM, et al. **Optimal workflow and process-based performance measures for endovascular therapy in acute ischemic stroke: analysis of the Solitaire FR thrombectomy for acute revascularization study.** *Stroke* 2014;45:2024–29 CrossRef Medline
8. Saver JL, Fonarow GC, Smith EE, et al. **Time to treatment with intravenous tissue plasminogen activator and outcome from acute ischemic stroke.** *JAMA* 2013;309:2480–88 CrossRef Medline
9. Goyal M, Menon BK, van Zwam WH, et al. **Endovascular thrombectomy after large-vessel ischaemic stroke: a meta-analysis of individual patient data from five randomised trials.** *Lancet* 2016;387:1723–31 CrossRef Medline
10. Zhang H, Prabhakar P, Sealock R, et al. **Wide genetic variation in the native pial collateral circulation is a major determinant of variation in severity of stroke.** *J Cereb Blood Flow Metab* 2010;30:923–34 CrossRef Medline
11. Menon BK, Smith EE, Coutts SB, et al. **Leptomeningeal collaterals are associated with modifiable metabolic risk factors.** *Ann Neurol* 2013;74:241–48 CrossRef Medline
12. Sargento-Freitas J, Pagola J, Rubiera M, et al. **Preferential effect of premorbid statins on atherothrombotic strokes through collateral circulation enhancement.** *Eur Neurol* 2012;68:171–76 CrossRef Medline
13. Hill MD, Martin RH, Mikulis D, et al. **Safety and efficacy of NA-1 in patients with iatrogenic stroke after endovascular aneurysm repair (ENACT): a phase 2, randomised, double-blind, placebo-controlled trial.** *Lancet Neurol* 2012;11:942–50 CrossRef Medline
14. Liu Z, Fan Y, Won SJ, et al. **Chronic treatment with minocycline preserves adult new neurons and reduces functional impairment after focal cerebral ischemia.** *Stroke* 2007;38:146–52 CrossRef Medline
15. Waring W. **Uric acid: an important antioxidant in acute ischaemic stroke.** *QJM* 2002;95:691–93 CrossRef Medline
16. Serles W, Gattringer T, Mutzenbach S, et al. **Endovascular stroke therapy in Austria: a nationwide 1-year experience.** *Eur J Neurol* 2016;23:906–11 CrossRef Medline
17. Hill MD, Goyal M, Demchuk AM, et al. **Ischemic stroke tissue-window in the new era of endovascular treatment.** *Stroke* 2015;46:2332–34 CrossRef Medline

Intracranial Applications of MR Imaging–Guided Focused Ultrasound

N. Khanna, D. Gandhi, A. Steven, V. Frenkel, and E.R. Melhem

ABSTRACT

SUMMARY: Initially used in the treatment of prostate cancer and uterine fibroids, the role of focused ultrasound has expanded as transcranial acoustic wave distortion and other limitations have been overcome. Its utility relies on focal energy deposition via acoustic wave propagation. The duty cycle and intensity of focused ultrasound influence the rate of energy deposition and result in unique physiologic and biomechanical effects. Thermal ablation via high-intensity continuous exposure generates coagulative necrosis of tissues. High-intensity, pulsed application reduces temporally averaged energy deposition, resulting in mechanical effects, including reversible, localized BBB disruption, which enhances neurotherapeutic agent delivery. While the precise mechanisms remain unclear, low-intensity, pulsed exposures can influence neuronal activity with preservation of cytoarchitecture. Its noninvasive nature, high-resolution, radiation-free features allow focused ultrasound to compare favorably with other modalities. We discuss the physical characteristics of focused ultrasound devices, the biophysical mechanisms at the tissue level, and current and emerging applications.

ABBREVIATIONS: FUS = focused ultrasound; MRgFUS = MR imaging–guided focused ultrasound; TMZ = temozolomide

The use of therapeutic ultrasound predates its role in diagnostic imaging. Early applications of therapeutic ultrasound were primarily in physical therapy for the treatment of musculoskeletal injuries, albeit in a low-energy, nonfocused manner.[1] More recently, higher energy focused ultrasound (FUS) has demonstrated enormous therapeutic and research potential via newly discovered, unique bioeffects. Therapeutic FUS relies on acoustic wave propagation directed at a specific focus, generating high-resolution focal energy deposition while sparing intervening and adjacent tissues. Acoustic waves can be generated by single-element transducers. Newer generation devices offer multielement phased array transducers, allowing electronic steering of the focal zone.[2]

Experimentation with neurologic FUS applications began in earnest more than 60 years ago with partial ablation of the basal ganglia in cats and monkeys in 1955 by Fry et al[3] and intracranial tumor therapy in humans performed by Heimburger[4] 3 decades later. Initially, impedance mismatch and nonuniformity at the soft-tissue-calvarial interface necessitated surgical craniotomy for intracranial FUS application. Once reliable transcranial propagation was achieved, the morbidity associated with craniotomy was no longer an obstacle in neurologic FUS application and the technique gained more widespread acceptance as a viable noninvasive alternative to current therapeutic options. Clinical and preclinical investigations into potential applications of the controlled deposition of mechanical energy, in the form of ultrasound, have since accelerated and yielded a variety of bioeffects based on the level of energy deposition. At high levels of deposition, tissue heating generates irreversible necrosis of the target area. As the temporally averaged rate of energy deposition is decreased, via decreasing the ultrasound intensity and duty cycle (ie, ratio of ON and OFF), mechanical effects can increase the permeability of the blood-brain barrier and influence neuronal activity, via both reversible suppression and stimulation.

Advances in Transcranial FUS

In 2002, the biggest obstacle in the translation of FUS to neurologic applications was overcome when Clement and Hynynen[5] achieved reproducible, high-resolution focal energy deposition via transcranial acoustic wave propagation, obviating craniotomy. This is accomplished via registration of data from CT interrogation of the calvaria, specifically to assess its attenuation, contour, and thickness. These data are registered with MR images and serve as input to the MR imaging–guided FUS (MRgFUS) appa-

From the Department of Diagnostic Radiology and Nuclear Medicine (N.K., D.G., A.S., V.F., E.R.M.) and Greenebaum Cancer Center (V.F.), University of Maryland School of Medicine, Baltimore, Maryland.

Paper previously presented in part at the Annual Meeting of the American Society of Neuroradiology and the Foundation of the ASNR Symposium, April 25–30, 2015; Chicago, Illinois.

Please address correspondence to Victor Frenkel, PhD, Department of Diagnostic Radiology and Nuclear Medicine, University of Maryland School of Medicine, Health Science Facility, 618A, Baltimore, MD 21201; e-mail: vfrenkel@som.umaryland.edu

http://dx.doi.org/10.3174/ajnr.A4902

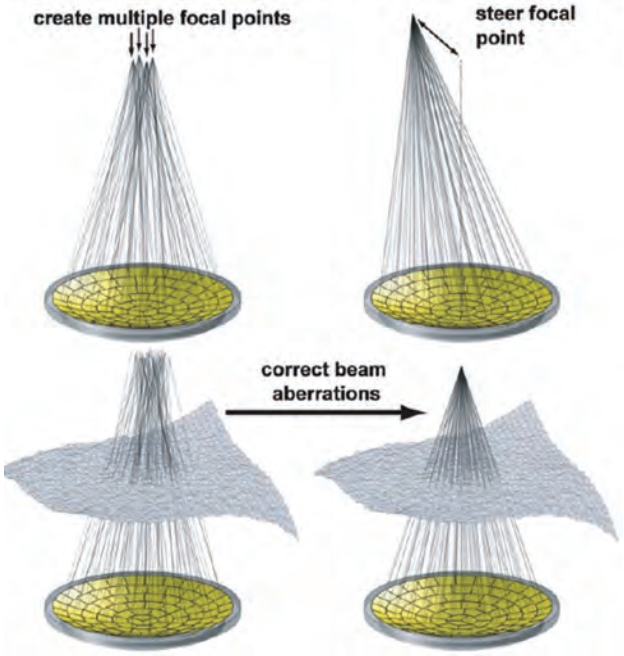

FIG 1. With a multielement, hemispheric phased array transducer, a single focus can be electronically steered (*upper right*), multiple focal points can be generated (*upper left*), and corrections can be achieved for aberrations in the beam path. Reprinted with permission from Tempany et al.[37]

ratus, which can individually steer up to 1024 ultrasound elements to compensate for predicted acoustic wave distortions at the soft-tissue–calvarial interface. Focused transcranial acoustic wave propagation can then be achieved with a resolution of approximately 1 mm.[5] The phased array transducer also offers the versatility of creating numerous focal points and hence treating larger volumes. This is currently being evaluated for generating regional hyperthermia, which may enhance the efficacy of chemotherapy and radiation therapy (Fig 1).[6]

Developments in real-time image guidance and monitoring have expanded the scope of FUS therapies, namely the integration of MR imaging–guided therapeutic systems. Early image guidance of FUS relied entirely on diagnostic ultrasound images for treatment planning and monitoring tissue-level effects, such as in the treatment of prostate cancer.[7] Current MR imaging–guided therapeutic systems offer superior soft-tissue detail, allowing preservation of nontarget tissues and accurate identification of tumor margins and other potential ROIs. Temperature maps via noninvasive, near-real-time MR thermometry enable validation of effective treatment for thermal therapies (ie, ablation, hyperthermia) and determination whether the nontargeted tissue in adjacent regions has been spared.

The versatility of the MRgFUS apparatus is a product of its ability to manipulate the volume and degree of energy deposition. The magnitude of local energy deposition generated by focused acoustic wave propagation is influenced by the intensity and duty cycle of the ultrasound application. High-intensity, continuous FUS application can generate marked focal temperature elevation, reaching up to 65°C or greater (with tissue devitalization generally achieved at temperatures exceeding 55°C)[8] within a matter of seconds. When FUS is applied in a pulsed, high-intensity fashion, cooling can occur between the pulses and the temporally averaged intensity can be lowered substantially. These factors lower the temperature elevations to just a few degrees Celsius. As a result, mechanical effects predominate on local cytoarchitecture, without irreversible thermal injury.[9] Further reduction in energy deposition is achieved with a pulsed low-intensity application, which may generate unique neuromodulatory effects with negligible temperature elevations (Fig 2).

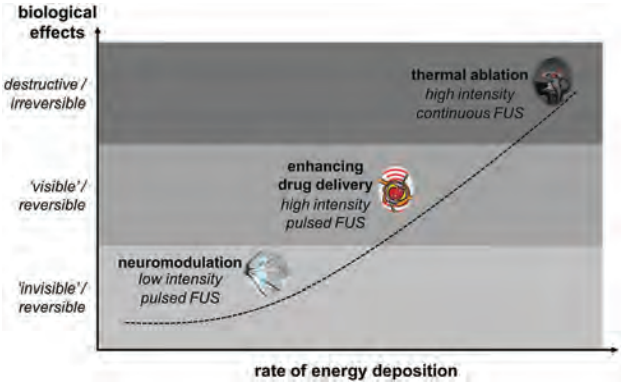

FIG 2. Unique biologic effects can be achieved over a range of energy-deposition rates by manipulating the intensity and duty cycle of the ultrasound application. These include neuromodulation, localized reversible enhancement of blood-brain barrier permeability, and thermal ablation.

High-Intensity, Continuous FUS

The therapeutic benefit of high-intensity continuous FUS application is related to the degree of localized temperature elevation, resulting in irreversible coagulative necrosis at the tissue level, and is the basis of ablative therapies. The treatment of benign prostatic hyperplasia and prostate cancer was the earliest clinical application of this form of FUS and used a transrectal transducer and a collinear ultrasound imaging transducer for both treatment planning and monitoring. Newer generation devices use MR imaging guidance and were first used for the treatment of uterine fibroids.[7] The use of MRgFUS in the treatment of uterine fibroids has since acquired FDA approval and is reimbursed by insurance providers on an individual basis. The advent of transcranial devices has provided the impetus for investigation into a variety of neurologic applications.

One of the more promising applications of FUS for thermal ablation has been in the treatment of medication-refractory essential tremor. While the exact etiology of the disorder is not entirely understood, disruption of the ventral intermediate nucleus of the thalamus, via stereotactic radiosurgery or deep brain stimulation, has been shown to be effective in the management of symptoms.[10] In 2013, Elias et al[11] demonstrated reliable improvement in tremor-related disability up to 1 year after MRgFUS-induced unilateral thalamotomy of the ventral intermediate nucleus. Other institutions have since successfully replicated these findings, and the procedure was recently FDA approved. Recent evidence also suggests a role for FUS-induced thermal ablation in cases of Parkinson disease refractory to pharmacologic intervention. In a small trial ($n = 13$), FUS-induced thermal ablation of the pallidothalamic tract resulted in significant reduction in symptoms as measured by the Unified Parkinson Disease Rating

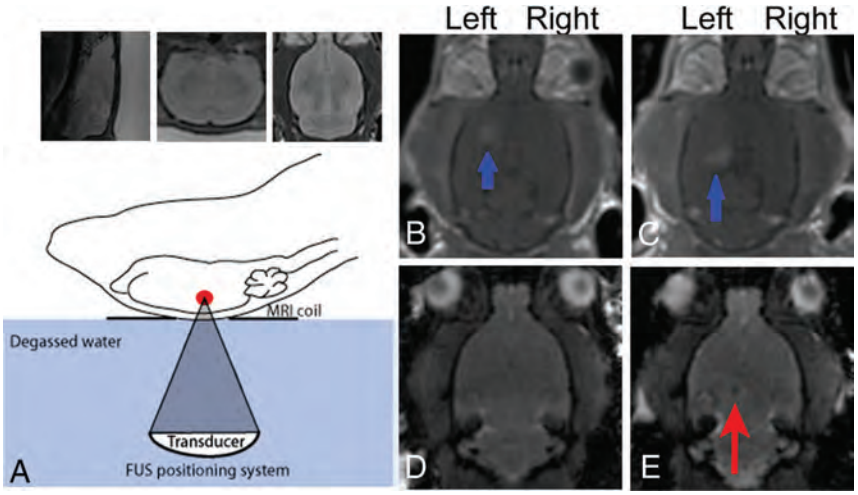

FIG 3. Application of MRgFUS for the delivery of iron-labeled neural stem cells. Schematic of the FUS apparatus (*lower left*). Sagittal, coronal, and axial T2-weighted images (*A*) are used to identify the intended targets of neural stem cell delivery in the left hippocampus and left striatum. T1-weighted, postcontrast images after local FUS sonication (*B* and *C*) demonstrate enhancement in the striatum and hippocampus (*blue arrows*) compatible with enhanced BBB permeability. Fast gradient-echo sequences are obtained before (*D*) and after (*E*) sonication, localizing a focus of hypointense signal (*red arrow*) confirming delivery of iron-labeled neural stem cells. Reprinted with permission from Burgess et al.[40]

Scale and patient assessment of global symptom relief. Patients undergoing MRgFUS-induced thermocoagulation of the pallidothalamic tract experienced a reduction in symptomatology that was comparable with that in stereotactic radiosurgery when effective parameters were applied.[12]

Similarly, MRgFUS-induced central lateral thalamotomy in patients with medication-refractory neuropathic pain syndrome has also been shown to result in symptomatic relief. In a small study ($n = 11$) performed in 2012, immediate pain relief was achieved during sonication in more than half the subjects. All except 1 patient experienced substantial symptomatic relief, which persisted 1 year after therapy (57% mean pain relief). The study included patients with both peripheral and central etiologies of neuropathic pain syndrome, and symptomatic benefit was similar in both groups.[13]

An effective and safe protocol for MRgFUS in the treatment of primary solid intracranial neoplasms remains more elusive. The infiltrative nature of primary gliomas makes ablation uniquely challenging. In a small clinical trial assessing the role of MRgFUS in the ablation of high-grade gliomas, coagulative necrosis and complete ablation of the tumors were not achieved in 3 patients undergoing MRgFUS treatment. After modification of the protocol, a fourth patient who underwent treatment had successful ablation of the tumor but with fatal intracranial hemorrhage a few days after treatment, possibly related to an underlying coagulopathy. Current understanding is that lower frequency application, as attempted in the fourth patient, seems to be associated with an increased risk of bleeding.[14] A universal protocol has not yet been established in the ablation of primary gliomas, and continued investigations are necessary.

High-Intensity, Pulsed FUS

By applying FUS in a pulsed mode rather than a continuous application, the temporally averaged rate of energy deposition is reduced. As a result, lower temperature elevations are achieved without irreversible thermal injury. Rather, mechanical effects will predominate, which may be used to enhance drug and gene delivery[9] via reversible localized enhanced permeability of the BBB (Fig 3).[15] Early investigations into FUS-induced BBB permeability enhancement were inconsistent and required acoustic energy levels that resulted in localized tissue damage in the region of treatment. Later development demonstrated that when these exposures were used in conjunction with ultrasound contrast agents in the form of "microbubbles," lower acoustic energies were required and BBB permeability was more reproducible. The underlying mechanism is related to the controlled oscillation of the bubbles by the varying pressure field of the ultrasound wave. It is theorized that bubble interactions with endothelial cells lead to the compromised integrity of the tight junctions and subsequent "leakiness" of the endothelial membrane.[16]

Enhanced drug delivery by using FUS is actively being investigated in several studies to determine a role in the treatment of CNS neoplasms.[17,18] Glioblastoma multiforme, the most common primary brain tumor in adults, is among the most lethal CNS neoplasms and has limited chemotherapeutic options. Temozolomide (TMZ) is one of the few agents that has shown a survival benefit in multiple large phase III trials, though posttreatment, 5-year mortality remains abysmal.[19] In a small preclinical study with a noninvasive glioma model, Wei et al[18] compared small-, medium-, and high-dose TMZ groups with a medium-dose TMZ + FUS group in regard to CSF/plasma TMZ concentrations, volume of tumor progression, and survival time in a rat model. The TMZ + FUS group demonstrated the highest TMZ CSF/plasma ratio, and MR imaging confirmed that the TMZ + FUS group showed the lowest rate of tumor progression compared with TMZ alone, regardless of concentration (Fig 4). Most important, the TMZ + FUS group was the only group to demonstrate a survival benefit compared with the control group (15% median survival time benefit).[18]

Enhanced CNS delivery via FUS has also been investigated by using different classes of therapeutic agents, including gene-carrying vectors, stem cells, and immunotherapies such as targeted antibodies.[20] Specifically in the case of Alzheimer disease, immunotherapy in the form of anti-amyloid-β plaque antibodies has yielded promising results.[21] Independent investigations by Raymond et al[22] and Jordão et al[23] have shown that FUS can be used to significantly increase CNS concentrations of anti-amyloid-β antibodies in a mouse model (approximately 3-fold in the Raymond et al group). By comparing the amyloid-β plaque burden between antibody and FUS + antibody cerebral hemispheres, the Jordão et al group further demonstrated a significant reduction in amyloid-β plaque burden in the antibody + FUS treatment hemisphere relative to the contralateral FUS-naive cerebral hemi-

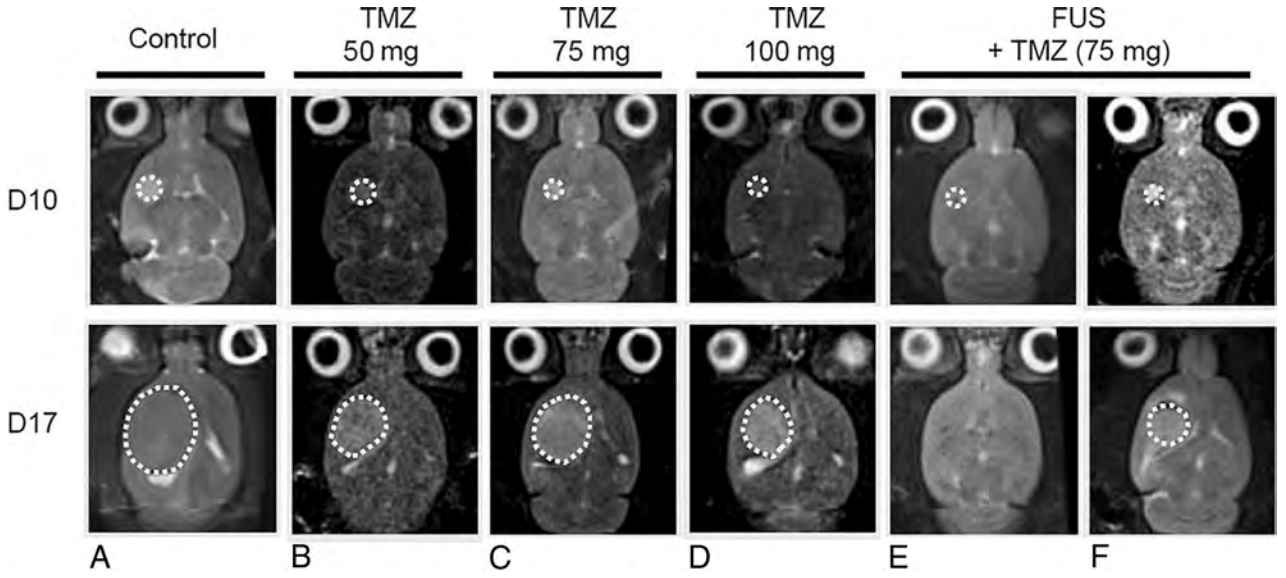

FIG 4. Comparison of TMZ versus TMZ + FUS. At day 10, tumors in all groups are similar in size, designating the start of treatments. At day 17, the FUS + TMZ group demonstrate the slowest rate of tumor growth as evidenced by the degree of T2-weighted signal. The FUS + TMZ group also shows the longest survival of any of the TMZ-only groups (not shown). Reprinted with permission from Wei et al.[18]

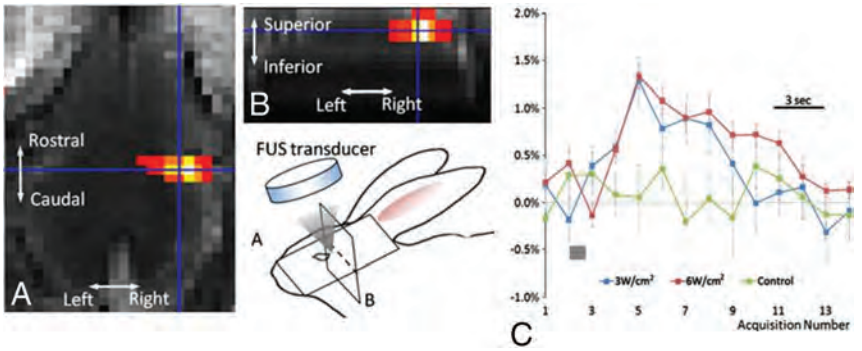

FIG 5. Neuromodulation of the rabbit motor cortex. An fMRI activation map shows increased blood oxygen level–dependent–weighted signal in the right motor cortex (*A* and *B*). The *blue crosshairs* on the fMRI images correspond to the sonication focus. Cartoon schematic illustrates the experimental setup and spatial orientation. The graph (*C*) demonstrates the percentage of blood oxygen level–dependent signal change as a function of the time/acquisition number at 2 different FUS intensities: 6 W/cm^2 (*red curve*) and 3 W/cm^2 (*blue curve*). The green dataset represents the control group. The *gray bars* indicate the sonication time. Reprinted with permission from Yoo et al.[28]

sphere. More recently, a novel modified FUS protocol developed by Leinenga and Götz[24] applied in a mouse model demonstrated that diffuse BBB permeability could be achieved via multiple sonication sites throughout the forebrain, reducing amyloid-β plaque burden without pharmacologic intervention. The etiology of amyloid-β plaque reduction is proposed to be related to enhancement of intrinsic microglial phagocytosis.[24]

Low-Intensity, Pulsed FUS

Neuromodulation, or the ability to reversibly influence neuronal activity, either via excitation or reversible suppression, has enormous therapeutic potential. Other neuromodulatory modalities have already been used extensively in the treatment of a variety of diseases. For instance, deep brain stimulation has gained widespread acceptance in the treatment of movement disorders, including Parkinson disease and essential tremor.[25] Electroconvulsive therapy[26] and, more recently, transcranial magnetic stimulation[27] have also demonstrated efficacy in the treatment of major depression. When used in a low-intensity manner, FUS can also produce local neuromodulatory effects creating negligible temperature elevations and complete preservation of target cytoarchitecture.[28]

The ability of ultrasound to influence neuronal activity was first established by Fry et al[29] in 1958 via ultrasound-induced reversible inhibition of visual-evoked potentials. As the role of FUS has expanded, so has the number of trials into the mechanisms and efficacy of ultrasound-induced neuromodulation. Mechanistic investigation into the effects of low-intensity ultrasound on neuronal electrophysiology by Tyler et al[30] in 2008 showed that ultrasound application triggered opening of sodium (Na^+) voltage-dependent channels, free calcium (Ca^{2+}) channels, and ultimately an increase in soluble *N*-ethylmaleimide sensitive fusion proteins attachment receptor–mediated synaptic vesicle exocytosis and synaptic transmission in excised hippocampal sections of mouse brain.[30] In vivo neurostimulation through an intact skull in mice has also been shown, without an increase in apoptosis or loss of BBB integrity. This was measured indirectly by using antibodies targeting apoptotic mediators and via a lack of intra-axial fluorescein isothiocyanate-dextran (10 kDa), which does not cross the BBB under normal conditions.[31]

More recently, Yoo et al[28] achieved reliable neurostimulation and reversible suppression by using remote low-intensity FUS in a rabbit model, as confirmed by fMRI and electroencephalographic recordings (Fig 5). Concurrent MR thermometry measured tem-

Clinical applications of focused ultrasound and the proposed mechanisms of action

	FUS Exposures and Effects on Biologic Tissues	
	Mechanism of Action	**Applications**
High-intensity continuous application	Thermal → coagulative necrosis	Thalamotomy: essential tremor,[11] chronic neuropathic pain,[13] obsessive-compulsive disorder[36] Pallidotomy: Parkinson disease[12] Solid tumor ablation[14]
High-intensity pulsed application	Oscillation of ultrasound "microbubble" contrast agents Thermal → regional hyperthermia Mechanical → radiation force–induced displacements	Enhanced agent CNS delivery[22] Enhanced chemotherapy/radiotherapy[37] Induction of microglial activation[27] Sonothrombolysis in ischemic stroke[38] Intracranial hematoma evacuation[39]
Low-intensity pulsed application	Mechanical → activation/inhibition of Na^+ and Ca^{2+}-gated ion channels	Noninvasive neuromodulation[33,34]

perature elevations of approximately 0.7°C, well below levels required to cause tissue devitalization.[8] Most important, the FUS exposures did not result in damage to the BBB as demonstrated by the absence of enhancement on postcontrast MR imaging or cytoarchitectural distortion as confirmed by histologic evaluation.[28] Low-intensity FUS for neuromodulation is one of the newest applications of FUS currently being investigated. Preliminary studies have been promising, and research is ongoing.

Advantages and Obstacles of FUS

High-intensity MRgFUS shares a great deal of therapeutic overlap with surgical resection and stereotactic radiosurgery, albeit with a few important distinctions. Both MRgFUS and radiosurgery compare favorably with surgical intervention in that both do not require surgical craniotomy. While radiosurgery is a mainstay in the treatment of intracranial neoplasms, its role in nonneoplastic pathologies is somewhat limited due to ionizing radiation exposure. In contradistinction, MRgFUS offers reliable, high-resolution energy deposition without radiation exposure or thermal injury to nontarget intracranial tissues.

As a tool for therapeutic agent delivery, FUS is the only available method of generating localized reversible BBB permeability in a noninvasive manner. Selective transport across the BBB is a challenge in ensuring CNS delivery.[32] A common obstacle in the development of CNS immunotherapy is the requirement of molecular modification to allow prohibitively large agents to traverse the BBB. While other noninvasive methods have been developed,[33] customized modification of each agent is required to take advantage of endogenous transport mechanisms, imposing a costly and time-intensive burden on translation to clinical trials. Use of an FUS-induced BBB opening would substantially decrease the size restrictions dictating molecular permeability and expedite assessment of clinical efficacy.[34]

FUS offers unique benefits as a therapeutic technique in influencing neuronal activity. FUS-induced neuromodulation does not require surgical craniotomy as is required for deep brain stimulation or subdural and epidural cortical stimulation. Other noninvasive systems, such as transcranial magnetic stimulation and electroconvulsive therapy can be effective; however, they offer inferior spatial resolution.[35] The superior spatial resolution offered by FUS could complement functional imaging modalities such as fMRI, to potentially serve as a powerful tool in functional connectivity studies.

Important obstacles remain in the development of FUS as a clinical tool. Further investigations into safe and effective protocols in the ablation of gliomas are needed because its role has lagged behind that of thalamotomy in the treatment of movement disorders and neuropathic pain. Achieving generalizability has also been challenging, most notably due to the limitations of acoustic accessibility in the ablation of superficial lesions or treatment envelope and in patient selection based on heat generation at the calvaria. Overcoming these limitations is actively being investigated.

CONCLUSIONS

The discovery of a noninvasive method of focusing mechanical energy, in the form of acoustic waves, within the parenchyma has heralded a new age of investigations into clinical and research applications. In the brief time since transcranial acoustic wave propagation was achieved, FUS has empirically demonstrated efficacy in the ablation of tissues, therapeutic agent delivery, and neuromodulation. The ability to focus acoustic wave propagation noninvasively on the scale of a few millimeters while manipulating the magnitude of energy deposition to create unique bioeffects offers versatility that is unparalleled in neurotherapeutics and research (Table). The role of FUS appears destined to expand as investigations into its utility continue at a rigorous pace.

Disclosures: Dheeraj Gandhi—*UNRELATED*: *Expert Testimony*: Occasionally (<1 year) provided expert testimony on medicolegal cases related to cerebrovascular disease; *Royalties*: Cambridge Press. *RELATED*: *Grants/Grants Pending*: Insightec, Medtronic, National Institutes of Health, Stryker. Victor Frenkel—*UNRELATED*: *Grants/Grants Pending*: Focused Ultrasound Foundation,* *Comments*: This was a 1-year grant of $100,000 to Dr Paul Fishman (Principal Investigator) of the VA Hospital affiliated with the University of Maryland School of Medicine. From this grant, I received 5% effort for my salary for 1 year, during which our article was conceived and written. The funding was, however, for my work on a preclinical study on using focused ultrasound to enhance stem cell delivery to the brain. It was not in any way related to working on this article. The Foundation is a nonprofit organization whose mandate is to increase awareness of focused ultrasound and its implementation in the clinic. This funding has ended, and we recently received notification from the VA System that our grant, which follows this work, is also to be funded. *Money paid to the institution.

REFERENCES

1. Lehmann JF. **The biophysical basis of biologic ultrasonic reactions with special reference to ultrasonic therapy.** *Arch Phys Med Rehabil* 1953;34:139–52 Medline
2. Haar GT, Coussios C. **High intensity focused ultrasound: physical**

principles and devices. *Int J Hyperthermia* 2007;23:89–104 CrossRef Medline
3. Fry WJ, Barnard JW, Fry EJ, et al. **Ultrasonic lesions in the mammalian central nervous system.** *Science* 1955;122:517–18 CrossRef Medline
4. Heimburger R. **Ultrasound augmentation of central nervous system tumor therapy.** *Indiana Med* 1985;78:469–76 Medline
5. Clement GT, Hynynen K. **A non-invasive method for focusing ultrasound through the human skull.** *Phys Med Biol* 2002;47:1219–36 CrossRef Medline
6. Madersbacher S, Pedevilla M, Vingers L, et al. **Effect of high-intensity focused ultrasound on human prostate cancer in vivo.** *Cancer Res* 1995;55:3346–51 Medline
7. Kennedy JE. **High-intensity focused ultrasound in the treatment of solid tumours.** *Nat Rev Cancer* 2005;5:321–27 CrossRef Medline
8. Meshorer A, Prionas SD, Fajardo LF, et al. **The effects of hyperthermia on normal mesenchymal tissues: application of a histologic grading system.** *Arch Pathol Lab Med* 1983;107:328–34 Medline
9. Frenkel V. **Ultrasound mediated delivery of drugs and genes to solid tumors.** *Adv Drug Deliv Rev* 2008;60:1193–208 CrossRef Medline
10. Pahwa R, Lyons KE, Wilkinson SB, et al. **Comparison of thalamotomy to deep brain stimulation of the thalamus in essential tremor.** *Mov Disord* 2001;16:140–43 Medline
11. Elias WJ, Huss D, Voss T, et al. **A pilot study of focused ultrasound thalamotomy for essential tremor.** *N Engl J Med* 2013;369:640–48 CrossRef Medline
12. Magara A, Bühler R, Moser D, et al. **First experience with MR-guided focused ultrasound in the treatment of Parkinson's disease.** *J Ther Ultrasound* 2014;2:11 CrossRef Medline
13. Jeanmonod D, Werner B, Morel A, et al. **Transcranial magnetic resonance imaging-guided focused ultrasound: noninvasive central lateral thalamotomy for chronic neuropathic pain.** *Neurosurg Focus* 2012;32:E1 CrossRef Medline
14. McDannold N, Clement G, Black P, et al. **Transcranial magnetic resonance imaging-guided focused ultrasound surgery of brain tumors: initial findings in 3 patients.** *Neurosurgery* 2010;66:323–32; discussion 332 CrossRef Medline
15. Hynynen K, McDannold N, Vykhodtseva N, et al. **Non-invasive opening of BBB by focused ultrasound.** *Acta Neurochir Suppl* 2003; 86:555–58 Medline
16. Sheikov N, McDannold N, Vykhodtseva N, et al. **Cellular mechanisms of the blood-brain barrier opening induced by ultrasound in presence of microbubbles.** *Ultrasound Med Biol* 2004;30:979–89 CrossRef Medline
17. Kinoshita M, McDannold N, Jolesz FA, et al. **Noninvasive localized delivery of Herceptin to the mouse brain by MRI-guided focused ultrasound-induced blood-brain barrier disruption.** *Proc Natl Acad Sci U S A* 2006;103:11719–23 CrossRef Medline
18. Wei KC, Chu PC, Wang HY, et al. **Focused ultrasound-induced blood-brain barrier opening to enhance temozolomide delivery for glioblastoma treatment: a preclinical study.** *PLoS One* 2013;8: e58995 CrossRef Medline
19. Stupp R, Hegi ME, Mason WP, et al; European Organisation for Research and Treatment of Cancer Brain Tumour and Radiation Oncology Groups, National Cancer Institute of Canada Clinical Trials Group. **Effects of radiotherapy with concomitant and adjuvant temozolomide versus radiotherapy alone on survival in glioblastoma in a randomised phase III study: 5-year analysis of the EORTC-NCIC trial.** *Lancet Oncol* 2009;10:459–66 CrossRef Medline
20. Kinoshita M, McDannold N, Jolesz FA, et al. **Targeted delivery of antibodies through the blood-brain barrier by MRI-guided focused ultrasound.** *Biochem Biophys Res Commun* 2006;340:1085–90 CrossRef Medline
21. Bard F, Cannon C, Barbour R, et al. **Peripherally administered antibodies against amyloid beta-peptide enter the central nervous system and reduce pathology in a mouse model of Alzheimer disease.** *Nat Med* 2000;6:916–19 CrossRef Medline
22. Raymond SB, Treat LH, Dewey JD, et al. **Ultrasound enhanced delivery of molecular imaging and therapeutic agents in Alzheimer's disease mouse models.** *PLoS One* 2008;3:e2175 CrossRef Medline
23. Jordão JF, Ayala-Grosso CA, Markham K, et al. **Antibodies targeted to the brain with image-guided focused ultrasound reduces amyloid-beta plaque load in the TgCRND8 mouse model of Alzheimer's disease.** *PLoS One* 2010;5:e10549 CrossRef Medline
24. Leinenga G, Götz J. **Scanning ultrasound removes amyloid-beta and restores memory in an Alzheimer's disease mouse model.** *Sci Transl Med* 2015;7:278ra233 CrossRef Medline
25. Benabid AL, Pollak P, Gervason C, et al. **Long-term suppression of tremor by chronic stimulation of the ventral intermediate thalamic nucleus.** *Lancet* 1991;337:403–06 CrossRef Medline
26. UK ECT Review Group. **Efficacy and safety of electroconvulsive therapy in depressive disorders: a systematic review and meta-analysis.** *Lancet* 2003;361:799–808 CrossRef Medline
27. Schutter DJ. **Antidepressant efficacy of high-frequency transcranial magnetic stimulation over the left dorsolateral prefrontal cortex in double-blind sham-controlled designs: a meta-analysis.** *Psychol Med* 2009;39:65–75 CrossRef Medline
28. Yoo SS, Bystritsky A, Lee JH, et al. **Focused ultrasound modulates region-specific brain activity.** *Neuroimage* 2011;56:1267–75 CrossRef Medline
29. Fry FJ, Ades HW, Fry WJ. **Production of reversible changes in the central nervous system by ultrasound.** *Science* 1958;127:83–84 CrossRef Medline
30. Tyler WJ, Tufail Y, Finsterwald M, et al. **Remote excitation of neuronal circuits using low-intensity, low-frequency ultrasound.** *PLoS One* 2008;3:e3511 CrossRef Medline
31. Tufail Y, Matyushov A, Baldwin N, et al. **Transcranial pulsed ultrasound stimulates intact brain circuits.** *Neuron* 2010;66:681–94 CrossRef Medline
32. Pardridge WM. **The blood-brain barrier: bottleneck in brain drug development.** *NeuroRx* 2005;2:3–14 CrossRef Medline
33. Shi N, Pardridge WM. **Noninvasive gene targeting to the brain.** *Proc Natl Acad Sci U S A* 2000;97:7567–72 CrossRef Medline
34. Choi JJ, Wang S, Tung YS, et al. **Molecules of various pharmacologically-relevant sizes can cross the ultrasound-induced blood-brain barrier opening in vivo.** *Ultrasound Med Biol* 2010;36:58–67 CrossRef Medline
35. Wagner T, Valero-Cabre A, Pascual-Leone A. **Noninvasive human brain stimulation.** *Annu Rev Biomed Eng* 2007;9:527–65 CrossRef Medline
36. Jung HH, Kim SJ, Roh D, et al. **Bilateral thermal capsulotomy with MR-guided focused ultrasound for patients with treatment-refractory obsessive-compulsive disorder: a proof-of-concept study.** *Mol Psychiatry* 2015;20:1205–11 CrossRef Medline
37. Tempany CM, McDannold NJ, Hynynen K, et al. **Focused ultrasound surgery in oncology: overview and principles.** *Radiology* 2011;259:39–56 CrossRef Medline
38. Burgess A, Huang Y, Waspe AC, et al. **High-intensity focused ultrasound (HIFU) for dissolution of clots in a rabbit model of embolic stroke.** *PLoS One* 2012;7:e42311 CrossRef Medline
39. Monteith SJ, Harnof S, Medel R, et al. **Minimally invasive treatment of intracerebral hemorrhage with magnetic resonance-guided focused ultrasound.** *J Neurosurg* 2013;118:1035–45 CrossRef Medline
40. Burgess A, Ayala-Grosso CA, Ganguly M, et al. **Targeted delivery of neural stem cells to the brain using MRI-guided focused ultrasound to disrupt the blood-brain barrier.** *PLoS One* 2011;6:e27877 CrossRef Medline

Hydrogel versus Bare Platinum Coils in Patients with Large or Recurrent Aneurysms Prone to Recurrence after Endovascular Treatment: A Randomized Controlled Trial

J. Raymond, R. Klink, M. Chagnon, S.L. Barnwell, A.J. Evans, J. Mocco, B.H. Hoh, A.S. Turk, R.D. Turner, H. Desal, D. Fiorella, S. Bracard, A. Weill, F. Guilbert, S. Lanthier, A.J. Fox, T.E. Darsaut, P.M. White, and D. Roy

ABSTRACT

BACKGROUND AND PURPOSE: Some patients are at high risk of aneurysm recurrence after endovascular treatment: patients with large aneurysms (Patients Prone to Recurrence After Endovascular Treatment PRET-1) or with aneurysms that have previously recurred after coiling (PRET-2). We aimed to establish whether the use of hydrogel coils improved efficacy outcomes compared with bare platinum coils.

MATERIALS AND METHODS: PRET was an investigator-led, pragmatic, multicenter, parallel, randomized (1:1) trial. Randomized allocation was performed separately for patients in PRET-1 and PRET-2, by using a Web-based platform ensuring concealed allocation. The primary outcome was a composite of a residual/recurrent aneurysm, adjudicated by a blinded core laboratory, or retreatment, intracranial bleeding, or mass effect during the 18-month follow-up. Secondary outcomes included adverse events, mortality, and morbidity (mRS > 2). The hypothesis was that hydrogel would decrease the primary outcome from 50% to 30% at 18 months, necessitating 125 patients per group (500 for PRET-1 and PRET-2).

RESULTS: The trial was stopped once 250 patients in PRET-1 and 197 in PRET-2 had been recruited because of slow accrual. A poor primary outcome occurred in 44.4% (95% CI, 35.5%–53.2%) of those in PRET-1 allocated to platinum compared with 52.5% (95% CI, 43.4%–61.6%) of patients allocated to hydrogel (OR, 1.387; 95% CI, 0.838–2.295; $P = .20$) and in 49.0% (95% CI, 38.8%–59.1%) in PRET-2 allocated to platinum compared with 42.1% (95% CI, 32.0%–52.2%) allocated to hydrogel (OR, 0.959; 95% CI, 0.428–1.342; $P = .34$). Adverse events and morbidity were similar. There were 3.6% deaths (1.4% platinum, 5.9% hydrogel; $P = .011$).

CONCLUSIONS: Coiling of large and recurrent aneurysms is safe but often poorly effective according to angiographic results. Hydrogel coiling was not shown to be better than platinum.

ABBREVIATION: PRET = Patients Prone to Recurrence After Endovascular Treatment

Endovascular coiling has revolutionized the management of intracranial aneurysms.[1,2] Coiling has been shown safe and effective in the treatment of ruptured aneurysms compared with surgical clipping.[3] Coiling is also frequently used to preventively treat unruptured aneurysms, even though it has never been proved superior to clipping or observation.[4,5] One drawback of coiling is the occurrence of residual or recurrent aneurysms at follow-up angiography in 20%–30% of patients.[6-8] The impact of recurrent aneurysms on long-term clinical outcomes remains unclear. They have infrequently been associated with subarachnoid hemorrhage, in the range of 0.1%–1% per year.[7,9] Nevertheless, concerns for recurrences have a number of clinical consequences,

Received November 8, 2016; accepted after revision December 14.

From the Departments of Radiology (J.R., A.W., F.G., D.R.) and Neurosciences (S.L.), Centre Hospitalier de l'Université de Montreal, Montreal, Quebec, Canada; Laboratory of Interventional Neuroradiology (R.K.), Research Centre of the Centre Hospitalier de l'Université de Montreal, Quebec, Canada; Department of Mathematics and Statistics (M.C.), Université de Montréal, Montreal, Quebec, Canada; Department of Neurological Surgery (S.L.B.), Oregon Health and Science University, Portland, Oregon; Department of Radiology and Medical Imaging (A.J.E.), University of Virginia, Charlottesville, Virginia; Department of Neurosurgery (J.M.), Mount Sinai Health System, New York, New York; Department of Neurosurgery (B.H.H.), University of Florida, Gainesville, Florida; Department of Neurosurgery (A.S.T., R.D.T.), Medical University of South Carolina, Charleston, South Carolina; Service de Neuroradiologie Diagnostique et Interventionnelle (H.D.), Centre Hospitalier Universitaire de Nantes, Nantes, France; Cerebrovascular Center (D.F.), Stony Brook University Medical Center, Stony Brook, New York; Département de Neuroradiologie Diagnostique et Interventionnelle (S.B.), Centre Hospitalier Universitaire de Nancy, Nancy, France; Department of Medical Imaging (A.J.F.), University of Toronto, Toronto, Ontario, Canada; Department of Surgery (T.E.D.), Division of Neurosurgery, University of Alberta Hospital, Edmonton, Alberta, Canada; and Stroke Research Group (P.M.W.), Institute of Neuroscience, Newcastle Upon Tyne, UK.

This work was supported by an unrestricted research grant from MicroVention Terumo.

Please address correspondence to Jean Raymond, MD, Centre Hospitalier de l'Université de Montréal, Notre-Dame Hospital, Department of Radiology, 1560 Sherbrooke East, Pavilion Simard, Suite Z12909, Montreal, Quebec, Canada H2L 4M1; e-mail: jean.raymond@umontreal.ca

Indicates open access to non-subscribers at www.ajnr.org

Indicates article with supplemental on-line tables.

Evidence-Based Medicine Level 1.

http://dx.doi.org/10.3174/ajnr.A5101

such as routine angiographic surveillance of nearly all patients, retreatment in 5%–15%, and, more recently, the emergence and growing use of potentially more effective but also potentially more risky alternatives, such as stent placement or flow diversion.[10-13]

A randomized trial comparing hydrogel and platinum coiling published in 2011 failed to confirm its primary composite endpoint in favor of hydrogel coils but demonstrated improved core laboratory adjudicated angiographic outcomes overall and in prespecified subgroups of medium (5.0–9.0 mm) and ruptured aneurysms.[11,14] There was no difference in retreatment rates. A recent systematic review of randomized trials concluded with a reduction of residual aneurysms after hydrogel compared with platinum coiling, but results were barely significant.[15] Recurrent aneurysms after platinum coiling are at high risk of re-recurring when retreated, but these patients were excluded from all published randomized trials.[8,14,16-18]

The Patients Prone to Recurrence After Endovascular Treatment (PRET) study was designed in 2007 to offer an alternative to platinum coiling in patients previously shown to be at high risk of recurrence: patients with large (≥10 mm) or recurrent aneurysms after coiling. The trial protocol was published in 2008.[19] We aimed to establish whether the use of hydrogel coils improved efficacy outcomes compared with bare platinum coils, without increasing procedural risks. Similar periprocedural (30 days) outcomes were reported for hydrogel and platinum coiling.[20] We now report the primary outcome of the trial: The primary hypothesis was that the use of hydrogel coils would decrease the proportion of residual or recurrent aneurysms from 50% to 30% (range from 50%–40% to 30%–21%) at 18 months compared with bare platinum coils.

MATERIALS AND METHODS

Study Design

PRET was an investigator-led, pragmatic, multicenter, international, randomized (1:1), controlled trial comparing a policy of using hydrogel versus bare platinum coils in the endovascular treatment of intracranial aneurysms. There were 25 participating clinical sites from 6 countries (United States, Canada, United Kingdom, France, Chile, Japan). The ClinicalTrials.gov registration number from the US National Institutes of Health is NCT00626912. All trial sites had local institutional review board approval. All patients (or legal representatives) signed a standardized informed consent form.

During the course of the trial, no change in methods or protocol occurred, but multiple different types of hydrogel coils were being manufactured, approved, and used.

Participants

Eligible patients, with an intracranial aneurysm requiring endovascular treatment, fell into 1 of 2 groups: PRET-1, with a large aneurysm (longest dimension, ≥10 mm, including any thrombosed portion), never treated; PRET-2, with an aneurysm of any size, presenting with a postcoiling recurrence requiring retreatment. There were few selection criteria: The patient was 18 years of age or older; life expectancy was >2 years; the aneurysm could be ruptured (World Federation of Neurologic Societies grade <IV) or unruptured; anatomy was such that endovascular treatment was considered possible with both types of coils; the endovascular operator was satisfied with using either type of coil, but no other type (such as polyglycolic acid/lactide copolymer coils); and the patient or authorized representative had given fully informed consent and had signed the consent form. Patients were not eligible if they met any of the following criteria: the presence of other aneurysms requiring treatment during the same session; the presence of an associated cerebral arteriovenous malformation; the primary intent of the procedure being parent vessel occlusion without simultaneous endovascular coiling of the aneurysm; and any absolute contraindication to endovascular treatment, angiography, or anesthesia.

Trial sites were tertiary centers experienced in the endovascular treatment of aneurysms with both platinum coils (at least 100 patients treated before enrollment) and hydrogel-coated coils (at least 10 patients previously treated).

Interventions

Standard local endovascular procedures were followed. Any locally approved bare platinum coil with controlled detachment was permitted, as were any assist devices believed necessary by the operator, provided they had local regulatory approval, excluding flow diverters, irrespective of the intended use indicated at randomization. Antiplatelet and anticoagulation regimens were left to the individual operator's judgment, according to the clinical practice at each site. When treatment allocation was to "platinum," types of coils other than bare platinum were forbidden. When treatment allocation was to "hydrogel," any coil of the hydrogel family was allowed but any bare platinum coil could also be used if the operator believed it was in the patient's best interest. Recommendations concerning hydrogel coil use pertaining to type, size, and sequence of introduction were issued but not enforced. No minimum percentage of hydrogel coils was prescribed; the protocol required "the substitution, as far as possible, of platinum by hydrogel coils, the operator always being allowed to use the coils he or she believes [are] appropriate at any time during the procedure."[15] "Successful hydrogel coiling" was predefined as two-thirds total coil lengths being hydrogel coils, to be used for explanatory analyses only. Other technical considerations such as preparing or steaming of hydrogel coils and the type of bare platinum coil were left entirely to the operator's discretion. The goal of the procedure was to occlude the aneurysm as completely as possible, keeping the risks of the procedure as low as possible.[15]

Outcomes

The primary outcome of the trial was the proportion of patients with a recurrence, defined as the following: 1) major angiographic recurrence of the lesion or the presence of a residual aneurysm at last angiographic follow-up, as determined by the core laboratory, blinded to treatment allocation; 2) retreatment of the same aneurysm by endovascular or surgical means during the 18-month follow-up period; and 3) an intracranial bleeding episode or the occurrence or progression of a mass effect in relation to the treated aneurysm during the follow-up period, as determined by the blinded Adverse Event Committee. Immediate treatment failures and missing follow-up angiographic data because of treat-

ment or aneurysm-related deaths or poor clinical outcomes (mRS > 2) were treated as primary outcome events.

Secondary outcomes included safety data, mortality and morbidity, and adverse events, defined as an event of any severity being possibly or probably related to the disease or the treatment and happening at any time during the 18-month follow-up. The independent Adverse Event Committee was responsible for the attribution of secondary outcome events. The protocol prespecified that morbidity would be defined per patient, according to the mRS score (mRS > 2). Adverse event reports and individual case report forms were cross-checked to determine the secondary safety endpoint for each patient. Periprocedure safety endpoints were reported. Delayed safety outcomes were categorized as the following: subarachnoid hemorrhage, progressive mass effect, stroke, transient ischemic events, inflammatory complications potentially related to coils, non-neurologic, retreatment-related, and others.

Number of Patients

Two hundred fifty subjects (125 in each group) were judged necessary to achieve 80% power at a 2-sided .0250 significance level to detect a difference of .20 (between .30 and .50) in primary outcome events between the intervention and control groups for patients in PRET-1 and PRET-2 separately, assuming a 10% proportion of patients lost during follow-up.[19]

Randomization

Randomized allocation (1:1) with minimization of risk factors was through the Web-based PRET application package (MedSciNet, Stockholm, Sweden; http://medscinet.com/), ensuring that allocation was concealed before the decision to include a patient. The minimization algorithm computes an imbalance score for each new patient on the basis of patient characteristics (the minimization criteria) and treatment assignments and characteristics of already-enrolled patients, with treatment with the lowest imbalance score being assigned; in addition, the minimization algorithm is dynamic in that it has a built-in random element for assigning patients to the treatment. We used the following minimization criteria: rupture status (yes, no); if the aneurysm was unruptured, planned use of an adjunct device (yes, no). From the moment of randomization, the patient was in the trial and accounted for in the analysis (intention-to-treat). PRET-1 and PRET-2 patient groups were randomized separately.

Masking and Trial Monitoring

Masking of the treatment teams was not possible. Patients were masked unless they specifically requested otherwise. The Adverse Event Committee and the Data Safety and Monitoring Committee, working independently from the Steering Committee, had access to masked data, but the Data Safety and Monitoring Committees could unmask groups whenever members thought that unmasking was mandatory to protect the safety of participants, though the need for unblinding did not arise during the trial. Monitoring of trial data quality was Web-based and performed by periodic review of data stored in the data base.

Data Collection

Data capture and management were held independent of the sponsor and funder on the secure servers of MedSciNet, ISO27000 and Statement on Auditing Standards-70 compliant. Details of data collection are given elsewhere.[20] Briefly, following registration, intervention, and discharge data collection, clinical follow-up data were recorded at 1, 6, and 18 months and angiographic follow-up imaging was performed at 6 and 18 months. Adverse events and additional interventions on the target aneurysm were reported at any time during the trial. When an additional intervention was planned following the 18-month angiographic follow-up, the form allowed the recording of this event (yes/no check box), though some sites also chose to complete an additional intervention form as well. Anonymized angiographic imaging data (catheter or noninvasive, including additional procedures) were sent in batches to the independent core laboratory (lead, P.M. White, Stroke Research Group, Institute of Neuroscience, Newcastle upon Tyne, United Kingdom) for adjudication of location, dimension, and occlusion state of the aneurysm. The core laboratory was masked to treatment allocation and treatment received. Assessment of the occlusion state was according to the revised 3-point Montreal scale; evolution (stable, better, worse) and occurrence of a major recurrence, defined as sufficiently large to technically allow placements of further coils, were recorded.[21]

Statistical Methods

All analyses were performed by the trial statistician (M.C.) according to the published trial protocol.[19] Analyses were Intent-to-treat. The primary outcome was studied by using odds ratios with 95% confidence intervals (platinum coiling as the reference), and groups were compared by using χ^2 tests. Multiple sensitivity analyses were performed for missing values. We performed exploratory stratified analyses, adjusting for rupture status, location, aneurysm size, and the use of adjunct devices. The median packing density was compared between hydrogel and platinum with Mann-Whitney *U* tests. Packing density is the volume of inserted coils divided by the aneurysm volume. Coil volume (V) was calculated by using the formula $V = \pi(c/2)^2 L$, where c is coil caliber and L is coil length for coils entered in the procedural case report forms. Aneurysm volumes (V_A) were determined by using a simple mathematic model $V_A = 4/3\ \pi\ ab\ (a + b)/2$, where a and b are half the long and short axes of the aneurysm, as entered on the case report forms. The number of deaths was compared with a Fisher exact test. To evaluate the possibility of different results for PRET-1 and PRET-2, we stratified descriptive and safety analyses by groups. All analyses were made with SPSS, Version 23 (IBM, Armonk, New York) by using a significance level of 5%.

Role of the Funding Source

The trial was sponsored by the Centre Hospitalier de l'Université de Montréal and funded by MicroVention Terumo. The sponsor and funder had no part in study design, data collection, analysis, or reporting and had no direct or indirect access to the data or source documents. The Steering Committee bears the sole responsibility for all aspects of the trial.

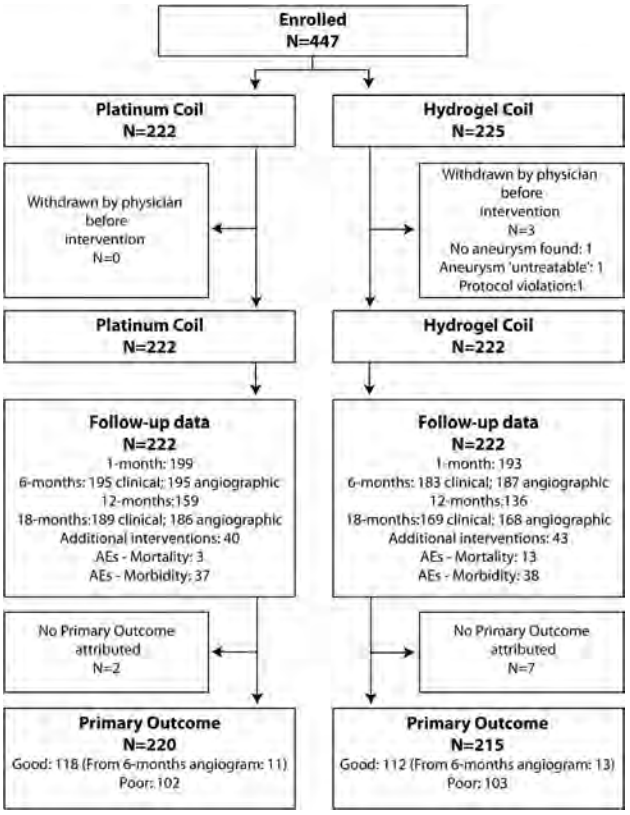

FIG 1. Trial profile. Patients screened are not reported because no eligibility logs were required per protocol. Four hundred forty-seven patients in PRET included 250 in PRET-1 and 197 in PRET-2 groups.

RESULTS

Patients were recruited between June 2007 and January 2014. On December 13, 2013, the Steering Committee decided to stop recruitment after the target number of patients ($n = 250$) had been recruited in PRET-1, but before reaching the target number of patients for PRET-2, because the trial was already 2 years behind schedule, recruitment rates were decreasing, and provisions had to be made to cover compensations to participating sites for the 18-month follow-up data. For each group, the number of participants who were randomly assigned, received intended treatment, and were analyzed for the primary outcome is illustrated in the trial profile (Fig 1). The number of screened patients cannot be provided because eligibility logs were not required per protocol. Four hundred forty-seven patients were recruited by 25 centers in 6 countries, 250 in PRET-1 and 197 in PRET-2.

The baseline patient and aneurysm characteristics are shown in Table 1. Groups were comparable.

Three patients (0.7%; 2 in PRET-1 and 1 in PRET-2; all 3 in the hydrogel group) were withdrawn before any treatment was attempted (1 protocol violation [World Federation of Neurological Societies IV after SAH]), 1 PRET-1 aneurysm judged untreatable, 1 patient in PRET-2 in whom no true recurrence was found). There were 1 crossover from hydrogel to platinum and 1 crossover from platinum to hydrogel, included in the intent-to-treat analyses.

For 9 patients (2.0%; 2 platinum; 7 hydrogel), the primary outcome could not be attributed because of withdrawn consent (2 hydrogel), lack of follow-up from unrelated mortality (1 hydrogel), or patients lost to follow-up (2 platinum; 4 hydrogel). Details are provided in On-line Table 1.

For 24 patients (5.4%; 11 platinum; 13 hydrogel), the 18-month follow-up angiogram was not available and the primary outcome was adjudicated by using the 6-month follow-up angiogram. For 17 patients (3.8%), the primary outcome was determined on the basis of a treatment failure and no further angiographic follow-up (no coil deployed: 3 platinum, 5 hydrogel; residual aneurysm: 4 platinum, 5 hydrogel).

The primary outcome, available for 435/447 patients (97.3%), was reached in 102/220 (46.4%) and 103/215 (47.9%) patients of the platinum and hydrogel groups, respectively (OR, 1.064; 95% CI, 0.730–1.550; $P = .747$). Each component of the composite primary outcome is detailed for PRET-1 and PRET-2 separately in Table 2. Results for predetermined subgroups (unruptured aneurysms, carotid aneurysms, use of stents, and location) are detailed in On-line Tables 2–4 and in the forest plots (Fig 2).

A poor primary outcome occurred in 55/124 (44.4%; 95% CI, 35.5%–53.2%) patients in PRET-1 with large aneurysms allocated to platinum compared with 63/120 (52.5%; 95% CI, 43.4%–61.6%) patients allocated to hydrogel (OR, 1.387; 95% CI, 0.838–2.295; $P = .204$).

In PRET-2 patients who had already presented with a recurrence, a poor primary outcome occurred in 47/96 (49.0%; 95% CI, 38.8%–59.1%) and 40/95 (42.1%; 95% CI, 32.0%–52.2%) patients allocated to platinum and hydrogel, respectively (OR, 0.959; 95% CI, 0.428–1.342; $P = .342$).

The angiographic outcome (residual or recurrent aneurysms) accounted for most primary outcome events (92.2%); the clinical components (SAH, mass effect, related morbidity or mortality; $n = 4$ each) accounted for 16/205 or 7.8% of primary outcome events. Forty-six patients (10.4%; 21 platinum, 25 hydrogel) were retreated during the 18-month follow-up, but 34 other retreatments (7.7%; 19 platinum, 15 hydrogel) were planned. Follow-up vascular imaging studies were performed by conventional angiography in 75% and 49% and by MRA in 25% and 51% of patients at 6 and 18 months, respectively.

Four different sensitivity analyses (excluding patients with no angiographic follow-up study from analyses [total $n = 426$]; counting the 9 patients with no primary outcome as good or poor [$n = 444$]; including the 3 patients withdrawn before treatment as treatment failures [$n = 447$]) did not change the results (On-line Table 5). Repeating all analyses, adjusting for aneurysm location, dimension of the long or short axis, width of the neck, rupture status, or use of stents, did not change the results.

Exploratory analyses, including only patients in whom the target length of hydrogel coils was met (103/120, 85.8% in PRET-1, and 88/95, 92.6% in PRET-2) and repeating all sensitivity analyses, did not show any significant difference between platinum and hydrogel ($P > .08$ in all cases). There was a significant difference between patients in PRET-1 and PRET-2 when patients lost, withdrawn, or without a primary outcome and when the hydrogel target was not met were excluded ($n = 395$) ($P = .025$) (On-line Table 6).

The median packing density of hydrogel-treated aneurysms (50.9%) was significantly higher ($P < .001$) than that in patients

Table 1: Baseline characteristics of patients and aneurysms

	PRET-1		PRET-2		PRET	
	Platinum	Hydrogel	Platinum	Hydrogel	Platinum	Hydrogel
Total No. patients randomized	125	125	97	100	222	225
Male sex	35 (28.0%)	33 (26.4%)	33 (34%)	27 (27.0%)	68 (30.6%)	60 (26.7%)
Mean age (SD) (yr)	59 (11)	58 (11)	57 (12)	56 (10)	58 (12)	57 (11)
Multiple aneurysms	36 (28.8%)	36 (28.8%)	23 (23.7%)	22 (22.0%)	59 (26.6%)	58 (25.8%)
Ruptured aneurysms						
No. (%) of treatment group	37 (29.6%)	35 (28%)	2 (2.1%)	5 (5.0%)	39 (17.6%)	40 (17.8%)
No. (%) WFNS > II	3 (8.1%)	8 (22.9%)	0	0	3 (7.7%)	8 (20.0%)
Unruptured aneurysms						
mRS at baseline 0–2	85 (96.6%)	90 (100.0%)	94 (98.9%)	94 (98.9%)	179 (97.8%)	184 (99.5%)
mRS at baseline 3–5	3 (3.4%)	0	1 (1.1%)	1 (1.1%)	4 (2.2%)	1 (0.5%)
No. (%) symptomatic	24 (27.3%)	18 (20%)	8 (8.4%)	9 (9.5%)	32 (17.5%)	27 (14.6%)
Aneurysm size (maximal dimension)						
Mean (SD) (mm)	13.3 (4.9)	12.7 (4.3)	8.6 (5.8)	8.3 (5.5)	11.3 (5.8)	10.7 (5.3)
≥10 mm	97 (77.6%)	96 (76.8%)	29 (29.9%)	25 (25.0%)	126 (56.8%)	121 (53.8%)
1.0–9.9 mm[a]	28 (22.4%)	29 (23.2%)	68 (70.1%)	75 (75.0%)	96 (43.2%)	104 (46.2%)
10.0–14.9 mm	59 (47.2%)	66 (52.8%)	16 (16.5%)	14 (14.0%)	75 (33.8%)	80 (35.6%)
15.0–19.9 mm	25 (20.0%)	24 (19.2%)	5 (5.2%)	7 (7.0%)	30 (13.5%)	31 (13.8%)
20.0–24.9 mm	8 (6.4%)	4 (3.2%)	6 (6.2%)	1 (1.0%)	14 (6.3%)	5 (2.2%)
≥25 mm	5 (4.0%)	2 (1.6%)	2 (2.1%)	3 (3.0%)	7 (3.2%)	5 (2.2%)
Aneurysm neck						
Mean (SD) (mm)	5.0 (2.1)	4.8 (1.6)	4.5 (2.5)	4.6 (2.3)	4.8 (2.3)	4.7 (1.9)
Neck ≥4.0 (mm)	88 (70.4%)	94 (75.2%)	53 (54.6%)	58 (58.0%)	141 (63.5%)	152 (67.6%)
Aneurysm location, anterior	96 (76.8%)	104 (83.2%)	69 (71.1%)	70 (70.0%)	165 (74.3%)	174 (77.3%)
Internal carotid	58 (46.4%)	69 (55.2%)	43 (44.3%)	40 (40.0%)	101 (45.5%)	109 (48.4%)
Anterior cerebral	23 (18.4%)	18 (14.4%)	21 (21.6%)	24 (24.0%)	44 (19.8%)	42 (18.7%)
Middle cerebral	15 (12.0%)	17 (13.6%)	5 (5.2%)	6 (6.0%)	20 (9.0%)	23 (10.2%)
Aneurysm location, posterior	29 (23.2%)	21 (16.8%)	28 (28.9%)	30 (30.0%)	57 (25.7%)	51 (22.7%)
Basilar	23 (18.4%)	13 (10.4%)	21 (21.6%)	19 (19.0%)	44 (19.8%)	32 (14.2%)
Other posterior	6 (4.8%)	8 (6.4%)	7 (7.2%)	11 (11.0%)	13 (5.9%)	19 (8.4%)
Intended use of adjunct device	41 (32.8%)	42 (33.6%)	35 (36.1%)	38 (38.0%)	76 (34.2%)	80 (35.6%)

Note:—WFNS indicates World Federation of Neurological Societies.

[a] PRET-1 aneurysms recruited as ≥10 mm on noninvasive imaging have been measured using fiducials as <10 mm by the core laboratory; median size was 8.6 mm (mean, 8.3 ± 1.3 mm).

Table 2: Primary outcome in all patients in PRET[a]

	PRET-1		PRET-2		PRET	
	Platinum (*n* = 124)	Hydrogel (*n* = 120)	Platinum (*n* = 96)	Hydrogel (*n* = 95)	Platinum (*n* = 220)	Hydrogel (*n* = 215)
Primary outcome	55 (44.4%)	63 (52.5%)	47 (49.0%)	40 (42.1%)	102 (46.4%)	103 (47.9%)
Major recurrence	33 (26.6%)	35 (29.2%)	33 (34.4%)	25 (26.3%)	66 (30.0%)	60 (27.9%)
Retreatment	11 (8.9%)	19 (15.8%)	10 (10.4%)	6 (6.3%)	21 (9.5%)	25 (11.6%)
Initial treatment failure	3 (2.4%)	1 (0.8%)	0 (0.0%)	4 (4.2%)	3 (1.4%)	5 (2.3%)
SAH	1 (0.8%)	1 (0.8%)	1 (1.0%)	1 (1.1%)	2 (0.9%)	2 (0.9%)
Mass effect	0 (0.0%)	1 (0.8%)	3 (3.1%)	0 (0.0%)	3 (1.4%)	1 (0.5%)
Related mortality	1 (0.8%)	3 (2.5%)	0 (0.0%)	0 (0.0%)	1 (0.5%)	3 (1.4%)
Related morbidity	2 (1.6%)	1 (0.8%)	0 (0.0%)	1 (1.1%)	2 (0.9%)	2 (0.9%)
Last observation carried forward[b]	4 (3.2%)	2 (1.7%)	0 (0.0%)	3 (3.2%)	4 (1.8%)	5 (2.3%)

[a] Data are numbers.

[b] Residual aneurysm at initial treatment and no angiographic follow-up.

with platinum coils (22.0%). Patients reaching the primary outcome had a significantly lower packing density ($P < .001$) than patients without a recurrence, whether platinum or hydrogel was used (Table 3).

The periprocedural morbidity, mortality, and adverse events (up to 1 month) have previously been published.[20] Twenty-seven additional adverse events (14 platinum, 13 hydrogel) occurred after 1 month. Eighteen were serious (7 platinum, 11 hydrogel). Details are provided in Table 4.

Adverse events attributed to inflammation at any time after the procedure (including the first 30 days after treatment) occurred in 6 patients (4 platinum, 2 hydrogel).

Morbidity according to the modified Rankin Scale and mortality are summarized in Table 5. There were 16 deaths (3.6%, 3 platinum, 13 hydrogel; $P = .011$). Two deaths (both hydrogel) related to the initial SAH were reported previously. Two other deaths, one 148 days after the procedure (platinum), the other at an unknown time from an unknown cause following treatment (hydrogel; the patient was lost to follow-up after 1-month) were not initially reported and have been adjudicated to be treatment-related delayed deaths. Two deaths 31 and 474 days after treatment were related to SAH at follow-up (hydrogel and platinum, respectively). Two deaths at 64 and 693 days were retreatment-related deaths (both hydrogel). Deaths unrelated to the aneurysm

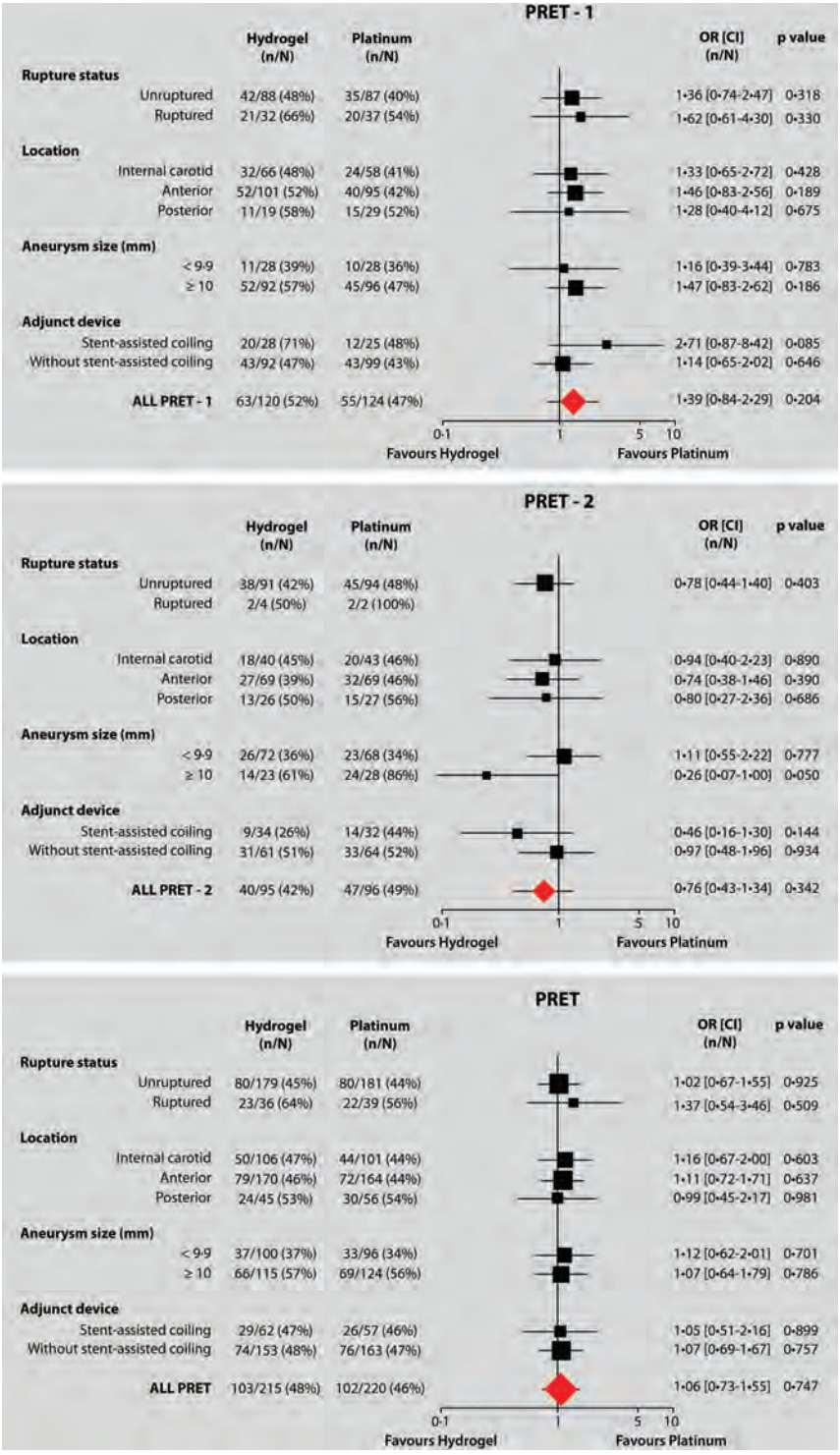

FIG 2. Subgroup analysis of primary outcome in PRET groups.

or its treatment were reported in 8 patients (1 platinum; 7 hydrogel). Details are provided in On-line Tables 7 and 8.

DISCUSSION

A randomized comparison did not show any significant difference between patients in the hydrogel and platinum groups when assessing the primary outcome—a composite of major angiographic recurrence and clinical status. This was true for both patients with large (PRET 1) and recurrent aneurysms (PRET 2) and for each component of the primary outcome. What is not surprising in these high-risk patients, angiographic outcomes were inferior compared with those in other coiling trials.[16,17,22,23] Safety endpoints were similar for the 2 groups, except for a greater number of deaths unrelated to the aneurysm or treatment (7 versus 1) in the hydrogel group. A careful review of individual cases indicates that this difference is probably a chance finding.

There were more missing primary outcomes in the hydrogel group ($n = 7$) than in the control group ($n = 2$). Although some of these outcomes were missing for reasons unrelated to treatment, reasons are not known for all patients. Sensitivity analyses indicated that missing data would not have affected trial results.

The median packing density of the hydrogel group was significantly higher than in the platinum group, but this finding did not translate into better long-term angiographic results. The volumetric packing density calculation assumes full hydrogel expansion, which might not occur in vivo. Preplanned analyses focusing on patients who have reached the "target hydrogel coiling strategy" did not show better results than those with platinum coiling. There was a correlation between packing density and recurrences for each group studied separately, suggesting that packing density is better understood as an index combining aneurysm characteristics (size, aspect ratio) and technical success of the coiling procedure (with any material) than as an independent mechanistic means to deliberately improve long-term results of embolization, at least with hydrogel in large and recurrent aneurysms.

Residual or recurrent aneurysms are signs that treatment may not be definitive. As expected, there were a few hemorrhagic episodes ($n = 4$ or 0.9%) during the 18-month follow-up, but 46 or 10.4% of patients were retreated and retreatments were planned for 34 other patients.

Inflammatory problems have previously been a concern with the use of hydrogel.[14,22,24-27] In PRET, adverse events that have been (rightly or wrongly) attributed to inflammation were transient and occurred rarely and with equal frequency in both groups.

Coiling of large and recurrent aneurysms proved safe.[20] There were few delayed adverse events after 1 month.

Treatment-related morbidity (4.0%) and mortality (0.7%) were relatively low for both groups. Unfortunately, the efficacy of coiling remains problematic, with poor long-term primary outcomes in nearly half of patients. Major angiographic recurrence rates were higher than those in other coiling studies,[8,28-30] but this finding was not unexpected for these high-risk patients; indeed, the trial hypothesized a 50% recurrence rate for the control group. Similar 50% recurrence rates for both hydrogel and platinum were reported for the subgroup of patients in the Hydrogel-Coated Coils versus Bare Platinum Coils for the Endovascular Treatment of Intracranial Aneurysms trial with >10-mm aneurysms.[14]

Whether patients treated with coiling should be followed to detect recurrences and whether recurrences should be retreated are questions that cannot be answered by the present data. We can only point out that despite retreatment, 3 patients in PRET-2 bled during follow-up; 2 others had progressive mass effect; residual or recurring aneurysms still occurred in >45% of patients; and re-retreatments were associated with serious adverse events in 3 patients.

How patients with large or recurrent aneurysms should be managed remains an open question. In the landmark International Subarachnoid Aneurysm Trial (ISAT), which has established the coiling of ruptured aneurysms compared with clipping, clinical outcomes of patients with aneurysms of >10 mm (n = 155) were similar (relative risk, 0.96; 95% CI, 0.65–1.42). Thus, clipping, reputed but not proved, at least for unruptured aneurysms,[31] to be more durable than coiling, is a reasonable option for some of these patients, though the long-term follow-up ISAT data con-

Table 3: Packing density versus primary outcome

	Platinum Primary Outcome (Angiographic Outcome Only)		Hydrogel Primary Outcome (Angiographic Outcome Only)		Total Primary Outcome (Angiographic Outcome Only)	
Packing Density[a]	No	Yes	No	Yes	No	Yes
PRET-1						
Valid No.	69	51	57	61	126	112
Percentile 25	14.72	11.92	33.91	18.55	18.28	13.79
Median	22.18	17.13	50.92	36.93	29.60	23.47
Median	35.52	27.61	89.26	58.88	53.60	46.90
PRET-2						
Valid No.	49	47	55	37	104	84
Percentile 25	18.15	6.02	34.62	11.64	24.46	7.37
Median	34.05	19.66	84.80	40.38	51.49	29.12
Percentile 75	60.15	43.21	172.95	94.72	111.77	65.92
PRET						
Valid No.	118	98	112	98	230	196
Percentile 25	15.23	7.65	34.27	17.91	21.81	12.55
Median	24.14	17.66	62.47	38.50	37.94	25.58
Percentile 75	43.72	35.71	114.34	71.66	74.87	50.58

[a] Packing density is coil volume (V) divided by aneurysm volume (VA). $V = \pi(c/2)^2 L$, where c is coil caliber and L is coil length. $VA = 4/3\ \pi\ ab\ (a + b)/2$, where a and b are half the long and short axes of the aneurysm.

Table 4: Adverse events[a]

	PRET-1		PRET-2		PRET	
	Platinum (n = 125)	Hydrogel (n = 123)	Platinum (n = 97)	Hydrogel (n = 99)	Platinum (n = 222)	Hydrogel (n = 222)
Total	24 (19.2%)	26 (21.1%)	13 (13.4%)	15 (15.2%)	37 (16.7%)	41 (18.5%)
SAH during follow-up	1 (0.8%)	0 (0.0%)	1 (1.0%)	2 (2.0%)	2 (0.9%)	2 (0.9%)
Mass effect	0 (0.0%)	1 (0.8%)	2 (2.1%)	0 (0.0%)	2 (0.9%)	1 (0.5%)
Stroke	1 (0.8%)	2 (1.6%)	1 (1.0%)	0 (0.0%)	2 (0.9%)	2 (0.9%)
TIA	0 (0.0%)	0 (0.0%)	0 (0.0%)	1 (1.0%)	0 (0.0%)	1 (0.5%)
Inflammatory	2 (1.6%)	0 (0.0%)	0 (0.0%)	0 (0.0%)	2 (0.9%)	0 (0.0%)
Subdural hematoma	0 (0.0%)	0 (0.0%)	0 (0.0%)	1 (1.0%)	0 (0.0%)	1 (0.5%)
Non-neurologic	3 (2.4%)	1 (0.8%)	0 (0.0%)	0 (0.0%)	3 (1.4%)	1 (0.5%)
Retreatment-related	1 (0.8%)	4 (3.3%)	2 (2.1%)	1 (1.0%)	3 (1.4%)	5 (2.3%)
Periprocedural event	16 (12.8%)	18 (14.6%)	7 (7.2%)	10 (10.1%)	23 (10.4%)	28 (12.6%)
Serious	15 (12.0%)	15 (12.2%)	5 (5.2%)	10 (10.1%)	20 (9.0%)	25 (11.3%)
Delayed	5 (4.0%)	7 (5.7%)	2 (2.1%)	4 (4.0%)	7 (3.2%)	11 (5.0%)
Periprocedure	10 (8.0%)	8 (6.5%)	3 (3.1%)	6 (6.1%)	13 (5.9%)	14 (6.3%)

[a] Adverse events were recorded during the trial. Periprocedural events (within 1 month of procedure) are lumped together. Data are numbers.

Table 5: Morbidity and mortality according to mRS at last follow-up[a]

	PRET-1		PRET-2		PRET	
mRS	Platinum (n = 125)	Hydrogel (n = 123)	Platinum (n = 97)	Hydrogel (n = 99)	Platinum (n = 222)	Hydrogel (n = 222)
0	88 (70.4%)	77 (62.6%)	60 (61.9%)	67 (67.7%)	148 (66.7%)	144 (64.9%)
1	19 (15.2%)	25 (20.3%)	23 (23.7%)	16 (16.2%)	42 (18.9%)	41 (18.5%)
2	7 (5.6%)	7 (5.7%)	10 (10.3%)	9 (9.1%)	17 (7.7%)	16 (7.2%)
3	1 (0.8%)	3 (2.4%)	3 (3.1%)	0 (0.0%)	4 (1.8%)	3 (1.4%)
4	5 (4.0%)	1 (0.8%)	1 (1.0%)	3 (3.0%)	6 (2.7%)	4 (1.8%)
5	2 (1.6%)	0 (0.0%)	0 (0.0%)	1 (1.0%)	2 (0.9%)	1 (0.5%)
6	3 (2.4%)	10 (8.1%)	0 (0.0%)	3 (3.0%)	3 (1.4%)	13 (5.9%)

[a] Data are numbers.

firm a low rebleed risk after de novo coiling and long-term outcome superiority over clipping.[9] Patients with large ruptured aneurysms could be offered participation in the ISAT II trial.[32] There are no randomized data for unruptured aneurysms, but a trial is ongoing.[4] Although meta-analyses of case series have reported improved angiographic results with stent-assisted coiling[12] or flow diversion[10] compared with historical coiling controls, preliminary results from the Flow Diversion in Intracranial Aneurysm Treatment trial have so far been below expectations.[11] Participation in these or other ongoing trials may be the best way to manage these high-risk patients.[33-36]

The PRET trial had several limitations. Operators could not be blinded to coil type. This may have affected case selection and coil selection and perhaps may have even modified the extent and completeness of the coiling procedure. Aneurysm volumes were not directly measured but were extrapolated from aneurysm dimensions; this method typically overestimates volumes and underestimates packing density. This is unlikely to have biased the comparison between groups. Recruitment was slowing down in the last years of enrollment, perhaps because treatment alternatives, such as flow diverters, were increasingly used for large and recurrent aneurysms. This may not affect the generalizability of conclusions, equally disappointing for both groups. The PRET-2 substudy was interrupted before the target number of patients was enrolled. Given the similarities in overall trial results, it is unlikely that a convincing difference between groups would have been shown had the trial reached its target. The relatively short 18-month follow-up was not completed by all patients, and the primary endpoint had to be imputed from the 6-month follow-up angiogram in 5.5% of patients. Short follow-up periods may not have captured all clinical consequences of recurrences, such as retreatments, along with the associated morbidity. Data monitoring was done on-line, with no local site visits to verify the data. Brain imaging studies were not imposed by protocol to verify the absence of asymptomatic complications. These perceived deficiencies are expected to affect treatment groups in a balanced manner.

ACKNOWLEDGMENTS

First and foremost, we acknowledge the support of patients and their relatives who agreed to participate in the study and who provided us with follow-up data. We also thank the medical, radiologic, and nursing staff of all participating centers. We are grateful to members of the Data Safety and Monitoring Committees (Sylvain Lanthier, Allan Fox). Implementing a study such as PRET requires considerable effort for a long time. Special thanks are due to Guylaine Gevry and her team at the PRET Coordination Head Office in Montreal for their outstanding work and indefectible commitment.

PRET Trial Collaborators

The PRET trial collaborators are listed in the order that participating sites joined the trial, with the number of patients recruited given in parentheses. Centre Hospitalier de l'Université de Montréal–Notre Dame Hospital, Montreal, Quebec, Canada: Principal Investigators, Jean Raymond, Alain Weill, and Daniel Roy; Coordinator, Ruby Klink (120). The Methodist Hospital, Houston, Texas: Principal Investigators, Richard Klucznik and Orlando Diaz; Coordinator, Marilyn Bautista (12). Kobe City Medical Center General Hospital, Kobe, Japan: Principal Investigators, Nobuyuki Sakai and Horotoshi Imamura (4). Medical University of South Carolina, Charleston, South Carolina: Principal Investigators, Aquilla Turk and Raymond Turner; Coordinator, Adrian Parker (26). State University of New York at Stony Brook University Medical Center, Stony Brook, New York: Principal Investigator, Henry Woo; Coordinators, Susan Fiore and Dawn Madigan (20). Oregon Health and Science University, Portland, Oregon: Principal Investigator, Stanley Barnwell; Coordinator, Sarah Ross-Jamieson (63). Cleveland Clinic, Cleveland, Ohio: Principal Investigator, Thomas Masaryk; Coordinator, Terese Wheeler (1). Centre Hospitalier Universitaire de Nancy-Hôpital Central, Nancy, France: Principal Investigator, Serge Bracard; special thanks to Dr Anne Laure Derelle (8). Leeds General Infirmary, Leeds, United Kingdom: Principal Investigator, Tony Goddard; Coordinator, Jonathan Pearce (also, central coordinator for the United Kingdom) (10). The Ottawa Hospital, Ottawa, Ontario, Canada: Principal Investigator, Marlise Santos; Coordinator, Betty Anne Schwarz (14). Instituto de Neurocirugía Dr Asenjo, Santiago, Chile: Principal Investigators, Juan-Gabriel Sordo Jara and Eduardo Bravo (14). University of Florida (Shands Hospital), Gainesville, Florida: Principal Investigators, J. Mocco and Brian Hoh; Coordinators, Bree Burks and Nicolle Wilson-Davis (29). University of Virginia Health System, Charlottesville, Virginia: Principal Investigator, Avery Evans; Coordinators, Claire McKinley and Thomas Tandy (39). Centre Hospitalier Universitaire de Nantes-Hôpital Guillaume et René Laennec, Nantes, France: Principal Investigator, Hubert Desal (23). West Virginia University Hospital, Morgantown, West Virginia: Principal Investigator, Jeffrey Carpenter; Coordinator, Jennifer Domico (8). State University of New York Upstate Medical University, Syracuse, New York: Principal Investigator, Eric Deshaies; Coordinators, Tina Craig, Kim Kasprowicz, Susan Hemingway, and Mark Villwock (10). University of Cincinnati Medical Center, Cincinnati, Ohio: Principal Investigator, Andrew Ringer; Coordinator, Rebecca Reinert (4). Washington University in St. Louis, St. Louis, Missouri: Principal Investigator, Christopher Moran; Coordinator, Angela Campbell (6). Queens Medical Centre, Nottingham, United Kingdom: Principal Investigator, Robert Lenthall; Coordinator, Alison Southam (12). Saint Francis Medical Center, Cape Girardeau, Missouri: Principal Investigator, Louis Caragine; Coordinators, Adrienne Jones and Kathy O'Howell (2). University of Oklahoma Health Sciences Center, Oklahoma City, Oklahoma: Principal Investigator, Steven Hoover; Coordinators, Brian Bridges and Bradley Hightower (11). Centre Hospitalier Sainte Anne, Paris, France: Principal Investigator, Olivier Naggara (2). University of Mississippi Health Care, Jackson, Mississippi: Principal Investigator, Razvan Buciuc; Coordinator, David Gordy (3). University of Alberta Hospital, Edmonton, Alberta, Canada: Principal Investigator, Tim E. Darsaut (2). Vanderbilt University Medical Center, Nashville, Tennessee: Principal Investigator, J. Mocco; Coordinators, Chesney Sarah Oravec and Jessica Sparks Marlin (4). Angiographic Core Laboratory: Phil White, Robin Sellar, Lynn Forrester, Newcastle and Edinburgh, UK.

Disclosures: Jean Raymond—*RELATED*: *Grant*: MicroVention, *Comments*: unrestricted investigator-led research grant*; *UNRELATED*: *Grants/Grants Pending*: Canadian Institutes of Health Research and Johnson & Johnson, DePuy Synthes (Codman Neuro), *Comments*: peer-review grant for Canadian UnRuptured Endovascular versus Surgery study and unrestricted investigator-led research grant for the Delta study, respectively.* Avery J. Evans—*RELATED*: *Grant*: MicroVention.* J. Mocco—*RELATED*: *Grant*: Stryker, Penumbra, Medtronic, *Comments*: research funding*; *UNRELATED*: *Consultancy*: TSP, Cerebrotech Medical, Rebound Medical, Pulsar Vascular, EndoStream; *Stock/Stock Options*: Blockade Medical, TSP, Cerebrotech Medical. Aquilla S. Turk—*RELATED*: *Grant*: Stryker, MicroVention, Penumbra, Medina Medical, Covidien, *Comments*: research funding*; *Consulting Fee or Honorarium*: Stryker, MicroVention, Penumbra, Medina Medical, *Comments*: honorarium, consulting; *Support for Travel to Meetings for the Study or Other Purposes*: Stryker, MicroVention, Penumbra, Medina Medical, *Comments*: coverage for airfare or hotel; *UNRELATED*: *Consultancy*: Stryker, MicroVention, Penumbra, Medina Medical; *Grants/Grants Pending*: Stryker, MicroVention, Penumbra, Medina Medical*; *Payment for Lectures Including Service on Speakers Bureaus*: Stryker, MicroVention, Penumbra, Medina Medical; *Stock/Stock Options*: Medina Medical, Three Rivers. Raymond D. Turner—*RELATED*: *Grant*: MicroVention, Penumbra, Medtronic, Pulsar Vascular, Sequent Medical, Stryker*; *Consulting Fee or Honorarium*: MicroVention, Penumbra, Medtronic, Pulsar Vascular, Sequent Medical, Stryker, Blockade Medical, Q'Apel Medical, Rebound Medical, Codman Neuro. David Fiorella—*RELATED*: *Grant*: Sequent Medical, MicroVention, National Institutes of Health, *Comments*: Principal Investigator responsibilities for trials,* funding indirectly related to study at hand; *Consulting Fee or Honorarium*: Sequent Medical, MicroVention, Medtronic, Stryker, Penumbra, *Comments*: proctoring and consulting; *Support for Travel to Meetings for the Study or Other Purposes*: Sequent Medical, MicroVention, Medtronic, Stryker, Penumbra; *UNRELATED*: *Consultancy*: Sequent Medical, MicroVention, Medtronic, Stryker, Penumbra, Codman Neuro/JNJ; *Payment for Lectures Including Service on Speakers Bureaus*: MicroVention, Penumbra; *Patents (Planned, Pending or Issued)*: Codman Neuro/Johnson & Johnson.* Alain Weill—*UNRELATED*: *Consultancy*: Balt Extrusion, *Comments*: member of the Adverse Event Committee of LEO 2 study, a registry of LEO stent used in France.* Philip M. White—*UNRELATED*: *Consultancy*: MicroVention, Codman Neuro, *Comments*: for educational training; *Grants/Grants Pending*: MicroVention Terumo for STABILISE thrombectomy trial*; *Travel/Accommodations/Meeting Expenses Unrelated to Activities Listed*: MicroVention Terumo. Daniel Roy—*RELATED*: *Grant:* MicroVention, *Comments*: unrestricted research fund for PRET.* *Money paid to the institution.

REFERENCES

1. Guglielmi G, Viñuela F, Dion J, et al. **Electrothrombosis of saccular aneurysms via endovascular approach, part 2: preliminary clinical experience.** *J Neurosurg* 1991;75:8–14 CrossRef Medline
2. Guglielmi G, Viñuela F, Sepetka I, et al. **Electrothrombosis of saccular aneurysms via endovascular approach, part 1: electrochemical basis, technique, and experimental results.** *J Neurosurg* 1991;75:1–7 CrossRef Medline
3. Molyneux A, Kerr R, Stratton I, et al; International Subarachnoid Aneurysm Trial (ISAT) Collaborative Group. **International Subarachnoid Aneurysm Trial (ISAT) of neurosurgical clipping versus endovascular coiling in 2143 patients with ruptured intracranial aneurysms: a randomised trial.** *Lancet* 2002;360:1267–74 CrossRef Medline
4. Darsaut TE, Findlay JM, Raymond J. **The design of the Canadian UnRuptured Endovascular versus Surgery (CURES) trial.** *Can J Neurol Sci* 2011;38:236–41 CrossRef Medline
5. Raymond J, Molyneux AJ, Fox AJ, et al; TEAM Collaborative Group. **The TEAM trial: safety and efficacy of endovascular treatment of unruptured intracranial aneurysms in the prevention of aneurysmal hemorrhages: a randomized comparison with indefinite deferral of treatment in 2002 patients followed for 10 years.** *Trials* 2008; 9:43 CrossRef Medline
6. Crobeddu E, Lanzino G, Kallmes DF, et al. **Review of 2 decades of aneurysm-recurrence literature, part 2: managing recurrence after endovascular coiling.** *AJNR Am J Neuroradiol* 2013;34:481–85 CrossRef Medline
7. Naggara ON, Lecler A, Oppenheim C, et al. **Endovascular treatment of intracranial unruptured aneurysms: a systematic review of the literature on safety with emphasis on subgroup analyses.** *Radiology* 2012;263:828–35 CrossRef Medline
8. Raymond J, Guilbert F, Weill A, et al. **Long-term angiographic recurrences after selective endovascular treatment of aneurysms with detachable coils.** *Stroke* 2003;34:1398–403 CrossRef Medline
9. Molyneux AJ, Birks J, Clarke A, et al. **The durability of endovascular coiling versus neurosurgical clipping of ruptured cerebral aneurysms: 18 year follow-up of the UK cohort of the International Subarachnoid Aneurysm Trial (ISAT).** *Lancet* 2015;385:691–97 CrossRef Medline
10. Brinjikji W, Murad MH, Lanzino G, et al. **Endovascular treatment of intracranial aneurysms with flow diverters: a meta-analysis.** *Stroke* 2013;44:442–47 CrossRef Medline
11. Raymond J, Gentric JC, Darsaut TE, et al. **Flow diversion in the treatment of aneurysms: a randomized care trial and registry.** *J Neurosurg* 2016 Nov 4:1–9. [Epub ahead of print] Medline
12. Hong Y, Wang YJ, Deng Z, et al. **Stent–assisted coiling versus coiling in treatment of intracranial aneurysm: a systematic review and meta-analysis.** *PLoS One* 2014;9:e82311 CrossRef Medline
13. Phan K, Huo YR, Jia F, et al. **Meta-analysis of stent-assisted coiling versus coiling-only for the treatment of intracranial aneurysms.** *J Clin Neurosci* 2016;31:15–22 CrossRef Medline
14. White PM, Lewis SC, Gholkar A, et al; HELPS trial collaborators. **Hydrogel-coated coils versus bare platinum coils for the endovascular treatment of intracranial aneurysms (HELPS): a randomised controlled trial.** *Lancet* 2011;377:1655–62 CrossRef Medline
15. Broeders JA, Ahmed Ali U, Molyneux AJ, et al. **Bioactive versus bare platinum coils for the endovascular treatment of intracranial aneurysms: systematic review and meta-analysis of randomized clinical trials.** *J Neurointerv Surg* 2016;8:898–908 CrossRef Medline
16. McDougall CG, Johnston SC, Gholkar A, et al; MAPS Investigators. **Bioactive versus bare platinum coils in the treatment of intracranial aneurysms: the MAPS (Matrix and Platinum Science) trial.** *AJNR Am J Neuroradiol* 2014;35:935–42 CrossRef Medline
17. Coley S, Sneade M, Clarke A, et al. **Cerecyte coil trial: procedural safety and clinical outcomes in patients with ruptured and unruptured intracranial aneurysms.** *AJNR Am J Neuroradiol* 2012;33: 474–80 CrossRef Medline
18. Molyneux AJ, Clarke A, Sneade M, et al. **Cerecyte coil trial: angiographic outcomes of a prospective randomized trial comparing endovascular coiling of cerebral aneurysms with either Cerecyte or bare platinum coils.** *Stroke* 2012;43:2544–50 CrossRef Medline
19. Raymond J, Roy D, White PM, et al; Icone Collaborative Group. **A randomized trial comparing platinum and hydrogel-coated coils in Patients Prone to Recurrence after Endovascular Treatment (the PRET trial).** *Interv Neuroradiol* 2008;14:73–83 Medline
20. Raymond J, Klink R, Chagnon M, et al; PRET Collaborative Group. **Patients prone to recurrence after endovascular treatment: periprocedural results of the PRET randomized trial on large and recurrent aneurysms.** *AJNR Am J Neuroradiol* 2014;35:1667–76 CrossRef Medline
21. Roy D, Milot G, Raymond J. **Endovascular treatment of unruptured aneurysms.** *Stroke* 2001;32:1998–2004 CrossRef Medline
22. White PM, Lewis SC, Nahser H, et al; HELPS Trial Collaboration. **HydroCoil Endovascular Aneurysm Occlusion and Packing Study (HELPS trial): procedural safety and operator-assessed efficacy results.** *AJNR Am J Neuroradiol* 2008;29:217–23 CrossRef Medline
23. Molyneux AJ, Kerr RS, Yu LM, et al; International Subarachnoid Aneurysm Trial (ISAT) Collaborative Group. **International subarachnoid aneurysm trial (ISAT) of neurosurgical clipping versus endovascular coiling in 2143 patients with ruptured intracranial aneurysms: a randomised comparison of effects on survival, dependency, seizures, rebleeding, subgroups, and aneurysm occlusion.** *Lancet* 2005;366:809–17 CrossRef Medline
24. Im SH, Han MH, Kwon BJ, et al. **Aseptic meningitis after embolization of cerebral aneurysms using hydrogel-coated coils: report of three cases.** *AJNR Am J Neuroradiol* 2007;28:511–12 Medline
25. Meyers PM, Lavine SD, Fitzsimmons BF, et al. **Chemical meningitis after cerebral aneurysm treatment using two second-generation aneurysm coils: report of two cases.** *Neurosurgery* 2004;55:1222 CrossRef Medline
26. Turner RD, Byrne JV, Kelly ME, et al. **Delayed visual deficits and monocular blindness after endovascular treatment of large and gi-**

ant paraophthalmic aneurysms. *Neurosurgery* 2008;63:469–74; discussion 474–75 CrossRef Medline
27. Xu DS, Hurley MC, Batjer HH, et al. **Delayed cranial nerve palsy after coiling of carotid cavernous sinus aneurysms: case report.** *Neurosurgery* 2010;66:E1215–16 CrossRef Medline
28. Byrne JV, Sohn MJ, Molyneux AJ, et al. **Five-year experience in using coil embolization for ruptured intracranial aneurysms: outcomes and incidence of late rebleeding.** *J Neurosurg* 1999;90:656–63 CrossRef Medline
29. Cognard C, Weill A, Castaings L, et al. **Intracranial berry aneurysms: angiographic and clinical results after endovascular treatment.** *Radiology* 1998;206:499–510 CrossRef Medline
30. Adams WM, Laitt RD. **Aneurysm remnants.** *Neurointerventionist* 2000;1:74–83
31. Kotowski M, Naggara O, Darsaut TE, et al. **Safety and occlusion rates of surgical treatment of unruptured intracranial aneurysms: a systematic review and meta-analysis of the literature from 1990 to 2011.** *J Neurol Neurosurg Psychiatry* 2013;84:42–48 CrossRef Medline
32. Darsaut TE, Jack AS, Kerr RS, et al. **International Subarachnoid Aneurysm Trial-ISAT, part II: study protocol for a randomized controlled trial.** *Trials* 2013;14:156 CrossRef Medline
33. Darsaut TE, Raymond J. **The design of the STenting in Aneurysm Treatments (STAT) trial.** *J Neurointerv Surg* 2012;4:178–81 CrossRef Medline
34. Raymond J, Darsaut TE, Guilbert F, et al. **Flow diversion in aneurysms trial: the design of the FIAT study.** *Interv Neuroradiol* 2011;17:147–53 Medline Medline
35. Turk AS 3rd, Martin RH, Fiorella D, et al. **Flow diversion versus traditional endovascular coiling therapy: design of the prospective LARGE aneurysm randomized trial.** *AJNR Am J Neuroradiol* 2014;35:1341–45 CrossRef Medline
36. Gory B, Bonafé A, Pierot L, et al. **Safety and efficacy of flow-diverter stents in endovascular treatment of intracranial aneurysm: interest of the prospective DIVERSION observational study.** *J Neuroradiol* 2014;41:93–96 CrossRef Medline

Reduced Patient Radiation Exposure during Neurodiagnostic and Interventional X-Ray Angiography with a New Imaging Platform

K. van der Marel, S. Vedantham, I.M.J. van der Bom, M. Howk, T. Narain, K. Ty, A. Karellas, M.J. Gounis, A.S. Puri, and A.K. Wakhloo

ABSTRACT

BACKGROUND AND PURPOSE: Advancements in medical device and imaging technology as well as accruing clinical evidence have accelerated the growth of the endovascular treatment of cerebrovascular diseases. However, the augmented role of these procedures raises concerns about the radiation dose to patients and operators. We evaluated patient doses from an x-ray imaging platform with radiation dose–reduction technology, which combined image noise reduction, motion correction, and contrast-dependent temporal averaging with optimized x-ray exposure settings.

MATERIALS AND METHODS: In this single-center, retrospective study, cumulative dose-area product inclusive of fluoroscopy, angiography, and 3D acquisitions for all neurovascular procedures performed during a 2-year period on the dose-reduction platform were compared with a reference platform. Key study features were the following: The neurointerventional radiologist could select the targeted dose reduction for each patient with the dose-reduction platform, and the statistical analyses included patient characteristics and the neurointerventional radiologist as covariates. The analyzed outcome measures were cumulative dose (kerma)-area product, fluoroscopy duration, and administered contrast volume.

RESULTS: A total of 1238 neurointerventional cases were included, of which 914 and 324 were performed on the reference and dose-reduction platforms, respectively. Over all diagnostic and neurointerventional procedures, the cumulative dose-area product was significantly reduced by 53.2% (mean reduction, 160.3 Gy $\times$ cm^2; $P < .0001$), fluoroscopy duration was marginally significantly increased (mean increase, 5.2 minutes; $P = .0491$), and contrast volume was nonsignificantly increased (mean increase, 15.3 mL; $P = .1616$) with the dose-reduction platform.

CONCLUSIONS: A significant reduction in patient radiation dose is achievable during neurovascular procedures by using dose-reduction technology with a minimal impact on workflow.

ABBREVIATIONS: CBCT = conebeam CT; CP_{KA} = cumulative dose (kerma)-area product; 3DRA = 3D rotational angiography; EAKR = phantom-entrance air kerma rate; IP_{DRT} = imaging platform with dose-reduction technology; IP_R = reference imaging platform; $K_{a,r}$ = air kerma rate at the fluoroscopic reference point; LAT = lateral plane of the biplane system; P_{KA} = dose (kerma)-area product; RAKR = image-receptor (detector) entrance air kerma rate

The advancement of neurointerventional practice offers increasingly safe and minimally invasive treatment for a variety of neurovascular diseases. In most cases, the benefits of neurointerventional treatment afforded by fluoroscopic image guidance clearly outweigh the associated radiation risks to patients, especially in comparison with invasive surgical alternatives.[1] However, the growing use of diagnostic procedures and complex fluoroscopy-guided interventions[2] has led to heightened concerns over ionizing radiation exposure to patients and staff.[3,4]

To address these concerns, a new commercially available angiographic imaging platform has been developed.[5] Its dose-reduction strategy applies to digital fluoroscopy and digital subtraction angiography, which accounts for approximately 70%–80% of the total patient radiation dose in vascular angiographic proce-

Received July 15, 2016; accepted after revision October 11.

From the Department of Radiology (K.v.d.M., S.V., M.H., T.N., K.T., A.K., M.J.G., A.S.P., A.K.W.), New England Center for Stroke Research, University of Massachusetts Medical School, Worcester, Massachusetts; and Philips Healthcare (I.M.J.v.d.B.), Best, the Netherlands.

This work was supported, in part, by a grant from Philips Healthcare.

K. van der Marel and S. Vedantham contributed equally to this work.

Paper previously presented at: Annual Meeting of the American Society of Neuroradiology and the Foundation of the ASNR Symposium, April 25–30, 2015; Chicago, Illinois; and Annual Meeting of the Society of NeuroInterventional Surgery, July 27–31, 2015; San Francisco, California.

Please address correspondence to Matthew J. Gounis, PhD, Department of Radiology, New England Center for Stroke Research, 55 Lake Ave N, Room SA-107R, Worcester, MA 01655; e-mail: Matthew.Gounis@umassmed.edu; @MattGounis

Indicates article with supplemental on-line table.
Indicates article with supplemental on-line photos

http://dx.doi.org/10.3174/ajnr.A5049

dures.[6,7] At the core of the system is an image postprocessing chain intended to yield diagnostic-quality DSA images at a lower radiation dose to the patient.[7] Key features of this image-processing chain are multiscale implementations of real-time motion correction, image contrast-dependent temporal averaging, and image noise reduction.[7] Lower dose acquisitions further allow the use of a smaller focal spot size, reducing magnification-dependent focal spot blur.[7] Additional hardware optimization includes the use of Cu beam filtration, depending on x-ray tube loading and a narrower x-ray pulse width.[8] Herein, these noise reduction algorithms and optimized exposure settings[7] will be collectively referred to as "dose-reduction technology," which is implemented on the dose-reduction x-ray imaging platform (IP_{DRT}).

Procedural dose reductions and the noninferiority of image quality by using IP_{DRT} have been described for iliac[9,10] and coronary angiography in adults[8,11-13] and in children.[13] For neuroangiographic procedures, a randomized, blinded review of consecutive DSA runs with dose-reduction technology targeting one-fourth of the standard radiation dose showed the ability to maintain diagnostic image quality.[7] A larger European study in 614 patients provided further evidence of significant reductions in total dose-area products of 62% and 65% for diagnostic and interventional procedures, respectively, while not significantly affecting fluoroscopy time, procedure duration, and the number of acquired images.[5]

A unique aspect of this study was that the neurointerventional radiologist with the dose-reduction platform had the flexibility to select, per case and per acquisition, a targeted dose reduction of 0%, 50%, or 75% as preferred, rather than using a protocol with a prespecified dose-reduction target.[5] This paradigm was investigated so that any equivocal image finding may be better visualized at different settings. Our study investigated the dose-reduction achieved in cumulative dose (kerma)-area product (CP_{KA}) by using such a flexible protocol for common interventional treatments and diagnostic examinations based on a retrospective review of all such procedures during a 2-year period in a North American academic practice. In addition, a key feature of this study that distinguishes it from prior studies was the inclusion of the neurointerventional radiologist (operator) and patient-specific factors as covariates in the statistical analyses.

Table 1: Maximum entrance air kerma rates for the 3 fluoroscopic modes I, II, and III on the reference and dose-reduction platforms[a]

Platform, Mode	Frames/Second	Filtration	Maximum EAKR (mGy/min)
Reference			
I	6	0.4 mm Cu +1 mm Al	22
II	12.5	0.4 mm Cu +1 mm Al	44
III	12.5	0.1 mm Cu +1 mm Al	79
DRT			
I	15	0.4 mm Cu +1 mm Al	11
II	15	0.4 mm Cu +1 mm Al	26
III	15	0.1 mm Cu +1 mm Al	62

Note:—DRT indicates dose-reduction technology.

[a] The operator chooses the fluoroscopy mode on the dose-reduction platform independent of the DSA program and the targeted dose-reduction setting used for angiography.

MATERIALS AND METHODS

This study was conducted in adherence to a protocol approved by our institutional review board and in compliance with the Health Insurance Portability and Accountability Act. Our institutional review board waived the requirement for informed consent for this retrospective study.

Included were neurointerventional and diagnostic procedures performed in 2 dedicated neurointerventional radiology suites during a 2-year time period from January 2, 2013, to December 30, 2014. Initially during approximately 1 year (January 2, 2013, to January 21, 2014), both neurointerventional suites (AlluraXper FD20/10 and FD20/20; Philips Healthcare, Best, the Netherlands) were not equipped with dose-reduction technology. In January 2014, dose-reduction technology was installed in 1 system (Allura Clarity FD20/10; Philips Healthcare). All procedures and examinations performed on this system subsequent to the installation of dose-reduction technology are referred to as performed on the IP_{DRT}. The other system (AlluraXper FD20/20) continued to be operated without dose-reduction technology. All procedures and examinations performed on this system and those performed on the FD20/10 system before installation of dose-reduction technology are referred to as performed on the "reference" platform (IP_R). For the FD20/20 system, the small and large focal spot sizes (nominal) were 0.4 and 0.7 mm in both planes. For the FD 20/10 system, which is equipped with a smaller detector in the lateral (LAT) plane, the small and large focal spot sizes (nominal) were 0.4 and 0.7 mm for the anteroposterior plane and 0.5 and 0.8 mm for the lateral plane.

The programmed maximum entrance air kerma rates (EAKRs) for each of the 3 available fluoroscopy modes were reduced for IP_{DRT} compared with IP_R. The frame rate, x-ray beam filtration, and maximum EAKR are summarized in Table 1 and were identical for both planes. For both platforms, fluoroscopic mode II was the default mode. For this mode, quality-control audits performed by an independent American Board of Radiology–certified diagnostic medical physicist encompassing the study period were collected and were used to validate the system-reported air kerma rate at the fluoroscopic reference point ($\dot{K}_{a,r}$) (Table 2). Because the deviations from unity for the ratios of measured and system-reported $\dot{K}_{a,r}$ were comparable with external dosimeter readings and positioning uncertainties,[14] no correction was performed

Table 2: Measured entrance air kerma rates for a typical patient examination and for the largest FOV in fluoroscopic mode II preferred for clinical imaging[a]

System	DRT	Plane	kV	Focal Spot (mm)	Measured EAKR (mGy/min)	$\dot{K}_{a,r}$ Ratio
FD 20/20	No	AP	68 ± 1	Small (0.4)	5.1 ± 0.2	1.03 ± 0.12
		LAT	69 ± 1	Small (0.4)	6.1 ± 1.0	1.00 ± 0.04
FD 20/10	Before	AP	68 ± 1	Small (0.4)	4.9 ± 1.0	1.07 ± 0.03
		LAT	72 ± 4	Small (0.5)	6.3 ± 3.4	0.97 ± 0.004
	After	AP	68 ± 1	Small (0.4)	2.8 ± 0.4	0.96 ± 0.08
		LAT	73 ± 2	Small (0.5)	4.4 ± 0.6	1.01 ± 0.1

Note:—AP indicates anteroposterior; DRT, dose-reduction technology.

[a] For each system, the selected kilovolt and x-ray focal spot along with its nominal size (millimeter) for each plane are summarized. For the FD 20/10 system, these values are reported before and after the installation of the DRT. The x-ray beam filtration is 0.4 mm Cu and 1 mm of Al for all systems, platforms, and planes.

Table 3: DSA programmed settings for the image-receptor (detector) entrance air kerma rate for a typical patient examination with the largest FOV on both platforms[a]

System	DRT	Acquisition Protocol	kV	Filtration	Focal Spot (mm)	Programmed RAKR (μGy/frame)
FD 20/20	No	Standard	80	0.1 mm Cu +1 mm Al	Large (AP/LAT: 0.7 mm)	4.0
FD 20/10	Before	Standard	80	0.1 mm Cu +1 mm Al	Large (AP: 0.7 mm; LAT: 0.8 mm)	4.0
	After	Quarter	75	0.1 mm Cu +1 mm Al	Small (AP: 0.4 mm; LAT: 0.5 mm)	0.7
		Half	78	No added filtration	Small (AP: 0.4 mm; LAT: 0.5 mm)	1.0
		Full	80	0.1 mm Cu +1 mm Al	Large (AP: 0.7 mm; LAT: 0.8 mm)	4.0

Note:—AP indicates anteroposterior; DRT, dose-reduction technology.

[a] The dose-reduction platform was equipped with 3 acquisition protocols in which the "full-dose" protocol reverts to the reference platform hardware and software settings ("standard" dose protocol). The programmed settings are identical for both planes in each system and for each acquisition protocol.

to system-reported data. Also, from Table 2, it can be inferred that for IP_{DRT}, the EAKR was approximately reduced by 50% compared with IP_R.

Regarding DSA acquisitions, the programmed settings for the image-receptor (detector) entrance air kerma rate (RAKR) for IP_R is shown in Table 3 and is referred to as "standard" acquisition protocol. The default setting programmed for the IP_{DRT} targeted an approximate 75% reduction in EAKR with respect to the IP_R, herein referred to as "quarter-dose" protocol. However, the neurointerventional radiologist, on the basis of patient-, procedure-, and acquisition-specific needs had the flexibility to select either the "quarter-dose" protocol; a "half-dose" protocol, which reduced the EAKR by approximately 50% with the dose-reduction technology; or, in rare circumstances, to revert to the reference platform hardware and software settings at 100% of the original dose, referred to as "full-dose" protocol and is identical to the "standard" protocol. The RAKRs for the 3 acquisition protocols are summarized in Table 3. The programmed settings were identical for both planes in each system and for each acquisition protocol.

Data Collection

The following information was retrospectively collected for each procedure or examination from the neurointerventional suites during the analyzed time period: procedure type classified into 10 categories (diagnostic angiography, aneurysm coil embolization, flow-diverter placement, intra-arterial vasospasm treatment, thrombectomy for acute ischemic stroke, stent-assisted aneurysm coiling, epistaxis treatment, carotid stent placement, brain AVM embolization, and dural AVF treatment), cumulative dose-area product in units of Gy $\times$ cm^2, total fluoroscopy duration (minutes), administered contrast volume (milliliter), names of the neurointerventional radiologists performing the procedure or examination labeled as "operators," and a selection of patient characteristics that may reflect differences in outcome measures. The collected patient characteristics included age, sex, body weight (kg), preprocedural blood pressure, and medical history such as hypertension, chronic obstructive pulmonary disorder, coronary artery disease, obesity, and diabetes mellitus. The patient characteristics were obtained from electronic medical records and procedure documents. Contrast volume was extracted from procedure documents. Cumulative dose (kerma)-area product and total fluoroscopy duration were extracted from procedure documents or retrieved from a Cloud-based dose-monitoring system (DoseWise Portal; Philips Healthcare). The dose-monitoring system gathered and anonymized system-generated dose-area product (P_{KA}) for each fluoroscopic, angiographic, and 3D imaging acquisition, and the CP_{KA} was aggregated from all acquisitions for that procedure. The CP_{KA} reported in this study is for the entire procedure and is inclusive of 3D rotational angiography (3DRA) and conebeam CT (CBCT), if performed, which do not benefit from dose-reduction technology enabled by the IP_{DRT} platform.

Data Preparation

A total of 1592 procedures were performed during the 2-year period in the 2 suites. After excluding spinal procedures (n = 260), cases with multiple or mixed treatment procedures (n = 11), partial diagnostic or partial/follow-up treatment studies (n = 14), other non-neurointerventional procedures (n = 25), and aneurysm-embolization procedures without coils or flow diverters (n = 4), we included data for the remaining cases (n = 1278). Cases with ≥1 missing outcome variable (n = 27) or patient-related factors (n = 13) were discarded, resulting in 1238/1592 (77.7%) cases available for analysis.

The 3 outcome variables of interest analyzed in the study were CP_{KA}, fluoroscopy duration, and administered contrast volume. Four interventional neuroradiologists performed these procedures. For procedures involving >1 operator, we could not accurately apportion the outcome variables. Therefore, any procedure involving >1 operator was coded as >1 operator. Patient medical history, with the exception of hypertension, was binary-coded for each condition. History of hypertension was combined with the preprocedural blood pressure measurement to generate a 4-point categoric scale: 0, no history of hypertension with preprocedural systolic and diastolic measurements of <140 and 90 mm Hg, respectively; 1, a history of hypertension and preprocedural systolic and diastolic measurements of <140 and 90 mm Hg, respectively; 2, no history of hypertension and preprocedural systolic and diastolic measurements of either ≥140 or ≥90 mm Hg, respectively; and, 3, a history of hypertension and preprocedural systolic and diastolic measurements of either ≥140 or ≥90 mm Hg, respectively.

Statistical Analysis

All statistical analyses were performed by using SAS 9.3 (SAS Institute, Cary, North Carolina). Generalized linear models were used to quantify the changes in the 3 outcome measures between the 2 neurointerventional imaging platforms. The outcome variables were appropriately Box-Cox transformed before statistical modeling. All models included the platform type (IP_{DRT} or IP_R)

and the neurointerventional procedure category as independent variables; and inclusion of covariates (operator, patient characteristics) was determined by using stepwise selection based on the corrected Akaike Information Criterion.[15] For each model, the least squares means and the confidence intervals for each platform and the Sidak multiple comparison–adjusted *P* values for the differences in least squares means between the 2 imaging platforms were obtained. The differences in least squares means between IP_{DRT} and IP_R and the percentage change were computed. Effects associated with $P < .05$ were considered statistically significant.

Table 4: Patient demographics and number of cases performed on each imaging platform[a]

	Reference Platform	Dose-Reduction Platform
No. of cases		
Diagnostic	654 (71.6%)	173 (53.4%)
Coil embolization	45 (5.0%)	42 (12.2%)
Flow diverter	58 (6.5%)	26 (7.6%)
Vasospasm	34 (3.7%)	26 (8.0%)
Thrombectomy	37 (4.1%)	19 (5.5%)
Stent-assisted coiling	27 (3.0%)	15 (4.4%)
Carotid stenting	25 (2.8%)	9 (2.6%)
Epistaxis	17 (1.9%)	5 (1.5%)
AVM	10 (1.1%)	6 (1.7%)
AVF	7 (0.8%)	3 (0.9%)
Total	914 (73.8%)	324 (26.2%)
Patient characteristics		
Age (yr)	57.4 ± 14.7	56.6 ± 15.2
Weight (kg)	79.3 ± 19.9	77.6 ± 18.4
Male	370 (40.5%)	134 (41.4%)
Female	544 (59.5%)	190 (58.6%)
Hypertension	276 (30.2%)	89 (27.5%)
Medical history		
Diabetes	113 (12.4%)	39 (12.0%)
CAD	67 (7.3%)	21 (6.5%)
COPD	61 (6.7%)	26 (8.0%)
Hypertension	496 (54.3%)	177 (54.6%)
Obesity	53 (5.8%)	17 (5.2%)
Operator		
1	59 (6.5%)	18 (5.6%)
2	433 (47.4%)	175 (54.0%)
3	249 (27.2%)	23 (7.1%)
4	79 (8.6%)	92 (28.4%)
Multiple	94 (10.3%)	16 (4.9%)

Note:—CAD indicates coronary artery disease; COPD, chronic obstructive pulmonary disorder.

[a] Data are presented as number (percentage) or mean ± SD. The number of patients with preprocedural hypertension is reported under "Patient characteristics," while the number of patients with a documented history of hypertension is reported under "Medical history."

RESULTS

Patient demographics and the number of cases are summarized in Table 4. Among the 1238 cases analyzed, 914 were performed on the IP_R and 324 were performed on the IP_{DRT}. The diagnostic examinations were 71.6% and 53.4% of the cases on the reference and dose-reduction platforms, respectively. All results are presented after adjusting for neurointerventional radiologist and patient characteristics in each model.

Procedural Cumulative Dose-Area Product

Overall and across all diagnostic examinations and neurointerventional procedures, the IP_{DRT} was associated with a significant reduction in procedural CP_{KA}, inclusive of all executed fluoroscopic, angiographic, and 3D imaging acquisitions (53.2%; mean reduction, 160.3 Gy × cm^2; $P < .0001$) compared with the IP_R (Table 5). Most cases were diagnostic procedures (Table 4) and yielded a 63.3% reduction (mean reduction, 88.2 Gy × cm^2; $P < .0001$) with IP_{DRT}. For diagnostic procedures, least squares means for the CP_{KA} were 139.4 Gy × cm^2 (95% CI, 131.6–147.6 Gy × cm^2) for the IP_R and 51.1 Gy × cm^2 (95% CI, 47–55.6 Gy × cm^2) for the IP_{DRT}. Across all interventional procedures, a 52.7% reduction (mean reduction, 171.8 Gy × cm^2; $P < .0001$) was observed with IP_{DRT} compared with IP_R, and the least squares means for the CP_{KA} were 326.3 Gy × cm^2 (95% CI, 295.5–360.4 Gy × cm^2) and 154.5 Gy × cm^2 (95% CI, 136–175.4 Gy × cm^2) for IP_R and IP_{DRT}, respectively. The reduction in CP_{KA} ranged from 30.5% for flow-diverter implants (mean reduction, 82.1 Gy × cm^2; $P = .0015$) to 73.8% for epistaxis (mean reduction, 251 Gy × cm^2; $P < .0001$). Also, with the exception of dural AVFs ($n = 7$ and 3 for IP_{DRT} and IP_R, respectively) and brain AVMs ($n = 10$ and 6 for IP_{DRT} and IP_R, respectively), all procedure types showed a significant reduction in CP_{KA} with the IP_{DRT} (Table 5 and Fig 1).

Table 5: Reduction achieved with the dose-reduction platform in comparison with the reference platform[a]

Procedure	CP_{KA} (Gy × cm^2)	Fluoroscopy Duration (min)	Contrast Volume (mL)
Diagnostic	88.2 (63.3%)[b]	−1.7 (−17.3%)[c]	−12.6 (−8.3%)
All interventions	171.8 (52.7%)[b]	−5.9 (−16.6)	−23.1 (−10.1%)
Coil embolization	166.3 (50.3%)[b]	−4.4 (−10.3%)	−37.3 (−13.7%)
Flow diverter	82.1 (30.5%)[c]	−14.9 (−55.1%)[c]	−34.6 (−15.5%)
Vasospasm	124.9 (71.1%)[b]	1.7 (11.1%)	9.4 (6.2%)
Thrombectomy	191.9 (60.2%)[b]	−5.1 (−17.8%)	2.9 (1.4%)
Stent-assisted coiling	112.1 (35.2%)[c]	−11.1 (−26.2%)	−72.6 (−27.1%)[c]
Carotid stenting	122.2 (55.7%)[b]	−1.7 (−6.7%)	17.6 (7.9%)
Epistaxis	251.0 (73.8%[b]	−7.4 (−22.7%)	73.7 (30.2%)
AVM	165.4 (26.2%)	−8.9 (−8.7%)	−105.3 (−43.2%)[c]
AVF	222.4 (37.6%)	−24.9 (−36.2%)	−51.3 (−15.6%)
Overall	160.3 (53.2%)[b]	−5.2 (−16.8%)[c]	−15.3 (−6.7%)

[a] Positive values indicate a reduction with the dose-reduction platform. Differences (percentage) in cumulative dose-area product, total fluoroscopy duration, and administered contrast volume were obtained from least squares means.

[b] $P < .0001$.

[c] $P < .05$.

Fluoroscopy Duration

Overall, the difference in total fluoroscopy duration between IP_{DRT} and IP_R was marginal ($P = .0491$) and resulted in a 5.2-minute (16.8%) increase with IP_{DRT} (Table 5 and Fig 2*A*). Procedure-related increases in fluoroscopy duration with the IP_{DRT} were found for diagnostic (an additional 1.7 minutes, $P = .0002$) and flow-diverter cases (an additional 14.9 minutes; $P = .0038$).

Administered Contrast Volume

Overall, the difference in administered contrast volume between IP_{DRT} and IP_R was nonsignificant ($P = .1616$) and resulted in a 15.3-mL (6.7%) increase with IP_{DRT} (Table 5 and Fig 2*B*). Increases in

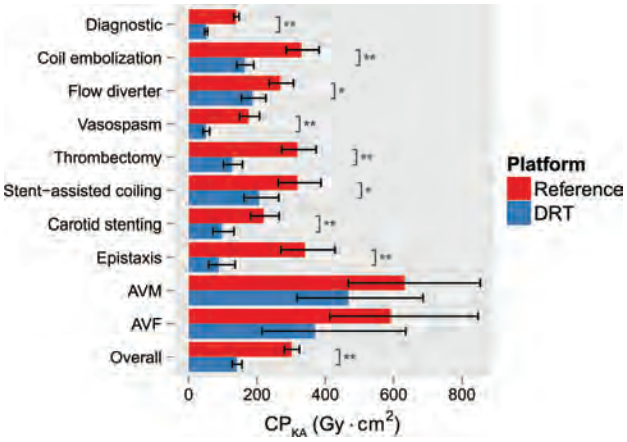

FIG 1. The cumulative dose-area product is significantly reduced with the dose-reduction technology platform. Bar graph and error bars represent least squares means and the associated 95% confidence intervals. Note a significant reduction in CP_{KA} between the dose-reduction technology and reference platforms. *Asterisk* indicates $P < .05$; *double asterisks*, $P < .0001$.

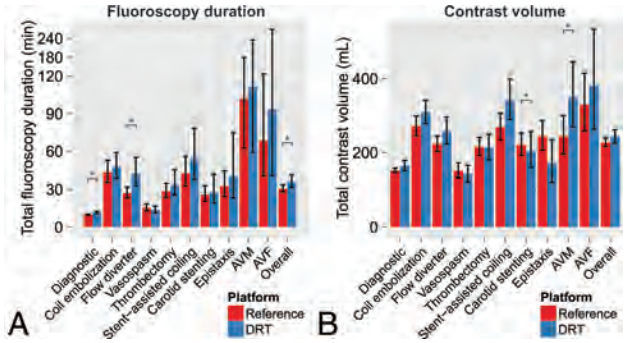

FIG 2. Least squares means and 95% confidence intervals of total fluoroscopy duration (*A*) and total administered contrast volume (*B*) are plotted for the reference and dose-reduction technology platforms. Note significant differences in fluoroscopy duration or contrast volume between the dose-reduction technology and reference platforms. *Asterisk* indicates $P < .05$; *double asterisks*, $P < .0001$.

administered contrast volume with the IP_{DRT} were observed for brain AVMs and stent-assisted coiling (Table 5 and Fig 2*B*).

DISCUSSION

While serious deterministic eye and skin injuries including cataracts are rare, erythema, and epilation as a consequence of interventional procedures are likely in a very small percentage of patients.[16,17] Several joint-society initiatives have been launched in response to increased recognition of the need to address such deterministic and long-term stochastic adverse events by carefully considering radiation exposure across medical imaging procedures, particularly in pediatric populations. The Image Wisely campaign was unveiled by the Joint Task Force on Adult Radiation Protection, an initiative established in 2009 by the American College of Radiology and the Radiological Society of North America.[18] Around the same time, the Alliance for Radiation in Pediatric Imaging introduced the Image Gently, Step Lightly campaign to encourage dose reduction in pediatric interventional radiologic procedures.[19]

General effort to minimize the risk of skin injury during fluoroscopic procedures entails using proper applied x-ray tube potential and beam filtration, limiting exposure duration for fluoroscopy, DSA, and non-DSA digital acquisitions, modifying the x-ray beam geometry by appropriate collimation and by placing the imaging detector close to the patient, and by ensuring minimal biplane overlap.[20] Besides educating interventional practitioners and technical staff on As Low As Reasonably Achievable practices, improvement in angiographic systems technology is needed to achieve further dose reductions while maintaining acceptable image quality.

The introduction of the IP_{DRT} with flexible selection of dose-reduction protocols to suit clinical needs was associated with an overall reduction in CP_{KA} of 53.2% across all diagnostic and interventional procedures in our academic neurointerventional practice. For diagnostic examinations, which constituted the largest fraction of studies, the mean CP_{KA} of 139.4 Gy × cm^2 (95% CI, 131.6–147.6 Gy × cm^2) observed in this study for the IP_R is lower than the 162.2 ± 231.7 Gy × cm^2 (95% CI, 129.0–195.4 Gy × cm^2) reported by Söderman et al.[5] In this study, the flexible use of dose-reduction protocols with the default setting of a quarter-dose protocol for the IP_{DRT} reduced the cumulative dose (kerma)-area product to 51.1 Gy × cm^2 (95% CI, 47–55.6 Gy × cm^2) constituting a 63.3% reduction with respect to the IP_R, similar to the 62% reduction in CP_{KA} with the fixed quarter-dose protocol reported by Söderman et al. Fig 3 shows a sample case highlighting improved visualization of perforators in diagnostic angiography with the half-dose and quarter-dose protocols.

Previous surveys of dose reports from a variety of interventional practices were used to infer reference dose values.[21-24] In addition, estimates of radiation doses for smaller groups of patients and for various neurointerventional procedures have been reported.[25-27] For the reference platform (IP_R), our CP_{KA} estimate of 139.4 Gy × cm^2 (95% CI, 131.6–147.6 Gy × cm^2) for diagnostic procedures is consistent with earlier reports by Kien et al[23] (173.9 ± 90.9 Gy × cm^2), D'Ercole et al[24] (142.1 ± 75.5 Gy × cm^2), Söderman et al[5] (162.2 ± 231.7 Gy × cm^2; 95% CI, 129.0–195.4 Gy × cm^2), and Alexander et al[25] (102.4 ± 43.4 Gy × cm^2). In addition, for aneurysm coil embolization, our CP_{KA} estimates of 330.3 Gy × cm^2 (95% CI, 285.6–381.9 Gy × cm^2) for IP_R are not markedly different from those reported by Miller et al[21] (282.7 Gy × cm^2; 95% CI, 261.1–304.3 Gy × cm^2), D'Ercole et al[28] (413 Gy × cm^2; 95% CI, 343–482 Gy × cm^2), Kien et al[23] (275.7 ± 145.1 Gy × cm^2), D'Ercole et al[24] (369.5 ± 162.3 Gy × cm^2), Vano et al[27] (293 ± 188 Gy × cm^2 and 317 ± 234 Gy × cm^2), and Alexander et al[25] (172.3 ± 67.7 Gy × cm^2).

The wide range of CP_{KA} reported in this and prior studies reflects the diverse nature of neurointerventional procedures performed with varying degrees of complexity, partly due to the expanded repository of neurointerventional devices such as Onyx (Covidien, Irvine, California), which is known to increase the procedure duration for AVM embolization,[29] and to the enhanced capabilities of the imaging equipment, such as the ability to perform 3DRA and CBCT. The procedural CP_{KA} reported in this study is inclusive of 3DRA and CBCT. Hence, caution is warranted while comparing results from this study with those of earlier studies, in which such 3D acquisitions were not prevalent, different devices were used, and case complexity

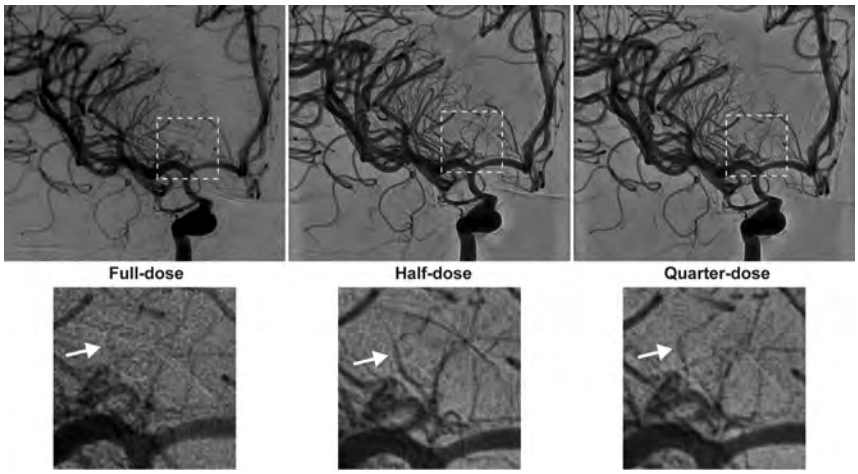

FIG 3. Diagnostic angiography was performed to assess the source of bleeding in a 43-year-old man who presented with diffuse SAH. During the examination, angiograms after contrast administration into the right ICA were obtained on IP_{DRT} platform by using the "full-dose" protocol (*left*), which is identical to the reference platform in terms of hardware and software settings, "half-dose" protocol (*middle*), and "quarter-dose" protocol (*right*). Magnified views of the *dashed area* highlight improved visualization of small perforators (*white arrows*) with the "half-dose" and "quarter-dose" protocols (*lower panels*).

was difficult to assess. The advantage of our analysis for comparison of IP_{DRT} and IP_R is that it is adjusted for operator and patient characteristics under identical practice standards with independent confirmation of system-reported CP_{KA}.

For the IP_{DRT}, the dose-reduction technology and the reduced air kerma rates are active only during 2D acquisitions such as fluoroscopy and DSA. For procedures requiring CBCT scans and depending on the number and type of CBCT scans, the relative benefit of the IP_{DRT} in terms of cumulative dose (kerma)-area product is reduced. For instance, flow-diverter placement at our institution commonly requires 3DRA before device deployment and at least 2 CBCT image volumes following implantation to confirm proper deployment and the absence of intraprocedural hemorrhage. Moreover, because flow-diverter placement is generally accompanied only by several angiograms before and after device deployment, the opportunities for dose reduction are relatively limited. For flow-diverter placement, the mean CP_{KA} for the IP_R and IP_{DRT} was 269.1 and 187 Gy × cm^2, respectively, constituting a significant ($P = .0015$) but relatively modest 30.5% reduction. Even in aneurysm coil embolization, an initial 3DRA and final CBCT are performed as standard of practice at our institution. Analysis of a subset of cases in which P_{KA} measurements were available separately for fluoroscopy, DSA, and CBCT suggests that there was no difference in the relative contribution of CBCT to the procedural CP_{KA} between the IP_R and IP_{DRT} for diagnostic cases, while results acquired on the IP_{DRT} indicate that the relative contribution of the CBCT to the CP_{KA} may vary with procedure type (On-line Figs 1 and 2 and On-line Table).

The study observed CP_{KA} reduction with the IP_{DRT} for each procedure type, with the exception of dural AVFs and brain AVMs. On occasion, an operator may repeat an acquisition at a higher dose for verification. However, in practice these situations arose sporadically, such as when examining highly complex brain AVMs, and rarely occurred during most of the diagnostic and other treatment procedures. The limited sample size for brain AVMs (10 and 6 treated on the IP_R and IP_{DRT}, respectively) and dural AVFs (7 and 3 treated on the IP_R and IP_{DRT}, respectively) could have also contributed to a nonsignificant reduction ($P > .15$) to the procedure CP_{KA}.

Despite significant reductions in CP_{KA} and across most procedure types, overall, we observed a marginal difference ($P = .0491$) in total fluoroscopy duration between the 2 platforms, with an additional 5.2 minutes of fluoroscopy duration with the IP_{DRT}. On our systems, the default is fluoroscopy mode II and is typically used for interventions. Generally, fluoroscopy mode I was used for diagnostic examinations, and fluoroscopy mode III was reserved for complex cases involving flow-diverter placement and AVM embolization. There was no indication that the use of these modes was different between the IP_R and the IP_{DRT}. Significant differences in total fluoroscopy duration between the 2 platforms were observed for diagnostic examinations ($P = .0002$) and flow-diverter placement ($P = .0038$), with an increase of 1.7 and 14.9 minutes, respectively, with IP_{DRT}. Additional analyses for these procedures indicated that the total fluoroscopy duration with IP_{DRT} increased for 1 operator by 2.3 minutes for diagnostic examinations ($P < .0001$) and 10.7 minutes for flow-diverter placement ($P = .0026$). Also, for flow-diverter placement, procedures involving >1 operator contributed to a substantial 34.5-minute ($P = .0203$) increase with IP_{DRT}. In our academic practice, the extent to which the assisting fellows are involved and the nature of their contribution to a case, depending on the procedure, may vary. Regarding the total administered contrast volume, overall, the difference between the 2 platforms was nonsignificant ($P = .1616$), with an increase of 15.3 mL (6.7%) with IP_{DRT}. Overall, the marginal increase in fluoroscopy duration and the nonsignificant change in administered contrast volume suggest that workflow was unaffected by the use of the IP_{DRT}.

Our study had limitations. This retrospective study precluded randomization of the operator and imaging platform. We did not analyze the partial contributions to CP_{KA} from fluoroscopy, angiography, and 3D imaging for all cases because these data were not recorded uniformly. For each procedure type, the sample-size distribution was not uniform for the 2 platforms in this retrospective study. Another confounding factor is the smaller x-ray detector for the LAT plane of the FD20/10 system, which was used for all IP_{DRT} examinations and part of the IP_R examinations. The smaller detector size may contribute to lower P_{KA} for that acquisition or may contribute to higher procedural CP_{KA}, because adjacent regions were additionally imaged when clinically needed. At our institution, all neurointerventional systems are from a single vendor; hence, our analysis is restricted to that vendor. Our study

considered CP_{KA} alone as the metric for analysis and does not address the skin-dose distribution and the peak skin dose[30] because the imaging geometry relative to the patient and anatomic region was not collected. CP_{KA} is relevant to the estimation of stochastic effects, while peak skin dose is directly related to skin effects.

CONCLUSIONS

The introduction of a dose-reduction platform was associated with a significant reduction of 53.2% in CP_{KA} over all procedure types, ranging from 30.5% to 73.8% for individual procedures compared with the reference platform without the noise-reduction algorithm from the same vendor. After adjustment for the operating neurointerventional radiologist and patient characteristics, our results demonstrate that significant dose reductions can be achieved for almost all the considered procedure types. Only marginal effects on total fluoroscopy duration and total administered contrast volume were observed, suggesting that the impact on workflow was minimal.

Disclosures: Imramsjah M.J. van der Bom—*UNRELATED*: *Employment*: Philips Healthcare; *Stock/Stock Options*: InNeuroCo. Matthew J. Gounis—*RELATED*: *Grant*: Philips Healthcare*; *UNRELATED*: *Consultancy*: Codman Neurovascular, Stryker Neurovascular; *Grants/Grants Pending*: National Institutes of Health, Asahi Intecc, Blockade Medical, CereVasc LLC, Codman Neurovascular, Cook Medical, Gentuity LLC, Fraunhofer Institute, InNeuroCo, Lazarus Effect, Medtronic, MicroVention/Terumo, Philips Healthcare, Silk Road, Spineology, Stryker Neurovascular, Wyss Institute*; *Stock/Stock Options*: InNeuroCo. Ajit S. Puri—*UNRELATED*: *Consultancy*: Stryker Neurovascular, Codman Neurovascular; *Grants/Grants Pending*: Stryker Neurovascular, Covidien*; *Stock/Stock Options*: InNeuroCo; *Travel/Accommodations/Meeting Expenses Unrelated to Activities Listed*: Stryker Neurovascular. Ajay K. Wakhloo—*RELATED*: *Grant*: Philips Healthcare, *Comments*: equipment support and research grant*; *Support for Travel to Meetings for the Study or other Purposes*: Philips Healthcare*; *UNRELATED*: *Consultancy*: Codman Neurovascular, Stryker Neurovascular; *Expert Testimony*: McCoy Law Firm, Coral Gables, Florida; *Payment for Lectures, including Service on Speakers Bureaus*: Harvard postgraduate course, Miami Cardiac and Vascular Institute; *Stock/Stock Options*: InNeuroCo, EpiEp, Penumbra; *Other*: Pulsar Medical, *Comments*: bridge loan. *Money paid to the institution.

REFERENCES

1. Molyneux AJ, Kerr RS, Yu LM, et al; International Subarachnoid Aneurysm Trial (ISAT) Collaborative Group. **International subarachnoid aneurysm trial (ISAT) of neurosurgical clipping versus endovascular coiling in 2143 patients with ruptured intracranial aneurysms: a randomised comparison of effects on survival, dependency, seizures, rebleeding, subgroups, and aneurysm occlusion.** *Lancet* 2005;366:809–17 CrossRef Medline
2. Grigoryan M, Chaudhry SA, Hassan AE, et al. **Neurointerventional procedural volume per hospital in United States: implications for comprehensive stroke center designation.** *Stroke* 2012;43:1309–14 CrossRef Medline
3. Stecker MS, Balter S, Towbin RB, et al; SIR Safety and Health Committee; CIRSE Standards of Practice Committee. **Guidelines for patient radiation dose management.** *J Vasc Interv Radiol* 2009; 20(suppl):S263–73 CrossRef Medline
4. Sánchez RM, Vano E, Fernández JM, et al. **Staff doses in interventional radiology: a national survey.** *J Vasc Interv Radiol* 2012;23: 1496–501 CrossRef Medline
5. Söderman M, Mauti M, Boon S, et al. **Radiation dose in neuroangiography using image noise reduction technology: a population study based on 614 patients.** *Neuroradiology* 2013;55:1365–72 CrossRef Medline
6. Pitton MB, Kloeckner R, Schneider J, et al. **Radiation exposure in vascular angiographic procedures.** *J Vasc Interv Radiol* 2012;23: 1487–95 CrossRef Medline
7. Söderman M, Holmin S, Andersson T, et al. **Image noise reduction algorithm for digital subtraction angiography: clinical results.** *Radiology* 2013;269:553–60 CrossRef Medline
8. Nakamura S, Kobayashi T, Funatsu A, et al. **Patient radiation dose reduction using an X-ray imaging noise reduction technology for cardiac angiography and intervention.** *Heart Vessels* 2016;31: 655–63 CrossRef Medline
9. van Strijen MJ, Grünhagen T, Mauti M, et al. **Evaluation of a noise reduction imaging technology in iliac digital subtraction angiography: noninferior clinical image quality with lower patient and scatter dose.** *J Vasc Interv Radiol* 2015;26:642–50.e1 CrossRef Medline
10. van den Haak RF, Hamans BC, Zuurmond K, et al. **Significant radiation dose reduction in the hybrid operating room using a novel x-ray imaging technology.** *Eur J Vasc Endovasc Surg* 2015;50:480–86 CrossRef Medline
11. Ten Cate T, van Wely M, Gehlmann H, et al. **Novel X-ray image noise reduction technology reduces patient radiation dose while maintaining image quality in coronary angiography.** *Neth Heart J* 2015; 23:525–30 CrossRef Medline
12. Eloot L, Thierens H, Taeymans Y, et al. **Novel X-ray imaging technology enables significant patient dose reduction in interventional cardiology while maintaining diagnostic image quality.** *Catheter Cardiovasc Interv* 2015;86:E205–12 CrossRef Medline
13. Haas NA, Happel CM, Mauti M, et al. **Substantial radiation reduction in pediatric and adult congenital heart disease interventions with a novel X-ray imaging technology.** *IJC Heart & Vasculature* 2015;6:101–09 CrossRef
14. Lin PJ, Schueler BA, Balter S, et al. **Accuracy and calibration of integrated radiation output indicators in diagnostic radiology: a report of the AAPM Imaging Physics Committee Task Group 190.** *Med Phys* 2015;42:6815–29 CrossRef Medline
15. Hurvich CM, Tsai CL. **Regression and time-series model selection in small samples.** *Biometrika* 1989;76:297–307 CrossRef
16. Balter S, Hopewell JW, Miller DL, et al. **Fluoroscopically guided interventional procedures: a review of radiation effects on patients' skin and hair.** *Radiology* 2010;254:326–41 CrossRef Medline
17. Faulkner K, Vañó E. **Deterministic effects in interventional radiology.** *Radiat Prot Dosimetry* 2001;94:95–98 CrossRef Medline
18. Brink JA, Amis ES Jr. **Image Wisely: a campaign to increase awareness about adult radiation protection.** *Radiology* 2010;257:601–02 CrossRef Medline
19. Sidhu M, Goske MJ, Connolly B, et al. **Image Gently, Step Lightly: promoting radiation safety in pediatric interventional radiology.** *AJR Am J Roentgenol* 2010;195:W299–301 CrossRef Medline
20. Norbash AM, Busick D, Marks MP. **Techniques for reducing interventional neuroradiologic skin dose: tube position rotation and supplemental beam filtration.** *AJNR Am J Neuroradiol* 1996;17: 41–49 Medline
21. Miller DL, Balter S, Cole PE, et al; RAD-IR study. **Radiation doses in interventional radiology procedures: the RAD-IR study, part I: overall measures of dose.** *J Vasc Interv Radiol* 2003;14:711–27 CrossRef Medline
22. Vano E, Järvinen H, Kosunen A, et al. **Patient dose in interventional radiology: a European survey.** *Radiat Prot Dosimetry* 2008;129: 39–45 CrossRef Medline
23. Kien N, Rehel JL, Etard C, et al. **Patient dose during interventional neuroradiology procedures: results from a multi-center study** [in French]. *J Radiol* 2011;92:1101–12 CrossRef Medline
24. D'Ercole L, Thyrion FZ, Bocchiola M, et al. **Proposed local diagnostic reference levels in angiography and interventional neuroradiology and a preliminary analysis according to the complexity of the procedures.** *Phys Med* 2012;28:61–70 CrossRef Medline
25. Alexander MD, Oliff MC, Olorunsola OG, et al. **Patient radiation exposure during diagnostic and therapeutic interventional neuroradiology procedures.** *J Neurointerv Surg* 2010;2:6–10 CrossRef Medline
26. Chohan MO, Sandoval D, Buchan A, et al. **Cranial radiation exposure during cerebral catheter angiography.** *J Neurointerv Surg* 2014; 6:633–36 CrossRef Medline

27. Vano E, Fernandez JM, Sanchez RM, et al. **Patient radiation dose management in the follow-up of potential skin injuries in neuroradiology.** *AJNR Am J Neuroradiol* 2013;34:277–82 CrossRef Medline
28. D'Ercole L, Mantovani L, Thyrion FZ, et al. **A study on maximum skin dose in cerebral embolization procedures.** *AJNR Am J Neuroradiol* 2007;28:503–07 Medline
29. Velat GJ, Reavey-Cantwell JF, Sistrom C, et al. **Comparison of N-butyl cyanoacrylate and Onyx for the embolization of intracranial arteriovenous malformations: analysis of fluoroscopy and procedure times.** *Neurosurgery* 2008;63:ONS73–78; discussion ONS78–80 Medline
30. Khodadadegan Y, Zhang M, Pavlicek W, et al. **Validation and initial clinical use of automatic peak skin dose localization with fluoroscopic and interventional procedures.** *Radiology* 2013;266:246–55 CrossRef Medline

The Efficacy of Shielding Systems for Reducing Operator Exposure during Neurointerventional Procedures: A Real-World Prospective Study

T.R. Miller, J. Zhuo, G. Jindal, R. Shivashankar, N. Beaty, and D. Gandhi

ABSTRACT

BACKGROUND AND PURPOSE: Neurointerventional surgery may expose patients and physician operators to substantial amounts of ionizing radiation. Although strategies for reducing patient exposure have been explored in the medical literature, there has been relatively little published in regards to decreasing operator exposure. The purpose of this study was to evaluate the efficacy of shielding systems in reducing physician exposure in a modern neurointerventional practice.

MATERIALS AND METHODS: Informed consent was obtained from operators for this Health Insurance Portability and Accountability Act–compliant, institutional review board–approved study. Operator radiation exposure was prospectively measured during 60 consecutive neurointerventional procedures from October to November 2013 using a 3-part lead shielding system. Exposure was then evaluated without lead shielding in a second 60-procedure block from April to May 2014. A radiation protection drape was randomly selected for use in half of the cases in each block. Two-way analysis of covariance was performed to test the effect of shielding systems on operator exposure while controlling for other covariates, including procedure dose-area product.

RESULTS: Mean operator procedure dose was 20.6 μSv for the entire cohort and 17.7 μSv when using some type of shielding. Operator exposure significantly correlated with procedure dose-area product, but not with other covariates. After we adjusted for procedure dose-area product, the use of lead shielding or a radiation protection drape significantly reduced operator exposure by 45% ($F = 12.54$, $P < .0001$) and 29% ($F = 7.02$, $P = .009$), respectively. The difference in protection afforded by these systems was not statistically significant ($P = .46$), and their adjunctive use did not provide additional protection.

CONCLUSIONS: Extensive lead shielding should be used as much as possible in neurointerventional surgery to reduce operator radiation exposure to acceptable levels. A radiation protection drape is a reasonable alternative when standard lead shielding is unavailable or impractical to use without neglecting strategies to minimize the dose.

ABBREVIATIONS: BMI = body mass index; PKA = air kerma area product

Advances in endovascular technology have led to the increasing use of minimally invasive, neurointerventional procedures for the diagnosis and treatment of cerebrovascular disease. While the efficacy of these fluoroscopically guided examinations is well-established, there is growing concern regarding the exposure of patients and medical personnel to ionizing radiation. Prior reports have demonstrated that exposure of patients and workers may not be negligible during interventional neuroradiology procedures, likely due to the complexity of some interventions and the use of digital subtraction angiography and biplane fluoroscopy.[1-7] Patient exposure may be high enough to result in deterministic effects such as skin erythema and epilation, while both patients and physician operators are potentially at risk from the stochastic effects of this radiation, namely carcinogenesis.[8-16]

Although multiple reports in the literature detail the risks of patient exposure to ionizing radiation during neurointerventional procedures, little has been published regarding exposure of the treating physician operators. Furthermore, the few reports available have either included a relatively small number of cases performed by a few experienced neurointerventionalists or, alternatively, have focused on quantifying the degree of protection afforded by personal protective equipment, such as lead glasses or caps.[1-4,17,18] While the use of such equipment remains an essential component of an overall strategy to protect medical personnel from scatter radiation, an equally important approach is to reduce the amount of scatter radiation

Received September 1, 2016; accepted after revision October 12.

From the Departments of Diagnostic Radiology, Neuroradiology (T.R.M., J.Z., G.J., R.S., D.G.), and Neurosurgery (N.B.), University of Maryland Medical Center, Baltimore, Maryland.

Please address correspondence to Timothy R. Miller, MD, University of Maryland Medical Center, Department of Radiology, 22 South Greene St, Baltimore, MD 21201; e-mail: tmiller5@umm.edu

http://dx.doi.org/10.3174/ajnr.A5038

reaching the physician operator. The latter may be achieved by minimizing the use of ionizing radiation in neurointerventions as much as clinically feasible and by the adjunctive deployment of shielding systems in the angiosuite. Strategies for minimizing radiation use in neurointerventional surgery have recently been described in detail by several groups and include the use of low-dose fluoroscope settings.[19-22] However, the efficacy of shielding systems in neurointerventional surgery has largely remained unstudied.

We therefore elected to prospectively evaluate operator exposure to scatter ionizing radiation in our neurointerventional practice while using various shielding systems.

MATERIALS AND METHODS

The institutional review board approved the research protocol for this single-center, HIPAA-compliant study. Operator radiation exposure was prospectively measured during 2 blocks of 60 consecutive neuroangiography procedures performed in roughly 6-week periods from October to November 2013 and April to May 2014. Physician operators participating in the study included attending neurointerventional radiologists ($n = 3$) and physician trainees specializing in the field ($n = 2$). All physician operators wore standard personal protective equipment during the study, including a lead vest and skirt and a thyroid shield. Written and verbal informed consent was obtained from physician operators. Patient consent was not obtained because their clinical care and radiation dose were unaffected by the research protocol.

During each 60-procedure block, operator exposure was measured during all neuroangiography procedures performed on an Artis zee biplane fluoroscopy unit (Siemens, Erlangen, Germany), consisting of two 40 × 30 cm flat panel image detectors in the anteroposterior and lateral planes. Along with operator radiation dose, fluoroscopy time, air kerma area product (PKA), procedure type (diagnostic versus intervention/treatment), and patient body mass index (BMI) were recorded for all procedures. Operator skin dose was measured by a personal electronic dosimeter (DMC 300; Mirion Technologies, Irvine California), which measures Hp(10), with a measurement range of 15 keV to 7 MeV for x-rays and gamma rays, a dose range from 1 μSv to 10 Sv, and an accuracy of at least ±20% (typical, ±10%). Body mass index was obtained from the patient's medical record. The specific type of intervention was not recorded (eg, aneurysm coiling, mechanical thrombectomy) because it was thought that other factors, including vessel tortuosity, plaque burden, and lesion morphology, would also play a critical role in determining overall procedure complexity. Consequently, our study design accounted for procedure complexity by taking into account the overall amount of ionizing radiation used during the procedure, as reflected by the PKA.

During the first 60 consecutive procedures, the personal dosimeter was attached to the left collar of the primary operator on top of the individual's lead vest and thyroid shield. If >1 physician participated in the procedure, the dosimeter was transferred between operators to ensure that it was always located on the primary operator standing closest to the fluoroscope. The dosimeter was left in the angiosuite on the patient's upper right thigh during all power-injected DSA runs while physician operators stood in the control room to avoid unnecessary radiation exposure. This procedure was used to standardize the relationship between measured operator exposure and the PKA. The dosimeter remained on the primary operator's left collar during all hand-injected DSA runs.

Standard radiation lead shielding was used in all cases, including an overhanging lead acrylic shield positioned over the patient's midabdomen (upper body shield), a lead apron skirt extending parallel to the fluoroscopy table on the side of the operator (lower body shield), and an approximately 2 × 1 m mobile barrier placed in front of the primary operator perpendicular to the angiography table. In addition, a disposable radiation-absorbing surgical drape (RADPAD; Worldwide Innovations & Technologies, Lenexa, Kansas), which has proved efficacious in reducing physician exposure during interventional cardiology and vascular interventional radiology procedures, was randomly selected to be used in half of cases.[23-31] If selected for use, the radiation protection drape was initially placed on the patient's right thigh below the femoral sheath insertion site and was subsequently transferred to the right lower abdomen once the catheter had been advanced into the thoracic aorta (Fig 1).

In the second half of the study, radiation exposure was again measured during 60 additional consecutive neuroangiography procedures performed in the same biplane angiosuite. However, in this portion of the study, the electronic dosimeter was placed at the collar level on an IV pole located on the opposite side of the angiosuite table immediately across from the primary operator and standard lead shielding. This step was to simulate operator exposure when lead shielding is not used because it was thought unethical to remove lead shielding from the side of the operator. Once again, a radiation protection drape was randomly selected for use in half of cases, this time positioned over the left lower abdomen. The dosimeter remained in the angiosuite throughout the procedure, including during power-injected DSA runs.

Operator radiation exposure was then analyzed according to the presence or absence of lead shielding and the radiation protection drape, yielding 4 groups (Table 1). One-way ANOVA was initially performed to test whether there were any group differences in procedure PKA, fluoroscopy time, and patient BMI. The Pearson correlation was used to analyze the simple relationship between operator radiation exposure and procedure PKA, fluoroscopy time, and patient BMI. Two-way analysis of covariance was performed to test the effect of lead shielding and the radiation protection drape on operator exposure, controlling for ≥1 of the other covariates (PKA, fluoroscopy time, patient BMI). Covariates were selected on the basis of whether they were significant explanatory variables in the multiple linear regression model with exposure dose as the response. A post hoc test with a Tukey correction was then performed to test for group differences in exposure dose, while controlling for the covariates. All statistical analysis was performed by using the computing environment R statistical and computing software (Version 3.2.0) (http://www.r-project.org). $P < .05$ was considered statistically significant.

RESULTS

Data were successfully collected from all eligible neurointerventional examinations in 2 blocks of 60 consecutive procedures. In

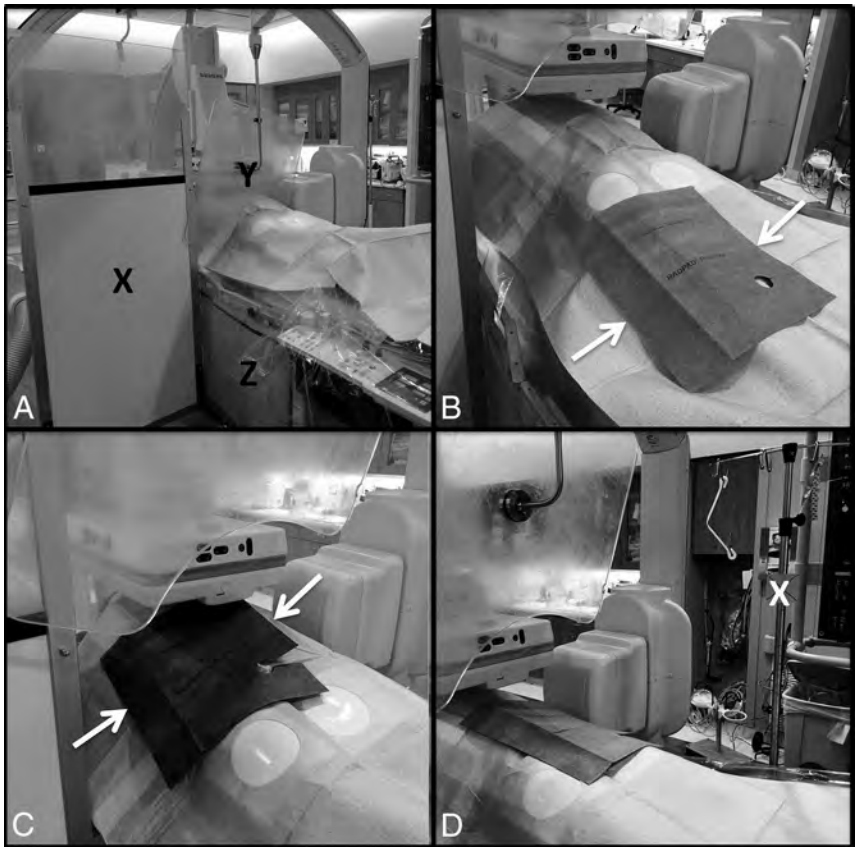

FIG 1. Configuration of shielding systems and dosimeter in the angiosuite. *A*, Positions of the mobile barrier (X), upper body shield (Y), and lower body shield (Z) are noted. *B*, Position of the radiation protection drape (*white arrows*) before sheath insertion and advancement of the diagnostic/intermediate catheter into the thoracic aorta. *C*, Position of the radiation protection drape (*white arrows*) during the remainder of the procedure. *D*, Position of the dosimeter (*white X*) in the second block of 60 patients, attached to an IV pole. The radiation protection drape is positioned over the left side of the patient.

Table 1: Shielding system groups

Group	Radiation Protection Drape	Standard Lead Shielding Systems
R0L0	−	−
R1L0	+	−
R0L1	−	+
R1L1	+	+

Note:—R0L1 indicates standard lead shielding; R0L0, no shielding; R1L0, use of the RADPAD drape; R1L1, concomitant use of the 2 shielding systems together; +, present; −, absent.

total, 71 diagnostic and 49 interventional neuroangiography procedures were included. During the initial investigation of operator radiation exposure data, 1 diagnostic procedure was excluded from further analysis due to a reported high operator exposure dose, which was out of proportion to the procedure PKA. This outlier may have occurred due to either improper dosimeter positioning or erroneous data entry. Consequently, data from 70 diagnostic and 49 therapeutic neurointerventional angiography procedures were included for further analysis (Table 2).

Mean operator radiation dose per procedure in the entire cohort was 20.6 ± 1.6 μSv and 17.7 ± 1.4 μSv for the 89 procedures in which exposure was measured by using some type of shielding system. The mean fluoroscopy time and PKA for the entire cohort were 44.6 ± 47.3 minutes and 149.3 ± 90.1 Gy × cm^2, respectively. Compared with therapeutic interventions, diagnostic examinations were associated with shorter fluoroscopy times (17.5 ± 1.4 minutes versus 83.3 ± 51.0 minutes, $P < .0001$) and lower PKA (132 ± 88 Gy × cm^2 versus 174 ± 88 Gy × cm^2, $P = .014$). The mean patient body mass index was 28.2 (range, 15.2–50.1).

One-way ANOVA testing demonstrated no statistically significant differences in the ratio of diagnostic-versus-interventional procedures ($F = 0.86$, $P = .47$), mean fluoroscopy time ($F = 0.433$, $P = .73$), mean PKA ($F = 0.53$, $P = .67$), or mean patient BMI (ANOVA, $F = 2.36$, $P = .08$) among the 4 shielding groups. Two-way analysis of the covariance showed that operator radiation exposure was highly correlated with procedure PKA, regardless of the shielding systems used ($r = 0.59$, $P < .0001$). Although fluoroscopy time ($r = 0.29$, $P = .0013$) and patient BMI ($r = -0.17$, $P = .062$) also correlated with operator radiation exposure, these covariates were no longer significant after taking PKA into account. Consequently, only PKA was included as a covariate in the final ANCOVA model for the effects of shielding systems on operator exposure dose.

ANCOVA revealed that the use of lead shielding ($F = 12.54$, $P < .0001$) and the radiation protection drape ($F = 7.02$, $P = .009$) significantly reduced operator exposure after adjusting for procedure PKA (Table 3). Post hoc tests comparing the adjusted operator exposure dose for the 4 shielding groups indicated that standard lead shielding (R0L1) reduced operator exposure to scatter radiation by nearly half (45%) compared with no shielding (R0L0) ($P < .001$). Use of the RADPAD drape (R1L0) was also associated with a significant but smaller reduction in operator exposure (29%) ($P = .026$). Finally, the concomitant use of the 2 shielding systems together (R1L1) failed to further reduce operator exposure to scatter radiation. The R1L1 group demonstrated a 44% reduction in operator exposure compared with no shielding (R0L0), essentially identical to standard lead shielding alone (R1L1 versus R0L1, $P = .99$).

DISCUSSION

Our results demonstrate that the consistent use of standard lead shielding can reduce the exposure of neurointerventionalists to scatter radiation by as much as 45%. More surprising is the 29% reduction in exposure afforded by the radiation protection drape. Although the drape had previously been shown to be effective in interventional cardiology and vascular interventional radiology procedures, physicians in these specialties often stand much closer to the irradiated portion of the patient's body, for example,

Table 2: Baseline group characteristics

Shielding Group	Mean FT (min)	Mean PKA (Gy × cm^2)	Mean Patient BMI	Intervention/Diagnostic
R0L0	41.63	148.43	25.9	12/18
R1L0	37.38	138.64	29.74	9/21
R0L1	54.08	164.11	29.48	14/16
R1L1	45.17	145.74	27.35	14/15

Note:—FT indicates fluoroscopy time; R0L1, standard lead shielding; R0L0, no shielding; R1L0, use of the RADPAD drape; R1L1, concomitant use of the 2 shielding systems together.

Table 3: Operator dose and adjusted dose reduction relative to R0L0

Shielding Group	Mean Operator Dose (μSv)	Standard Error	Dose Relative to R0L0: Adjusted for PKA	Significance
R0L0	29.1	0.212	NA	NA
R1L0	19.5	0.211	0.78	$P < .001$
R0L1	17.7	0.211	0.55	$P = .026$
R1L1	15.9	0.213	0.56	$P < .001$

Note:—NA indicates not applicable; R0L1, standard lead shielding; R0L0, no shielding; R1L0, use of the RADPAD drape; R1L1, concomitant use of the 2 shielding systems together.

next to the thorax during cardiac pacemaker/defibrillator placement. In these instances, the drape is placed directly adjacent to the irradiated body part, where it is in an optimal position to shield the operator from scatter radiation. In contradistinction, neurointerventionalists using femoral artery access typically stand much farther away from the x-ray target (ie, head and neck), and it was uncertain whether placing the drape over the patient's lower abdomen would still be effective. However, despite the greater distance between operator and x-ray source, the drape still significantly reduced operator exposure.

The current study failed to show a further reduction in operator dose when augmenting lead shielding with the radiation protection drape. However, we still use the inexpensive, easy-to-use drape in our practice because we believe it may provide additional radiation protection in certain situations. These include procedures requiring greater radiation exposure of the pelvis (eg, difficult femoral artery access, femoral artery injury), spinal angiography, and studies using brachial or radial artery access. Although not evaluated in the current study, the drape may be more effective in these instances due to a combination of increased proximity of the operator to the irradiated body part and an inability to optimally position all lead shielding components. For example, the overhanging lead shield is impractical to use during femoral sheath insertion, while the stand-alone lead shield is similarly unworkable when using a brachial artery approach.

Furthermore, although we consistently use extensive lead shielding in our practice, this is likely not the case for all neurointerventionalists. Overhanging and stand-alone lead shielding can be cumbersome to use, particularly during complex interventions such as aneurysm coiling, which often require oblique positioning of the fluoroscopy tubes. In these instances, the working space available for lead shields is often reduced, making them difficult or impractical to use. Moreover, some practices may be limited in their use of lead shielding, either because it is not readily available or due to physical constraints within the angiography suite. In situations in which lead shielding is not ideal, either due to operator preference or limitations of a particular practice, a radiation protection drape may be a reasonable alternative for scatter radiation protection.

Operator exposure was highly correlated with PKA. As discussed in the "Materials and Methods" section, procedure PKA is a reasonable measure of overall procedure complexity, potentially accounting for a diverse array of difficult-to-anticipate variables, including intervention type, experience of the operators, vessel tortuosity, and vessel plaque burden. After we accounted for this correlation, neither procedure type nor patient BMI significantly impacted operator dose. Before the current study, we had speculated that patient BMI might impact operator exposure secondary to increased scatter radiation production while imaging over the superiormost aspect of the thorax and lower neck. The latter occurs during catheterization of cervical vessels and can represent a significant percentage of procedure time in diagnostic cerebral angiograms, particularly with tortuous vessel anatomy. However, any increase in scatter radiation generated by larger size patients was too small to be detected.

Operator exposure was modest in the current study: 20.6 μSv per procedure for the entire cohort and 17.7 μSv when using some types of shielding. Given these results, it is highly unlikely that an operator in our practice would exceed the annual occupational limit of 20 mSv. Although comparison with prior studies can be challenging due to differences in methodology, other authors have typically noted higher operator doses during neurointerventional procedures. For example, Moritake et al[5] reported an average entrance dose at the operator's left collar of 50 μGy/μSv ($n = 32$), Kemerink et al[2] found an average entry dose at the operator's neck of 74 μGy/μSv ($n = 31$), and Bor et al[18] noted a mean entry dose of 28.8 μGy/μSv in the region of the thyroid ($n = 57$). We believe that the meticulous use of shielding systems in most of our cases contributed to the relatively low operator exposure, though other factors, including fluoroscope settings, likely played a role.

The current study has several limitations, which reflect some of the practical challenges of measuring operator radiation exposure during everyday clinical practice. First, our measured operator dose likely overestimates true physician exposure during clinical practice secondary to leaving the dosimeter in the angiosuite during power-injected DSA runs. However, this practice allowed us to standardize the relationship between measured operator exposure and procedure PKA. In addition, estimated operator exposure in the second half of the study may have been slightly greater than in the first half due to the dosimeter being located on the side of the lateral fluoroscope x-ray source. This feature, in turn, may have led to a mild overestimation of the efficacy of lead shielding. However, the difference was thought likely to be small because the lateral tube is almost exclusively used when imaging over the head and upper neck, where the greater distance of the operator/dosimeter from the irradiated body part would likely minimize any such variation. Finally, small variations in positioning of the dosimeter during the first half of the study, when operators wore the dosimeter, may have also affected our results. However, it was not practical to attach the dosimeter to a fixed position such as an IV pole on the right side of the angiosuite table because it would have interfered with the work of physician operators. Despite these issues, our results help to quantify the degree of protection afforded by shielding systems in neurointerventional

surgery and have demonstrated that such systems may help limit physician exposure to acceptable levels in a modern neurointerventional practice.

CONCLUSIONS

Extensive lead shielding should be used as much as possible in neurointerventional surgery to reduce operator radiation exposure to acceptable levels. A radiation protection drape is a reasonable alternative when standard lead shielding is unavailable or impractical to use without neglecting strategies to minimize the dose.

Disclosures: Timothy R. Miller—*UNRELATED*: *Grants/Grants Pending*: University of Maryland, *Comments*: Medtronic industry grant for already published research pertaining to comparison of the classic-versus-second-generation Flex Pipeline Embolization Device paid to University of Maryland Medical Center Radiology Department; Stryker industry grant for the Trevo Retriever Registry Post Market Surveillance paid to the University of Maryland Medical Center Radiology Department; Medtronic industry grant for Apollo, Onyx, Delivery Micro Catheter Post Market Safety Study paid to the University of Maryland Medical Center Radiology Department; *Pending*: MicroVention industry grant for the Pivotal Study of the FRED Stent System in the Treatment of Intracranial Aneurysms paid to the University of Maryland Medical Center Radiology Department.* Gaurav Jindal—*UNRELATED*: *Grants/Grants Pending:* Stryker, MicroVention, Codman, Medtronic, Comments: research grants*; *Payment for Lectures including Service on Speakers Bureaus*: Internal Medicine Department at the Union Memorial Hospital in Baltimore, Maryland. Dheeraj Gandhi—*UNRELATED*: *Royalties*: Cambridge Press. *Money paid to the institution.

REFERENCES

1. Sans Merce M, Korchi AM, Kobzeva L, et al. **The value of protective head cap and glasses in neurointerventional radiology.** *J Neurointerv Surg* 2016;8:736–40 CrossRef Medline
2. Kemerink GJ, Frantzen MJ, Oei K, et al. **Patient and occupational dose in neurointerventional procedures.** *Neuroradiology* 2002;44:522–28 CrossRef Medline
3. Tavares JB, Sacadura-Leite E, Matoso T, et al. **The importance of protection glasses during neuroangiographies: a study on radiation exposure at the lens of the primary operator.** *Interv Neuroradiol* 2016;22:368–71 CrossRef Medline
4. Layton KF, Kallmes DF, Cloft HJ, et al. **Radiation exposure to the primary operator during endovascular surgical neuroradiology procedures.** *AJNR Am J Neuroradiol* 2006;27:742–43 Medline
5. Moritake T, Matsumaru Y, Takigawa T, et al. **Dose measurement on both patients and operators during neurointerventional procedures using photoluminescence glass dosimeters.** *AJNR Am J Neuroradiol* 2008;29:1910–17 CrossRef Medline
6. Lekovic GP, Kim LJ, Gonzalez LF, et al. **Radiation exposure during endovascular procedures.** *Neurosurgery* 2008;63:ONS81–85; discussion ONS85–86 Medline
7. Alexander MD, Oliff MC, Olorunsola OG, et al. **Patient radiation exposure during diagnostic and therapeutic interventional neuroradiology procedures.** *J Neurointerv Surg* 2010;2:6–10 CrossRef Medline
8. Committee on Health Effects of Exposure to Low Levels of Ionizing Radiations. *Health Effects of Exposure to Low Levels of Ionizing Radiations: Time for Reassessment?* National Academy Press: Washington, DC; 1998
9. Thierry-Chef I, Simon SL, Land CE, et al. **Radiation dose to the brain and subsequent risk of developing brain tumors in pediatric patients undergoing interventional neuroradiology procedures.** *Radiat Res* 2008;170:553–65 CrossRef Medline
10. Orbach DB, Stamoulis C, Strauss KJ, et al. **Neurointerventions in children: radiation exposure and its import.** *AJNR Am J Neuroradiol* 2014;35:650–56 CrossRef Medline
11. Venneri L, Rossi F, Botto N, et al. **Cancer risk from professional exposure in staff working in cardiac catheterization laboratory: insights from the National Research Council's Biological Effects of Ionizing Radiation VII Report.** *Am Heart J* 2009;157:118–24 CrossRef Medline
12. Amis ES Jr, Butler PF, Applegate KE, et al; American College of Radiology. **American College of Radiology white paper on radiation dose in medicine.** *J Am Col Radiol* 2007;4:272–84 CrossRef Medline
13. Vano E, Fernandez JM, Sanchez RM, et al. **Patient radiation dose management in the follow-up of potential skin injuries in neuroradiology.** *AJNR Am J Neuroradiol* 2013;34:277–82 CrossRef Medline
14. Peterson EC, Kanal KM, Dickinson RL, et al. **Radiation-induced complications in endovascular neurosurgery: incidence of skin effects and the feasibility of estimating risk of future tumor formation.** *Neurosurgery* 2013;72:566–72 CrossRef Medline
15. Roguin A, Goldstein J, Bar O. **Brain tumours among interventional cardiologists: a cause for alarm? Report of four new cases from two cities and a review of the literature.** *EuroIntervention* 2012;7:1081–86 CrossRef Medline
16. Roguin A, Goldstein J, Bar O, et al. **Brain and neck tumors among physicians performing interventional procedures.** *Am J Cardiol* 2013;111:1368–72 CrossRef Medline
17. Chohan MO, Sandoval D, Buchan A, et al. **Cranial radiation exposure during cerebral catheter angiography.** *J Neurointerv Surg* 2014;6:633–36 CrossRef Medline
18. Bor D, Cekirge S, Türkay T, et al. **Patient and staff doses in interventional neuroradiology.** *Radiat Prot Dosimetry* 2005;117:62–68 Medline
19. Kahn EN, Gemmete JJ, Chaudhary N, et al. **Radiation dose reduction during neurointerventional procedures by modification of default settings on biplane angiography equipment.** *J Neurointerv Surg* 2016;8:819–23 CrossRef Medline
20. Schneider T, Wyse E, Pearl MS. **Analysis of radiation doses incurred during diagnostic cerebral angiography after the implementation of dose reduction strategies.** *J Neurointerv Surg* 2016 Apr 7. [Epub ahead of print] CrossRef Medline
21. Pearl MS, Torok C, Wang J, et al. **Practical techniques for reducing radiation exposure during cerebral angiography procedures.** *J Neurointerv Surg* 2015;7:141–45 CrossRef Medline
22. Honarmand AR, Shaibani A, Pashaee T, et al. **Subjective and objective evaluation of image quality in biplane cerebral digital subtraction angiography following significant acquisition dose reduction in a clinical setting.** *J Neurointerv Surg* 2016 Apr 6. [Epub ahead of print] CrossRef Medline
23. Simons GR, Orrison WW Jr. **Use of a sterile, disposable, radiation-absorbing shield reduces occupational exposure to scatter radiation during pectoral device implantation.** *Pacing Clin Electrophysiol* 2004;27:726–29 CrossRef Medline
24. Sawdy JM, Gocha MD, Olshove V, et al. **Radiation protection during hybrid procedures: innovation creates new challenges.** *J Invasive Cardiol* 2009;21:437–40 Medline
25. Power S, Mirza M, Thakorlal A, et al. **Efficacy of a radiation absorbing shield in reducing dose to the interventionalist during peripheral endovascular procedures: a single centre pilot study.** *Cardiovasc Intervent Radiol* 2015;38:573–78 CrossRef Medline
26. Politi L, Biondi-Zoccai G, Nocetti L, et al. **Reduction of scatter radiation during transradial percutaneous coronary angiography: a randomized trial using a lead-free radiation shield.** *Catheter Cardiovasc Interv* 2012;79:97–102 CrossRef Medline
27. Murphy JC, Darragh K, Walsh SJ, et al. **Efficacy of the RADPAD protective drape during real world complex percutaneous coronary intervention procedures.** *Am J Cardiol* 2011;108:1408–10 CrossRef Medline
28. Kloeze C, Klompenhouwer EG, Brands PJ, et al. **Editor's choice–Use of disposable radiation-absorbing surgical drapes results in significant dose reduction during EVAR procedures.** *Eur J Vasc Endovasc Surg* 2014;47:268–72 CrossRef Medline
29. King JN, Champlin AM, Kelsey CA, et al. **Using a sterile disposable protective surgical drape for reduction of radiation exposure to interventionalists.** *AJR Am J Roentgenol* 2002;178:153–57 CrossRef Medline
30. Jones MA, Cocker M, Khiani R, et al. **The benefits of using a bismuth-containing, radiation-absorbing drape in cardiac resynchronization implant procedures.** *Pacing Clin Electrophysiol* 2014;37:828–33 CrossRef Medline
31. Germano JJ, Day G, Gregorious D, et al. **A novel radiation protection drape reduces radiation exposure during fluoroscopy guided electrophysiology procedures.** *J Invasive Cardiol* 2005;17:469–72 Medline

Measured Head CT/CTA Skin Dose and Intensive Care Unit Patient Cumulative Exposure

R.D. Nawfel and G.S. Young

ABSTRACT

BACKGROUND AND PURPOSE: Estimates of cumulative CT/CTA radiation dose based on volumetric CT dose index have raised concern that neurological intensive care unit patient exposures may reach thresholds for deterministic skin injury. Because the accuracy of volumetric CT dose index for this purpose in unknown, we set out to directly measure head CT and CTA peak skin dose, assess the relationship of volumetric CT dose index to measured peak skin dose, and determine whether multiple CT/CTA exposures in typical patients in the neurological intensive care unit produce cumulative doses approaching or exceeding single-dose deterministic thresholds for skin injury.

MATERIALS AND METHODS: In a prospective study from 2011–2013, nanoDot optical stimulated luminescence dosimeters were used to measure head CT/CTA peak skin dose in 52 patients (28 female, 24 male; mean age, 63 years) divided equally between 2 CT scanners. Volumetric CT dose index and dose-length product were recorded for each examination. Peak skin dose was also measured on an acrylic skull phantom in each scanner. A 2-tailed, unpaired *t* test was used to compare mean patient skin doses between the 2 scanners. The measured peak skin doses were then used to calculate cumulative peak skin dose in 4 typical patients in intensive care units who received multiple CT/CTA scans.

RESULTS: Head CT/CTA peak skin dose agreed between scanners in patients and phantoms: (scanner 1 CT/CTA: patients, 39.2 ± 3.7 mGy and 98.9 ± 5.3 mGy, respectively, versus phantom, 40.0 mGy and 105.4 mGy, respectively; scanner 2 CT/CTA: patients, 42.9 ± 9.4 mGy and 98.8 ± 7.4 mGy, respectively, versus phantom, 37.6 mGy and 95.2 mGy, respectively). Volumetric CT dose index overestimated peak skin dose by a factor of 1.4–1.9 depending on examination and CT scanner. Cumulative doses in 4 patients in the intensive care unit estimated from measured CT/CTA peak skin dose ranged from 1.9–4.5 Gy.

CONCLUSIONS: Directly measured radiation skin doses from head CT/CTA patient examinations are substantially lower than volumetric CT dose index. Measured peak skin dose confirms that multiple head CT/CTA examinations in representative patients in the neurological intensive care unit may produce cumulative doses exceeding the single-dose deterministic threshold for skin injury.

ABBREVIATIONS: CAK = cumulative air kerma; $CTDI_{vol}$ = volumetric CT dose index; ICU = intensive care unit; PSD = peak skin dose

Patients in the neurological intensive care unit (ICU) require rapid, accurate head CT and CTA diagnosis and monitoring to guide therapy of critical neurologic emergencies such as infarction and hemorrhage associated with high short-term risk of death or severe disability.[1,2] Although 1 head CT/CTA exposure falls in the low-dose radiation range that poses no risk of deterministic effects,[3,4] cumulative radiation doses from multiple head CT/CTA scans combined with angiography over 1–3 weeks in patients in the ICU have been reported to range from 0.46–8.32 Gy by using equipment-displayed dose data[5] and 0.22–1.8 Gy by using dosimeters.[6] These doses approach or exceed the accepted 2-Gy single-dose deterministic threshold for skin injury, above which erythema (skin redness) and epilation (hair loss) may occur. The frequency and severity of radiation skin damage increases with dose. Transient erythema and epilation may be observed hours after a single exposure to 2–5 Gy and usually resolve by 24 hours without long-term sequelae. Latent effects, typically seen weeks after single-dose exposure to >5 Gy, may lead to permanent epilation and dermal atrophy or induration. Desquamation, ulceration, and necrosis are typically not seen with single doses <10 Gy.[7,8] Although skin effects have been produced in a small number of patients by a series of much higher radiation dose exposures from conventional cerebral angiography and/or high-

Received June 7, 2016; accepted after revision October 13.

From the Department of Radiology (R.D.N., G.S.Y.), Brigham and Women's Hospital, Boston, Massachusetts; Department of Radiology (G.S.Y.), Dana Farber Cancer Institute, Boston, Massachusetts; and Department of Radiology (R.D.N., G.S.Y.), Harvard Medical School, Boston, Massachusetts.

The authors contributed equally to this work.

Please address correspondence to Geoffrey S. Young, MD, Department of Radiology, Brigham and Women's Hospital, 75 Francis St, Boston, MA 02115; e-mail: gsyoung@partners.org

http://dx.doi.org/10.3174/ajnr.A5040

Table 1: Patient demographics by scanner

	Scanner 1 (Siemens)		Scanner 2 (Toshiba)	
	CTA Head	Routine Head	CTA Head	Routine Head
No. of patients	13	13	13	13
Female	6	4	11	7
Male	7	9	2	6
Mean age ± SD	67.6 ± 11.8	60.8 ± 15.6	59.3 ± 13.6	63.1 ± 21.6

Table 2: CT/CTA technique

Scan/Phase	Tube Potential (kVp)	Tube Current (mA)[a]	mAs_{eff}[a]	Rot. Time (sec)	Beam Width (mm)	Pitch	Scan Length (mm)
Scanner 1							
Head CT							
Head	120	450	450	1	16 × 1.2		195
Head CTA							
Head	120	450	450	1	16 × 1.2		156
Premonitoring[b]	120	182	60	0.33	1 × 10		10
Monitoring[b]	120	182	60	0.33	1 × 10		10
CTA head	120	342	174	0.33	20 × 0.6	0.65	180
Delayed head	120	585	450	0.5	20 × 0.6	0.65	171
Scanner 2							
Head CT							
Head	120	250	286	0.75	32 × 0.5	0.65	160
Helical	120	250	286	0.75	32 × 0.5	0.65	160
Head CTA							
Helical	120	250	286	0.75	32 × 0.5	0.65	160
Premonitoring[b]	120	50	25	0.5	4 × 0.5		2
Monitoring[b]	120	50	25	0.5	4 × 0.5		0
Helical	120	250	196	0.5	64 × 0.5	0.64	160
Helical	120	250	196	0.5	64 × 0.5	0.64	160

Note:—mAs_{eff} indicates effective mAs; Rot., rotation.
[a] Tube current and mAs_{eff} were variable for Monitoring phase.
[b] Scan over region of chest.

Table 3: PSD and $CTDI_{vol}$ from head CT/CTA by scanner (mGy)

	Scanner 1		Scanner 2	
	CTA[a]	CT	CTA[a]	CT
Patients[b]				
PSD	98.9 ± 5.3	39.2 ± 3.7	98.8 ± 7.4	42.9 ± 9.4
$CTDI_{vol}$	187 ± 15.1	68.4 ± 2.5	142 ± 3.6	64.6 ± 1.5
Phantom				
PSD	105	40.0	95.2	37.6
$CTDI_{vol}$	167	68.8	139	62.4

[a] $CTDI_{vol}$ is total of all phases exposing head.
[b] Dose for patient exams is given as mean ± standard deviation.

dose CT perfusion,[9-15] no skin effects have been reported in the much larger group of more typical patients in the ICU who are exposed to multiple low-dose fractions from CT/CTA without CT perfusion or repeated high-dose angiograms.

Volumetric CT dose index ($CTDI_{vol}$), the most frequently used dose descriptor, does not accurately represent dose to the patient. In particular, $CTDI_{vol}$ has been shown to overestimate skin dose to the head,[9,10,16-18] and thus is not a reliable metric for predicting risk of head CT/CTA radiation–induced skin injury. To estimate skin dose for patients in the ICU exposed to multiple CT/CTA and neurointerventional studies over a short period of time requires combining doses from multiple CT/CTA scans with angiographic dose estimates. We directly measured peak skin dose (PSD) from head CT/CTA examinations and determined if multiple examination exposures in typical patients in the neurological ICU result in cumulative doses approaching or exceeding deterministic thresholds for skin injury.

MATERIALS AND METHODS

Institutional review board approval was obtained for this prospective study performed at the Brigham and Women's Hospital. Patient informed consent was waived by the institutional review board. Between March 2011 and June 2013, skin dose was measured by using dosimeters applied to 52 randomly selected patients, and $CTDI_{vol}$ was recorded during head CT/CTA examinations on 2 CT scanners representing the most disparate architectures available at our institution: a conventional 40-detector CT scanner and a 320-detector conebeam CT. Doses were measured on 26 patients scanned on scanner 1 (40 detector row CT scanner; Siemens Somatom Definition AS, Siemens, Erlangen, Germany), and 26 patients on scanner 2 (320 detector rows; Aquilion ONE CT scanner, Toshiba Medical Systems, Tokyo, Japan). On each scanner, 13 patients received a head CTA examination, and 13 patients received a routine head CT examination (Table 1). Scanning protocols are given in Tables 2 and 3. A single technologist collected examination data on each scanner, placed the dosimeters on patients, and performed the scan. CT examination dose metrics, $CTDI_{vol}$, and dose-length product were also recorded for each patient examination. The $CTDI_{vol}$ specified for CTA examinations was defined as the sum of $CTDI_{vol}$ values from phases scanning over the head only; premonitoring and monitoring phases were not included in the calculation because these exposures occur to the chest rather than the head.

Patient and phantom head sizes were determined by measuring head thickness on CT images as the transverse anteroposterior (*AP*) and lateral diameters (*LAT*) by using the CT console software. The effective diameter was calculated as the square root of the product of the anteroposterior and lateral thickness: $(AP \times LAT)^{1/2}$.

Study Group Skin Dose Measurement

Doses were measured with optically stimulated luminescence dosimeters at 4 locations with respect to the surface of the patient's head. The same measurements were performed on the acrylic skull phantom (Fig 1*A*). The optical stimulated luminescence dosimeters used were 1 cm × 1 cm aluminum oxide–based nanoDots[19] (Landauer, Glenwood, Illinois) and were read by using a microStar reader (Landauer). The microStar reader was calibrated according to manufacturer's user manual recommendations by using 5 control nanoDots provided with the dosimetry system. The dosimeters were tested for reproducibility with 5 exposure measurements in air at 120 kVp. They demonstrated very good reproducibility (coefficient of variation, 0.01).

Two nanoDots were placed on the surface of the patient's head: 1 on the forehead (Fig 1*B*) and 1 on the back of the head. Two nanoDots were also placed at locations on the head holder adjacent to the left and right temporal bone. At these lateral locations, the dosimeters were placed on the head holder instead of the patient's head to avoid disturbing the patient. Each individual patient's PSD was specified as the maximum of the 4 measurements.

Skin Dose Measurement Correction Factor

Skin dose was measured at both temporal locations on an acrylic skull phantom and corresponding locations on the head holder while using the same clinical protocols and scan parameters (Table 2). The standard filters used provide 6.8-mm Al equivalent filtration for scanner 1 and 4.8-mm Al equivalent filtration for scanner 2. Tube current modulation was used for CTA, and fixed mAs was used for routine head CT on both scanners. Detector configuration and collimation for CTA were 20 rows × 0.6 mm for scanner 1 and 64 rows × 0.5 mm for scanner 2. The ratio of the skin dose measured at the temporal location of the phantom and the dose at the corresponding location on the head holder was used as a correction factor to estimate patient temporal skin dose from the head holder measurements acquired during patient examinations. The mean correction factor was 1.33 ± 0.10 when averaged over all examination techniques. This factor of 1.33 was multiplied by the dose measured at the head holder locations for patient examinations.

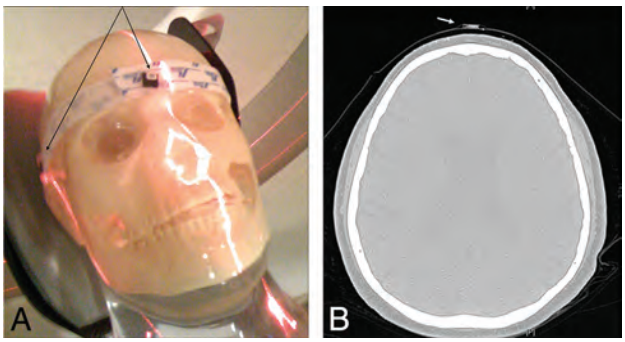

FIG 1. *A*, Acrylic skull phantom with nanoDots at forehead and lateral locations. *B*, Patient CT image with nanoDot on forehead.

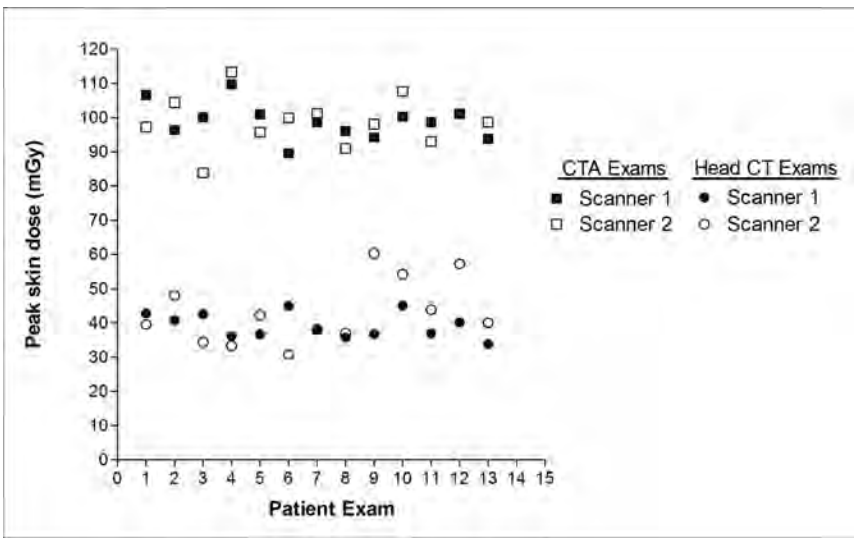

FIG 2. PSD distribution for all 52 patient examinations on both scanners. PSD was very comparable between scanners for the same patient examination. On average, the PSD for CTA examinations was more than twice that of routine head CT examinations. Note that 2 data points coincide for examination 7 (head CT) and examination 12 (head CTA).

Statistical Analysis

Mean, standard deviation, and coefficient of variation were calculated for all doses and size measurements. Correlations were also calculated to compare doses between patient groups and patient dose values with corresponding values on the phantom. A 2-tailed, unpaired *t* test was used to compare mean patient skin doses between the 2 scanners.

Estimate of Patient Skin Dose from Neurointerventional Imaging

Doses were measured with optical stimulated luminescence dosimeters at the same 4 locations on the surface of the acrylic skull phantom (Fig 1*A*) during 2 separate trials by using an interventional x-ray fluoroscopy imaging system (Innova 3100; GE Healthcare, Milwaukee, Wisconsin) with examination technique factors typically used during neurointerventional imaging, producing a total of 8 dose measurements. The maximum dose to the phantom for each assessment was specified as the PSD of the 4 measurements. The total cumulative air kerma (CAK) was also recorded from the imaging system display for each trial. This is specified as the CAK at the interventional reference point.[20] The PSD to CAK ratio was calculated for each assessment.[21]

Predicting Patient Skin Dose for ICU Clinical Examinations

Patients in the ICU who received between 12 and 27 total CT examinations and several cerebral angiograms over a period of 2–4 weeks were identified. In accordance with hospital radiation safety practice, these patients were examined for evidence of radiation-induced skin injury or hair loss. PSD measurements from the 52-patient study group were used to estimate cumulative doses to these patients in the ICU having the same examinations. For interventional angiography examinations, the PSD to CAK ratio, together with the total patient examination CAK, was used to estimate the cumulative skin dose for patients in the ICU who had previously received multiple cerebral angiograms. Total cumulative skin dose was calculated by adding the PSD estimates from CT to the skin dose estimate from angiography.

RESULTS

The maximum optical stimulated luminescence dose was measured in the forehead location in 14 patient examinations, in the left temporal location in 23 patient examinations, in the right temporal location in 15 patient examinations, and at the back of the head location in no patient examinations.

The mean PSD for CTA examinations (98.9 ± 5.3 mGy) and for routine head CT examinations (39.2 ± 3.7 mGy) per-

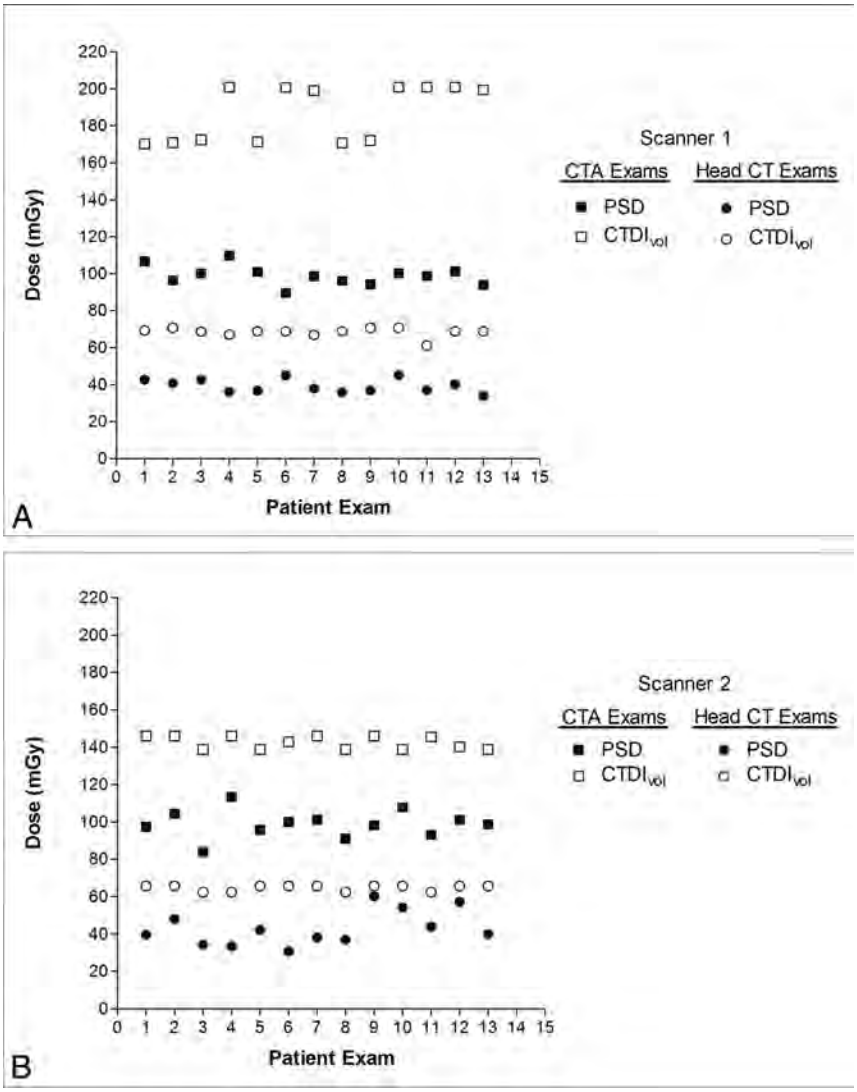

FIG 3. *A*, PSD and $CTDI_{vol}$ for all patients examined on scanner 1. *B*, PSD and $CTDI_{vol}$ for all patients examined on scanner 2. $CTDI_{vol}$ overestimated PSD for all patient examinations on each scanner for both CTA examinations and routine head CT examinations.

formed on scanner 1 agreed well with PSD measured on the acrylic head phantom: 105.4 mGy and 40.0 mGy, respectively (Table 3). In addition, for scanner 2, the mean PSDs for CTA examinations (98.8 ± 7.4 mGy) and routine head CT examinations (42.9 ± 9.4 mGy) were very comparable with corresponding phantom measurements: 95.2 mGy and 37.6 mGy, respectively. In general, the PSD for CTA examinations was slightly more than double that of routine head CT examinations (Fig 2). The difference in mean PSD for corresponding examinations on both scanners 1 and 2 were not statistically significant (CTA examinations, $P = .97$; routine head CT examinations, $P = .19$).

$CTDI_{vol}$ overestimated PSD for all patient examinations on both scanners 1 and 2 as illustrated in Fig 3. The mean $CTDI_{vol}$ was an overestimate of the PSD for all patient examinations and phantom scans (Table 3). $CTDI_{vol}$ was very comparable for routine head examinations performed on both scanners; however, for CTA examinations, the $CTDI_{vol}$ was approximately 24% (142/187) lower on scanner 2 compared with scanner 1. The difference between mean $CTDI_{vol}$ for scanners 1 and 2 was statistically significant for both CTA ($P < .0001$) and routine head CT ($P < .0001$).

Effect of Patient Head Size

The mean effective diameters were 17.4 ± 0.7 cm and 16.8 ± 0.8 cm for patients examined on scanners 1 and 2, respectively. The effective diameter of the phantom was 16.6 cm. Figure 4 demonstrates the variation in PSD with patient size for all 52 patient examinations on both scanners. On neither scanner was there a significant correlation between PSD and patient head size for corresponding patient examinations (scanners 1 and 2 CTA examinations, $R^2 = 0.0008$ and $R^2 = 0.006$, respectively; scanners 1 and 2 routine head CT examinations, $R^2 = 0.0001$ and $R^2 = 0.285$, respectively).

Comparison of Dose Descriptors

Patient and phantom $CTDI_{vol}$ overestimated the measured PSD for both head CTA and head CT on average by 65% (range, 44%–89%). The $CTDI_{vol}$ to PSD ratio ranged from 1.4 ± 0.5 to 1.9 ± 2.8 for the various examinations and scanners. This overestimation was statistically significant ($P < .0001$) (Table 3).

Skin Dose from Neurointerventional Imaging

The PSDs measured on the surface of the acrylic skull phantom for 2 separate assessments are given in Table 4. Using the total CAK (mGy) from each trial, the PSD to CAK ratio was determined to be 0.45. This is consistent with literature documenting that CAK overestimates PSD.[21] When the total CAK was known, the PSD to CAK ratio was used to estimate the cumulative skin dose from patient examinations performed on the same interventional imaging system by multiplying the total CAK by 0.45.

Total Patient Skin Dose from Multiple Imaging Examinations

Table 5 provides 4 examples of patients having multiple CTA and routine CT examinations of the head over a period of days to weeks. These patients also had several cerebral angiograms over the same time period. The PSD for these patients' CT examinations was calculated by multiplying the mean PSD obtained from optical stimulated luminescence measurements by the corresponding number of CTA or routine head CT examinations that the patient received. These calculated PSDs for CT were added to cumulative skin dose estimated from cerebral angiography by using the phantom measurement–based conversion above. Total cumulative skin dose ranged from 1.9–4.8 Gy for these patients.

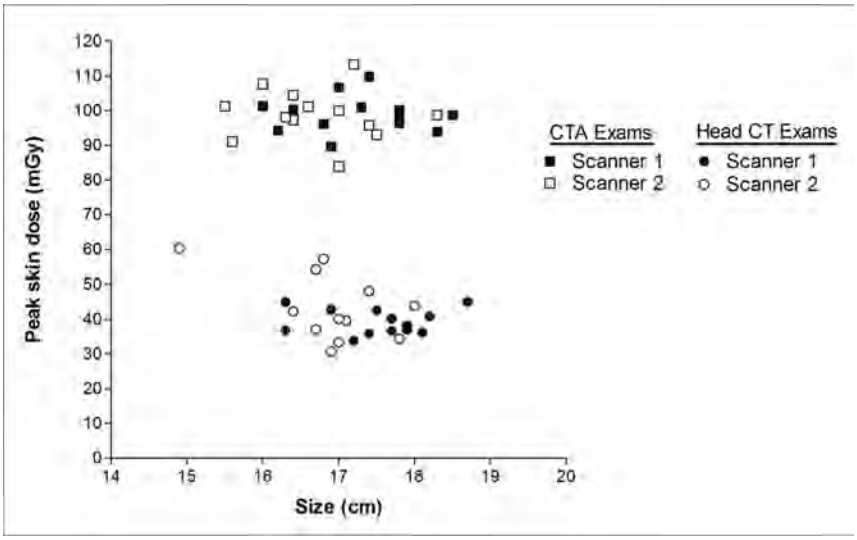

FIG 4. PSD versus patient size for all patient examinations on both scanners. Patient size is specified as the effective diameter, calculated from anteroposterior and lateral thickness measurements of patient's head. There was no significant correlation between PSD and patient head size for corresponding patient examinations on each scanner.

Table 4: Angiographic phantom CAK and PSD (mGy)

	CAK	PSD	PSD/CAK
Trial 1	73	33.1	0.45
Trial 2	101	45.1	0.45

Table 5: Illustrative ICU patient CT/CTA and cerebral angiography exposures[a]

	Patient 1	Patient 2	Patient 3	Patient 4
No. of CTA	12	8	8	8
PSD (mGy)	1187	791	791	791
No. of head CT	2	7	4	18
PSD (mGy)	78	274	157	706
No. of cerebral angiograms	11	9	2	14
Cumulative skin dose (mGy)[b]	2667	1574	908	3261
Total skin dose, all exams (mGy)	3932	2639	1856	4758
Time interval for all exams (days)	30	18	16	31

[a] All patient CT exams performed on scanner 1.
[b] Cumulative skin dose for cerebral angiography predicted from phantom measurements.

Skin Effects

No evidence of radiation-induced skin injury or hair loss was detected in any patient.

DISCUSSION

CT and CTA are effective essential diagnostic tools for managing patients with stroke, intracranial hemorrhage, brain trauma, and other critical neurologic conditions. Typical patients undergoing multiple CTA and routine head CT scans, and in some cases cerebral angiography, may receive cumulative doses approaching accepted thresholds for deterministic radiation skin injuries such as erythema and epilation. In addition, these cumulative exposures may reach thresholds associated with cataract induction, a latent deterministic effect that may occur at single doses lower than 2 Gy.[22] Importantly, the dose thresholds for these deterministic effects have primarily been studied in the setting of single exposure rather than multiple exposures separated by days or weeks. Because tissue-protective and DNA-repair effects usually occur within 24 hours, the actual threshold for induction of deterministic injury by cumulative low-dose exposures remains unknown and may be substantially higher.[8] There is compelling preclinical evidence that biologic effects of low-dose and low–dose rate exposures are qualitatively distinct from well-studied high-dose and high–dose rate exposures.[4,23] In addition, clinical experience, as in the 4 patients from the ICU whom we studied, suggests that CT radiation–induced skin injury is very rarely observed in typical patients in the neurological ICU. Clearly, more study of the effects of cumulative CT radiation is needed to assess risk in this group. The first step in determining the actual effects of cumulative low-dose radiation is to accurately measure skin dose resulting from multiple head CT/CTA. To address this, we measured dose in a sample of patients undergoing CT/CTA on the 2 different CT scanners at our institution with the most dissimilar architectures.

In the 4 patients reported, as is typical of the adult neurological ICU population, the radiation risk is outweighed by the immediate risk of death or severe permanent disability. These patients received a large number of imaging examinations (14–30 over a period of 2–4 weeks); however, reducing the number of these examinations would compromise treatment and is likely not in the best interest of the patient. The mean PSD from the CT study groups allowed us to predict PSD from these 4 patient examinations because direct patient measurement was not available. The range in total cumulative skin dose was estimated to be 1.9–4.8 Gy, which is at or above the threshold for deterministic effects, consistent with the initial dose-measurement feasibility study by Mamourian et al[6] in patients with SAH. We agree with the investigators' conclusions that radiation awareness and accurate dose assessment of these hospitalized patients are important, but caution that because these risks are much less of a concern than the immediate risk of death and severe disability in these patients, cumulative dose estimates should not be the basis for decreasing clinically indicated imaging studies or decreasing CT dose at the expense of diagnostic image quality.[24]

Nevertheless, surveillance for immediate or delayed skin injury may be reasonable in selected patients in the ICU who survive to leave the hospital after undergoing multiple CT examinations with high cumulative doses. Occasionally, transient erythema may be observed after coronary or cerebral angio-intervention, and epilation has been reported in a number of patients exposed to inadvertent high exposures during CT perfusion.[7,8,10-13] In contrast, deterministic skin effects have not been reported in the large number of patients in the ICU exposed over the course of weeks to similar cumulative doses from multiple daily CT and CTA; however, it is possible that these effects occur but have gone undetected. Despite this remote possibility, it seems unlikely that

such skin effects are occurring at a frequency or severity comparable with well-documented single-dose exposures. This clinical experience is consistent with the radiation biology literature showing that exposure to multiple low-dose fractions of radiation stimulates immediate DNA repair, cellular protective changes, apoptosis, and tissue effects that are substantially different from the effects of a single or several high-dose radiation exposures.[23] Although these contemporary biologic data and recent epidemiologic analyses have cast substantial doubt on the validity of the linear no-threshold model for estimating low-dose radiation effects, some controversy persists in the radiation biology literature, causing concern among patients and physicians.[3,4,23] Although the predicted low-level decades-delayed stochastic risks of radiation-induced carcinogenesis are very difficult to investigate clinically, direct DNA and cellular effect of radiation and rapid deterministic skin effects should be far easier to study and may help to directly address this controversy. Valid accurate estimates of patient exposure are needed as a first step toward such research.

In this study, measurement results from CT examinations demonstrated that phantom skin doses were a reasonable approximation of patient skin doses. Thus, results from phantom measurements were used when direct patient measurements were not otherwise available. Our results indicate that PSD was consistent for all patients on a particular scanner when comparing the same patient examination. This result would allow us to predict the PSD reasonably well for other patients who may receive head CTA or CT examinations on either of these scanners. In contrast, the mean $CTDI_{vol}$ overestimated the mean PSD by a factor ranging from 1.4 ± 0.5 to 1.9 ± 2.8 depending on the specific CT protocol and scanner, and there is some interpatient variation in the relationship of $CTDI_{vol}$ and PSD (Fig 3*B*). These findings confirm that $CTDI_{vol}$ alone is inadequate as an indicator of patient radiation dose and potential for radiation-induced deterministic effects. As such, though a correction factor for $CTDI_{vol}$ specific to each scanner and protocol would be possible, we chose not to use $CTDI_{vol}$, but instead to calculate cumulative individual patient dose for our 4 patients from the ICU directly from PSD measurements on the relevant scanner and protocol.

Prediction of patient skin dose in a single patient undergoing multiple scans by using dose measurements on multiple patients is a limitation of this study. This was unavoidable because of the logistical challenges of placing and retrieving the dosimeters on patients who are critically ill and may be scanned at any time of day or night. Our data indicate that there was a high degree of consistency between PSD on different scanners for the same CT examination protocol and that the head phantom served as an acceptable alternative to patient dose measurements, particularly for assessment of skin dose during cerebral angiography. For these reasons, we believe our method provided a reasonable initial basis for dose quantification. Although direct measurements on the same patient having multiple examinations would have been a more valid means of data collection, this would have been extremely cumbersome in the most critically ill patients. Although our measurement results were useful in calculating the PSD for examinations and protocols on our scanners, the results of this study reflect the scanners and imaging protocols specifically at our institution.

CONCLUSIONS

Directly measured head CT/CTA PSD was reasonably consistent for a given examination across patients and CT scanners. Using these scanner- and protocol-specific PSD measurements to predict doses to 4 typical patients in the neurological ICU exposed to multiple CT/CTA examinations, we found cumulative skin doses ranged from 1.9–4.8 Gy, at or above the threshold for single-dose deterministic skin effects, but we observed no skin effects. Further study correlating diagnostic CT exposure in patients in the ICU with direct cellular, DNA, and deterministic skin effects is needed to investigate what if any risk these cumulative exposures impart. Meanwhile, cumulative dose estimates should not be used to justify reduction in individual CT scan dose at the expense of diagnostic image quality or to limit the number of otherwise clinically indicated scans in critically ill patients in the neurological ICU.

Disclosures: Geoffrey Young—*UNRELATED*: *Grants*: Dr. Young received no salary or direct research support relevant to the research reported in this paper. Toshiba Medical Systems provided research support to the Department of Radiology of Brigham and Women's Hospital to support research on neurologic CT/CTA unrelated to radiation dose or the research reported in this paper.

REFERENCES

1. Mokin M, Kass-Hout T, Kass-Hout O, et al. **Intravenous heparin for the treatment of intraluminal thrombus in patients with acute ischemic stroke: a case series.** *J Neurointerv Surg* 2013;5:144–50 CrossRef Medline
2. Camargo EC, Furie KL, Singhal AB, et al. **Acute brain infarct: detection and delineation with CT angiographic source images versus nonenhanced CT scans.** *Radiology* 2007;244:541–48 CrossRef Medline
3. Wall BF, Kendall GM, Edwards AA, et al. **What are the risks from medical x-rays and other low dose radiation?** *Br J Radiol* 2006;79:285–94 CrossRef Medline
4. Tubiana M, Feinendegen LE, Yang C, et al. **The linear no-threshold relationship is inconsistent with radiation biologic and experimental data.** *Radiology* 2009;251:13–22 CrossRef Medline
5. Wong JM, Ho AL, Lin N, et al. **Radiation exposure in patients with subarachnoid hemorrhage: a quality improvement target.** *J Neurosurg* 2013;119:215–20 CrossRef Medline
6. Mamourian AC, Young H, Stiefel MF. **Cumulative radiation dose in patients admitted with subarachnoid hemorrhage: a prospective study using a self-developing film badge.** *AJNR Am J Neuroradiol* 2010;31:1787–90 CrossRef Medline
7. Koenig TR, Wolff D, Mettler FA, et al. **Skin injuries from fluoroscopically guided procedures: part 1, characteristics of radiation injury.** *AJR Am J Roentgenol* 2001;177:3–11 CrossRef Medline
8. Balter S, Hopewell JW, Miller DL, et al. **Fluoroscopically guided interventional procedures: a review of radiation effects on patients' skin and hair.** *Radiology* 2010;254:326–41 CrossRef Medline
9. Zhang D, Cagnon CH, Villablanca JP, et al. **Estimating peak skin and eye lens dose from neuroperfusion examinations: use of Monte Carlo based simulations and comparisons to $CTDI_{vol}$, AAPM Report No. 111, and ImPACT dosimetry tool values.** *Med Phys* 2013;40:091901 CrossRef Medline
10. Zhang D, Cagnon CH, Villablanca JP, et al. **Peak skin and eye lens radiation dose from brain perfusion CT based on Monte Carlo simulation.** *AJR Am J Roentgenol* 2012;198:412–17 CrossRef Medline
11. Hoang JK, Wang C, Frush DP, et al. **Estimation of radiation exposure for brain perfusion CT: standard protocol compared with deviations in protocol.** *AJR Am J Roentgenol* 2013;201:W730–34 CrossRef Medline
12. Imanishi Y, Fukui A, Niimi H, et al. **Radiation-induced temporary hair loss as a radiation damage only occurring in patients who had**

the combination of MDCT and DSA. *Eur Radiol* 2005;15:41–46 CrossRef Medline
13. Hirata M, Sugawara Y, Fukutomi Y, et al. **Measurement of radiation dose in cerebral CT perfusion study.** *Radiat Med* 2005;23:97–103 Medline
14. Diekmann S, Siebert E, Juran R, et al. **Dose exposure of patients undergoing comprehensive stroke imaging by multidetector-row CT: comparison of 320-detector row and 64-detector row CT scanners.** *AJNR Am J Neuroradiol* 2010;31:1003–09 CrossRef Medline
15. Yamauchi-Kawara C, Fujii K, Aoyama T, et al. **Radiation dose evaluation in multidetector-row CT imaging for acute stroke with an anthropomorphic phantom.** *Br J Radiol* 2010;83:1029–41 CrossRef Medline
16. Bauhs JA, Vrieze TJ, Primak AN, et al. **CT dosimetry: comparison of measurement techniques and devices.** *Radiographics* 2008;28:245–53 CrossRef Medline
17. McCollough CH, Leng S, Yu L, et al. **CT dose index and patient dose: they are *not* the same thing.** *Radiology* 2011;259:311–16 CrossRef Medline
18. Rong X, Cody D. **How accurate is estimating CT skin dose based on CTDI?** *Med Phys* 2010;37:3463 CrossRef
19. Patient Monitoring Solutions nanoDot Dosimeter [technical specifications]. Glenwood, IL: Landauer Inc; 2010
20. Stecker MS, Balter S, Towbin RB, et al. **Guidelines for patient radiation dose management.** *J Vasc Interv Radiol* 2009;20:S263–73 CrossRef Medline
21. Miller DL, Balter S, Cole PE, et al. **Radiation doses in interventional radiology procedures: the RAD-IR study: part II: skin dose.** *J Vasc Interv Radiol* 2003;14:977–90 CrossRef Medline
22. Miller DL, Schueler BA, Balter S. **New recommendations for occupational radiation protection.** *J Am Coll Radiol* 2012;9:366–68 CrossRef
23. Averbeck D. **Does scientific evidence support a change from the LNT model for low-dose radiation risk extrapolation?** *Health Phys* 2009;97:493–504 CrossRef Medline
24. Durand DJ. **A rational approach to the clinical use of cumulative effective dose estimates.** *AJR Am J Roentgenol* 2011;197:160–62 CrossRef Medline

Effects of Radiation Exposure on the Cost-Effectiveness of CT Angiography and Perfusion Imaging in Aneurysmal Subarachnoid Hemorrhage

J. Ivanidze, R.A. Charalel, I. Shuryak, D. Brenner, A. Pandya, O.N. Kallas, K. Kesavabhotla, A.Z. Segal, M.S. Simon, and P.C. Sanelli

ABSTRACT

BACKGROUND AND PURPOSE: CT angiography and perfusion imaging is an important prognostic tool in the management of patients with aneurysmal subarachnoid hemorrhage. The purpose of this study was to perform a cost-effectiveness analysis of advanced imaging in patients with SAH, incorporating the risks of radiation exposure from CT angiography and CT perfusion imaging.

MATERIALS AND METHODS: The risks of radiation-induced brain cancer and cataracts were incorporated into our established decision model comparing the cost-effectiveness of CT angiography and CT perfusion imaging and transcranial Doppler sonography in SAH. Cancer risk was calculated by using National Cancer Institute methodology. The remaining input probabilities were based on literature data and a cohort at our institution. Outcomes were expected quality-adjusted life years gained, costs, and incremental cost-effectiveness ratios. One-way, 2-way, and probabilistic sensitivity analyses were performed.

RESULTS: CT angiography and CT perfusion imaging were the dominant strategies, resulting in both better health outcomes and lower costs, even when incorporating brain cancer and cataract risks. Our results remained robust in 2-way sensitivity analyses varying the prolonged latency period up to 30 years, with either brain cancer risk up to 50 times higher than the upper 95% CI limit or the probability of cataracts from 0 to 1. Results were consistent for scenarios that considered either symptomatic or asymptomatic patients with SAH. Probabilistic sensitivity analysis confirmed our findings over a broad range of selected input parameters.

CONCLUSIONS: While risks of radiation exposure represent an important consideration, CT angiography and CT perfusion imaging remained the preferred imaging compared with transcranial Doppler sonography in both asymptomatic and symptomatic patients with SAH, with improved health outcomes and lower health care costs, even when modeling a significantly higher risk and shorter latency period for both cataract and brain cancer than that currently known.

ABBREVIATIONS: CTAP = CT angiography and CT perfusion; NCI = National Cancer Institute; QALY = quality-adjusted life year; TCD = transcranial Doppler sonography

Aneurysmal subarachnoid hemorrhage is a devastating illness with the reported incidence estimated as 14.5 per 100,000 person years in the United States.[1] SAH is associated with a mortality of 15%, and approximately 58% of survivors experience functional disability, with global cognitive impairment being a major contributor to poor functional status.[2] SAH is also associated with a considerable economic burden, with average inpatient costs of $150,101 for patients with symptomatic vasospasm in the United States and $110,310 for patients without symptomatic vasospasm.[3] A study conducted in the United Kingdom in 2010 found the total annual economic burden of SAH to be approximately £510 million ($873.5 million),[4] accounting for outpatient care, cerebrovascular rehabilitation, and social services. The same study found an estimated annual total of 74,807 quality-adjusted life years (QALYs) lost due to SAH. Therefore, SAH is associated with a substantial burden on health care resources, most of which are related to the long-term effects of functional and cognitive disability.

The marked increase in CT use during the past several decades

Received August 16, 2016; accepted after revision October 3.

From the Departments of Radiology (J.I., R.A.C., O.N.K., K.K., P.C.S.), Neurology (A.Z.S.), and Internal Medicine and Public Health (M.S.S.), Weill Cornell Medical College, NewYork-Presbyterian Hospital, New York, New York; Department of Radiology (I.S., D.B.), NewYork-Presbyterian Hospital, Columbia University Medical Center, New York, New York; Department of Health Policy and Management (A.P.), Harvard T.H. Chan School of Public Health, Boston, Massachusetts; and Department of Radiology (M.S.S., P.C.S.), Northwell Health, Manhasset, New York.

This work was supported by the Radiological Society of North America Research and Education Foundation (Resident Research Grant RR1429 to Jana Ivanidze).

Preliminary results of this work were presented as an oral scientific paper presentation at: Annual Meeting of the Radiological Society of North America, November 30 to December 5, 2014; Chicago, Illinois.

Please address correspondence to Jana Ivanidze, MD, PhD, Department of Radiology, NewYork-Presbyterian Hospital/Weill Cornell Medicine, New York, NY 10065; e-mail: jai9018@nyp.org; @jana_ivanidze

http://dx.doi.org/10.3174/ajnr.A5034

Table 1: Input parameters added into the decision analytic model incorporating the effects of radiation exposure

Input Parameter	Value	Source
Probability of brain cancer	27.35 per 100,000 person years	Calculated using NCI methodology (Berrington de Gonzalez et al,[15] see main text for further details)
Probability of cataract	0.0025	Yuan et al[13]
Latency of brain cancer	10.7 yr	Kranzinger et al[12]
Latency of cataract	6 yr	Henk et al[14]
Utility of brain cancer	0.69	de Rooij et al[19]
Utility of cataract	0.86	Kallmes and Kallmes[20]
Cost of brain cancer	$49,301.70	de Rooij et al[19]
Cost of cataract	$2692	Kallmes and Kallmes[20]

Table 2: Lifetime brain cancer risks[a]

Age at Treatment (yr)	Sex	Life Expectancy (mRS Score)	Lifetime Brain Cancer Risk (per 100,000 Individuals) (Mean) (95% CI)
70	M	Normal (0–2)	8.14 (1.52–23.82)
70	M	Reduced (3–5)	2.33 (0.44–6.82)
70	F	Normal (0–2)	2.47 (0.52–6.84)
70	F	Reduced (3–5)	0.66 (0.14–1.83)
50	M	Normal (0–2)	27.35 (5.25–80.16)[b]
50	M	Reduced (3–5)	5.26 (1.01–15.40)
50	F	Normal (0–2)	7.32 (1.55–20.36)
50	F	Reduced (3–5)	1.39 (0.29–3.85)

[a] Risks were calculated using NCI methodology (https://irep.nci.nih.gov/radrat/), adjusted for life expectancy.[15] The average dose for a CT+CTA+CTP examination was estimated from published literature.[16]

[b] To assume a conservative approach, we used the highest modeled risk (50-year-old male patient with normal life expectancy) for our base case scenario.

has revolutionized the practice of medicine and is associated with a marked rise in administered radiation doses.[5] This increase in radiation dose is attributable, in part, to the increased speed of image acquisition, allowing multiphase examinations to evaluate greater coverage of the body and provide functional information. This has resulted in a significant increase in the population's cumulative exposure to ionizing radiation and concern for the potential increase in cancer risk.[6] In 2009, the US Food and Drug Administration issued a notification regarding the safety of CT perfusion in administering high radiation doses.[7] Consequently, there has been a focus on reducing radiation exposure from medical imaging and evaluating the appropriate use of CT.[8]

The purpose of our study was to incorporate the short- and long-term risks of ionizing radiation exposure from CT angiography and CT perfusion (CTAP) imaging into our established cost-effectiveness decision model of patients with aneurysmal subarachnoid hemorrhage[9] to determine whether the risks of radiation-induced brain cancer and cataracts would potentially alter the model results. In our previous work, which did not include the downstream effects of radiation exposure from CTAP on health outcomes and health care costs, our model results indicated that CTAP is the preferred imaging strategy compared with transcranial Doppler sonography (TCD), leading to improved clinical outcomes and lower health care costs in patients with SAH.[9] Our hypothesis is that CTAP will remain the preferred imaging strategy in patients with SAH due to its relatively low risk from radiation exposure coupled with the high morbidity and mortality rates in this patient population.

MATERIALS AND METHODS

Model Structure

Our established decision-analysis model was developed by using the TreeAge Pro software program (Version 2013.1.0; TreeAge Software, Williamstown, Massachusetts).[9] The model compares the health and economic consequences of 2 imaging strategies for management of SAH: TCD and CTAP. Following aneurysmal rupture, patients with SAH are classified as either symptomatic or asymptomatic for complications such as vasospasm and/or delayed cerebral ischemia. The test result of either TCD or CTAP leads to management options, including no treatment (patient observation), immediate treatment with medical hypertensive therapy, and further testing by using digital subtraction angiography with potential interventional treatment. The organization of the branches in the model is based on the Guidelines for the Management of Aneurysmal Subarachnoid Hemorrhage published by the American Heart Association/American Stroke Association[10] and a clinical decision-making algorithm derived from consultation with 4 neurologists specializing in neurointensive care at New York-Presbyterian Hospital Weill Cornell Campus for specific clinical scenarios.

Patient Population

The base case scenario is a 50-year-old patient, representing the average age in a previously described SAH cohort at our institution.[9] Inclusion criteria for the empiric patient cohort are described in detail in our previously published decision analytic model.[9] Briefly, this cohort included adult patients with documented aneurysmal SAH at admission enrolled in an internal review board–approved prospective diagnostic accuracy trial at our institution. Patients underwent aneurysm repair and were monitored in the neurologic intensive care unit, as per the standard of care. Patients were defined as symptomatic if they had documented clinical deterioration with the occurrence of focal neurologic impairment or a decrease of at least 2 points on the Glasgow Coma Scale that was new and not attributable to other causes. Patients who did not experience the above symptoms were defined as asymptomatic. All patients were imaged with CTAP on the day of occurrence of symptoms or on days 6–8 in case of asymptomatic patients. Patients who had negative CTAP findings were managed conservatively. Patients who had positive CTAP findings received medically induced hypertensive therapy as per standard guidelines.[11] Patients who did not respond to medical therapy proceeded to angiographic testing. If angiographic testing was positive for vasospasm, patients were treated intraprocedurally with intra-arterial verapamil.

Input Probabilities

Input Parameters Derived from Published Literature. Table 1 lists all input parameters incorporated in our expanded decision analytic model incorporating the effects of radiation exposure. All other preexisting input parameters are described in detail in our previously published decision analytic model.[9] Probabilities were

Table 3: Cost-effectiveness analysis results: overall patient population[a]

Strategy	Cost ($)	Incremental Cost ($)	Effectiveness (QALYs)	Incremental Effectiveness (QALYs)	Incremental Cost-Effectiveness Ratio ($/QALY)
CTAP	147,116	–	13.81	–	
TCD	154,718	7601	13.62	−0.1972	Dominated

[a] CTAP imaging strategy is used as the reference in the incremental cost-effectiveness results.

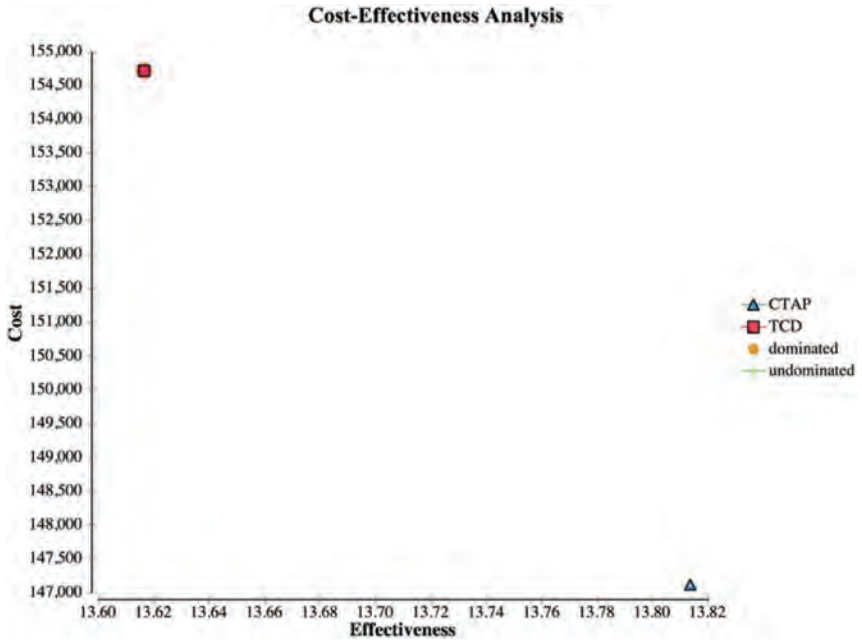

FIG 1. Cost-effectiveness analysis results. The CTAP strategy had greater QALYs and lower cost than the TCD strategy after incorporating the risks of brain cancer and cataract.

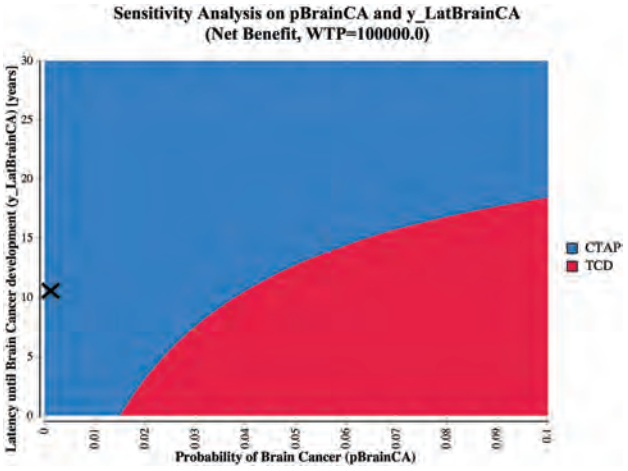

FIG 2. Two-way sensitivity analysis on the probability of brain cancer and the latency of brain cancer overall in the patient population. The CTAP strategy is indicated in blue, and the TCD strategy is indicated in red. *X* denotes the base case (latency of brain cancer = 10.7 years based on published literature; modeled probability of brain cancer = 0.0002725; 95% CI, 0.000053–0.000802). A willingness-to-pay (WTP) threshold of $100,000 was assumed.

calculated by using a conditionally dependent multinomial prediction model.

A mean brain cancer latency of 10.7 years after exposure was used in the model based on published literature.[12] The risk of cataract from radiation exposure related to CTAP was estimated at 0.0025 based on published literature.[13] The average latency of cataract is reported as 6 years after exposure.[14]

Risks from Radiation Exposure. Lifetime brain cancer risk from CTAP was calculated by using National Cancer Institute (NCI) methodology (https://irep.nci.nih.gov/radrat/) and adjusted for life expectancy.[15] As demonstrated in Table 2, the risks differed on the basis of patient sex, age, and life expectancy. We conservatively elected to use the highest modeled risk as the base case risk of radiation-induced brain cancer included in the model, which was 27.25 per 100,000 persons per year (95% CI, 5.3–80.2 per 100,000) in a 50-year-old male patient with normal life expectancy (Table 2). The average brain effective dose from NCCT/CTAP used in the risk calculation was 16.4 mSv (range, 11.8–27.3 mSv), and the mean dose-length product was 6790.0 mGy × cm, based on published literature.[16] Of note, this mean effective dose has been further decreased in recent years, with published studies citing comprehensive acute stroke protocol NCCT/CTAP doses of up to 10.6 mSv.[17] However, we sought a conservative approach and elected to use the higher mean effective dose of 16.4 mSv because the empiric patient cohort used as a basis for our decision analytic model had received this dose. Furthermore, our model results would represent the higher limit of radiation exposure from CTAP imaging in this cohort.

Outcomes

Health Outcomes. Outcome health states reflect functional outcomes from SAH, incorporating quality-of-life impairments associated with cataract formation and developing brain cancer.

The probabilities for long-term clinical outcomes from SAH, representing health states, were categorized as recovered (mRS, 0–2), disability (mRS, 3–5), or death (mRS, 6) and were derived from the International Subarachnoid Aneurysm Trial.[1]

Utility Weights and Quality-Adjusted Life Years. Utilities were calculated as a weighted average from a systematic review of utilities assigned according to mRS scores. The utilities of recovered and disability were 0.80 and 0.22, respectively.[18] Life expectancies in each health state were derived from literature review as 28 years for recovered (mRS, 0–2),[19] and 10.8 years for disability (mRS, 3–5).[20] Death was assigned a value of zero for both life years and utility.

The utility of brain cancer of 0.692 was assumed on the basis of published literature.[21] The utility of cataract of 0.86 was assumed on the basis of published literature.[22]

Table 4: One-way sensitivity analysis results: probability of cataract[a]

Probability of Cataract	Strategy	Cost ($)	Effectiveness (QALYs)	Incremental Cost ($)	Incremental Effectiveness (QALYs)	Incremental Cost-Effectiveness Ratio ($/QALY)
0	CTAP	147,110	13.81	0	0	
0	TCD	154,719	13.62	7608.40	−0.20	Dominated
0.2	CTAP	147,625	13.80	0	0	
0.2	TCD	154,719	13.62	7094.12	−0.18	Dominated
0.4	CTAP	148,139	13.78	0	0	
0.4	TCD	154,719	13.62	6579.84	−0.17	Dominated
0.6	CTAP	148,653	13.77	0	0	
0.6	TCD	154,719	13.62	6065.56	−0.15	Dominated
0.8	CTAP	149,168	13.75	0	0	
0.8	TCD	154,719	13.62	5551.28	−0.13	Dominated
1	CTAP	149,682	13.73	0	0	
1	TCD	154,719	13.62	5037.00	−0.12	Dominated

[a] In a 1-way sensitivity analysis, CTAP remained the optimal strategy when varying the probability of cataract from 0.0 to 1.0.

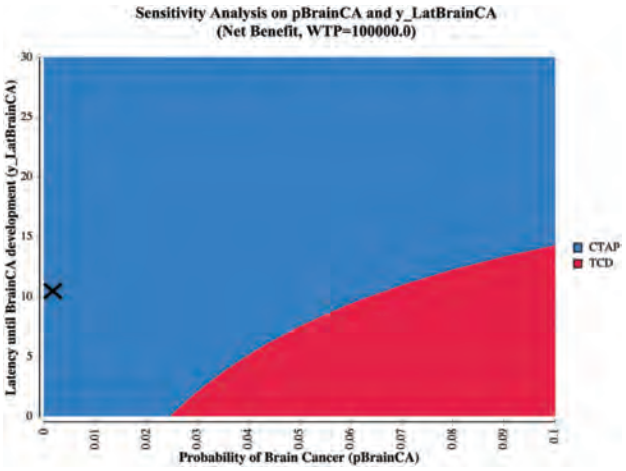

FIG 3. Two-way sensitivity analysis on the probability of brain cancer and the latency of brain cancer and subanalysis of the asymptomatic patient population. The CTAP strategy is indicated in blue, and the TCD strategy is indicated in red. *X* denotes the base case (latency of brain cancer = 10.7 years based on published literature; modeled probability of brain cancer = 0.0002725; 95% CI, 0.000053–0.000802). A willingness-to-pay (WTP) threshold of $100,000 was assumed.

Health outcomes were expressed as quality-adjusted-life years gained for each imaging strategy. Lifetime QALYs were calculated by multiplying the sum of the number of years spent in each health state by the utility associated with that state.

Cost Outcomes. Evaluation of costs included only direct medical costs; indirect costs such as loss of earnings through inability to work were omitted according to standard methods in performing cost-effectiveness analyses in the United States. Imaging costs were based on the 2012 Medicare rates (including both technical and professional fees) based on the Current Procedural Terminology codes. The 2012 rates were chosen to maintain consistency with our empiric cohort. The total costs for long-term care in each health state were estimated from the literature and multiplied by the life expectancy. Current values for both benefits and costs were calculated by discounting the original values at a rate of 3% per year, as recommended for cost-effectiveness analyses in the United States.[23] Costs of brain cancer[24] and cataract surgery[25] were estimated on the basis of published literature.

Statistical Analyses

Incremental cost-effectiveness ratios were calculated as well as the incremental cost per QALY gained. Univariable and multivariable sensitivity analyses were performed to determine the independent and combined effect of input parameter uncertainty. A willingness-to-pay threshold of $100,000/QALY was assumed on the basis of previously published work.[9] Two-way sensitivity analyses were performed to evaluate the impact of the following: 1) the probability of brain cancer and latency until brain cancer development, and 2) the probability of cataract and latency until cataract development based on model results. A scenario analysis considering only asymptomatic patients was also performed.

To assess overall model uncertainty, we conducted probabilistic sensitivity analysis in which 10,000 simulations were performed. The selected key variables were assumed to have triangular distributions. In a separate probabilistic sensitivity analysis, the range of the probability of brain cancer was extended to incorporate an upper limit of 5% (>50 times the upper limit of the 95% confidence interval), and 10,000 simulations of the model were repeated.

RESULTS

The per-person cost for the CTAP strategy was $147,116. The per-person cost for the TCD strategy was $154,718. The CTAP strategy resulted in a gain of 13.81 QALYs. The TCD strategy resulted in a gain of 13.62 QALYs (Table 3). Because the CTAP strategy resulted in lower cost and greater gains in QALYs, the CTAP strategy was dominant over the TCD strategy. When we varied the probability of brain cancer, the CTAP strategy remained cost-effective at $100,000/QALY as long as the risk of brain cancer remained lower than approximately 4%, compared with 0.03% in the base case. This threshold value was 50 times greater than the upper limit of the 95% confidence interval (0.08%) (Figs 1 and 2). Our results remained robust when varying the latency of brain cancer onset from 0.1 years to 30 years at base case brain cancer risk (Fig 2).

In 2-way sensitivity analysis, the CTAP strategy remained dominant over the TCD strategy under all circumstances when the probability of cataract was varied from 0 to 1 and cataract

Table 5: Cost-effectiveness analysis results: asymptomatic patient population subanalysis[a]

Strategy	Cost ($)	Incremental Cost ($)	Effectiveness (QALYs)	Incremental Effectiveness (QALYs)	Incremental Cost-Effectiveness Ratio ($/QALY)
CTAP	145,247	–	13.86	–	
TCD	156,272	11,024	13.51	−0.3517	Dominated

[a] CTAP imaging strategy is used as the reference in the incremental cost-effectiveness results.

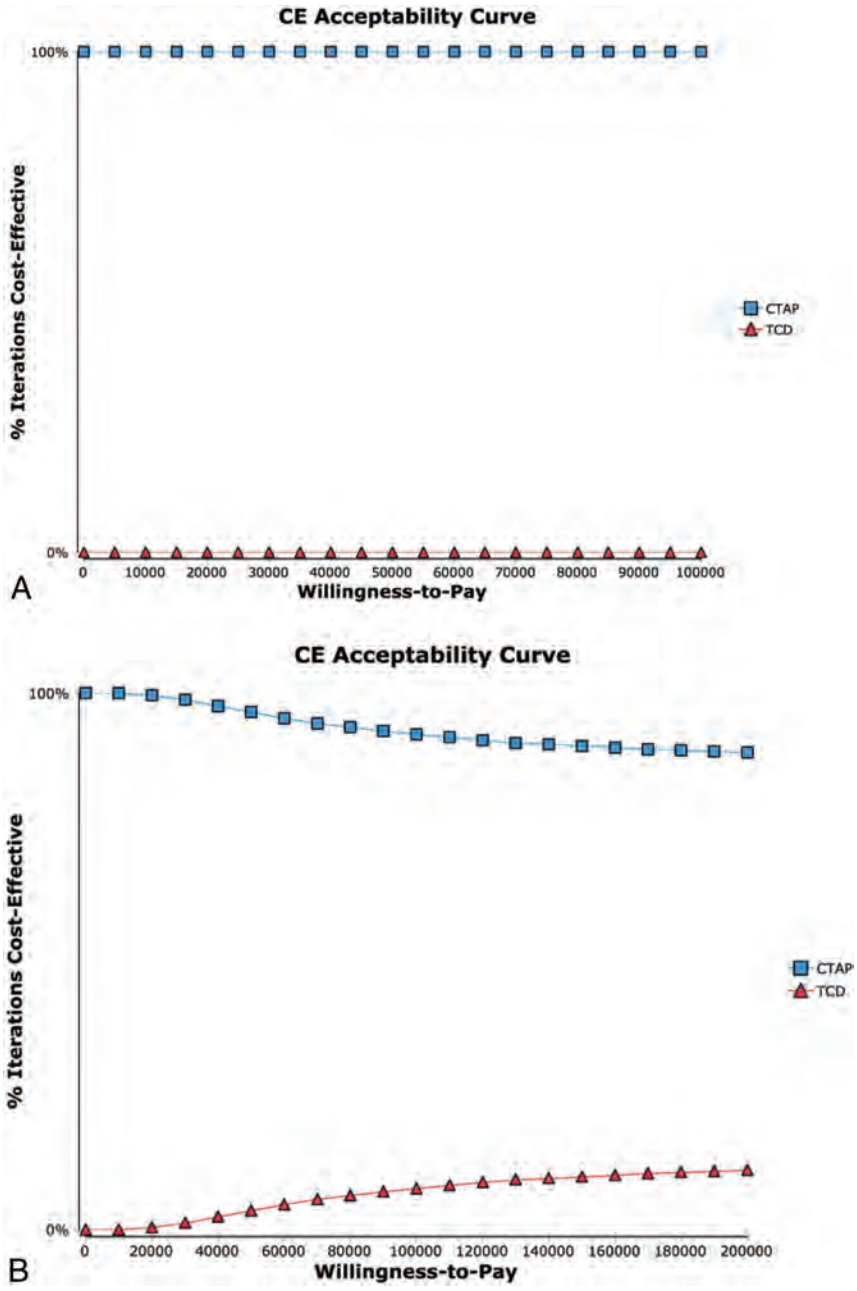

FIG 4. Cost-effectiveness (CE) acceptability curves. CE acceptability curves were calculated incorporating distributions reported in the literature and the probability of brain cancer as modeled on the basis of NCI methodology (*A*, see Table 1) and, in a separate subanalysis, incorporating an upper limit of the probability of brain cancer of 5% (ie, >50 times higher than the calculated 95% confidence interval upper limit of 80.16 per 100,000, *B*).

latency was varied from 0.1 to 30 years. Table 4 demonstrates results of a 1-way sensitivity analysis varying the probability of cataract from 0 to 1 when there was no condition for which TCD was preferred.

A scenario analysis of asymptomatic patients with SAH did not change the results; CTAP remained the dominant strategy compared with TCD (Fig 3 and Table 5).

In probabilistic sensitivity analysis, CTAP was the preferred strategy in 100% of iterations across a broad range of willingness-to-pay threshold values (Fig 4*A*). When the upper limit of the probability distribution for developing brain cancer was increased to 5% (compared with the upper limit of the 95% confidence interval, 0.08%; Table 2), CTAP was still preferred in >92% of iterations at a willingness-to-pay value below $100,000/QALY (Fig 4*B*).

DISCUSSION

Our model demonstrates that while the development of brain cancer and cataract from radiation exposure in patients undergoing CTAP is an important consideration, it does not alter CTAP as the preferred imaging strategy in SAH compared with TCD. Similar to our prior analysis that did not incorporate these radiation-induced complications, we found that CTAP leads to greater quality-adjusted life expectancy for patients with SAH and lower health care costs after incorporating brain cancer and cataract risk. These findings were robust across a broad range of plausible values and remained consistent even after modeling a significantly higher risk and shorter latency period than known from current literature. Moreover, we conservatively elected to use the highest modeled risk (50-year-old male patient with normal life expectancy) for our base case scenario. This age approximates the median age of a patient with SAH in published cohorts.[1] If we had assumed a higher age or additional comorbidities, results would have been even more favorable for CTAP because of lower lifetime brain cancer risk (Table 2).

In recent years, CTAP has become increasingly recognized as an important prognostic tool in patients with SAH, especially given the recognized importance of cerebral blood flow evaluation in the prediction of poor clinical outcomes.[26] Moreover, recent studies have shown that blood-brain barrier permeability evaluation with CTAP may become an important early prognostic marker of global cerebral edema[27] and delayed cerebral isch-

emia.[28] Early identification of these complications before they become apparent on noncontrast CT further increases the utility of CTAP. Furthermore, CTAP radiation doses have gradually decreased in recent years in an effort to decrease radiation exposure to the patient, with published studies citing comprehensive acute stroke protocol NCCT/CTAP doses of up to 10.6 mSv.[17] Therefore, the radiation risk assumed in our model may, in fact, be overestimated, further supporting CTAP as the superior imaging technique in patients with SAH.

While radiation risk is an important consideration when selecting the appropriate imaging technique, our study shows that after we account for the risk of developing radiation-induced brain cancer and the risk of developing radiation-induced cataract, CTAP remains the superior imaging technique in patients with SAH, resulting in improved clinical outcomes and lower health care costs. This has important implications in the clinical decision-making for the management of patients with SAH, supporting the use of CTAP imaging.

The main limitation of our study is that a decision-modeling study design was performed instead of a prospective randomized clinical trial. Decision analytic models can help inform clinical decision-making by considering all potential consequences, incorporating the best available evidence, and considering uncertainty in estimates. Such models are particularly useful when randomized controlled trials are not feasible, such as in the case of gauging the contribution of radiation exposure effects on management strategies for SAH. This scenario is particularly relevant in this study given the long-term latency period associated with radiation-induced brain cancer. Another limitation in decision modeling is the variability of the input parameters. However, we performed several types of sensitivity analyses (1-way, 2-way, and probabilistic) to assess the variability of each input in the model results.

CONCLUSIONS

While there have been, to our knowledge, no randomized trials directly comparing the impact of different imaging modalities on clinical outcomes of patients with SAH, recent publications have demonstrated the added benefit of CTAP imaging in the detection of vasospasm and perfusion deficits.[9,29] Moreover, CT perfusion imaging has the added benefit of evaluating delayed cerebral ischemia, an important SAH complication and determinant of poor clinical outcomes in SAH,[26] which is particularly important given the limitations of clinical examination[30] and TCD[31] in this patient population.

Until recently, the focus has been on avoiding any kind of radiation exposure related to CT-based imaging, focusing on sonography-based methods instead. However, our study shows that the significant health benefits of CTAP outweigh the risks related to radiation exposure, even when modeling a far greater brain cancer risk than has been determined by using NCI methodology.

Future studies assessing the clinical and cost effectiveness of other imaging studies associated with radiation exposure should include the short- and long-term effects of radiation exposure to provide a comprehensive analysis of the benefits and risks for a given patient population.

Disclosures: Jana Ivanidze—*RELATED*: *Grant*: Radiological Society of North America Research and Education Foundation Resident Research Grant, *Comments*: Resident Research Grant (awarded to J.I.) 2014–2015.

REFERENCES

1. Molyneux AJ, Kerr RS, Birks J, et al; ISAT Collaborators. **Risk of recurrent subarachnoid haemorrhage, death, or dependence and standardised mortality ratios after clipping or coiling of an intracranial aneurysm in the International Subarachnoid Aneurysm Trial (ISAT): long-term follow-up.** *Lancet Neurol* 2009;8:427–33 CrossRef Medline
2. Springer MV, Schmidt JM, Wartenberg KE, et al. **Predictors of global cognitive impairment 1 year after subarachnoid hemorrhage.** *Neurosurgery* 2009;65:1043–50; discussion 1050–51 CrossRef Medline
3. Chou CH, Reed SD, Allsbrook JS, et al. **Costs of vasospasm in patients with aneurysmal subarachnoid hemorrhage.** *Neurosurgery* 2010;67:345–51; discussion 351–52 CrossRef Medline
4. Rivero-Arias O, Gray A, Wolstenholme J. **Burden of disease and costs of aneurysmal subarachnoid haemorrhage (aSAH) in the United Kingdom.** *Cost Eff Resour Alloc* 2010;8:6 CrossRef Medline
5. Smith-Bindman R, Lipson J, Marcus R, et al. **Radiation dose associated with common computed tomography examinations and the associated lifetime attributable risk of cancer.** *Arch Intern Med* 2009; 169:2078–86 CrossRef Medline
6. Amis ES Jr, Butler PF; American College of Radiology. **ACR white paper on radiation dose in medicine: three years later.** *J Am Coll Radiol* 2010;7:865–70 CrossRef Medline
7. Wintermark M, Lev MH. **FDA investigates the safety of brain perfusion CT.** *AJNR Am J Neuroradiol* 2010;31:2–3 CrossRef Medline
8. Goehler A, Gazelle GS. **Examining the use of comparative and cost-effectiveness analyses in radiology.** *AJR Am J Roentgenol* 2014;203: 939–44 CrossRef Medline
9. Sanelli PC, Pandya A, Segal AZ, et al. **Cost-effectiveness of CT angiography and perfusion imaging for delayed cerebral ischemia and vasospasm in aneurysmal subarachnoid hemorrhage.** *AJNR Am J Neuroradiol* 2014;35:1714–20 CrossRef Medline
10. Meyers PM, Schumacher HC, Higashida RT, et al; Joint Writing Group of the Technology Assessment Committee, Society of NeurolnterventionalSurgery, Society of Interventional Radiology, Joint Section on Cerebrovascular Neurosurgery of the American Association of Neurological Surgeons and Congress of Neurological Surgeons, Section of Stroke and Interventional Neurology of the American Academy of Neurology. **Reporting standards for endovascular repair of saccular intracranial cerebral aneurysms.** *J Neurointerv Surg* 2010;2:312–23 CrossRef Medline
11. Miller JA, Dacey RG Jr, Diringer MN. **Safety of hypertensive hypervolemic therapy with phenylephrine in the treatment of delayed ischemic deficits after subarachnoid hemorrhage.** *Stroke* 1995;26: 2260–66 CrossRef Medline
12. Kranzinger M, Jones N, Rittinger O, et al. **Malignant glioma as a secondary malignant neoplasm after radiation therapy for craniopharyngioma: report of a case and review of reported cases.** *Onkologie* 2001;24:66–72 Medline
13. Yuan MK, Tsai DC, Chang SC, et al. **The risk of cataract associated with repeated head and neck CT studies: a nationwide population-based study.** *AJR Am J Roentgenol* 2013;201:626–30 CrossRef Medline
14. Henk JM, Whitelocke RA, Warrington AP, et al. **Radiation dose to the lens and cataract formation.** *Int J Radiat Oncol Boil Phys* 1993;25: 815–20 CrossRef Medline
15. Berrington de Gonzalez A, Iulian Apostoaei A, Veiga LH, et al. **RadRAT: a radiation risk assessment tool for lifetime cancer risk projection.** *J Radiol Prot* 2012;32:205–22 CrossRef Medline
16. Mnyusiwalla A, Aviv RI, Symons SP. **Radiation dose from multidetector row CT imaging for acute stroke.** *Neuroradiology* 2009;51: 635–40 CrossRef Medline
17. Diekmann S, Siebert E, Juran R, et al. **Dose exposure of patients undergoing comprehensive stroke imaging by multidetector-row CT: comparison of 320-detector row and 64-detector row CT scanners.** *AJNR Am J Neuroradiol* 2010;31:1003–09 CrossRef Medline
18. Post PN, Stiggelbout AM, Wakker PP. **The utility of health states after stroke: a systematic review of the literature.** *Stroke* 2001;32: 1425–29 CrossRef Medline
19. de Rooij NK, Linn FH, van der Plas JA, et al. **Incidence of subarach-**

noid haemorrhage: a systematic review with emphasis on region, age, gender and time trends. *J Neurol Neurosurg Psychiatry* 2007;78:1365–72 CrossRef Medline
20. Kallmes DF, Kallmes MH. **Cost-effectiveness of angiography performed during surgery for ruptured intracranial aneurysms.** *AJNR Am J Neuroradiol* 1997;18:1453–62 Medline
21. McCarter H, Furlong W, Whitton AC, et al. **Health status measurements at diagnosis as predictors of survival among adults with brain tumors.** *J Clin Oncol* 2006;24:3636–43 CrossRef Medline
22. Busbee BG, Brown MM, Brown GC, et al. **Cost-utility analysis of cataract surgery in the second eye.** *Ophthalmology* 2003;110:2310–17 CrossRef Medline
23. Weinstein MC, Siegel JE, Gold MR, et al. **Recommendations of the Panel on Cost-Effectiveness in Health and Medicine.** *JAMA* 1996;276:1253–58 CrossRef Medline
24. Martino J, Gomez E, Bilbao JL, et al. **Cost-utility of maximal safe resection of WHO grade II gliomas within eloquent areas.** *Acta Neurochir (Wien)* 2013;155:41–50 CrossRef Medline
25. Camejo MD, Rupani MK, Rebenitsch RL. **A comparative analysis of the cost of cataract surgery abroad and in the United States.** *Indian J Ophthalmol* 2014;62:748–49 CrossRef Medline
26. Sanelli PC, Anumula N, Johnson CE, et al. **Evaluating CT perfusion using outcome measures of delayed cerebral ischemia in aneurysmal subarachnoid hemorrhage.** *AJNR Am J Neuroradiol* 2013;34:292–98 CrossRef Medline
27. Ivanidze J, Kallas ON, Gupta A, et al. **Application of blood-brain barrier permeability imaging in global cerebral edema.** *AJNR Am J Neuroradiol* 2016;37:1599–603 CrossRef Medline
28. Ivanidze J, Kesavabhotla K, Kallas ON, et al. **Evaluating blood-brain barrier permeability in delayed cerebral infarction after aneurysmal subarachnoid hemorrhage.** *AJNR Am J Neuroradiol* 2015;36:850–54 CrossRef Medline
29. Dankbaar JW, de Rooij NK, Velthuis BK, et al. **Diagnosing delayed cerebral ischemia with different CT modalities in patients with subarachnoid hemorrhage with clinical deterioration.** *Stroke* 2009;40:3493–98 CrossRef Medline
30. Schmidt JM, Wartenberg KE, Fernandez A, et al. **Frequency and clinical impact of asymptomatic cerebral infarction due to vasospasm after subarachnoid hemorrhage.** *J Neurosurg* 2008;109:1052–59 CrossRef Medline
31. Carrera E, Schmidt JM, Oddo M, et al. **Transcranial Doppler for predicting delayed cerebral ischemia after subarachnoid hemorrhage.** *Neurosurgery* 2009;65:316–23; discussion 323–24 CrossRef Medline

Genetics of Von Hippel-Lindau Disease

D.C. Dwyer and R.K. Tu

ABBREVIATIONS: VHL = Von Hippel Lindau; pVHL = VHL protein; HIF = hypoxia-inducible factor

Von Hippel-Lindau (VHL) disease is a rare, autosomal dominant syndrome that is associated with the development of tumors in a variety of organ systems, most commonly hemangioblastoma of the central nervous system and retina.[1] The ocular manifestations of the disease were first independently described by 2 ophthalmologists, Treacher Collins in 1894[2] and Eugene von Hippel in 1904.[3] Both recognized families with angiomatous retinal growths and described them in the medical literature. In 1927, Arvid Lindau,[4] a Swedish pathologist, recognized that these retinal lesions were associated with an increased risk of developing hemangioblastomas of the central nervous system. Since then, VHL disease has been associated with many other lesions, including clear cell renal carcinoma, pheochromocytoma, endolymphatic sac tumors, epididymal and broad ligament cystadenomas, and islet-cell tumors.[5] The prevalence of VHL disease is estimated to be between 1 in 31,000 and 1 in 53,000.[6,7]

DIAGNOSIS

The diagnosis of VHL is often made by using clinical criteria. Patients with a family history of VHL are diagnosed with the disease in the presence of 1 additional tumor—a CNS hemangioblastoma, pheochromocytoma, or clear cell renal carcinoma. Those without a family history must have 2 CNS hemangioblastomas or 1 CNS hemangioblastoma with either a pheochromocytoma or clear cell renal carcinoma.[8,9] With the current understanding of the genetic basis for VHL disease and the availability of molecular genetic testing, the diagnosis of VHL disease may be made in individuals who do not satisfy the clinical diagnostic criteria.

Despite the increased availability and detection rate of genetic testing, negative results are not always definitive. Up to 20% of tumors in individuals with VHL disease result from de novo mutations, and these individuals do not have a family history of the disease.[10] Furthermore, many de novo mutations result in mosaicism, in which patients may have clinical signs of the disease but test negative genetically for it because not all tissues carry the mutation.[11]

MOLECULAR GENETICS

VHL disease is an autosomal dominantly inherited disorder with marked variability in penetrance and phenotype. The *VHL* gene is located on the short arm of chromosome 3 (3p25–26) with its coding sequence represented in 3 exons.[12,13] The gene encodes 2 protein isoforms, a full-length 30-kDa protein (pVHL30) and a smaller 19-kDa protein (pVHL19), generated by alternative translation initiation.[14] The *VHL* gene is evolutionarily conserved and is expressed in all organ systems, not exclusively those affected by VHL disease.[15]

Patients with VHL disease have an inactivating germline mutation in 1 copy of the *VHL* gene and 1 normally functioning wild type allele. Tumor development depends on mutation of the remaining wild type allele in a susceptible target organ. A wide variety of germline mutations have been identified, but the largest group consists of deletions that alter exon sequences.[16] The remaining mutations are due to nonsense mutations or missense substitutions. A complex classification system has been described to correlate genotype and phenotype, but it is less useful for clinical management because an individual may move from one subtype to another.[17]

FUNCTION OF THE TUMOR SUPPRESSOR PROTEIN

The *VHL* gene product is a tumor-suppressor protein that influences many cellular pathways but is best characterized by its function in the oxygen-sensing pathway. The VHL protein (pVHL) has a critical role in regulating a transcription factor called hypoxia-inducible factor (HIF). In the presence of functioning pVHL and normoxic conditions, pVHL binds to a subunit of HIF and acts as a ubiquitin ligase, leading to the destruction of HIF via

From the Virginia Commonwealth University School of Medicine (D.C.D.), Richmond, Virginia; Department of Radiology (R.K.T.), George Washington University Hospital, Washington, DC; and Progressive Radiology (R.K.T.), Falls Church, Virginia.

Please address correspondence to Raymond K. Tu, MD, MS, FACR, Department of Radiology, George Washington University, 2121 K Street NW, Suite 100, Washington, DC 20037; e-mail: Raymond.Tu@progressiveradiology.net

http://dx.doi.org/10.3174/ajnr.A5032

proteasomal degradation. In the presence of functioning pVHL and hypoxic conditions, pVHL is unable to form a ubiquitin ligase and HIF is not degraded. This outcome allows HIF to induce transcription of genes involved in diverse processes including angiogenesis, proliferation, metabolism, and apoptosis (eg, *VEGF*, *PDGFβ*, *TGFα*). In the presence of nonfunctioning pVHL, HIF will not be degraded regardless of oxygen conditions. This feature allows the inappropriate overproduction of hypoxia-inducible messenger RNAs and unregulated cell growth—the hallmark of pVHL-defective cells.[13,18-20]

ROLE OF IMAGING

Imaging plays a crucial role in the diagnosis and surveillance of VHL disease, particularly with identification of CNS hemangioblastomas. These are the most common tumors in VHL disease, affecting 60%–80% of all patients and are the presenting feature in approximately 40% of cases.[11,21,22] VHL disease accounts for approximately one-third of patients with CNS hemangioblastomas. The most common site is the cerebellum (44%–72%), followed by the spinal cord (13%–50%), brain stem (10%–25%), and supratentorial structures (1%).[18,23]

Imaging is also crucial in the identification and surveillance of lesions outside the CNS, including the pancreas, kidneys, adrenal glands, and reproductive organs. Identification of renal carcinoma is of particular importance because it is the major malignant neoplasm of VHL disease and one of the leading causes of mortality.[19] Although retinal hemangioblastomas are the second most common tumor in VHL disease, they are typically only detectable by examination of the dilated eye.[18]

Screening is critical in all patients with VHL disease regardless of symptoms because lesions are treatable. Indeed, the morbidity and mortality of VHL disease has been significantly reduced during the past 20 years due to advanced screening and surgical techniques.[6] Particular screening guidelines vary among different centers but typically include renal, brain, and spinal cord imaging at regular intervals.[24,25]

REFERENCES

1. Maher ER, Neumann, HP, Richard S. **von Hippel-Lindau disease: a clinical and scientific review.** *Eur J Hum Genet* 2011;19:617–23 CrossRef Medline
2. Collins ET. **Intra-ocular growths (two cases, brother and sister, with peculiar vascular new growth, probably primarily retinal, affecting both eyes).** *Trans Ophthal Soc U K* 1894;14:141–49
3. Von Hippel E. **Üeber eine sehr seltene Erkrankung der Netzhaut.** *Albrecht von Græfe's Archiv für Ophthalmologie* 1904;59:83–106 CrossRef
4. Lindau A. **Zur frage der angiomatosis retinae und ihrer hirncomplikation.** *Acta Ophthalmol Scand* 1927;4:193–226
5. Maher ER, Kaelin WG Jr. **von Hippel-Lindau disease.** *Medicine (Baltimore)* 1997;76:381–91 CrossRef Medline
6. Taouli B, Ghouadni M, Corréas JM, et al. **Spectrum of abdominal imaging findings in von Hippel-Lindau disease.** *AJR Am J Roentgenol* 2003;181:1049–54 CrossRef Medline
7. Hes FJ, Feldberg MA. **Von Hippel-Lindau disease: strategies in early detection (renal-, adrenal-, pancreatic masses).** *Eur Radiol* 1999;9:598–610 CrossRef Medline
8. Melmon KL, Rosen SW. **Lindau's disease: review of the literature and study of a large kindred.** *Am J Med* 1964;36:595–617 CrossRef Medline
9. Lamiell JM, Salazar FG, Hsia YE. **von Hippel-Lindau disease affecting 43 members of a single kindred.** *Medicine (Baltimore)* 1989;68:1–29 CrossRef Medline
10. Richards FM, Payne SJ, Zbar B, et al. **Molecular analysis of de-novo germline mutations in the von Hippel-Lindau disease gene.** *Hum Mol Gen* 1995;4:2139–43 CrossRef Medline
11. Sgambati MT, Stolle C, Choyke PL, et al. **Mosaicism in von Hippel-Lindau disease: lessons from kindreds with germline mutations identified in offspring with mosaic parents.** *Am J Hum Genet* 2000;66:84–91 CrossRef Medline
12. Seizinger BR, Rouleau GA, Ozelius LJ, et al. **Von Hippel-Lindau disease maps to the region of chromosome 3 associated with renal cell carcinoma.** *Nature* 1988;332:268–69 CrossRef Medline
13. Latif F, Tory K, Gnarra J, et al. **Identification of the von Hippel-Lindau disease tumor suppressor gene.** *Science* 1993;260:1317–20 CrossRef Medline
14. Renbaum P, Duh FM, Latif F, et al. **Isolation and characterization of the full-length 3′ untranslated region of the human von Hippel-Lindau tumor suppressor gene.** *Hum Genet* 1996;98:666–71 CrossRef Medline
15. Richards FM, Schofield PN, Fleming S, et al. **Expression of the von Hippel-Lindau disease tumour suppressor gene during human embryogenesis.** *Hum Mol Genet* 1996;5:639–44 CrossRef Medline
16. Franke G, Bausch B, Hoffmann MM, et al. **Alu-Alu recombination underlies the vast majority of large VHL germline deletions: molecular characterization and genotype-phenotype correlations in VHL patients.** *Hum Mutat* 2009;30:776–86 CrossRef Medline
17. Gossage L, Eisen T, Maher ER. **VHL, the story of a tumour suppressor gene.** *Nat Rev Cancer* 2015;15:55–64 CrossRef Medline
18. Shanbhogue KP, Hock M, Fatterpaker G, et al. **von Hippel-Lindau disease: review of genetics and imaging.** *Radiol Clin North Am* 2016;54:409–22 CrossRef Medline
19. Maher ER, Yates JR, Harries R, et al. **Clinical features and natural history of von Hippel-Lindau disease.** *Q J Med* 1990;77:1151–63 CrossRef Medline
20. Nordstrom-O'Brien M, van der Luijt RB, van Rooijen E, et al. **Genetic analysis of von Hippel-Lindau disease.** *Hum Mutat* 2010;31:521–37 CrossRef Medline
21. Courcoutsakis NA, Prassopoulos PK, Patronas NJ. **Aggressive leptomeningeal hemangioblastomatosis of the central nervous system in a patient with von Hippel-Lindau disease.** *AJNR Am J Neuroradiol* 2009;30:758–60 CrossRef Medline
22. Wanebo JE, Lonser RR, Glenn GM, et al. **The natural history of central nervous system hemangioblastomas in patients with von Hippel-Lindau disease.** *J Neurosurg* 2003;98:82–94 CrossRef Medline
23. Slater A, Moore NR, Huson SM. **The natural history of cerebellar hemangioblastomas in von Hippel-Lindau disease.** *AJNR Am J Neuroradiol* 2003;24:1570–74 Medline
24. Leung RS, Biswas SV, Duncan M, et al. **Imaging features of von Hippel-Lindau Disease.** *Radiographics* 2008;28:65–79 CrossRef Medline
25. Tomura N, Ito Y, Matsuoka H, et al. **PET findings of intramedullary tumors of the spinal cord using [18F] FDG and [11C] methionine.** *AJNR Am J Neuroradiol* 2013;34:1278–83 CrossRef Medline

Transverse Sinus Stenosis Is the Most Sensitive MR Imaging Correlate of Idiopathic Intracranial Hypertension

P.P. Morris, D.F. Black, J. Port, and N. Campeau

ABSTRACT

BACKGROUND AND PURPOSE: Patients with idiopathic intracranial hypertension have transverse sinus stenosis on gadolinium-bolused MRV, but other MR imaging signs are less consistently seen. Our aim was to demonstrate that transverse sinus stenosis could be identified on conventional MR imaging, and this identification would allow improved diagnostic sensitivity to this condition.

MATERIALS AND METHODS: MR imaging and MRV images from 63 patients with idiopathic intracranial hypertension and 96 controls were reviewed by using 3 independent procedures. MRV images were graded for the presence and degree of stenosis of the transverse sinus. Postgadolinium coronal T1-weighted sequences were evaluated independent of MRV. The dimensions of the proximal and distal transverse sinus were measured from the MRV examinations, and the cross-sectional area of the transverse sinus was calculated. Correlation among the 3 modes of evaluation of the transverse sinus was conducted by using Wilcoxon/Kruskal-Wallis, Pearson, and Spearman ρ nonparametric statistical techniques.

RESULTS: Transverse sinus stenosis was identified bilaterally on MRV in 94% of patients with idiopathic intracranial hypertension and in 3% of controls. On coronal T1 postgadolinium MR images, transverse sinus stenosis was identified in 83% of patients with idiopathic intracranial hypertension and 7% of controls. Previously described MR imaging signs of intracranial hypertension were identified in 8%–61% of patients with idiopathic intracranial hypertension. Correlation among the 3 modes of evaluation was highly significant ($P < .0001$).

CONCLUSIONS: Even without the assistance of an MRV sequence, neuroradiologists can validly identify bilateral transverse sinus stenosis in patients with intracranial hypertension more reliably than other previously described MR imaging findings in this condition. We conclude that transverse sinus stenosis is the most useful and sensitive imaging indicator of this disease state.

ABBREVIATIONS: IIH = idiopathic intracranial hypertension; TS = transverse sinus

Primary idiopathic intracranial hypertension (IIH), alternatively known as pseudotumor cerebri, is a little-understood condition characterized by unexplained elevation of intracranial pressure. The diagnosis is established by the Modified Dandy Criteria, which, in essence, means an opening pressure at lumbar puncture of >250 mm of water in adults and >280 mm in children, with no definable etiology.[1] The condition is known to be more prevalent in young adult women, especially those with an elevated body mass index,[2,3] older men with obstructive sleep apnea,[4-7] and patients with a variety of endocrine conditions.[4,8] It is associated with the use of several medications, most notably vitamin A derivatives and tetracycline antibiotics.[9,10] Headache is the most consistent symptom experienced by patients, though back and shoulder discomfort can be reported too. Papilledema progressing to variable degrees of transient or permanent visual loss is a familiar but not necessarily a sine qua non manifestation. Idiopathic intracranial hypertension in children can present with features less commonly seen in adults, most particularly signs of intracranial mass effect, including cranial nerve deficits, most notably in cranial nerve VI.[11] The prolonged debilitation and suffering associated with this condition can be substantial. Symptoms may overlap those seen in migraine, and misdiagnosis creates delays that may have substantial comorbidities. The most concerning complication of untreated or treatment-resistant IIH is visual loss, which can progress rapidly and become irreversible once the patient becomes symptomatic. Therefore, it is important to recognize and diagnose this condition clinically and on imaging studies as early as possible.

Several brain MR imaging findings have been associated with the diagnosis of idiopathic intracranial hypertension. These in-

Received September 12, 2016; accepted after revision November 2.

From the Department of Radiology, Mayo Clinic, Rochester, Minnesota.

Please address correspondence to Pearse Morris, MB, BCh, Department of Radiology, Mayo Clinic, 200 First Street SW, Rochester, MN 55905; e-mail: morris.ppearse@mayo.edu

http://dx.doi.org/10.3174/ajnr.A5055

clude an appearance of an empty sella (>50% vacancy of the sella with a concave upper surface of the pituitary gland), optic nerve sheath dilation, vascular distension and protrusion of the optic papillae with advanced papilledema, "slit ventricles," and a bright spot at the optic nerve head on diffusion-weighted imaging. However, published sensitivity and prevalence of these findings are inconsistent, ranging between 6% and 66%.[12] When a gadolinium-bolused MRV sequence is available, bilateral transverse sinus (TS) stenosis of >50% degree is seen in 93% of patients with IIH, suggesting that this is the most sensitive imaging characteristic of this condition.[13,14] However, unless the specific diagnosis of IIH has been canvassed in advance and the imaging sequences have been protocoled accordingly, in most instances, the reading neuroradiologist will not have an MRV sequence available to assist in making this diagnosis. Therefore, it is very likely that in a substantial proportion of cases of IIH, only a conventional set of MR images will be obtained and the diagnosis is likely to be missed.

The purpose of this study was to attempt to define the sensitivity with which neuroradiologists might be capable of perceiving signs of TS stenosis on non-MRV imaging, specifically by focusing on the coronal postgadolinium T1-weighted images. In the authors' experience, TS stenosis was identifiable on coronal T1 with gadolinium contrast imaging in a high proportion of patients with IIH, and we conjectured that it might be possible to improve one's sensitivity to this disease state by emphasizing the utility of this sequence, even when an MRV examination has not been performed.

MATERIALS AND METHODS

Subjects

We conducted a retrospective study with institutional review board approval of images acquired during a 5-year period (2010–2015) in 63 adult and teenage patients in whom the diagnosis of IIH was established according to the Modified Dandy Criteria. Patients were identified by searching key words in the electronic medical records. Only patients who had available images from both a gadolinium-bolused MRV examination and a pre-/postgadolinium MR imaging examination during the period of review were included. Patients who had already undergone a therapeutic shunting procedure, such as a ventriculoperitoneal shunt or lumbar-peritoneal shunt were excluded from the study. Ongoing or already initiated medical therapy did not preclude inclusion in the study. Electronic medical records were reviewed for clinical parameters such as symptom profile, age, weight, body mass index, opening pressure at lumbar puncture, visual symptoms, and duration of symptoms.

A control group of 96 patients without IIH was identified from a consecutive list of MR imaging/MRV studies performed during the same period (Table 1). Inclusion criteria were adult age between 18 and 60 years and availability of gadolinium-bolused MRV images and pre-/postgadolinium MR images from the same period. Patients with obvious intracranial pathology, such as intracranial masses, hydrocephalus, venous thrombosis, or postsurgical/traumatic derangement of the dural sinuses, and so forth, were excluded. Control patients carried a variety of diagnoses centered on migraine, migraine variants, or headache not otherwise specified.

Table 1: Clinical characteristics of patients with idiopathic intracranial hypertension and controls

	IIH (*n* = 63)	Controls (*n* = 96)	*P* Value
Age (mean) (yr)	31.6 ± 10.6	35.5 ± 9.8	
Female/male	58:5	72:24	
BMI	36.5 ± 8.2	27.5 ± 6.4	<.0001
Duration of symptoms (mean) (yr)	4.9 ± 6.8		
CSF opening pressure (mm H_2O) (mean)	356.9 ± 89		

Note:—BMI indicates body mass index.

MR Imaging and MRV Review

MR and MRV images were reviewed independently of one another. Each case was reviewed independently by 2 neuroradiologists. A randomized list of subjects in each instance was provided to each neuroradiologist in an approximately 50:50 mix of IIH and control cases.

In their review of the MR images, the reviewing neuroradiologists were asked to score each case in a categoric "yes/no" manner for the presence or absence of conventional signs of idiopathic intracranial hypertension. They were also asked to evaluate the coronal T1 postgadolinium images of the TS and decide "yes/no" for whether they perceived a segment of >50% stenosis on either side or both sides (Fig 1). Criteria for the diagnosis of TS stenosis included signs of collapse of the sinus on itself, particularly in comparison with more posterior images on the same sequence; signs of herniation of the contour of the brain into the expected location of the sinus ("internal cephalocele"); or clear absence of a definable sinus on ≥1 section.

Review of the MRV sequences was conducted in a similarly blinded, randomized manner. Neuroradiologists were asked to categorically decide whether TS stenosis of >50% was present on 1 or both sides. Second, a score for the point of maximal narrowing for each TS was recorded by using a 0–4 quartile scale (Fig 2).[13]

Finally, the raw data images from each MRV examination in 60 patients with IIH and the first 40 controls were reviewed for direct measurement of the dimensions of the TS with electronic calipers on the PACS screen. Orthogonal measurements were obtained of the TS, and the cross-sectional area was calculated on the assumption of a roughly triangular configuration of the sinus as (width × height) / 2. The cross-sectional area of each sinus was calculated in 2 locations. A proximal measurement was performed approximately 1.5 cm lateral to the torcular when the TS was seen to have assumed a steady horizontal course. A distal measurement was obtained at the point of maximal stenosis. In the absence of a definable stenosis or narrowing, TS measurements were obtained distally at the apex of the upward curve of the TS proximal to the sigmoid sinus.

The interpretation of the MRV examination, reviewed independent of the coronal postgadolinium sequence, was compared with the original clinical interpretation in the electronic records if it was available. Approximately 40% of the MR imaging/MRV examinations in this study were conducted at a 3T magnetic field strength, and the remainder at 1.5T. Postgadolinium comparison T1-weighted imaging was performed by using our routine clinical protocols and consisted of T1-based volumetric acquisitions,

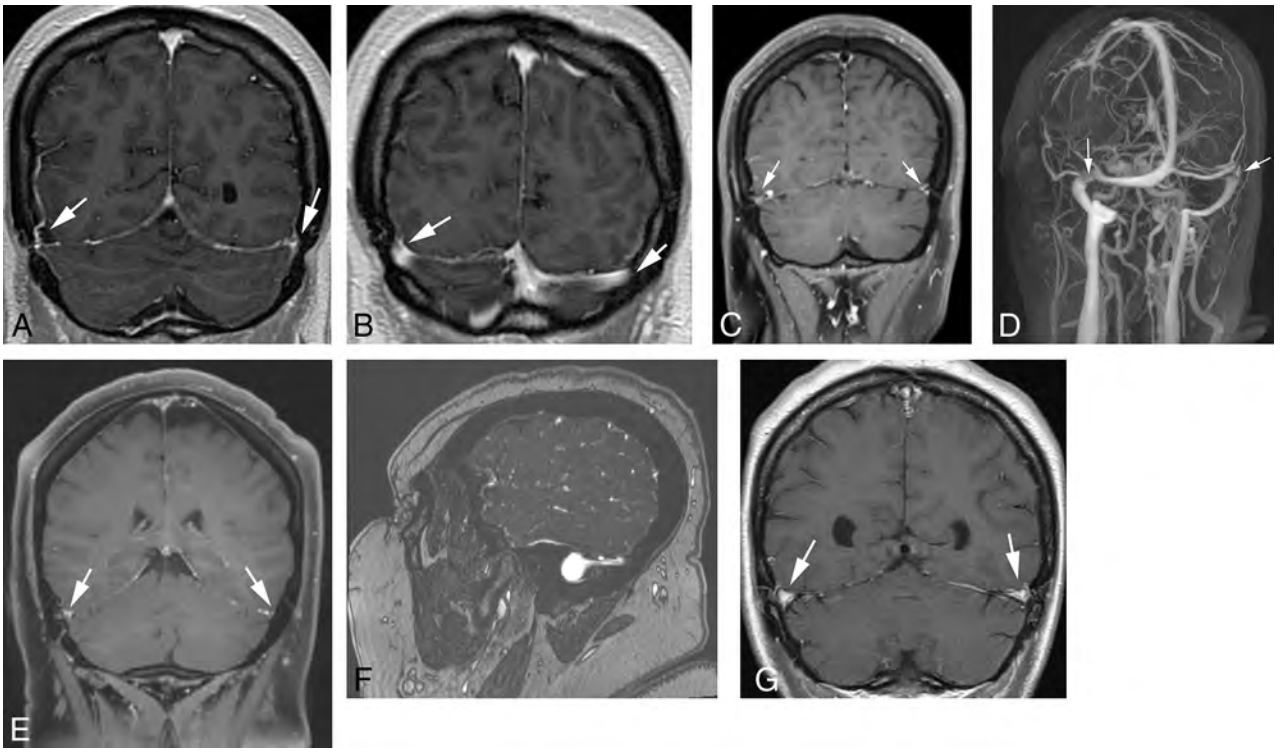

FIG 1. *A–C*, Transverse sinus stenosis on coronal T1 postgadolinium MR imaging. *A* and *B*, Images from a 43-year-old female patient with idiopathic intracranial hypertension. CSF opening pressure was 380 mm H_2O. Postgadolinium coronal 3D fast-spoiled gradient recalled images, section thickness = 2.4 mm, demonstrate stenosis of the transverse sinuses bilaterally (*arrows*). The expected Δ configuration is distorted and collapsed bilaterally (*A*). This is more easily appreciated on images from within the same study by comparing with the images of the same sinuses more posteriorly (*B*). *C* and *D*, Images from a 36-year-old female patient with IIH. CSF opening pressure was 370 mm H_2O. Postgadolinium T1-weighted image (*C*) with coronal reformatting from a 3D acquisition, with a section thickness = 2 mm, TR = 650 ms, TE = 12 ms; and oblique projectional image from a gadolinium-bolused MRV sequence, with TR = 3.83 ms and TE = 1.39 ms. Stenoses of the transverse sinuses are evident on both images (*arrows*). *E* and *F*, Coronal T1-weighted image from a 32-year-old female patient with IIH. CSF opening pressure was 304 mm H_2O. Virtually complete collapse of the transverse sinuses can be discerned bilaterally (*arrows*). A sagittal raw data image (*F*) from the gadolinium-bolused MRV, section thickness = 0.66 mm, suggests an appearance of herniation of the temporo-occipital tissues into the transverse sinus space. *G*, By contrast, an image from a control patient, a 49-year-old woman with multiple medical problems but no specific explanation for her symptoms of headache. A coronal postgadolinium T1-weighted image, section thickness = 4 mm, shows the expected Δ configuration (*arrows*) of the preserved transverse sinuses bilaterally.

such as sampling perfection with application-optimized contrasts by using different flip angle evolution (SPACE sequence; Siemens, Erlangen, Germany) or CUBE (GE Healthcare, Milwaukee, Wisconsin), fast spin-echo, and conventional spin-echo techniques without and with fat saturation. A few examinations performed at other institutions and included in this study were obtained by using spoiled gradient-recalled or MPRAGE techniques, which are characterized by robust intrasinus signal due to rephasing phenomena. These constituted <10% of the studies.

Data Analysis

Data were stored by using Excel spreadsheets (Microsoft, Redmond, Washington) and were analyzed by using JMP Pro 11.2 for Mac (SAS Institute, Cary, North Carolina). The Student *t* test was used for comparing the incidence of MR imaging and MRV findings between groups. Ordinate and categoric variables were correlated with continuous variables by using nonparametric statistical procedures, including Wilcoxon/Kruskal-Wallis rank sums, the Pearson correlation coefficient, and the Spearman ρ.

RESULTS

Subjects

Patients with IIH and control subjects were similar in overall profile (Table 1). Patients with IIH had a slightly greater preponderance of women and a higher body mass index than control subjects.

MR Imaging Interpretation

Bilateral TS stenosis was discerned in 83% of patients with IIH with the coronal postgadolinium T1-weighted images and in 7% of controls ($P < .0001$) (Table 2). The nature of the TS stenosis was often a collapse or flattening of the expected contours of the dural sinus. However, 50% of subjects demonstrated a uni- or bilateral pattern of effective herniation of temporo-occipital tissue into the expected location of the sinus, with the margins being presumably constrained by the bony edges of the dural sinus along the inner calvaria. This appearance is referred to as "an internal cephalocele" by the authors. Unilateral TS stenosis or hypoplasia was perceived in an additional 9% of controls. Other MR imaging signs of IIH were seen with less sensitivity. Signs of an "empty sella" were discerned in 53% of patients with IIH and 5%

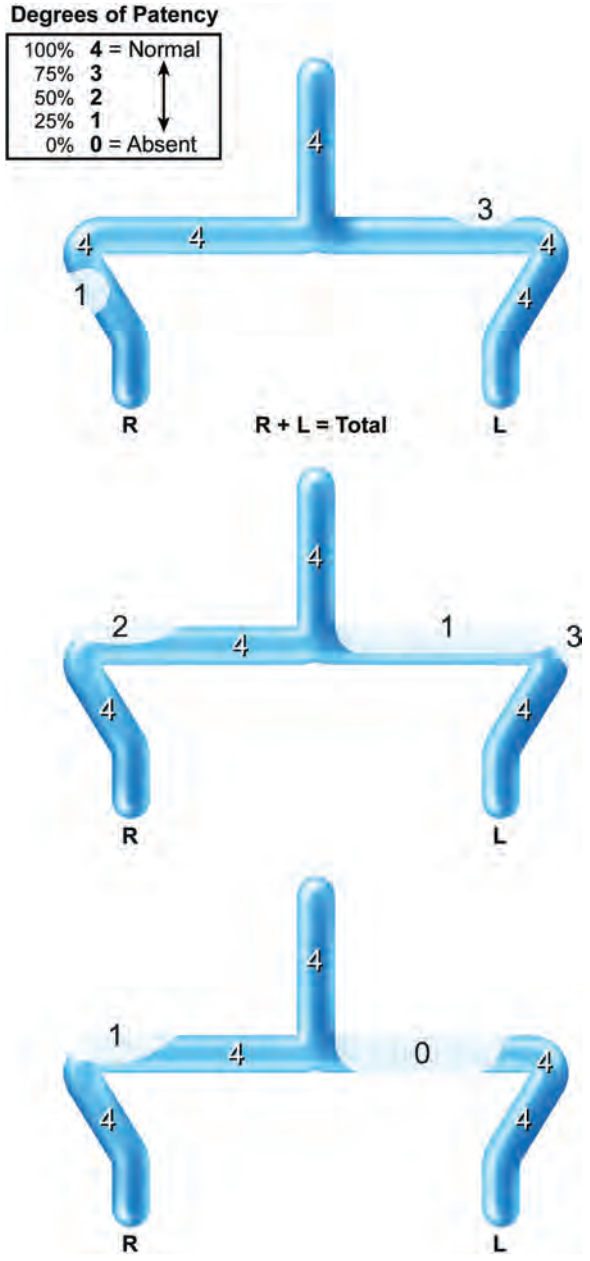

FIG 2. Schema for scoring transverse sinus patency based on Farb et al (2003).[13] Transverse sinuses were rated by using the MRV, MIP, and raw data images on a 5-point scale bilaterally between 0 (absent) and 4 (full expected contour of a normally sized transverse sinus). The scoring system does not discern etiologies of the narrowing, merely the degree of patency/stenosis on each side. A maximum possible score of 8 would, therefore, indicate full patency on each side. R indicates right; L, left.

of controls. Optic nerve sheath distension (>6 mm in transverse dimensions) was seen in 63% of patients with IIH and 4% of controls. Papilledema and DWI changes were less frequent (Table 2).

MRV Interpretation

Bilateral TS stenosis of >50% was perceived categorically in 94% of patients with IIH compared with 3% of controls ($P < .0001$). When we compared the quartile scores of the configuration of the TS bilaterally (left + right score; maximum, 8), patients with IIH

Table 2: Results—MRI findings, interpreted independently of MRV findings

Retrospective Study Interpretation	IIH (*n* = 63)	Controls (*n* = 96)
Empty sella	34 (53%)	5 (5%)
Dilated optic nerve sheath of >6 mm	40 (63%)	4 (4%)
DWI bright spot at fundus	6 (9%)	1 (1%)
Papilledema	20 (34%)	4 (4%)
Bilateral TS stenosis on coronal T2 post gadolinium	53 (83%)	7 (7%)
Internal cephalocele into the transverse sinus	32 (50%)	0

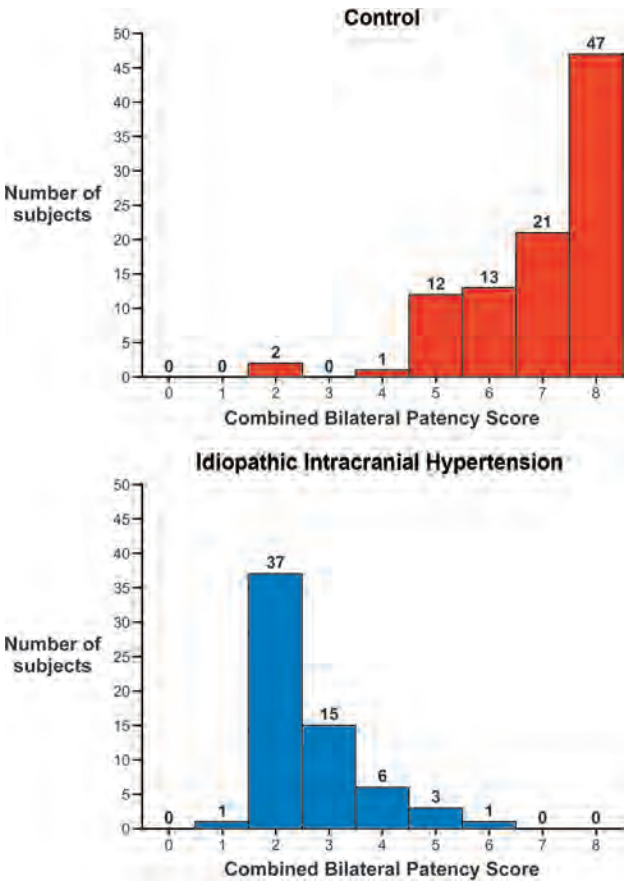

FIG 3. Patency scores on MRV interpretation. A summation of left and right patency scores, maximal normal = 8, was performed on the blinded readings of the MRV images independent of clinical data or the MR imaging appearance. The scatter of scores shows a clear discernment between patients with IIH and controls. Almost all controls scored ≥5, while patients with IIH almost all scored ≤5.

scored almost exclusively <5 and were thus discernible from controls, who almost all scored ≥5 ($P < .0001$) (Fig 3).

MRV Cross-Sectional Area Measurements

Calculation of the narrowed distal segment of the TS in patients with IIH showed a substantial reduction compared with controls measured in the same location (Table 3). The left and right distal transverse sinus showed an 88% and 86% reduction in mean cross-sectional area, respectively, in patients with IIH compared with controls. The summation of the left and right total outflow cross-sectional area was similarly affected. A lesser degree of sinus narrowing was detectable on statistical analysis more posteriorly

Table 3: Results—MRV cross-sectional area measurements on transverse sinuses

	Left TS Proximal (Mean) (mm^2)	Left TS Distal	Right TS Proximal	Right TS Distal	Left + Right Proximal	Left + Right Distal
Controls	24.7 ± 14.1	23.9 ± 10.7	37.5 ± 15.9	29.9 ± 11.4	62.2 ± 19.3	53.8 ± 15.4
IIH	19.2 ± 13.3	2.9 ± 2.1	28.4 ± 14.2	4.1 ± 4.1	47.5 ± 2.4	7.1 ± 4.8
P value (1-way ANOVA)	NS	.0001	.0003	.0001	.0001	.0001

Note:—NS indicates not significant.

in the sinuses, particularly on the right side. However, the proximal effect was less evident visually in individual cases.

Correlation and Multivariate Analysis

Analysis of the correlation among the MR imaging observations, the MRV interpretation, and the direct measurement of the TS dimensions showed strong consistency, indicating that the reviewers' perceptions of MR imaging findings of TS stenosis were valid. Correlation with the Spearman ρ between the MR imaging interpretation of categoric TS patency/stenosis on the one hand and the MRV grading scale on the other showed a highly significant correspondence for all subjects ($P < .0001$). Despite some statistical groups being small in the subanalysis (eg, few patients with IIH had normal-appearing sinuses), this statistical robustness held up in the analysis by diagnostic group (controls, $P < .002$; IIH group, $P < .028$).

Similarly, the validity of the reviewers' interpretation of the coronal MR images was upheld by the correlation between the MR imaging diagnosis of TS stenosis and the direct measurement of the cross-sectional area of the TS (Spearman $\rho = -.7504$, $P < .0001$).

Comparison with Original Clinical Reports

Many of the subjects with IIH in this group were imaged with a variety of MR imaging and MRV studies during the time course of this retrospective review, including studies from outside institutions. Approximately 33% of subjects with IIH had at least 1 earlier MRV interpretation, which the reviewers in this study would have retrospectively revised. Findings of TS narrowing or stenosis documented in this study were previously ascribed on ≥1 occasion in 33% of this patient group to "hypoplasia," "arachnoid granulations," or "anatomic variability in the absence of other signs of idiopathic intracranial hypertension."

DISCUSSION

Idiopathic intracranial hypertension is a poorly understood condition, the hallmark of which is elevation of CSF opening pressure without an identifiable intracranial mass or ventriculomegaly.[1,15-17] It shares many similarities with a condition of visual impairment and intracranial pressure observed in astronauts after prolonged exposure to conditions of microgravity.[18-20] It may also share common pathophysiologic pathways with acute mountain sickness, a condition in which recent MR imaging studies have focused on alterations of arterial inflow, cerebral white matter diffusivity, and venous outflow restriction.[21] Explanations for the mechanisms underlying IIH have focused on overproduction of CSF; impaired resorption of CSF[22]; dysautoregulation of cerebral blood flow[23]; dysregulation of fluid homeostasis, among others, in turn mediated by underlying endocrinopathies; fluid and electrolyte shifts with subtle white matter edema[24]; dysregulation of aquaporin 1 and aquaporin 4 receptors[16,25,26]; or proinflammatory states[27,28] due to mitochondrial dysregulation or circulating signaling leptins.[29-32]

A preponderance of evidence suggests a high incidence of IIH in women of childbearing age with an elevated body mass index, supporting hypotheses that metabolic or hormonal factors may play a strong role.[2,3] However, evidence supporting a single etiologic sequence of pathophysiology has not been consistent. Some volumetric studies have suggested alterations of CSF volume or brain volume as the explanation for elevated acranial pressure.[33-35] Studies of cerebral perfusion by using xenon-enhanced CT, MR perfusion, and SPECT have not identified a consistent pattern of hyperperfusion or hypoperfusion.[36,37] Since the observation that stenoses of the transverse sinuses are seen in 94% of patients with IIH,[13,14,38] speculation has been raised that venous outflow obstruction could play a role in the genesis of IIH,[39] but reversibility of this finding with effective medical therapy and reduction of intracranial pressure suggests that venous occlusive findings are secondary to the elevated intracranial pressure and not vice versa.[40-42]

Secondary effects of chronically elevated acranial pressure from any cause include optic nerve sheath distension, papilledema, flattening of the posterior globe, and flattening and depression of the diaphragma sellae. These secondary effects determine the structural alterations that may be detectable on imaging studies in patients with IIH on which neuroradiologists rely to make this diagnosis. Long-established MR imaging signs of IIH include optic nerve sheath distension,[12,43,44] empty sella appearance,[44,45] enhancement of the vessels at the optic papilla,[12,43,44,46-48] meningocele formation,[49] or restriction of diffusion at the optic nerve head.[50] However, the sensitivity of these MR imaging signs in patients with IIH varies widely between studies, with reported rates of between 6% and 72%.[51] MR imaging studies in pediatric patients in whom anesthesia helps to eliminate eye motion show greater sensitivity to ocular findings of IIH, with optic nerve sheath distension seen in 88% of pediatric patients in 1 study.[52] Generally, sensitivity rates in adult studies tend to be substantially lower with greater published emphasis on the specificity of these findings. The issue of specificity of the finding of TS stenosis is not addressed in this article due to the selective nature of the control population, mostly presenting with nonspecific headache conditions. The utility of the MR imaging/MRV signs we describe in patients with IIH lies in their sensitivity in allowing the neuroradiologist to alert the treating clinician to what may have been previously an overlooked or unsuspected diagnosis.

More useful may be the effect of sustained intracranial hypertension on the transverse dural sinuses. Farb et al[13] reported that stenosis of the transverse sinuses on gadolinium-bolused MR venography is detectable in 94% of patients with IIH, making this

a more sensitive diagnostic indicator in adults than previously established MR imaging signs. However, in most instances when a patient with IIH is imaged, an MRV sequence will not be included with the study unless the diagnosis of IIH is strongly suspected in advance and a specific request for an MRV has been submitted. Therefore, it seems reasonable to conclude that without an MRV sequence being available in most instances, neuroradiologic sensitivity to the diagnosis of IIH will be limited. Furthermore, even when an MRV sequence has been obtained, the nature of transverse sinus narrowing in some patients may seem nonspecific when consideration is given to entities such as anatomic asymmetry, indentations in the contrast column due to arachnoid granulations, or sequelae of previous episodes of dural sinus thrombosis. In this retrospective study, potentially helpful findings in 33% of the MRV sequences in patients with IIH were downplayed or dismissed in ≥1 of the original clinical radiology reports. It might be conjectured that the significance of observations of transverse sinus narrowing was downplayed by the original interpreting radiologist because of the absence of other more "established" signs of idiopathic intracranial hypertension, but our study was not constructed to examine this particular question. We surmise that the diagnosis of IIH on neuroradiologic interpretation may be thus stymied on 2 levels: First, when an MRV sequence is not available, the neuroradiologist is at a disadvantage in not having the most consistent anatomic correlate of IIH demonstrated to best advantage (ie, MRV signs of TS stenosis). Second, when an MRV is available, findings of TS stenosis may be confused with perceptions of anatomic variability and asymmetry and so forth.

We acknowledge that our study is limited in several respects, including its retrospective nature. Our IIH group was carefully screened and diagnosed by using the Modified Dandy Criteria and, as such, represents one of the largest cohorts in this field of publication. However, our control group was of a more heterogeneous composition, mostly diagnosed with migraine or migraine-variant headache. As we retrospectively reviewed the clinical notes, it appeared conceivable that this control group may even contain a number of patients with undiagnosed idiopathic intracranial hypertension. Although this is partially conjectural on our part, it could form an explanation for why a small number (3%) of the controls demonstrated bilateral TS stenosis. Moreover, the observation in this study that a small number of controls demonstrated unilateral or bilateral TS stenosis is consistent with previous authors' experiences. The control group described by Farb et al[13] demonstrated a 6.7% rate of bilateral TS narrowing, while Ayanzen et al[53] found that 31% of patients with normal MR imaging findings showed substantial flow gaps in the TS on MRV. Similar rates of TS interruptions were reported by Bono et al[54] in a population of patients with normal CSF pressures who presented with a variety of headache and psychiatric diagnoses. The MRV and MR imaging techniques used in our study also varied and evolved during the 5 years of retrospective review, with images with a variety of section thicknesses (2–5 mm), T1-based techniques, and 1.5 and 3T scanners. However, we believe that these methodologic shortcomings do not detract substantively from our observations pertaining to the core IIH cohort.

CONCLUSIONS

Our retrospective study is consistent with previous imaging studies of idiopathic intracranial hypertension and demonstrates that TS stenosis/collapse is the most consistent anatomic finding in a group of patients with this condition. Our findings of a 93% incidence of TS stenosis on MRV in this group of patients replicates those of previous studies.[13,14,38] More useful, however, is that we have demonstrated that more careful scrutiny of the appearance of the transverse sinuses on coronal T1 postgadolinium imaging can help neuroradiologists almost completely compensate for the handicap of not having an MRV sequence on hand in this patient group. Additionally, our study suggests that neuroradiologists may need to be more critical in the degree of latitude they exercise in the interpretation of TS narrowing as anatomic variability. The absence of alternative MR imaging signs of IIH in TS narrowing should not deter the neuroradiologist from giving strong consideration to this diagnosis in the appropriate clinical setting.

REFERENCES

1. Friedman DI, Liu GT, Digre KB. **Revised diagnostic criteria for the pseudotumor cerebri syndrome in adults and children.** *Neurology* 2013;81:1159–65 CrossRef Medline
2. Daniels AB, Liu GT, Volpe NJ, et al. **Profiles of obesity, weight gain, and quality of life in idiopathic intracranial hypertension (pseudotumor cerebri).** *Am J Ophthalmol* 2007;143:635–41 CrossRef Medline
3. Ko MW, Chang SC, Ridha MA, et al. **Weight gain and recurrence in idiopathic intracranial hypertension: a case-control study.** *Neurology* 2011;76:1564–67 CrossRef Medline
4. Fraser JA, Bruce BB, Rucker J, et al. **Risk factors for idiopathic intracranial hypertension in men: a case-control study.** *J Neurol Sci* 2010; 290:86–89 CrossRef Medline
5. Thurtell MJ, Trotti LM, Bixler EO, et al. **Obstructive sleep apnea in idiopathic intracranial hypertension: comparison with matched population data.** *J Neurol* 2013;260:1748–51 CrossRef Medline
6. Wall M, Purvin V. **Idiopathic intracranial hypertension in men and the relationship to sleep apnea.** *Neurology* 2009;72:300–01 CrossRef Medline
7. Wardly DE. **Intracranial hypertension associated with obstructive sleep apnea: a discussion of potential etiologic factors.** *Med Hypotheses* 2014;83:792–97 CrossRef Medline
8. Soelberg Sørensen P, Gjerris F, Svenstrup B. **Endocrine studies in patients with pseudotumor cerebri: estrogen levels in blood and cerebrospinal fluid.** *Arch Neurol* 1986;43:902–06 CrossRef Medline
9. Tabassi A, Salmasi AH, Jalali M. **Serum and CSF vitamin A concentrations in idiopathic intracranial hypertension.** *Neurology* 2005;64: 1893–96 CrossRef Medline
10. Warner JE, Larson AJ, Bhosale P, et al. **Retinol-binding protein and retinol analysis in cerebrospinal fluid and serum of patients with and without idiopathic intracranial hypertension.** *J Neuroophthalmol* 2007;27:258–62 CrossRef Medline
11. Cinciripini GS, Donahue S, Borchert MS. **Idiopathic intracranial hypertension in prepubertal pediatric patients: characteristics, treatment, and outcome.** *Am J Ophthalmol* 1999;127:178–82 CrossRef Medline
12. Maralani PJ, Hassanlou M, Torres C, et al. **Accuracy of brain imaging in the diagnosis of idiopathic intracranial hypertension.** *Clin Radiol* 2012;67:656–63 CrossRef Medline
13. Farb RI, Vanek I, Scott JN, et al. **Idiopathic intracranial hypertension: the prevalence and morphology of sinovenous stenosis.** *Neurology* 2003;60:1418–24 CrossRef Medline
14. Higgins JN, Gillard JH, Owler BK, et al. **MR venography in idiopathic intracranial hypertension: unappreciated and misunderstood.** *J Neurol Neurosurg Psychiatry* 2004;75:621–25 CrossRef Medline

15. Friedman DI, Jacobson DM. **Diagnostic criteria for idiopathic intracranial hypertension.** *Neurology* 2002;59:1492–95 CrossRef Medline
16. Baykan B, Ekizoğlu E, Altıokka Uzun G. **An update on the pathophysiology of idiopathic intracranial hypertension alias pseudotumor cerebri.** *Agri* 2015;27:63–72 CrossRef Medline
17. Ducros A, Biousse V. **Headache arising from idiopathic changes in CSF pressure.** *Lancet Neurol* 2015;14:655–68 CrossRef Medline
18. Wilson MH, Imray CH, Hargens AR. **The headache of high altitude and microgravity: similarities with clinical syndromes of cerebral venous hypertension.** *High Alt Med Biol* 2011;12:379–86 CrossRef Medline
19. Wilson MH, Wright A, Imray CH. **Intracranial pressure at altitude.** *High Alt Med Biol* 2014;15:123–32 CrossRef Medline
20. Nelson ES, Mulugeta L, Myers JG. **Microgravity-induced fluid shift and ophthalmic changes.** *Life (Basel)* 2014;4:621–65 CrossRef Medline
21. Sagoo RS, Hutchinson CE, Wright A, et al; Birmingham Medical Research and Expedition Society. **Magnetic resonance investigation into the mechanisms involved in the development of high-altitude cerebral edema.** *J Cereb Blood Flow Metab* 2017;37:319–31 CrossRef Medline
22. Chazal J, Janny P, Georget AM, et al. **Benign intracranial hypertension: a clinical evaluation of the CSF absorption mechanisms.** *Acta Neurochir Suppl (Wien)* 1979;28:505–08 Medline
23. Bateman GA. **Idiopathic intracranial hypertension: priapism of the brain?** *Med Hypotheses* 2004;63:549–52 CrossRef Medline
24. Moser FG, Hilal SK, Abrams G, et al. **MR imaging of pseudotumor cerebri.** *AJR Am J Roentgenol* 1988;150:903–09 CrossRef Medline
25. King LS, Nielsen S, Agre P. **Aquaporin-1 water channel protein in lung: ontogeny, steroid-induced expression, and distribution in rat.** *J Clin Invest* 1996;97:2183–91 CrossRef Medline
26. Zador Z, Bloch O, Yao X, et al. **Aquaporins: role in cerebral edema and brain water balance.** *Prog Brain Res* 2007;161:185–94 CrossRef Medline
27. Sinclair AJ, Ball AK, Burdon MA, et al. **Exploring the pathogenesis of IIH: an inflammatory perspective.** *J Neuroimmunol* 2008;201–02:212–20 CrossRef Medline
28. Skau M, Brennum J, Gjerris F, et al. **What is new about idiopathic intracranial hypertension? An updated review of mechanism and treatment.** *Cephalalgia* 2006;26:384–99 CrossRef Medline
29. Dhungana S, Sharrack B, Woodroofe N. **Cytokines and chemokines in idiopathic intracranial hypertension.** *Headache* 2009;49:282–85 CrossRef Medline
30. Lampl Y, Eshel Y, Kessler A, et al. **Serum leptin level in women with idiopathic intracranial hypertension.** *J Neurol Neurosurg Psychiatry* 2002;72:642–43 CrossRef Medline
31. Samancı B, Samancı Y, Tüzün E, et al. **Evidence for potential involvement of pro-inflammatory adipokines in the pathogenesis of idiopathic intracranial hypertension.** *Cephalalgia* 2016 May 18. [Epub ahead of print] Medline
32. Sheldon CA, Kwon YJ, Liu GT, et al. **An integrated mechanism of pediatric pseudotumor cerebri syndrome: evidence of bioenergetic and hormonal regulation of cerebrospinal fluid dynamics.** *Pediatr Res* 2015;77:282–89 CrossRef Medline
33. Joynt RJ, Sahs AL. **Brain swelling of unknown cause.** *Neurology* 1956;6:801–03 Medline
34. Johnston I. **Reduced C.S.F. absorption syndrome: reappraisal of benign intracranial hypertension and related conditions.** *Lancet* 1973;2:418–21 Medline
35. Malm J, Kristensen B, Markgren P, et al. **CSF hydrodynamics in idiopathic intracranial hypertension: a long-term study.** *Neurology* 1992;42:851–58 CrossRef Medline
36. Bicakci K, Bicakci S, Aksungur E. **Perfusion and diffusion magnetic resonance imaging in idiopathic intracranial hypertension.** *Acta Neurol Scand* 2006;114:193–97 CrossRef Medline
37. Lorberboym M, Lampl Y, Kesler A, et al. **Benign intracranial hypertension: correlation of cerebral blood flow with disease severity.** *Clin Neurol Neurosurg* 2001;103:33–36 CrossRef Medline
38. Sander K, Poppert H, Etgen T, et al. **Dynamics of intracranial venous flow patterns in patients with idiopathic intracranial hypertension.** *Eur Neurol* 2011;66:334–38 CrossRef Medline
39. Woodall MN, Nguyen KD, Alleyne CH Jr, et al. **Bilateral transverse sinus stenosis causing intracranial hypertension.** *BMJ Case Rep* 2013;2013 CrossRef
40. Rohr A, Dorner L, Stingele R, et al. **Reversibility of venous sinus obstruction in idiopathic intracranial hypertension.** *AJNR Am J Neuroradiol* 2007;28:656–59 Medline
41. King JO, Mitchell PJ, Thomson KR, et al. **Cerebral venography and manometry in idiopathic intracranial hypertension.** *Neurology* 1995;45:2224–28 CrossRef Medline
42. Fraser JA, Leung AE. **Reversibility of MRI features of pseudotumor cerebri syndrome.** *Can J Neurol Sci* 2014;41:530–32 CrossRef Medline
43. Agid R, Farb RI, Willinsky RA, et al. **Idiopathic intracranial hypertension: the validity of cross-sectional neuroimaging signs.** *Neuroradiology* 2006;48:521–27 CrossRef Medline
44. Ridha MA, Saindane AM, Bruce BB, et al. **Magnetic resonance imaging findings of elevated intracranial pressure in cerebral venous thrombosis versus idiopathic intracranial hypertension with transverse sinus stenosis.** *Neuroophthalmology* 2013;37:1–6 CrossRef Medline
45. Yuh WT, Zhu M, Taoka T, et al. **MR imaging of pituitary morphology in idiopathic intracranial hypertension.** *J Magn Reson Imaging* 2000;12:808–13 Medline
46. Brodsky MC, Vaphiades M. **Magnetic resonance imaging in pseudotumor cerebri.** *Ophthalmology* 1998;105:1686–93 CrossRef Medline
47. Butros SR, Goncalves LF, Thompson D, et al. **Imaging features of idiopathic intracranial hypertension, including a new finding: widening of the foramen ovale.** *Acta Radiol* 2012;53:682–88 CrossRef Medline
48. Saindane AM, Bruce BB, Riggeal BD, et al. **Association of MRI findings and visual outcome in idiopathic intracranial hypertension.** *AJR Am J Roentgenol* 2013;201:412–18 CrossRef Medline
49. Lloyd KM, DelGaudio JM, Hudgins PA. **Imaging of skull base cerebrospinal fluid leaks in adults.** *Radiology* 2008;248:725–36 CrossRef Medline
50. Salvay DM, Padhye LV, Huecker JB, et al. **Correlation between papilledema grade and diffusion-weighted magnetic resonance imaging in idiopathic intracranial hypertension.** *J Neuroophthalmol* 2014;34:331–35 CrossRef Medline
51. Bidot S, Saindane AM, Peragallo JH, et al. **Brain imaging in idiopathic intracranial hypertension.** *J Neuroophthalmol* 2015;35:400–11 CrossRef Medline
52. Görkem SB, Doğanay S, Canpolat M, et al. **MR imaging findings in children with pseudotumor cerebri and comparison with healthy controls.** *Childs Nerv Syst* 2015;31:373–80 CrossRef Medline
53. Ayanzen RH, Bird CR, Keller PJ, et al. **Cerebral MR venography: normal anatomy and potential diagnostic pitfalls.** *AJNR Am J Neuroradiol* 2000;21:74–78 Medline
54. Bono F, Lupo MR, Lavano A, et al. **Cerebral MR venography of transverse sinuses in subjects with normal CSF pressure.** *Neurology* 2003;61:1267–70 CrossRef Medline

Effects of MRI Protocol Parameters, Preload Injection Dose, Fractionation Strategies, and Leakage Correction Algorithms on the Fidelity of Dynamic-Susceptibility Contrast MRI Estimates of Relative Cerebral Blood Volume in Gliomas

K. Leu, J.L. Boxerman, and B.M. Ellingson

ABSTRACT

BACKGROUND AND PURPOSE: DSC perfusion MR imaging assumes that the contrast agent remains intravascular; thus, disruptions in the blood-brain barrier common in brain tumors can lead to errors in the estimation of relative CBV. Acquisition strategies, including the choice of flip angle, TE, TR, and preload dose and incubation time, along with post hoc leakage-correction algorithms, have been proposed as means for combating these leakage effects. In the current study, we used DSC-MR imaging simulations to examine the influence of these various acquisition parameters and leakage-correction strategies on the faithful estimation of CBV.

MATERIALS AND METHODS: DSC-MR imaging simulations were performed in 250 tumors with perfusion characteristics randomly generated from the distributions of real tumor population data, and comparison of leakage-corrected CBV was performed with a theoretic curve with no permeability. Optimal strategies were determined by protocol with the lowest mean error.

RESULTS: The following acquisition strategies (flip angle/TE/TR and contrast dose allocation for preload and bolus) produced high CBV fidelity, as measured by the percentage difference from a hypothetic tumor with no leakage: 1) 35°/35 ms/1.5 seconds with no preload and full dose for DSC-MR imaging, 2) 35°/25 ms/1.5 seconds with 1/4 dose preload and 3/4 dose bolus, 3) 60°/35 ms/2.0 seconds with 1/2 dose preload and 1/2 dose bolus, and 4) 60°/35 ms/1.0 second with 1 dose preload and 1 dose bolus.

CONCLUSIONS: Results suggest that a variety of strategies can yield similarly high fidelity in CBV estimation, namely those that balance T1- and T2*-relaxation effects due to contrast agent extravasation.

ABBREVIATIONS: AIF = arterial input function; Bidir = bidirectional leakage correction algorithm; CNR = contrast-to-noise ratio; EES = extravascular extracellular space; K^{trans} = efflux rate of contrast agent from the vasculature; rCBV = relative CBV; Unidir = unidirectional leakage correction algorithm

DSC-MR imaging is a PWI technique based on the indicator-dilution theory,[1] which uses the first pass of a paramagnetic contrast agent to estimate cerebrovascular parameters, including relative CBV (rCBV) and CBF.[2,3] A primary clinical application for rCBV includes the evaluation of brain tumor vascularity and angiogenesis; however, neovascularity within neoplasms tends to have elevated vascular permeability, resulting in contrast agent leakage into the extravascular extracellular space (EES) and violation of assumptions made by the indicator-dilution theory. These "leakage effects," which can be either T1-weighted, which would cause underestimation of the rCBV, or T2*-weighted, which would cause overestimation of the rCBV, greatly depend on the acquisition strategy and protocol used for DSC-MR imaging signal acquisition.[4] To address these problems, strategies have been proposed for reducing the influence of contrast agent leakage, many focusing on T1-weighted artifact reduction, including use of low flip angles,[5] dual-echo acquisitions,[6-8] preload administration,[9] and/or postprocessing leakage-correction algorithms.[10-13]

Previous studies have used a combination of these strategies to reduce extravasation-induced error of CBV estimates; however,

Received July 17, 2016; accepted after revision October 4.

From the University of California, Los Angeles Brain Tumor Imaging Laboratory (K.A.B.L., B.M.E.), Center for Computer Vision and Imaging Biomarkers; Department of Bioengineering (K.A.B.L., B.M.E.), Henry Samueli School of Engineering and Applied Science; and University of California, Los Angeles Neuro-Oncology Program (B.M.E.), University of California, Los Angeles, Los Angeles, California; Departments of Radiological Sciences (A.B.L., B.M.E.) and Biomedical Physics (B.M.E.), David Geffen School of Medicine, University of California, Los Angeles, Los Angeles, California; and Department of Diagnostic Imaging (J.L.B.), Rhode Island Hospital and Alpert Medical School of Brown University, Providence, Rhode Island.

This work was supported by the American Cancer Society Research Scholar Grant RSG-15-003-01-CCE (B.M.E.); the National Brain Tumor Society Research Grant (B.M.E.); the Siemens Healthcare Research Grant (B.M.E.); and the University of California, Los Angeles Medical Scientist Training Program (K.A.B.L.).

Please address correspondence to Benjamin M. Ellingson, PhD, UCLA Brain Tumor Imaging Laboratory, Departments of Radiology, Biomedical Physics, Bioengineering, and Psychiatry, and Radiological Sciences and Psychiatry, David Geffen School of Medicine, University of California, Los Angeles, 924 Westwood Blvd, Suite 615, Los Angeles, CA 90024; e-mail: ellingson@mednet.ucla.edu

Indicates article with supplemental on-line table.

Indicates article with supplemental on-line photo.

http://dx.doi.org/10.3174/ajnr.A5027

these approaches have primarily been evaluated empirically. The goal of this study was to systematically evaluate, with simulation, the effects of various leakage-correction strategies on the fidelity of CBV estimation using simulated DSC-MR imaging data derived from the convolution theory[14] and recent developments by Quarles et al.[15] We hypothesized that this approach could provide insight into the interaction of pulse sequence parameters, preload dosing, and leakage-correction algorithms that are not readily determined experimentally.

MATERIALS AND METHODS

Simulation Procedure

The following common DSC-MR imaging protocol variables were evaluated by using simulations: pulse sequence parameters, including flip angle, TE, and TR; preload dose and incubation time; truncation of the DSC-MR imaging dataset after first pass to limit postbolus leakage contamination; and postprocessing leakage-correction algorithms. Simulated DSC-MR imaging signal curves for brain tumors were generated via the following: 1) selection of pulse sequence parameters; 2) construction of the DSC-MR imaging relaxivity–time-series without leakage for "ground truth rCBV"; 3) construction of the leakage-affected intravascular and EES contrast agent concentration–time-series based on tumor characteristics; and 4) estimation of CBV by using no leakage correction, unidirectional leakage correction (Unidir) as described by Boxerman et al,[10] or bidirectional leakage correction (Bidir) accounting for bidirectional contrast agent flux between the vasculature and EES.[11,13]

Simulated DSC-MR Imaging Relaxation Rate–Time Curve

The simulated DSC-MR imaging relaxation rate–time curve is derived from the gradient-echo signal equation, which has signal contributions from both T1 and T2. When the MR imaging signal intensities, which have arbitrary units, are converted to $(\Delta R_2^*(t)$, in units of 1/s, these contributions are modeled for a single-shot gradient-echo EPI acquisition as the following[15]:

$$1)\quad \Delta R_2^*(t) = r_{2,P}^* v_P C_p(t) + r_{2,E}^* v_E C_E(t) + K_P v_P v_E |C_P - C_E| - \frac{1}{TE} \times \left(\ln \frac{1 - E_1 \times e^{-TR \times r_1 \times C_T(t)}}{1 - E_1} - \ln \frac{1 - \cos\alpha \times E_1 \times e^{-TR \times r_1 \times C_T(t)}}{1 - \cos\alpha \times E_1} \right)$$

where α is the flip angle; $E_1 = e^{-TR/T_{10}}$; subscripts E, I, and P represent the extravascular, intracellular, and plasma compartments, respectively; v represents the volume fraction; K represents "calibration susceptibility factors"; C represents contrast agent concentration; and r_1 and r_2^* are the T1 and T2 gadolinium relaxivities, respectively. The first term, $r_{2,P}^* C_p(t)$ represents the T2* contribution of the plasma concentration of contrast agent; the second term, $r_{2,E}^* C_E(t)$ represents the extravascular extracellular contrast agent contribution to T2*; $K_P V_P V_E |C_P - C_E|$, represents the T2*-weighted contribution owing to the difference in the concentration of contrast agent between the vasculature and the EES; and

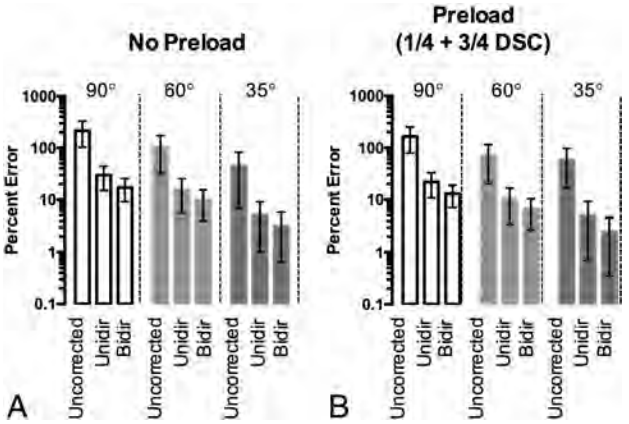

FIG 1. Effect of the flip angle on recovery of CBV (TE = 35 ms/TR = 1.0 second). *A*, Percentage error (with 95% CI) of the estimated CBV for different flip angles and leakage-correction strategies, without the use of preload, compared with ground truth CBV. *B*, Percentage error (with 95% CI) of the estimated CBV for different flip angles and leakage-correction strategies, with use of 1/4 dose preload, compared with ground truth CBV.

$-\frac{1}{TE} \times \left(\ln \frac{1 - E_1 \times e^{-TR \times r_1 \times C_T(t)}}{1 - E_1} - \ln \frac{1 - cos\alpha \times E_1 \times e^{-TR \times r_1 \times C_T(t)}}{1 - \cos\alpha \times E_1} \right)$ represents the T1 contribution of contrast agent in both the plasma and EES.

Pulse Sequence Parameters

We tested all combinations of the following DSC-MR imaging parameters: flip angle = 35°, 60°, and 90°; TE = 15, 25, 35, 45, and 55 ms; TR = 1.0, 1.5, and 2.0 seconds; fractional preload + bolus dosage = ¼ + ¾ (6 mmol/L total, single dose), ½ + ½ (6 mmol/L total, single dose), and 1 + 1 (12 mmol/L total, double dose), in which a different value of peak arterial input function (AIF) concentration would simply scale all relaxivity–time curves proportionally.

Construction of Blood Plasma and EES Concentration

A generic AIF, which models the input of contrast agent into the tissue vasculature, was generated by using the following γ-variate-like approximation:

$$2)\qquad C_\alpha(t) = A(t/t_p^2)e^{-t/t_p} + B(-e^{-t/t_p}),$$

where A = 200 mmol/L s, B = 1.75 mmol/L, and t_p = 2 seconds (from Simpson et al[16]) and the peak concentration was 6.0 mmol/L for the full dose and scaled appropriately for the preload dosages and postpreload bolus injections. For preload simulations, the composite AIF was constructed as the superposition of the preload injection AIF and the bolus AIF was delayed by the specified incubation time.

The blood plasma contrast agent concentration was computed by convolving the AIF with an exponential residue function, where the residue function describes the tracer retention; the convolution is used to describe the AIF as a series of narrow, instantaneous boluses of contrast agent; and the CBF factor accounts for the proportionality of the concentration in the vasculature to the delivered blood[14]:

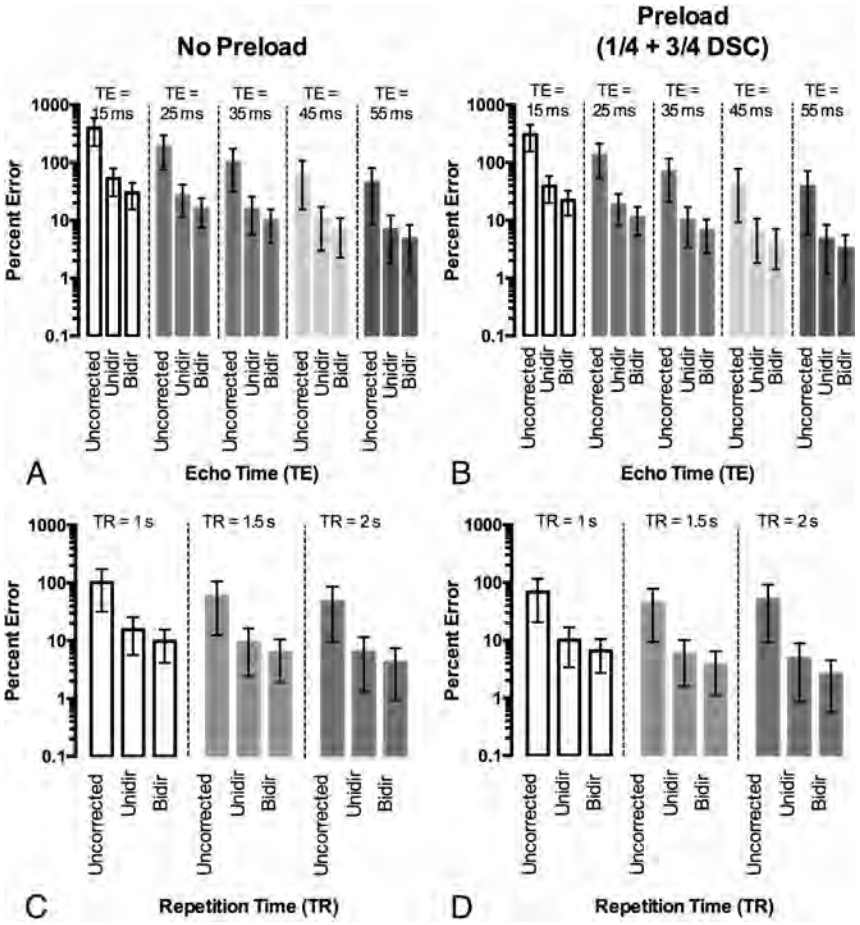

FIG 2. Effect of TE and TR on CBV accuracy with flip angle = 60°. *A*, Percentage error in CBV estimation for different TEs by using TR = 1.0 second without preload. *B*, Percentage error in CBV estimation for different TEs by using TR = 1.0 second with 1/4 dose preload. *C*, Percentage error in CBV estimation for different TRs with a 60° flip angle and TE = 35 ms with no preload. *D*, Percentage error in CBV estimation for different TRs with a 60° flip angle and TE = 35 ms with a 1/4 dose preload.

$$3) \qquad C_p(t) = \frac{\rho}{k_H} \times CBF \times \int_0^t C_\alpha(\tau) \times e^{-\frac{t-\tau}{MTT}}\, d\tau,$$

where ρ is the density of brain tissue (1.04 g/mL), and k_H is the hematocrit difference between capillaries and large vessels (0.73).[17]

The EES contrast agent concentration was computed by using a 2-compartment pharmacokinetic model as follows:

$$4) \qquad C_E(t) = K^{trans} \times \int_0^t C_\alpha(\tau) \times e^{-\left(\frac{K^{trans}}{v_e}\right) \times (t-\tau)}\, d\tau,$$

where K^{trans} describes the efflux rate of contrast agent from the vasculature, often equated with permeability, and K^{trans}/v_e describes the rate of contrast agent influx back into the vasculature.

The relaxivity-time curves were obtained from Equation 1. For each relaxivity–time curve, the baseline signal was calculated as the median of the first 30 seconds of the signal.

Tissue, Contrast Agent, and Noise Characteristics

Specific tumor characteristics were estimated on the basis of previous data from Schmiedeskamp et al,[17] including CBV = 5 mL/100 g, CBF = 60 mL/100 g/min, and $T_{20}^* = 0.05$ seconds. The blood volume fraction, v_p, was set equal to $\rho/k_H \times CBV$. Relaxivity values for gadobutrol (Gadavist; Bayer Schering Pharma, Berlin, Germany) were assumed to be $r_1 = 3.6$ mmol/L^{-1}s^{-1} [18], $r_{2,P}{}^* = 87$ mmol/L^{-1}s^{-1},[19] and $r_{2,E}^* = 30$ mmol/L^{-1}s^{-1}.[7] Monte Carlo simulations were performed by using the following values: $K^{trans} = 0.214 \pm 0.04$ minute^{-1} (range = 0.114 − 0.318), $v_e = 0.722 \pm 0.17$ (range = 0.259 − 0.985), $T_{10} = 1.59 \pm 0.40$ seconds (range = 0.84 − 2.87), $r_{2,P}^* = 87.0 \pm 17.4$ mmol/$^{-1}$s^{-1} (range = 42.4 − 132), and $r_{2,E}^* = 30 \pm 6$ mmol/L^{-1}s^{-1} (range = 14.4 − 45.5). v_e was limited to a maximum of 1, and T_{10} was limited to a minimum of white matter (832 ms).[20]

K^{trans} and v_e were chosen by using the average values and SDs from Zhang et al.[21] T_{10} was estimated from variable flip angle mapping from 25 glioblastomas (5 precontrast T1 flip angle maps were acquired for each patient [2°, 5°, 10°, 15°, 30°]) and fitted by using a Levenberg-Marquardt nonlinear approach to the gradient-echo signal equation. The variances for $r_{2,P}^*$ and $r_{2,E}^*$ are, to the best of our knowledge, not well-defined in the literature and were chosen to be 20% to approximately match the SDs of the other parameters. K_P, the susceptibility calibration factor, was chosen to generate a 40% peak signal drop in gray matter, for which CBF = 60 mL/100 g/min and CBV = 4 mL/100 g were chosen.[22] The whole-brain average was selected as the average of 1000 white matter voxels (including noise), with CBF = 25 mL/100 g/min and CBV = 2 mL/100 g.

Contrast-to-noise ratio (CNR) was first measured in a sample of 25 human glioblastomas (flip angle = 35°, TE = 32 ms, and TR = 1.8 seconds), which had a CNR of 40.5. To model noise added by the TE and TR used, we scaled the CNR by $C \times \sin(\alpha) \times e^{-TE/T_2^*}(1 - e^{-TR/T_1}) \Big/ \sin(35°) \times e^{-0.032}/T_2^*(1 - e^{-1.8/T_1})$, where the numerator incorporates the dose (C) of the new protocol and TE, TR, the flip angle, and the denominator scales the CNR according to the parameters used in acquiring the human data.

The CNR, which is defined with the following equation, was used to calculate SD[23,24]:

$$5) \qquad CNR = \frac{\Delta R_{2,max}^*}{\sigma},$$

where $\Delta R_{2,max}^*$ is the maximum value of ΔR_2^* and σ is the SD of the Gaussian noise added to each time point. Gaussian noise was added with mean of zero and a SD of σ.

Leakage Correction Algorithms

Uncorrected CBV was computed by integrating $\Delta R_2^*(t)$, while leakage-corrected CBV was obtained by using either Unidir[10] or Bidir[11,13] leakage-correction algorithms. The "ground truth" $(\Delta R_2^*(t)_{gt})$ estimate of CBV was calculated under conditions of no noise with $K^{trans} = 0$. The percentage error from ground truth was calculated for uncorrected and leakage-corrected CBV estimates with added noise.

Effects of Preload Incubation Time and Truncation of the DSC Time-Series

To estimate the effects of preload incubation time, we compared estimates of CBV with delays of 5–10 minutes between preload and bolus injection. To estimate the effects of truncating $\Delta R_2^*(t)$ on CBV estimates, we compared CBV estimates by using the first 30, 60, 90, or 120 seconds of the postbaseline $\Delta R_2^*(t)$ as well as the entire 150-second data.

Monte Carlo Simulations to Estimate CBV Confidence Intervals

For each set of pulse sequence parameters, Gaussian noise was added to each time point with normal distribution (zero mean, SD equal to the maximum signal scaled by the CNR), and tumor characteristics were generated according to the normal distributions described previously. A Monte Carlo simulation was conducted by using 250 randomly chosen tumors, with random noise, for each set of pulse sequence parameters. Percentage error was calculated by using the computed CBV and the ground truth CBV. The 95% confidence intervals of percentage error were subsequently generated for the uncorrected CBV, and each of the leakage-correction algorithms and are shown in each of the figures. For Figs 1–3, 1 particular protocol (flip angle = 60°, TE = 35 ms, TR = 1.0 s, ¼ preload dose + ¾ DSC-MR imaging, waiting time = 5 minutes) was chosen as the template based on American Society of Functional Neuroradiology recommendations,[25] with variations to only 1 of the parameters shown for each subfigure. For Fig 4, all combinations of flip angle, TR, TE, and preload dosage were evaluated. For all figures, integration of the relaxivity–time curve was performed from the injection time point to the end (2.5 minutes), unless otherwise noted.

RESULTS

Without preload, there is reduced T1-weighting and increased T2*-weighting with smaller flip angles as manifested by higher $\Delta R_2^*(t)$, best seen in the "tail" (On-line Fig 1*A*). Preload administration increases T2*-weighting of the signal (On-line Fig 1*B*). In this case, without preload, the 35° relaxivity–time curve is closest to ground truth $(\Delta R_2^*(t)_{gt})$, while the 60° and 35° curves are equally close to the truth curve after preload (¼ dose + ¾ dose DSC-MR imaging). On the basis of the formula used for CNR, the 35° flip angle also yielded the most noise, as exemplified in the preload DSC-MR imaging curve. For both nonpreload and preload administration, Unidir-corrected $\Delta R_2^*(t)$ varied more from $\Delta R_2^*(t)_{gt}$ across all tested flip angles compared with Bidir-corrected $\Delta R_2^*(t)$, particularly right after the first pass of the bolus (On-line Fig 1*C–F*). Figure 1*A*, -*B* illustrates the percentage errors for uncorrected, Unidir, and Bidir CBV estimates, compared with

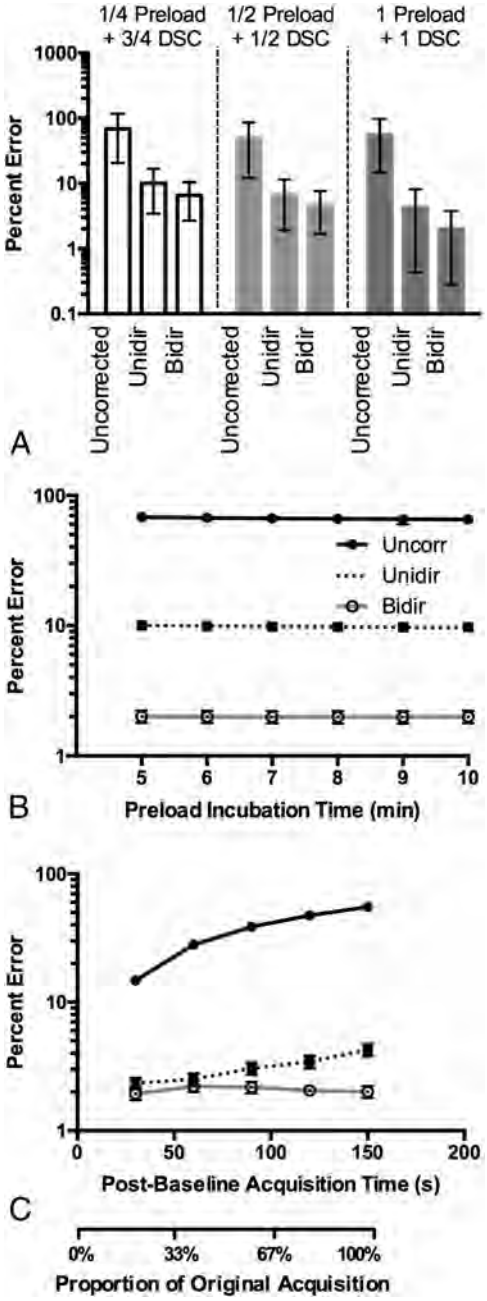

FIG 3. Effects of preload dosage, incubation time, and truncation of corrected $\Delta R_2^*(t)$ on CBV fidelity. *A*, Percentage errors in CBV for each preload dosage with 95% CI. The best performance was obtained with 1-dose preload and 1-dose DSC-MR imaging bolus when using TE = 35 ms, TR = 1.0 second, and flip angle = 60°. Note the increased T2*-weighting from a full-dose preload decreases the CBV error when using these acquisition parameters. *B*, Effects of preload incubation time on CBV estimation when using preload. *C*, Effects of truncation of the $\Delta R_2^*(t)$ curves and leakage-correction strategies on CBV estimation when using a 1-dose preload followed by a 1-dose DSC bolus injection.

$\Delta R_2^*(t)_{gt}$, for different flip angles. With this particular combination of TR/TE/preload dosage, the 35° flip angle had the lowest error. Furthermore, error after both Unidir and Bidir leakage corrections tracked with error in the uncorrected CBV (ie, the lower error in uncorrected CBV corresponded with lower error after leakage correction). For all tested flip angles, uncorrected CBV

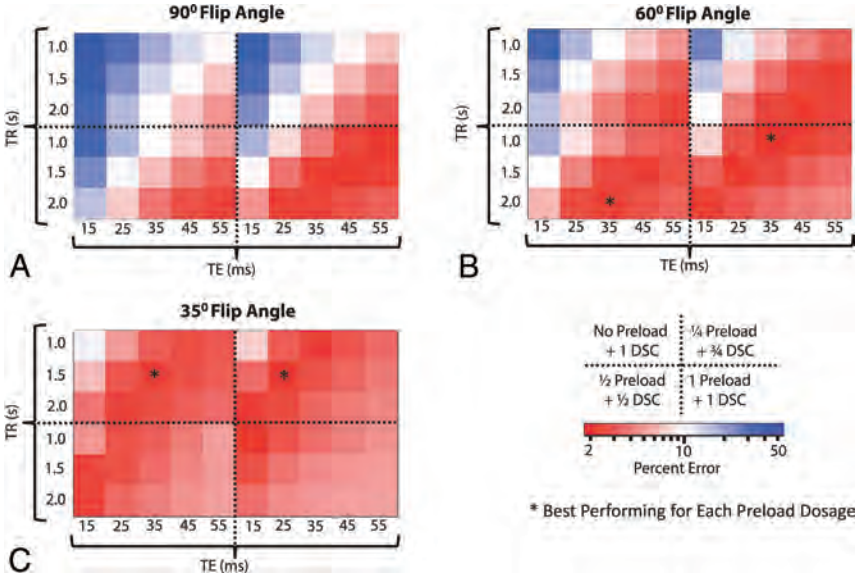

FIG 4. Heat map diagrams depicting the percentage error in the CBV estimation for combinations of acquisition protocols with Bidir. Each quadrant within each subfigure represents a different preload dose. Each subfigure represents a different flip angle: 90° (*A*), 60° (*B*), and 35° (*C*). Optimal strategies balance T1-weighted and T2*-weighted effects from contrast agent extravasation via a combination of TE, TR, and preload. *Red boxes* indicate acquisition protocols with minimum error, while *blue boxes* indicate protocols with poor CBV fidelity (high error compared with ground truth).

estimates had the highest error, followed by the Unidir and then the Bidir estimates.

Results indicate longer TEs increase the T2*-weighting of $\Delta R_2^*(t)$ (On-line Fig 2*A*, -*B*; flip angle = 60°, TR = 1.0 second). Without preload (Fig 2*A*), TE = 55 ms yielded the most accurate $\Delta R_2^*(t)$ for all 3 correction strategies by using all leakage-correction strategies. With ¼ dose preload (Fig 2*B*), TE = 45–55 ms had smaller error than without preload, though the 55 ms performed slightly better. Post hoc leakage-correction error tracked with uncorrected error in these examples. Results also suggest an increased T2*-weighting (or decreased T1-weighting) with longer TRs (On-line Fig 2*C*, -*D*). Independent of preload, TR ≥ 1.5 seconds yielded $\Delta R_2^*(t)$ with less error compared with $\Delta R_2^*(t)_{gt}$ for a 60° flip (Fig 2*C*, -*D*) for the chosen flip angle, TE, and preload dosage. In general, CBV error with the 3 methods was linearly correlated.

Preload primarily increases T2*-weighting and reduces T1-weighting in $\Delta R_2^*(t)$ (On-line Fig 3*A*; flip angle = 60°, TE = 35 ms, TR = 1.5 seconds). For these parameters, 1 preload + 1 bolus dosing yielded higher $\Delta R_2^*(t)$ fidelity compared with ground truth $\Delta R_2^*(t)$ than the ¼ + ¾ and ½ + ½ dosing schemes (Fig 3*A*). Even though the ½ + ½ and 1 + 1 dosing schemes had approximately the same uncorrected CBV percentage error, the post hoc leakage-correction algorithms benefited from the higher CNR that the full DSC-MR imaging dose provides. Results also suggest that preload does not act by decreasing the concentration-dependent rate of contrast agent efflux, but rather by decreasing baseline tissue T1 before bolus injection, as well as increasing T2*-weighting, as evidenced by identical wash-in rates and concentration-dependent reductions in baseline T1 (On-line Fig 3*B*, -*C*).

With incubation times of 5–10 minutes, the change in CBV error is virtually similar, with a slight, gradual decrease in error from 5 to 10 minutes (Fig 3*B*). Next, because CBV is computed from the integration of $\Delta R_2^*(t)$, 1 strategy for mitigating leakage effects is truncating $\Delta R_2^*(t)$ after the first pass. As expected, the less data used for computing CBV, the lower is the percentage error for uncorrected CBV. For Unidir CBV, mean percentage error is lowest when 30 seconds is used and gradually increases with time. For Bidir CBV, percentage error was approximately the same for all cutoff times (Fig 3*C*).

The protocol with the lowest overall mean percentage error used a 60° flip angle, TE/TR = 35/1000 ms with 1 dose preload, by using the bidirectional correction; however, there were multiple protocols whose 95% CIs overlapped (On-line Table), suggesting there are several strategies that could be used to get similar CBV estimates. In general, the best performing strategies (dark red areas in Fig 4 and On-line Fig 4) were those that balanced both T1- and T2*-weighting secondary to contrast agent extravasation, with a mean uncorrected CBV error of <70% for all the "optimal" strategies with 1 total dose of contrast and <80% for those with 2 total doses of contrast agent, as opposed to a much larger error for other protocols. Preload did not necessarily depress percentage error, as evidenced by the 35° flip angle, in which higher preload dosages could "overshoot" the "ground truth." The acquisition strategies with the lowest mean error in this simulation (flip angle/TE/TR) for each preload dosing were the following: 1) with no preload and full dose for DSC-MR imaging: 35°/35 ms/1.5 seconds; 2) with ¼ dose preload and ¾ dose bolus: 35°/25 ms/1.5 seconds; 3) with ½ dose preload and ½ dose bolus: 60°/35 ms/2.0 seconds; and 4) with 1-dose preload and 1-dose bolus: 60°/35 ms/1.0 second. The 90° flip angle only appeared as an optimal strategy with 1-dose preload and 1-dose bolus.

DISCUSSION

The purpose of this study was to evaluate the influence of various DSC-MR imaging acquisition strategies and post hoc leakage-correction algorithms on the fidelity of the estimation. In general, the performance of both leakage-correction algorithms improves as the leakage-contaminated $\Delta R_2^*(t)$ curve more closely approximates $\Delta R_2^*(t)_{gt}$. Furthermore, a much more "homogeneous" performance is seen for the double dose because many more protocols were "optimal" with the double dose. This finding would seem to imply that this scheme is less sensitive to the physiologic variations that would impact the estimates of $\Delta R_2^*(t)$.

As has been established previously, increased T2*-weighted leakage results from a lower flip angle, longer TR, longer TE, and higher preload dosage.[15,26] Given that the errors before and after leakage correction are generally correlated, the optimal strategies minimize errors in uncorrected rCBV, which can be accom-

plished by balancing T1- and T2*-weighted leakage effects. Therefore, the optimal protocols balance these 2 opposing effects so that the DSC-MR imaging curves do not deviate too much from the ground truth. For example, a TR of 1.0 second, which is relatively T1-weighted, can be offset with a full dose of preload, which is quite T2*-weighted. Some of the optimal protocols, on the other hand, take a middle-of-the-road approach (ie, 60° flip angle or TE = 35 ms) so that none of the parameters cause the DSC-MR imaging curves to be overly affected by T1-weighted or T2*-weighted leakage effects.

Our results also suggest that the mechanism by which preload increases CBV fidelity is by increasing T2*-weighting and decreasing T1-weighting of the $\Delta R_2^*(t)$ curves rather than by decreasing the flux of contrast agent diffusion into the EES. While preload and postprocessing leakage-correction algorithms have been shown to work synergistically in many cases, including intermediate-to-high flip angle acquisitions,[9] it is also possible for preload to overcompensate and worsen the deviation of the leakage-contaminated $\Delta R_2^*(t)$ curve compared with the ground truth; Hu et al[27] drew the same conclusion. Furthermore, sufficient preload correction was found between 6 and 10 minutes, which agrees with the findings of Hu et al[27] and Kassner et al.[28]

The bidirectional leakage correction accounts for backward flux of contrast agent and was shown to reduce CBV error compared with the unidirectional leakage correction in all 180 acquisition scenarios tested. Both leakage-correction algorithms work by first performing a least-squares fit of the model-generated corrected $\Delta R_2^*(t)$ curve plus the leakage term, and then subtracting the original $\Delta R_2^*(t)$ curve by the calculated leakage term. Thus, if the computed leakage term does not include back flux of contrast agent, it can cause the corrected $\Delta R_2^*(t)$ curve to adopt a shape noticeably different from C_p (Equation 3), thereby overestimating and underestimating the ground truth curve immediately following the first pass of the bolus. Thus, CBV estimates obtained by using the unidirectional algorithm have approximately twice the error compared with estimates obtained by using the bidirectional leakage-correction algorithm.

The study has several notable limitations. First, we did not account for errors arising from either variations in MTT (including bolus dispersion) or bolus delay, both of which would serve to increase the percentage error for the leakage-correction algorithms presented in the study due to MTT sensitivity. Therefore, the percentage errors are meant to be relative, with many of the optimal protocols providing a balance between T1 and T2* leakage effects over the population of tumors. Another limitation is the lack of more sophisticated integration of all of the effects of microvascular and microcellular morphologies on DSC-MR imaging data, including, but not limited to, the arbitrary geometry of the underlying vessels.[29,30] Furthermore, the noise modeled does not take into account potential sources, such as coil quality, section thickness, and the use of a global AIF. Much of the population data used for these tumors were acquired in small cohorts, and a study in a larger population would be required for more accurate modeling of the tumor population characteristics, particularly r_2^*. Finally, the results in the simulation warrant validation in real patients. Testing every combination of MR imaging protocol is infeasible in real patients. Furthermore, it is currently impossible to ascertain the ground truth rCBV; however, these results could be validated in real brain tumors by using an extension of the Paulson and Schmainda[4] methodology, in which the top performing protocols are tested against each other for variability between scans.

CONCLUSIONS

The current study demonstrates that the choice of image acquisition and preload dosing and/or fractionation has tremendous impact on the fidelity of CBV estimation. Results suggest that a variety of acquisition strategies can be used to obtain similar accuracy of CBV estimation, while the bidirectional leakage-correction algorithm aids in minimizing errors in CBV estimation under all scenarios. To compute the most accurate CBV, one should focus on standardizing a DSC-MR imaging acquisition strategy that minimizes errors in the underlying leakage-contaminated $\Delta R_2^*(t)$ curve by balancing T1 and T2* contamination effects over the tumor population, which will, in turn, reduce the residual errors in CBV estimation following leakage correction.

Disclosures: Benjamin M. Ellingson—*UNRELATED: Consultancy:* MedQIA, Siemens, Roche, Agios Pharmaceuticals, Bristol-Meyer Squib, Nativis, Insys Therapeutics, Omniox; *Grants/Grants Pending*: Siemens, Roche.

REFERENCES

1. Meier P, Zierler KL. **On the theory of the indicator-dilution method for measurement of blood flow and volume.** *J Appl Physiol* 1954;6:731–44 Medline
2. Essig M, Nguyen TB, Shiroishi MS, et al. **Perfusion MRI: the five most frequently asked clinical questions.** *AJR Am J Roentgenol* 2013;201:W495–510 CrossRef Medline
3. Petrella JR, Provenzale JM. **MR perfusion imaging of the brain: techniques and applications.** *AJR Am J Roentgenol* 2000;175:207–19 CrossRef Medline
4. Paulson ES, Schmainda KM. **Comparison of dynamic susceptibility-weighted contrast-enhanced MR methods: recommendations for measuring relative cerebral blood volume in brain tumors.** *Radiology* 2008;249:601–13 CrossRef Medline
5. Cha S, Knopp EA, Johnson G, et al. **Intracranial mass lesions: dynamic contrast-enhanced susceptibility-weighted echo-planar perfusion MR imaging.** *Radiology* 2002;223:11–29 CrossRef Medline
6. Vonken EJ, van Osch MJ, Bakker CJ, et al. **Measurement of cerebral perfusion with dual-echo multi-slice quantitative dynamic susceptibility contrast MRI.** *J Magn Reson Imaging* 1999;10:109–17 Medline
7. Schmiedeskamp H, Straka M, Newbould RD, et al. **Combined spin- and gradient-echo perfusion-weighted imaging.** *Magn Reson Med* 2012;68:30–40 CrossRef Medline
8. Skinner JT, Robison RK, Elder CP, et al. **Evaluation of a multiple spin- and gradient-echo (SAGE) EPI acquisition with SENSE acceleration: applications for perfusion imaging in and outside the brain.** *Magn Reson Imaging* 2014;32:1171–80 CrossRef Medline
9. Boxerman JL, Prah DE, Paulson ES, et al. **The role of preload and leakage correction in gadolinium-based cerebral blood volume estimation determined by comparison with MION as a criterion standard.** *AJNR Am J Neuroradiol* 2012;33:1081–87 CrossRef Medline
10. Boxerman JL, Schmainda KM, Weisskoff RM. **Relative cerebral blood volume maps corrected for contrast agent extravasation significantly correlate with glioma tumor grade, whereas uncorrected maps do not.** *AJNR Am J Neuroradiol* 2006;27:859–67 Medline
11. Leu K, Boxerman JB, Cloughesy TF, et al. **Improved leakage correction for single-echo dynamic susceptibility contrast (DSC) perfusion MRI estimates of relative cerebral blood volume (rCBV) in**

high-grade gliomas by accounting for bidirectional contrast agent exchange. *AJNR Am J Neuroradiol* 2016;37:1440–46
12. Bjornerud A, Sorensen AG, Mouridsen K, et al. **T1- and T2*-dominant extravasation correction in DSC-MRI, Part I, theoretical considerations and implications for assessment of tumor hemodynamic properties.** *J Cereb Blood Flow Metab* 2011;31:2041–53 CrossRef Medline
13. Leu K, Boxerman JL, Lai A, et al. **Bidirectional contrast agent leakage correction of dynamic susceptibility contrast (DSC)-MRI improves cerebral blood volume estimation and survival prediction in recurrent glioblastoma treated with bevacizumab.** *J Magn Reson Imaging* 2016;44:1229–37 CrossRef Medline
14. Ostergaard L, Weisskoff RM, Chesler DA, et al. **High resolution measurement of cerebral blood flow using intravascular tracer bolus passages, Part I: mathematical approach and statistical analysis.** *Magn Reson Med* 1996;36:715–25 CrossRef Medline
15. Quarles CC, Gochberg DF, Gore JC, et al. **A theoretical framework to model DSC-MRI data acquired in the presence of contrast agent extravasation.** *Phys Med Biol* 2009;54:5749–66 CrossRef Medline
16. Simpson NE, He Z, Evelhoch JL. **Deuterium NMR tissue perfusion measurements using the tracer uptake approach, I: optimization of methods.** *Magn Reson Med* 1999;42:42–52 Medline
17. Schmiedeskamp H, Andre JB, Straka M, et al. **Simultaneous perfusion and permeability measurements using combined spin- and gradient-echo MRI.** *J Cereb Blood Flow Metab* 2013;33:732–43 CrossRef Medline
18. Pintaske J, Martirosian P, Graf H, et al. **Relaxivity of gadopentetate dimeglumine (Magnevist), gadobutrol (Gadovist), and gadobenate dimeglumine (MultiHance) in human blood plasma at 0.2, 1.5, and 3 Tesla.** *Invest Radiol* 2006;41:213–21 CrossRef Medline
19. Kjolby BF, Østergaard L, Kiselev VG. **Theoretical model of intravascular paramagnetic tracers effect on tissue relaxation.** *Magn Reson Med* 2006;56:187–97 CrossRef Medline
20. Wansapura JP, Holland SK, Dunn RS, et al. **NMR relaxation times in the human brain at 3.0 Tesla.** *J Magn Reson Imaging* 1999;9:531–38 Medline
21. Zhang N, Zhang L, Qiu B, et al. **Correlation of volume transfer coefficient Ktrans with histopathologic grades of gliomas.** *J Magn Reson Imaging* 2012;36:355–63 CrossRef Medline
22. Wu O, Østergaard L, Koroshetz WJ, et al. **Effects of tracer arrival time on flow estimates in MR perfusion-weighted imaging.** *Magn Reson Med* 2003;50:856–64 CrossRef Medline
23. van Osch MJ, Vonken EJ, Viergever MA, et al. **Measuring the arterial input function with gradient echo sequences.** *Magn Reson Med* 2003;49:1067–76 CrossRef Medline
24. Vonken EP, van Osch MJ, Bakker CJ, et al. **Simultaneous quantitative cerebral perfusion and Gd-DTPA extravasation measurement with dual-echo dynamic susceptibility contrast MRI.** *Magn Reson Med* 2000;43:820–27 Medline
25. Welker K, Boxerman J, Kalnin A, et al; American Society of Functional Neuroradiology MR Perfusion Standards and Practice Subcommittee of the ASFNR Clinical Practice Committee. **ASFNR recommendations for clinical performance of MR dynamic susceptibility contrast perfusion imaging of the brain.** *AJNR Am J Neuroradiol* 2015;36:E41–51 CrossRef Medline
26. Liu HL, Wu YY, Yang WS, et al. **Is Weisskoff model valid for the correction of contrast agent extravasation with combined T1 and T2* effects in dynamic susceptibility contrast MRI?** *Med Phys* 2011; 38:802–09 CrossRef Medline
27. Hu LS, Baxter LC, Pinnaduwage DS, et al. **Optimized preload leakage-correction methods to improve the diagnostic accuracy of dynamic susceptibility-weighted contrast-enhanced perfusion MR imaging in posttreatment gliomas.** *AJNR Am J Neuroradiol* 2010;31: 40–48 CrossRef Medline
28. Kassner A, Annesley DJ, Zhu XP, et al. **Abnormalities of the contrast re-circulation phase in cerebral tumors demonstrated using dynamic susceptibility contrast-enhanced imaging: a possible marker of vascular tortuosity.** *J Magn Reson Imaging* 2000;11:103–13 Medline
29. Pathak AP, Ward BD, Schmainda KM. **A novel technique for modeling susceptibility-based contrast mechanisms for arbitrary microvascular geometries: the finite perturber method.** *Neuroimage* 2008;40:1130–43 CrossRef Medline
30. Semmineh NB, Xu J, Boxerman JL, et al. **An efficient computational approach to characterize DSC-MRI signals arising from three-dimensional heterogeneous tissue structures.** *PLoS One* 2014;9: e84764 CrossRef Medline

Diagnostic Accuracy of T1-Weighted Dynamic Contrast-Enhanced–MRI and DWI-ADC for Differentiation of Glioblastoma and Primary CNS Lymphoma

X. Lin, M. Lee, O. Buck, K.M. Woo, Z. Zhang, V. Hatzoglou, A. Omuro, J. Arevalo-Perez, A.A. Thomas, J. Huse, K. Peck, A.I. Holodny, and R.J. Young

ABSTRACT

BACKGROUND AND PURPOSE: Glioblastoma and primary CNS lymphoma dictate different neurosurgical strategies; it is critical to distinguish them preoperatively. However, current imaging modalities do not effectively differentiate them. We aimed to examine the use of DWI and T1-weighted dynamic contrast-enhanced–MR imaging as potential discriminative tools.

MATERIALS AND METHODS: We retrospectively reviewed 18 patients with primary CNS lymphoma and 36 matched patients with glioblastoma with pretreatment DWI and dynamic contrast-enhanced–MR imaging. VOIs were drawn around the tumor on contrast-enhanced T1WI and FLAIR images; these images were transferred onto coregistered ADC maps to obtain the ADC and onto dynamic contrast-enhanced perfusion maps to obtain the plasma volume and permeability transfer constant. Histogram analysis was performed to determine the mean and relative ADC_{mean} and relative 90th percentile values for plasma volume and the permeability transfer constant. Nonparametric tests were used to assess differences, and receiver operating characteristic analysis was performed for optimal threshold calculations.

RESULTS: The enhancing component of primary CNS lymphoma was found to have significantly lower ADC_{mean} (1.1×10^{-3} versus 1.4×10^{-3}; $P < .001$) and relative ADC_{mean} (1.5 versus 1.9; $P < .001$) and relative 90th percentile values for plasma volume (3.7 versus 5.0; $P < .05$) than the enhancing component of glioblastoma, but not significantly different relative 90th percentile values for the permeability transfer constant (5.4 versus 4.4; $P = .83$). The nonenhancing portions of glioblastoma and primary CNS lymphoma did not differ in these parameters. On the basis of receiver operating characteristic analysis, mean ADC provided the best threshold (area under the curve = 0.83) to distinguish primary CNS lymphoma from glioblastoma, which was not improved with normalized ADC or the addition of perfusion parameters.

CONCLUSIONS: ADC was superior to dynamic contrast-enhanced–MR imaging perfusion, alone or in combination, in differentiating primary CNS lymphoma from glioblastoma.

ABBREVIATIONS: AUC = area under the curve; DCE = dynamic contrast-enhanced; $-_{5\%tile}$ = 5th percentile; GBM = glioblastoma; K^{trans} = permeability transfer constant; *MGMT* = *O(6)-methylguanin-DNA-methyltransferase*; $-_{90\%tile}$ = 90th percentile; PCNSL = primary CNS lymphoma; r- = relative or normalized; Ve = extravascular extracellular volume; Vp = blood plasma volume

The standard of care for glioblastoma (GBM) dictates maximum safe resection.[1] In contrast, efforts at resection in primary CNS lymphoma (PCNSL) are discouraged due to lack of survival benefits and an increase in postoperative deficits.[2,3] Given the distinct prognostic implications and the differing surgical planning and treatment options for PCNSL and GBM, their preoperative differentiation is important in patients presenting with an enhancing brain tumor. MR imaging features of PCNSL and GBM are highly variable and overlapping,[4,5] rendering the differentiation difficult when based solely on conventional MR imaging.

Several studies have suggested the usefulness of diffusion-weighted imaging–derived ADC maps in differentiating PCNSL

Received July 22, 2016; accepted after revision October 7.

From the Departments of Neurology (X.L., A.O., A.A.T.), Radiology (M.L., O.B., V.H., J.A.-P., A.I.H., R.J.Y.), Epidemiology and Biostatistics (K.M.W., Z.Z.), Pathology (J.H.), Medical Physics (K.P.), and The Brain Tumor Center (V.H., A.O., A.I.H., R.J.Y.), Memorial Sloan Kettering Cancer Center, New York, New York; and Department of Neurology (X.L.), National Neuroscience Institute, Singapore.

X. Lin and M. Lee contributed equally to the article as co-first authors.

This work was supported in part by National Institutes of Health/National Cancer Center Support Grant P30 CA008748. M. Lee's research was funded, in part, through the National Institutes of Health Memorial Sloan Kettering Cancer Center Medical Student Summer Fellowship program.

Please address correspondence to Robert J. Young, MD, Neuroradiology Service, Department of Radiology, Memorial Sloan Kettering Cancer Center, 1275 York Ave, New York, NY 10065; e-mail: youngr@mskcc.org

Indicates open access to non-subscribers at www.ajnr.org
Indicates article with supplemental on-line photo.
http://dx.doi.org/10.3174/ajnr.A5023

from GBM.[6,7] Due to its higher cellularity compared with GBM, PCNSL has been shown to exhibit lower ADC values.[6,7] The use of dynamic MR imaging perfusion techniques has also been of growing interest. In pathologic studies, PCNSL and GBM exhibited varying degrees of increased vascular permeability and perfusion.[8,9] T2*-weighted DSC studies have suggested the discriminative value of cerebral blood volume; however, the results have been inconsistent.[10-12] More recent studies have suggested the effectiveness of T1-weighted dynamic contrast-enhanced (DCE) perfusion in differentiating PCNSL from GBM.[13,14] DCE-MR imaging measures fractional blood plasma volume per unit volume of tissue (Vp) and time-dependent leakage (permeability transfer constant [K^{trans}]), which reflect tissue perfusion and leakiness, respectively.[15,16] Compared with DSC, DCE perfusion has the advantages of higher spatial resolution, better quantification of microvascular leakiness and perfusion, and increased resistance to susceptibility artifacts.[16,17]

In this study, we aimed to examine the use of DCE-MR imaging and DWI-ADC as potential discriminative tools and to define cutoff (threshold) values for DWI-ADC and DCE perfusion parameters that would be sensitive and specific for PCNSL. We hypothesized that PCNSL would have greater diffusion restriction, while GBM would have greater leakiness and perfusion.

MATERIALS AND METHODS

Patient Selection

This study is an institutional review board–approved retrospective single-institution study performed under a waiver of informed consent. All Health Insurance Portability and Accountability Act regulations were followed. We queried institutional and departmental data bases for all patients with histologically confirmed newly diagnosed PCNSL between January 2011 and December 2014 who had pretreated DWI- and DCE-MR imaging scans available for analysis. As part of our hospital routine practice, all histology was verified by 1 of 2 neuropathologists, both of whom had >8 years of experience in neuropathology. We excluded patients under the following conditions: 1) systemic lymphoma, 2) nonparenchymal PCNSL, 3) having undergone chemotherapy before PCNSL diagnosis, and 4) a known history of testing positive for human immunodeficiency virus. A GBM cohort, matched for age and sex, was selected from an institutional data base of newly diagnosed patients with GBM who had histologic confirmation and preoperative DWI and DCE-MR imaging.

Patient charts were reviewed for demographic characteristics, functional status at initial tumor diagnosis, and clinical outcome data. For patients with PCNSL, we collected serum lactate dehydrogenase results obtained within 1 month of tumor diagnosis; for patients with GBM, we collected the available tumor molecular profile, including *O(6)-methylguanin-DNA-methyltransferase* (*MGMT*) methylation, *isocitrate dehydrogenase* (*IDH*) mutation, and epidermal growth factor receptor (EGFR) mutation status.

MR Imaging

MR imaging sequences were acquired with a 1.5 or 3T MR imaging scanner (Signa Excite, HDx, and Discovery 750; GE Healthcare, Milwaukee, Wisconsin) and a standard 8-channel head coil. Gadopentetate dimeglumine (Magnevist; Bayer HealthCare Pharmaceuticals, Wayne, New Jersey) was injected via a venous catheter (18–21 ga) at doses based on patient body weight (0.2 mL/kg body weight; maximum, 20 mL) at 2–3 mL/s. DWI was acquired in the transverse plane by using a spin-echo, echo-planar imaging sequence with the following parameters: TR/TE = 8000/104.2 ms; diffusion gradient encoding in 3 orthogonal directions; b=1000 s/mm^2; FOV = 240 mm; matrix size = 128 × 128 pixels; section thickness = 5 mm; section gap = 1 mm; and number of average = 2. ADC values were calculated with the following parameters: ADC = $[\ln(S / S_0)] / b$, where S is the signal intensity of the ROI obtained through 3 orthogonally oriented DWIs or diffusion trace images, S_0 is the signal intensity of the ROI acquired through reference T2-weighted images, and b is the gradient b factor with a value of 1000 s/mm^2. ADC maps were calculated on a pixel-by-pixel basis.

DCE-MR imaging of the brain was acquired after DWI scans as part of a standard clinical protocol with an axial 3D T1WI echo-spoiled gradient echo sequence (TR = 4–5 ms; TE = 1–2 ms; section thickness = 5 mm; flip angle = 25°; FOV = 24 cm; matrix = 256 × 128; temporal resolution = 5–6 seconds; number of sections = 10–15; and total time = 3.3–4 minutes). Ten phases were acquired preinjection followed by a 30-phase dynamic injection imaging and a 40-mL saline flush. Matching contrast-enhanced T1-weighted (TR/TE = 600/8 ms; thickness = 5 mm) images were also obtained, along with standard sequences including T2-weighted images, FLAIR images, and susceptibility-weighted images. T1 mapping provides a method to calculate the T1 value of each voxel during the noncontrast phase and has been shown not to significantly alter DCE quantification.[18,19] Hence, we do not perform T1 mapping for DCE correction at our institution, and it was not available for image processing in this study.

Image Postprocessing and Analysis

ADC maps, DCE-MR imaging perfusion raw data, contrast-enhanced T1WI, and FLAIR images were transferred to an off-line workstation.

Postprocessing

DCE-MR imaging perfusion data were processed with FDA-approved commercial software (nordicICE; NordicNeuroLab, Bergen, Norway). The signal-to-noise ratio and arterial input function were optimized individually for each patient. For the arterial input function, an appropriate artery was semiautomatically selected to characterize the input function curve and concentration-time curve.[20] The linear assumption between change in signal intensity and gadolinium concentration was made to convert the signal intensity curve to a concentration-time curve. Curves showing an optimal relationship between arterial input function and the concentration-time curve were selected. We used the perfusion analysis method based on the 2-compartment pharmacokinetic model proposed by Tofts et al[20] to calculate pharmacokinetic parameters, including Vp and K^{trans} and to display the results as parametric maps.

Table 1: Patient clinical data

Characteristics	GBM	PCNSL
No. of patients	36	18
Sex	22 men, 14 women	11 men, 7 women
Mean age (range) at diagnosis (yr)	68.6 (46–88)	68.7 (47–84)
Tumor type	Glioblastoma multiforme	Diffuse large B-cell lymphoma
Median KPS (range)	90 (60–100)	70 (50–90)
LDH (U/L) (median) (range)		203 (117–334)
MGMT (No.)	Methylated (10)	
	Unmethylated (19)	
	Not available (7)	
IDH (No.)	Mutated (1)	
	Wild-type (30)	
	Not available (5)	
EGFR amplification/mutation (No.)	Positive (22)	
	Negative (8)	
	Not available (6)	

Note:—KPS indicates Karnofsky performance status; LDH, lactate dehydrogenase.

Table 2: Imaging results

Imaging Parameter at Enhancing Tumor (median)	PCNSL (n = 12)	GBM (n = 24)	P Value	AUC
ADC_{mean} (mm^2/s)	1.1×10^{-3}	1.4×10^{-3}	<.001	0.826
$rADC_{mean}$	1.5	1.9	<.001	0.773
$rADC_{5\%tile}$	1.1	1.1	.99	–
$rVp_{90\%tile}$	3.7	5.0	.006	0.728
$rK^{trans}_{90\%tile}$	5.4	4.4	.83	–

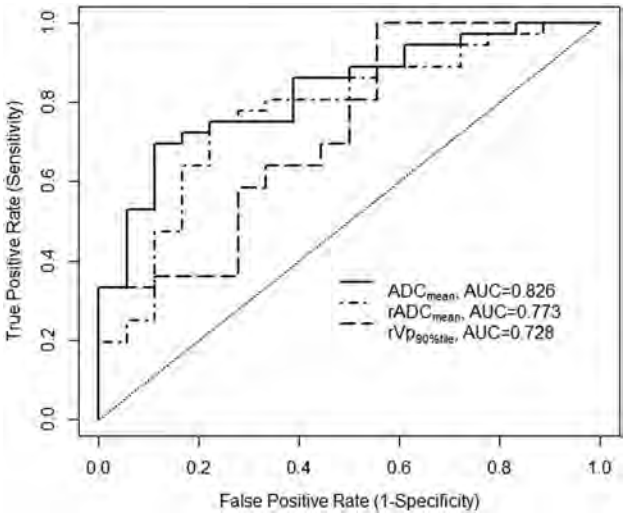

FIG 1. Area under the curve for apparent diffusion coefficient and blood plasma volume. Area under the curve for ADC_{mean}, $rADC_{mean}$, and $rVp_{90\%tile}$ demonstrating the highest AUC value for ADC_{mean}. There are no statistically significantly differences among the 3 AUCs.

Image Analysis

Two experienced operators (1 radiology fellow with 3 years and 1 medical student with 1 year of experience) manually outlined a VOI around the enhancing lesion on contrast-enhanced T1WI and the peritumoral nonenhancing lesion on FLAIR images; the 2 operated independently. The VOI was constructed by summing ROIs drawn around the lesion on all axial sections by the 2 operators, and the final VOI was approved by a board-certified neuroradiologist with 10 years of experience in MR imaging and functional imaging. VOIs were transferred to the ADC, Vp, and K^{trans} parametric maps, and the corresponding measurements were recorded for the all enhancing and nonenhancing lesions. Minimum values of zero pixels were removed. To reduce variability related to scanner heterogeneity, contrast, and patient physiology (eg, cardiac output), we normalized all parameters to normal brain by placing ROIs (standardized area of 40–60 mm^2) in the normal-appearing white matter of the contralateral hemisphere at the midlevel of the tumor.[21-23] The ROI was placed on the contrast-enhanced T1-weighted images and then transferred to the VP and K^{trans} maps and adjusted, if necessary, to avoid potential outlier areas that may harbor subtle microvascular leakage. The ADC, Vp, and K^{trans} measurements were binned, and histogram analysis was performed to determine the mean and 90th percentile normalized values for Vp (rVp_{mean}; $rVp_{90\%tile}$) and K^{trans}, and the mean and fifth percentile normalized values for ADC ($rADC_{mean}$, $rADC_{5\%tile}$). The 90th percentile for Vp and K^{trans} characterizes the portion of the tumor with the highest perfusion, while the fifth percentile for ADC determines the portion of the tumor with the greatest degree of restricted diffusion. To facilitate comparisons with prior studies, we also recorded absolute (non-normalized) ADC_{mean} and $ADC_{5\%tile}$ values.

Statistical Analysis

Wilcoxon rank sum tests were conducted to assess differences between GBM and PCNSL groups for normalized ADC, K^{trans}, and Vp parameters. Measurements from enhancing and nonenhancing lesions were analyzed separately. The significance of P values was adjusted by using the false discovery rate approach. Receiver operating characteristic analysis was performed for the parameters with statistically significant differences, and the area under the curve (AUC) was computed.[24] Optimal thresholds were estimated with consideration for sensitivity and specificity. Overall survival was estimated by using the Kaplan-Meier method, starting from the date of tumor diagnosis until death. Patients who did not die during the study period were censored at the date of last available follow-up. Statistical analysis was performed by using R statistical and computing software (http://www.r-project.org/), including the "ROCR" and "survival" packages. We retrospectively reviewed all patients with pretreated primary CNS lymphoma who underwent evaluation with DCE-MR imaging at our center and selected a GBM cohort matched for age and sex; hence, a sample size calculation was not performed for this study.

RESULTS

Patient Population

We identified 18 patients with PCNSL (11 men; mean age, 68.7 years) and 36 matched patients with GBM (22 men; mean age, 68.6 years) who met all the inclusion criteria. The patient-selection process and clinical data are summarized in On-line Fig 1 and Table 1, respectively.

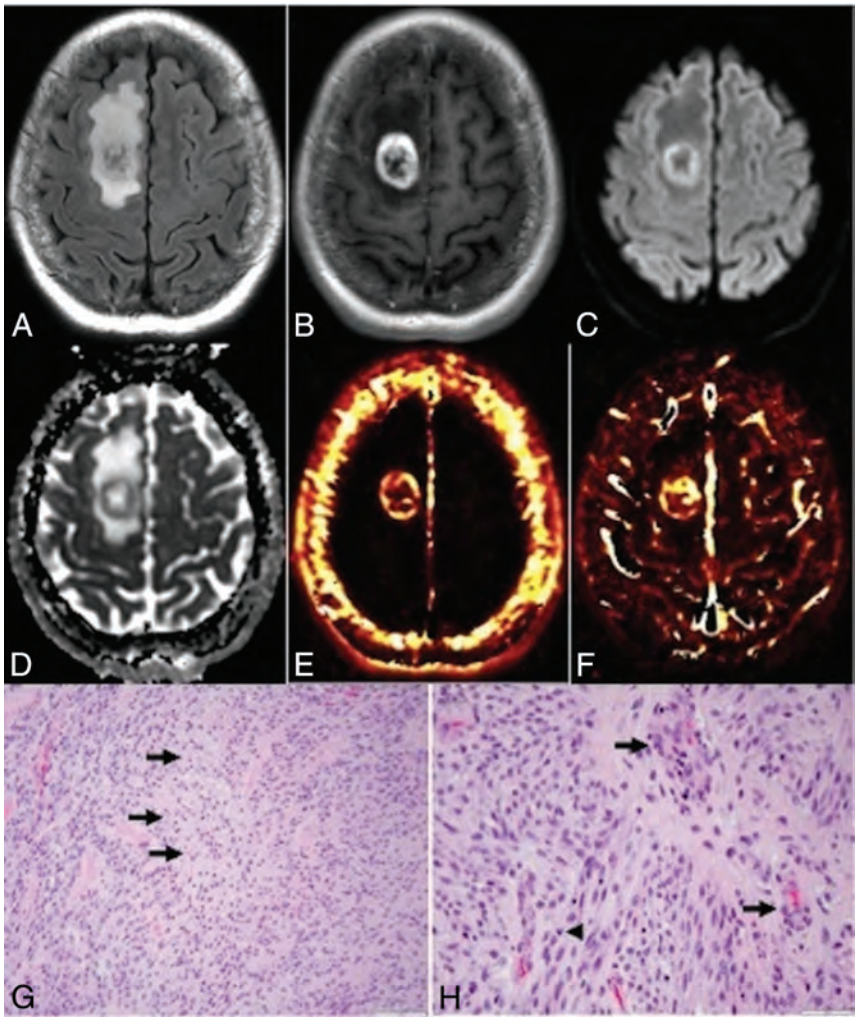

FIG 2. Glioblastoma. Axial FLAIR (*A*), contrast-enhanced TI-weighted (*B*), diffusion-weighted (*C*), ADC (*D*), permeability transfer constant (E), and plasma volume (*F*) images reveal a heterogeneously enhancing tumor in the right frontal lobe with peripheral diffusion restriction (low on ADC, *D*), increased leakiness (*E*), and increased perfusion (*F*). These findings suggest areas of cellular tumor with marked neovascularity and areas of necrosis. Micrographs (*G* and *H*) show high glial neoplasm with necrosis (*G*, *arrows*), microvascular proliferations (*H*, *arrows*), and mitotic activity (*H*, *arrowhead*), consistent with a diagnosis of glioblastoma. Magnification ×20 (*G*) and ×40 (*H*).

In the PCNSL and GBM cohorts, the median Karnofsky performance status at tumor diagnosis was 70 and 90, respectively. At last follow-up, all except 1 (94.4%) patient with PCNSL were alive, with a median follow-up of 22.1 months. One patient died 21.3 months after diagnosis, and the 12-month overall survival in the PCNSL cohort was 100%. The 12-month overall survival in the GBM cohort was 48.5% (95% CI, 29.6%–64.9%).

In the PCNSL cohort, the mean serum lactate dehydrogenase was 203.1 U/L (range, 117.0–334.0 U/L). Among GBM samples with available *MGMT* methylation ($n = 29$), *IDH* mutation ($n = 31$), and EGFR mutation ($n = 30$) status, 10 (34.5%) were *MGMT* methylated, 1 (3.2%) was *IDH* mutated, and 22 (73.3%) were EGFR mutant.

Imaging Findings

The imaging results are summarized in Table 2 and Fig 1, and representative PCNSL and GBM cases are shown in Figs 2 and 3.

ADC

For the enhancing lesions, the median $rADC_{mean}$ was lower for PCNSL than for GBM (PCNSL versus GBM, 1.5 versus 1.9; $P < .001$). On the basis of receiver operating characteristic analysis, a $rADC_{mean}$ threshold of <1.7 indicated PCNSL with a specificity of 78% and sensitivity of 75%. For the nonenhancing lesions, the $rADC_{mean}$ was not significantly different ($P = .21$). When tested without normalization to a ratio, the median ADC_{mean} of the enhancing lesions was also lower in PCNSL than in GBM (1.1×10^{-3} mm^2/s versus 1.4×10^{-3} mm^2/s; $P < .001$); an ADC_{mean} threshold of $<1.3 \times 10^{-3}$ mm^2/s indicated PCNSL with a specificity of 89% and sensitivity of 69%. There was no significant difference in the AUCs for ADC_{mean} and $rADC_{mean}$ ($P = .88$).

DCE-MR Imaging

For the enhancing lesions, the median $rVp_{90\%tile}$ was lower for PCNSL than for GBM (3.7 versus 5.0; $P = .006$), while the median $K^{trans}{}_{90\%tile}$ was not significantly different ($P = .83$) between the two. For the nonenhancing lesions, neither $rVp_{90\%tile}$ nor the $rK^{trans}{}_{90\%tile}$ was significantly different ($P \geq .16$). If one optimized specificity and sensitivity, a $rVp_{90\%tile}$ threshold of <4.6 indicated PCNSL with a specificity of 72% and sensitivity of 58%. The AUC for $rVp_{90\%tile}$ was not significantly different from that for ADC_{mean} ($P = .87$) or $rADC_{mean}$ ($P = .66$).

Combining ADC and DCE-MR Imaging

If one combined ADC_{mean} and $rVp_{90\%tile}$ at the enhancing lesion, a binary threshold of $ADC_{mean} < 1.3 \times 10^{-3}$ mm^2/s and $rVp_{90\%tile} < 4.6$ predicted PCNSL with a specificity of 61% and a sensitivity of 83%. Conversely, a binary threshold of $ADC_{mean} \geq 1.3 \times 10^{-3}$ mm^2/s and $rVp_{90\%tile} \geq 4.6$ predicted GBM with a specificity of 94% and sensitivity of 47%.

DISCUSSION

We retrospectively examined the use of ADC and DCE in differentiating pretreated PCNSL from GBM. We found that ADC_{mean}, $rADC_{mean}$, and $rVp_{90\%tile}$, but not rK^{trans} in the enhancing regions, distinguished PCNSL and GBM (Table 2). An ADC_{mean} threshold of 1.3×10^{-3} mm^2/s discriminated PCNSL and GBM with the best specificity and sensitivity; a binary threshold that combined ADC_{mean} and $rVp_{90\%tile}$ values was helpful for predicting GBM but less so for PCNSL.

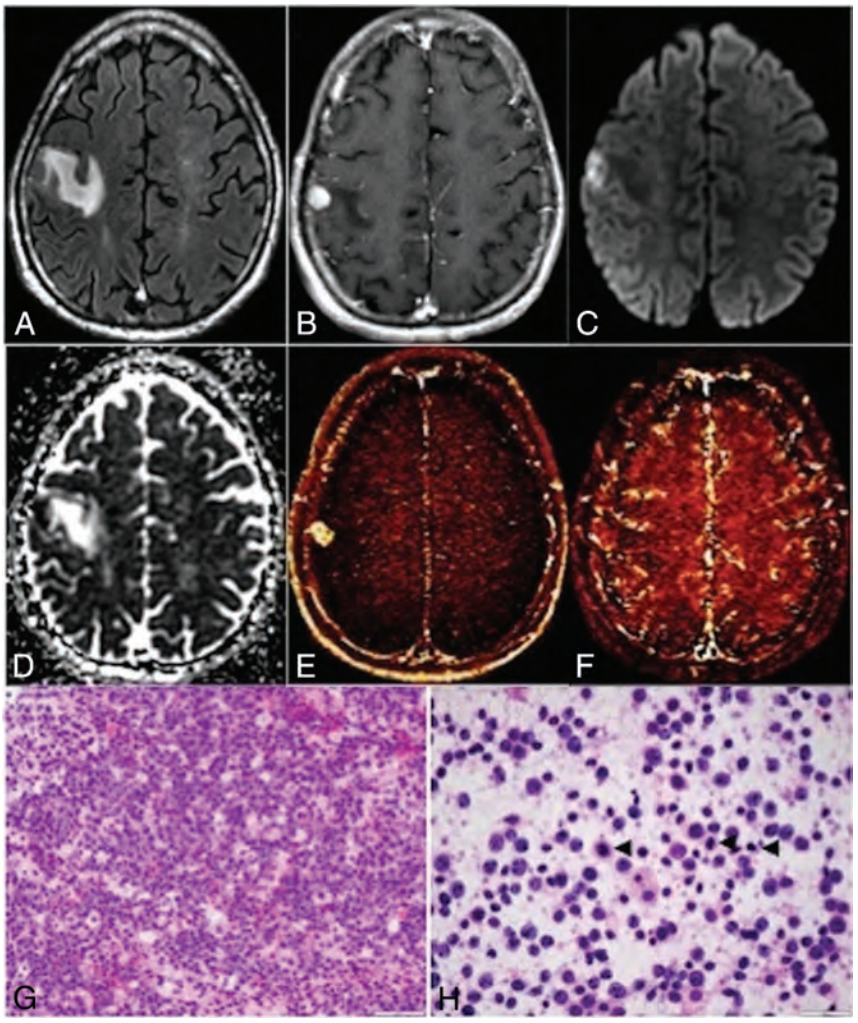

FIG 3. Primary CNS lymphoma. Axial FLAIR (*A*), contrast-enhanced TI-weighted (*B*), diffusion-weighted (*C*), ADC (*D*), permeability transfer constant (*E*), and plasma volume (*F*) images show an enhancing tumor in the right frontal lobe with diffusion restriction (*D*), increased leakiness (high on K^{trans}, *E*), and only slightly increased perfusion (slightly high on Vp, *F*). These findings indicate cellular tumor without marked neovascularity, typical for primary CNS lymphoma. Micrographs (*G* and *H*) show high-grade lymphoid proliferation with obvious mitotic activity in the cytology preparation (*H*, *arrowheads*). Magnification ×40 (*G* and *H*).

Our study findings are consistent with previous studies demonstrating significantly lower ADC in PCNSL than in GBM.[6,7,25,26] In a subset of these studies, DWI results were correlated with histologic information and showed a clear inverse relationship between ADC and tumor cellularity,[6,7,26] suggesting that untreated PCNSL has higher tumor density than untreated GBM. In contrast to these studies, we also studied relative normalized ADC values but did not find any improved discriminative performance with $rADC_{mean}$ over absolute $ADC_{mean.}$ We therefore advocate the use of ADC_{mean}, which is a simpler and more direct measurement than $rADC_{mean}$, to distinguish PCNSL and GBM.

Our study also examined the use of the DCE-MR imaging technique and showed that rVp was able to distinguish PCNSL from GBM. Vp was not part of the original Tofts model and was introduced later in the modified Tofts model to account for intravascular tracer.[15] In gliomas, Vp has been shown to differentiate tumor grade.[27] However, Vp has not be shown to be useful in differentiating PCNSL from GBM.[14] Our study, to the best of our knowledge, is the first to demonstrate the discriminating value of $rVp_{90\%tile}$; this positive finding may be related to our choice of a normalized parameter to reduce interscanner, interrater, and interpatient variability.

K^{trans} is the other commonly measured DCE-MR imaging parameter. It measures the degree of increase in T1 due to contrast accumulation in tissue and can be affected by multiple factors such as blood flow and capillary wall surface area. In general, it is used to represent leakiness due to capillary permeability and blood-brain barrier disruption.[16] A study by Kickingereder et al[13] showed that PCNSL had significantly higher K^{trans} than GBM and further correlated these radiologic findings with histologic demonstration of destroyed vessel architecture in the 11 PCNSLs and intact vascular integrity in the 60 GBMs. With CT perfusion imaging, K^{trans} was also shown to be significantly higher in PCNSL than in GBM in one study[28] but not in a subsequent study[29]; this latter negative study was attributed to the use of the Patlak model, which fails to account for backflow of contrast agent from the extravascular extracellular space to the blood plasma, compromising K^{trans} measurement. Our study also showed a trend for higher K^{trans} in PCNSL than in GBM, but the difference was not statistically significant.

Our results indicated that rVp is not superior to ADC for identifying PCNSL, and a combined model including $rVp_{90\%tile}$ and ADC_{mean} is not superior to either technique alone. Perfusion MR imaging has been suggested as a valuable part of the imaging strategy for the differential diagnosis of undiagnosed brain masses.[30,31] In addition, perfusion MR imaging has demonstrated additional value in gliomas with correlations to glioma grade, *EGFR* gene amplification and vIII status, *MGMT* methylation status, time-to-progression, and overall survival.[21,32-37] Therefore, while not superior for differential diagnosis purposes, DCE-MR imaging may be helpful to support the presumptive diagnosis of PCNSL when marked hyperperfusion is absent, and it can be considered to provide important prognostic data about tumor vascularity and leakiness independent of data about tumor cellularity.

Unlike previous studies that examined imaging parameters solely at contrast-enhancing regions, we evaluated imaging parameters at both enhancing and nonenhancing regions but failed to show any added discriminative value. This outcome suggests

that increases in tumor cellularity, microvascular permeability, and vascular proliferation are less marked in nonenhancing areas of different brain tumors compared with contrast-enhancing regions. Although nonenhancing regions in glioblastomas are known to include a combination of tumor and peritumoral edema,[38] quantification of tumor-related imaging characteristics is dependent on the relative abundance of tumor cells and may be diluted by the amount of edema.[26]

Our study has several potential limitations. First, we did not examine all DCE-MR imaging parameters, including extravascular extracellular volume (Ve), which was shown in 1 study to differentiate PCNSL from other brain tumors.[14] This study by Abe et al[14] used a DCE-MR imaging sequence with a shorter-than-standard acquisition time, however, which potentially overestimates K^{trans} and underestimates Vp and Ve,[39] thereby limiting the generalizability of the results. In addition, the physiologic meaning of Ve remains elusive, with conflicting studies demonstrating its correlation with tumor cellularity.[7,26,40] The use of Ve is further refuted by an earlier study that failed to show a significant difference in Ve between PCNSL and GBM.[13] We did not evaluate Ve in our study and, instead, chose ADC as a more reliable and widely applied marker of tumor cellularity.[7,26] Second, we did not evaluate the performance of other conventional MR imaging parameters such as the presence of necrosis and rim enhancement. Previous studies have shown that PCNSL has variable degrees of T1 and T2 intensities, extent of necrosis, and pattern of contrast enhancement—suggesting that these features are unreliable in distinguishing lymphoma from other CNS lesions.[41,42] Consequently, in 1 prior study, the use of rim enhancement and central necrosis resulted in misclassification of 3 (17.6%) of 17 PCNSLs and malignant gliomas.[30] Given the statistical limitations of our relatively small sample size of patients with PCNSL who underwent DCE-MR imaging, we chose to focus our study on examining ADC, rather than all the other conventional MR imaging parameters. Our small sample size also limited our ability to use cross-validation to assess the operating characteristics and validate the sensitivities and specificities of the cutoff values determined in our study. Third, we did not account for the presence of microbleed, which may confound ADC and DCE-MR imaging results. However, the additional step of eliminating microbleed by using an additional SWI sequence may pose impractical constraints and limit the applicability of our study. Fourth, due to the lack of the routine use of MR spectroscopy in this retrospective study, we were unable to evaluate the utility of MR spectroscopy, which has been shown to distinguish PCNSL from GBM in 1 study with a specificity exceeding 90%.[43] The added value of MR spectroscopy in discriminating the diagnoses should be incorporated in future prospective studies. Fifth, the manual drawing and transfer of VOIs to parametric maps could have introduced variability. We sought to reduce the variability by having all VOIs drawn by operators who had at least 1 year of experience and reviewed by an experienced board-certified neuroradiologist and by exploiting the histogram function to interrogate only the most abnormal parts of the tumor.

CONCLUSIONS

Pretreatment differentiation of PCNSL and GBM is challenging. Our study suggests that DCE-MR imaging is helpful in identifying PCNSL, though rVp did not outperform ADC and a combined model did not outperform either metric alone. Further prospective studies are needed to confirm these findings.

ACKNOWLEDGMENTS

We thank Ms Joanne Chin for her editorial work in the preparation of this manuscript.

Disclosures: Robert J. Young—*UNRELATED*: *Consultancy*: Agios Glioma Advisory Board, *Comments*: honorarium; *Grants/Grants Pending*: Dana Foundation.* *Money paid to the institution.

REFERENCES

1. Marko NF, Weil RJ, Schroeder JL, et al. **Extent of resection of glioblastoma revisited: personalized survival modeling facilitates more accurate survival prediction and supports a maximum-safe-resection approach to surgery.** *J Clin Oncol* 2014;32:774–82 CrossRef Medline
2. Bataille B, Delwail V, Menet E, et al. **Primary intracerebral malignant lymphoma: report of 248 cases.** *J Neurosurg* 2000;92:261–66 CrossRef Medline
3. DeAngelis LM, Yahalom J, Heinemann MH, et al. **Primary CNS lymphoma: combined treatment with chemotherapy and radiotherapy.** *Neurology* 1990;40:80–86 CrossRef Medline
4. Koeller KK, Smirniotopoulos JG, Jones RV. **Primary central nervous system lymphoma: radiologic-pathologic correlation.** *Radiographics* 1997;17:1497–526 CrossRef Medline
5. Rees JH, Smirniotopoulos JG, Jones RV, et al. **Glioblastoma multiforme: radiologic-pathologic correlation.** *Radiographics* 1996;16:1413–38; quiz 62–63 Medline
6. Doskaliyev A, Yamasaki F, Ohtaki M, et al. **Lymphomas and glioblastomas: differences in the apparent diffusion coefficient evaluated with high b-value diffusion-weighted magnetic resonance imaging at 3T.** *Eur J Radiol* 2012;81:339–44 CrossRef Medline
7. Guo AC, Cummings TJ, Dash RC, et al. **Lymphomas and high-grade astrocytomas: comparison of water diffusibility and histologic characteristics.** *Radiology* 2002;224:177–83 CrossRef Medline
8. Molnár PP, O'Neill BP, Scheithauer BW, et al. **The blood-brain barrier in primary CNS lymphomas: ultrastructural evidence of endothelial cell death.** *Neuro Oncol* 1999;1:89–100 CrossRef Medline
9. Jain RK, di Tomaso E, Duda DG, et al. **Angiogenesis in brain tumours.** *Nat Rev Neurosci* 2007;8:610–22 CrossRef Medline
10. Xing Z, You RX, Li J, et al. **Differentiation of primary central nervous system lymphomas from high-grade gliomas by rCBV and percentage of signal intensity recovery derived from dynamic susceptibility-weighted contrast-enhanced perfusion MR imaging.** *Clin Neuroradiol* 2014;24:329–36 CrossRef Medline
11. Toh CH, Wei KC, Chang CN, et al. **Differentiation of primary central nervous system lymphomas and glioblastomas: comparisons of diagnostic performance of dynamic susceptibility contrast-enhanced perfusion MR imaging without and with contrast-leakage correction.** *AJNR Am J Neuroradiol* 2013;34:1145–49 CrossRef Medline
12. Kickingereder P, Wiestler B, Sahm F, et al. **Primary central nervous system lymphoma and atypical glioblastoma: multiparametric differentiation by using diffusion-, perfusion-, and susceptibility-weighted MR imaging.** *Radiology* 2014;272:843–50 CrossRef Medline
13. Kickingereder P, Sahm F, Wiestler B, et al. **Evaluation of microvascular permeability with dynamic contrast-enhanced MRI for the differentiation of primary CNS lymphoma and glioblastoma: radiologic-pathologic correlation.** *AJNR Am J Neuroradiol* 2014;35:1503–08 CrossRef Medline
14. Abe T, Mizobuchi Y, Nakajima K, et al. **Diagnosis of brain tumors**

using dynamic contrast-enhanced perfusion imaging with a short acquisition time. *Springerplus* 2015;4:88 CrossRef Medline
15. Bergamino M, Bonzano L, Levrero F, et al. **A review of technical aspects of T1-weighted dynamic contrast-enhanced magnetic resonance imaging (DCE-MRI) in human brain tumors.** *Phys Med* 2014; 30:635–43 CrossRef Medline
16. Cha S. **Update on brain tumor imaging: from anatomy to physiology.** *AJNR Am J Neuroradiol* 2006;27:475–87 Medline
17. Essig M, Shiroishi MS, Nguyen TB, et al. **Perfusion MRI: the five most frequently asked technical questions.** *AJR Am J Roentgenol* 2013;200:24–34 CrossRef Medline
18. Haacke EM, Filleti CL, Gattu R, et al. **New algorithm for quantifying vascular changes in dynamic contrast-enhanced MRI independent of absolute T1 values.** *Magn Reson Med* 2007;58:463–72 CrossRef Medline
19. Jung SC, Yeom JA, Kim JH, et al. **Glioma: application of histogram analysis of pharmacokinetic parameters from T1-weighted dynamic contrast-enhanced MR imaging to tumor grading.** *AJNR Am J Neuroradiol* 2014;35:1103–10 CrossRef Medline
20. Tofts PS, Brix G, Buckley DL, et al. **Estimating kinetic parameters from dynamic contrast-enhanced T(1)-weighted MRI of a diffusable tracer: standardized quantities and symbols.** *J Magn Reson Imaging* 1999;10:223–32 Medline
21. Arevalo-Perez J, Thomas AA, Kaley T, et al. **T1-weighted dynamic contrast-enhanced MRI as a noninvasive biomarker of epidermal growth factor receptor vIII status**. *AJNR Am J Neuroradiol* 2015;36: 2256–61 CrossRef Medline
22. Thomas AA, Arevalo-Perez J, Kaley T, et al. **Dynamic contrast enhanced T1 MRI perfusion differentiates pseudoprogression from recurrent glioblastoma.** *J Neurooncol* 2015;125:183–90 CrossRef Medline
23. Zhang M, Gulotta B, Thomas A, et al. **Large-volume low apparent diffusion coefficient lesions predict poor survival in bevacizumab-treated glioblastoma patients.** *Neuro Oncol* 2016;18: 735–43 CrossRef Medline
24. DeLong ER, DeLong DM, Clarke-Pearson DL. **Comparing the areas under two or more correlated receiver operating characteristic curves: a nonparametric approach.** *Biometrics* 1988;44: 837–45 CrossRef Medline
25. Yamashita K, Yoshiura T, Hiwatashi A, et al. **Differentiating primary CNS lymphoma from glioblastoma multiforme: assessment using arterial spin labeling, diffusion-weighted imaging, and ^{18}F-fluorodeoxyglucose positron emission tomography.** *Neuroradiology* 2013; 55:135–43 CrossRef Medline
26. Kono K, Inoue Y, Nakayama K, et al. **The role of diffusion-weighted imaging in patients with brain tumors.** *AJNR Am J Neuroradiol* 2001;22:1081–88 Medline
27. Lüdemann L, Grieger W, Wurm R, et al. **Quantitative measurement of leakage volume and permeability in gliomas, meningiomas and brain metastases with dynamic contrast-enhanced MRI.** *Magn Reson Imaging* 2005;23:833–41 CrossRef Medline
28. Warnke PC, Timmer J, Ostertag CB, et al. **Capillary physiology and drug delivery in central nervous system lymphomas.** *Ann Neurol* 2005;57:136–39 CrossRef Medline
29. Schramm P, Xyda A, Klotz E, et al. **Dynamic CT perfusion imaging of intra-axial brain tumours: differentiation of high-grade gliomas from primary CNS lymphomas.** *Eur Radiol* 2010;20:2482–90 CrossRef Medline
30. Al-Okaili RN, Krejza J, Woo JH, et al. **Intraaxial brain masses: MR imaging-based diagnostic strategy—initial experience.** *Radiology* 2007;243:539–50 CrossRef Medline
31. Omuro AM, Leite CC, Mokhtari K, et al. **Pitfalls in the diagnosis of brain tumours.** *Lancet Neurol* 2006;5:937–48 CrossRef Medline
32. Arevalo-Perez J, Peck KK, Young RJ, et al. **Dynamic contrast-enhanced perfusion MRI and diffusion-weighted imaging in grading of gliomas.** *J Neuroimaging* 2015;25:792–98 CrossRef Medline
33. Gupta A, Young RJ, Shah AD, et al. **Pretreatment dynamic susceptibility contrast MRI perfusion in glioblastoma: prediction of EGFR gene amplification.** *Clin Neuroradiol* 2015;25:143–50 CrossRef Medline
34. Jain KK, Sahoo P, Tyagi R, et al. **Prospective glioma grading using single-dose dynamic contrast-enhanced perfusion MRI.** *Clinical Radiol* 2015;70:1128–35 CrossRef Medline
35. Ahn SS, Shin NY, Chang JH, et al. **Prediction of methylguanine methyltransferase promoter methylation in glioblastoma using dynamic contrast-enhanced magnetic resonance and diffusion tensor imaging.** *J Neurosurg* 2014;121:367–73 CrossRef Medline
36. Choi HS, Kim AH, Ahn SS, et al. **Glioma grading capability: comparisons among parameters from dynamic contrast-enhanced MRI and ADC value on DWI.** *Korean J Radiol* 2013;14:487–92 CrossRef Medline
37. Law M, Young RJ, Babb JS, et al. **Gliomas: predicting time to progression or survival with cerebral blood volume measurements at dynamic susceptibility-weighted contrast-enhanced perfusion MR imaging.** *Radiology* 2008;247:490–98 CrossRef Medline
38. Wen PY, Macdonald DR, Reardon DA, et al. **Updated response assessment criteria for high-grade gliomas: Response Assessment in Neuro-Oncology working group.** *J Clin Oncol* 2010;28:1963–72 CrossRef Medline
39. Larsson C, Kleppesto M, Rasmussen I Jr, et al. **Sampling requirements in DCE-MRI based analysis of high grade gliomas: simulations and clinical results.** *J Magn Reson Imaging* 2013;37:818–29 CrossRef Medline
40. Mills SJ, Soh C, Rose CJ, et al. **Candidate biomarkers of extravascular extracellular space: a direct comparison of apparent diffusion coefficient and dynamic contrast-enhanced MR imaging–derived measurement of the volume of the extravascular extracellular space in glioblastoma multiforme.** *AJNR Am J Neuroradiol* 2010;31: 549–53 CrossRef Medline
41. Johnson BA, Fram EK, Johnson PC, et al. **The variable MR appearance of primary lymphoma of the central nervous system: comparison with histopathologic features.** *AJNR Am J Neuroradiol* 1997;18: 563–72 Medline
42. Slone HW, Blake JJ, Shah R, et al. **CT and MRI findings of intracranial lymphoma.** *AJR Am J Roentgenol* 2005;184:1679–85 CrossRef Medline
43. Aburano H, Ueda F, Yoshie Y, et al. **Differences between glioblastomas and primary central nervous system lymphomas in 1H-magnetic resonance spectroscopy.** *Jpn J Radiol* 2015;33:392–403 CrossRef Medline

MR Fingerprinting of Adult Brain Tumors: Initial Experience

C. Badve, A. Yu, S. Dastmalchian, M. Rogers, D. Ma, Y. Jiang, S. Margevicius, S. Pahwa, Z. Lu, M. Schluchter, J. Sunshine, M. Griswold, A. Sloan, and V. Gulani

ABSTRACT

BACKGROUND AND PURPOSE: MR fingerprinting allows rapid simultaneous quantification of T1 and T2 relaxation times. This study assessed the utility of MR fingerprinting in differentiating common types of adult intra-axial brain tumors.

MATERIALS AND METHODS: MR fingerprinting acquisition was performed in 31 patients with untreated intra-axial brain tumors: 17 glioblastomas, 6 World Health Organization grade II lower grade gliomas, and 8 metastases. T1, T2 of the solid tumor, immediate peritumoral white matter, and contralateral white matter were summarized within each ROI. Statistical comparisons on mean, SD, skewness, and kurtosis were performed by using the univariate Wilcoxon rank sum test across various tumor types. Bonferroni correction was used to correct for multiple-comparison testing. Multivariable logistic regression analysis was performed for discrimination between glioblastomas and metastases, and area under the receiver operator curve was calculated.

RESULTS: Mean T2 values could differentiate solid tumor regions of lower grade gliomas from metastases (mean, 172 ± 53 ms, and 105 ± 27 ms, respectively; $P = .004$, significant after Bonferroni correction). The mean T1 of peritumoral white matter surrounding lower grade gliomas differed from peritumoral white matter around glioblastomas (mean, 1066 ± 218 ms, and 1578 ± 331 ms, respectively; $P = .004$, significant after Bonferroni correction). Logistic regression analysis revealed that the mean T2 of solid tumor offered the best separation between glioblastomas and metastases with an area under the curve of 0.86 (95% CI, 0.69–1.00; $P < .0001$).

CONCLUSIONS: MR fingerprinting allows rapid simultaneous T1 and T2 measurement in brain tumors and surrounding tissues. MR fingerprinting–based relaxometry can identify quantitative differences between solid tumor regions of lower grade gliomas and metastases and between peritumoral regions of glioblastomas and lower grade gliomas.

ABBREVIATIONS: CW = contralateral white matter; GBM = glioblastoma multiforme; *IDH1* = *isocitrate dehydrogenase 1*; LGG = lower grade glioma; MET = metastasis; MRF = MR fingerprinting; PW = peritumoral white matter; ST = solid tumor

Glioblastoma multiforme is the most common malignant primary brain tumor with an age-adjusted incidence rate of 3.19/100,000.[1,2] Brain metastases account for 48%–51% of all intracranial neoplasms, with an annual incidence of 8.3–14.3/100,000.[2,3] Early differentiation between primary and metastatic malignant brain tumors ensures selection of appropriate diagnostic and management options and also provides accurate prognostic information early in the course of management.[3,4] The ability to differentiate primarily vasogenic edema (as seen around metastatic lesions) and edema with neoplastic cellular infiltration (as seen around glioblastomas) can allow accurate delineation of the tumor margin and aid therapeutic planning and has the potential to positively affect patient outcome.[5] More fundamentally,

Received July 14, 2016; accepted after revision October 11.

From the Department of Radiology (C.B., S.D., D.M., S.P., J.S., M.G., V.G.), University Hospitals Cleveland Medical Center and Case Western Reserve University, Cleveland, Ohio; School of Medicine (A.Y., M.R., Z.L.), Department of Biomedical Engineering (Y.J., M.G., V.G.), and Department of Epidemiology and Biostatistics (S.M., M.S.), Case Western Reserve University, Cleveland, Ohio; and Departments of Neurosurgery and Pathology (A.S.), University Hospitals–Cleveland Medical Center, Seidman Cancer Center and the Case Comprehensive Cancer Center, Cleveland, Ohio.

Conflict of interest: Dan Ma, Vikas Gulani, Mark Griswold, and Jeffrey Sunshine receive research support from Seimens. Chaitra Badve, Dan Ma, Yun Jiang, Andrew Sloan, Jeffrey Sunshine, Mark Griswold, and Vikas Gulani have a pending patent application on this work.

This work was supported by National Institutes of Health 1R01BB017219 award (Principal Investigator: Dr. Mark Griswold) and 1R01EB016728 award (Principal Investigators: Drs. Mark Griswold and Vikas Gulani).

Paper previously presented at: Annual Meeting of the American Society of Neuroradiology and the Foundation of the ASNR Symposium, May 17–22, 2014; Montreal, Quebec, Canada; Annual Meeting of the Radiological Society of North America, November 30–December 5, 2014; Chicago, Illinois.

Please address correspondence to Chaitra Badve, MD, Department of Radiology, University Hospitals Cleveland Medical Center and Case Western Reserve University, 11100 Euclid Ave, Cleveland, OH 44106; e-mail: chaitra.badve@uhhospitals.org

Indicates open access to non-subscribers at www.ajnr.org
Indicates article with supplemental on-line appendix and tables.
Indicates article with supplemental on-line photo.

http://dx.doi.org/10.3174/ajnr.A5035

it is necessary to understand the differences among biologic characteristics of various tumor types to better comprehend complex aggressive tumor behavior and lack of response to treatment, particularly in the case of glioblastomas.[6] Advanced MR imaging studies such as perfusion imaging, diffusion tensor imaging, and MR spectroscopy have demonstrated some utility in discriminating brain metastases from glioblastomas and identifying areas of peritumoral infiltration.[7-14] However, there remains a need for a simple, rapid, quantitative, and noninvasive method to probe tissue characteristics in patients with brain tumors by exploiting subtle changes in the microenvironment that may not be appreciated by the human eye on standard qualitative clinical images.

MR fingerprinting (MRF) is a recently introduced MR imaging technique in which pseudorandomized acquisition parameters are used to simultaneously quantify multiple tissue properties, including T1 and T2 relaxation times.[15] The sequence design results in a signal evolution in each voxel, which depends on the T1 and T2 of tissue in that voxel. On the basis of Bloch equations, a dictionary of all possible signal evolutions is simulated with acquisition parameters from the used sequence and all possible T1 and T2 combinations. Selecting the dictionary entry that is best correlated with the voxel signal time course identifies the best dictionary match for each voxel. The T1 and T2 times used to construct the dictionary entry are identified as the relaxation time measurements for that voxel.[15-17]

In this study, we evaluated the ability of MR fingerprinting–derived T1 and T2 relaxometry to differentiate the 3 common types of intra-axial brain tumors (glioblastomas, lower grade gliomas, and metastases). Using these parameters, we also explored the T1 and T2 properties of peritumoral white matter in various tumor types.

MATERIALS AND METHODS

This Health Insurance Portability and Accountability Act–compliant study was approved by the institutional review board and was performed at University Hospitals Cleveland medical center as a part of larger prospective protocol evaluating preliminary applications of MRF. Informed written consent was obtained from all participants. The inclusion criterion was the presence of an untreated intra-axial neoplasm. Exclusion criteria were all contraindications for MR imaging.

Subjects

Thirty-one patients with newly diagnosed brain tumors were included. Seventeen patients with glioblastoma multiforme (GBMs), 8 with metastases (METs), and 6 with WHO grade II glial neoplasms (lower grade gliomas [LGGs]) were included in this study. The LGG group included 5 oligodendrogliomas and 1 oligoastrocytoma. One of the patients with brain metastasis presented with an unknown primary malignancy and was later diagnosed with adenocarcinoma of the esophagus. The primary malignancies in other patients with brain metastases included adenocarcinoma of the lung, breast, colon, and esophagus and 1 case of melanoma. The metastatic melanoma lesion included in this study did not show hyperintense signal on precontrast T1-weighted images. One of the patients with GBM had undergone a stereotactic biopsy sampling from a portion of the tumor at an outside institution before MR fingerprinting; the biopsy tract was well-defined and was avoided during the ROI analysis. There was no other history of brain surgery, radiation, or significant cerebral trauma in any of the participants. In patients with metastases, 5 had not received any systemic therapy; 2 had completed systemic chemotherapy 2 and 5 months, respectively, before the appearance of brain metastasis; and 1 patient with breast cancer developed a brain metastasis while on systemic chemotherapy for the primary malignancy. The final histopathologic diagnosis was available in all patients (13 total resections, 16 partial resections, and 2 biopsies). Patient demographics, including age and sex, were noted; note was also made if patients had been treated with steroids at the time of MRF imaging. For all gliomas, *isocitrate dehydrogenase 1* (*IDH1*) status was assessed by using a monoclonal antibody to *IDH1* R132.

MR Imaging and Processing

All patients were scanned at 3T (Verio and Magnetom Skyra; Siemens, Erlangen, Germany) by using a 20-channel head coil. MRF acquisitions were incorporated in a clinical MR imaging brain study and were acquired before gadolinium-based contrast agent administration in all subjects. The MRF acquisition was planned on whole-brain clinical standard FLAIR images and, depending on the tumor size, 3–5 MRF sections were acquired through each lesion. The MRF acquisition consisted of a True FISP sequence with parameters as follows; FOV, 300 × 300 mm^2; matrix, 256 × 256; section thickness, 5 mm; flip angle variable, 0°–60°; TR variable, 8.7–11.6 ms; sinc radiofrequency pulse with a duration of 800 μs; and a time-bandwidth product of 2. For every section, 3000 time points were acquired with a total acquisition time of 30.8 seconds.[15]

A dictionary of signal evolutions that could arise from the pulse sequence by using all possible combinations of T1, T2, and off-resonance frequency was generated with a total of 287,709 signal time courses. The ranges of T1 and T2 were chosen on the basis of potentially encountered ranges of these properties, with T1 values between 100 and 3000 ms and T2 values between 10 and 500 ms. The total simulation time was 5.3 minutes. The vector dot product between the measured signal and each dictionary entry was calculated, and the entry yielding the highest dot product was selected as the closest match to the acquired signal.[15] The final output consisted of T1, T2, proton-density, and off-resonance maps for each section, of which only T1 and T2 maps were used for quantitative analysis.

ROI Analysis

A fellowship-trained neuroradiologist (reader 1) who was blinded to the final pathology analyzed the quantitative T1 and T2 maps as follows: Of 31 patients scanned, all GBMs and METs demonstrated enhancement on postgadolinium T1-weighted images, 2 of 6 LGGs were completely nonenhancing, and the remaining 4 LGG lesions showed patchy minimal enhancement. ROIs were drawn in 3 specific areas for each tumor with axial FLAIR and postcontrast T1-weighted images for reference. The solid tumor (ST) region was defined as the enhancing region in tumors with postcontrast enhancement or an expansile FLAIR hyperintensity region in nonenhancing/minimally enhancing tumors. The peri-

tumoral white matter (PW) region was defined as white matter within 1 cm of the enhancing or expansile FLAIR hyperintense tumor margin. One patient with GBM was excluded from the solid tumor analysis because the entire tumor was necrotic with a thin enhancing rim and had no solid-appearing component. In a cerebellar metastatic lesion, the solid tumor measurements were excluded because the entire tumor had hemorrhagic products within. The peritumoral region measurements for these 2 patients were included in the analysis.

The largest possible ROIs were drawn in ST and PW regions that met the previously outlined criteria, while excluding areas of hemorrhage, calcification, or necrosis in these regions. ROIs drawn in PW were restricted to white matter regions while avoiding inclusion of gray matter structures. Finally, contralateral white matter (CW) regions were defined as normal-appearing white matter in the contralateral hemisphere, excluding nonspecific white matter signal abnormalities in older patients. If normal-appearing white matter was not available in the same lobe in the contralateral hemisphere, the ROI was placed in another contralateral lobe. The size of the ROI depended on the lesion size and homogeneity and ranged from 0.32 to 12 cm^2 (median, 1.7 cm^2) for ST, from 0.25 to 2.5 cm^2 (median, 0.96 cm^2) for PW, and from 0.16 to 2.0 cm^2 (median, 1.0 cm^2) for CW. Areas with imaging artifacts (in 1 patient) and prior biopsy tracts (in 1 patient) were avoided. Utmost care was taken to follow the region criteria and avoid partial volume averaging with different tissue types in the vicinity. The output of this analysis consisted of distributional summary parameters for each ROI based on T1 and T2 relaxation times of each voxel within the ROI. ROI output from reader 1 was exclusively used for all statistical analysis. All data processing and analysis were performed in Matlab (MathWorks, Natick, Massachusetts).

Interobserver Concordance

A second reader (a board-certified radiologist, also blinded to the final pathology) delineated ROIs in ST and PW regions of all tumors. The measurements from reader 2 were used only for assessment of interobserver concordance. The ROIs of readers 1 and 2 were compared by means of the Pearson correlation coefficient and intraclass correlation coefficient.

Statistical Analysis

For tumor analysis, distributional parameters were calculated as an output of ROI analysis, including mean, median, mode, SD, skewness, kurtosis, and 10th, 25th, 75th, and 90th percentile values. While the mean, median, and mode are measures of central tendency, the SD measures variability, skewness measures lack of symmetry in the distribution of T1 or T2 across voxels, and the kurtosis measures whether the distribution is heavy-tailed or light-tailed relative to the normal distribution. Pearson correlation coefficients among the mean, median, mode, and 10th, 25th, 75th, and 90th percentiles by type of tissue (ST, PW, or CW) were above 0.90 with many >0.95, indicating that examination of multiple measures from this group would likely be redundant and 1 representative measure could be used instead (see the On-line Appendix and On-line Tables 1–6 for correlation analysis). The mean was selected from all the highly correlated parameters because it is conventionally the most commonly used measure of central tendency. On the other hand, the SD, skewness, and kurtosis were not highly intercorrelated with each other or with the central tendency and percentile measures. Thus, the mean, along with SD, skewness, and kurtosis, were selected for further analyses. These parameters (mean, SD, skewness, and kurtosis) were examined to compare ST and PW regions from each tumor group with the CW. The Wilcoxon signed rank test was used for this analysis. Wilcoxon rank sum tests were used to compare mean, SD, skewness, and kurtosis of ST and PW regions across the 3 tumor types. All results were corrected for multiple-comparison testing by using the Bonferroni correction method, and results significant both with and without multiple-testing correction are reported. With the Bonferroni correction, statistical significance was reached if the P value was $<0.05/k$, where k = number of tests. When comparing tumor types, we set k to 12 (3 pair-wise comparisons $\times$ 4 parameters), and when comparing tumors versus CW, k was set to 8 (2 ROIs $\times$ 4 parameters), resulting in thresholds for statistical significance of $P < .0042$ and .0063, respectively. Multiple logistic regression analysis with a forward stepwise selection model was used to examine which parameters were the best predictors for distinguishing GBMs and METs. At a given step, the most significant predictor with $P < .05$ was entered. The area under the receiver operating characteristic curve was calculated by using the predicted probability from this model as a classifier. All statistical analyses were performed by using SAS 9.4 software (SAS Institute, Cary, North Carolina).

RESULTS

Table 1 summarizes patient demographics for the 3 tumor groups. Patients with lower grade gliomas were younger compared with patients with GBMs and metastases, as expected. Among the 3 tumor groups, there were no differences in the proportion of patients on steroids. There were no differences in T1 and T2 values between patients with and without steroid treatment when compared by tumor type. There were no differences in CW measurements for the 3 groups to suggest significant age effects on normal brain parenchyma (data not shown). All GBMs were negative for *IDH1*, whereas 4 of 6 LGGs were positive for *IDH1*. Figure 1 is an example of MRF-derived T1 and T2 maps and ROI delineation in 1 of the study participants with an enhancing brain tumor. Another example of ROI delineation in a nonenhancing brain tumor is provided in the On-line Figure.

The means and SDs of the mean, SD, skewness, and kurtosis parameters for T1 and T2 for solid/enhancing regions of different tumor types are outlined in Table 2. For all tumor types combined, the mean and SD based on T1 and T2 of solid tumor regions were significantly different from contralateral white matter, even after adjusting for multiple comparison testing (Table 2).

The mean and SD of the PW region of GBMs were significantly different when compared with the CW with $P < .0001$. The comparison of the mean of the PW region of METs and CW yielded a $P = .0078$; this was not significant after multiple-comparison correction. There were no differences between the mean and SD of the PW of LGGs compared with CW. Figure 2 is a scatterplot of mean T1 versus T2 of ST and PW regions of all tumor types with contralateral white matter measurements.

Table 1: Patient demographics

	GBM (*n* = 17)	LGG (*n* = 6)	Metastasis (*n* = 8)	*P* Value
Age, yr (mean) (range)	61.4 ± 9.2 (45–76)	46.5 ± 12.1 (38–67)	63.5 ± 8.6 (48–76)	.03[a]
Sex (No.)				
Female	8 (47.1%)	2 (33.3%)	5 (62.5%)	.57[b]
Male	9 (52.9%)	4 (66.7%)	3 (37.5%)	
Steroids (No.)[c]				
Yes	5 (29.4%)	1 (16.7%)	3 (37.5%)	.77[b]
No	12 (70.6%)	5 (83.3%)	5 (62.5%)	
IDH1 (No.)				
Positive	0 (0.0%)	4 (66.7%)	NA	.003[d]
Negative	11 (100.0%)	1 (16.7%)[e]	NA	

Note:—NA indicates not applicable.

[a] *P* value from the Kruskal-Wallis test. Results of the Wilcoxon rank sum tests showed that the LGG group differed in age from the GBM and metastasis groups (*P* = .014 and .023, respectively) and that the GBM and metastasis groups did not differ in age (*P* = .68).

[b] *P* value from an exact version of the Pearson χ^2 test comparing proportions in the 3 groups.

[c] Wilcoxon rank sum test revealed no differences in T1 and T2 values when patients with the presence and absence of steroid treatment were compared by tumor type.

[d] *P* value from the Fisher exact test comparing GBM and LGG groups.

[e] *IDH1* status of 1 patient with LGG was unknown.

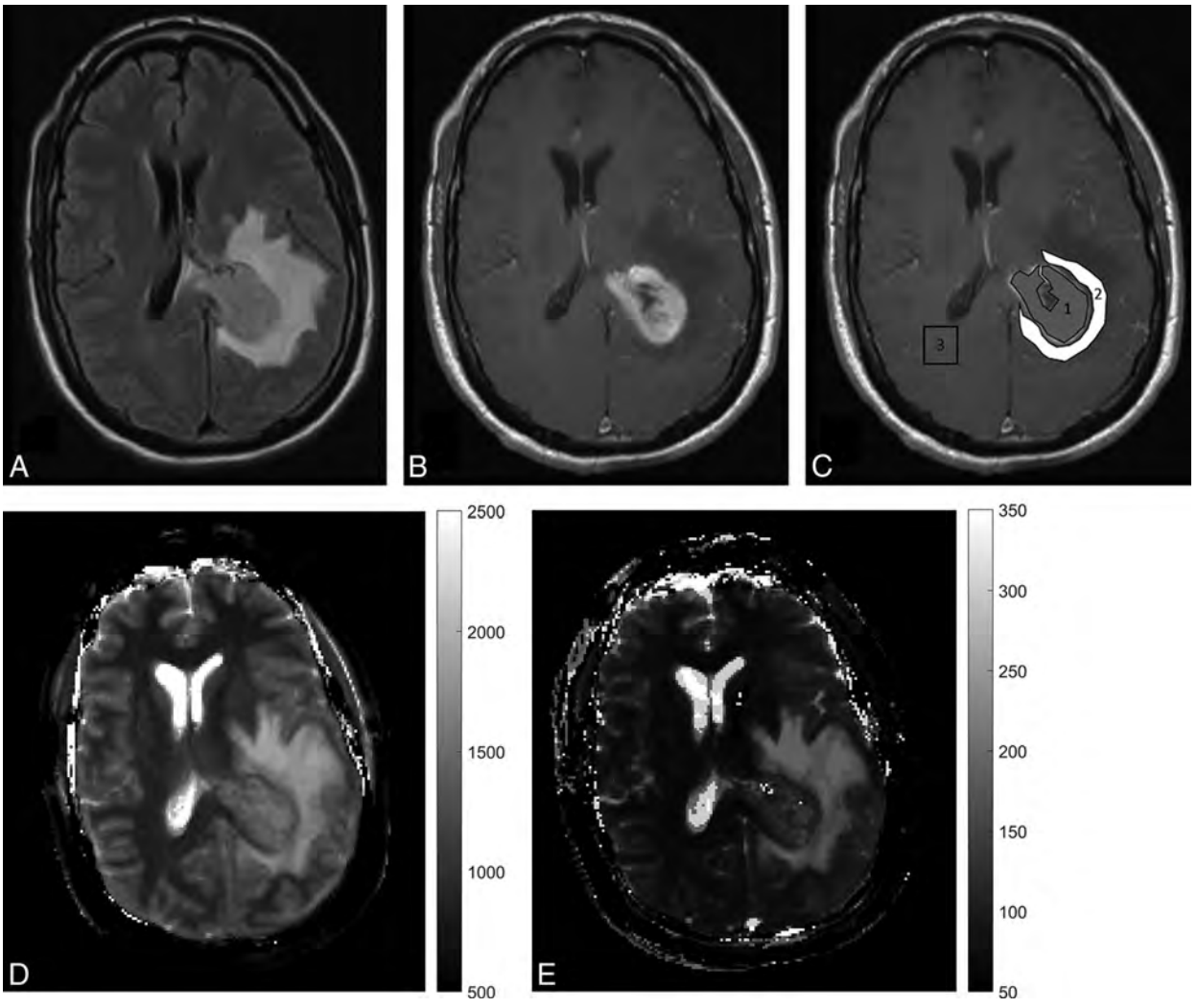

FIG 1. A study patient, a 45-year-old man presenting with severe headaches and altered sensorium with glioblastoma. *A* and *B*, FLAIR and contrast-enhanced T1-weighted images from the clinical scan, which demonstrate a left periatrial enhancing lesion with peritumoral FLAIR hyperintensity. *C*, Postcontrast T1-weighted image with ROI overlay. The central gray ROI shows a solid enhancing tumor region, the white ROI shows a peritumoral white matter region, and the blank ROI in the contralateral hemisphere denotes the contralateral white matter measurement. *D* and *E*, MRF-derived quantitative T1 and T2 maps.

Wilcoxon rank sum test analysis of ST and PW regions of GBMs versus METs showed differences between multiple histogram parameters for T1 and T2 only before Bonferroni correction (Table 2). Analysis of ST regions of GBMs versus LGGs showed no significant difference in nearly all T1 and T2 parameters (except T2 skewness). There were, however, several differences between

Table 2: Mean ± standard deviation of mean, SD, skewness, and kurtosis of T1 and T2 from various tumor regions and contralateral white matter in 3 tumor types with results from the Wilcoxon rank sum test[a] and the Wilcoxon signed rank test[b]

ROI	Parameter	Tissue Type[a]			All Tissue Types Combined (n = 31)[b]
		GBM (n = 17)[c]	Metastasis (n = 8)[c]	LGG (n = 6)	
ST	Mean	1639 ± 247 (v MET $P \leq .05$)	1324 ± 273 (v LGG $P \leq .05$)	1600 ± 197	1558 ± 271 (v CW $P < .0063$)[d]
T1	SD	133 ± 50	116 ± 63	120 ± 26	126 ± 49 (v CW $P < .0063$)[d]
	Skewness	0.01 ± 0.66	0.38 ± 0.56	0.16 ± 0.52	0.12 ± 0.61
	Kurtosis	3.06 ± 0.96	3.23 ± 0.58	3.26 ± 1.11	3.14 ± 0.90
ST	Mean	138 ± 22 (v MET $P \leq .05$)	105 ± 27 (v LGG $P < .0042$)[d]	172 ± 53	137 ± 37 (v CW $P < .0063$)[d]
T2	SD	21 ± 9	17 ± 9	22 ± 12	20 ± 9 (v CW $P < .0063$)[d]
	Skewness	0.77 ± 1.43 (v LGG $P \leq .05$)	0.67 ± 0.97	−0.28 ± 0.68	0.54 ± 1.25
	Kurtosis	6.38 ± 8.61	5.49 ± 6.54	2.88 ± 0.61	5.47 ± 7.19
PW	Mean	1578 ± 331 (v LGG $P < .0042$)[d]	1382 ± 188 (v LGG $P \leq .05$)	1066 ± 218	1429 ± 338 (v CW $P < .0063$)[d]
T1	SD	124 ± 59 (v LGG, MET $P \leq .05$)	75 ± 27	73 ± 15	101 ± 52 (v CW $P < .0063$)[d]
	Skewness	−0.06 ± 0.44 (v LGG $P \leq .05$)	−0.10 ± 0.39 (v LGG $P \leq .05$)	0.54 ± 0.56	0.04 ± 0.50
	Kurtosis	2.73 ± 0.81	2.84 ± 0.53	3.12 ± 0.97	2.83 ± 0.77 (v CW $P \leq .05$)
PW	Mean	140 ± 27 (v LGG $P \leq .05$)	119 ± 27 (v LGG $P \leq .05$)	102 ± 43	127 ± 33 (v CW $P < .0063$)
T2	SD	17 ± 7 (v LGG, MET $P \leq .05$)	12 ± 7	10 ± 3	14 ± 7 (v CW $P < .0063$)
	Skewness	0.39 ± 1.51 (v LGG $P \leq .05$)	0.39 ± 0.85 (v LGG $P \leq .05$)	0.71 ± 0.53	0.45 ± 1.20
	Kurtosis	5.68 ± 11.82	4.99 ± 2.84	3.45 ± 1.40	5.07 ± 8.80
CW	Mean	927 ± 133	911 ± 39	873 ± 61	912 ± 104
T1	SD	40 ± 11	44 ± 12	36 ± 10	40 ± 11
	Skewness	0.27 ± 0.51	0.45 ± 0.55	0.13 ± 0.69	0.29 ± 0.55
	Kurtosis	3.22 ± 1.13	3.09 ± 0.57	3.54 ± 1.32	3.25 ± 1.04
CW	Mean	69 ± 9	72 ± 6	72 ± 17	70 ± 11
T2	SD	5 ± 2	5 ± 1	6 ± 3	5 ± 2
	Skewness	0.20 ± 1.60	0.27 ± 0.95	0.58 ± 0.95	0.31 ± 1.33
	Kurtosis	4.85 ± 7.07	3.96 ± 2.07	3.82 ± 1.73	4.41 ± 5.32

Note:—v indicates versus (when compared to).

[a] When comparing tumor types by rank sum tests, P values $< .0042$ (0.05/12) were statistically significant after Bonferroni correction. P values labeled as $P \leq .05$ have unadjusted P values $\leq .05$ but are not statistically significant after Bonferroni correction.

[b] When comparing tumor tissue vs CW by signed rank tests, P values $< .0063$ (0.05/8) were statistically significant after Bonferroni correction.

[c] For solid tumor analysis for GBMs (n = 16) and for METs (n = 7) (see "ROI Analysis" in "Materials and Methods" for further details).

[d] P value statistically significant after Bonferroni correction.

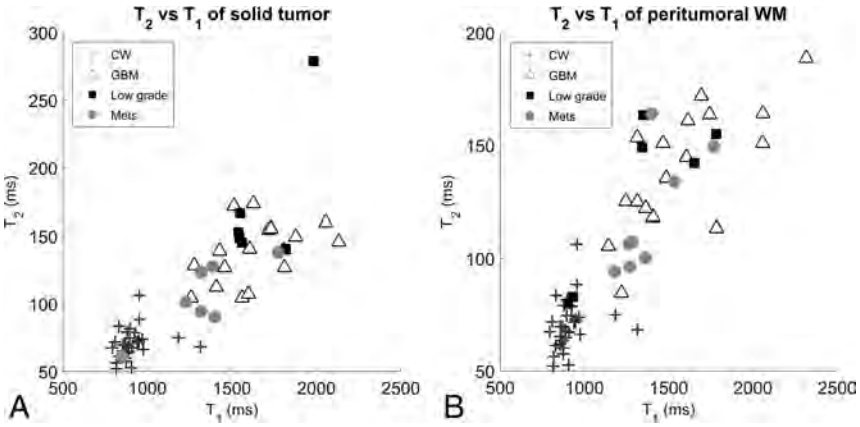

FIG 2. Scatterplot of T1-versus-T2 measurements in all tumor types for the solid tumor region (*A*) and the peritumoral white matter region (*B*).

GBMs and LGGs when T1 and T2 parameters of peritumoral white matter were compared, with differences in mean T1 remaining significant even after Bonferroni correction. Lastly, several ST and PW region parameters were significantly different between LGGs and METs, with differences in the mean T2 of ST remaining significant even after Bonferroni correction.

On the basis of a stepwise selection model for multiple logistic regressions to differentiate between GBMs and METs, the best differentiation was obtained by using the single-predictor mean T2 relaxometry of the ST region. With this parameter, the area under the ROC curve was 0.86 (95% CI. 0.69–1.00) with a P value $< .0001$. When added individually to the model with a mean T2 from the ST region, none of the other parameters significantly improved the ability of the model to discriminate GBMs and METs.

Interobserver Concordance

The Pearson correlation coefficients for T1 and T2 of the ST region were 0.90 and 0.83, respectively, and the Pearson correlation coefficients for T1 and T2 of the PW region were 0.88 and 0.91, respectively. According to the guidelines for clinical significance, intraclass correlation coefficients for all measures (ST T1, ST T2, PW T1, and PW T2) were excellent (intraclass correlation coefficients = 0.90, 0.83, 0.88, and 0.89, respectively).[18]

DISCUSSION

This study describes the application of MRF in quantifying tissue relaxation times in primary glial and metastatic brain tumors. MRF can identify quantifiable relaxometry differences between solid tumor regions of lower grade gliomas and metastatic brain lesions. MRF relaxometry also identifies significant differences in the peritumoral region of GBMs compared with LGGs.

A variety of advanced imaging techniques, including perfusion imaging, DTI, MR spectroscopy, and molecular imaging such as positron emission tomography, have been used for advanced brain tumor evaluation during the past decade with mixed success.[7-14] In particular, perfusion imaging has been shown to have utility in differentiating metastases from GBMs and in differentiating various glioma grades.[8,11] DTI has shown promising results for tumor margin delineation and identification of tumor infiltration.[12,14] PET imaging with FDG has been modestly successful in differentiating glioma grades but remains limited in utility because of a lack of specificity and significant background uptake.[19,20] Molecular imaging with newer PET agents holds significant promise; however, it needs further evaluation with larger scale studies.[20-22] Despite all these advances, no single neuroimaging technique has emerged that can be easily, reliably, and consistently used in a day-to-day setting to differentiate intra-axial brain tumors on the basis of both their origin and histopathologic grading. The problem of tissue discrimination is even more challenging in a posttherapy setting in which there is the possibility of pesudoprogression, pseudoresponse, and development of radiation necrosis.[23,24] Although a combination of these sophisticated neuroimaging techniques along with conventional MR imaging can improve different aspects of brain tumor diagnostics, they involve significant financial and time limitations and technical challenges.[23-25]

MRF is a new technique that provides multiparametric quantitative information in an ultrafast single acquisition, which can be easily performed in the framework of a present day clinical setup.[15-17] Recent studies have looked into improving on the MRF acquisition parameters to make them more robust, improving the reconstruction algorithms, and acquiring newer quantitative parameters from this technique.[26-28] Given its multiparametric capabilities and repeatability, this technique has the capability of becoming a useful MR imaging biomarker.[29,30] Although the clinical applications and utility of this technique have not been assessed so far, the in vivo quantitation data in healthy volunteers and patients are emerging.[31-33]

Differentiation between GBM and solitary metastasis by using conventional imaging can be challenging due to several overlapping imaging characteristics, and surgical sampling is frequently necessary for the final diagnosis. While the history of previous malignancy and the multiplicity of lesions is usually a reliable indicator of brain metastases, recent studies suggest that about 14% of all patients with brain metastases have an unknown primary malignancy and up to 46% of patients present with a single brain metastasis.[2,3] Conversely, by using modern MR imaging techniques, nearly 35% of patients with newly diagnosed GBM have multiple enhancing lesions, significantly higher than previous estimates, which ranged from 0.5% to 20%.[34] Early differentiation of primary and metastatic malignant brain tumors is essential for prompt, appropriate, and cost-efficient diagnosis and treatment; coordination of multidisciplinary care; and assessment for clinical trials.[3,4] Our results demonstrate that MRF-derived relaxometry may be useful in differentiating solid tumor regions of lower grade gliomas and metastases.

While the differences between solid tumor regions of GBMs and metastases neared significance, there were no significant differences between ST regions of LGGs and GBMs. T1 and T2 values of tissue depend on local cellularity, water content, structural organization, and the presence and concentration of lipids, proteins, macromolecules, and paramagnetic substances.[35] The relaxometry differences between ST regions of LGGs and METs probably reflect differences based on the distinct tissue of origin in the 2 groups and a higher concentration of certain lipids and macromolecules in glial lesions.[9,36] Lack of demonstrable T1 and T2 differences between solid tumor regions of LGGs and GBMs also suggests that these values are probably driven by the type of cellularity and tissue of origin; and given the common glial origin, it may be difficult to differentiate different grades of gliomas. The role of lineage cannot be assessed in this study given the lack of subjects with pure astrocytoma pathology of a single grade. The subtle differences in skewness of T2 between GBMs and LGGs could potentially be a reflection of higher cellular density, anaplasia, or microvascular proliferation in GBMs compared with LGGs.[37-39] Although the observed differences in T1 and T2 relaxation times of different tumor types are not entirely unexpected on the basis of our knowledge of qualitative images, being able to evaluate these differences quantitatively may be of potential benefit not only in the diagnosis and grading of brain tumors but also for other purposes such as treatment planning, monitoring therapy, and recurrence assessment.

Several pathologic and imaging studies have shown that the peritumoral white matter of glial tumors and METs differs in cellular and molecular content.[35-39] Metastatic lesions have little evidence of histologic invasion and are primarily surrounded by vasogenic edema beyond the contrast-enhancing margins. Conversely, the FLAIR signal abnormality beyond the enhancing margins in gliomas, particularly GBMs, contains infiltrative cells mixed with vasogenic edema.[13,40-44] The presence of neoplastic cells has also been identified in peritumoral regions as far as 2.5 cm from the enhancing tumor margin in white matter regions without any corresponding signal abnormality on T2-weighted images.[14,40] Thus, CT and conventional MR imaging are not helpful in establishing tumor margins in gliomas in general and GBMs in particular. In our study, the ROIs in the peritumoral white matter were drawn to encompass white matter located within 1 cm of the enhancing margin/expansile FLAIR margin of the tumor. With this method, differentiation between ST and PW regions of FLAIR hyperintense tumors is particularly challenging. The T1 difference between the PW of GBMs and LGGs could potentially be influenced by the ROI technique used in this study. Further work with a larger sample size and perhaps an automated ROI delineation technique will be useful to verify whether discrepant tissue characteristics can indeed be reflected in measurable T1 differences. Analysis of PW in our study also reveals some additional subtle trends alluding to the heterogeneity of PW in GBM compared with METs and LGGs, with nonsignificant differences in SD and skewness. Carefully designed larger sample size

prospective studies with 3D volumetric MRF acquisition and targeted histologic correlation are necessary to identify quantifiable differences in PW of various tumor types and to better understand the exact histopathologic correlates of these findings.

Several studies have used MR relaxometry for brain tumor diagnosis in the past with mixed success.[45-51] Recently, there has been renewed interest in evaluating the role of relaxometry in the assessment of nonenhancing tumor burden and response to antiangiogenic drug therapy.[52-55] Although most of these recent studies focus on the role of T2 relaxometry, a recent study has demonstrated that T1 mapping may play a significant role in earlier detection of recurrent tumor in patients on antiangiogenic therapy. MRF differs from the methodology used in these studies in a few respects. MRF is a rapid imaging technique that allows simultaneous T1 and T2 measurements from a single acquisition in <30 seconds. The initial phantom studies have demonstrated better accuracy and efficiency compared with standard T1 and T2 measurement techniques.[7] A recent article demonstrated the in vivo sensitivity of MRF in identifying aging-related changes in asymptomatic volunteers.[32] The newer FISP-based sequence is less susceptible to field inhomogeneities compared with the True FISP–based acquisition used in this study and could serve as a robust quantitation tool for future studies.[16,17] Development of a rapid 3D MRF technique has opened avenues for whole-brain coverage with near-isotropic spatial resolution with the potential for applications in tumor imaging and beyond.[56]

There are some limitations to this proof-of-concept study, including the small sample size, heterogeneity of the study population and tumor type, and lack of correlation of the imaging findings with genomic and molecular markers. The authors acknowledge that given the small sample size, even a few outliers could influence the study outcome significantly; therefore, it is difficult to draw any definite conclusions from these results. Further validation with an appropriately powered larger sample study and perhaps with automated tumor-segmentation technique with whole-brain volumetric data will ensure that the results are generalizable and robust. A well-designed prospective study with adequate power will allow the examination of multivariable models to distinguish tissues of origin on the basis of MRF distributional parameters. The role of MRF in differentiating the various potential tissues of origin in brain metastases also warrants further exploration. If additional studies validate and improve on our results, MRF may have a role in the imaging evaluation of brain tumors.

CONCLUSIONS

This study demonstrates the application of MR fingerprinting in the quantitative evaluation of glioblastomas, metastases, and lower grade gliomas, in which MRF-based relaxometry can identify quantitative differences between solid tumor regions of lower grade gliomas and metastases and between peritumoral regions of glioblastomas and lower grade gliomas. MRF offers the capability of rapidly generating quantitative relaxometry maps of brain tumors in a clinical setting. The utility of this technique needs to be further explored in larger sample studies.

Disclosures: Dan Ma—*RELATED*: *Grant*: National Institutes of Health.* Shivani Pahwa—*RELATED*: *Grant*: Siemens Healthcare, *Comments*: research support from Siemens.* Mark Schluchter—*RELATED*: *Grant*: National Institutes of Health.* Jeffrey Sunshine—*RELATED*: *Grant*: Siemens, *Comments*: sponsored research grant*; *UNRELATED*: *Patents (Planned, Pending, or Issued)*: Siemens and Case Western Reserve University, *Comments*: MRI technical patents not covering this article.* Mark Griswold—*RELATED*: *Grant*: Siemens*; *UNRELATED*: *Grants/Grants Pending*: Siemens*; *Patents (Planned, Pending, or Issued)*: Siemens, GE Healthcare, Bruker. Vikas Gulani—*RELATED*: *Grant:* National Institutes of Health, Siemens, *Comments*: Case Western Reserve University and University Hospitals receive research support from the National Institutes of Health and Siemens*; *Support for Travel to Meetings for the Study or Other Purposes*: National Institutes of Health, Siemens, *UNRELATED*: *Grants/Grants Pending*: National Institutes of Health, *Comments*: multiple additional National Institutes of Health grants*; *Patents (Planned, Pending, or Issued)*: Siemens.* *Money paid to the institution.

REFERENCES

1. Thakkar JP, Dolecek TA, Horbinski C, et al. **Epidemiologic and molecular prognostic review of glioblastoma.** *Cancer Epidemiol Biomarkers Prev* 2014;23:1985–96 CrossRef Medline
2. Ostrom QT, Gittleman H, Liao P, et al. **CBTRUS statistical report: primary brain and central nervous system tumors diagnosed in the United States in 2007–2011.** *Neuro Oncol* 2014;16(suppl 4):iv1–63 CrossRef Medline
3. Nayak L, Lee EQ, Wen PY. **Epidemiology of brain metastases.** *Curr Oncol Rep* 2012;14:48–54 CrossRef Medline
4. Sperduto PW, Chao ST, Sneed PK, et al. **Diagnosis-specific prognostic factors, indexes, and treatment outcomes for patients with newly diagnosed brain metastases: a multi-institutional analysis of 4,259 patients.** *Int J Radiat Oncol Biol Phys* 2010;77:655–61 CrossRef Medline
5. Giese A, Bjerkvig R, Berens ME, et al. **Cost of migration: invasion of malignant gliomas and implications for treatment.** *J Clin Oncol* 2003;21:1624–36 CrossRef Medline
6. Smith C, Ironside JW. **Diagnosis and pathogenesis of gliomas.** *Current Diagnostic Pathology* 2007;13:180–92 CrossRef
7. Bulakbasi N, Kocaoglu M, Ors F, et al. **Combination of single-voxel proton MR spectroscopy and apparent diffusion coefficient calculation in the evaluation of common brain tumors.** *AJNR Am J Neuroradiol* 2003;24:225–33 Medline
8. Cha S, Lupo JM, Chen MH, et al. **Differentiation of glioblastoma multiforme and single brain metastasis by peak height and percentage of signal intensity recovery derived from dynamic susceptibility-weighted contrast-enhanced perfusion MR imaging.** *AJNR Am J Neuroradiol* 2007;28:1078–84 CrossRef Medline
9. Crisi G, Orsingher L, Filice S. **Lipid and macromolecules quantitation in differentiating glioblastoma from solitary metastasis: a short-echo time single-voxel magnetic resonance spectroscopy study at 3 T.** *J Comput Assist Tomogr* 2013;37:265–71 CrossRef Medline
10. Fan G, Sun B, Wu Z, et al. **In vivo single-voxel proton MR spectroscopy in the differentiation of high-grade gliomas and solitary metastases.** *Clin Radiol* 2004;59:77–85 CrossRef Medline
11. Halshtok Neiman O, Sadetzki S, Chetrit A, et al. **Perfusion-weighted imaging of peritumoral edema can aid in the differential diagnosis of glioblastoma mulltiforme versus brain metastasis.** *Isr Med Assoc J* 2013;15:103–05 Medline
12. Kinoshita M, Goto T, Okita Y, et al. **Diffusion tensor-based tumor infiltration index cannot discriminate vasogenic edema from tumor-infiltrated edema.** *J Neurooncol* 2010;96:409–15 CrossRef Medline
13. Min ZG, Niu C, Rana N, et al. **Differentiation of pure vasogenic edema and tumor-infiltrated edema in patients with peritumoral edema by analyzing the relationship of axial and radial diffusivities on 3.0T MRI.** *Clin Neurol Neurosurg* 2013;115:1366–70 CrossRef Medline
14. Price SJ, Jena R, Burnet NG, et al. **Improved delineation of glioma margins and regions of infiltration with the use of diffusion tensor imaging: an image-guided biopsy study.** *AJNR Am J Neuroradiol* 2006;27:1969–74 Medline
15. Ma D, Gulani V, Seiberlich N, et al. **Magnetic resonance fingerprinting.** *Nature* 2013;495:187–92 CrossRef Medline
16. Jiang Y, Ma D, Seiberlich N, et al. **MR fingerprinting using fast imaging with steady state precession (FISP) with spiral readout.** *Magn Reson Med* 2015;74:1621–31 CrossRef Medline
17. Chen Y, Jiang Y, Pahwa S, et al. **MR fingerprinting for rapid quanti-**

tative abdominal imaging. *Radiology* 2016;279:278–86 CrossRef Medline
18. Cicchetti DV. **Guidelines, criteria, and rules of thumb for evaluating normed and standardized assessment instruments in psychology.** *Psychol Assess* 1994;6:284–90 CrossRef
19. Wong TZ, Van der Westhuizen GJ, Coleman RE. **Positron emission tomography imaging of brain tumors.** *Neuroimaging Clin of N Am* 2002;12:615–26 CrossRef Medline
20. Pauleit D, Stoffels G, Bachofner A, et al. **Comparison of 18 F-FET and 18 F-FDG PET in brain tumors.** *Nuclear Med Biol* 2009;36:779–87 CrossRef Medline
21. Becherer A, Karanikas G, Szabó M, et al. **Brain tumor imaging with PET: a comparison between [18F] fluorodopa and [11C] methionine.** *Eur J Nucl Med Mol Imaging* 2003;30:1561–67 CrossRef Medline
22. Kamson DO, Juhász C, Buth A, et al. **Tryptophan PET in pretreatment delineation of newly-diagnosed gliomas: MRI and histopathologic correlates.** *J Neurooncol* 2013;112:121–32 CrossRef Medline
23. Clarke JL, Chang S. **Pseudoprogression and pseudoresponse: challenges in brain tumor imaging.** *Cur Neurol Neurosci Rep* 2009;9:241–46 CrossRef Medline
24. Henson JW, Ulmer S, Harris GJ. **Brain tumor imaging in clinical trials.** *AJNR Am J Neuroradiol* 2008;29:419–24 CrossRef Medline
25. Gempt J, Soehngen E, Förster S, et al. **Multimodal imaging in cerebral gliomas and its neuropathological correlation.** *Eur J Radiol* 2014;83:829–34 CrossRef Medline
26. Zhao B, Setsompop K, Ye H, et al. **Maximum likelihood reconstruction for magnetic resonance fingerprinting.** *IEEE Trans Med Imaging* 2016;35:1812–23 CrossRef Medline
27. Assländer J, Glaser SJ, Hennig J. **Pseudo steady-state free precession for MR-fingerprinting.** *Magn Reson Med* 2016 Apr 15. [Epub ahead of print] CrossRef Medline
28. Buonincontri G, Sawiak SJ. **MR fingerprinting with simultaneous B1 estimation.** *Magn Reson Med* 2016;76:1127–35 CrossRef Medline
29. European Society of Radiology (ESR). **Magnetic resonance fingerprinting: a promising new approach to obtain standardized imaging biomarkers from MRI.** *Insights Imaging* 2015;6:163–65 CrossRef Medline
30. Jiang Y, Ma D, Keenan KE, et al. **Repeatability of magnetic resonance fingerprinting T1 and T2 estimates assessed using the ISMRM/NIST MRI system phantom.** *Magn Reson Med* 2016 Oct 27. [Epub ahead of print] CrossRef Medline
31. Hamilton JI, Jiang Y, Chen Y, et al. **MR fingerprinting for rapid quantification of myocardial T1, T2, and proton spin density.** *Magn Reson Med* 2016 Apr 1. [Epub ahead of print] CrossRef Medline
32. Badve C, Yu A, Rogers M, et al. **Simultaneous T1 and T2 brain relaxometry in asymptomatic volunteers using magnetic resonance fingerprinting.** *Tomography* 2015;1:136–44 CrossRef Medline
33. Cloos MA, Alon L, Geppert C, et al. **Rapid T1 and T2 mapping of the hip articular cartilage with radial MR fingerprinting.** In: *Proceedings of the Annual Meeting and Exhibition* of the *International Society for Magnetic Resonance in Medicine,* Toronto, Ontario, Canada. May 30 to June 5, 2015; Scientific Session: Cartilage Imaging (0113).
34. Thomas RP, Xu LW, Lober RM, et al. **The incidence and significance of multiple lesions in glioblastoma.** *J Neurooncol* 2013;112:91–97 CrossRef Medline
35. Deoni SC. **Quantitative relaxometry of the brain.** *Top Magn Reson Imaging* 2010;21:101–13 CrossRef Medline
36. Opstad KS, Murphy MM, Wilkins PR, et al. **Differentiation of metastases from high-grade gliomas using short echo time 1H spectroscopy.** *J Magn Reson Imaging* 2004;20:187–92 CrossRef Medline
37. Maher EA, Furnari FB, Bachoo RM, et al. **Malignant glioma: genetics and biology of a grave matter.** *Genes Dev* 2001;15:1311–33 CrossRef Medline
38. Louis DN, Ohgaki H, Wiestler OD, et al. **The 2007 WHO classification of tumours of the central nervous system.** *Acta Neuropathol* 2007;114:97–109 Medline
39. Ma L, Song ZJ. **Differentiation between low-grade and high-grade glioma using combined diffusion tensor imaging metrics.** *Clin Neurol Neurosurg* 2013;115:2489–95 CrossRef Medline
40. Kelly PJ, Daumas-Duport C, Kispert DB, et al. **Imaging-based stereotaxic serial biopsies in untreated intracranial glial neoplasms.** *J Neurosurg* 1987;66:865–74 CrossRef Medline
41. Palfi S, Swanson KR, De Boüard S, et al. **Correlation of in vitro infiltration with glioma histological type in organotypic brain slices.** *Br J Cancer* 2004;91:745–52 Medline
42. Deng Z, Yan Y, Zhong D, et al. **Quantitative analysis of glioma cell invasion by diffusion tensor imaging.** *J Clin Neurosci* 2010;17:1530–36 CrossRef Medline
43. Wang W, Steward CE, Desmond PM. **Diffusion tensor imaging in glioblastoma multiforme and brain metastases: the role of p, q, L, and fractional anisotropy.** *AJNR Am J Neuroradiol* 2009;30:203–08 Medline
44. Watanabe M, Tanaka R, Takeda N. **Magnetic resonance imaging and histopathology of cerebral gliomas.** *Neuroradiology* 1992;34:463–69 CrossRef Medline
45. Wagnerova D, Herynek V, Malucelli A, et al. **Quantitative MR imaging and spectroscopy of brain tumours: a step forward?** *Eur Radiol* 2012;22:2307–18 CrossRef Medline
46. Damadian R. **Tumor detection by nuclear magnetic resonance.** *Science* 1971;171:1151–53 CrossRef Medline
47. Araki T, Inouye T, Suzuki H, et al. **Magnetic resonance imaging of brain tumors: measurement of T1—work in progress.** *Radiology* 1984;150:95–98 CrossRef Medline
48. Komiyama M, Yagura H, Baba M, et al. **MR imaging: possibility of tissue characterization of brain tumors using T1 and T2 values.** *AJNR Am J Neuroradiol* 1987;8:65–70 Medline
49. Just M, Thelen M. **Tissue characterization with T1, T2, and proton density values: results in 160 patients with brain tumors.** *Radiology* 1988;169:779–85 CrossRef Medline
50. Kjaer L, Thomsen C, Gjerris F, et al. **Tissue characterization of intracranial tumors by MR imaging. In vivo evaluation of T1- and T2-relaxation behavior at 1.5 T.** *Acta Radiol* 1991;32:498–504 CrossRef Medline
51. Newman S, Haughton V, Yetkin Z, et al. **T1, T2 and proton density measurements in the grading of cerebral gliomas.** *Eur Radiol* 1993;3:49–52
52. Ellingson BM, Cloughesy TF, Lai A, et al. **Quantification of edema reduction using differential quantitative T2 (DQT2) relaxometry mapping in recurrent glioblastoma treated with bevacizumab.** *J Neurooncol* 2012;106:111–19 CrossRef Medline
53. Lescher S, Jurcoane A, Veit A, et al. **Quantitative T1 and T2 mapping in recurrent glioblastomas under bevacizumab: earlier detection of tumor progression compared to conventional MRI.** *Neuroradiology* 2015;57:11–20 CrossRef Medline
54. Hattingen E, Jurcoane A, Daneshvar K, et al. **Quantitative T2 mapping of recurrent glioblastoma under bevacizumab improves monitoring for non-enhancing tumor progression and predicts overall survival.** *Neuro Oncol* 2013;15:1395–404 CrossRef Medline
55. Ellingson BM, Lai A, Nguyen HN, et al. **Quantification of nonenhancing tumor burden in gliomas using effective T2 maps derived from dual-echo turbo spin-echo MRI.** *Clin Cancer Res* 2015;21:4373–83 CrossRef Medline
56. Ma D, Hamilton J, Jiang Y, et al. **Fast 3D magnetic resonance fingerprinting (MRF) for whole brain coverage in less than 3 minutes.** In: *Proceedings of the Annual Meeting and Exhibition of the International Society for Magnetic Resonance in Medicine,* Singapore. May 7–13, 2016; Electronic Poster Session: Acquisition, Reconstruction and Analysis 1 (3180)

Lower Magnetization Transfer Ratio in the Forceps Minor Is Associated with Poorer Gait Velocity in Older Adults

S. Seiler, L. Pirpamer, B. Gesierich, E. Hofer, M. Duering, D. Pinter, E. Jouvent, F. Fazekas, J.-F. Mangin, H. Chabriat, S. Ropele, and R. Schmidt

ABSTRACT

BACKGROUND AND PURPOSE: Gait disturbances in the elderly are disabling and a major public health issue but are poorly understood. In this multimodal MR imaging study, we used 2 voxel-based analysis methods to assess the voxelwise relationship of magnetization transfer ratio and white matter hyperintensity location with gait velocity in older adults.

MATERIALS AND METHODS: We assessed 230 community-dwelling participants of the Austrian Stroke Prevention Family Study. Every participant underwent 3T MR imaging, including magnetization transfer imaging. Voxel-based magnetization transfer ratio–symptom mapping correlated the white matter magnetization transfer ratio of each voxel with gait velocity. To assess a possible relationship between white matter hyperintensity location and gait velocity, we applied voxel-based lesion-symptom mapping.

RESULTS: We found a significant association between the magnetization transfer ratio within the forceps minor and gait velocity (β = 0.134; 95% CI, 0.011–0.258; P = .033), independent of demographics, general physical performance, vascular risk factors, and brain volume. White matter hyperintensities did not significantly change this association.

CONCLUSIONS: Our study provides new evidence for the importance of magnetization transfer ratio changes in gait disturbances at an older age, particularly in the forceps minor. The histopathologic basis of these findings is yet to be determined.

ABBREVIATIONS: MNI = Montreal Neurological Institute; MTI = magnetization transfer imaging; MTR = magnetization transfer ratio; SPPB = Short Physical Performance Battery; VLSM = voxel-based lesion symptom mapping; VMTRSM = voxel-based MTR symptom mapping; WMH = white matter hyperintensity

Gait abnormalities in older adults are common.[1,2] They are associated with falls[3,4] and represent a serious public health issue.[1,5] A complex brain network manages supraspinal gait control.[6] White matter hyperintensities (WMHs) are common and not necessarily related to clinical symptoms. However on a group level, widespread WMHs have been associated with gait dysfunction, probably as the consequence of disruption of the supraspinal gait network,[7-9] and were related to gait performance in several studies,[10-13] but results are conflicting.[9,14,15] One explanation for conflicting results might be that as reported for cognitive decline,[16-18] widespread, invisible, and highly variable microstructural changes in normal-appearing white matter also contribute to gait abnormalities in addition to visible lesions. This hypothesis is supported by 2 DTI studies that reported the higher mean diffusivity and lower fractional anisotropy in the genu of the corpus callosum to be correlated with poorer gait performance independent of visible WMHs.[14,19]

Complementary information on microstructural brain tissue alterations may come from magnetization transfer imaging (MTI). Other than DTI, which offers information on brain tissue organization,[20] MTI offers information on tissue composition.[21] Magnetization transfer ratio (MTR) is one of the few MR imaging measures that have been validated postmortem to represent a direct marker of myelin content.[22]

The only study on MTR and gait found that lower MTR was associated with poorer gait performance, independent of WMHs.[23]

Received May 8, 2016; accepted after revision October 12.

From the Department of Neurology (S.S., L.P., E.H., D.P., F.F., S.R., R.S.) and Institute of Medical Informatics, Statistics and Documentation (E.H.), Medical University of Graz, Graz, Austria; Institute for Stroke and Dementia Research (B.G., M.D.), Klinikum der Universität München, Ludwig-Maximilians-University, Munich, Germany; Department of Neurology (E.J., H.C.), Institut National de la Santé et de la Recherche Médicale, UMR-740, Centre Hospitalo-Universitaire Lariboisière, Paris, France; and Neurospin (J.-F.M.), Commissariat à l'Energie Atomique et aux Energies Alternatives Saclay, Gif/Yvette, France.

This work was supported by the FP6 ERA-NET NEURON grant (01 EW1207/Mechanisms of Small Vessel Related Brain Damage and Cognitive Impairment) and by the Austrian Science Fund project I904.

Parts of the data were presented at the Annual Meeting of the Austrian Alzheimer Society, October 24–25, 2014; Villach, Austria.

Please address correspondence to Reinhold Schmidt, MD, Department of Neurology, Clinical Division of Neurogeriatrics, Medical University Graz, Auenbruggerplatz 22, A-8036 Graz, Austria; e-mail: reinhold.schmidt@medunigraz.at

Indicates open access to non-subscribers at www.ajnr.org

Indicates article with supplemental on-line table.

http://dx.doi.org/10.3174/ajnr.A5036

In this large multimodal MR imaging study, we used voxel-based MTR symptom mapping (VMTRSM) and voxel-based lesion symptom mapping (VLSM) to identify those brain areas in which MTR or WMH-related tissue alterations relate to gait velocity. We hypothesized that alterations, if any, would mainly be located within the frontal white matter because intact fontal subcortical pathways have been reported to be crucial for maintenance of gait performance at a higher level.[6,24]

MATERIALS AND METHODS

Study Subjects

The study sample is drawn from the Austrian Stroke Prevention Family Study, a prospective single-center community-based study designed to assess the cerebral effects of vascular risk factors in the healthy elderly population of the City of Graz, Austria. The Austrian Stroke Prevention Family Study represents an extension of the Austrian Stroke Prevention Study, which was established in 1991.[25] Between 2006 and 2013, study participants of the Austrian Stroke Prevention Study and their first-degree relatives were invited to enter the Austrian Stroke Prevention Family Study. Individuals were excluded from the study if they had a history of neuropsychiatric disease, including previous cerebrovascular attacks and dementia, or abnormal neurologic examination findings, determined on the basis of a structured clinical interview and a physical and neurologic examination performed by a board-certified neurologist. None of the study participants had a history or MR imaging findings suggestive of normal pressure hydrocephalus. There were also no subjects with a history or signs of heart failure in the study. None of the study participants had uncorrected visual impairment. A total of 381 individuals from 169 families were included in the study. The number of members per family ranged from 2 to 6. All individuals underwent MR imaging, except for 26 who had contraindications. Thus, MTI scans were available in 355 subjects. The participants' ages ranged from 35 to 82 years. We focused on age-related decline in gait velocity and thus included all 230 subjects 60 years of age and older in the current analysis.

The ethics committee of the Medical University of Graz, Austria, approved the study protocol, and written informed consent was obtained from all subjects.

Measurement of Gait Velocity

Study participants were asked to walk a total distance of 8 meters with 3 turns at their usual, self-selected pace on level ground. None of the study participants needed walking aids. Time was measured with a stopwatch. The faster of the 2 trials was used for the subsequent analyses. We chose gait velocity because it can be measured quickly and in a clinical setting without instrumental efforts. It has been shown to be a good measure of mobility in elderly individuals.[15]

Measurement of Cognition and General Physical Performance

Scores of memory and executive function were assessed as described previously.[26]

General physical performance was assessed by using the Short Physical Performance Battery (SPPB).[27]

Vascular Risk Factors

Assessment of vascular risk factors included arterial hypertension, diabetes mellitus, hypercholesterolemia, hypertriglyceridemia, hyperuricemia, cardiac disease, peripheral vascular disease, and venous thrombotic disease and was determined on the basis of history and measurements at the examination as previously described.[26]

MR Imaging

MR imaging was performed on a 3T whole-body scanner (Magnetom TrioTim; Siemens, Erlangen, Germany) and included conventional imaging and MTI. The MTI sequence was based on a spoiled 3D gradient-echo sequence (TR = 40 ms, TE = 7.38 ms, flip angle = 15°, number of sections = 40, section thickness = 3 mm, in-plane resolution = 0.86 × 0.86 mm) performed with and without a Gaussian-shaped magnetization transfer saturation pulse.

The conventional protocol included an axial FLAIR sequence (TR = 1000 ms, TE = 69 ms, TI = 2500 ms, number of sections = 40, section thickness = 3 mm, no intersection-gap, in-plane resolution = 0.86 × 0.86 mm^2) and a high-resolution T1-weighted 3D sequence with magnetization preparation and whole-brain coverage (TR = 1900 ms, TE = 2.19 ms, TI = 900 ms, flip angle = 9°, isotropic resolution = 1 mm).

For assessment of microbleeds, a T2* sequence was used (TR = 35 ms, TE = 14.7 ms, flip angle = 15°, number of sections = 64, section thickness = 2 mm, no intersection-gap, in-plane resolution = 0.90 × 0.90 mm^2).

Visual MR Imaging Rating

White matter hyperintensities and silent nonlacunar and lacunar infarcts were recorded on FLAIR images as previously described.[26] Microbleeds were recorded on T2*-weighted images following the definition of Greenberg et al.[28]

Generation of WMH and MTR Maps

WMH maps were generated by using a custom-written Interactive Data Language program (DispImage; Exelis Visual Information Solutions, Boulder, Colorado) as described previously.[29] Two highly experienced raters segmented WMHs on FLAIR images by combined region-growing and local thresholding following manual selection.[29] The total lesion volume in cubic millimeters was calculated by multiplying the lesion area by the section thickness. WMH volumes in white matter tracts were calculated by overlaying the probabilistic white matter tract atlas (25% probability), provided within the Oxford Centre for fMRI of the Brain Software Library (FSL; http://www.fmrib.ox.ac.uk/fsl),[30] on the normalized WMH maps.

MTR maps were calculated according to the formula MTR = (M0 − MSS)/M0, where M0 represents the signal intensity of a voxel without any radiofrequency saturation and MSS is the signal intensity of the same voxel obtained with the radiofrequency saturation pulse.[21]

For the subsequent steps, tools from FSL[31] were used.

Because we found that MTR provides good contrast in performing tissue segmentation, gray matter, white matter, and CSF partial volume maps were derived from the MTR-weighted scans

by using FSL FAST (FMRIB Automated Segmentation Tool; http://fsl.fmrib.ox.ac.uk/fsl/fslwiki/FAST).[32]

The T1, FLAIR, and MTR-weighted scans were brain-extracted by using the FSL Brain Extraction Tool (http://fsl.fmrib.ox.ac.uk/fsl/fslwiki/BET).[33]

The resulting skull-stripped T1-weighted images were nonlinearly registered to the Montreal Neurological Institute-152 standard space template (MNI 152) by using FSL FNIRT (FMRIB Nonlinear Image Registration Tool; http://fsl.fmrib.ox.ac.uk/fsl/fslwiki/FNIRT).[31]

Then, the brain-extracted FLAIR and MTR scans were linearly registered to the corresponding brain-extracted T1-weighted images by using FLIRT (FMRIB Linear Image Registration Tool; http://www.fmrib.ox.ac.uk/).[34]

We used the transformation matrices from these steps to warp FLAIR and white matter MTR maps to the MNI-152 standard space template. WMH maps were transformed to the MNI-152 standard space template in the same way.

The resulting white matter MTR maps in standard space were eroded by 1 voxel to reduce partial volume effects resulting from "edge" voxels. To produce more normally distributed data, reduce noise, and account for the intersubject and registration variability,[35] we smoothed the MTR maps with a 4-mm Gaussian kernel.

A mean white matter MTR mask was created and thresholded to exclude MTR values below 20%.[17] We chose this threshold to exclude voxels from CSF and to further reduce the spurious effects of partial volume effects caused by the white matter–gray matter transition zone.

Anatomic structures containing clusters of voxels in which MTR related significantly to gait velocity were localized by overlaying the probabilistic white matter tract atlas (25% probability), provided within FSL,[30] on the normalized white matter MTR maps. As in voxelwise analysis, we eroded the segmentations of these tracts by 1 voxel to reduce CSF artifacts at "edge" zones. The resulting "core" white matter mean MTR was used in subsequent analyses.

Statistical Analysis

General Statistical Analysis. Assumptions of normal distribution were tested with the Kolmogorov-Smirnov test. Normally distributed variables are reported as mean ± SD, and non-normally distributed variables, as median and interquartile range. WMH volume had a skewed distribution containing zero values; therefore, the value 2 was added to the volumes before natural log-transformation. To relate demographic, clinical, and imaging characteristics of the study participants to gait velocity, we categorized subjects into quartiles according to gait velocity distribution. One-way analysis of variance, with quartiles of walking speed as fixed factors and demographic, clinical, and imaging characteristics as outcome variables, and χ^2 tests were performed to test significant associations with normally and non-normally distributed variables, respectively. Variables significantly ($P < .05$) associated with gait speed in these analyses were entered as covariates in the VMTRSM and ROI analyses described in the subsequent paragraphs. Correlations between MTR and gait velocity were calculated by using the Pearson correlation coefficient. Linear multiple regression analysis tested an independent relationship between MTR and gait velocity. To test a possible dose-effect relationship, we used analysis of covariance with MTR quartiles as fixed factors and walking speed as the dependent variable. Age, sex, height, brain volume, general physical performance, presence of vascular risk factors, and MR imaging findings significantly associated with walking speed in the univariate analysis were entered as covariates in the regression analysis and the ANCOVA.

To assess mediating effects of executive function scores on the relationship between MTR and gait velocity, we used bootstrapped models as described by Preacher and Hayes.[36]

Voxel-Based MTR Symptom Mapping. To find associations between MTR values within a voxel and gait velocity, we used the permutation-based statistical interference tool for nonparametric testing (FSL Randomize tool; http://fsl.fmrib.ox.ac.uk/fsl/fslwiki/Randomise/UserGuide).[31] Five thousand permutations were performed to build the null distribution, and significant associations were determined by selecting the threshold-free cluster-enhancement option. To correct for multiple comparisons, a family-wise error–adjusted P value $< .05$ was considered statistically significant because voxel-based analyses test thousands of voxels separately. If we controlled the family-wise error, the chance of ≥ 1 false-positive across all voxels was lower than 5%. Age, sex, height, brain volume, general physical performance, and variables that were univariatey associated with walking speed were entered as covariates.

ROI Analysis. To identify white matter tracts in which mean MTR correlates with gait velocity, we overlaid the probabilistic white matter tract atlas[30] provided within FSL on significant voxels from the VMTRSM analysis.

The mean MTR within identified tracts was calculated in standard space by using FSLMATHS (http://fsl.fmrib.ox.ac.uk/fsl/fslwiki/Fslutils). We eroded identified tracts by 1 voxel to reduce possible CSF contamination and partial volume effects from "edge" voxels. The mean MTR in the resulting "skeletonized" tracts was used in the subsequent linear multiple regression analysis.

A possible dose-effect relation of MTR within identified tracts and gait velocity was investigated by means of analysis of covariance with MTR in quartiles.

Age, sex, height, general physical performance, brain volume, and variables univariate-associated with walking speed were entered as covariates in the linear multiple regression analysis and the analysis of covariance. A P value $< .05$ was considered statistically significant.

Voxel-Based Lesion Symptom Mapping. Nonparametric mapping was used to relate WMH location to gait velocity.[37] One thousand permutations were performed to build the null distribution, and the Brunner-Munzel test was applied for statistical significance.[38] Briefly, permutation testing is a procedure that compares a test statistic to a null distribution derived from the dataset of interest itself. Permuting how the dependent and independent variables are paired typically derives the permutation null distribution. When the null hypothesis is true (no effect), the observed pairings should be no more likely to generate an extreme test statistic than any other.[39] Voxels affected in <7 subjects were not considered for analysis. Correction for multiple testing was

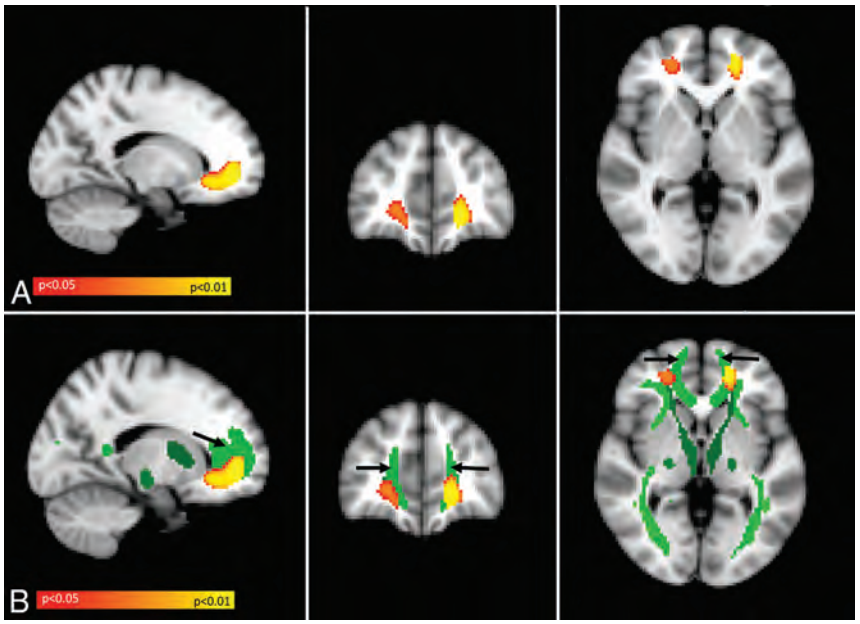

FIG 1. Result of voxel-based MTR symptom-mapping analysis. *A*, Yellow/orange represents MTR voxels positively related to gait velocity. The statistical map is superimposed on the MNI-152 standard space template and is family-wise error–corrected for multiple comparisons ($P < .05$). The result is independent of age, sex, height, the presence of microbleeds, SPPB total score, diabetes, hyperuricemia, and brain volume. *B*, The statistical map shown in *A* (MTR voxels positively related to gait velocity) is now superimposed on the Johns Hopkins University DTI-based white matter tract atlas. Shades of green indicate different white matter tracts, as defined by the atlas. Most of the MTR voxels positively related to gait velocity (yellow/orange) are located within the forceps minor (light green frontal tract, indicated by *black arrows*).

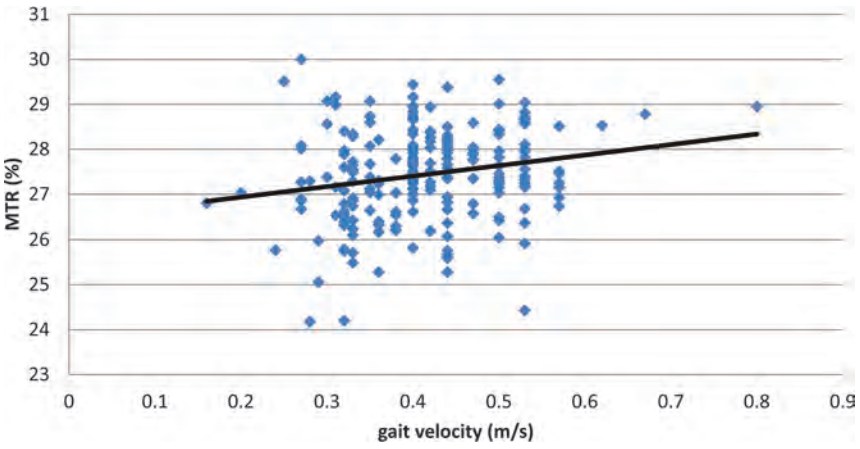

FIG 2. Correlation ($r = 0.20$; 95% CI, 0.08–0.32; $P = .002$) between walking speed (x-axis, meters/second) and MTR within the forceps minor (y-axis, percentage). *r* indicates the Pearson correlation coefficient.

achieved by permutation-generated family-wise error thresholds. Age, sex, height, and brain volume were entered as covariates. To identify the localization of significant voxels within major white matter tracts, we used the probabilistic white matter tract atlas[30] provided within FSL.

RESULTS

Characteristics of the Study Population

Demographic, clinical, and imaging characteristics of the study participants are summarized in the On-line Table. Individuals who walked slower were significantly older and shorter, their general physical performance was worse, and they more often had diabetes compared with their faster counterparts. Slower participants performed worse on executive function tasks and had more microbleeds on brain imaging. WMHs and cardiac disease did not relate to gait velocity.

Imaging Data

In the voxel-based MTR symptom-mapping analysis, we found significant clusters of MTR voxels that were positively correlated with gait velocity bilaterally within the frontal white matter (Fig 1*A*). The association remained significant after correction for multiple comparisons and adjustment for age, sex, height, brain volume, general physical performance, microbleeds, diabetes, and hyperuricemia. To examine the spatial relationship between these clusters and major white matter tracts, we projected significant clusters from the VMTRSM analysis on the probabilistic white matter tract atlas in MNI space. As shown in Fig 1*B*, there was substantial overlap with the forceps minor.

Given the prominent association of MTR voxels and walking speed within the forceps minor, we assessed the mean MTR of the forceps minor in standard space and used a linear regression model, adjusted for age, sex, height, brain volume, general physical performance, microbleeds, diabetes, and hyperuricemia to determine the association between forceps minor MTR and gait velocity. Higher mean MTR within the forceps minor was positively related to gait velocity ($\beta = 0.134$; 95% CI, 0.011–0.258; $P = .033$) (Fig 2). This association remained virtually unchanged when global WMH volume or WMH volume within the forceps minor was added to the analysis ($\beta = 0.162$; 95% CI, 0.024–0.307; $P = .029$; and $\beta = 0.136$; 95% CI, 0.013–0.261; $P = .030$, respectively). Because the correlation between MTR and walking speed seemed to be dependent on a few outliers who walked quite fast, we repeated the regression analysis and excluded participants with walking speeds ± 1.5 SDs from the population mean. This step did not substantially alter the direction or strength of the association ($\beta = 0.117$; 95% CI, −0.012–0.248; $P = .076$).

We examined executive function as a confounder because it related significantly to gait velocity in the univariate analysis. Indeed, executive function attenuated the effect of forceps minor MTR on gait speed, and there remained only a nonsignificant trend ($\beta =$

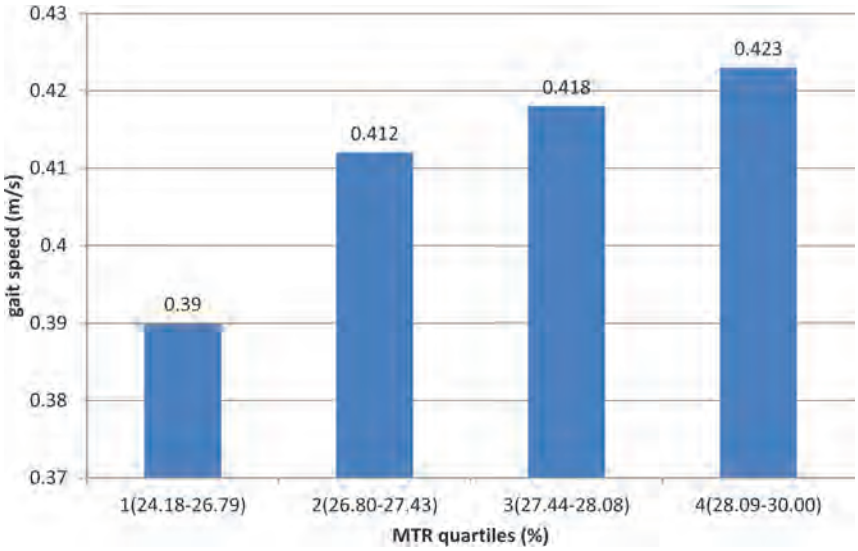

FIG 3. Analysis of covariance results. The mean MTR (percentage) of the forceps minor was divided into quartiles (x-axis). The first quartile was the lowest. Ranges of the MTR quartiles are as follows: quartile 1, 24.18–26.79; quartile 2, 26.80–27.43; quartile 3, 27.44–28.08; quartile 4, 28.09–30.00. Values on the y-axis represent the estimated mean walking speed in meters/second of subjects within each quartile, adjusted for age, sex, height, SPPB total score, the presence of microbleeds, diabetes, hyperuricemia, and brain volume. Increasing MTR values within the forceps minor are related to higher gait velocity in a dose-dependent manner (*P* for linear trend = .031).

0.123; 95% CI, −0.002–0.243; $P = .054$). A Preacher and Hayes[36] bootstrap method showed that executive dysfunction had no significant mediation effect on the association between MTR and gait velocity (indirect effect, 0.016; bootstrapped standard error, 0.013; bootstrapped 95% CI, −0.0047–0.0460).

Figure 3 illustrates the associations between quartiles of mean MTR distribution in the forceps minor and gait velocity. Analysis of covariance, which we corrected for age, sex, height, brain volume, general physical performance, microbleeds, diabetes, and hyperuricemia, showed an independent linear dose-effect relationship between forceps minor-MTR quartiles and gait velocity (*P* for linear trend = .031).

VLSM identified no voxel clusters in which WMHs related significantly to slower gait speed.

DISCUSSION

In this study of older adults free of stroke, dementia, and other neurologic diseases, we used 2 observer-independent methods to identify micro- and macrostructural determinants of gait velocity. We found a dose-dependent association between MTR values in the forceps minor and gait velocity, independent of age, sex, height, general physical performance, diabetes, hyperuricemia, brain volume, microbleeds, and WMH volume. Lower MTR, suspected of representing decreased myelin content,[17,22] related to slower gait velocity. VLSM showed no voxel clusters in which WMHs were significantly related to a slower gait velocity. Different results of MTR and WMH analysis in the current study are not surprising in light of the work of Wong et al,[40] who reported no significant relationship among MTR, WMH, and cerebrovascular risk factors, suggesting an independent pathophysiology for each measure.

Our results are in line with MTR and DTI findings in normal aging and in patients with cerebral small-vessel disease.[14,19,24] The only MTR study in healthy, older adults described a relationship between whole-brain MTR and gait velocity.[23] The authors of this investigation quantified MTR changes globally by using histogram-based metrics. This is a very robust approach, but it fails to provide information on the location of MTR changes that relate to gait. Our voxelwise approach overcomes this limitation and thus extended previous results by identifying MTR alterations within the forceps minor as important determinants of walking speed. de Laat et al[24] studied 429 individuals 50–85 years of age with cerebral small-vessel disease. These authors found loss of white matter integrity in the corpus callosum, particularly the genu where the forceps minor crosses. Similar results were reported by Della Nave et al[14] and Bhadelia et al,[19] who also showed that participants with abnormal gait had lower fractional anisotropy in the genu of the corpus callosum. Even though DTI probes brain tissue organization rather than brain tissue composition like MTI, previous DTI results largely resemble our MTR findings.[20,21] Microstructural brain tissue changes in the forceps minor were consistently linked with gait disturbances both in normal aging and in patients with cerebral small-vessel disease.[14,19]

The forceps minor is a large fiber bundle that connects the bilateral prefrontal cortices of the hemispheres,[8,41] which play an important role in motor control, especially in older adults.[42] Intact interhemispheric connections may be important for maintaining motor control at a high level.[43] We observed no significant relationship between WMHs or lacunes and gait performance in our community-dwelling sample. Conversely, individuals with a higher number of microbleeds had slower gait velocity. This is partly in line with 1 recent study that reported an association between microbleeds, but not WMHs and gait velocity, in community-dwelling adults.[44] Microbleeds occur in the wake of cerebral small-vessel disease, and their presence relates to microstructural brain tissue changes.[45] However, neither the inclusion of WMHs nor of lacunes or microbleeds in the regression analysis changed the association between MTR of the forceps minor and gait velocity significantly.

The 2 previous DTI studies[14,19] also found that DTI measures in the genu of the corpus callosum remained significantly associated with poorer gait performance after adding WMH volume to the analysis. Considering that more widespread WMHs seen in elderly individuals are a marker of coexisting cerebral small-vessel disease, previous results and the results of the current study indicate that factors other than cerebral small-vessel disease may also play an important role in the development of gait disturbances during aging. Postmortem studies that correlate MTR and DTI measures with brain tissue alterations are thus likely to im-

prove our pathophysiologic understanding of age-related gait abnormalities.

The current study has several strengths. It is the largest cohort study on gait performance using voxel-based MTR mapping to date. The study is community-based, with prospectively planned radiologic and clinical protocols. With MTI, images with a much higher spatial resolution and signal-to-noise ratio can be produced than is possible with DTI acquisitions. There are also no echo-planar imaging–induced artifacts. The high scan resolution allowed accurate registration of scans and segmentation of tissue types and WMHs. A thorough post-processing procedure and rigorous quality control of segmentations reduced the effects of coregistration errors and CSF contamination to a minimum.

There are also limitations. The study has a cross-sectional design. Other potential underlying mechanisms for our findings, beyond a direct causal relationship between microstructural damage and disturbances in gait velocity, are possible. Among them are peripheral neuromuscular disease, the presence of hip and joint disease, or visual disturbances or cognitive dysfunction. We had expected peripheral neuromuscular disease and hip and joint diseases to be reflected in the SPPB total score, which was considered a confounder in our regression model. Inclusion of the SPPB total score did not significantly alter our results, arguing against a large effect of general physical performance on the relationship between forceps minor MTR and gait velocity.

When we added executive function scores to the regression analysis, the relationship between MTR of the forceps minor and walking speed was attenuated. There remained only a nonsignificant trend. In contrast to authors in previous studies who reported executive functions exerting mediating effects on the relationship between structural brain changes and gait,[46,47] we were unable to confirm that executive function is a mediator in the association between forceps minor MTR and gait speed in the current investigation. It is likely that the effect of MTR on gait became nonsignificant when the executive function score was introduced simply because a trivial amount of variance was explained in addition to the model without inclusion of results of executive function testing. Participants were directed to walk at their "usual pace," allowing them to make a personal choice between a range of gait speeds. This could have biased our results. However, usual gait speed correlated well with the SPPB score in our study and was shown to relate significantly to disability in previous work.[27] Previous data even suggest that usual gait speed alone is nearly as good a predictor of disability outcome as extensive physical testing.[27]

The lack of an association between heart disease and walking speed might have been caused by the rather short walking distance (8 m) and the possibility of walking at a normal pace in our study. It was described previously that the presence of heart disease rather affects long-distance walking tests.[48] We realize that we tested the association between voxel values and walking speed in a far larger number of voxels in MTR analysis that compose the whole white matter than in the lesion-based analysis. Consequently, the risk of finding associations due to chance alone is probably higher in the MTR analyses, and by contrast, the risk of missing associations that actually exist is probably higher in the lesion-based analysis. In this study, besides family-wise error control, the symmetry of our findings in both hemispheres is a strong argument against findings due to chance alone.

The variance of the VMTRSM analyses was substantial. The reason for this large variability of results, which hampers the utility of findings, is unclear. It remains to be seen whether other methods of image analysis such as Tract-Based Spatial Statistics (TBSS; http://fsl.fmrib.ox.ac.uk/fsl/fslwiki/TBSS)[49] might resolve this problem.

Some subjects originated from the same families. This might lead to correlated errors in the statistical models. FSL includes no regular option to correct voxelwise analyses for family structure. Including, for instance, random effects would be very difficult to interpret. However, we consider this a minor issue here, given the small number of subjects per family.

Our voxelwise approach is neither useful nor intended to diagnose a single subject. However, our results broaden the pathophysiologic understanding of MTR and gait disturbances in aging. Future longitudinal studies might use high-resolution, 3D MTR scans to tailor reliable predictors for gait disturbances in older age.

CONCLUSIONS

Our study provides new evidence for the importance of MTR changes in gait disturbances at an older age, particularly in the forceps minor. Identification of the causes and the histopathologic origin of these MR imaging–detected tissue alterations is important because therapeutic measures may be derived.

Disclosures: Stephan Seiler—*RELATED*: *Grant*: *Comments*: This work was supported by FP6 ERA-NET NEURON grant (01EW1207) and by the Austrian Science Fund project I904*; *Support for Travel to Meetings for the Study or Other Purposes*: *Comments*: Travel costs for a study group meeting I attended (at Zuers, Austria) were covered by the grants indicated above.* Marco Duering—*RELATED*: *Grant*: European Union FP6 ERA-NET NEURON Grant*; *Support for Travel to Meetings for the Study or Other Purposes*: European Union FP6 ERA-NET NEURON Grant*; *UNRELATED*: *Grants/Grants Pending*: German Center for Neurodegenerative Diseases Inter-Site Project Else Kröner-Fresenius-Stiftung*; *Payment Lectures including Service on Speakers Bureaus*: Bayer Vital GmbH, *Comments*: lectures. Jean-Francois Mangin—*RELATED*: *Grant*: Mechanisms of Small Vessel Related Brain Damage and Cognitive Impairment*. Hugues Chabriat—*UNRELATED*: *Board Membership:* Servier, *Comments*: clinical trial preparation*; *Consultancy*: Johnson & Johnson, *Comments*: Data and Safety Monitoring Board. Reinhold Schmidt—*RELATED*: *Grant*: FP6 ERA-NET NEURON grant (01EW1207) and the Austrian Science Fund project I904.* *Money paid to the institution.

REFERENCES

1. Verghese J, LeValley A, Hall CB, et al. **Epidemiology of gait disorders in community-residing older adults.** *J Am Geriatr Soc* 2006;54:255–61 CrossRef Medline
2. Mertz KJ, Lee DC, Sui X, et al. **Falls among adults: the association of cardiorespiratory fitness and physical activity with walking-related falls.** *Am J Prev Med* 2010;39:15–24 CrossRef Medline
3. Verghese J, Buschke H, Viola L, et al. **Validity of divided attention tasks in predicting falls in older individuals: a preliminary study.** *J Am Geriatr Soc* 2002;50:1572–76 CrossRef Medline
4. Kang HG, Dingwell JB. **Effects of walking speed, strength and range of motion on gait stability in healthy older adults.** *J Biomech* 2008;41:2899–905 CrossRef Medline
5. Mahlknecht P, Kiechl S, Bloem BR, et al. **Prevalence and burden of gait disorders in elderly men and women aged 60–97 years: a population-based study.** *PLoS One* 2013;8:e69627 CrossRef Medline
6. la Fougère C, Zwergal A, Rominger A, et al. **Real versus imagined locomotion: a [18F]-FDG PET-fMRI comparison.** *Neuroimage* 2010;50:1589–98 CrossRef Medline

7. Jones DK, Lythgoe D, Horsfield MA, et al. **Characterization of white matter damage in ischemic leukoaraiosis with diffusion tensor MRI.** *Stroke* 1999;30:393–97 CrossRef Medline
8. Catani M, ffytche DH. **The rises and falls of disconnection syndromes.** *Brain* 2005;128:2224–39 CrossRef Medline
9. Novak V, Haertle M, Zhao P, et al. **White matter hyperintensities and dynamics of postural control.** *Magn Reson Imaging* 2009;27:752–59 CrossRef Medline
10. Murray ME, Senjem ML, Petersen RC, et al. **Functional impact of white matter hyperintensities in cognitively normal elderly subjects.** *Arch Neurol* 2010;67:1379–85 CrossRef Medline
11. Baezner H, Blahak C, Poggesi A, et al; LADIS Study Group. **Association of gait and balance disorders with age-related white matter changes: the LADIS study.** *Neurology* 2008;70:935–42 CrossRef Medline
12. Poggesi A, Gouw A, van der Flier W, et al. **Cerebral white matter changes are associated with abnormalities on neurological examination in non-disabled elderly: the LADIS study.** *J Neurol* 2013;260:1014–21 CrossRef Medline
13. Soumare A, Elbaz A, Zhu Y, et al. **White matter lesions volume and motor performances in the elderly.** *Ann Neurol* 2009;65:706–15 CrossRef Medline
14. Della Nave R, Foresti S, Pratesi A, et al. **Whole-brain histogram and voxel-based analyses of diffusion tensor imaging in patients with leukoaraiosis: correlation with motor and cognitive impairment.** *AJNR Am J Neuroradiol* 2007;28:1313–19 CrossRef Medline
15. Guttmann CR, Benson R, Warfield SK, et al. **White matter abnormalities in mobility-impaired older persons.** *Neurology* 2000;54:1277–83 CrossRef Medline
16. Seiler S, Pirpamer L, Hofer E, et al. **Magnetization transfer ratio relates to cognitive impairment in normal elderly.** *Front Aging Neurosci* 2014;6:263 CrossRef Medline
17. Seiler S, Ropele S, Schmidt R. **Magnetization transfer imaging for in vivo detection of microstructural tissue changes in aging and dementia: a short literature review.** *J Alzheimers Dis* 2014;42(suppl 3):S229–37 CrossRef Medline
18. Tuladhar AM, van Norden AG, de Laat KF, et al. **White matter integrity in small vessel disease is related to cognition.** *Neuroimage Clin* 2015;7:518–24 CrossRef Medline
19. Bhadelia RA, Price LL, Tedesco KL, et al. **Diffusion tensor imaging, white matter lesions, the corpus callosum, and gait in the elderly.** *Stroke* 2009;40:3816–20 CrossRef Medline
20. Mori S, Zhang J. **Principles of diffusion tensor imaging and its applications to basic neuroscience research.** *Neuron* 2006;51:527–39 CrossRef Medline
21. Graham SJ, Henkelman RM. **Understanding pulsed magnetization transfer.** *J Magn Reson Imaging* 1997;7:903–12 CrossRef Medline
22. Schmierer K, Scaravilli F, Altmann DR, et al. **Magnetization transfer ratio and myelin in postmortem multiple sclerosis brain.** *Ann Neurol* 2004;56:407–15 CrossRef Medline
23. Rosano C, Sigurdsson S, Siggeirsdottir K, et al. **Magnetization transfer imaging, white matter hyperintensities, brain atrophy and slower gait in older men and women.** *Neurobiol Aging* 2010;31:1197–204 CrossRef Medline
24. de Laat KF, Tuladhar AM, van Norden AG, et al. **Loss of white matter integrity is associated with gait disorders in cerebral small vessel disease.** *Brain* 2011;134:73–83 CrossRef Medline
25. Schmidt R, Lechner H, Fazekas F, et al. **Assessment of cerebrovascular risk profiles in healthy persons: definition of research goals and the Austrian Stroke Prevention Study (ASPS).** *Neuroepidemiology* 1994;13:308–13 CrossRef Medline
26. Schmidt R, Fazekas F, Kapeller P, et al. **MRI white matter hyperintensities: three-year follow-up of the Austrian Stroke Prevention Study.** *Neurology* 1999;53:132–39 CrossRef Medline
27. Guralnik JM, Ferrucci L, Pieper CF, et al. **Lower extremity function and subsequent disability: consistency across studies, predictive models, and value of gait speed alone compared with the short physical performance battery.** *J Gerontol A Biol Sci Med Sci* 2000;55:M221–31 CrossRef Medline
28. Greenberg SM, Vernooij MW, Cordonnier C, et al; Microbleed Study Group. **Cerebral microbleeds: a guide to detection and interpretation.** *Lancet Neurol* 2009;8:165–74 CrossRef Medline
29. Plummer DL. **DispImage: a display and analysis tool for medical images.** *Revista di Neuroradiologica* 1992;5:489–95 CrossRef
30. Hua K, Zhang J, Wakana S, et al. **Tract probability maps in stereotaxic spaces: analyses of white matter anatomy and tract-specific quantification.** *Neuroimage* 2008;39:336–47 CrossRef Medline
31. Jenkinson M, Beckmann CF, Behrens TE, et al. **FSL.** *Neuroimage* 2012;62:782–90 CrossRef Medline
32. Zhang Y, Brady M, Smith S. **Segmentation of brain MR images through a hidden Markov random field model and the expectation-maximization algorithm.** *IEEE Trans Med Imaging* 2001;20:45–57 CrossRef Medline
33. Smith SM. **Fast robust automated brain extraction.** *Hum Brain Mapp* 2002;17:143–55 CrossRef Medline
34. Jenkinson M, Smith S. **A global optimisation method for robust affine registration of brain images.** *Med Image Anal* 2001;5:143–56 CrossRef Medline
35. Ashburner J, Friston KJ. **Voxel-based morphometry: the methods.** *Neuroimage* 2000;11:805–21 CrossRef Medline
36. Preacher KJ, Hayes AF. **Asymptotic and resampling strategies for assessing and comparing indirect effects in multiple mediator models.** *Behav Res Methods* 2008;40:879–91 CrossRef Medline
37. Rorden C, Karnath HO, Bonilha L. **Improving lesion-symptom mapping.** *J Cogn Neurosci* 2007;19:1081–88 CrossRef Medline
38. Kimberg DY, Coslett HB, Schwartz MF. **Power in voxel-based lesion-symptom mapping.** *J Cogn Neurosci* 2007;19:1067–80 CrossRef Medline
39. Winkler AM, Ridgway GR, Webster MA, et al. **Permutation inference for the general linear model.** *Neuroimage* 2014;92:381–97 CrossRef Medline
40. Wong KT, Grossman RI, Boorstein JM, et al. **Magnetization transfer imaging of periventricular hyperintense white matter in the elderly.** *AJNR Am J Neuroradiol* 1995;16:253–38 Medline
41. Montero-Odasso M, Verghese J, Beauchet O, et al. **Gait and cognition: a complementary approach to understanding brain function and the risk of falling.** *J Am Geriatr Soc* 2012;60:2127–36 CrossRef Medline
42. Chao YP, Cho KH, Yeh CH, et al. **Probabilistic topography of human corpus callosum using cytoarchitectural parcellation and high angular resolution diffusion imaging tractography.** *Hum Brain Mapp* 2009;30:3172–87 CrossRef Medline
43. Seidler RD, Bernard JA, Burutolu TB, et al. **Motor control and aging: links to age-related brain structural, functional, and biochemical effects.** *Neurosci Biobehav Rev* 2010;34:721–33 CrossRef Medline
44. Stijntjes M, de Craen AJ, van der Grond J, et al. **Cerebral microbleeds and lacunar infarcts are associated with walking speed independent of cognitive performance in middle-aged to older adults.** *Gerontology* 2016;62:500–07 CrossRef Medline
45. Akoudad S, de Groot M, Koudstaal PJ, et al. **Cerebral microbleeds are related to loss of white matter structural integrity.** *Neurology* 2013;81:1930–37 CrossRef Medline
46. Ezzati A, Katz MJ, Lipton ML, et al. **The association of brain structure with gait velocity in older adults: a quantitative volumetric analysis of brain MRI.** *Neuroradiology* 2015;57:851–61 CrossRef Medline
47. Nadkarni NK, Nunley KA, Aizenstein H, et al; Health ABC Study. **Association between cerebellar gray matter volumes, gait speed, and information-processing ability in older adults enrolled in the health ABC study.** *J Gerontol A Biol Sci Med Sci* 2014;69:996–1003 CrossRef Medline
48. Pasma JH, Stijntjes M, Ou SS, et al. **Walking speed in elderly outpatients depends on the assessment method.** *Age (Dordr)* 2014;36:9736 CrossRef Medline
49. Smith SM, Jenkinson M, Johansen-Berg H, et al. **Tract-based spatial statistics: voxelwise analysis of multi-subject diffusion data.** *Neuroimage* 2006;31:1487–505 CrossRef Medline

Evaluation of Encephaloduroarteriosynangiosis Efficacy Using Probabilistic Independent Component Analysis Applied to Dynamic Susceptibility Contrast Perfusion MRI

A.N. Laiwalla, F. Kurth, K. Leu, R. Liou, J. Pamplona, Y.C. Ooi, N. Salamon, B.M. Ellingson, and N.R. Gonzalez

ABSTRACT

BACKGROUND AND PURPOSE: Indirect cerebral revascularization has been successfully used for treatment in Moyamoya disease and symptomatic intracranial atherosclerosis. While angiographic neovascularization has been demonstrated after surgery, measurements of local tissue perfusion are scarce and may not reflect the reported successful clinical outcomes. We investigated probabilistic independent component analysis and conventional perfusion parameters from DSC-MR imaging to measure postsurgical changes in tissue perfusion.

MATERIALS AND METHODS: In this prospective study, 13 patients underwent unilateral indirect cerebral revascularization and DSC-MR imaging before and after surgery. Conventional perfusion parameters (relative cerebral blood volume, relative cerebral blood flow, and TTP) and probabilistic independent components that reflect the relative contributions of DSC signals consistent with arterial, capillary, and venous hemodynamics were calculated and examined for significant changes after surgery. Results were compared with postsurgical DSA studies to determine whether changes in tissue perfusion were due to postsurgical neovascularization.

RESULTS: Before surgery, tissue within the affected hemisphere demonstrated a high probability for hemodynamics consistent with venous flow and a low probability for hemodynamics consistent with arterial flow, whereas the contralateral control hemisphere demonstrated the reverse. Consistent with symptomatic improvement, the probability for venous hemodynamics within the affected hemisphere decreased with time after surgery ($P = .002$). No other perfusion parameters demonstrated this association. Postsurgical DSA revealed an association between an increased preoperative venous probability in the symptomatic hemisphere and neovascularization after surgery.

CONCLUSIONS: Probabilistic independent component analysis yielded sensitive measurements of changes in local tissue perfusion that may be associated with newly formed vasculature after indirect cerebral revascularization surgery.

ABBREVIATIONS: EDAS = encephaloduroarteriosynangiosis; ICA = independent component analysis; ICAS = intracranial atherosclerosis; MMD = Moyamoya disease; rCBF = relative cerebral blood flow; rCBV = relative cerebral blood volume

Encephaloduroarteriosynangiosis (EDAS) is a form of indirect cerebral revascularization, which has been successfully used as a treatment in Moyamoya disease (MMD) and symptomatic intracranial atherosclerosis (ICAS) in adults.[1-8] In principle, extracranial arterial branches are surgically redirected below the dura mater and apposed to hypoperfused brain tissue. This procedure results in the sprouting of new vessels that gradually form new anastomoses with the intracranial circulation, improving perfusion and reducing the risk of stroke.[7] In a recently published report on treatment outcomes with EDAS, the rate of stroke was 2.4% (5.6% in patients with ICAS, 0% in patients with MMD) within 2 years after the operation.[9] These rates are lower than the previously observed rates for medical treatment (15%) or angioplasty and stent placement (21%) in the SAMMPRIS (Stenting vs. Aggressive Medical Management for Preventing Recurrent Stroke in Intracranial Stenosis) trial.[10,11]

Multiple imaging modalities have been used to assess the extent of indirect revascularization in patients with MMD and ICAS. Conventional angiography, CTA, and MRA have demonstrated neovascularization within the EDAS operative territory through transdural and transpial collateral vessels.[12,13] Increased donor superficial temporal artery and middle meningeal artery vessel sizes and a decrease in preoperative native collaterals fol-

Received November 17, 2015; accepted after revision October 17, 2016.

From the Departments of Neurosurgery (A.N.L., Y.C.O.) and Radiology (K.L., J.P., N.S., B.M.E.), David Geffen School of Medicine, University of California, Los Angeles, Los Angeles, California; and Department of Neurosurgery (F.K., R.L., N.R.G.), Cedars
Sinai Medical Center, Los Angeles, California.

This work is supported by the Ruth and Raymond Stotter Endowed Chair in Neurosurgery and the National Institutes of Health award K23NS079477.

Please address correspondence to Nestor R. Gonzalez, MD, Cedars Sinai Medical Center, 127 S San Vicente Blvd, Suite A6600, Los Angeles, CA 90048,
e-mail: nestor.gonzalez@cshs.org

Indicates open access to non-subscribers at www.ajnr.org

Indicates article with supplemental on-line photos.

http://dx.doi.org/10.3174/ajnr.A5041

Table 1: Study participants—characteristics, history of TIA, and stroke and imaging data at the time of the first and last scan relative to the operation and the number of observations

ID	Age (yr)	Sex	Diagnosis	Events Pre- and Postoperation		Imaging Data	
				Pre-	Post-	Time Range (days)	Time Points
1	55	F	ICAS	TIA		−19–373	5
2	65	F	ICAS	Stroke	TIA	−14–364	4
3	75	F	ICAS	Stroke		107–365	4
4	66	F	ICAS	TIA + Stroke		99–372	4
5	63	M	ICAS	Stroke		−14–370	4
6	55	F	MMD	Stroke		−71–172	3
7	23	F	MMD	Stroke		−4–94	2
8	67	M	ICAS	TIA		−7–190	2
9	56	F	MMD	TIA		−7–135	2
10	47	F	ICAS	Stroke		−3–186	3
11	70	F	ICAS	TIA + Stroke		−15	1
12	35	F	MMD	TIA + Stroke		116	1
13	35	F	MMD	TIA		437	1

Note:—ID indicates identification.

lowing EDAS have also been reported.[5,12,14,15] Beyond anatomic changes, investigating tissue perfusion is necessary because alterations in tissue perfusion are dynamic processes that may not correlate directly with structural changes.[16,17] In MMD, xenon-enhanced CT scanning, SPECT, blood oxygen level–dependent cerebrovascular-reactivity MR imaging, and PET studies have shown improved cerebrovascular reactivity in territories of the intervened hemisphere.[12,18,19] In addition, CT perfusion and DSC-MR imaging studies found improved postoperative cerebral hemodynamics through TTP, relative cerebral blood flow (rCBF), and relative cerebral blood volume (rCBV) measures.[16,20] Yet, the association between local tissue perfusion following EDAS with structural changes and clinical outcomes is still unclear.

Probabilistic independent component analysis (ICA) of DSC-MR imaging allows improved differentiation of physiologic and pathophysiologic cerebral hemodynamics through the extraction of spatiotemporal blood supply patterns.[21] It is a data-driven, multivariate approach that has been applied to functional MR imaging, electroencephalographic recordings, and, recently, DSC-MR imaging data in glioblastoma, in which it demonstrated the ability to discern tumor from normal vasculature and characterize tumor perfusion patterns.[22-27] The objective of this study was to apply ICA to DSC-MR imaging data to evaluate hemodynamic changes after EDAS, to assess whether this method can detect changes consistent with structural imaging measures, and to compare the results with classic perfusion measures—that is, by quantitatively separating the DSC-MR imaging time-series data in each image voxel into independent temporal patterns consistent with arterial, capillary, and venous hemodynamics, we hypothesized that probabilistic ICA would detect subtle changes in vascularity that may not be captured by classic perfusion measures. We further hypothesized that brain regions in adults with symptomatic ICAS or MMD would contain tissue with a high venous probability, suggesting hemodynamics consistent with delayed venous flow. Additionally, we posited that a favorable increase in tissue perfusion within the surgical hemisphere after EDAS would reduce this venous probability and that this reduction would be associated with neovascularization as measured with postoperative digital subtraction angiography.

MATERIALS AND METHODS

Study Design

We performed a prospective study of adult patients (23–75 years of age) with TIA or nonsevere stroke attributed to 70%–99% intracranial stenosis of a major intracranial artery and confirmed by conventional angiography. All patients presented with persistent strokes or TIAs despite optimal medical management, as established in the SAMMPRIS trial.[10] Patients with ICAS or MMD were included in this study, with the former enrolled in the ongoing EDAS Surgical Indirect Revascularization for Symptomatic Intracranial Arterial Stenosis (ERSIAS) trial (clinicaltrials.gov No. NCT01819597). Patients with MMD received the same imaging and therapy as those with ICAS through the ERSIAS protocol. All participants provided informed consent before taking part, and the study was conducted with institutional review board approval (No. 12-000439; University of California, Los Angeles).

Study Participants

Thirteen patients (female/male ratio: 11:2; mean age, 54.77 ± 15.66 years) who underwent unilateral EDAS surgery and DSC-MR imaging from 2013 to 2014 were included (see Table 1 for an overview of all enrolled patients). Eight of the patients were diagnosed with ICAS, and 5, with MMD. Of the 13 patients, 8 had DSC-MR imaging data at multiple time points, including 1 pre- and up to 4 postoperatively (ie, at approximately 3, 6, 9, and 12 months after the operation). The exact timing of the imaging studies was recorded in days after the operation, yielding negative numbers for preoperative scans (Table 1). For 12 of the 13 patients, postoperative DSA studies were performed to document the extent of newly formed vessels from the donor artery. These studies were used to compare potential perfusion changes with the actual observed sprouting of new vessels. One patient (patient 11) died of a myocardial infarction before these postoperative studies were performed.

Preoperative Evaluation

All patients underwent preoperative imaging that included DSA and/or MR imaging. DSA of all patients revealed severe stenosis in the intracranial cerebral vasculature that corresponded to their clinical symptoms. EDAS was considered for treatment on the basis of clinical need, including ischemic symptoms within 30 days and evidence of hypoperfusion and poor collateral flow (American Society of Interventional and Therapeutic Neuroradiology/Society of Interventional Radiology grades 0–2).

Surgical Technique

The EDAS surgical technique has been previously described.[5,7] In brief, the superficial temporal artery is identified and dissected with its surrounding galeal cuff. A craniotomy is performed, and the dura

is opened in cruciate fashion, preserving the middle meningeal artery branches. The dural layers are separated, the inner avascular layer is removed, and the arachnoid is widely opened with microdissection under the surgical microscope. The superficial temporal artery is subsequently sutured to the edges. The burr-holes and inner table of the bone flap are trimmed to prevent kinking and compression of the superficial temporal artery on its replacement. Patients remain in intensive medical management during and after the operation with antiplatelets, high-dose statins, and strict control of blood pressure and glycemia.

MR Images

All MR imaging data were collected on a 1.5T (Avanto; Siemens, Erlangen, Germany) or 3T MR imaging system (Trio, Prisma, or Skyra; Siemens). Each patient underwent follow-up studies on the same MR imaging scanner that was used for their original preoperative baseline scan. Standard anatomic MR imaging sequences included a sagittal T1-weighted image, along with axial T2-weighted and FLAIR images. A 10- to 20-mL (0.1 mmol/kg body weight) dose of gadobenate dimeglumine contrast agent was administered during DSC-MR imaging (gradient-echo EPI: TE/TR = 23/1210 ms [1.5T], TE/TR = 32/1840 ms [3T], 35° flip angle, 120 time points, bolus injection after 20–25 baseline images, 16–20 sections, 5-mm section thickness with no intersection gap, 128 × 128 matrix size, 24-cm FOV). rCBV, rCBF, and TTP were computed via the commercially available postprocessing software (IB Neuro, Version 2.0; Imaging Biometrics, Elm Grove, Wisconsin). Sagittal and axial postcontrast T1-weighted images were obtained following DSC perfusion images.

Probabilistic Independent Component Analysis

Technical and mathematic details regarding the probabilistic ICA algorithm are described in Beckmann and Smith.[28] In the current study, we implemented the probabilistic ICA algorithm by using the MELODIC program from the FMRIB Software Library (FSL; http://fsl.fmrib.ox.ac.uk/fsl/fslwiki/MELODIC). Briefly, probabilistic ICA was applied to the raw DSC-MR imaging data throughout the entire brain to identify 3 statistically independent temporal components plus noise.[22] These 3 independent components were then manually identified as "arterial," "venous," and "capillary" components based on their temporal hemodynamic profiles, in which the arterial component had the shortest TTP, the venous component had the longest TTP, and the capillary component had the smallest signal amplitude and an intermediate TTP. For verification of this empiric categorization, the components were checked via their respective spatial patterns to ensure that the arterial component covered the circle of Willis and the venous component contained the choroidal plexus. Next, the posterior probability of the DSC time signal for each independent component compared with noise was calculated for each image voxel. This calculation resulted in 3 unique brain maps reflecting the relative probability of a voxel having a DSC time-series consistent with arterial, venous, or capillary hemodynamic profiles. These resulting probability maps were then used for subsequent analyses.

Image Registration

All conventional and perfusion images for each subject were registered to the axial, postcontrast T1-weighted images at the first postoperative time point by using a 12-*df* affine transformation with a mutual information cost function (in FSL). If required, 9-*df* manual alignment was subsequently performed (tkregister2, FreeSurfer; surfer.nmr.mgh.harvard.edu). Three investigators (A.N.L., B.M.E., K.L.) verified adequate alignment of the images by consensus.

ROIs

ROIs were manually drawn on baseline postcontrast T1-weighted images around the surgical graft site and on a mirrored region within the contralateral hemisphere. Because all images were aligned between baseline and postsurgical follow-up, a single set of ROIs was used for comparison. The mean values of all 6 measures (arterial probability, capillary probability, venous probability, rCBV, rCBF, and TTP) within these 2 ROIs (surgical and contralateral) were calculated for each patient and evaluation time point.

Statistical Analysis

The calculated ROI-wise values (probabilities for arterial, capillary, and venous components, as well as rCBV, rCBF, and TTP) were used as the dependent measures in a statistical model. The association between time after the operation (independent variable) and the imaging measures of interest (dependent variable) was calculated by using a general linear model and permutation testing. This approach allowed accounting for interindividual differences among the participants by including "subject" as a factor of no interest and assessing interactions between surgical and control hemispheres by modeling appropriate interactions. Correlation coefficients were calculated from the *t* values on the basis of the effective *dfs*. Because none of the measures of interest can be assumed to be normally distributed in this small sample, significance was established by using a Monte Carlo simulation with 10,000 permutations.[29] Specifically, the null hypothesis was that there is no association between the time after the operation and the measures of interest (dependent variables), so all observed differences were explained by interindividual variability and noise. This entails that no systematic changes occur in either measurement with time, which means that under the null hypothesis it is inconsequential at which time relative to surgery the measure was taken. While we controlled for interindividual differences, the time after the operation can thus be interchanged at random, without yielding a less significant correlation or interaction under the null hypothesis. The null hypothesis can be rejected at $P \leq .05$, however, if random permutations of the time after the operation yield less significant results in at least 95% of all cases. With 6 different measures of interest, we controlled the type I error by applying a Bonferroni correction for multiple comparisons (ie, significance was determined at $P < .0083$). Seeing that previous analyses focused on MMD, and not ICAS, and that the underlying disease may be a modifying factor for the results, we repeated the statistical analysis for each disease group as a post hoc analysis and additionally calculated the interaction between disease group and

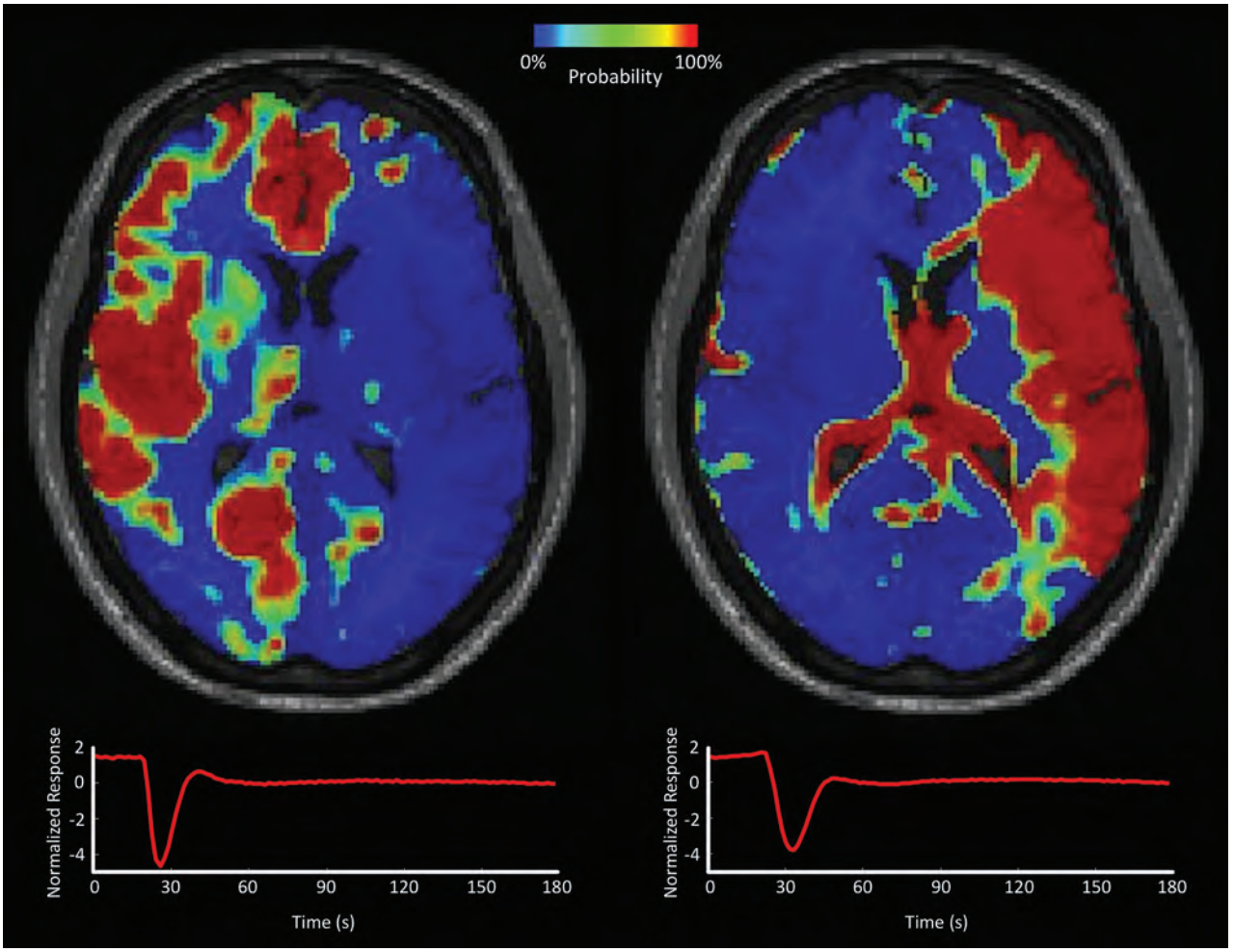

FIG 1. Probabilistic independent component analysis of presurgical DSC-MR imaging of a patient undergoing EDAS. Probability maps of arterial (left) and venous (right) components are shown on an axial section. The respective time courses show a delayed response in the venous component. The color bar indicates local probability. Note the high probability for the venous component in the left hemispheric cortex, which is the symptomatic side.

postsurgical changes. The analysis was performed in Matlab (Version 7.12; MathWorks, Natick, Massachusetts).

In addition, standard plots of the probability of arterial, venous, and capillary components within the prescribed ROIs with time in the complete sample and descriptive statistics were generated for demographic and clinical assessments to characterize the study population. Additional plots were created for rCBF, rCBV, and TTP. For comparison with the individual DSA studies, plots of the changes within the arterial and venous component with time for each individual patient were created. These analyses were conducted by using JMP (Version 11; SAS Institute, Cary, North Carolina).

Clinical Analysis

Patient data were reviewed up to 24 months following EDAS surgery to evaluate TIA, stroke, and death.

Role of the Funding Source

None of the funding sources had any role in the collection or interpretation of data or any influence on the writing or decision to submit the manuscript.

RESULTS

Probabilistic ICA of the asymptomatic control hemisphere revealed a lower probability of belonging to the venous component than to the arterial component at baseline (mean probability: arterial, 0.40 ± 0.08, versus venous, 0.16 ± 0.07). In the preoperative symptomatic hemisphere, the probabilities of arterial and venous components were inverted (mean probability: venous, 0.46 ± 0.19, versus arterial, 0.23 ± 0.09). This inversion is depicted in the preoperative probabilistic map of arterial and venous components shown in Fig 1 for a representative patient. Visually, the maps showed striking asymmetry between the right and left frontal cortices, with a higher venous probability in the left frontoparietal cortex (symptomatic site) compared with contralateral tissue. Images for several axial sections of this patient are shown in On-line Fig 1.

With time, baseline values of venous and arterial probabilities were maintained in the asymptomatic control side (Fig 2). There was no significant correlation between the time after the operation and the venous probability of this asymptomatic hemisphere. After the operation, however, the high venous probabilities of the operative side (preoperative mean probability, 0.46 ± 0.19, versus

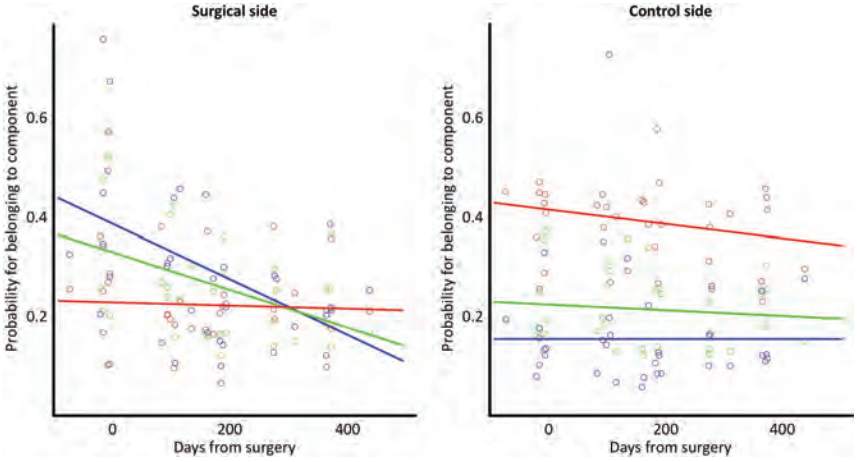

FIG 2. Temporal changes in the mean local probability of the tissue to belong to either the arterial (red), venous (blue), or capillary (green) component. The dominance of the venous component at baseline in the symptomatic hemisphere indicates delayed perfusion. Note the normalization in dominance with time, suggesting an accelerated perfusion of the surgical region.

Table 2: Significance of the association between the time after the operation and the measurements of interest within the surgical side, the contralateral side, and their interaction

	P Interaction	*r* Surgical Side	*P* Surgical Side	*r* Control Side	*P* Control Side
Artery	.258	0.024	.418	−0.109	.194
Vein	.001[a]	−0.426	.002[a]	0.051	.281
Capillary	.009	−0.332	.020	−0.003	.489
rCBF	.270	−0.017	.444	−0.116	.226
rCBV	.404	0.157	.121	0.113	.192
TTP	.120	0.181	.151	0.260	.039

Note:—*P* indicates probability; *r*, correlation coefficient.
[a] Significant results after correction for multiple comparisons using a Bonferroni correction.

12-month probability, 0.23 ± 0.09) decreased with time, while the arterial probabilities remained largely unchanged. This outcome was also reflected in a significant negative correlation between the time after the operation and the venous probability of this symptomatic hemisphere ($P = .002$). The association between venous probability and the time after the operation was significantly stronger on the surgical side compared with the control side ($P = .001$), in which no significant correlation between any perfusion measure and time after the operation was detected. After approximately 9 months, probabilities of the individual components of the surgical side appeared inverted to reflect patterns similar to those of the nonsurgical side. No other interactions between hemispheres (control versus surgical) or correlations with time after the operation survived the correction for multiple comparisons for any other perfusion measurement. Table 2 provides a detailed overview of *P* values and correlation coefficients. Although no significant findings were observed for the classic measures, rCBV, rCBF, and TTP, the respective plots can be found in On-line Fig 2 for completeness.

Post hoc analyses for each etiology group revealed a significant negative correlation between the venous probability and time after the operation of the surgical hemisphere in patients with ICAS ($P = .004$); this correlation was not significant for patients with MMD, likely due to the small sample size. An interaction between subgroup and time after the operation did not yield any significant results, thus not supporting a difference between ICAS and MMD. Notably, the study was not designed to separately evaluate each etiology group; however, the striking magnitude of the effect of the operation in the ICAS group reached statistical significance in this post hoc analysis. No other perfusion measure showed significant changes after the operation in that subgroup analysis.

Exploration of individual arterial and venous components in the surgical hemispheres of each patient did not demonstrate the pattern of increased venous probability across all patients. Of all 13 patients, 3 did not show an increased venous probability preoperatively. Fig 3 depicts examples from 1 patient with and 1 patient without increased venous probability. A direct comparison with postoperative DSA studies revealed that the 3 patients who did not show increased venous probabilities preoperatively did not develop new collaterals from the EDAS surgery. However, all other patients who had an inversion of the components did develop new collaterals from the donor vessel after the operation. This observation suggests that measures of venous probability may be a surrogate for neovascularization. An overview of the direct comparisons in all patients is given in On-line Fig 3.

Clinical Results

No patient had a stroke within the 24-month follow-up period. The 3 patients who did not develop postoperative collaterals had improvement in the degree of intracranial arterial stenosis and did not develop strokes; this outcome was attributed to the medical management. One of the 14 patients (patient 2) had a TIA at 1–6 months postoperatively. Further TIAs were not observed during the follow-up period for this patient. None of the other 12 patients had a TIA postoperatively.

DISCUSSION

Collaterals are of critical importance in maintaining cerebral perfusion in patients with intracranial arterial stenosis.[30] EDAS facilitates the formation of new collaterals between redirected extracranial arterial branches and the intracranial circulation.[7] The extent of revascularization following EDAS is traditionally focused on the anatomic investigation of collaterals by conventional angiography. However, consideration of the functional effects is also necessary because alterations in tissue perfusion may not correlate directly with structural changes.[16,17,31,32] The goal of this study was to explore perfusion MR imaging measurements to better characterize tissue perfusion following EDAS. No significant relationships were found between conventional perfusion measures (rCBV, rCBF, and TTP) and the time after EDAS surgery. By applying probabilistic ICA, however, a significant change was observed in the surgical hemisphere that corresponded to the clinical observation of protection from stroke and a reduced risk

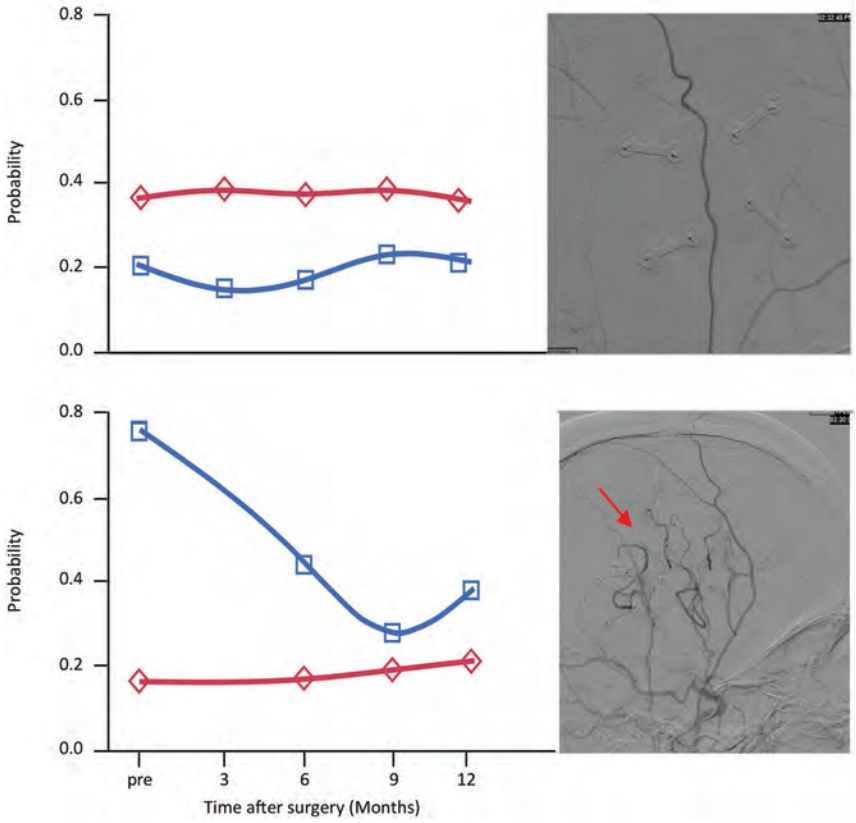

FIG 3. Comparison between the results from probabilistic ICA and the postoperative DSA studies in 2 sample patients. The results for the arterial and venous component are shown on the left, with the arterial component in red and the venous component in blue. The sagittal view of the respective postoperative DSA study is depicted directly to the right side of these graphs. Upper part: Note that this patient did not exhibit the pattern of an inversion of the probabilities as presented in Fig 2 for the whole sample. The respective postoperative DSA study does not show any new anastomoses between the donor artery and the intracranial vasculature. Lower part: This patient exhibited an inversion of the probabilities on the surgical side with a postoperative decrease of the venous component. The newly formed anastomoses with the intracranial arteries are indicated with a *red arrow*.

of TIA after EDAS, in agreement with prior publications reporting these beneficial clinical effects.[7,9] Specifically, the nonsurgical (control) hemisphere was found to have a constant, high arterial probability and low venous and capillary probabilities, suggesting that the raw DSC signal was most consistent with a rapid arterial hemodynamic pattern. Because this asymptomatic hemisphere was not affected by intracranial arterial stenosis, no perfusion deficit was expected.

In contrast, the symptomatic hemisphere, in which there was intracranial arterial stenosis and thus made the patient eligible for EDAS revascularization, had high venous and capillary probabilities and a low arterial probability at baseline, suggesting that most tissue near the surgical site expressed patterns more similar to delayed venous hemodynamics. This shift toward a higher probability of the venous component within the symptomatic hemisphere can be interpreted as a slower perfusion in this region. After EDAS surgery, the elevated probability for the venous component significantly decreased with time; this decrease led to an inversion of the probability pattern at 9 months. This suggests a normalization of the blood flow characteristics, with faster arrival and clearing of the contrast agent in the tissue due to higher perfusion after EDAS. In other words, after EDAS surgery, tissue perfusion changes in that it becomes less delayed than before the operation, thus less resembling venous blood flow characteristics. This interpretation is consistent with the clinical observation that symptoms improved in all cases following EDAS surgery.

While we also observed a significant negative correlation between the time after the operation and venous probability in the surgical hemisphere within the ICAS group, no significant correlation between the time after the operation and any perfusion measure was found within the MMD group. The interaction between patient group and time after the operation was not significant, indicating that the response to the operation did not differ between patients with ICAS and those with MMD. Nonsignificant results within the MMD group may rather be due to the relatively small sample size; this study was not designed to investigate each group independently. As shown in Table 1, the MMD group comprised only 5 of the 13 patients, and future analysis based on a larger dataset is desirable to further evaluate these findings.

The comparison with postoperative DSA studies confirms that improvement in perfusion was associated with formation of new collaterals. Patients who did not develop new collaterals from the donor vessel did not show an increased venous probability in the surgical hemisphere according to the results from the probabilistic ICA. These patients also exhibited a reduction in the stenosis of the qualifying artery in DSA angiography with time, which may be why they did not develop new collaterals, because the innate source of cerebral irrigation was sufficient to prevent them from developing symptoms. This effect has been reported in cases of intensive medical management alone, which was maintained in all patients undergoing EDAS in this study.[11,33] While this observation supports the notion that the decrease in the venous probability derived from probabilistic ICA acts as a surrogate for revascularization, it raises a second interesting question: One might inquire whether the observed relationship between increased venous probability and postoperative revascularization might qualify as a marker for patient selection and/or serve as a valuable tool for surgical planning and monitoring. While this question is beyond the scope of this initial study, it is well worth following up in a larger systematic study. Furthermore, because the clinical outcome after EDAS is likely to be superior to medical therapy alone, it will be important to assess whether such an observation may be reason enough for withholding or delaying an operation.[9-11]

In the setting of MMD, improved cerebral perfusion following indirect revascularization has been demonstrated by using tradi-

tional neuroimaging modalities. In a recent study with 12 pediatric patients with MMD, SPECT revealed improvement in basal perfusion and cerebrovascular reactivity in the MCA surgical territory, approximately 3 months following revascularization by EDAS surgery.[34] In a similar study in 17 pediatric patients with MMD who underwent EDAS, SPECT at approximately 5 months (153 ± 110 days) showed significant improvement in the cerebrovascular reserve, with nonsignificant improvement of the basal CBF.[19] Furthermore, perfusion MR imaging in 13 children with MMD demonstrated delayed presurgical TTP enhancement compared with controls, which was significantly reduced following EDAS.[16] CT perfusion was also used to evaluate multiple burr-hole revascularization in ischemic adult MMD.[20] Six-month follow-up CT perfusion showed postoperative increases in CBF, with decreases in MTT and TTP. Our results, however, do not demonstrate the same magnitude of change in traditional perfusion measures in patients undergoing EDAS. Some of the differences can be expected because most data in this study stem from adult patients with ICAS, usually of advanced age, in whom extensive neovascularization after EDAS is not necessarily anticipated. In addition, the relatively small overall sample size and limited coverage of time points may have contributed to the nonsignificant findings with conventional perfusion measures. The significant results found with probabilistic ICA may indicate a higher sensitivity of this technique to perfusion changes, warranting further studies to validate its use to monitor EDAS effects and potentially as a selection tool to identify subjects who would benefit most from indirect revascularization.

First developed in the engineering field of signal processing, ICA has been applied to fMRI for the separation of functional networks in task-related and task-free fMRI studies and to EEG to resolve differences between evoked responses.[25,27,35-38] More recently, ICA has been used to separate and distinguish phases of cerebral perfusion. Separation of the mixed dynamic signals of DSC-MR imaging into independent source signals provides spatiotemporal hemodynamic information on local perfusion for cerebral vasculature and parenchyma.[37,39] In a study of 12 patients with unilateral carotid stenosis, this method differentiated normal arterial, stenotic arterial, and stenotic-side parenchymal phases; this finding suggests that stenosis and poor collateral circulation resulted in delayed contrast perfusion through parenchyma on the side of the stenosis.[37] Additionally, probabilistic ICA applied to neuro-oncology allowed the detection of abnormal tumor vasculature, distinguishing tumor from normal tissue and potentially serving as a biomarker to predict responses to antiangiogenic drugs.[22,40] The present study suggests that the use of this method can be expanded to surgical planning and monitoring for EDAS in patients with ICAS. Despite recent concern about gadolinium deposits after repeat use, postcontrast MR imaging is standard in the stroke protocols of many institutions and DSC-MR imaging can be performed concurrently without additional contrast administration.[41,42] While the clinical significance of gadolinium deposits after repeat use still remains unknown, the application of probabilistic ICA to DSC-MR imaging may prove beneficial for surgical planning and monitoring for EDAS.[41,42] These potential benefits may thus outweigh the risk of gadolinium; however, further investigation is warranted.

CONCLUSIONS

The current results indicate that probabilistic ICA of DSC-MR imaging data is a sensitive technique for monitoring changes in perfusion after EDAS surgery in patients with ICAS and MMD. Hypoperfused brain regions had a high probability of perfusion characteristics, consistent with venous hemodynamics, and this elevated probability decreased as newly formed collaterals became evident.

Disclosures: Nestor R. Gonzalez—*RELATED*: *Grant*: National Institutes of Health, *Comments*: National Institutes of Health, National Institute of Neurological Disorders and Stroke, K23NS079477–01A1.* *Money paid to the institution.

REFERENCES

1. Adelson PD, Scott RM. **Pial synangiosis for Moyamoya syndrome in children.** *Pediatr Neurosurg* 1995;23;26–33 Medline
2. Matsushima T, Inoue T, Ikezaki K, et al. **Multiple combined indirect procedure for the surgical treatment of children with Moyamoya disease: a comparison with single indirect anastomosis and direct anastomosis.** *Neurosurg Focus* 1998;5;e4 Medline
3. Sainte-Rose C, Oliveira R, Puget S, et al. **Multiple bur hole surgery for the treatment of Moyamoya disease in children.** *J Neurosurg* 2006;105(6 suppl):437–43 Medline
4. Scott RM, Smith JL, Robertson RL, et al. **Long-term outcome in children with moyamoya syndrome after cranial revascularization by pial synangiosis.** *J Neurosurg* 2004;100(2 suppl pediatrics):142–49 Medline
5. Dusick JR, Gonzalez NR, Martin NA. **Clinical and angiographic outcomes from indirect revascularization surgery for Moyamoya disease in adults and children: a review of 63 procedures.** *Neurosurgery* 2011;68:34–43; discussion 43 CrossRef Medline
6. Dusick JR, Liebeskind DS, Saver JL, et al. **Indirect revascularization for nonmoyamoya intracranial arterial stenoses: clinical and angiographic outcomes.** *J Neurosurg* 2012;117:94–102 CrossRef Medline
7. Gonzalez NR, Liebeskind DS, Dusick JR, et al. **Intracranial arterial stenoses: current viewpoints, novel approaches, and surgical perspectives.** *Neurosurg Rev* 2013;36:175–84; discussion 184–85 CrossRef Medline
8. Starke RM, Komotar RJ, Connolly ES. **Optimal surgical treatment for Moyamoya disease in adults: direct versus indirect bypass.** *Neurosurg Focus* 2009;26:E8 CrossRef Medline
9. Gonzalez NR, Dusick JR, Connolly M, et al. **Encephaloduroarteriosynangiosis for adult intracranial arterial steno-occlusive disease: long-term single-center experience with 107 operations.** *J Neurosurg* 2015;123:654–61 CrossRef Medline
10. Chimowitz MI, Lynn MJ, Derdeyn CP, et al; SAMMPRIS Trial Investigators. **Stenting versus aggressive medical therapy for intracranial arterial stenosis.** *N Engl J Med* 2011;365:993–1003 CrossRef Medline
11. Derdeyn CP, Chimowitz MI, Lynn MJ, et al; Stenting and Aggressive Medical Management for Preventing Recurrent Stroke in Intracranial Stenosis Trial Investigators. **Aggressive medical treatment with or without stenting in high-risk patients with intracranial artery stenosis (SAMMPRIS): the final results of a randomised trial.** *Lancet* 2014;383:333–41 CrossRef Medline
12. Ginat DT, Smith ER, Robertson RL, et al. **Imaging after direct and indirect extracranial-intracranial bypass surgery.** *AJR Am J Roentgenol* 2013;201:W124–32 CrossRef Medline
13. Blauwblomme T, Lemaitre H, Naggara O, et al. **Cerebral blood flow improvement after indirect revascularization for pediatric Moyamoya disease: a statistical analysis of arterial spin-labeling MRI.** *AJNR Am J Neuroradiol* 2016;37:706–12 CrossRef Medline
14. Yoon HK, Shin HJ, Lee M, et al. **MR angiography of moyamoya disease before and after encephaloduroarteriosynangiosis.** *AJR Am J Roentgenol* 2000;174:195–200 CrossRef Medline
15. Robertson RL, Burrows PE, Barnes PD, et al. **Angiographic changes**

after pial synangiosis in childhood moyamoya disease. *AJNR Am J Neuroradiol* 1997;18:837–45 Medline
16. Lee SK, Kim DI, Jeong EK, et al. **Postoperative evaluation of moyamoya disease with perfusion-weighted MR imaging: initial experience.** *AJNR Am J Neuroradiol* 2003;24:741–47 Medline
17. Liebeskind DS, Sanossian N. **How well do blood flow imaging and collaterals on angiography predict brain at risk?** *Neurology* 2012;79: S105–09 CrossRef Medline
18. Sam K, Poublanc J, Sobczyk O, et al. **Assessing the effect of unilateral cerebral revascularization on the vascular reactivity of the non-intervened hemisphere: a retrospective observational study.** *BMJ Open* 2015;5:e006014 CrossRef Medline
19. Oh SW, Kim YK, Kim SK, et al. **Hemodynamic improvement of anterior cerebral artery territory perfusion induced by bifrontal encephalo(periosteal) synangiosis in pediatric patients with moyamoya disease: a study with brain perfusion SPECT.** *Ann Nucl Med* 2012;26:47–57 CrossRef Medline
20. Dai DW, Zhao WY, Zhang YW, et al. **Role of CT perfusion imaging in evaluating the effects of multiple burr hole surgery on adult ischemic Moyamoya disease.** *Neuroradiology* 2013;55:1431–38 CrossRef Medline
21. Lu CF, Chou YC, Guo WY, et al. **Brain MR perfusion image segmentation using independent component analysis and hierarchical clustering.** *Conf Proc IEEE Eng Med Biol Soc* 2007;2007:5547–50 Medline
22. LaViolette PS, Cohen AD, Prah MA, et al. **Vascular change measured with independent component analysis of dynamic susceptibility contrast MRI predicts bevacizumab response in high-grade glioma.** *Neuro Oncol* 2013;15:442–50 CrossRef Medline
23. Damoiseaux JS, Rombouts SA, Barkhof F, et al. **Consistent resting-state networks across healthy subjects.** *Proc Natl Acad Sci U S A* 2006;103:13848–53 CrossRef Medline
24. Calhoun VD, Liu J, Adali T. **A review of group ICA for fMRI data and ICA for joint inference of imaging, genetic, and ERP data.** *Neuroimage* 2009;45:S163–72 CrossRef Medline
25. Onton J, Westerfield M, Townsend J, et al. **Imaging human EEG dynamics using independent component analysis.** *Neurosci Biobehav Rev* 2006;30:808–22 CrossRef Medline
26. Delorme A, Makeig S. **EEGLAB: an open source toolbox for analysis of single-trial EEG dynamics including independent component analysis.** *J Neurosci Methods* 2004;134:9–21 CrossRef Medline
27. Smith SM, Fox PT, Miller KL, et al. **Correspondence of the brain's functional architecture during activation and rest.** *Proc Natl Acad Sci U S A* 2009;106:13040–45 CrossRef Medline
28. Beckmann CF, Smith SM. **Probabilistic independent component analysis for functional magnetic resonance imaging.** *IEEE Trans Med Imaging* 2004;23:137–52 CrossRef Medline
29. Nichols K, Holmes A. **Non-parametric procedures.** *Statistical Parametric Mapping* 2007;253–72 CrossRef
30. Macchi C, Catini C, Federico C, et al. **Magnetic resonance angiographic evaluation of circulus arteriosus cerebri (circle of Willis): a morphologic study in 100 human healthy subjects.** *Ital J Anat Embryol* 1996;101:115–23 Medline
31. Lee SC, Jeon JS, Kim JE, et al. **Contralateral progression and its risk factor in surgically treated unilateral adult moyamoya disease with a review of pertinent literature.** *Acta Neurochir (Wien)* 2014;156: 103–11 CrossRef Medline
32. Amin-Hanjani S, Singh A, Rifai H, et al. **Combined direct and indirect bypass for moyamoya: quantitative assessment of direct bypass flow over time.** *Neurosurgery* 2013;73: 962–67; discussion 967–68 CrossRef Medline
33. Ryu WS, Park SS, Kim YS, et al. **Long-term natural history of intracranial arterial stenosis: an MRA follow-up study.** *Cerebrovasc Dis* 2014;38:290–96 CrossRef Medline
34. Kim YI, Phi JH, Paeng JC, et al. **In vivo evaluation of angiogenic activity and its correlation with efficacy of indirect revascularization surgery in pediatric Moyamoya disease.** *J Nucl Med* 2014;55: 1467–72 CrossRef Medline
35. Calamante F, Gadian DG, Connelly A. **Delay and dispersion effects in dynamic susceptibility contrast MRI: simulations using singular value decomposition.** *Magn Reson Med* 2000;44:466–73 Medline
36. Wu O, Østergaard L, Weisskoff RM, et al. **Tracer arrival timing-insensitive technique for estimating flow in MR perfusion-weighted imaging using singular value decomposition with a block-circulant deconvolution matrix.** *Magn Reson Med* 2003;50:164–74 CrossRef Medline
37. Kao YH, Teng MM, Liu KC, et al. **Hemodynamic segmentation of MR perfusion images in patients with unilateral carotid stenosis using independent component analysis.** *J Magn Reson Imaging* 2008; 28:1125–32 CrossRef Medline
38. McKeown MJ, Makeig S, Brown GG, et al. **Analysis of fMRI data by blind separation into independent spatial components.** *Hum. Brain Mapp* 1998;6:160–88 Medline
39. Kao YH, Guo WY, Wu YT, et al. **Hemodynamic segmentation of MR brain perfusion images using independent component analysis, thresholding, and Bayesian estimation.** *Magn Reson Med* 2003;49: 885–94 CrossRef Medline
40. LaViolette PS, Daun MK, Paulson ES, et al. **Effect of contrast leakage on the detection of abnormal brain tumor vasculature in high-grade glioma.** *J Neurooncol* 2014;16:543–49 CrossRef Medline
41. Ramalho J, Semelka RC, Ramalho M, et al. **Gadolinium-based contrast agent accumulation and toxicity: an update.** *AJNR Am J Neuroradiol* 2016;37:1192–98 CrossRef Medline
42. Stojanov D, Aracki-Trenkic A, Benedeto-Stojanov D. **Gadolinium deposition within the dentate nucleus and globus pallidus after repeated administrations of gadolinium-based contrast agents-current status.** *Neuroradiology* 2016;58:433–441 CrossRef Medline

In Vivo Assessment of the Impact of Regional Intracranial Atherosclerotic Lesions on Brain Arterial 3D Hemodynamics

C. Wu, S. Schnell, P. Vakil, A.R. Honarmand, S.A. Ansari, J. Carr, M. Markl, and S. Prabhakaran

ABSTRACT

BACKGROUND AND PURPOSE: Intracranial atherosclerosis induces hemodynamic disturbance, which is not well-characterized, particularly in cerebral flow redistribution. We aimed to characterize the impact of regional stenotic lesions on intracranial hemodynamics by using 4D flow MR imaging.

MATERIALS AND METHODS: 4D flow MR imaging was performed in 22 symptomatic patients (mean age, 68.4 ± 14.2 years) with intracranial stenosis (ICA, $n = 7$; MCA, $n = 9$; basilar artery, $n = 6$) and 10 age-appropriate healthy volunteers (mean age, 60.7 ± 8.1 years). 3D blood flow patterns were visualized by using time-integrated pathlines. Blood flow and peak velocity asymmetry indices were compared between patients and healthy volunteers in 4 prespecified arteries: ICAs, MCAs, and anterior/posterior cerebral arteries.

RESULTS: 3D blood flow pathlines demonstrated flow redistribution across cerebral arteries in patients with unilateral intracranial stenosis. For patients with ICA stenosis compared with healthy volunteers, significantly lower flow and peak velocities were identified in the ipsilateral ICA ($P = .001$ and $P = .001$) and MCA ($P < .001$ and $P = .001$), but higher flow, in the ipsilateral PCA ($P < .001$). For patients with MCA stenosis, significantly lower flow and peak velocities were observed in the ipsilateral ICA ($P = .009$ and $P = .045$) and MCA ($P < .001$ and $P = .005$), but significantly higher flow was found in the ipsilateral posterior cerebral artery ($P = .014$) and anterior cerebral artery ($P = .006$). The asymmetry indices were not significantly different between patients with basilar artery stenosis and the healthy volunteers.

CONCLUSIONS: Regional intracranial atherosclerotic lesions not only alter distal arterial flow but also significantly affect ipsilateral collateral arterial hemodynamics.

ABBREVIATIONS: ACA = anterior cerebral artery; AI-F = flow rate asymmetry index; AI-V = peak velocity asymmetry index; BA = basilar artery; ICAD = intracranial atherosclerotic disease; PCA = posterior cerebral artery; PC-MRA = phase-contrast MR angiogram; VENC = velocity encoding

Intracranial atherosclerotic disease (ICAD) is characterized by narrowing and blockage of the major intracranial arteries due to accumulation of atherosclerotic plaques within the vessel wall. It represents one of the most common causes of ischemic stroke worldwide, with higher occurrence rates in Asians, Hispanics, and blacks than in whites.[1]

Patients with symptomatic ICAD have a high risk of stroke recurrence, particularly those with high-grade (70%–99%) stenosis.[2] Currently, aggressive medical management is recommended for the treatment of ICAD. However, approximately 12% of patients with ICAD experience a recurrent stroke within the first year.[3] Therefore, careful risk stratification and monitoring of ICAD are paramount. In particular, hemodynamic failure may impart a high risk in a subset of patients with ICAD. Local hemodynamic alterations secondary to ICAD, particularly in the locations proximal and distal to the stenosis, may be useful markers of recurrent stroke risk.[4,5] Because DSA is invasive, noninvasive alternatives such as sonography and 2D phase-contrast MR imaging have been used to measure hemodynamic changes in patients with ICAD, classify stenosis severity, predict risk of recurrent stroke, and detect in-stent restenosis after stent placement.[6-9] However, these techniques may be limited by low reproducibility, an inadequate insonation window, or insufficient anatomic coverage. In addition, the impact of atherosclerotic lesions on the hemodynamics in other vascular territories and the redistribution

Received June 20, 2016; accepted after revision October 26.

From the Department of Biomedical Engineering (C.W., M.M.), McCormick School of Engineering, Northwestern University, Chicago, Illinois; Departments of Radiology (C.W., S.S., P.V., A.R.H., S.A.A., J.C., M.M.), Neurological Surgery (S.A.A.), and Neurology (S.P.), Feinberg School of Medicine, Northwestern University, Chicago, Illinois; and Philips Healthcare (C.W.), Gainesville, Florida.

This work was supported by American Heart Association Predoctoral Fellowship 14PRE18370014 and American Heart Association Scientist Development Grant 16SDG30420005.

Please address correspondence to Can Wu, PhD, Department of Radiology, Northwestern University, 737 N Michigan Ave, Suite 1600, Chicago, IL 60611; e-mail: canwu2016@u.northwestern.edu

Indicates article with supplemental on-line tables.

http://dx.doi.org/10.3174/ajnr.A5051

of cerebral blood flow through circle of Willis collaterals are not well-characterized. Furthermore, a 3D characterization of the stenosis-induced hemodynamic changes across the entire cerebral vasculature and a comparison of the hemodynamics between patients with ICAD and age-controlled healthy volunteers have not been previously reported, to our knowledge.

4D flow MR imaging (ie, time-resolved 3D phase-contrast MR imaging with 3-directional velocity-encoding) provides reliable flow measurements consistent with 2D phase-contrast MR imaging and offers additional benefits, including retrospective flow quantification at any vessel location within the imaging volume and 3D blood flow visualization of the entire vasculature.[10-12] Recently, 4D flow MR imaging has attracted increasing interest in the assessment of intracranial hemodynamics in patients with cerebrovascular diseases, such as intracranial aneurysms, vein of Galen malformation, and cerebral arteriovenous malformation.[13-17]

The purpose of this study was to evaluate the impact of regional intracranial atherosclerotic lesions on cerebral artery hemodynamics in comparison with healthy volunteers by using 4D flow MR imaging.

MATERIALS AND METHODS

Study Subjects

Between 2012 and 2014, clinical records of symptomatic patients with ICAD who had undergone 4D flow MR imaging were retrospectively reviewed ($n = 26$). The study included only patients with moderate (50%–70%) to severe (>70%) symptomatic intracranial stenosis. DSA, the criterion standard for stenosis measurement, is associated with a small but noticeable risk of complications; moreover, in the absence of an endovascular intervention, it is unreasonable to mandate its use. Alternatively, CTA has excellent diagnostic accuracy with a sensitivity and specificity of >97% compared with DSA.[18] TOF-MRA has been demonstrated to be a reliable tool for assessing intracranial artery stenosis,[19] but contrast-enhanced MRA was superior to TOF-MRA for the detection of ICA stenosis.[20] In our study, stenosis severity was evaluated on the basis of clinically available CTA or a combination of TOF-MRA and contrast-enhanced MRA with a circle of Willis FOV. Two patients with near-occlusion stenosis were excluded because flow analysis was not possible due to slow flow, and 2 additional patients with bilateral stenosis were also excluded. Twenty-two patients (mean age, 68.4 ± 14.2 years; 10 women) and 10 age-appropriate healthy volunteers (mean age, 60.7 ± 8.1 years; 4 women) were included (Table). The stenosed vessels for patients with ICAD were as follows: unilateral intracranial ICA ($n = 7$) with stenosis locations in the cavernous ($n = 5/7$) and petrous ($n = 2/7$) segments, unilateral MCA ($n = 9$), and the basilar artery (BA, $n = 6$). The study was conducted in accordance with a protocol approved by the local institutional review board, which permitted retrospective chart review. Informed consent was obtained from all healthy volunteers.

MR Imaging

All measurements were performed on a 1.5T or 3T MR imaging scanner (Magnetom Avanto or Skyra; Siemens, Erlangen, Germany). 4D flow MR imaging was performed after standard T1-MPRAGE and 3D TOF-MRA sequences. Cerebral 3D blood flow was measured by using 4D flow MR imaging with 3-directional velocity-encoding and 3D volumetric coverage of the major intracranial vessels (see Fig 1 for the volume coverage). The scan was prospectively gated with electrocardiography R waves produced by chest leads. Pulse sequence parameters were as follows: TR = 5.4 ms, TE = 2.8 ms, flip angle = 15°, velocity sensitivity (velocity-encoding [VENC]) = 100 cm/s, FOV = 220 × 160 mm^2, band-

Demographics and clinical features of the 22 patients with ICAD and 10 age-appropriate healthy volunteers included in the study[a]

	Subject Groups		
	Healthy Volunteers	Patients with ICAD	*P* Values
Subject characteristics			
No.	10	22	–
Age (yr)	60.7 ± 8.1	68.4 ± 14.2	.124
Sex (male/female)	6:4	12:10	–
Height (m)	1.74 ± 0.12	1.71 ± 0.11	.503
Weight (kg)	79.8 ± 13.7	76.0 ± 14.8	.557
Body mass index (kg/m^2)	26.2 ± 2.9	26.0 ± 3.9	.878
Stenosed vessels			
ICA (moderate/severe)	–	7 (4/3)	–
MCA (moderate/severe)	–	9 (3/6)	–
BA (moderate/severe)	–	6 (2/4)	–

Note:—– indicates not applicable.

[a] "Moderate" and "severe" indicate stenosis of 50%–70% and >70%, respectively. *P* values are calculated using the Mann-Whitney *U* test; $P < .05$ was considered statistically significant.

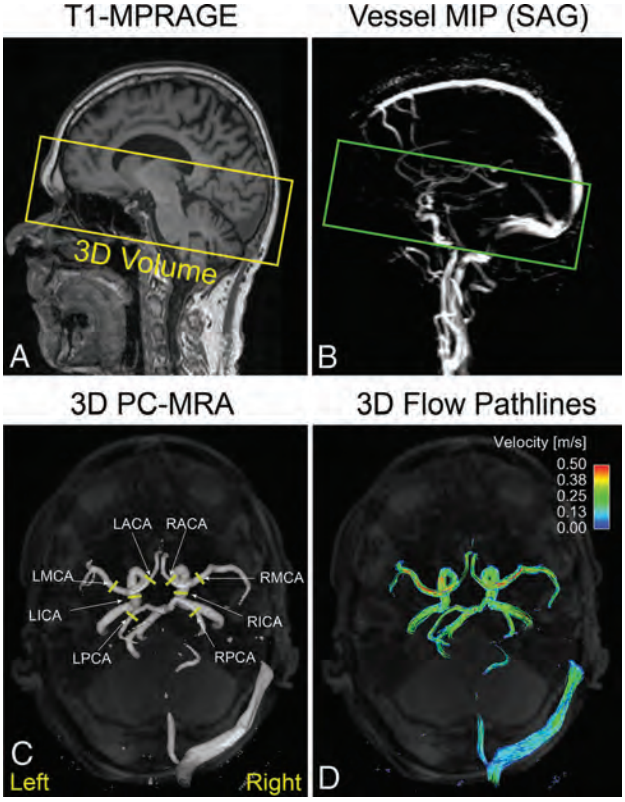

FIG 1. Sagittal T1-weighted MPRAGE (*A*) and vessel MIP (*B*) images of the head show the 3D volume coverage for 4D flow imaging. A 3D phase-contrast MR angiogram was derived from the 4D flow data and was used for positioning 2D analysis planes in the major cerebral arteries (*C*). Time-integrated 3D pathlines illustrate the cumulative flow path of the vessels within the 3D PC-MRA volume over 1 cardiac cycle (*D*). L indicates left; R, right.

width = 445 Hz/pixel, temporal resolution = 43 ms, voxel size = (1.1–1.2) × (1.1–1.2) × (1.2–1.4) mm^3, acceleration factor R = 2 (generalized autocalibrating partially parallel acquisition), acquisition time = 15–20 minutes depending on the heart rate of the subjects.

3D Blood Flow Visualization

All 4D flow MR imaging data were preprocessed by using an in-house software programmed in Matlab (MathWorks, Natick, Massachusetts), as previously described.[21] The preprocessing included random noise reduction as well as corrections for velocity aliasing and phase offsets from Maxwell cross-terms and eddy currents. In addition, a 3D phase-contrast MR angiogram (PC-MRA) was derived from the magnitude and phase-difference data (Fig 1*C*). The preprocessed data were then further analyzed in a 3D visualization software package (EnSight; CEI, Apex, North Carolina). Cerebral 3D blood flow was visualized by using time-integrated 3D pathlines, which illustrated the collective pathline traces of 25,000 virtual particles equally distributed within the 3D PC-MRA over 1 cardiac cycle (Fig 1*D*). The color coding of the pathlines reflects the magnitude of blood flow velocities in the vasculature. For display purposes, a velocity window of 0–50 cm/s was used to better visualize the flow patterns in the low-velocity vascular territories (eg, poststenosis, posterior circulation, and so forth).

Vascular Flow Quantification

As illustrated in Fig 1*C*, for normal cerebral vessels (ie, all vessels of healthy volunteers and those vessels without stenosis in patients), 2D analysis planes were manually positioned perpendicular to 4 prespecified pairs of cerebral arteries by using the 3D PC-MRA for anatomic orientation (ICA: between the lacerum C3 and cavernous C4 segments; MCA: middle M1 segment; anterior cerebral artery [ACA]: middle A1 segment; posterior cerebral artery [PCA]: middle P2 segment). For the stenosed vessel, an analysis plane was placed at approximately 1 cm distal to the location of the stenosis to measure poststenotic flow. For each analysis plane, volumetric flow rate (milliliter/second) and peak velocities (meter/second) were calculated. The flow analysis was performed by a scientist (C.W.) with >7 years of MR imaging research experience. A recent study by our group reported an excellent inter-observer agreement (Lin concordance correlation coefficient, $\rho_c = 0.996$) for quantitative blood flow and velocity measurements in intracranial arteries.[12] The same criterion was applied for quantitative flow assessment in this study.

Flow and Velocity Asymmetry Indices

Absolute cerebral blood flow and velocity values are age- and sex-dependent.[12,22] Thus, the flow/velocity ratios (asymmetry indices) between the affected (left) and nonaffected (right) arteries were used to compare the differences between patients with ICAD and healthy volunteers to minimize the impact of age and sex on flow analysis. The absolute values of the velocities and flow rates are shown in On-line Tables 1–4.

Asymmetry indices were calculated as the ratios of the flow rate (AI-F) and peak velocities (AI-V) between the affected and nonaffected side (affected/nonaffected) for patients with unilateral ICA and MCA stenosis or between the left and right sides (left/right) for healthy volunteers and patients with BA stenosis. In addition, schematic vascular flow models were created to characterize the normal cerebral flow distribution and stenosis-induced flow redistribution in the ipsilateral cerebral arteries compared with the contralateral counterparts.

Statistical Analysis

The asymmetry indices in each subgroup were illustrated by using box-and-whisker plots. Mann-Whitney *U* tests were used to compare the asymmetry indices between patient subgroups and healthy volunteers. In addition, posterior-to-anterior flow ratios, the ratios of the posterior flow (PCA flow) and anterior flow (summation of ACA and MCA flow), were compared between patients with BA stenosis and healthy volunteers by using a Mann-Whitney *U* test. All statistical analyses were performed by using the MedCalc software package (Version 14.8.1; MedCalc Software, Mariakerke, Belgium). $P < .05$ was considered statistically significant.

RESULTS

Study Cohort

Demographics and clinical features of the patients with ICAD and healthy volunteers are summarized in the Table. There were no significant differences between healthy volunteers and patients with ICAD in terms of age, height, weight, and body mass index.

3D Visualization of Intracranial Hemodynamics

3D flow pathlines in healthy volunteers demonstrated symmetric blood flow velocities and patterns in all prespecified cerebral arteries (Fig 2*A*, an example of the volunteers). In contrast, blood flow was compromised at the location of arterial stenosis (*thick yellow arrows*) compared with the contralateral counterpart (*thin white arrows*) in patients with unilateral ICA (Fig 2*B*) and unilateral MCA (Fig 2*C*) stenosis. Additionally, we observed elevated ipsilateral PCA flow in the patients with ICA stenosis (*small pink arrow*, Fig 2*B*) as well as increased ipsilateral ACA flow in the patients with MCA stenosis (*small pink arrow*, Fig 2*C*). Although blood flow was substantially decreased in the stenosed BA (*thick yellow arrow*, Fig 2*D*), no side-to-side flow difference was observed in a patient with BA stenosis (Fig 2*D*).

Flow and Peak Velocity Asymmetry Indices

For patients with ICA stenosis compared with healthy volunteers, the flow rate and peak velocity asymmetry indices (affected/nonaffected ratios) were both significantly lower in the ICA (Fig 3*A*, AI-F: 0.40 ± 0.17 versus 0.97 ± 0.06, $P = .001$; Fig 4*A*, AI-V: 0.57 ± 0.16 versus 0.95 ± 0.09, $P = .001$) and MCA (Fig 3*B*, AI-F: 0.55 ± 0.23 versus 0.99 ± 0.06, $P < .001$; Fig 4*B*, AI-V: 0.72 ± 0.18 versus 1.04 ± 0.13, $P = .002$). In contrast, the flow asymmetry index was significantly higher in the PCA (Fig 3*C*, AI-F: 1.55 ± 0.33 versus 1.00 ± 0.06, $P < .001$).

For patients with MCA stenosis compared with healthy volunteers, the flow and velocity asymmetry indices were both significantly lower in the ICA (Fig 3*A*, AI-F: 0.77 ± 0.27 versus 0.97 ± 0.06, $P = .009$; Fig 4*A*, AI-V: 0.84 ± 0.18 versus 0.95 ± 0.09, $P = .045$) and MCA (Fig 3*B*, AI-F: 0.45 ± 0.24 versus 0.99 ± 0.06, $P <$

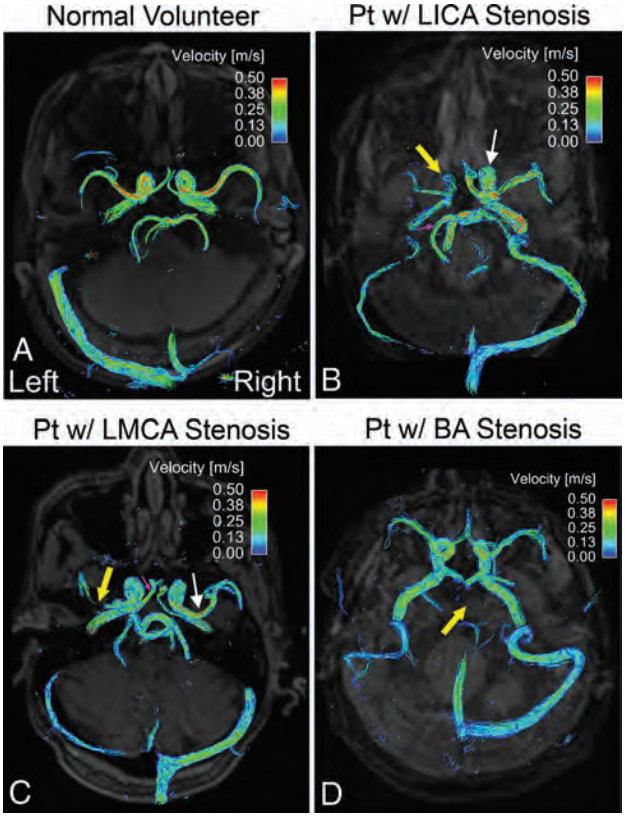

FIG 2. Time-integrated 3D pathlines illustrate symmetric and coherent flow velocities of the left and right cerebral arteries in a healthy volunteer (*A*). Reduced blood flow velocities are observed in the stenosed vessel (*thick yellow arrows*) compared with the contralateral counterpart (*thin white arrows*) in 2 patients with left ICA (*B*) and left MCA (*C*) stenosis. The *pink arrows* indicate augmented ipsilateral collateral flow. In a patient with BA stenosis (*D*), blood flow velocity is substantially decreased in the severely stenosed BA (*thick yellow arrow*; pathlines are invisible due to slow flow) but shows no significant side-to-side difference of flow velocities in the bilateral cerebral arteries. w/ indicates with.

.001; Fig 4*B*, AI-V: 0.68 ± 0.27 versus 1.04 ± 0.13, $P = .005$). By comparison, the indices were significantly higher in the PCA (Fig 3*C*, AI-F: 1.33 ± 0.49 versus 1.00 ± 0.06, $P = .014$) and ACA (Fig 3*D*, AI-F: 1.57 ± 0.54 versus 1.02 ± 0.19, $P = .006$; Fig 4*D*, AI-V: 1.29 ± 0.39 versus 0.99 ± 0.13, $P = .042$).

The flow and velocity asymmetry indices were not significantly different between patients with BA stenosis and healthy volunteers in any prespecified location. However, the posterior-to-anterior flow ratios in patients with BA stenosis (0.23 ± 0.05) were significantly lower ($P = .030$) compared with the healthy volunteers (0.37 ± 0.16).

ICAD Flow-Redistribution Model

Figure 5 illustrates the normal and stenosed schematic vascular flow models that include the 4 prespecified artery pairs. For the normal vascular model (Fig 5*A*), blood flow was comparable in the cerebral artery pairs. However, in the ICA stenosis model (Fig 5*B*), blood flow decreased in the ipsilateral ICA and MCA, but increased in the ipsilateral PCA compared with the contralateral counterparts. In the MCA stenosis model (Fig 5*C*), blood flow decreased in the ipsilateral ICA and MCA, but increased in the ipsilateral PCA and ACA. In contrast, there were no side-to-side flow differences in the BA stenosis model (Fig 5*D*).

DISCUSSION

The results of this study demonstrate the potential of 4D flow MR imaging for the comprehensive evaluation of intracranial hemodynamics in patients with ICAD. The findings demonstrate that focal intracranial atherosclerotic lesions not only alter vascular flow dynamics in the stenotic artery but also significantly influence the regional hemodynamics in other vascular territories. Indeed, unilateral intracranial atherosclerotic lesions cause cerebral blood flow redistribution across ipsilateral circle of Willis collaterals.

Catheter cerebral angiography, though invasive, remains the definitive diagnostic tool for the quantification of stenosis severity and assessment of collateral flow. Intracranial atherosclerotic lesions are dynamic and may progress or regress with time, and symptomatic ICAD involves a high recurrence rate.[1,23] Thus, regular monitoring of the lesions may provide quantitative metrics of hemodynamic alternations, which may predict stroke risk and response to therapy. Noninvasive imaging modalities, such as MRA and transcranial Doppler, have high accuracy in excluding intracranial stenosis. However, these techniques may result in over- or underestimation of the stenosis due to dephasing artifacts, flow signal loss, or inadequate insonation window.[24]

Currently, intracranial hemodynamic disturbance in patients with ICAD is primarily assessed by sonography or quantitative MRA (2D PC-MRA).[6,8,9,25-27] However, very few studies have been performed to characterize the 3D blood flow disturbance and flow redistribution across the major cerebral arteries in patients with ICAD. An early study by Hope et al[28] reported that TOF-MRA overestimated stenosis, and 4D flow MR imaging velocity measurements could improve the accuracy of the diagnosis. Hemodynamic measurements using 3D blood flow patterns can enhance anatomic vessel imaging in that the quantitative hemodynamic information not only improves diagnosis but can potentially be used in prognosis and risk stratification.

The impact of regional atherosclerotic lesions on the flow redistribution across cerebral vessels remains incompletely understood. Using quantitative MRA, Ruland et al[29] observed elevated ipsilateral PCA flow in patients with ICA or MCA stenosis. van Everdingen et al[30] reported reduced ipsilateral MCA flow in patients with ICA occlusion. In our study, we found decreased ipsilateral MCA flow and increased ipsilateral PCA flow in patients with ICA or MCA stenosis, which is in agreement with the previous findings. Additionally, we identified increased ipsilateral ACA flow in patients with MCA stenosis.

Previous studies have demonstrated that the interhemispheric differences of cerebral flow parameters in healthy subjects were not significant. An early study by Sorteberg et al[31] reported that there were only minor side-to-side differences of blood flow velocities in healthy adults and a difference of >14% was considered abnormal in the ICAs and MCAs. Obata et al[32] also identified no significant difference between left and right ICA flow in healthy subjects. We corroborated these findings in healthy volunteers and noted significant side-to-side flow dif-

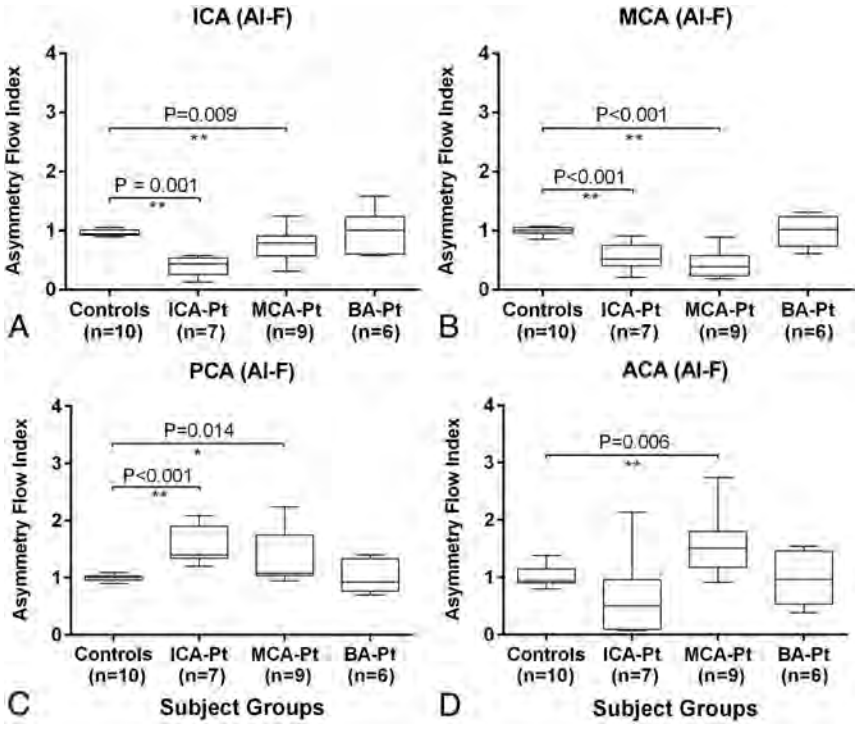

FIG 3. Asymmetry index of the blood flow in 4 major cerebral vessel locations (*A*, ICA; *B*, MCA; *C*, PCA; and *D*, ACA) in patients with stenosis in the ICA ($n = 7$), MCA ($n = 9$), and BA ($n = 6$) compared with age-appropriate healthy volunteers ($n = 10$). Single and double *asterisks* indicate significant differences with $.01 \leq P < .05$ and $P < .01$, respectively. ICA-Pt, MCA-Pt, and BA-Pt are patients with ICA, MCA, and BA stenosis, respectively.

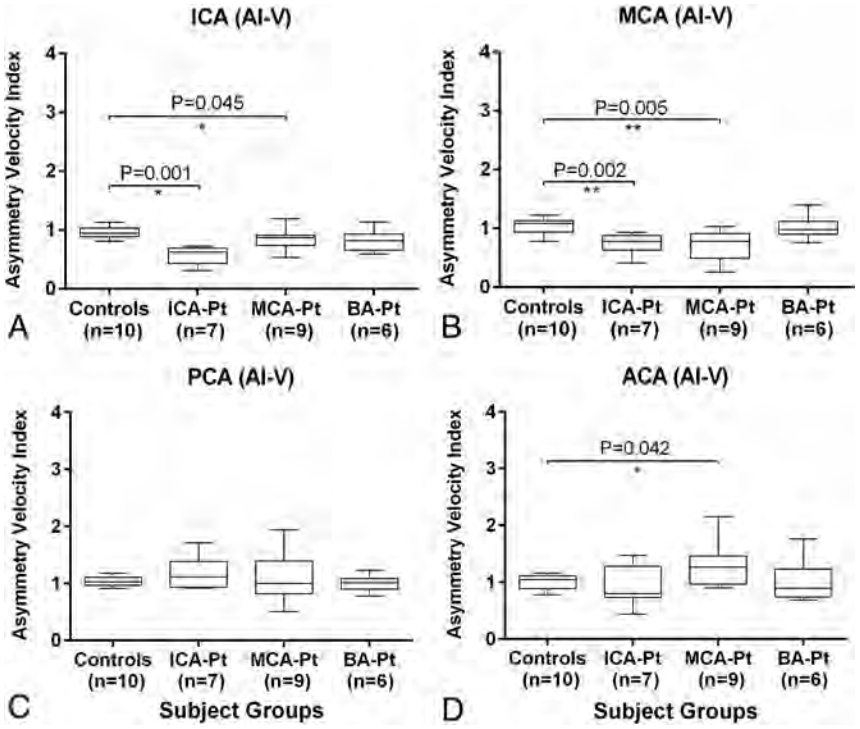

FIG 4. Asymmetry index of the peak velocities in 4 major cerebral vessel locations (*A*, ICA; *B*, MCA; *C*, PCA; and *D*, ACA) in patients with stenosis in the ICA ($n = 7$), MCA ($n = 9$), and BA ($n = 6$) compared with age-appropriate healthy volunteers ($n = 10$). Single and double *asterisks* indicate significant differences with $.01 \leq P < .05$ and $P < .01$, respectively. ICA-Pt, MCA-Pt, and BA-Pt are patients with ICA, MCA, and BA stenosis, respectively.

ferences in symptomatic patients with unilateral ICA or MCA stenosis, consistent with prior observations.[29,30,33]

Collateral flow has been recognized as an independent predictor of recurrent stroke risk in patients with symptomatic intracranial atherosclerosis.[34] In patients with unilateral ICA stenosis, we observed significantly decreased flow in the ipsilateral ICA and MCA but increased flow in the ipsilateral PCA, indicating possible PCA-to-MCA collateral flow pathways to maintain necessary perfusion pressure in the MCA territory. The finding is consistent with previous studies that reported higher blood flow or velocities in the ipsilateral PCA in patients with ICA lesions.[29,35] Similarly, in patients with unilateral MCA stenosis, we identified significantly decreased flow in the ipsilateral ICA and MCA but increased flow in the ipsilateral ACA and PCA, suggesting potential ACA-to-MCA and PCA-to-MCA collateral flow pathways via leptomeningeal anastomoses.[36] The finding also agrees with previous reports that have shown elevated flow or velocities in the ipsilateral ACA and PCA in patients with MCA stenosis or occlusion.[37,38] In contrast, no side-to-side differences of the flow parameters were observed in patients with BA stenosis, indicating no interhemispheric difference of BA flow distribution. However, significantly lower posterior-to-anterior flow ratios in patients with BA stenosis compared with healthy volunteers indicate hemodynamic compromise in the posterior circulation.

For image acquisition, 1.5T and 3T MR imaging scanners were used, depending on the availability of the scanners. However, previous studies have shown that the influence of different field strengths on quantitative blood flow assessment was minor.[10,39] Quantitative flow measurements in intracranial vessels and the thoracic aorta were not significantly different between 1.5T and 3T.

Limitations

The small number of patients in each stenosis subgroup is a major limitation of the study, which precludes a systematic analysis of the association between stenosis severity and quantitative flow parameters and the influence of differ-

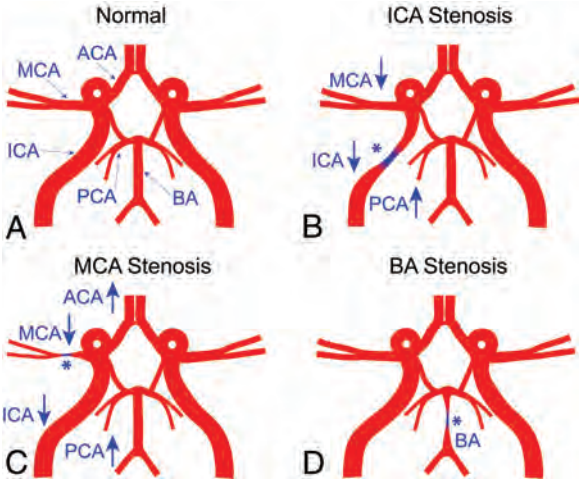

FIG 5. Schematic cerebral vascular models (*A*, normal; *B*, ICA stenosis; *C*, MCA stenosis; and *D*, BA stenosis) illustrate the impact of regional stenotic lesions on blood flow in other cerebral vascular territories. The *asterisk* represents the location of the stenosis. The up arrow and down arrow indicate a relative increase or decrease of flow in the local vessel compared with the contralateral counterpart in patients with intracranial atherosclerosis.

ent vascular variants of the circle of Willis (eg, ACA or PCA hypoplasia) and intracranial atherosclerotic risk factors (eg, diabetes, hypertension, hypercholesterolemia, and so forth) on cerebral hemodynamics. The flow analysis was restricted to patients with moderate and severe stenosis because greater hemodynamic alterations are expected in this group of patients compared with patients with mild stenosis. In addition, dominant ACA and PCA flow and potential blood flow redistribution across the ipsilateral circle of Willis collaterals (ie, through anterior/posterior communicating arteries) might be confounding factors to the collateral flow analysis. Further studies with larger patient cohorts, including those with mild stenosis, are warranted to investigate the impact of different vascular morphology, stenosis severity, and atherosclerosis risk factors on intracranial hemodynamic changes. Nevertheless, to our knowledge, this is the largest cohort to date for 3D blood flow visualization of stenosis-induced intracranial flow redistribution as well as a quantitative comparison of flow and velocity asymmetry in the major cerebral arteries between patients with ICAD and healthy volunteers.

The current 4D flow MR imaging technique is also limited by insufficient spatial resolution for the characterization of blood flow at sites of critical or severe stenosis. Instead, poststenotic flow was used to represent the regional flow in the stenotic artery. The in-plane resolution of 1.1–1.2 mm in this study was appropriate for measuring blood flow in the large cerebral arteries (eg, ICAs and MCAs). However, the accuracy of flow quantification in the smaller arteries (eg, ACAs and PCAs) may be compromised by partial volume effects. In addition, flow measurements in the posterior communicating artery and leptomeningeal collaterals are not possible. Therefore, a higher magnetic field (7T) with increased spatial resolution may be required for improved flow assessment in the smaller vessels.

The wide use of 4D flow MR imaging in clinical applications is hindered by its relatively long scanning time. Noticeable effort has been made to accelerate data acquisition by using non-Cartesian sampling or compressed sensing techniques. For example, the phase contrast with vastly undersampled isotropic projection reconstruction sequence based on a highly undersampled 3D radial acquisition enables a total imaging time of <8 minutes.[40] Basha et al[41] reported an acceleration factor of 7 by using randomly undersampled echo-planar imaging with compressed sensing reconstruction. A recent study by Dyvorne et al[42] has demonstrated the feasibility of an abdominal 4D flow MR imaging scan in a single breath-hold by combining spiral sampling and dynamic compressed sensing. In addition, the limited availability of the 4D flow MR imaging sequence further hinders its wide implementation in clinical sites.

In addition, single-VENC 4D flow MR imaging includes an inherent trade-off related to the selection of an optimal VENC. On the one hand, the VENC should be higher than the maximum expected velocity to avoid velocity aliasing. On the other hand, a VENC that is too high undermines the reliability for detecting slow flow (eg, reduced flow in the stenosed vessels) because the velocity noise level is proportional to the VENC. Dual- or multi-VENC techniques have been proposed to extend the dynamic range of velocities that can be reliability assessed.[43,44] Complex flow characteristics (eg, disturbed or turbulent flow fluctuations associated with vascular stenosis) cause flow-related signal loss and present another challenge for accurate poststenotic flow assessment. Ultrashort TE 4D flow MR imaging has been shown to provide more reliable stenotic flow quantification.[45,46] A recent study by Petersson et al[47] reported a stack-of-spiral technique, which provided more favorable stenotic flow assessment against the conventional Cartesian counterpart.

CONCLUSIONS

The study demonstrates the potential of 4D flow MR imaging for comprehensive hemodynamic characterization in patients with intracranial atherosclerosis. The results indicate that regional atherosclerotic lesions can not only alter local vascular flow dynamics but also significantly influence the hemodynamics in other vascular territories, potentially due to collateral flow recruitment. 4D flow MR imaging provides additional hemodynamic information that may assist in elucidating the pathophysiology and autoregulation mechanism in intracranial atherosclerosis and in predicting the risk of recurrent stroke.

Disclosures: Can Wu—*RELATED*: *Grant*: American Heart Association, *Comments*: American Heart Association Predoctoral Fellowship 14PRE18370014.* Sameer Ansari—*UNRELATED*: *Grants/Grants Pending*: Radiological Society of North America, American Heart Association, and National Institutes of Health grants.* James Carr—*UNRELATED*: *Board Membership*: Bayer AG, *Comments*: Advisory Board; *Grants/Grants Pending*: Bayer AG, Siemens.* Shyam Prabhakaran—*UNRELATED*: *Grants/Grants Pending*: National Institute of Neurological Disorders and Stroke, Patient-Centered Outcomes Research Institute*; *Royalties*: UpToDate. *Money paid to the institution.

REFERENCES

1. Arenillas JF. **Intracranial atherosclerosis: current concepts.** *Stroke* 2011;42:S20–23 CrossRef Medline
2. Jeng JS, Tang SC, Liu HM. **Epidemiology, diagnosis and management of intracranial atherosclerotic disease.** *Expert Rev Cardiovasc Ther* 2010;8:1423–32 CrossRef Medline
3. Chimowitz MI, Lynn MJ, Derdeyn CP, et al; SAMMPRIS Trial Investigators. **Stenting versus aggressive medical therapy for intracranial arterial stenosis.** *N Engl J Med* 2011;365:993–1003 CrossRef Medline
4. Prabhakaran S, Warrior L, Wells KR, et al. **The utility of quantitative magnetic resonance angiography in the assessment of intracranial in-stent stenosis.** *Stroke* 2009;40:991–93 CrossRef Medline

5. Prabhakaran S, Wells KR, Jhaveri MD, et al. **Hemodynamic changes following Wingspan stent placement–a quantitative magnetic resonance angiography study.** *J Neuroimaging* 2011;21:e109–13 CrossRef Medline
6. Amin-Hanjani S, Alaraj A, Calderon-Arnulphi M, et al. **Detection of intracranial in-stent restenosis using quantitative magnetic resonance angiography.** *Stroke* 2010;41:2534–38 CrossRef Medline
7. Amin-Hanjani S, Rose-Finnell L, Richardson D, et al; VERiTAS Study Group. **Vertebrobasilar Flow Evaluation and Risk of Transient Ischaemic Attack and Stroke study (VERiTAS): rationale and design.** *Int J Stroke* 2010;5:499–505 CrossRef Medline
8. Baumgartner RW, Mattle HP, Schroth G. **Assessment of ≥50% and <50% intracranial stenoses by transcranial color-coded duplex sonography.** *Stroke* 1999;30:87–92 CrossRef Medline
9. Wang L, Xing Y, Li Y, et al. **Evaluation of flow velocity in unilateral middle cerebral artery stenosis by transcranial Doppler.** *Cell Biochem Biophys* 2014;70:823–30 CrossRef Medline
10. Bammer R, Hope TA, Aksoy M, et al. **Time-resolved 3D quantitative flow MRI of the major intracranial vessels: initial experience and comparative evaluation at 1.5T and 3.0T in combination with parallel imaging.** *Magn Reson Med* 2007;57:127–40 CrossRef Medline
11. Markl M, Frydrychowicz A, Kozerke S, et al. **4D flow MRI.** *J Magn Reson Imaging* 2012;36:1015–36 CrossRef Medline
12. Wu C, Honarmand AR, Schnell S, et al. **Age-related changes of normal cerebral and cardiac blood flow in children and adults aged 7 months to 61 years.** *J Am Heart* 2016;5:pii: e002657 CrossRef Medline
13. Ansari SA, Schnell S, Carroll T, et al. **Intracranial 4D flow MRI: toward individualized assessment of arteriovenous malformation hemodynamics and treatment-induced changes.** *AJNR Am J Neuroradiol* 2013;34:1922–28 CrossRef Medline
14. Schnell S, Ansari SA, Vakil P, et al. **Three-dimensional hemodynamics in intracranial aneurysms: influence of size and morphology.** *J Magn Reson Imaging* 2014;39:120–31 CrossRef Medline
15. Wu C, Ansari SA, Honarmand AR, et al. **Evaluation of 4D vascular flow and tissue perfusion in cerebral arteriovenous malformations: influence of Spetzler-Martin grade, clinical presentation, and AVM risk factors.** *AJNR Am J Neuroradiol* 2015;36:1142–49 CrossRef Medline
16. Wu C, Schnell S, Markl M, et al. **Combined DSA and 4D flow demonstrate overt alterations of vascular geometry and hemodynamics in an unusually complex cerebral AVM.** *Clin Neuroradiol* 2015 Oct 16. [Epub ahead of print] CrossRef Medline
17. Wu C, Schoeneman SE, Kuhn R, et al. **Complex alterations of intracranial 4D hemodynamics in vein of Galen aneurysmal malformations during staged endovascular embolization.** *Operative Neurosurg* 2016;12:239–49 CrossRef
18. Nguyen-Huynh MN, Wintermark M, English J, et al. **How accurate is CT angiography in evaluating intracranial atherosclerotic disease?** *Stroke* 2008;39:1184–88 CrossRef Medline
19. Choi CG, Lee DH, Lee JH, et al. **Detection of intracranial atherosclerotic steno-occlusive disease with 3D time-of-flight magnetic resonance angiography with sensitivity encoding at 3T.** *AJNR Am J Neuroradiol* 2007;28:439–46 Medline
20. Debrey SM, Yu H, Lynch JK, et al. **Diagnostic accuracy of magnetic resonance angiography for internal carotid artery disease: a systematic review and meta-analysis.** *Stroke* 2008;39:2237–48 CrossRef Medline
21. Bock J, Kreher BW, Hennig J, et al. **Optimized pre-processing of time-resolved 2D and 3D phase contrast MRI data.** In: *Proceedings of the Scientific Meeting and Exhibition of the International Society for Magnetic Resonance in Medicine*, Berlin, Germany. May 19–25, 2007:3138
22. Bakker SL, de Leeuw FE, den Heijer T, et al. **Cerebral haemodynamics in the elderly: the Rotterdam Study.** *Neuroepidemiology* 2004;23:178–84 CrossRef Medline
23. Akins PT, Pilgram TK, Cross DT 3rd, et al. **Natural history of stenosis from intracranial atherosclerosis by serial angiography.** *Stroke* 1998;29:433–38 CrossRef Medline
24. Khan M, Naqvi I, Bansari A, et al. **Intracranial atherosclerotic disease.** *Stroke Res Treat* 2011;2011:282845 CrossRef Medline
25. Amin-Hanjani S, Du XJ, Zhao MD, et al. **Use of quantitative magnetic resonance angiography to stratify stroke risk in symptomatic vertebrobasilar disease.** *Stroke* 2005;36:1140–45 CrossRef Medline
26. Mizuma A, Ishikawa T, Kajihara N, et al. **Dynamic cross-sectional changes of the middle cerebral artery in atherosclerotic stenosis detected by 3.0-Tesla MRI.** *Neurol Res* 2014;36:795–99 CrossRef Medline
27. Zhao L, Barlinn K, Sharma VK, et al. **Velocity criteria for intracranial stenosis revisited: an international multicenter study of transcranial Doppler and digital subtraction angiography.** *Stroke* 2011;42:3429–34 CrossRef Medline
28. Hope TA, Hope MD, Purcell DD, et al. **Evaluation of intracranial stenoses and aneurysms with accelerated 4D flow.** *Magn Reson Imaging* 2010;28:41–46 CrossRef Medline
29. Ruland S, Ahmed A, Thomas K, et al. **Leptomeningeal collateral volume flow assessed by quantitative magnetic resonance angiography in large-vessel cerebrovascular disease.** *J Neuroimaging* 2009;19:27–30 CrossRef Medline
30. van Everdingen KJ, Kappelle LJ, Klijn CJ, et al. **Clinical features associated with internal carotid artery occlusion do not correlate with MRA cerebropetal flow measurements.** *J Neurol Neurosurg Psychiatry* 2001;70:333–39 CrossRef Medline
31. Sorteberg W, Langmoen IA, Lindegaard KF, et al. **Side-to-side differences and day-to-day variations of transcranial Doppler parameters in normal subjects.** *J Ultrasound Med* 1990;9:403–09 Medline
32. Obata T, Shishido F, Koga M, et al. **Three-vessel study of cerebral blood flow using phase-contrast magnetic resonance imaging: effect of physical characteristics.** *Magn Reson Imaging* 1996;14:1143–48 CrossRef Medline
33. Brint SU, Al-Khalidi HR, Vatel B, et al. **MCA flow asymmetry is a marker for cerebrovascular disease.** *Neurol Res* 1996;18:163–67 CrossRef Medline
34. Liebeskind DS, Cotsonis GA, Saver JL, et al; Warfarin–Aspirin Symptomatic Intracranial Disease (WASID) Investigators. **Collateral circulation in symptomatic intracranial atherosclerosis.** *J Cereb Blood Flow Metab* 2011;31:1293–301 CrossRef Medline
35. Zanette EM, Fieschi C, Bozzao L, et al. **Comparison of cerebral angiography and transcranial Doppler sonography in acute stroke.** *Stroke* 1989;20:899–903 CrossRef Medline
36. Brozici M, van der Zwan A, Hillen B. **Anatomy and functionality of leptomeningeal anastomoses: a review.** *Stroke* 2003;34:2750–62 CrossRef Medline
37. Brass LM, Duterte DL, Mohr JP. **Anterior cerebral artery velocity changes in disease of the middle cerebral artery stem.** *Stroke* 1989;20:1737–40 CrossRef Medline
38. Uemura A, O'Uchi T, Kikuchi Y, et al. **Prominent laterality of the posterior cerebral artery at three-dimensional time-of-flight MR angiography in M1-segment middle cerebral artery occlusion.** *AJNR Am J Neuroradiol* 2004;25:88–91 Medline
39. Strecker C, Harloff A, Wallis W, et al. **Flow-sensitive 4D MRI of the thoracic aorta: comparison of image quality, quantitative flow, and wall parameters at 1.5 T and 3 T.** *J Magn Reson Imaging* 2012;36:1097–103 CrossRef Medline
40. Gu T, Korosec FR, Block WF, et al. **PC VIPR: a high-speed 3D phase-contrast method for flow quantification and high-resolution angiography.** *AJNR Am J Neuroradiol* 2005;26:743–49 Medline
41. Basha TA, Akçakaya M, Goddu B, et al. **Accelerated three-dimensional cine phase contrast imaging using randomly undersampled echo planar imaging with compressed sensing reconstruction.** *NMR Biomed* 2015;28:30–39 CrossRef Medline
42. Dyvorne H, Knight-Greenfield A, Jajamovich G, et al. **Abdominal 4D flow MR imaging in a breath hold: combination of spiral sampling and dynamic compressed sensing for highly accelerated acquisition.** *Radiology* 2015;275:245–54 CrossRef Medline
43. Ha H, Kim GB, Kweon J, et al. **Multi-VENC acquisition of four-dimensional phase-contrast MRI to improve precision of velocity**

field measurement. *Magn Reson Med* 2016;75:1909–19 CrossRef Medline
44. Schnell S, Rose MJ, Wu C, et al. **Improved assessment of aortic hemodynamics by k-t accelerated dual-VENC 4D flow MRI in pediatric patients.** *J Cardiovasc Magn Reson* 2016;18(suppl):O96 CrossRef
45. Kadbi M, Negahdar M, Cha JW, et al. **4D UTE flow: a phase-contrast MRI technique for assessment and visualization of stenotic flows.** *Magn Reson Med* 2015;73:939–50 CrossRef Medline
46. O'Brien KR, Myerson SG, Cowan BR, et al. **Phase contrast ultrashort TE: a more reliable technique for measurement of high-velocity turbulent stenotic jets.** *Magn Reson Med* 2009;62:626–36 CrossRef Medline
47. Petersson S, Dyverfeldt P, Sigfridsson A, et al. **Quantification of turbulence and velocity in stenotic flow using spiral three-dimensional phase-contrast MRI.** *Magn Reson Med* 2016;75:1249–55 CrossRef Medline

A Fully Automated, Atlas-Based Approach for Superior Cerebellar Peduncle Evaluation in Progressive Supranuclear Palsy Phenotypes

G. Nicoletti, M.E. Caligiuri, A. Cherubini, M. Morelli, F. Novellino, G. Arabia, M. Salsone, and A. Quattrone

ABSTRACT

BACKGROUND AND PURPOSE: The superior cerebellar peduncle is damaged in progressive supranuclear palsy. However, alterations differ between progressive supranuclear palsy with Richardson syndrome and progressive supranuclear palsy-parkinsonism. In this study, we propose an automated tool for superior cerebellar peduncle integrity assessment and test its performance in patients with progressive supranuclear palsy with Richardson syndrome, progressive supranuclear palsy-parkinsonism, Parkinson disease, and healthy controls.

MATERIALS AND METHODS: Structural and diffusion MRI was performed in 21 patients with progressive supranuclear palsy with Richardson syndrome, 9 with progressive supranuclear palsy-parkinsonism, 20 with Parkinson disease, and 30 healthy subjects. In a fully automated pipeline, the left and right superior cerebellar peduncles were first identified on MR imaging by using a tractography-based atlas of white matter tracts; subsequently, volume, mean diffusivity, and fractional anisotropy were extracted from superior cerebellar peduncles. These measures were compared across groups, and their discriminative power in differentiating patients was evaluated in a linear discriminant analysis.

RESULTS: Compared with those with Parkinson disease and controls, patients with progressive supranuclear palsy with Richardson syndrome showed alterations of all superior cerebellar peduncle metrics (decreased volume and fractional anisotropy, increased mean diffusivity). Patients with progressive supranuclear palsy-parkinsonism had smaller volumes than those with Parkinson disease and controls and lower fractional anisotropy than those with Parkinson disease. Patients with progressive supranuclear palsy with Richardson syndrome had significantly altered fractional anisotropy and mean diffusivity in the left superior cerebellar peduncle compared with those with progressive supranuclear palsy-parkinsonism. Discriminant analysis with the sole use of significant variables separated progressive supranuclear palsy-parkinsonism from progressive supranuclear palsy with Richardson syndrome with 70% accuracy and progressive supranuclear palsy-parkinsonism from Parkinson disease with 74% accuracy.

CONCLUSIONS: We demonstrate the feasibility of an automated approach for extracting multimodal MR imaging metrics from the superior cerebellar peduncle in healthy subjects and patients with parkinsonian. We provide evidence that structural and diffusion measures of the superior cerebellar peduncle might be valuable for computer-aided diagnosis of progressive supranuclear palsy subtypes and for differentiating patients with progressive supranuclear palsy-parkinsonism from with those with Parkinson disease.

ABBREVIATIONS: FA = fractional anisotropy; MD = mean diffusivity; PD = Parkinson disease; PSP = progressive supranuclear palsy; PSP-P = progressive supranuclear palsy-parkinsonism; PSP-RS = progressive supranuclear palsy with Richardson syndrome; SCP = superior cerebellar peduncle

Progressive supranuclear palsy (PSP) is a neurodegenerative disorder characterized by a symmetric akinetic-rigid syndrome with vertical supranuclear palsy and falls.[1] It is characterized by deposition of tau, with pathologic findings and degeneration affecting the white matter, particularly brain stem tracts, with less involvement of the cortex.[2,3] Advanced neuroimaging studies using MR imaging[4,5] and diffusion tensor imaging[6,7] have confirmed the presence of a more severe involvement of white matter rather than cortical gray matter in PSP pathology. In particular, imaging alterations have been found in the superior cerebellar peduncles (SCPs), part of the dentatorubrothalamic tract that connects the dentate nucleus of the cerebellum to the ventrolateral thalamus, which in turn projects to the premotor cortex. Abnormal DTI measures of SCP were reported in patients with progressive supranuclear palsy with Richardson syndrome (PSP-RS).[8]

Received January 18, 2016; accepted after revision October 24.

From the Institute of Bioimaging and Molecular Physiology (G.N., M.E.C., A.C., F.N., M.S., A.Q.), National Research Council, Catanzaro, Italy; and Institute of Neurology (M.M., G.A., A.Q.), University "Magna Graecia", Catanzaro, Italy.

Please address correspondence to Giuseppe Nicoletti, MD, Institute of Bioimaging and Molecular Physiology, National Research Council, Viale Europa, 88100 Catanzaro, Italy; e-mail: g.nicoletti@unicz.it


Indicates article with supplemental on-line photo.

http://dx.doi.org/10.3174/ajnr.A5048

Other studies have found DTI alterations in the corpus callosum, internal capsules, and long-range white matter tracts.[7,9-13] Recently, DTI metrics were used to distinguish the 2 variants of PSP,[14,15] the so-called progressive supranuclear palsy-parkinsonism (PSP-P), which is characterized by an asymmetric onset, resting tremor, poor response to levodopa, and PSP-RS, in which early falls and vertical supranuclear gaze palsy occur earlier than they do in the former variant. These studies agreed that MR imaging– and DTI-based metrics are able to reliably evaluate brain changes due to PSP in vivo, thus providing further insight into disease physiopathology. Because an error rate of 10%–30% has been reported in a clinical study with pathologic analysis,[16] clinical criteria are not sufficient to make a correct diagnosis, especially at earlier stages of illness. The use of these quantitative measures in clinical practice would help improve the accuracy of the diagnostic process, especially in the attempt to have early differentiation of parkinsonian syndromes or the 2 disease phenotypes. However, the extraction of these metrics is not straightforward in everyday clinical practice because of the advanced techniques that need to be implemented; hence, an easy method to quickly obtain relevant quantities would be very useful in the diagnostic work-up.

The authors aimed to use a simple, atlas-based tool for the automatic assessment of SCP volume and microstructural integrity; this approach is very useful to correctly diagnose patients with parkinsonian syndromes.

MATERIALS AND METHODS

Patients

This study was approved by the local ethics committee of our institution (Institute of Neurology, University Magna Graecia of Catanzaro, Italy), and all subjects provided written informed consent before enrollment. Thirty subjects who met the clinical research criteria for probable or possible PSP[17] and 20 with a diagnosis of Parkinson disease (PD)[18] (mean age, 66.2 ± 3.0 years) were included in this study. The PSP group was divided into 9 patients with PSP-P (mean age, 70.1 ± 4.8 years) and 21 with PSP-RS (mean age, 71.9 ± 5.9 years). All patients were examined at the Institute of Neurology, University Magna Graecia, Catanzaro, Italy, between June 2013 and June 2014, by a movement disorders specialist and PSP expert (G.N.). All subjects underwent detailed clinical evaluations. The patient's disability was assessed by using the Unified Parkinson's Disease Rating Scale–Motor Examination,[19] and disease severity, by using the Hohen and Yahr scale.[20] Onset of falls and supranuclear gaze palsy within 2 years was associated with a diagnosis of PSP-RS, while patients were diagnosed as having PSP-P if they presented with oculomotor slowness or backward falls at 2 years from disease onset, asymmetry of limb signs, and moderate/good improvement in bradykinesia and rigidity after levodopa administration. All patients with PSP-RS had probable PSP; 7 patients with PSP-P had probable PSP, and 2 patients with PSP-P had possible PSP. When MR imaging was performed, all patients with PSP-P were classified as PSP-P, even though the onset of the disease in some patients could be confused with an idiopathic PD. To examine cognitive functions, we administered the Mini-Mental State Examination.[21] Thirty healthy subjects were also recruited. All controls performed within normal limits on standardized neurologic and neuropsychological testing.

MR Imaging Acquisition and Processing

All participants underwent the same MR imaging protocol. Patients were examined by using a 3T Discovery MR750 scanner (GE Healthcare, Milwaukee, Wisconsin). The MR imaging protocol included whole-brain, 3D, T1-weighted (BRAVO; GE Healthcare, Milwaukee, Wisconsin), spoiled gradient recalled-echo imaging (TE/TR = 3.7/9.2 ms, flip angle = 12°, voxel size = 1 × 1 × 1 mm^3), diffusion tensor imaging (b=1000 s/mm^2, diffusion-weighting along 27 noncollinear gradient directions, matrix size = 128 × 128, 80 axial sections, number of b=0 images = 4, NEX = 2, voxel size = 2 × 2 × 2 mm^3), and fast fluid-attenuated inversion recovery axial images (TR/TE = 9500/100 ms, matrix size = 512 × 512, FOV = 24 cm, thirty-six 4-mm sections, gap = 0 mm).

FLAIR images were visually checked to assess vascular lesions in each patient. The extent and possible etiology of white matter hyperintensities were not different across patients, independent of the group. Moreover, none of the participants showed infratentorial lesions that could affect volumetric and diffusion measures in the SCP.

A graphic description of our fully automated processing workflow is shown in Fig 1. Image processing was performed by using FSL (http://www.fmrib.ox.ac.uk/fsl).[22] Brain tissue volume, normalized for subject head size, was estimated with the SIENAX tool (http://fsl.fmrib.ox.ac.uk/fsl/fslwiki/SIENA).[23,24] SIENAX starts by extracting brain and skull images from the single whole-head input data.[25] The brain image is then affine-registered to Montreal Neurological Institute-152 space (by using the skull image to determine the registration scaling); this processing step is primarily to obtain the volumetric scaling factor, to normalize subsequently extracted measures for head size. Moreover, SIENAX provides the partial volume estimates for the different tissues in the brain. In particular, in this study, we exploited the white matter partial volume estimates to exclude CSF voxels from the analysis, as will be further explained in the next section.

Head motion and image distortions induced by eddy currents in the DTI data were corrected by applying a 3D full-affine (mutual-information cost function) alignment of each image to the mean no-diffusion-weighting (B0) image. After distortion correction, DTI data were averaged and concatenated into 28 (1 mean B0 + 27 B1000) volumes. A diffusion tensor model was fit at each voxel, generating fractional anisotropy (FA) and mean diffusivity (MD) maps. The FA maps were then registered to whole-brain-extracted T1-weighted images by using a full-affine (correlation-ratio cost function) alignment with nearest neighbor resampling. The calculated transformation matrix was then applied to the MD maps with identical resampling options.[26]

ROI Extraction

To localize ROIs for the left and right SCPs on the T1 images and coregistered DTI maps of each subject, we used the tractography-based atlas of human brain connections (http://www.natbrainlab.com/), obtained from tractography data of 40 healthy adults mapped onto a common reference space (Montreal Neurological Institute).[27] This atlas provides probability maps of each recon-

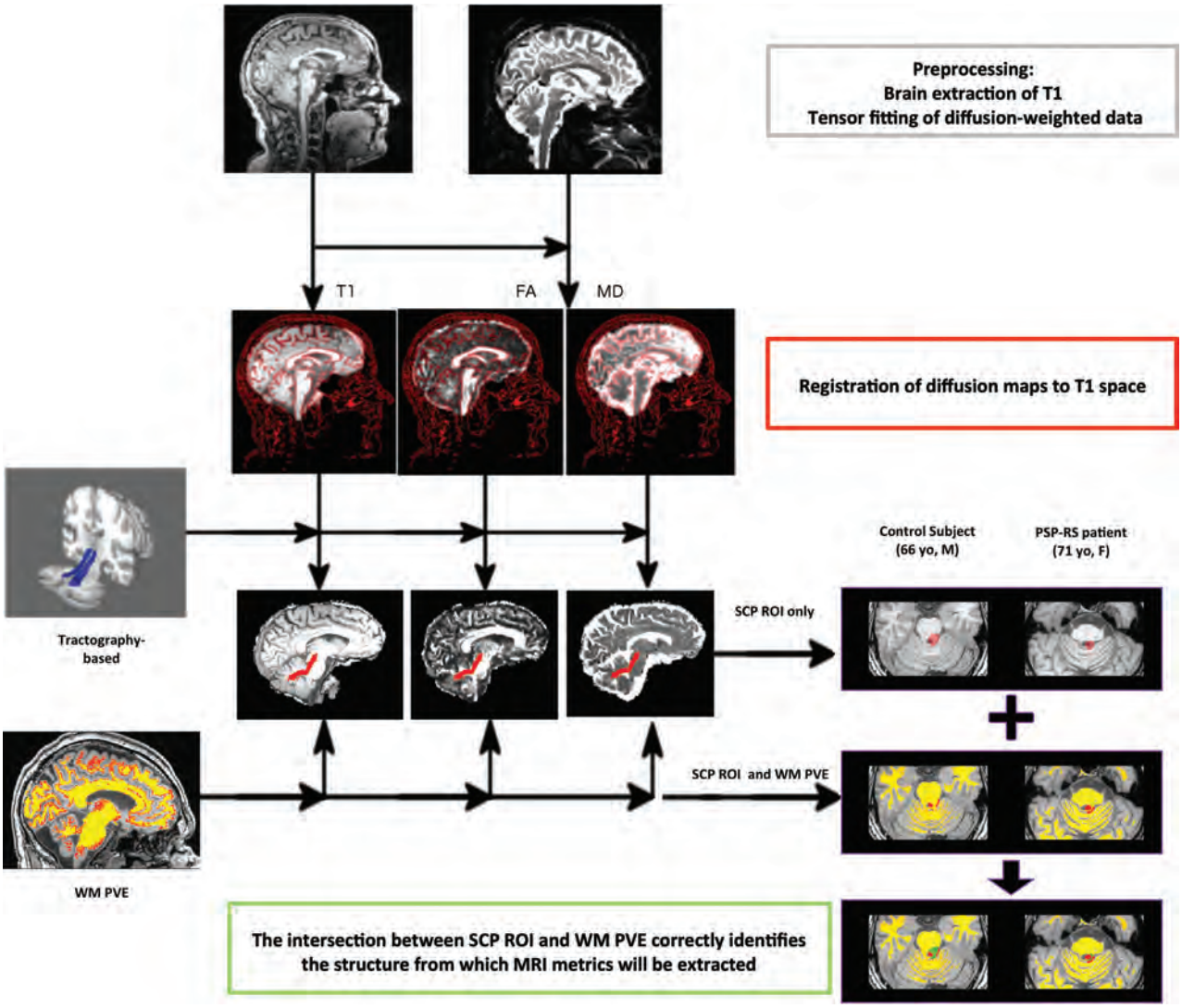

FIG 1. Image-processing workflow. The coregistration of different sequences allows the extraction of multimodal parameters from an ROI.

structed bundle: each voxel value ranges from 0 to 1 and represents the proportion of subjects in which that same voxel was part of the bundle. Thus, we thresholded the bilateral SCP probability maps at 0.3 so that each included voxel was represented in at least 30% of the subjects from whom the atlas was obtained. This threshold was chosen on the basis of the overlap of the ROI with the anatomic regions in the template.

Subsequently, ROIs were warped in each subject's T1 space in the following manner: First, the Montreal Neurological Institute-152 template was nonlinearly registered to each subject's T1 image by using the FMRIB Nonlinear Registration Tool (FNIRT; http://fsl.fmrib.ox.ac.uk/fsl/fslwiki/FNIRT); afterward, the resulting warp field was applied to the SCP binary masks. Before extracting MR imaging metrics from selected ROIs, we performed a processing step to account for confounding effects due to CSF contamination. In particular, each subject's WM partial volume estimate was thresholded at 0.75, to retain only those voxels that belonged to WM with a probability of at least 75%. The resulting mask was then used, in combination with the SCP ROIs, to automatically extract right and left SCP volumes, average FAs, and average MDs for each subject.

A 2-step quality check was performed to ensure validity of the image-processing pipeline: First, the contrast-to-noise ratio of the included scans had to be excellent; second, to exclude CSF contamination, an expert visually inspected the outcome of nonlinear registration between ROIs and T1-weighted images.

Statistical Analyses

The difference in sex distribution between patients and control subjects and among groups of patients with different movement disorders was evaluated with the χ^2 test. The Shapiro-Wilk test was used to assess normal distribution of continuous variables. Differences in normal clinical variables among the study groups were assessed by using 2-tailed, 2-sample *t* tests, while the Mann-Whitney *U* test was used for non-normally distributed variables. The threshold for statistical significance was set at .05 after Bonferroni correction for multiple comparisons. Differences in the multimodal imaging variables across groups were evaluated by analysis of variance, with age, sex, and disease duration as covariates. The Tukey honest significant difference test was used to identify pair-wise differences between groups, corrected for multiple comparisons. Pearson correlation analysis was used to eval-

Table 1: Demographic, clinical, and neuroimaging features in patients with PSP-P, PSP-RS, PD, and healthy controls

	PSP-P (*n* = 9)	PSP-RS (*n* = 21)	PD (*n* = 20)	HC (*n* = 30)
Age (mean) (yr)	70.1 ± 4.8	71.9 ± 5.9	66.2 ± 3.0	67.2 ± 7.2
Sex, % male	100%	57%	50%	47%
Disease duration (mean) (yr)	6.3 ± 3.7	3.1 ± 1.4	7.5 ± 3.7	–
MMSE (mean)	22.1 ± 3.6	19.0 ± 5.4	23.2 ± 3.3	–
UPDRS-III (mean)	22.8 ± 17.7	39.3 ± 7.7	27.1 ± 9.1	–
HY (mean)	2.9 ± 0.7	3.4 ± 0.8	2.2 ± 0.5	–
SCP right				
Volume (No. of voxels) (mean)	5652 ± 1172	5282 ± 753	6907 ± 1306	6569 ± 944
FA (mean)	0.44 ± 0.05	0.40 ± 0.05	0.48 ± 0.04	0.45 ± 0.02
MD ($\times 10^{-3}$ mm^2/s) (mean)	0.873 ± 0.06	0.949 ± 0.170	0.851 ± 0.089	0.833 ± 0.031
SCP left				
Volume (No. of voxels) (mean)	5315 ± 1121	4812 ± 701	6369 ± 1205	5961 ± 894
FA (mean)	0.44 ± 0.04	0.39 ± 0.05	0.47 ± 0.04	0.45 ± 0.02
MD ($\times 10^{-3}$ mm^2/s (mean)	0.895 ± 0.061	0.974 ± 0.074	0.874 ± 0.066	0.857 ± 0.023

Note:—HC indicates healthy controls; MMSE, Mini-Mental State Examination; UPDRS-III, Unified Parkinson's Disease Rating Scale–Motor Examination; HY, Hohen and Yahr score.

uate the relationship between MR imaging parameters and clinical variables. All statistical analyses were performed with R software (http://www.R-project.org).

Linear Discriminant Analysis

After performing comparisons of the MR imaging variables across different groups, we studied the discriminant power of these measures. In particular, we applied linear discriminant analysis on our dataset, to identify the following: which variables perform better in separating the groups and what is the predictive power of these measures (ie, how is a new subject classified on the basis of these measures?). We can define a total covariance matrix C, as the combination of 2 components:

1) The between-subjects covariance matrix (B), which represents the covariance of the different variable means.

2) The within-subjects covariance matrix (W), which represents the covariance of the distances between individual values and group means.

This relationship is expressed by the following equation: $C = B + W$, which is a generalization of 1-way analysis of variance in the case of a dataset with multiple variables. In this context, a discriminant analysis searches for a combination of variables that maximize either the $B \times C^{-1}$, in which case the approach is descriptive and the constraint is that the total variance (C) of the linear combination of variables equals 1, or the $B \times W^{-1}$ term, in which case the approach is predictive and the within variance (W) of the correlation equals 1.

In this study, we first performed the analysis in descriptive mode on a dataset comprising all MR imaging metrics, measured on all the study participants, divided according to the diagnosis. Subsequently, we tested the predictive approach by building 2 different models that included only the variables that were significant in group-wise comparisons. In particular, we were interested in identifying which variables could better differentiate the 2 PSP phenotypes (first model) or PSP-P and PD (second model). In both cases, leave-one-out cross-validation was used. Leave-one-out cross-validation works as follows: At each iteration, the linear discriminant model is trained on all subjects except 1, which is used to test the predictive power of the model. The accuracy is computed across all iterations and is used to evaluate the model.

RESULTS

Patients

Table 1 shows the demographic and clinical characteristics of the patients. At the examination, age was higher in the patients with PSP-RS compared with healthy controls ($P = .02$) and patients with PD ($P = .01$). Those with PSP-RS also had significantly shorter disease duration compared with those with PD ($P = .0001$) and PSP-P ($P = .02$). Differences in Hohen and Yahr stages were found in those with PD ($P = .0004$) and PSP-RS ($P = .001$) compared with patients with PSP-P. Subjects with PSP-RS had significantly higher Unified Parkinson's Disease Rating Scale–Motor Examination scores compared with those with PSP-P ($P = .002$) and PD ($P = .0004$).

There was no significant correlation between clinical and imaging variables. The only significant correlation surviving correction for multiple comparisons was the one found in patients with PD between the Hohen and Yahr score and age ($r = 0.78$, $P < .05$).

ROI Analysis

Table 1 also summarizes values of volume, FA, and MD of the right and left SCPs in the different groups. Figure 2 shows the boxplots for the MR imaging metrics that were considered in the analysis. *P* values for the different comparisons can be found in Table 2.

Both PSP subtypes showed significant damage to the SCP. In particular, patients with PSP-RS showed alterations of all metrics (decreased volume, decreased FA, and increased MD) bilaterally compared with patients with PD and control subjects. Patients with PSP-P had a bilateral SCP volume decrease compared with controls and decreased SCP volume and FA bilaterally compared with those with PD.

In the comparison between PSP subtypes, we found significant differences in the left SCP. In particular, patients with PSP-RS had significantly decreased FA values ($P = .007$) and significantly increased MD values ($P = .003$) in this structure.

Finally, we found an increase in FA in patients with PD compared with controls, in the right SCP.

Linear Discriminant Analysis

On-line Fig 1 shows a graphic representation of the descriptive discriminant analysis. In particular, each subject is projected on a

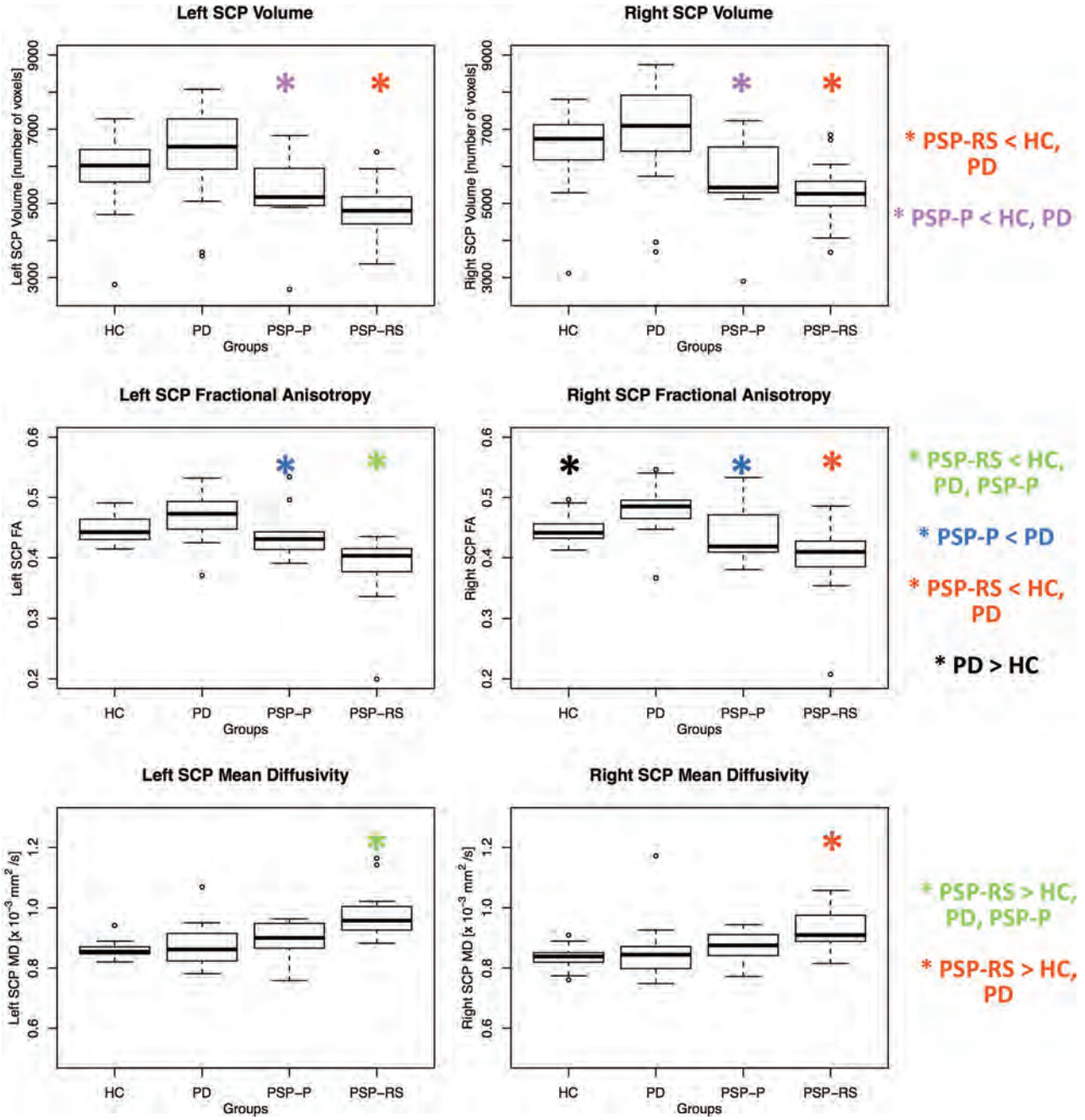

FIG 2. Box-and-whisker plots of volumes, FA, and MD of the right and left SCPs in patients and controls.

plane defined by the linear discriminant components. Each group is represented by an ellipse. The ellipse center indicates the means (between-variances), while the ellipse area is proportional to within-variances.

In the first predictive discriminant analysis model, we included FA and MD values from the left SCP because they were significantly different between the 2 PSP phenotypes. The accuracy of the model reached 70%, with MD as the best predictor (coefficients of the linear discriminant for MD = 9.67 and for FA = −7.87). In the second model, instead, volume and FA from bilateral SCPs were used to discriminate patients with PD from those with PSP-P. This model reached an accuracy of 74%, with FA values performing better than volume in separating the 2 groups (coefficients of the linear discriminant analyses: −29.6 and 18.7 for FA of right and left SCPs, respectively; −0.002 and 0.001 for right and left SCP volumes, respectively).

DISCUSSION

In the present study, we introduced a fully automated pipeline for the assessment of SCP integrity in patients with PSP, PD, and healthy subjects. The proposed method takes advantage of an atlas-based ROI approach that allowed the automated individuation of the SCP, thus avoiding time-consuming and highly user-dependent manual measurements. We also tested the ability of this tool to distinguish the 2 PSP subtypes. By assessing volume and diffusion metrics of the SCP, we found significant differences

Table 2: *P* values from the statistical tests among different groups after correction for multiple comparisons (Tukey test)[a]

	PD vs HC	PSP-P vs HC	PSP-RS vs HC	PSP-P vs PD	PSP-RS vs PD	PSP-P vs PSP-RS
Age	1	1	.02[b]	0.1	.01[b]	1
Sex	.1	.0001[b]	.1	.008[b]	1	.01[b]
Disease duration	–	–	–	1	.0001[b]	.02[b]
MMSE	–	–	–	1	.01[b]	1
UPDRS-III	–	–	–	1	.0022[b]	.002[b]
HY	–	–	–	.0004[b]	.94	.001[b]
SCP right						
Volume	.66	.008[b]	.00005[b]	.001[b]	.000004 [b]	.95
FA	.01[b]	.66	.0005[b]	.004[b]	1.45×10^{-8}[b]	.16
MD	.89	.38	.0003[b]	.77	.01[b]	.31
SCP left						
Volume	.44	.03[b]	.00008[b]	.002[b]	.000002[b]	.81
FA	.15	.58	.0000005[b]	.03[b]	9.33×10^{-10}[b]	.007[b]
MD	.70	.16	9.30×10^{-10}[b]	.67	.000001[b]	.003[b]

Note:— HC indicates healthy controls; MMSE, Mini-Mental State Examination; UPDRS-III, Unified Parkinson's Disease Rating Scale-Motor Examination; HY, Hohen and Yahr score.

[a] Sex differences were assessed with χ^2 tests. Age differences were assessed with ANOVA. Disease duration differences were assessed using ANCOVA, with age and sex as covariates. Other clinical and imaging differences were assessed with ANCOVA, with age, sex, and disease duration, as covariates. Correction for multiple comparisons was performed with the Tukey honest significant difference test.

[b] Significant.

between PSP-P and PSP-RS in MD and FA of the left SCP, with the latter phenotype more severely damaged. As expected, both PSP phenotypes showed extensive alterations of multimodal MR imaging metrics compared with patients with PD and controls. Discriminant analysis of the significantly different metrics allowed separation of the 2 PSP subtypes with an accuracy of 70% and could also distinguish PSP-P from PD with an accuracy of 74%.

By using a quick and fully automated pipeline, we were able to analyze a predefined ROI (ie, SCP) on different MR imaging sequences, thus collecting information in different scales (ie, macroscopic volume and microstructural integrity). SCP identification and evaluation were performed by an atlas-based approach. The use of an atlas has multiple benefits. First, it facilitates the identification of brain structures on MR imaging in healthy subjects and patients.[27] Second, it avoids a manual ROI definition, which is a time-consuming and strongly user-dependent procedure; this feature raised the level of reproducibility of this study. Despite heavy SCP damage present in PSP, which could hamper the identification of the structure, the quality check of images performed in this study confirmed that the grade of superimposition between the SCP masks and the T1 images was appropriate.

The choice of the ROI for analyses was because atrophy of the SCP is a well-known postmortem finding in patients with PSP.[3] This bundle is composed of efferent cerebellar fibers, mainly originating from the dentate nucleus, which decussate and project via the red nucleus to the contralateral ventrolateral nucleus of the thalamus. SCP fibers that project to the reticular and vestibular nuclei of the brain stem may be involved in the pathophysiology of postural instability in PSP. Moreover, damage of SCP fibers that contributes to the control of smooth pursuit movements may contribute to gaze palsy in this disorder.[28] In previous studies, we investigated MR imaging alterations in SCP and infratentorial structures of patients with PD, PSP, and multiple system atrophy with predominant parkinsonian signs,[29-31] but we had not yet considered the 2 PSP phenotypes separately.

Two recent studies have found differences between PSP-RS and PSP-P by using volumetry of brain stem structures[14] or DTI metrics.[15] In the former, the authors concluded that SCP was relatively spared in patients with PSP-P, but not in those with PSP-RS; in the latter, instead, the authors demonstrated the utility of combining DTI metrics to the well-known Magnetic Resonance Parkinsonism Index.[31] Our findings are in line with results from both studies, because patients with PSP-RS were found more severely damaged in most comparisons and DTI metrics helped uncover differences between subtypes that could not be found by volume alone.

In this study, patients with PSP-RS showed bilateral alterations of all SCP metrics compared with controls and patients with PD, whereas compared with patients with PSP-P, they showed altered diffusion metrics in the left SCP only. This finding suggests that the right SCP might be equally damaged between the 2 phenotypes, while the left SCP seems to be relatively spared in PSP-P. The presence of unilateral significant differences in SCP between PSP-P and PSP-RS is not surprising and is in line with the asymmetric clinical presentation of PSP-P.[32] The presence of left-sided damage in PSP-RS is also in line with results from a recent study investigating white matter loss in PSP.[33]

The integrity of the SCP, which characterized patients with PD in this study, supported the robustness of our automated method, confirming the notion that this structure is not involved in PD. Increased MD and decreased FA values in the SCP in PSP compared with PD have also been reported previously.[34,35] Patients with PD showed increased FA in the SCP compared not only with patients with PSP but also with healthy controls. Despite pathologic alterations being usually associated with decreases of this metric, increases of FA have also been reported and are thought to characterize a selective degeneration of white matter bundles in regions of crossing fibers.[36] Thus, in the present study, the higher FA found in patients with PD could be the result of different pathologic processes that do not hamper the microstructural integrity of the entire SCP as we found in PSP-RS but rather cause the loss of connections with an orientation different from the principal diffusion direction of the SCP.

Results of the discriminant analysis between PSP phenotypes seem to encourage the adoption of this automated approach in

clinical practice, though at the present time, this is not yet feasible. In fact, validation is still needed on larger cohorts and, at the same time, in assessing the reliability of the method in individual subjects, possibly with confirmed postmortem diagnosis. Despite these well-known limitations, however, the accuracy of 70% obtainable with the sole use of diffusion metrics extracted from the left SCP suggests that our tool could be valuable in the clinical diagnostic process, possibly integrated with other measures that currently aid the diagnosis (eg, the Magnetic Resonance Parkinsonian Index).

Overall, our findings demonstrate the following: 1) Automatic extraction of multimodal MR imaging metrics from the SCP is feasible not only in healthy controls but also in patients with PD and PSP; 2) damage to the SCP is present in the 2 forms of PSP with a different degree of severity: more severe in PSP-RS than in PSP-P, despite the significantly longer disease duration in the latter form; 3) SCP metrics in patients with PD were comparable with those extracted from healthy subjects; 4) the in vivo microstructural changes observed in SCP with DTI are in line with abnormalities detected in previous postmortem studies; 5) the degenerative process seems to begin on one side of the SCP and then progresses in the contralateral structure; and 6) damage to the SCP as detected by volume and FA might improve differentiation of PSP-P and PD in an early stage of the disease.

There are some limitations to our study: First, the population was relatively small. Second, we did not have postmortem confirmation to reach the criterion standard diagnosis and cannot fully exclude misdiagnosis. Third, the tool still needs validation on larger cohorts of patients and on MR imaging scans acquired with different parameters.

CONCLUSIONS

With a fully automated analysis pipeline, we were able to rapidly extract MR imaging markers that helped identify different patterns of SCP damage, not only between PSP-P and PSP-RS but also between PSP-P and PD. This approach was implemented with minimal user intervention, which guarantees reproducibility of the results and avoids the time-consuming procedures required for manual segmentation of ROIs. The proposed pipeline could be useful if integrated into the current diagnostic process, to improve early diagnosis of PD and different parkinsonian syndromes, especially in the most ambiguous cases.

REFERENCES

1. Steele JC, Richardson JC, Olszewski J. **Progressive supranuclear palsy: a heterogeneous degeneration involving the brain stem, basal ganglia and cerebellum with vertical gaze and pseudobulbar palsy, nuchal dystonia and dementia.** *Arch Neurol* 1964;10:333–59 CrossRef Medline
2. Hauw JJ, Daniel SE, Dickson D, et al. **Preliminary NINDS neuropathologic criteria for Steele-Richardson-Olszewski syndrome (progressive supranuclear palsy).** *Neurology* 1994;44:2015–19 CrossRef Medline
3. Tsuboi Y, Slowinski J, Josephs KA, et al. **Atrophy of superior cerebellar peduncle in progressive supranuclear palsy.** *Neurology* 2003;60:1766–69 CrossRef Medline
4. Josephs KA, Whitwell JL, Dickson DW, et al. **Voxel-based morphometry in autopsy proven PSP and CBD.** *Neurobiol Aging* 2008;29:280–89 CrossRef Medline
5. Price S, Paviour D, Scahill R, et al. **Voxel-based morphometry detects patterns of atrophy that help differentiate progressive supranuclear palsy and Parkinson's disease.** *Neuroimage* 2004;23:663–69 CrossRef Medline
6. Erbetta A, Mandelli ML, Savoiardo M, et al. **Diffusion tensor imaging shows different topographic involvement of the thalamus in progressive supranuclear palsy and corticobasal degeneration.** *AJNR Am J Neuroradiol* 2009;30:1482–87 CrossRef Medline
7. Nilsson C, Markenroth Bloch K, Brockstedt S, et al. **Tracking the neurodegeneration of parkinsonian disorders: a pilot study.** *Neuroradiology* 2007;49:111–19 CrossRef Medline
8. Seppi K, Poewe W. **Brain magnetic resonance imaging techniques in the diagnosis of parkinsonian syndromes.** *Neuroimage Clin N Am* 2010;20:29–55 CrossRef Medline
9. Canu E, Agosta F, Baglio F, et al. **Diffusion tensor magnetic resonance imaging tractography in progressive supranuclear palsy.** *Mov Disord* 2011;26:1752–55 CrossRef Medline
10. Knake S, Belke M, Menzler K, et al. **In vivo demonstration of microstructural brain pathology in progressive supranuclear palsy: a DTI study using TBSS.** *Mov Disord* 2010;25:1232–38 CrossRef Medline
11. Padovani A, Borroni B, Brambati SM, et al. **Diffusion tensor imaging and voxel based morphometry study in early progressive supranuclear palsy.** *J Neurol Neurosurg Psychiatry* 2006;77:457–63 CrossRef Medline
12. Wang J, Wai Y, Lin WY, et al. **Microstructural changes in patients with progressive supranuclear palsy: a diffusion tensor imaging study.** *J Magn Reson Imaging* 2010;32:69–75 CrossRef Medline
13. Whitwell JL, Master AV, Avula R, et al. **Clinical correlates of white matter tract degeneration in progressive supranuclear palsy.** *Arch Neurol* 2011;68:753–60 CrossRef Medline
14. Longoni G, Agosta F, Kostić VS, et al. **MRI measurements of brainstem structures in patients with Richardson's syndrome. Progressive supranuclear palsy-parkinsonism, and Parkinson's disease.** *Mov Disord* 2011;26:247–55 CrossRef Medline
15. Agosta F, Pievani M, Svetel M, et al. **Diffusion tensor MRI contributes to differentiate Richardson's syndrome from PSP-parkinsonism.** *Neurobiol Aging* 2012;33:2817–26 CrossRef Medline
16. Jankovic J, Rajput AH, McDermott MP, et al. **The evolution of diagnosis in early Parkinson disease: Parkinson Study Group.** *Arch Neurol* 2000;57:369–72 CrossRef Medline
17. Litvan I, Agid Y, Calne D, et al. **Clinical research criteria for the diagnosis of progressive supranuclear palsy (Steele-Richardson-Olszewski syndrome): report of the NINDS-SPSP international workshop.** *Neurology* 1996;47:1–9 CrossRef Medline
18. Calne DB, Snow BJ, Lee C. **Criteria for diagnosing Parkinson's disease.** *Ann Neurol* 1992;32(suppl):S125–27 CrossRef Medline
19. Fahn S, Elton R, members of the UPDRS Development Committee. **Unified Parkinson's Disease Rating Scale.** In: Fahn S, Marsden CD, Calne DB, Goldstein M, eds. *Recent Developments in Parkinson's Disease.* Florham Park, NJ: Macmillan Healthcare Information; 1987:153–64
20. Hoehn MM, Yahr MD. **Parkinsonism: onset, progression and mortality.** *Neurology* 1967;17:427–42 CrossRef Medline
21. Folstein MF, Folstein SE, McHugh PR. **'Mini-Mental State': a practical method for grading the cognitive state of patients for the clinician.** *J Psychiatry Res* 1975;12:189–98 CrossRef Medline
22. Jenkinson M, Beckmann CF, Behrens TE, et al. **FSL.** *Neuroimage* 2012;62:782–90 CrossRef Medline
23. Smith SM, De Stefano N, Jenkinson M, et al. **Normalized accurate measurement of longitudinal brain change.** *J Comput Assist Tomogr* 2001;25:466–75 CrossRef Medline
24. Smith SM, Zhang Y, Jenkinson M, et al. **Accurate, robust and automated longitudinal and cross-sectional brain change analysis.** *Neuroimage* 2002;17:479–89 CrossRef Medline
25. Smith SM. **Fast robust automated brain extraction.** *Hum Brain Mapp* 2002;17:143–55 CrossRef Medline
26. Cherubini A, Péran P, Caltagirone C, et al. **Aging of subcortical nuclei: microstructural, mineralization and atrophy modifications**

measured in vivo using MRI. *Neuroimage* 2009;48:29–36 CrossRef Medline
27. Thiebaut de Schotten M, Ffytche DH, Bizzi, et al. **Atlasing location, asymmetry and inter-subject variability of white matter tracts in the human brain with MR diffusion tractography.** *Neuroimage* 2011;54 1:49–59 CrossRef Medline
28. Ohtsuka K, Igarashi Y, Chiba S. **Cerebellar peduncle lesion without saccadic abnormalities.** *Ophthalmologica* 1992;204:44–48 CrossRef Medline
29. Nicoletti G, Tonon C, Lodi R, et al. **Apparent diffusion coefficient of the superior cerebellar peduncle differentiates progressive supranuclear palsy from Parkinson's disease.** *Mov Disord* 2008;23: 2370–6 CrossRef Medline
30. Nicoletti G, Rizzo G, Barbagallo G, et al. **Diffusivity of cerebellar hemispheres enables discrimination of cerebellar or parkinsonian multiple system atrophy from progressive supranuclear palsy-Richardson syndrome and Parkinson disease.** *Radiology* 2013;267: 843–50. CrossRef Medline
31. Quattrone A, Nicoletti G, Messina D, et al. **MR imaging index for differentiation of progressive supranuclear palsy from Parkinson disease and the Parkinson variant of multiple system atrophy.** *Radiology* 2008;246:214–21 CrossRef Medline
32. William DR, de Silva R, Paviour DC, et al. **Characteristics of two distinct clinical phenotypes in pathologically proven progressive supranuclear palsy: Richardson's syndrome and PSP-parkinsonism.** *Brain* 2005;128:1247–58 CrossRef Medline
33. Agosta F, Kostic VS, Galantucci S, et al. **The in vivo distribution of brain tissue loss in Richardson's syndrome and PSP-parkinsonism: a VBM-DARTEL study.** *Eur J Neurosci* 2010;32:640–47 CrossRef Medline
34. Worker A, Blain C, Jarosz J, et al. **Diffusion tensor imaging of Parkinson disease, multiple system atrophy and progressive supranuclear palsy: a tract-based spatial statistics study.** *Plos One* 2014;9: e112638 CrossRef Medline
35. Meijer FJ, van Rumund A, Tuladhar A, et al. **Conventional 3T brain MRI and diffusion tensor imaging in the diagnostic workup of early stage parkinsonism.** *Neuroradiology* 2015;57:655–69 CrossRef Medline
36. Douaud G, Behrens TE, Poupon C, et al. **In vivo evidence for the selective subcortical degeneration in Huntington's disease.** *Neuroimage* 2009;46:958–66 Medline

Basilar Artery Changes in Fabry Disease

R. Manara, R.Y. Carlier, S. Righetto, V. Citton, G. Locatelli, F. Colas, M. Ermani, D.P. Germain, and A. Burlina

ABSTRACT

BACKGROUND AND PURPOSE: Dolichoectasia of the basilar artery is a characteristic finding of Fabry disease. However, its prevalence, severity, and course have been poorly studied. This study quantitatively evaluated, by MRA, a panel of basilar artery parameters in a large cohort of patients with Fabry disease.

MATERIALS AND METHODS: Basilar artery mean diameter, curved length, "origin-to-end" linear distance (linear length), and tortuosity index ([curved length ÷ linear length] − 1) were retrospectively measured on 1.5T MRA studies of 110 patients with Fabry disease (mean age, 39.4 ± 18.6 years; 40 males) and 108 control patients (mean age, 42.0 ± 18.2 years; 40 males).

RESULTS: Patients with Fabry disease had increased basilar artery mean diameter ($P < .001$) and basilar artery linear length ($P = .02$) compared with control patients. Basilar artery curved length and tortuosity index correlated with age in both groups ($P < .001$), whereas basilar artery linear length correlated with age only in patients with Fabry disease ($P = .002$). Patients with Fabry disease showed a basilar artery curved length mean increase of 4.2% (9.7% in male patients with Fabry disease versus male control patients), whereas the basilar artery mean diameter had a mean increase of 12.4% (14.3% in male patients with Fabry disease versus male control patients). Male patients with Fabry disease had increased basilar artery mean diameter, curved length, and tortuosity index compared with female patients with Fabry disease ($P = .04$, $P = .02$, and $P < .001$, respectively) and male control patients ($P < .001$, $P = .01$, and $P = .006$, respectively). Female patients with Fabry disease demonstrated an age-dependent increase of basilar artery mean diameter that became significant ($P < .001$) compared with female control patients above the age of 45 years.

CONCLUSIONS: The basilar artery of patients with FD is subjected to major remodeling that differs according to age and sex, thus providing interesting clues about the pathophysiology of cerebral vessels in Fabry disease.

ABBREVIATION: FD = Fabry disease

Fabry disease (OMIM 301500; FD) is a rare X-linked (Xq22.1) disease caused by mutations in the *GLA* gene causing deficiency of the hydrolase α-galactosidase A (α-GalA, E.C. 3.2.1.22).[1] The enzyme deficiency results in impaired sphingolipid catabolism with lysosomal accumulation of upstream metabolites (mainly globotriaosylceramide [Gb_3] and its deacylated compound globotriaosylsphingosine [lysoGb$_3$]). All organs are involved, with major damage to the kidneys, heart, and nervous system. The brain might present white matter vascular-like abnormalities, TIAs, and stroke at a young age,[2] suggesting that micro- and macroangiopathy might have a pivotal role in the pathogenesis of brain lesions. Indeed, both small and large blood vessels have been consistently shown to present functional and morphologic changes in patients with FD.[3-5] Increased vessel tortuosity has been found in the retina[6] and in the skin,[7,8] and intracranial artery dolichoectatic changes have been repeatedly observed in patients with FD during both pathologic and neuroimaging evaluations.[9-17]

Hitherto, most of the latter studies either referred to small samples or evaluated single specific aspects of artery dolichoectasia (such as the vessel lumen diameter). In addition, these studies

Received August 20, 2016; accepted October 6.

From the Sezione di Neuroscienze (R.M.), University of Salerno, Salerno, Italy; Radiology Division (R.Y.C., F.C.) and Division of Medical Genetics (F.C., D.P.G.), University of Versailles, Versailles, France; Department of Neurosciences (S.R., V.C., M.E.), University of Padova, Padova, Italy; S. Giovanni e Ruggi d'Aragona Hospital (G.L.), Salerno, Italy; and Neurological Unit (A.B.), St. Bassiano Hospital, Bassano del Grappa, Italy.

D.P.G. and A.B. should be considered co–senior authors.

Please address correspondence to Alessandro Burlina, MD, PhD, Neurological Unit, St. Bassiano Hospital, Via dei Lotti 40, 36061 Bassano del Grappa, Italy; e-mail: alessandro.burlina@aslbassano.it

Indicates open access to non-subscribers at www.ajnr.org

Indicates article with supplemental on-line appendix and tables.

http://dx.doi.org/10.3174/ajnr.A5069

FIG 1. MIP of an MRA study in *A*, a 41-year-old male patient with FD and *B*, a control patient. Note a mild increase of the tortuosity of the basilar artery and a more evident increase of the lumen diameter (compare the basilar artery with the contiguous ICA) *C*, Drawing of a tortuous basilar artery showing the real curved length (*dashed line*) and the linear distance between the basilar artery extremes (*dotted line*).

applied different quantification methods or semiquantitative scores for the severity of the intracranial FD-related vessel changes, leading to conflicting results about the role of sex, age, and treatments.

Our retrospective, transversal, case-control MRA study quantitatively investigated the morphologic basilar artery lumen changes (Fig 1) by applying a comprehensive panel of measurements encompassing all aspects of vessel dolichoectasia (diameter, length, and tortuosity) on a large cohort of patients with FD, aiming to provide a detailed picture of FD-related basilar artery changes according to age and sex.

MATERIALS AND METHODS

Patients

One hundred thirteen patients with FD underwent MR imaging and MRA and were retrospectively analyzed. Three patients were excluded for anatomic reasons (see below): therefore, 110 patients with FD were considered (mean age, 39.4 ± 18.6 years; range, 6–75 years; 40 males). The diagnosis of FD was confirmed by α-galactosidase A enzyme activity and *GLA* mutation identification. All patients gave written informed consent.

One hundred ten patients with no history of head trauma, neurosurgery, or other neurologic or psychiatric disease who underwent MRI and MRA for headache or TIA were analyzed. Two patients were excluded for anatomic reasons (see below): therefore, 108 patients (mean age, 42.0 ± 18.2 years; range: 4–76 years; 40 males) represented our control group.

MR Technique

All MR examinations of patients and control patients were performed between 2007–2014 with 1.5T scanners (Achieva or Intera; Philips Healthcare, Best, the Netherlands) with a standard quadrature head coil.

The MR study protocol included conventional T1-weighted and FLAIR axial images covering the whole brain and a TOF-MRA sequence for the evaluation of the main intracranial arteries. The latter sequence was acquired with the following parameters: TR, 23 ms; TE, 2.274 ms; section thickness, 1.4 mm; acquisition matrix, 512 × 512; and FOV, 16 cm on the Intera scanner and TR, 25 ms; TE, 6.906 ms; section thickness, 1 mm; acquisition matrix, 512 × 512; and FOV, 16 cm on the Achieva scanner.

Basilar Artery Evaluation

All MRIs were evaluated by 2 neuroradiologists (R.M., V.C.) to exclude concomitant posterior cranial fossa lesions that could potentially interfere with the cisternal course of the basilar artery (eg, neoplasms, abscesses, and parenchymal or vascular malformations). No patient with FD or healthy patient was excluded for this reason, and in no case was there disagreement between neuroradiologists.

The mean basilar artery diameter was measured by a neuroradiologist (R.M.) on the acquisition MRA axial sections with a commercially available image viewer (Medstation version 4.9; Exprivia, Molfetta, Italy) at 3 points, namely the starting, middle, and ending points of the basilar artery after adjusting the image window (On-line Appendix).

The basilar artery anatomic length (curved length of the whole cisternal segment) and the linear distance between the proximal and distal extremities of the basilar artery (linear length) were measured by a neuroradiologist (S.R.) with commercially available software (InSpace, syngo MR Workplace; Siemens, Erlangen, Germany) dedicated to the vessel analysis (On-line Appendix). Because the basilar artery landmarks were 1) the conjunction of the 2 vertebral arteries (starting point) and 2) the basilar artery bifurcation into the 2 posterior cerebral arteries (ending point), patients with FD and control patients with agenesia of 1 vertebral artery or of the precommunicating segment of 1 or both posterior cerebral arteries were excluded from the study (2 control patients and 3 patients with FD, including a woman harboring a persistent trigeminal artery).

In addition, the tortuosity index was calculated as follows, according to previous studies[18]:

$$\text{Tortuosity Index} = (\text{curved length} \div \text{linear length}) - 1$$

This index is equal to 0 when the vessel is perfectly straight, and the index increases with the relative increase of the curved length with respect to the linear length (Fig 1*C*).

In 15 patients, all of the aforementioned variables were remeasured after 3 months by 2 of the coauthors (R.M., S.R.) to assess intrarater and interrater reproducibility.

Statistical Analysis

The Student *t* test was performed to compare quantitative normally distributed variables between patients with FD and control patients and between subgroups. Analysis of covariance was used to test the dependence of groups, omitting the effect of age. The linear relationships between age and diameter, length, and tortuosity measures were evaluated by using the Pearson coefficient. Reproducibility of the measurements was also tested by Pearson coefficient. Significance level was set at $P < .05$.

RESULTS

Main findings are presented in On-line Table 1. FD and control groups did not differ for age ($P = .30$) or sex ($P = .91$). All measurements (mean diameter, curved length, linear length, and tortuosity index) showed very high interrater and intrarater agreement ($r \geq 0.9$).

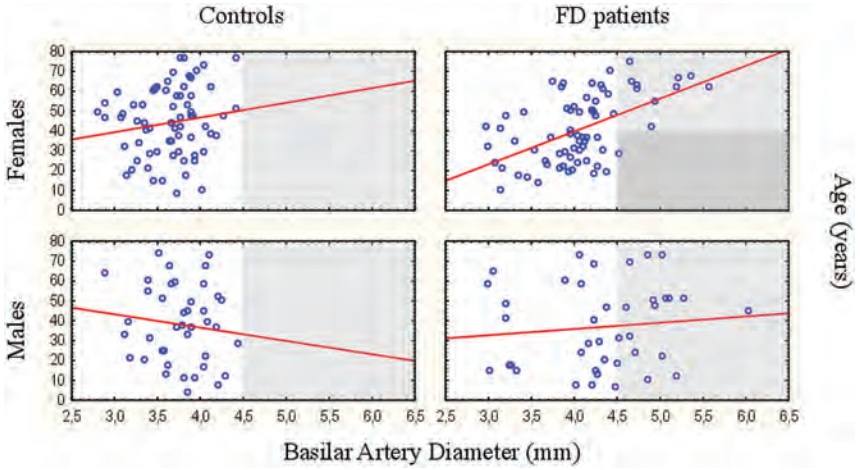

FIG 2. Mean basilar artery diameter findings in our study population (patients with FD and control patients) subdivided according to sex (*circles* represent the value in each patient). This composite plot shows sex- and age-related differences among subgroups; note that a mean basilar artery diameter greater than 4.5 mm could be found at any age among male Fabry patients and almost only after the age of 40 among female Fabry patients.

Diameter Analysis

Compared with control patients, patients with FD had increased mean basilar artery diameter (4.16 ± 0.62 mm versus 3.70 ± 0.36 mm; $P < .001$); the mean basilar artery diameter showed mild correlation with age among patients with FD ($r = 0.3$; $P = .001$) and no correlation among control patients.

When subgrouping according to sex, the basilar artery diameter did not correlate with age among male patients with FD and male and female control patients. In contrast, female patients with FD showed a good correlation between age and basilar artery diameter ($r = 0.54$) (Fig 2).

Male patients with FD had increased mean basilar artery diameter compared with female patients with FD (4.32 ± 0.72 mm versus 4.07 ± 0.55 mm; $P = .04$) and male control patients (4.32 ± 0.72 mm versus 3.78 ± 0.36 mm; $P < .001$). Female patients with FD had increased mean basilar artery diameter compared with female control patients (4.07 ± 0.55 mm versus 3.66 ± 0.36 mm; $P < .001$). No difference was found between male and female control patients (3.70 ± 0.36 mm versus 3.66 ± 0.36 mm).

We divided patients and control patients according to sex and age (younger or older than 45 years); male patients with FD showed increased mean basilar artery diameter compared with control patients at any age, whereas female patients with FD differed from control patients only in the older subgroup.

A diagnostic criterion based on a mean basilar artery diameter >4.42 mm had a specificity of 97.2% and a sensitivity of 28.2%.

Length and Tortuosity Analysis

Compared with control patients, patients with FD had increased linear length (28.34 ± 4.03 mm versus 27.18 ± 3.32 mm; $P = .02$) and showed a trend toward increased curved length (31.13 ± 5.38 mm versus 29.88 ± 4.79 mm; $P = .07$). As a consequence, the tortuosity index did not differ between patients with FD and control patients (0.097 ± 0.083 versus 0.099 ± 0.113; $P = .86$). Curved length and tortuosity index showed a positive correlation with age in both the patient and control groups ($P < .001$). In contrast, the linear length correlated with age only in the FD group ($P = .002$).

Male patients with FD had increased curved length and tortuosity index compared with female patients with FD (32.72 ± 5.81 mm versus 30.21 ± 4.92 mm; $P = .02$ and 0.132 ± 0.094 versus 0.077 ± 0.070; $P < .001$, respectively) and male control patients (32.72 ± 5.81 mm versus 29.83 ± 4.5 mm; $P = .01$ and 0.132 ± 0.094 versus 0.075 ± 0.085; $P = .006$). No significant difference was observed between male and female control patients. No significant difference was found between female patients with FD and female control patients after adjusting for age.

Analysis of Diameter Versus Length and Tortuosity

The mean basilar artery diameter showed no correlation with curved length and tortuosity index in control patients and showed a mild correlation ($r = 0.35$ and $r = 0.43$, respectively) in patients with FD.

The curved length showed a mean increase of 4.2% in patients with FD compared with control patients (9.7% in male patients with FD compared with male control patients), whereas the mean lumen diameter (ie, circumference) showed a mean increase of 12.4% in patients with FD compared with control patients (14.3% in male patients with FD compared with male control patients).

DISCUSSION

This MRA study quantitatively investigated the morphologic basilar artery lumen changes in FD, showing the progressive and profound vessel remodeling that ultimately leads to basilar artery dolichoectasia. In particular, patients with FD presented increased basilar artery diameter, length, and tortuosity that differed significantly according to patient sex and age.

Basilar Artery Diameter Changes

Ectasia of intracranial arteries has been qualitatively observed in patients with FD at both pathologic and neuroimaging evaluation.[9-13] A few studies applied a semiquantitative or quantitative approach with MRA 3D reconstructions (2 studies with 1.5T and 1 with 3T scanner),[14-16,19] T2 axial images (van der Tol L, personal communication), either T2 axial images or MRA,[17] or axial partitions of MRA (present study). Despite different methods, sequences, and scanners used for the measurement and the different ways to present study findings (different patient subgrouping, mean or median value, etc), all studies consistently showed the increase of the basilar artery diameter in patients with FD compared with control patients (On-line Table 2).

As expected for an X-linked disease, the basilar artery diameter in FD was shown to be significantly greater among male patients compared with female patients in all previous studies except one.[19] The latter discordant result might have depended on the

small sample size (5 males versus 7 females) or on the age of the sex subgroups considered in the study (mean age of female study participants, >40 years). In fact, according to our findings, the basilar artery diameter appears to already be enlarged in male patients with FD at a young age, whereas women show significant basilar artery changes only above the age of 45 years. The different behavior of basilar artery diameter according to sex is interesting for several reasons. For example, it limits the efficacy of basilar artery diameter as a criterion for differentiating female patients with FD from patients with multiple sclerosis, as recently suggested.[20] In fact, the diagnostic dilemma usually involves young women aged less than 45 years with neurologic symptoms and nonspecific white matter signal abnormalities.[20] In addition, because WM changes also seem to appear early in female patients with FD, but basilar artery changes occur later in women, macroangiopathy seems to have no role or a minimal role in the appearance of white matter signal abnormalities. Therefore, micro- and macroangiopathy might present different time courses in FD.

Length and Tortuosity of the Basilar Artery

The approach applied in this study provides quantitative information on the effect of FD on the elongation of the basilar artery. Indirect data have been provided by previous case reports, case series, and small studies based on qualitative evaluations (On-line Table 3).[9,10,13] Recently, Politei et al[17] applied a semiquantitative approach with the Smoker criteria. According to the Smoker criteria, in addition to a basilar diameter greater than 4.5 mm, the position of the top of the basilar artery (indicative of the length of the artery) and the basilar artery position with respect to the midline (indicative of the tortuosity of the artery) also concur in the identification of dolichoectasic basilar arteries. Politei et al[17] found an increased rate of dolichoectasia in patients with FD, especially among males (55.5% of male patients with FD versus 34.8% of female patients with FD; $P = .09$). Unfortunately, this study did not include a control population and did not provide the weight of each item (diameter, elongation, and tortuosity) in determining dolichoectasia in the FD population, hampering their precise analysis.

In the present study, FD-related vessel elongation was directly demonstrated by the increased curved length (effective length of the basilar artery in its 3D cisternal course) in male patients with FD compared with female patients with FD and control patients. In addition, patients with FD showed increased linear distance between the proximal and distal extremities of the basilar artery. The concomitant cranial displacement of the top of the basilar artery likely determines a higher score at the second item of the Smoker criteria, thus contributing to the high rate of dolichoectasia observed in patients with FD.[17] The measurement of both curved and linear basilar artery length allowed us to precisely quantify the basilar artery tortuosity by a tortuosity index. Although the concomitant increase of the linear length partly hampered the efficacy in detecting basilar artery tortuosity changes, this measure further highlighted the sex-related artery vulnerability in FD, showing a significantly increased basilar artery tortuosity in male patients with FD compared with both female patients with FD and male control patients. Although the Smoker score is easily applicable to conventional T2 axial images and is certainly less time-consuming, the quantitative evaluation of linear length, curved length, and tortuosity index on 3D-TOF MRA proved to be highly reproducible in our study, providing a powerful and reliable tool for the follow-up of the natural history of artery changes in FD over the years as well as the monitoring of any therapeutic intervention.

Evolution of Basilar Artery Changes

The evolution of basilar artery changes is an obvious phenomenon that can be inferred by the fact that megadolicho-arteries do not appear, or at least have never been reported, in pediatric patients with FD. Nonetheless, the characterization of the evolution of basilar artery changes in FD remains rather elusive. Azevedo et al[19] found increased basilar artery diameter values in older patients with FD, whereas Fellgiebel et al[14,15] and Uçeyler et al[16] found no association with age. The present study showed that the basilar artery diameter increases significantly with age in the female subgroup, whereas male patients with FD and both male and female control patients do not change significantly over time. According to these findings, male patients with FD already present increased mean basilar artery diameter at a young age, with scarce changes over time, whereas female patients with FD progress from values that do not differ from control patients to values that do not differ from male patients with FD. Altogether, these contradictory findings underlie 1) the heterogeneity of basilar artery involvement in FD and 2) the difficulty in extrapolating complex phenomena in rare diseases without well-designed, long-lasting longitudinal studies in large patient cohorts with sex- and age-matched control patients. For example, the lack of evolution of basilar artery diameter in men might be related to a higher early mortality in patients with more severe intracranial artery involvement. Because stroke is associated with an increased basilar artery diameter in the healthy population[21] and stroke occurs at a younger age in male patients with FD,[2] a biased selection might have altered basilar artery diameter age-dependent findings in a transverse study design.

Hitherto, the evolution of basilar artery elongation has never been addressed, and all the information can be driven only from the present study, which necessarily requires further validation. According to our findings, basilar artery elongation seems to be an age-dependent phenomenon recognizable in both patients with FD and control patients. Nonetheless, patients with FD also present an age-dependent significant increase of the linear distance between the proximal and distal extremities of the basilar artery, which likely results in cranial ectopia of its distal extremity.

Altogether, these artery changes involving diameter, length, and tortuosity might explain the high rate of dolichoectasia previously detected semiquantitatively in patients with FD.[17]

Ectasia Versus Elongation

Dolichoectatic changes might represent different faces of the same phenomenon (ie, the structural disruption of the artery vessel wall) or underlie different pathogenic mechanisms. Actually,

diameter, curved length, and tortuosity index showed no correlation among control patients and displayed a relatively weak relationship within the FD cohort. In addition, the severity of the curved length and diameter changes in the FD cohort compared with control patients demonstrates that the artery wall is nearly 3 times more vulnerable circumferentially than longitudinally. This observation seems to be consistent with functional and pathologic findings in FD that report the primary involvement of the smooth muscle cells in the accumulation of globotriaosylceramide, reduced sympathetic innervation of proximal cerebral arteries, and enhanced release of nitric oxide from endothelial cells.[5] Because the smooth muscle cell tone is pivotal in controlling the vessel radius according to brain parenchyma metabolic need, media layer dysfunction might manifest prevalently as ectasia and, only to a lesser extent, elongation. The presence of basilar artery ectasia in other lysosomal storage disorders, like late-onset Pompe disease, might support the role of metabolite accumulation within the smooth muscle cells.[22,23]

Diagnostic Role of Basilar Artery Changes in FD

Limits inherent to the measurement of the basilar artery diameter and to scanners, sequences, and methods applied have been discussed above. For example, the evaluation of the basilar artery diameter on MRA most likely leads to an underestimation compared with T2 axial findings because MRA represents only the vessel lumen, whereas T2 imaging measurement includes the vessel wall. In addition, sequences with long TR and TE (T2 imaging) are prone to CSF pulsation artifacts around the basilar artery that might alter the measurement of the vessel diameter. Sequences on different scanners might differ for resolution, with a considerable impact on the measurement of the basilar artery diameter. Nonetheless, at least 2 further anatomic and methodologic aspects need to be discussed. In contrast to the internal carotid artery, the basilar artery shows high diameter variability even among patients who do not have FD (2.8–4.4 mm in the present study, but also 1.2–5.5 mm).[16] The caliper variability of the vertebral arteries and the rather common variants of the circle of Willis involving the precommunicating P1 segment of the posterior cerebral arteries might significantly influence the basilar artery diameter, hampering its diagnostic value. In fact, nearly 20% of P1 segments are hypoplastic, and the blood flow of the postcommunicating P2 segment might be partly or completely sustained by the ipsilateral internal carotid artery via the posterior communicating artery. A significant basilar artery diameter increment in a patient with FD with unilateral or bilateral P1 segment hypoplasia would probably not lead to "increased" values compared with the normal mean value. This anatomic variability might result in a decreased sensitivity of basilar artery diameter cutoff values when looking for a high specificity (a cutoff of 4.42 mm in the present study had a specificity of 97.2%, but a sensitivity of 28.1%), especially among young women, in whom the differences between patients and control patients are less evident, if there are any.

The methodologic aspect regards the variability of the diameter according to image windowing. Previous studies did not specify the window parameters used for the evaluation of the basilar artery diameter because they depend on the investigator's choice and on image features that might vary from patient to patient, even when using the same sequence parameters. Different image windowing might lead to the inclusion or exclusion of a pixel at the border of the vessel. Because the pixel size is usually 0.3–0.4 mm and the mean basilar artery diameter in control patients is approximately 3.7 mm, different image windowing might lead to a 10%–20% variability in the measure obtained. This fact might partly explain the difficulty of replicating cutoff values in different studies. A previous study investigated 25 patients with FD and showed that a basilar artery diameter cutoff of 2.98 mm could differentiate patients with FD from young patients without FD who have had a stroke with a specificity of 88.5% and a sensitivity of 84%.[15] Another study on 87 patients with FD demonstrated that a basilar artery diameter cutoff of 3.2 mm had a sensitivity of 87% and a specificity of 86% in discriminating male patients with FD from male control patients (no difference was found between male patients with FD and male patients without FD who have had a stroke or among female subgroups).[16]

Therefore, to minimize the measurement variability, we applied an easily replicable standardized method to optimize and standardize the image windowing throughout the study (On-line Appendix). Indeed, we obtained outstanding interrater and intrarater reproducibility of the basilar artery diameter measurements. Nonetheless, because differences in image windowing, sequences, sequence parameters, and scanners might significantly impact the final measure of the vessel diameter, center-specific normative values are likely required, and literature cutoff values can hardly be used in a diagnostic setting of FD. Taking into account the anatomic variability of the circle of Willis, the use of the basilar artery diameter as a unique marker of FD appears rather inefficient.

Similarly, basilar artery linear and curved length and the relative tortuosity index proved to retain very poor diagnostic utility because of the largely overlapping findings between patients with FD and control patients. These limits are minimized in a longitudinal study design because the anatomy of the circle of Willis does not change significantly over time, thus allowing precise monitoring of the basilar artery dolichoectatic changes.

To note, the inclusion of patients with headache and TIA in our control group might represent a possible drawback of the study. Even though no study has shown basilar artery changes in patients with headache and TIA, these patients may potentially present initial dolichoectatic abnormalities that might have hampered the recognition of FD basilar artery changes. According to this hypothesis, basilar artery changes in FD may be even more evident when using healthy patients as control patients. However, a positive control group has the advantage of being closer to a clinical setting, where some of the abovementioned vascular changes have been proposed for diagnostic purposes.

CONCLUSIONS

The panel of measurements (artery diameter, length, and tortuosity) applied in this study provides some relevant hints about the pathophysiology of vessel remodeling in FD. Moreover, our study provides an interesting tool for monitoring the natural course of

basilar artery changes and the possible response to treatments. Despite these findings, basilar artery measures seem to retain limited value in a routine diagnostic setting unless a highly selective basilar artery diameter cutoff is considered.

Disclosures: Renzo Manara—*UNRELATED*: *Payment for Lectures (including service on Speakers Bureaus)*: Biomarin, Merks, Shire, *Comments*: honoraria for lectures. Giampiero Locatelli—*UNRELATED*: *Travel/Accommodations/Meeting Expenses Unrelated to Activities Listed:*, *Comments*: Boston paid fees for congresses and courses about interventional neuroradiology (approximately €700 per course or congress). Dominique Germain—*UNRELATED*: *Consultancy*: Sanofi-Genzyme, Shire; *Grants/Grants Pending*: Amicus, Sanofi-Genzyme, Shire*; *Payment for Lectures (including service on Speakers Bureaus)*: Sanofi-Genzyme, Shire; *Travel/Accommodations/Meeting Expenses Unrelated to Activities Listed*: Sanofi-Genzyme, Shire. Alessandro Burlina—*UNRELATED*: *Board Membership*: Sanofi-Genzyme, *Comments*: approximately €2000 as member of the European Advisory Board of the Fabry Registry, which is sponsored by Sanofi-Genzyme; *Payment for Lectures (Including Service on Speakers Bureaus)*:, *Comments*: approximately €3000; *Travel/Accommodations/Meeting Expenses Unrelated to Activities Listed:*, *Comments*: related to the payment of lectures or seminars.*Money paid to institution.

REFERENCES

1. Germain DP. **Fabry disease.** *Orphanet J Rare Dis* 2010;5:30 CrossRef Medline
2. Kolodny E, Fellgiebel A, Hilz MJ, et al. **Cerebrovascular involvement in Fabry disease: current status of knowledge.** *Stroke* 2015;46:302–13 CrossRef Medline
3. Boutouyrie P, Laurent S, Laloux B, et al. **Non-invasive evaluation of arterial involvement in patients affected with Fabry disease.** *J Med Genet* 2001;38:629–31 CrossRef Medline
4. Boutouyrie P, Laurent S, Laloux B, et al. **Arterial remodelling in Fabry disease.** *Acta Paediatr Suppl* 2002;91:62–66 CrossRef Medline
5. Rombach SM, Twickler TB, Aerts JM, et al. **Vasculopathy in patients with Fabry disease: current controversies and research directions.** *Mol Genet Metab* 2010;99:99–108 CrossRef Medline
6. Orssaud C. **Ocular manifestations in Fabry disease: a survey of 32 hemizygous male patients.** *Ophthalmic Genet* 2003;24:129–39 CrossRef Medline
7. Zampetti A, Gnarra M, Borsini W, et al. **Vascular endothelial growth factor (VEGF-a) in Fabry disease: association with cutaneous and systemic manifestations with vascular involvement.** *Cytokine* 2013;61:933–39 CrossRef Medline
8. Michaud L. **Vascular tortuosities of the upper eyelid: a new clinical finding in Fabry patient screening.** *J Ophthalmol* 2013;2013:207573 CrossRef Medline
9. Garzuly F, Maródi L, Erdös M, et al. **Megadolichobasilar anomaly with thrombosis in a family with Fabry's disease and a novel mutation in the alpha-galactosidase A gene.** *Brain* 2005;128:2078–83 CrossRef Medline
10. Maisey DN, Cosh JA. **Basilar artery aneurysm and Anderson-Fabry disease.** *J Neurol Neurosurg Psychiatry* 1980;43:85–87 CrossRef Medline
11. Jardim L, Vedolin L, Schwartz IV, et al. **CNS involvement in Fabry disease: clinical and imaging studies before and after 12 months of enzyme replacement therapy.** *J Inherit Metab Dis* 2004;27:229–40 CrossRef Medline
12. Gupta S, Ries M, Kotsopoulos S, et al. **The relationship of vascular glycolipid storage to clinical manifestations of Fabry disease: a cross-sectional study of a large cohort of clinically affected heterozygous women.** *Medicine (Baltimore)* 2005;84:261–68 CrossRef Medline
13. Ginsberg L, Manara R, Valentine AR, et al. **Magnetic resonance imaging changes in Fabry disease.** *Acta Paediatr Suppl* 2006;95:57–62 CrossRef Medline
14. Fellgiebel A, Keller I, Marin D, et al. **Diagnostic utility of different MRI and MR angiography measures in Fabry disease.** *Neurology* 2009;72:63–68 CrossRef Medline
15. Fellgiebel A, Keller I, Martus P, et al. **Basilar artery diameter is a potential screening tool for Fabry disease in young stroke patients.** *Cerebrovasc Dis* 2011;31:294–99 CrossRef Medline
16. Uçeyler N, Homola GA, Guerrero González H, et al. **Increased arterial diameters in the posterior cerebral circulation in men with Fabry disease.** *PLoS One* 2014;9:e87054 CrossRef Medline
17. Politei J, Schenone AB, Burlina A, et al. **Vertebrobasilar dolichoectasia in Fabry disease: the earliest marker of neurovascular involvement?** *J Inborn Errors Metab Screen* 2014; DOI: 10.1177/2326409814541246
18. Manara R, Gabrieli J, Citton V, et al. **Intracranial internal carotid artery changes in acromegaly: a quantitative magnetic resonance angiography study.** *Pituitary* 2014;17:414–22 CrossRef Medline
19. Azevedo E, Mendes A, Seixas D, et al. **Functional transcranial Doppler: presymptomatic changes in Fabry disease.** *Eur Neurol* 2012;67:331–37 CrossRef Medline
20. Böttcher T, Rolfs A, Tanislav C, et al. **Fabry disease - underestimated in the differential diagnosis of multiple sclerosis?** *PLoS One* 2013;8:e71894 CrossRef Medline
21. Pico F, Labreuche J, Gourfinkel-An I, et al. **Basilar artery diameter and 5-year mortality in patients with stroke.** *Stroke* 2006;37:2342–47 CrossRef Medline
22. Sacconi S, Bocquet JD, Chanalet S, et al. **Abnormalities of cerebral arteries are frequent in patients with late-onset Pompe disease.** *J Neurol* 2010;257:1730–33 CrossRef Medline
23. Laforêt P, Petiot P, Nicolino M, et al. **Dilative arteriopathy and basilar artery dolichoectasia complicating late-onset Pompe disease.** *Neurology* 2008;27:70:2063–66 CrossRef Medline

Toward Precision and Reproducibility of Diffusion Tensor Imaging: A Multicenter Diffusion Phantom and Traveling Volunteer Study

E.M. Palacios, A.J. Martin, M.A. Boss, F. Ezekiel, Y.S. Chang, E.L. Yuh, M.J. Vassar, D.M. Schnyer, C.L. MacDonald, K.L. Crawford, A. Irimia, A.W. Toga, P. Mukherjee, and the TRACK-TBI Investigators

ABSTRACT

BACKGROUND AND PURPOSE: Precision medicine is an approach to disease diagnosis, treatment, and prevention that relies on quantitative biomarkers that minimize the variability of individual patient measurements. The aim of this study was to assess the intersite variability after harmonization of a high-angular-resolution 3T diffusion tensor imaging protocol across 13 scanners at the 11 academic medical centers participating in the Transforming Research and Clinical Knowledge in Traumatic Brain Injury multisite study.

MATERIALS AND METHODS: Diffusion MR imaging was acquired from a novel isotropic diffusion phantom developed at the National Institute of Standards and Technology and from the brain of a traveling volunteer on thirteen 3T MR imaging scanners representing 3 major vendors (GE Healthcare, Philips Healthcare, and Siemens). Means of the DTI parameters and their coefficients of variation across scanners were calculated for each DTI metric and white matter tract.

RESULTS: For the National Institute of Standards and Technology diffusion phantom, the coefficients of variation of the apparent diffusion coefficient across the 13 scanners was <3.8% for a range of diffusivities from 0.4 to 1.1 × 10^{-6} mm^2/s. For the volunteer, the coefficients of variations across scanners of the 4 primary DTI metrics, each averaged over the entire white matter skeleton, were all <5%. In individual white matter tracts, large central pathways showed good reproducibility with the coefficients of variation consistently below 5%. However, smaller tracts showed more variability, with the coefficients of variation of some DTI metrics reaching 10%.

CONCLUSIONS: The results suggest the feasibility of standardizing DTI across 3T scanners from different MR imaging vendors in a large-scale neuroimaging research study.

ABBREVIATIONS: AD = axial diffusivity (units of 10^{-3} mm^2/s); CoV = coefficient of variation; FA = fractional anisotropy; MD = mean diffusivity (units of 10^{-3} mm^2/s); NIST = National Institute of Standards and Technology; PVP = polyvinylpyrrolidone; RD = radial diffusivity (units of 10^{-3} mm^2/s); TBI = traumatic brain injury; TRACK-TBI = Transforming Research and Clinical Knowledge in Traumatic Brain Injury

The new paradigm of precision medicine relies on quantitative biomarkers validated for their accuracy and efficacy. They must also be standardized so that precise and reproducible measurements can be made despite differences in instrumentation and procedures.[1] Medical imaging can provide many clinically useful biomarkers; however, the precision of its metrics must first be established in large-scale multisite studies that encompass the range of scanning hardware and software used to acquire the data.

DTI studies of patients with traumatic brain injury (TBI) show alterations of white matter microstructure in many tracts, across the range of severe, moderate, and mild TBI.[2-5] However, TBI is a highly heterogeneous pathology in cause, severity, and clinical course. New standardized clinical and imaging biomarkers are needed to enhance outcome prediction and for triage to the most appropriate therapeutic interventions. Transforming Research and Clinical Knowledge in TBI (TRACK-TBI), a National Insti-

Received May 1, 2016; accepted after revision October 10.

From the Departments of Radiology and Biomedical Imaging (E.M.P., A.J.M., F.E., Y.S.C., E.L.Y., P.M.), Neurological Surgery and Brain and Spinal Injury Center (M.J.V.), and Bioengineering and Therapeutic Sciences (P.M.), University of California, San Francisco, San Francisco, California; National Institute of Standards and Technology (M.A.B.), Boulder, Colorado; Brain and Spinal Cord Injury Center (E.L.Y., M.J.V., P.M.), San Francisco General Hospital and Trauma Center, San Francisco, California; Department of Psychology (D.M.S.), University of Texas, Austin, Texas; Department of Neurological Surgery (C.L.M.), University of Washington, Seattle, Washington; and Mark and Mary Stevens Neuroimaging and Informatics Institute (K.L.C., A.I., A.W.T.), University of Southern California, Los Angeles, California.

This research was funded by National Institutes of Health grant U01 NS086090.

Grant funding support for investigators: A.J.M., NIH R01EB012031, NIH U01NS086090, NIH R21CA186140, NIH R01CA194533, Voyager Therapeutics, Quest Diagnostics Incorporated; E.L.Y., NIH U01 NS086090, DoD W81XWH-14–2-0176, D.M.S., DoD-Navy W911QY-14-C-0070, NIH U01NS086090, NIH R01AG046460; C.L.M., NIH R01HD083126, DoD PT108802-SC104833-S1, NIH U01NS086090, DoD W81XWH-14–2-0176; A.I., NIH R44 NS 081792, NIH U01NS086090; A.W.T., NIH R01MH094343, NIH P41EB015922, NIH U01NS086090; and P.M., NIH R24MH106096, NIH R01HD072074, NIH U01 NS086090, DoD W81XWH-14–2-0176, DoD W81XWH-13–1-0494, GE 114-2014-GES-0001.

Please address correspondence to Pratik Mukherjee, MD, PhD, Department of Radiology and Biomedical Imaging, University of California, San Francisco, China Basin, 185 Berry St, San Francisco, CA 94107; e-mail: pratik.mukherjee@ucsf.edu

http://dx.doi.org/10.3174/ajnr.A5025

tutes of Health–funded study, began in October 2013 with the goal of enrolling 3000 patients with TBI at 11 enrollment sites across the United States. The objective was to create a large, high-quality data base that integrates clinical, imaging, proteomic, genomic, and outcome measures to establish more precise methods for TBI diagnosis and prognosis.[6] The first critical element for a multicenter imaging study is to minimize the intersite variability. Biomarkers derived from DTI metrics must be optimally robust with respect to differences in the acquisition hardware and software across medical centers.[7] Intersite differences can originate from variations in scanner manufacturer; hardware characteristics such as field strength, gradient strength, and speed; and the type of radiofrequency coil, software version, site-specific quality control procedures, and adherence to the research protocol.[8]

Diffusion phantom and human volunteer studies are needed to assess the reproducibility and variability of the imaging data. Previous studies have shown DTI variability on test-retest studies,[9-20] but only 3 previous articles[7,21,22] have studied systematic DTI variability due to intrinsic differences between different MR imaging systems in an isotropic phantom and in a human volunteer, either within a single site or across sites. However, these prior investigations were limited to relatively few sites in the case of multicenter studies, to 1.5T scanners or a combination of 1.5T and 3T scanners, to a DTI protocol with low angular resolution, and, in 1 case, to nonharmonized DTI by using different protocols at different sites.

In this study, we assessed the intersite precision of DTI metrics from a harmonized high-angular-resolution DTI protocol across thirteen 3T scanners at the 11 sites enrolling patients for the TRACK-TBI study. High-angular-resolution diffusion imaging, which requires the acquisition of ≥30 diffusion gradient directions per scan, has been proposed to improve the accuracy and reliability of DTI metrics compared with standard DTI acquisitions with fewer directions.[23,24] In addition to the traveling human volunteer, data were acquired from a novel isotropic diffusion phantom developed at the National Institute of Standards and Technology (NIST), which allows precise assessment of the range of diffusivities that might be encountered in healthy and pathologic brain tissue.

MATERIALS AND METHODS

All study procedures were approved by the institutional review boards of all 11 enrollment sites of the TRACK-TBI multicenter study.

The initial diffusion phantom and human brain data were acquired from all 13 scanners at the 11 sites within a 4-month time period at the beginning of the study. The acquisition, processing, and analysis of the isotropic diffusion phantom data were performed by a PhD MR imaging physicist (A.J.M), who is a Professor of Radiology with 25 years of experience in industry and academia. The traveling volunteer brain imaging data were processed and analyzed by a PhD scientist (E.M.P.) with 8 years of experience in diffusion tensor image processing and analysis in TBI. All of the imaging analysis was overseen by a board-certified neuroradiologist (P.M.) with 20 years of experience with DTI research and who is the director of the imaging core and a Principal Investigator of the multicenter study.

NIST Isotropic Diffusion Phantom

Diffusion MR imaging was acquired from a prototype isotropic diffusion phantom in a 3D-printed shell developed at the NIST and from the brain of a traveling healthy volunteer (male, 49 years of age) on thirteen 3T MR imaging scanners at 11 different sites by using 8- or 12-channel head radiofrequency coils. Isotropic phantoms are used to calibrate diffusivities, so a full DTI acquisition or identical parameters with the traveling volunteer sequences is not a requirement. The main objective of the isotropic phantoms is to verify the precision of the principal axis diffusivities because all DTI metrics are computed from these diffusivities.

The diffusion phantom was scanned at $b=0$, 500, and 900 s/mm^2 with 1.1-mm in-plane resolution and 5-mm sections, by using 3 orthogonal directions and 4 signal averages. An 11-section protocol was used and the image stack was prescribed such that the sections were centered on the phantom and intersected vials within the phantom cross-sectionally.

Traveling Volunteer

The traveling volunteer was scanned once at each center during the same session as the NIST phantom. All volunteer scans were acquired within a 4-month interval. Additionally, from one of the sites (site 3), 2 DTI scans were acquired on the same day from the human traveling volunteer, 30 months after the first DTI acquisition from this volunteer. The characteristics of the scanners for each site and parameters of acquisition from the traveling volunteer in each site are reported in Table 1. The DTI protocol is based on the "Enhanced DTI" standard established by the Alzheimer Disease Neuroimaging Initiative 2 study for GE Healthcare scanners (http://adni.loni.usc.edu/wpcontent/uploads/2010/05/ADNI2_GE_22_E_DTI.pdf), except that 64 diffusion directions were used at most sites instead of 60 directions to accommodate the Siemens in-product DTI sequence in specifying the number of directions. In brief, the protocol consists of a multislection spin-echo echo-planar sequence with 2.7-mm isotropic spatial resolution and a b-value of 1300 s/mm^2, with 8 additional brain volumes acquired at $b=0$ s/mm^2.

All the images were inspected, and none had any major artifacts. One of the advantages of using high-angular-resolution diffusion imaging is that a corrupted image in any single direction has a minimal effect on the fitting or metrics. Thus, images from high-angular-resolution diffusion imaging produce more accurate and reliable results than lower angular resolution acquisitions.

Preparation and Processing of the NIST Isotropic Diffusion Phantom

We established an array of thirteen 20-mL vials containing variable amounts of the polymer polyvinylpyrrolidone (PVP) (Fig 1).[25] PVP containing vials, with mass fractions of 0%, 10%, 20%, 30%, 40%, and 50% were arranged in a plane, with 0% PVP (deionized water) at the center and increasing concentrations of PVP in 2 rings around the central vials. Vials were contained in a spheric water-tight vessel. The phantom was transported between

Table 1: DTI acquisition protocol for the 11 academic medical centers[a]

Site	Scanner	Vendor	Model and Field (Tesla)	Software Version	Head Coil (Channels)	Voxel Size	Flip Angle	TR (ms)	TE (ms)	Directions	Sections	Matrix	b-Value	B0
1	Trio	Siemens	Trio 3T	syngo MR B17	12	2.7	90°	9000	94	64	64	128 × 84	1300	8
2a	Skyra	Siemens	Skyra 3T	syngo MR D13	12	2.7	90°	9000	92	64	59	128 × 84	1300	8
2b	Trio	Siemens	Trio 3T	syngo MR B17	12	2.7	90°	9000	94	64	59	128 × 84	1300	8
3	MR750	GE	MR750 3T	DV24.0_RO1_1344	8	2.7	90°	9050	81	60	59	128 × 128	1300	8
4	Signa	GE	Signa 3T	HD16.0_V02_1131a	8	2.7	90°	14,000	83	60	54	128 × 128	1000	8
5	Trio	Siemens	Trio 3T	syngo MB B17	12	2.7	90°	9000	94	64	59	128 × 84	1300	8
6	Trio	Siemens	Trio 3T	syngo MR B17	12	2.7	90°	9000	94	64	59	128 × 84	1300	8
7a	MR750	GE	MR750 3T	DV24.0_R01_1344	8	2.7	90°	9000	81	60	59	128 × 128	1300	8
7b	Trio	Siemens	Trio 3T	syngo MR B17	12	2.7	90°	9000	94	64	59	128 × 84	1300	8
8	Skyra	Siemens	Skyra 3T	syngo MR D13	20	2.7	90°	9000	92	64	59	128 × 84	1300	8
9	Signa	GE	Signa 3T	HD16.0_V02_1131a	8	2.7	90°	14,000	88	60	54	128 × 128	1300	8
10	Achieva	Phillips	Achieva 3T	U3.2.3, U3.2.3.1	8	2.7	90°	9000	71	64	59	128 × 125	1300	8
11	Ingenia	Phillips	Ingenia 3T	U5.1.2, U5.1.2.0	15	2.7	90°	9000	94	64	59	128 × 126	1300	8

[a] Sites 2 and 7 participated in the study with 2 different scanners each.

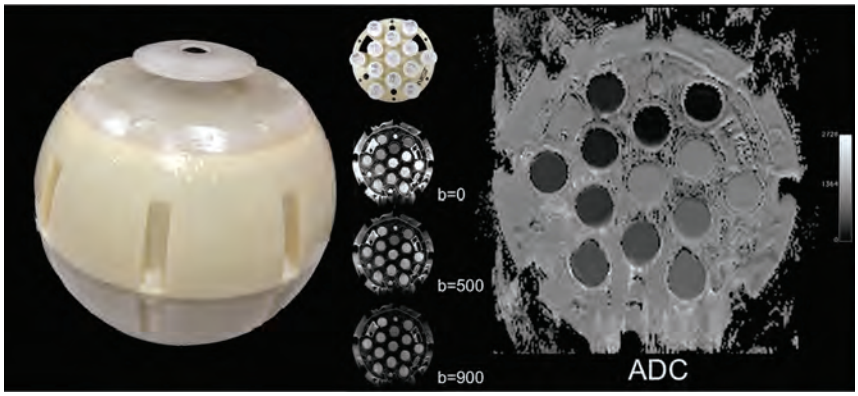

FIG 1. Prototype isotropic diffusion phantom in a 3D-printed shell from the National Institute of Standards and Technology.

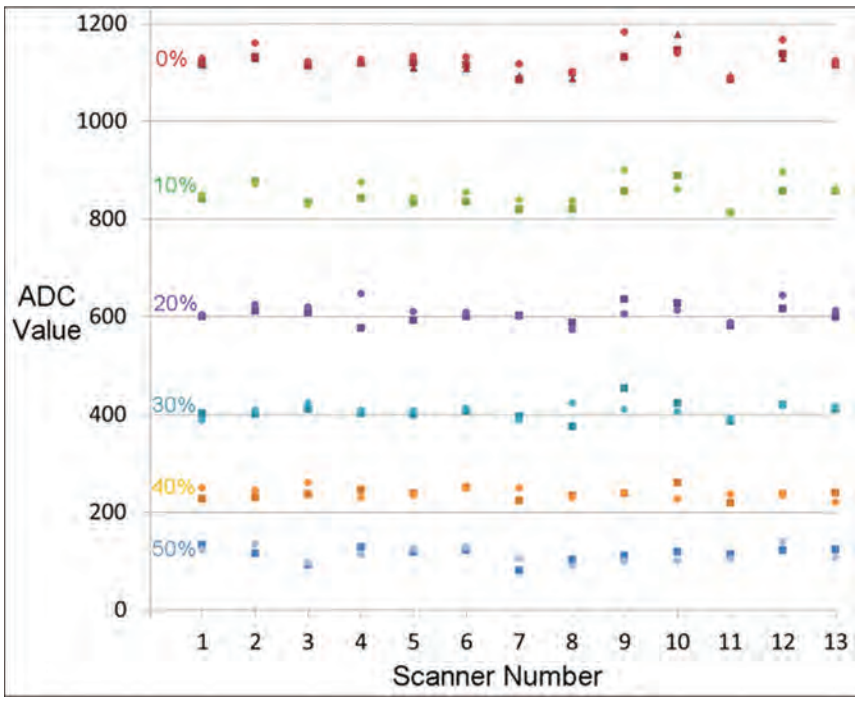

FIG 2. ADC measurements obtained across all 13 scanners in TRACK-TBI. The measured ADC in units of 10^{-6} mm^2/s for vials containing 0%–50% PVP are plotted for each TRACK-TBI MR imaging system. The NIST phantom allows 3 measures of 0% PVP and 2 measures of each of the 10%–50% PVP concentrations. Data are shown for the central vial (*triangle*), inner vials (*squares*), and outer vials (*circles*) of the phantom.

sites in a dry state in a foam enclosure. On arrival at each site, the phantom was initially packed with ice and placed in a refrigerator. In parallel, a slurry of ice and water was prepared and allowed to equilibrate for 1–2 hours. Ice water was then added to the phantom along with as much additional ice as could be accommodated; the phantom was returned to the refrigerator and left overnight (8–10 hours). In the morning, additional ice was packed into the phantom and left in an insulated container until imaged (within 2 hours).

DTI Preprocessing and Analysis for the Traveling Volunteer

DTI preprocessing and analysis were performed by using tools from the Oxford Centre for Functional MR Imaging of the Brain (FMRIB) Software Library (FSL (http://www.fmrib.ox.ac.uk/fsl)).

First, images were corrected for eddy current distortions and motion by using an average of the 8 b=0 s/mm^2 volumes as a reference. The registered images were skull-stripped by using the FSL Brain Extraction Tool (http://fsl.fmrib.ox.ac.uk/fsl/fslwiki/BET). All the resulting brain masks were visually inspected. Fractional anisotropy (FA) maps were calculated by using the FMRIB Diffusion Toolbox (http://fsl.fmrib.ox.ac.uk/fsl/fslwiki/FDT).[26] After calculation of the FA map, a voxelwise statistical analysis of the FA data was performed by using Tract-Based Spatial Statistics (TBSS; http://fsl.fmrib.ox.ac.uk/fsl/fslwiki/TBSS).[27,28] Within the TBSS pipeline, FA data were aligned into the common FMRIB58 FA template, which is in Montreal Neurological Institute 152 at-

las standard space, by using the nonlinear registration algorithm FMRIB Nonlinear Registration Tool (FNIRT; http://fsl.fmrib.ox.ac.uk/fsl/fslwiki/FNIRT).[29]

Next, a mean FA image was created from the images for all the subjects' serial scans at different sites in this common space and thinned to generate a mean FA white matter skeleton that represented the center of all tracts common to the entire group of scans. The FA white matter skeleton was thresholded to FA > 0.2 to exclude gray matter and voxels containing partial volume effects with gray matter. This process ensured that each dataset skeleton was in the group space while also representing the center of the subject's unique white matter bundles. The aligned FA volume was then projected onto the skeleton by filling the skeleton with FA values from the nearest relevant tract center. This was achieved for each skeleton voxel by searching perpendicular to the local skeleton structure for the maximum value in the FA image of the subject. Mean FA, mean diffusivity (MD), axial diffusivity (AD), and radial diffusivity (RD) values were obtained from the FA skeleton map of each scan.

Specific fasciculi were studied by using masks obtained from the FSL Jülich histologic atlas (http://neuro.debian.net/pkgs/fsl-juelich-histological-atlas.html) mapped on the standard Montreal Neurological Institute space and resampled to 1-mm resolution. Binary mask images from the fasciculi of interest were used to mask the individual FA (skeletonized) maps previously registered to the Montreal Neurological Institute standard space by using the nonlinear tools in the TBSS procedure. We included 15 large main fasciculi. Mean FA, MD, AD, and RD values were obtained from each subject's white matter skeleton and each of the skeletonized ROIs.

Table 2: Mean ADC, SD, and CoV for each concentration of PVP

	All MR Imaging Systems (n = 13)			Trio Only (n = 5)		
Vial	Mean ADC	SD	CoV	Mean ADC	SD	CoV
0% PVP	1123	23	2.1%	1105	15	1.4%
10% PVP	850	24	2.8%	829	13	1.6%
20% PVP	607	19	3.1%	596	14	2.3%
30% PVP	408	16	3.8%	399	16	4.0%
40% PVP	238	11	4.6%	237	13	5.5%
50% PVP	113	15	13.0%	105	16	15.2%

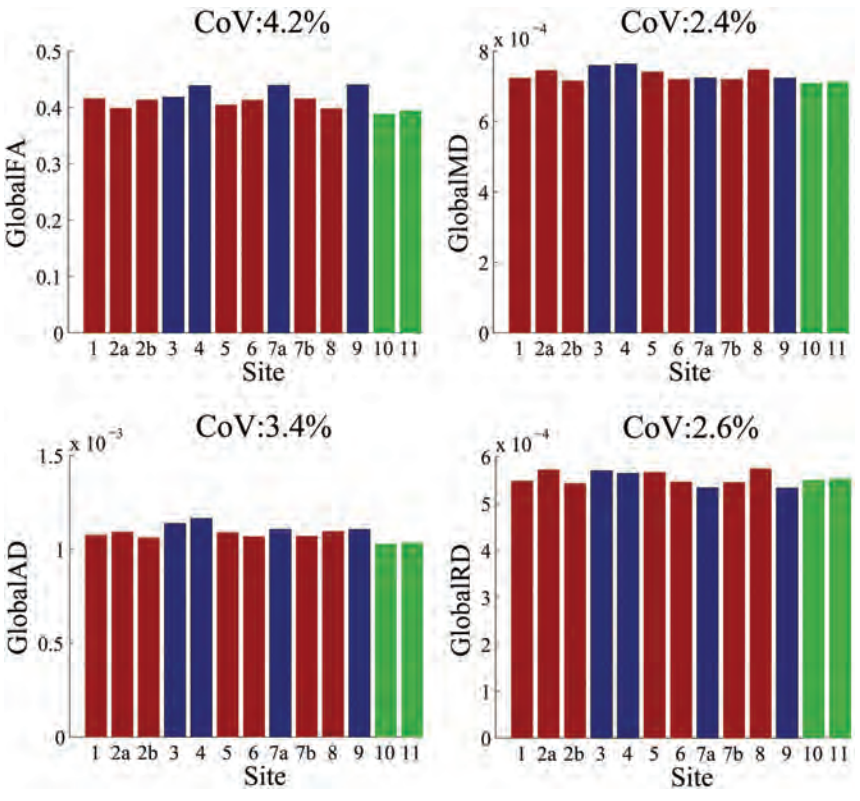

FIG 3. Global non-normalized DTI parameters and CoV across sites. Red indicates Siemens; Blue, GE Healthcare; Green, Phillips Healthcare. By order of sites, see Table 1.

Statistical Analysis

NIST Isotropic Diffusion Phantom. ADC images were reconstructed, and ROI analysis was performed. ADC values were quantified in the center section, which corresponded to the central plane of the phantom. A circular ROI measuring 1.2–1.3 cm^2 was placed in the center of each of the 13 vials, and the mean ADC value was determined. A mean ADC and its coefficient of variation (CoV), which is obtained from calculating the SD divided by the average, were established for each vial across all sites.

Traveling Volunteer. The CoV was calculated for each DTI metric in the whole white matter skeleton and for each fasciculus to summarize the amount of variation across scanners at the 11 sites. Furthermore, we also calculated a normalized CoV for each of the preselected ROIs, in which each DTI metric was divided by its corresponding mean value per site, as has been performed in prior DTI studies of TBI.[30,31]

RESULTS

NIST Isotropic Diffusion Phantom

There were 3 ADC measures for the three 0% PVP vials and 2 measures each for the paired 10%, 20%, 30%, 40%, and 50% PVP vials. The differences between the inner and outer rings of vials were not statistically significant ($P > .05$). Figure 2 shows the consistency of ADC measurements within and across systems. Table 2 provides the mean, SD, and CoV for each concentration of PVP. Data are shown for the full set of TRACK-TBI systems and for a subset of systems that shared the same manufacturer and model (Siemens Trio). The latter is the most common scanner type in TRACK-TBI study, with no more than 2 of any other system. The CoV is <3.8% for concentrations of PVP of <30% w/w. The CoV is slightly decreased if a single scanner type is considered. At 40% and 50% w/w PVP, the diffusivity decreased and the resulting CoV became larger.

Traveling Volunteer

Whole-brain DTI measurements across sites are shown in Fig 3. The CoV for global white matter skeleton DTI parameters within and across scanners was

Table 3: Mean DTI parameters across all 13 scanners and their CoV

	FA	CoV%[a]	CoV%[b]	MD	CoV%[a]	CoV%[b]	AD	CoV%[a]	CoV%[b]	RD	CoV%[a]	CoV%[b]
Global	0.41	4.16	NA	0.73	2.44	NA	1.08	3.41	NA	0.55	2.57	NA
SLFl	0.44	2.64	3.93	0.70	4.14	2.34	1.06	4.04	1.51	0.52	4.66	3.75
SLFr	0.43	3.38	2.44	0.71	2.56	0.99	1.07	3.38	1.07	0.53	2.60	1.68
SFOl	0.46	3.60	4.47	0.65	4.68	3.30	1.00	3.94	2.56	0.47	5.86	4.80
SFOr	0.45	4.72	4.22	0.67	4.94	3.62	1.03	4.82	2.55	0.50	5.90	5.19
CSTl	0.56	5.18	2.36	0.69	6.95	6.10	1.16	7.10	6.20	0.45	8.67	7.04
CSTr	0.58	5.39	3.22	0.67	6.61	5.71	1.14	6.61	5.37	0.43	8.97	7.46
CINGl	0.54	4.35	3.47	0.72	3.57	1.95	1.21	3.28	1.93	0.48	5.68	3.85
CINGr	0.50	4.42	2.69	0.74	3.77	1.66	1.20	4.43	1.79	0.51	4.39	2.65
GenuCC	0.67	5.29	3.52	0.76	4.04	4.45	1.47	3.10	1.99	0.41	10.11	9.82
BodyCC	0.66	2.60	3.32	0.82	3.05	1.97	1.56	2.66	1.97	0.44	5.41	4.18
SpleniumCC	0.74	2.56	2.20	0.70	3.11	2.26	1.44	2.76	1.68	0.32	7.30	5.81
ACRl	0.45	5.10	2.84	0.73	2.88	2.17	1.13	3.40	1.63	0.53	4.00	3.15
ACRr	0.44	5.22	3.15	0.72	4.09	3.05	1.13	4.75	2.39	0.52	4.56	3.93
PCRl	0.46	2.18	3.94	0.74	3.64	1.89	1.15	3.38	1.45	0.54	4.22	3.17
PCRr	0.46	2.86	2.30	0.74	2.82	1.64	1.13	2.83	1.99	0.54	3.49	1.79
ALICl	0.55	4.84	2.49	0.70	3.75	2.42	1.19	4.91	2.10	0.45	5.05	3.88
ALICr	0.54	6.22	3.10	0.71	3.63	2.35	1.20	4.85	2.22	0.46	5.55	4.09
PLICl	0.66	2.99	4.05	0.65	6.23	4.47	1.24	6.16	3.36	0.36	4.38	3.42
PLICr	0.64	3.78	3.54	0.67	4.38	2.78	1.25	4.44	1.84	0.38	6.95	5.67
PTRl	0.55	2.13	3.26	0.80	4.40	2.65	1.36	4.78	2.16	0.52	4.37	3.38
PTRr	0.52	3.08	1.96	0.78	3.42	1.31	1.29	3.96	1.01	0.52	3.76	1.97
ECl	0.38	7.31	4.06	0.76	2.77	1.89	1.10	3.67	1.22	0.60	3.77	2.78
ECr	0.37	7.75	4.12	0.78	2.73	1.39	1.11	4.20	1.55	0.62	3.20	1.77
UNCl	0.42	7.66	6.05	0.77	5.66	4.90	1.14	6.00	4.27	0.58	7.03	6.55
UNCr	0.43	5.57	2.94	0.75	5.97	5.00	1.14	6.60	4.84	0.56	6.29	5.43

Note:—r indicates right; l, left; SLF, superior longitudinal fasciculus; SFO, superior fronto-occipital fasciculus; CST, corticospinal tract; CC, corpus callosum; CING, cingulum corticospinal tract; ACR, anterior corona radiata; PCR, posterior corona radiata; PLIC, posterior limb of internal capsule; ALIC, anterior limb of internal capsule; PTR, posterior thalamic radiation; EC, external capsule; UNC, uncinate fasciculus; NA, not applicable.

[a] CoV across sites.

[b] CoV across sites normalized by the mean FA.

<5%, showing consistency comparable with the NIST diffusion phantom results. Table 3 and Fig 4 report the mean of the DTI parameters of each of the 14 white matter tracts (left and right sides) and the CoV extracted from the DTI parameters and their normalized values. For FA, MD, AD, and RD values, the CoV was ≤5% for most tracts both within and across scanners (Tables 3 and 4). The CoV of normalized DTI values was less than that of non-normalized DTI values.

DISCUSSION

In this study of intersite variability of DTI by using both an isotropic phantom and a human volunteer, the 3T high-angular-resolution diffusion imaging protocol yielded CoVs below 5% for FA, MD, AD, and RD, averaged over the white matter skeleton of the whole brain. This finding demonstrates acceptably low intersite variation despite the 3 different scanner vendors and 6 different scanner models across the 11 centers. When examining the DTI parameters for specific tracts, we found better measurement precision in large central tracts than in small peripheral white matter, with reduced variability (lower CoV) when normalizing the values by the global DTI parameters per site. The low intersite variability of diffusion metrics was confirmed by ADC results across all 13 scanners from the NIST diffusion phantom over a range of values characteristic of the healthy human brain, as well as high and low values caused by pathology such as TBI.

The NIST has developed a series of MR imaging isotropic diffusion phantoms to enable stable measurements to mimic human tissue responses to MR imaging in a predictable and repeatable way for use in calibrating MR imaging scanners. The NIST isotropic diffusion phantom in the present study contained variable amounts of the PVP, which, at different concentrations, has shown properties similar to those of healthy brain tissue.[25] The different concentrations in each of the vials corresponded with the expected degrees of diffusivity and showed minimal variation between scanners. The relatively poor CoV seen at very low diffusivities likely comes from the selected range of b-values, which were limited to values of 0, 500, and 900 s/mm^2. Incorporation of a larger b-value is likely to substantially improve the variance in high-PVP-concentration vials, and we have recently adapted our protocol to include a b=2000 s/mm^2 value as well.

The results of our study, with CoVs ranging from 2% to 5%, generally concur with those of prior investigations of intersite DTI measurements in healthy subjects.[9,10,18-20] In a very recent study, Kamagata et al[17] scanned 7 volunteers at 2 sites, both with 3T Achieva scanners (Philips Healthcare). With several analytic methods, including voxelwise comparison with TBSS, atlas-based analysis, and tract-specific analysis, they reported a CoV intersite variability of <4% in the case of tract-specific analysis and a CoV of <6% by using the atlas-based analysis. Even if the parameters of acquisition, scanners, and approaches of all these studies vary, the CoV seems to be a reliable and stable measure for intersite variation. However, all these studies compared groups of different healthy subjects, adding confounding factors due to intersubject biologic variability. In our study, this large source of variation was eliminated by using the same subject across all 13 scanners.

MR imaging phantoms enable more precise measurement of diffusivity values against known standards than is possible by us-

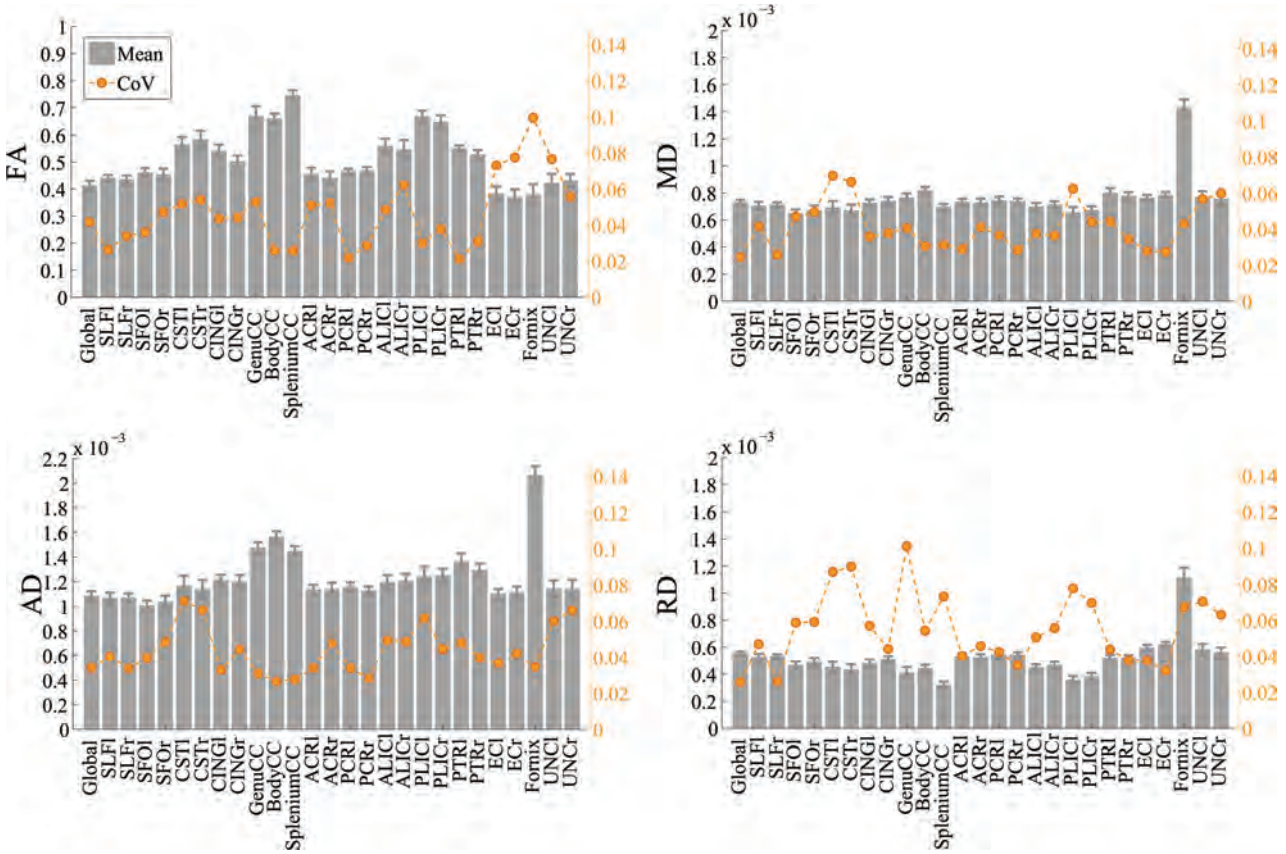

FIG 4. Graphic representation of CoVs across all 13 scanners. The coefficient of variation (percentage) is in orange. Mean non-normalized DTI parameters are in gray. r indicates right; l, left; SLF, superior longitudinal fasciculus; SFO, superior fronto-occipital fasciculus; CST, corticospinal tract; CC, corpus callosum; CING, cingulum corticospinal tract; ACR, anterior corona radiata; ALIC, anterior limb of internal capsule; PCR, posterior corona radiata; PLIC, posterior limb of internal capsule; PTR, posterior thalamic radiation; EC, external capsule; UNC, uncinate fasciculus.

ing a living human brain. To our knowledge, only 3 multisite studies have previously assessed the intersite reliability of DTI measures in both a traveling volunteer and an isotropic diffusion phantom. In the most recent study, Grech-Sollars et al[22] assessed the reproducibility of DTI in an ice water phantom and in 9 healthy volunteers across 8 scanners (1.5T Avanto; 1.5T Symphony; Siemens; 3T Achieva) at 5 sites, all by using different DTI acquisition parameters. The phantom used in that study consisted of 5 tubes filled with distilled water and 1 tube with sucrose. Despite the considerable variability across scanners and DTI protocols, the authors reported robustness across 1.5T and 3T scanners with CoVs computed from the non-normalized DTI values ranging from 1% to 7.4%.

Zhu et al[21] evaluated the intra- and intersite differences in DTI measurements in 3 centers, all with 1.5T GE Healthcare Signa scanners, in a travelling human volunteer and a phantom fabricated with cells in a cylindric polycarbonate container filled with 3 chemicals (cyclic alcanes). Their normalized bias scores results suggested that the intersite variation, though relatively small among scanners of the same vendor, significantly affects DTI measurement accuracy and precision. In Walker et al,[8] the investigators proposed a 2-step analysis for assessing phantom data in multisite DTI studies. These results were part of a pediatric brain development study at 5 sites with 1.5T scanners and the American College of Radiology MR imaging–accreditation phantom, consisting of 10 mmol of nickel chloride and sodium chloride. The results suggested that initial outlier identification is important for accurate assessment of inter- and intrasite variability and for identification of problems with data acquisition.

Our study offers several advances over these previous multisite DTI standardization studies. The novel NIST diffusion phantom has a much larger and more granular range of diffusivities, from 0.1 to 1.1 mm^2/s with 6 distinct ADC values, compared with phantoms used in prior reports. This feature allows more precise calibration of the DTI values expected in healthy and pathologic brain tissue. We restricted the study to 3T scanners to avoid systematic differences due to field strength and because the much higher signal-to-noise ratio compared with 1.5T scanners enables measurement of DTI metrics such as FA with much less uncertainty.[18] Our use of a harmonized high-angular-resolution diffusion imaging protocol with 60+ diffusion directions also allows more precise quantitation of DTI metrics.[23,24] A prior multicenter DTI standardization study of 2 traveling volunteers in five 3T scanners (3 Trio scanners and 2 Signa scanners) also used a high-angular-resolution diffusion imaging protocol with 33 diffusion directions and found good concordance of FA and MD values across sites.[19] Consistent with our results, these authors concluded that the comparability of DTI measures between different magnets supports the feasibility of multisite clinical trials by using DTI as an outcome measure. However, they reported

Table 4: Intrascanner DTI measures for site 3 and their CoV

	FA	CoV%[a]	CoV%[b]	MD	CoV%[a]	CoV%[b]	AD	CoV%[a]	CoV%[b]	RD	CoV%[a]	CoV%[b]
Global	0.41	0.73	NA	0.76	0.16	NA	1.13	0.19	NA	0.57	0.42	NA
SLFl	0.43	0.52	0.53	0.74	1.30	1.17	1.12	1.12	1.26	0.55	1.50	1.10
SLFr	0.43	3.08	3.79	0.73	1.12	1.19	1.10	0.27	0.16	0.55	2.04	2.38
SFOl	0.44	4.03	3.33	0.70	4.31	4.16	1.08	2.75	2.82	0.51	6.08	5.65
SFOr	0.45	1.94	1.43	0.73	0.19	0.13	1.13	0.85	0.66	0.53	1.28	0.94
CSTl	0.59	3.81	3.19	0.68	1.16	1.03	1.20	1.46	1.44	0.42	4.50	4.08
CSTr	0.61	3.62	2.94	0.65	2.18	2.02	1.16	0.57	0.59	0.40	4.65	4.23
CINGl	0.52	1.75	1.23	0.77	1.34	1.27	1.27	1.34	1.15	0.52	2.13	1.92
CINGr	0.48	2.65	2.23	0.78	1.40	1.26	1.24	1.38	1.37	0.54	2.49	2.16
GenuCC	0.67	0.94	0.21	0.80	0.60	0.45	1.55	0.40	0.26	0.42	1.80	1.39
BodyCC	0.54	0.46	0.29	0.87	1.79	1.64	1.62	1.58	1.69	0.49	2.18	1.76
SpleniumCC	0.75	0.97	0.27	0.70	1.86	1.72	1.47	1.07	1.20	0.31	3.73	3.31
ACRl	0.46	0.97	0.80	0.77	0.05	0.11	1.20	0.42	0.26	0.55	0.43	0.40
ACRr	0.46	0.57	0.97	0.77	0.27	0.21	1.21	0.06	0.16	0.55	0.50	0.57
PCRl	0.47	0.22	0.55	0.75	0.72	0.79	1.17	0.83	0.97	0.54	0.63	0.62
PCRr	0.46	1.02	0.64	0.74	1.13	1.11	1.14	1.34	1.15	0.54	1.29	1.22
ALICl	0.56	3.00	2.44	0.75	1.81	1.71	1.29	1.51	1.32	0.48	3.60	3.31
ALICr	0.55	2.87	2.28	0.77	0.92	1.07	1.33	2.73	2.66	0.50	1.49	1.09
PLICl	0.66	1.29	0.64	0.72	2.94	2.82	1.36	2.20	2.36	0.40	4.22	3.82
PLICr	0.66	0.82	0.98	0.71	0.70	0.57	1.35	0.18	0.35	0.40	1.74	1.56
PTRl	0.55	1.36	0.74	0.83	1.71	1.68	1.42	1.01	1.20	0.53	2.67	2.41
PTRr	0.53	0.67	1.13	0.80	1.46	1.31	1.33	1.71	1.80	0.53	1.25	0.84
ECl	0.41	3.16	2.45	0.79	1.12	0.96	1.17	1.14	0.99	0.60	2.23	1.81
ECr	0.40	1.70	1.17	0.81	0.48	0.34	1.18	0.37	0.18	0.63	1.05	0.69
Fornix	0.39	5.87	5.17	0.13	1.13	1.00	2.01	1.05	0.89	0.10	3.19	2.78
UNCl	0.44	6.63	5.96	0.84	6.53	6.38	1.29	4.17	4.22	0.62	9.17	8.75
UNCr	0.44	4.17	3.53	0.84	3.47	3.36	1.28	2.00	2.15	0.61	5.13	4.76

Note:—r indicates right; l, left; SLF, superior longitudinal fasciculus; SFO, superior fronto-occipital fasciculus; CST, corticospinal tract; CC, corpus callosum; CING, cingulum corticospinal tract; ACR, anterior corona radiata; PCR, posterior corona radiata; PLIC, posterior limb of internal capsule; ALIC, anterior limb of internal capsule; PTR, posterior thalamic radiation; EC, external capsule; UNC, uncinate fasciculus, NA, not applicable.

[a] CoV across sites.

[b] CoV across sites normalized by the mean FA.

greater intersite variability in DTI metrics than we found, with an average white matter CoV of 6.8% for FA and 4.1% for MD.

Despite having many more scanners (13 versus 5) and many more scanner models (6 versus 2) than Fox et al,[19] we found a global white matter CoV of 4.2% for FA and 2.4% for MD. This finding is likely due to the hand-drawn ROI measurements of Fox et al, which introduce intrarater and interrater variability, compared with the fully automated DTI measurements of the present study using TBSS, which has the added advantage of evaluating white matter throughout the entire brain instead of only a few selected regions. In addition, when estimating the FA CoV of a specific tract (ie, the anterior corona radiata) from a prior DTI study of mild TBI,[5] we found a 5% CoV for the anterior corona radiata, known to be commonly injured after mild TBI,[2] across the pooled group of patients with complicated mild TBIs and controls, with a statistically significant mean difference of 3% between patient and control groups at $P < .05$. Thus, the interscanner variation of FA observed in this tract in the current study across 13 different 3T scanners of various types is similar to the intersubject variability of FA on a single scanner.[5]

A limitation of our study is that only a single volunteer could be assessed at all sites, given the travel expenses involved in flying multiple volunteers to be scanned at 11 different medical centers located throughout the United States. Also, intrasite scan-rescan reliability was obtained at only 1 site, though with the same human subject scanned across all of the sites. Our results indicate, as expected, that the variability of DTI metrics is less within the same scanner (Table 4) than across different scanners (Table 3). There were small variations in the DTI protocol performed at each site due to hardware or software idiosyncrasies of each vendor platform; however, low intersite variability was achieved despite these minor protocol differences. This study was designed to measure the magnitude of variability, but the many possible sources of variation due to scanner hardware and software factors, as well as dozens of pulse sequence parameters, are beyond the scope of this study. This subject remains an open area in the DTI literature, which requires future investigation. The application of newly developed methods to retrospectively compensate for intersite differences in diffusion MR imaging acquisition by using correction factors may further reduce the variability of DTI metrics in multisite studies and improve reproducibility,[20] including for longitudinal data.[32] This application is particularly important for the investigation of smaller peripheral white matter tracts in which intersite variation is higher than in large central white matter regions.

CONCLUSIONS

By using a novel isotropic diffusion phantom and a traveling volunteer, we have demonstrated the feasibility of standardizing DTI on 3T scanners from all 3 major MR imaging vendors across the 11 patient enrollment sites of the TRACK-TBI study. Our findings support the viability and reproducibility of large-scale multisite DTI projects to validate diffusion-based biomarkers for TBI and many other neurologic and psychiatric disorders in the coming era of precision medicine.

ACKNOWLEDGMENTS

We gratefully acknowledge the MR imaging technologists and study coordinators from all sites of the TRACK-TBI study. We also acknowledge the pioneering efforts of the Quantitative Imaging Biomarkers Alliance of the Radiological Society of North America, especially their contributions to previous designs of an isotropic diffusion phantom that led to the development of the NIST diffusion phantom.

Data used in preparation of this article were obtained from the Transforming Research and Clinical Knowledge in Traumatic Brain Injury (TRACK-TBI) project. As such, there are investigators within TRACK-TBI that contributed to the design and implementation and/or provided data but did not participate in analysis or writing of this report. A complete listing of TRACK-TBI investigators can be found at: http://tracktbi.ucsf.edu/organization-and-leadership.

Disclosures: Alastair Martin—*RELATED*: *Grant*: National Institutes of Health, *Comments*: NIH U01NS086090 (Principal Investigator, Dr. Geoffrey T. Manley) "Transforming Research and Clinical Knowledge in Traumatic Brain Injury"*; *Support for Travel to Meetings for the Study or Other Purposes*: National Institutes of Health, *Comments*: NIH U01NS086090 (Principal Investigator, Dr. Geoffrey T. Manley) "Transforming Research and Clinical Knowledge in Traumatic Brain Injury."* Michael A. Boss—*UNRELATED*: *Patents (Planned, Pending, or Issued)*: National Institute of Standards and Technology, *Comments*: The phantom shell design was submitted for a patent, "MRI Phantom, Method for Making Same and Acquiring an MRI," application No. 20150323639, The author has not received any payment related to this patent application.* Frank Ezekiel—*RELATED*: *Grant*: National Institutes of Health.* David M. Schnyer—*RELATED*: *Grant*: National Institute of Neurological Disorders and Stroke*; *UNRELATED*: *Grants/Grants Pending*: National Institute of Mental Health.* Christine L. MacDonald—*RELATED*: *Grant*: National Institutes of Health, *Comments*: 1U01NS086090-01 "Transforming Research and Clinical Knowledge in Traumatic Brain Injury"*; *UNRELATED*: *Consultancy*: Sinapis Pharma, *Comments*: I received payment for consultancy to Sinapis Pharma unrelated to this article; *Employment*: University of Washington, *Comments*: I am employed at the University of Washington; *Grants/Grants Pending*: R01HD083126, *Comments*: I received an RO1 grant from National Institutes of Health/National Institute of Neurological Disorders and Stroke for research unrelated to this article; *Payment for Lectures including Service on Speakers Bureaus*: University of Tennessee Health Sciences, Neurology Grand Grounds University of Hawaii, Pathology Chronic Traumatic Encephalopathy (CTE) Conference, *Comments*: I was an invited speaker to university and symposium lectures; I received payment for invited speaking engagements during the prior 36-month period unrelated to this article. Karen L. Crawford—*RELATED*: *Grant*: National Institutes of Health*; *UNRELATED*: *Employment*: University of Southern California; *Grants/Grants Pending*: National Institutes of Health, Alzheimer's Association, Michael J. Fox Foundation.* Arthur W. Toga—*RELATED*: *Grant*: National Institutes of Health*; *UNRELATED*: *Employment*: University of Southern California; *Grants/Grants Pending*: National Institutes of Health, Alzheimer's Association, Michael J. Fox Foundation.* Pratik Mukherjee—*UNRELATED*: *Board Membership*: GE-National Football League Medical Advisory Board, *Comments*: No payment has been received by me or my institution in the prior 36 months for my service on this board; *Payment for Lectures including Service on Speakers Bureaus*: GE Healthcare, *Comments*: Webinar. *Money paid to the institution.

REFERENCES

1. Collins FS, Varmus H. **A new initiative on precision medicine.** *N Engl J Med* 2015;372:793–95 CrossRef Medline
2. Niogi SN, Mukherjee P, Ghajar J, et al. **Extent of microstructural white matter injury in postconcussive syndrome correlates with impaired cognitive reaction time: a 3T diffusion tensor imaging study of mild traumatic brain injury.** *AJNR Am J Neuroradiol* 2008; 29:967–73 CrossRef Medline
3. Newcombe V, Chatfield D, Outtrim J, et al. **Mapping traumatic axonal injury using diffusion tensor imaging: correlations with functional outcome.** *PLoS One* 2011;6:e19214 CrossRef Medline
4. Palacios EM, Sala-Llonch R, Junque C, et al. **White matter integrity related to functional working memory networks in traumatic brain injury.** *Neurology* 2012;78:852–60 CrossRef Medline
5. Yuh EL, Cooper SR, Mukherjee P, et al; TRACK-TBI INVESTIGATORS. **Diffusion tensor imaging for outcome prediction in mild traumatic brain injury: a TRACK-TBI study.** *J Neurotrauma* 2014;31:1457–77 CrossRef Medline
6. Yue JK, Vassar MJ, Lingsma HF, et al; TRACK-TBI Investigators. **Transforming research and clinical knowledge in traumatic brain injury pilot: multicenter implementation of the common data elements for traumatic brain injury.** *J Neurotrauma* 2013;30:1831–44 CrossRef Medline
7. Hsu W, Markey MK, Wang MD. **Biomedical imaging informatics in the era of precision medicine: progress, challenges, and opportunities.** *J Am Med Inform Assoc* 2013;20:1010–13 CrossRef Medline
8. Walker L, Curry M, Nayak A, et al; Brain Development Cooperative Group. **A framework for the analysis of phantom data in multicenter diffusion tensor imaging studies.** *Hum Brain Mapp* 2013;34: 2439–54 CrossRef Medline
9. Pagani E, Hirsch JG, Pouwels PJ, et al. **Intercenter differences in diffusion tensor MRI acquisition.** *J Magn Reson Imaging* 2010;31: 1458–68 CrossRef Medline
10. Vollmar C, O'Muircheartaigh J, Barker GJ, et al. **Identical, but not the same: intra-site and inter-site reproducibility of fractional anisotropy measures on two 3.0T scanners.** *Neuroimage* 2010;51: 1384–94 CrossRef Medline
11. Jansen JF, Kooi ME, Kessels AG, et al. **Reproducibility of quantitative cerebral T2 relaxometry, diffusion tensor imaging, and 1H magnetic resonance spectroscopy at 3.0 Tesla.** *Invest Radiol* 2007;42: 327–37 CrossRef Medline
12. Bisdas S, Bohning DE, Besenski N, et al. **Reproducibility, interrater agreement, and age-related changes of fractional anisotropy measures at 3T in healthy subjects: effect of the applied b-value.** *AJNR Am J Neuroradiol* 2008;29:1128–33 CrossRef Medline
13. Takao H, Hayashi N, Kabasawa H, et al. **Effect of scanner in longitudinal diffusion tensor imaging studies.** *Hum Brain Mapp* 2012;33: 466–77 CrossRef Medline
14. Magnotta VA, Matsui JT, Liu D, et al. **Multicenter reliability of diffusion tensor imaging.** *Brain Connect* 2012;2:345–55 CrossRef Medline
15. Huang L, Wang X, Baliki MN, et al. **Reproducibility of structural, resting-state BOLD and DTI data between identical scanners.** *PLoS One* 2012;7:e47684 CrossRef Medline
16. Veenith TV, Carter E, Grossac J, et al. **Inter subject variability and reproducibility of diffusion tensor imaging within and between different imaging sessions.** *PLoS One* 2013;8:e65941 CrossRef Medline
17. Kamagata K, Shimoji K, Hori M, et al. **Intersite reliability of diffusion tensor imaging on two 3T scanners.** *Magn Reson Med Sci* 2015; 14:227–33 CrossRef Medline
18. Polders DL, Leemans A, Hendrikse J, et al. **Signal to noise ratio and uncertainty in diffusion tensor imaging at 1.5, 3.0, and 7.0 Tesla.** *J Magn Reson Imaging* 2011;33:1456–63 CrossRef Medline
19. Fox RJ, Sakaie K, Lee JC, et al. **A validation study of multicenter diffusion tensor imaging: reliability of fractional anisotropy and diffusivity values.** *AJNR Am J Neuroradiol* 2012;33:695–700 CrossRef Medline
20. Mirzaalian H, de Pierrefeu A, Savadjiev P, et al. **Harmonizing diffusion MRI data across multiple sites and scanners.** *Med Image Comput Comput Assist Interv* 2015;9349:12–19 CrossRef Medline
21. Zhu T, Hu R, Qiu X, et al. **Quantification of accuracy and precision of multi-center DTI measurements: a diffusion phantom and human brain study.** *Neuroimage* 2011;56:1398–411 CrossRef Medline
22. Grech-Sollars M, Hales PW, Miyazaki K, et al. **Multi-centre reproducibility of diffusion MRI parameters for clinical sequences in the brain.** *NMR Biomed* 2015;28:468–85 CrossRef Medline
23. Mukherjee P, Berman JI, Chung SW, et al. **Diffusion tensor MR imaging and fiber tractography: theoretic underpinnings.** *AJNR Am J Neuroradiol* 2008;29:632–41 CrossRef Medline
24. Mukherjee P, Chung SW, Berman JI, et al. **Diffusion tensor MR imaging and fiber tractography: technical considerations.** *AJNR Am J Neuroradiol* 2008;29:843–52 CrossRef Medline

25. Pierpaoli C, Sarlls J, Nevo U, et al. **Polyvinylpyrrolidone (PVP) water solutions as isotropic phantoms for diffusion MRI studies.** In: *Proceedings of the Annual Meeting and Exhibition of the International Society for Magnetic Resonance in Medicine,* Honolulu, Hawaii. April 18–24, 2009:1414
26. Behrens TE, Johansen-Berg H, Woolrich MW, et al. **Non-invasive mapping of connections between human thalamus and cortex using diffusion imaging.** *Nat Neurosci* 2003;6:750–57 CrossRef Medline
27. Smith SM, Jenkinson M, Johansen-Berg H, et al. **Tract-based spatial statistics: voxelwise analysis of multi-subject diffusion data.** *Neuroimage* 2006;31:1487–505 CrossRef Medline
28. Smith SM, Jenkinson M, Woolrich MW, et al. **Advances in functional and structural MR image analysis and implementation as FSL.** *Neuroimage* 2004;23(suppl 1):S208–19 CrossRef Medline
29. Andersson JL, Jenkinson M, Smith S. **Non-linear registration, aka spatial normalisation.** http://www.fmrib.ox.ac.uk/analysis/techrep/. FMRIB technical report TR07JA2. Published June 28, 2007
30. Galanaud D, Perlbarg V, Gupta R, et al; Neuro Imaging for Coma Emergence and Recovery Consortium. **Assessment of white matter injury and outcome in severe brain trauma: a prospective multicenter cohort.** *Anesthesiology* 2012;117:1300–10 CrossRef Medline
31. Dinkel J, Drier A, Khalilzadeh O, et al; for NICER (Neuro Imaging for Coma Emergence and Recovery) Consortium. **Long-term white matter changes after severe traumatic brain injury: a 5-year prospective cohort.** *AJNR Am J Neuroradiol* 2014;35:23–29 CrossRef Medline
32. Venkatraman VK, Gonzalez CE, Landman B, et al. **Region of interest correction factors improve reliability of diffusion imaging measures within and across scanners and field strengths.** *Neuroimage* 2015;119:406–16 CrossRef Medline

Predictive Utility of Marketed Volumetric Software Tools in Subjects at Risk for Alzheimer Disease: Do Regions Outside the Hippocampus Matter?

T.P. Tanpitukpongse, M.A. Mazurowski, J. Ikhena, and J.R. Petrella, for the Alzheimer's Disease Neuroimaging Initiative

ABSTRACT

BACKGROUND AND PURPOSE: Alzheimer disease is a prevalent neurodegenerative disease. Computer assessment of brain atrophy patterns can help predict conversion to Alzheimer disease. Our aim was to assess the prognostic efficacy of individual-versus-combined regional volumetrics in 2 commercially available brain volumetric software packages for predicting conversion of patients with mild cognitive impairment to Alzheimer disease.

MATERIALS AND METHODS: Data were obtained through the Alzheimer's Disease Neuroimaging Initiative. One hundred ninety-two subjects (mean age, 74.8 years; 39% female) diagnosed with mild cognitive impairment at baseline were studied. All had T1-weighted MR imaging sequences at baseline and 3-year clinical follow-up. Analysis was performed with NeuroQuant and Neuroreader. Receiver operating characteristic curves assessing the prognostic efficacy of each software package were generated by using a univariable approach using individual regional brain volumes and 2 multivariable approaches (multiple regression and random forest), combining multiple volumes.

RESULTS: On univariable analysis of 11 NeuroQuant and 11 Neuroreader regional volumes, hippocampal volume had the highest area under the curve for both software packages (0.69, NeuroQuant; 0.68, Neuroreader) and was not significantly different ($P > .05$) between packages. Multivariable analysis did not increase the area under the curve for either package (0.63, logistic regression; 0.60, random forest NeuroQuant; 0.65, logistic regression; 0.62, random forest Neuroreader).

CONCLUSIONS: Of the multiple regional volume measures available in FDA-cleared brain volumetric software packages, hippocampal volume remains the best single predictor of conversion of mild cognitive impairment to Alzheimer disease at 3-year follow-up. Combining volumetrics did not add additional prognostic efficacy. Therefore, future prognostic studies in mild cognitive impairment, combining such tools with demographic and other biomarker measures, are justified in using hippocampal volume as the only volumetric biomarker.

ABBREVIATIONS: AD = Alzheimer disease; ADAS-13 = 13-item Alzheimer's Disease Assessment Scale; ADNI = Alzheimer's Disease Neuroimaging Initiative; ADNI-GO = Alzheimer's Disease Neuroimaging Initiative–Grand Opportunities; AUC = area under the curve; HOC = Hippocampal Occupancy Score; MCI = mild cognitive impairment; NQ = NeuroQuant; NR = Neuroreader; ROC = receiver operating characteristic

Alzheimer disease (AD) is a progressive neurodegenerative disease leading to synaptic dysfunction, neuronal death, and brain atrophy. Atrophy of specific medial temporal lobe structures, such as the hippocampus, amygdala, and parahippocampal gyrus, has been associated with the future development of AD in numerous research studies.[1-9] However, use of this information

Received April 21, 2016; accepted after revision October 31.

From the Department of Radiology (T.P.T., M.A.M., J.R.P.), Duke University Medical Center, Durham, North Carolina; and Duke University School of Medicine (J.I.), Durham, North Carolina.

Data used in preparation of this article were obtained from the Alzheimer's Disease Neuroimaging Initiative data base (adni.loni.usc.edu). Thus, the investigators within the ADNI contributed to the design and implementation of ADNI and/or provided data but did not participate in analysis or writing of this report. A complete listing of ADNI investigators can be found at http://adni.loni.usc.edu/wp-content/uploads/how_to_apply/ADNI_Acknowledgement_List.pdf.

Data collection and sharing for this project were funded by the ADNI (National Institutes of Health Grant U01 AG024904) and DOD-ADNI (Department of Defense award number W81XWH-12–2-0012). ADNI is funded by the National Institute on Aging, the National Institute of Biomedical Imaging and Bioengineering, and through generous contributions from the following: AbbVie, the Alzheimer's Association, Alzheimer's Drug Discovery Foundation, Araclon Biotech, BioClinica, Biogen, Bristol-Myers Squibb, CereSpir Inc, Eisai Inc, Elan Pharmaceuticals, Eli Lilly and Company, EUROIMMUN, F. Hoffmann-La Roche Ltd and its affiliated company Genentech, Fujirebio Diagnostics, GE Healthcare, IXICO, Janssen Alzheimer Immunotherapy Research & Development, Johnson & Johnson Pharmaceutical Research & Development LLC, Lumosity, Lundbeck, Merck & Co, Meso Scale Diagnostics LLC, NeuroRx Research, NeuroTrack Technologies, Novartis Pharmaceuticals Corporation, Pfizer, Piramal Imaging, Servier, Takeda Pharmaceutical Company, and Transition Therapeutics. The Canadian Institutes of Health Research is providing funds to support ADNI clinical sites in Canada. Private sector contributions are facilitated by the Foundation for the National Institutes of Health (www.fnih.org). The grantee organization is the Northern California Institute for Research and Education, and the study is coordinated by the Alzheimer's Disease Cooperative Study at the University of California, San Diego. ADNI data are disseminated by the Laboratory for Neuro Imaging at the University of Southern California.

Please address correspondence to Jeffrey R. Petrella, MD, Duke University Hospital, Department of Radiology, Box 3808, Durham, NC 27710; e-mail: jeffrey.petrella@duke.edu

Indicates open access to non-subscribers at www.ajnr.org

http://dx.doi.org/10.3174/ajnr.A5061

in the clinical care of patients with memory impairment for prognosis remains challenging.[10,11] Medial temporal lobe volume assessments of MR images with visual ratings or manual or semimanual volumetric processing have been difficult to implement in a busy clinical environment due to the high interobserver variability of raters and/or the time-consuming nature of obtaining these measurements.[12] These problems have been addressed through the use of fully automated segmentation algorithms available in commercial software programs, providing the user with immediate, detailed volumetric analysis of the hippocampus and other brain regions, which is more sensitive than visual analysis.[13]

Because the atrophy pattern in prodromal AD is spatially distributed, including regions beyond the hippocampus, such as the lateral and inferior temporal lobe, parietal lobe, and cingulate gyrus,[14] incorporation of such information may enhance the prognostic capability of these currently available tools. Indeed, pattern-analysis techniques, incorporating whole-brain morphologic information,[15-19] have been harnessed for this purpose and have shown a high prognostic value in individual patients. Such techniques, however, have not yet been implemented in commercially available products. The purpose of this study was to assess the prognostic efficacy of using the complete set of raw volumetric measures available in 2 fully automated, commercially available brain volumetric software packages. Such tools have been FDA 510(k) cleared for clinical use but have not yet been validated for specific diagnostic or prognostic purposes in AD. We sought to determine whether combining volumetrics by using multivariable approaches, including machine learning,[20-22] would add to the prognostic efficacy of individual measures alone, such as hippocampal volume, in predicting conversion from mild cognitive impairment (MCI) to AD. We hypothesized that the multivariable approach would enhance the prognostic value of already existing individual measures available in commercial volumetric software.

MATERIALS AND METHODS

Subjects

All subject data were available through the Alzheimer's Disease Neuroimaging Initiative (ADNI), a multicenter trial with a publicly available data base (adni.loni.usc.edu).[15] The ADNI was launched in 2003 as a public-private partnership, led by Principal Investigator Michael W. Weiner, MD. The primary goal of the ADNI has been to test whether MR imaging, PET, other biologic markers, and clinical and neuropsychological assessment can be combined to measure the progression of MCI and early AD. For up-to-date information, see www.adni-info.org.

All subjects classified as having MCI under ADNI-1 or late MCI under Alzheimer's Disease Neuroimaging Initiative–Grand Opportunities (ADNI-GO), with baseline MR imaging and a baseline and 3-year clinical assessment available on or before November 11, 2013, were selected.

Conversion of MCI to AD was based on the National Institute of Neurological Disorders and Stroke and the Alzheimer's Disease and Related Disorders Association criteria for probable or possible AD, determined by review from a committee according to protocol guidelines. Those subjects who did not fulfill these criteria for conversion were defined as nonconverters, including subjects with MCI and those who reverted to a normal state.

Image Acquisition and Image Analysis

All subjects underwent brain MR imaging at 1.5T or 3T with sagittal 3D T1-weighted (MPRAGE) scans. Further details on the MR imaging scanner protocol and MR image acquisition are available elsewhere (http://adni.loni.usc.edu/methods/documents/mri-protocols/). Because we selected only subjects with late MCI from the ADNI-GO, all subjects were therefore previous members of ADNI-1 and had their original scan with the ADNI-1 protocol. The MPRAGE sequence was processed with NeuroQuant (NQ; CorTechs Labs, San Diego, California) (Original Version 1.0), which is a commercially available automated image-analysis software program (http://www.cortechslabs.com/neuroquant/). Separate left and right volumes, available in the generated morphometry report, were combined into a total volume for the following 11 brain regions (features): amygdala, caudate, cerebellum, cortical gray matter, forebrain parenchyma, hippocampus, inferior lateral ventricle, lateral ventricle, pallidum, putamen, and thalamus.

In addition, the MPRAGE sequence was also processed with Neuroreader (NR; Brainreader Aps, Horsens, Denmark), another commercially available software program for volumetric segmentation (http://brainreader.net/).[23] Both NQ and NR are FDA 510(k) cleared and "intended for automatic labeling, visualization and volumetric quantification of segmentable brain structures from a set of MR images" (http://www.accessdata.fda.gov/cdrh_docs/pdf6/K061855.pdf and https://www.accessdata.fda.gov/cdrh_docs/pdf14/K140828.pdf). Because the NR volumetric report yielded many more regions compared with NQ, 11 regions yielding the best individual predictions were chosen from the NR morphometry report to keep the models equally parsimonious. Combined bilateral volumes were obtained for the following 11 brain regions (features): amygdala, cerebellum, frontal lobe, hippocampus, lateral ventricle, occipital lobe, parietal lobe, putamen, temporal lobe, thalamus, and ventral diencephalon. Technical aspects of these commercial software packages have been previously described in detail.[24,25]

Of note, all ADNI studies included 2 echo-spoiled gradient echo/MPRAGE sequences performed back-to-back, the original and a repeat sequence accelerated by parallel imaging. In cases in which the original MPRAGE sequence could not be processed by the NR or NQ programs, the repeat MPRAGE sequence was used instead. If processing also failed on the repeat sequence, with either NR or NQ, the case was excluded from all further analysis. All image processing and analyses were performed by 2 authors (T.P.T. and J.I.). Sample segmentations from NQ and NR are shown in Fig 1*A*.

Statistical Analysis

We compared demographics between the MCI converter and nonconverter groups by using a 2-sample Student *t* test, assuming equal variance when appropriate. To assess the prognostic performance of individual features and multivariable models combining the features, we used the receiver operating characteristic (ROC) curve methodology. Area under the curve (AUC) was used to summarize the performance. Comparison of AUCs was performed by using the method of Delong et al.[26]

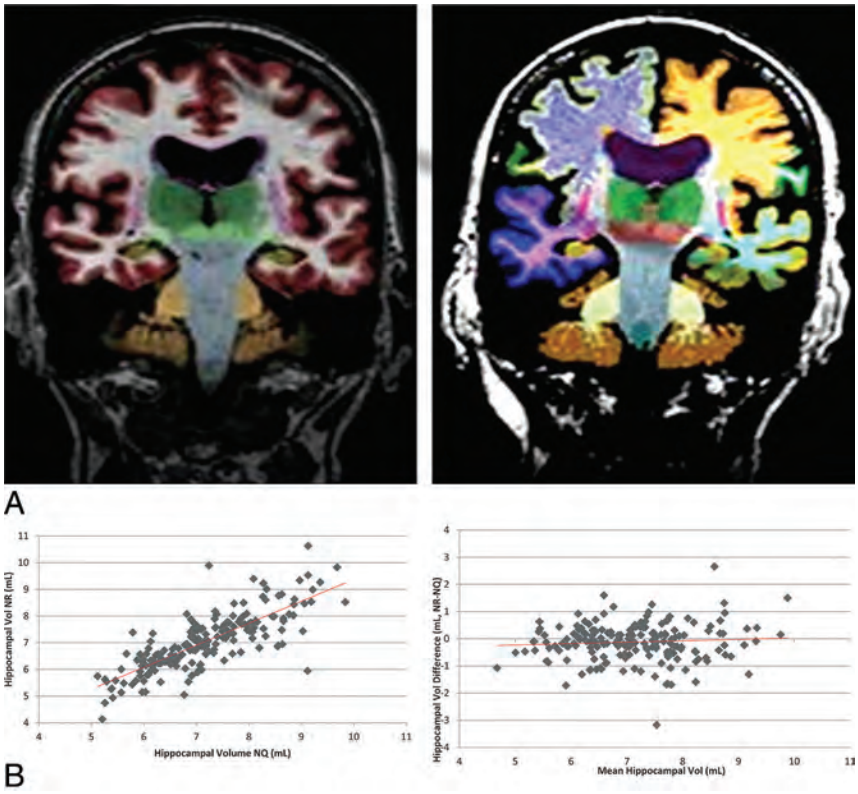

FIG 1. Example of NeuroQuant (*A*, *left*) and Neuroreader (*A*, *right*) color segmentations in the same subject and hippocampal scatter (*B*, *left*) and Bland-Altman plots (*B*, *right*). Note the high correlation ($r = 0.79$, $P < .05$) of hippocampal volumetrics between software packages across all subjects and the small underestimation bias (−0.12 mL, $P < .05$) of NR with respect to NQ.

Table 1: Characteristics of study populations[a]

Characteristic	All Patients	MCI (Nonconverter)	MCI to AD (Converter)	*P* Value
No.	192	107	85	
Age (yr)	74.8 ± 7.3	74.7 ± 7.6	75.0 ± 6.9	.7604
Sex				.3262
Female	75 (39)	38 (36)	37 (44)	
Male	117 (61)	69 (64)	48 (56)	
Education (yr)	15.7 ± 2.9	15.7 ± 3.0	15.6 ± 2.8	.7637
ADAS-13 (baseline)	17.7 ± 6.4	15.2 ± 6.1	20.9 ± 5.3	<.0001
MMSE (baseline)	27.1 ± 1.7	27.6 ± 1.7	26.5 ± 1.6	<.0001

Note:—MMSE indicates Mini-Mental State Examination.

[a] MCI or AD status was determined at 3-year follow-up by the ADNI criteria. Data are means. Percentages listed in parentheses are rounded to the nearest percentage.

To test whether a combination of the features would outperform models based on a single brain region, we constructed 2 multivariable models: a classic multivariable logistic regression model and a more novel machine-learning method called the Random Forest Classifier.[27] For the Random Forest Classifier, 2000 trees were used. The leave-one-out cross-validation method was used for training and testing of the multivariable models. In addition to the data-driven multivariable models, we also tested one a priori multivariable model, known as the Hippocampal Occupancy (HOC) score, defined as the ratio of hippocampal volume to the sum of hippocampal and inferior lateral ventricle volumes. This measure is thought to differentiate individuals with congenitally small hippocampi from those with degeneration.[28] The HOC score for each separate hemisphere was averaged to provide a single composite measurement. Because inferior lateral ventricle (temporal horn) volume was not available for NR, this measure was calculated only with NQ.

To assess correlations between assessment of the same volume by the NQ and NR software, we used the Pearson correlation. Statistical analyses were performed with Matlab, Version 8.1.0.604 R2013a (MathWorks, Natick, Massachusetts); R statistical and computing software, Version 3.1.3 (http://www.r-project.org); and JMP, Version 11.0 (SAS Institute, Cary, North Carolina) software packages.

RESULTS

Initially 281 subjects were identified in the ADNI databases who met the inclusion criteria. Eighty-four (29.9%) subjects were excluded due to failure to generate an NQ morphometry report. Five (1.8%) subjects were excluded for other reasons, including failure to generate an NR morphometry report. A total of 192 remaining subjects met the inclusion and exclusion criteria. All subjects had a 3-year clinical follow-up visit recorded. Mean follow-up was 3.05 ± 0.14 years (range, 2.47–3.63 years). All 192 included subjects were diagnosed as having MCI at baseline, and all started under the ADNI-1 protocol. At the end of the 3-year follow-up, 186/192 subjects had their 3-year evaluation under the ADNI-1 protocol and 6/192 subjects had their 3-year evaluation under the ADNI-GO protocol. For the 192 subjects, at the 3-year follow-up, the final diagnosis was AD in 85/192 (44.3%), MCI in 99/192 (51.6%), and healthy in 8/192 (4.2%).

Characteristics of the study populations are listed in Table 1. Two subjects did not have the 13-item Alzheimer's Disease Assessment Scale (ADAS-13) scores at baseline. There were no significant differences ($P > .05$) between the MCI (nonconverter) and AD (converter) groups in terms of age, sex, or education. There was a significant difference ($P < .0001$) in the ADAS-13 score at baseline and the Mini-Mental State Examination score at baseline between the 2 groups. The AUC for predicting conversion at baseline was 0.76 and 0.68 for the ADAS-13 and Mini-Mental State Examination, respectively.

AUC values for NQ and NR are listed in Table 2. With NQ, the most predictive feature for conversion of MCI to AD was hippocampal volume, with an AUC of 0.69. The most predictive feature for NR was also hippocampal volume, with an AUC of 0.68. The multivariable analysis did not improve on either of these.

Table 2: AUC values for different brain regions separated by software package (NQ, NR) and method of analysis (univariable-multivariable)

Feature	AUC NQ (95% CI)	AUC NR (95% CI)
Univariable analysis		
Hippocampus	0.69 (0.61–0.76)	0.68 (0.60–0.76)
Amygdala	0.67 (0.59–0.74)	0.65 (0.57–0.73)
Cerebellum	0.58 (0.49–0.66)	0.57 (0.49–0.66)
Putamen	0.58 (0.50–0.66)	0.62 (0.54–0.70)
Thalamus	0.56 (0.47–0.64)	0.56 (0.48–0.64)
Lateral ventricle	0.54 (0.46–0.62)	0.54 (0.46–0.62)
Pallidum	0.52 (0.43–0.60)	NA
Caudate	0.51 (0.42–0.59)	NA
Cortical gray matter	0.64 (0.56–0.72)	NA
Forebrain parenchyma	0.62 (0.54–0.70)	NA
Inferior lateral ventricle	0.60 (0.52–0.68)	NA
Temporal lobe	NA	0.63 (0.55–0.71)
Parietal lobe	NA	0.61 (0.53–0.69)
Frontal lobe	NA	0.60 (0.52–0.68)
Occipital lobe	NA	0.59 (0.51–0.68)
Ventral diencephalon	NA	0.51 (0.43–0.60)
Multivariable analysis		
Logistic regression	0.63 (0.55–0.71)	0.65 (0.58–0.73)
Random forest	0.60 (0.52–0.68)	0.62 (0.54–0.71)

Note:—NA indicates not applicable.

Table 3: Pearson correlation coefficients for NQ and NR volumetrics in regions with the same name

Feature	Pearson Coefficient (*r*)	95% CI	*P* Value
Thalamus	0.60	0.51–0.69	<.001
Putamen	0.61	0.51–0.69	<.001
Lateral ventricles	0.99	0.99–0.99	<.001
Hippocampus	0.79	0.72–0.83	<.001
Cerebellum	0.87	0.83–0.90	<.001
Amygdala	0.71	0.64–0.78	<.001

Intracranial volume normalization did not result in improvement of the performance of hippocampal volume in the linear model (AUC = 0.65 for NQ, and 0.61 for NR), and adding age as a covariate to the normalized intracranial hippocampal volumes did not result in improvement (AUC = 0.66 for NQ and 0.62 for NR).

With the NR, the AUC value for the hippocampus was significantly greater ($P < .05$) than the AUC value for the cerebellum, lateral ventricle, and the thalamus. With the NQ, the AUC value for the hippocampus was significantly greater ($P < .05$) than the AUC value for the caudate, cerebellum, lateral ventricle, pallidum, putamen, and thalamus.

There was no statistically significant difference in AUC values by using hippocampal volumes obtained by NR versus NQ ($P = .657$).

Pearson correlation coefficients are listed in Table 3. There was a statistically significant correlation between NQ and NR absolute volumes in all compatible regions tested: thalamus, lateral ventricle, hippocampus, cerebellum, putamen, and amygdala ($P < .05$). The scatterplot and Bland-Altman plot for hippocampal volume are shown in Fig 1*B*. There was a small bias for NR with respect to NQ of −0.12 mL (95% CI, −0.02 to −0.22 mL).

The AUC for the HOC score was 0.64 (95% CI, 0.56–0.72). There was no statistically significant difference in AUC values by using the NQ HOC score versus NQ hippocampal volume ($P = .1827$).

DISCUSSION

Our study, with the complete set of raw volumetric measures available in 2 fully automated, commercially available brain volumetric software packages, confirms previous studies documenting the prognostic utility of hippocampal volume in patients with MCI. Indeed, hippocampal volumes provided the highest prognostic value of all individual regions available in both the NQ and NR volumetric reports. Multivariable analysis, including the use of a cross-validated machine-based learning classifier algorithm, which incorporated other brain regions available in these software packages, did not provide additional predictive value compared with a model based on just hippocampal volumes. The results of our study are in agreement with previous studies that have found hippocampal volumes to be most predictive of conversion of MCI to AD, with little added benefit from additional brain regions. For example, a large study of patients in the ADNI using semiautomated methods reported that hippocampal volumes were the most predictive of conversion compared with other regional and whole-brain measures.[29] Automated volumetric measurements of the hippocampus also had high predictive values for conversion.[2] A 2-year clinical follow-up study of patients with MCI with manual methods demonstrated that baseline hippocampal volumes had high predictive value.[5] Despite the differences in segmentation techniques (manual, semiautomated, and automated) among the 3 studies, all these studies reported that hippocampal volumes were the most predictive of MCI conversion.

On the other hand, a number of previous studies have implicated brain regions other than the hippocampus as either adding to the prognostic value of hippocampal volume or having prognostic value in their own right, though direct comparison with our study is limited due to differences in methodologies and primary outcomes. In one study using manual methods, a bivariate model of hippocampal volumes and follow-up changes to either ventricular volume or whole-brain volume was shown to have prognostic value in predicting conversion of MCI to AD.[7] Another study with automated methods found that amygdala and caudate nucleus volumes were predictive of MCI conversion, whereas hippocampal volumes were not.[12] A separate study with automated methods reported that deep gray matter structures, including the amygdala, thalamus, putamen, and nucleus accumbens, were predictive of conversion of MCI to AD, in addition to the hippocampus.[30] Temporal horn volumes were shown to be more predictive than hippocampal volumes in one study using semiautomated methods,[31] whereas the left lateral temporal lobe and left parietal cortex were the most predictive factors in another study using automated methods.[32]

A likely reason for discrepancies with these studies is that volume loss in AD-affected regions is correlated with that of the hippocampus, and these collinear effects are therefore lost in the multivariable model when one accounts for hippocampal volume. For example, in our study, volume of the hippocampus was highly correlated with that of the amygdala ($r = 0.71$) and cortical gray matter ($r = 0.52$) for NQ, and amygdala ($r = 0.75$) and temporal lobe ($r = 0.57$) for NR. Another explanation for the differences in results, compared with our study, could be the use of different segmentation methods. In our study, we used an automated segmentation method with NQ and NR, which may be

less accurate in measuring smaller and deeper structures compared with manual or semiautomated segmentation methods.

Also of note in this study, the HOC score, a composite index of hippocampal and temporal horn volume, did not outperform hippocampal volume alone. The HOC score has been advocated as a more accurate measurement of hippocampal tissue loss, which accounts for individual variations in hippocampal size by accounting for temporal horn volume. In our study population, temporal horn volume was somewhat collinear with hippocampal volume ($r = -0.33$), and we did not find the HOC to be more predictive of conversion than hippocampal volume alone, suggesting that the additional variance added by temporal horn volume might be redundant information and/or noise. Although temporal horn volume was a significant predictor of conversion in the univariable logistic regression model, it lost significance when hippocampal volume was added to the model and negligibly increased the AUC. Nevertheless, our results do not exclude the possibility that combining these 2 measures may be helpful in the preclinical or mild dementia phases of the disease spectrum.

Our study has several limitations. It was theoretically possible that the ROC area for hippocampal volume might have been larger if hippocampal volumes were normalized to intracranial volume and adjusted for age.[33] Such corrections might adjust for bias across subjects since ICV-normalized and age-adjusted values are already available in the volumetric reports. Nevertheless, for our primary analysis, we chose to use the raw values, in keeping with our purpose of comparing single-versus-combined measures within the same subjects, which should not be affected by normalizing by intracranial volume, a practice that could introduce additional noise into the measures. Although age may differentially affect various brain regions, we did not have age-adjusted values available for most regions in the NQ volumetric report and therefore did not include these measures in our primary analysis. Even so, secondary analyses of hippocampal volume with intracranial volume normalization, as well as including age as a covariate in the linear model, did not yield additional prognostic efficacy. Of note, 1 group, the Coalition Against Major Diseases, reported higher AUC values for the prediction of MCI conversion to AD (in 2 years) in their de novo analysis, based on automated hippocampal volume obtained by several methods: 0.7565 (LEAP; Learning Embeddings for Atlas Propagation, http://www.ixico.com/additional-information/leap-analysis), 0.7516 (NeuroQuant), 0.7536 (FreeSurfer; http://surfer.nmr.mgh.harvard.edu), and 0.7290 (HMAPS; Hippocampus Multi-Atlas Propagation and Segmentation).[34] However, the same committee also reported a range of AUC values between 0.60 and 0.77 based on their literature review, and our results are within this range.

Both the NQ and NR programs provide a large number of data values (55 for the general morphometry report through NQ, 140 for the NR report) that we did not fully include in our machine-based learning classifier program. Increasing the number of features can hurt the performance of a classifier, given a limited sample size. Initially, we found that the addition of the full dataset resulted in a worse predictive value for MCI conversion, which we speculate was due to overfitting of the training samples. This is a common phenomenon when the number of predictor variables is high compared with the number of subjects in the training set.[35] Hence, we decided to limit our analysis to the most promising features provided in the NQ and NR volumetric reports.

In some cases, we were not able to process the MR images for the baseline sequence, which excluded some patients from the study, all of whom were chosen through the ADNI data base. In total, 89 of 281 patients were excluded due to inadequate NQ or NR morphometry data. This was most often due to patient age and sex missing from the anonymized header information, a requirement of the NQ processing pipeline but a situation unlikely to occur in clinical practice because these are standard DICOM data fields. In addition, some patients had inadequate MPRAGE sequences due to technical factors, including motion, which we were not able to segment by using the NQ or NR programs; in these cases, we substituted a repeat MPRAGE sequence. Despite occasional differences in our ability to process a particular sequence, we found a strong linear correlation ($r > 0.60$) between NQ and NR for all compatible regions tested. Of interest, for hippocampal volume, there was a small underestimation bias for NR with respect to NQ, which may be attributable to different segmentation algorithms. Two outliers were noted, showing differences of approximately ± 3 mL between software packages, which were attributable to segmentation differences.

Another limitation is that we did not incorporate biomarkers, neuropsychological assessments, or longitudinal imaging measures in our study. Rather, we sought to limit our study to testing the prognostic efficacy of 2 commercially available brain volumetric software packages in their own right, rather than by using additional data, which might confound direct comparisons. Of note, the Mini-Mental State Examination and ADAS-13 AUC scores were as high as, or higher than, those of hippocampal volume alone, in agreement with previous studies looking at the prognostic efficacy of multiple biomarkers in MCI.[36] This result is not surprising given that a dichotomous end point measure, conversion, was used to assess cognitive decline, and cognitive measures at baseline would be expected to strongly predict how close a subject is to the point of conversion. Future effort in evaluating the prognostic efficacy of these software packages should involve combining volumetric data with a suite of biomarkers and neuropsychological assessments by using machine-based learning approaches and continuous, rather than categoric, outcomes of cognitive decline. Subject factors such as financial or socioeconomic ones also remained unadjusted in the analysis. These factors would unlikely affect the within-subject design and were omitted to keep the comparison straightforward between single-versus-multiple volumetric outputs directly available from the imaging software packages.

Despite these limitations, our study had several strengths, including a large sample size of 192 patients through the ADNI data base. Indeed, ADNI uses a wide variety of vendor platforms, field strengths, and harmonized pulse sequences that patients are likely to encounter in future clinical settings. We also selected patients with 3-year clinical follow-up, which provided a more accurate designation of future conversion status, compared with studies with shorter follow-up duration.

CONCLUSIONS

Of the multiple regional volume measures available in current FDA-cleared brain volumetric software, hippocampal volume remains the best single predictor of MCI conversion to AD at 3-year follow-up. Combining volumetrics, by using multivariable approaches including a machine-learning classifier, does not appear to add additional prognostic efficacy. Therefore, future prognostic studies in mild cognitive impairment, combining such tools with demographic and other biomarker measures, are justified in using hippocampal volume as the only volumetric biomarker.

ACKNOWLEDGMENTS

The authors thank Dr. James Brewer (for NeuroQuant) and Dr. Jamila Ahdidan (for Neuroreader) for providing comments for this article.

Disclosures: Jeffrey R. Petrella—*UNRELATED*: *Board Membership*: Piramal Healthcare, *Comments*: advisory board; *Payment for Lectures including Service on Speakers Bureaus*: Eli Lilly, *Comments*: Speakers Bureau. J. Ikhena was funded by the 2015 RSNA Research Medical Student Grant #RMS1504.

REFERENCES

1. deToledo-Morrell L, Stoub TR, Bulgakova M, et al. **MRI-derived entorhinal volume is a good predictor of conversion from MCI to AD.** *Neurobiol Aging* 2004;25:1197–203 CrossRef Medline
2. Fritzsche KH, Stieltjes B, Schlindwein S, et al. **Automated MR morphometry to predict Alzheimer's disease in mild cognitive impairment.** *Int J Comput Assist Radiol Surg* 2010;5:623–32 CrossRef Medline
3. Douaud G, Menke RA, Gass A, et al. **Brain microstructure reveals early abnormalities more than two years prior to clinical progression from mild cognitive impairment to Alzheimer's disease.** *J Neurosci* 2013;33:2147–55 CrossRef Medline
4. Wang PN, Lirng JF, Lin KN, et al. **Prediction of Alzheimer's disease in mild cognitive impairment: a prospective study in Taiwan.** *Neurobiol Aging* 2006;27:1797–806 CrossRef Medline
5. Eckerström C, Olsson E, Borga M, et al. **Small baseline volume of left hippocampus is associated with subsequent conversion of MCI into dementia: the Göteborg MCI study.** *J Neurol Sci* 2008;272:48–59 CrossRef Medline
6. Varon D, Barker W, Loewenstein D, et al; Alzheimer's Disease Neuroimaging Initiative. **Visual rating and volumetric measurement of medial temporal atrophy in the Alzheimer's Disease Neuroimaging Initiative (ADNI) cohort: baseline diagnosis and the prediction of MCI outcome.** *Int J Geriatr Psychiatry* 2015;30:192–200 CrossRef Medline
7. Jack CR Jr, Shiung MM, Weigand SD, et al. **Brain atrophy rates predict subsequent clinical conversion in normal elderly and amnestic MCI.** *Neurology* 2005;65:1227–31 CrossRef Medline
8. Desikan RS, Fischl B, Cabral HJ, et al. **MRI measures of temporoparietal regions show differential rates of atrophy during prodromal AD.** *Neurology* 2008;71:819–25 CrossRef Medline
9. Devanand DP, Pradhaban G, Liu X, et al. **Hippocampal and entorhinal atrophy in mild cognitive impairment: prediction of Alzheimer disease.** *Neurology* 2007;68:828–36 CrossRef Medline
10. Petrella JR, Coleman RE, Doraiswamy PM. **Neuroimaging and early diagnosis of Alzheimer disease: a look to the future.** *Radiology* 2003;226:315–36 CrossRef Medline
11. Petrella JR. **Neuroimaging and the search for a cure for Alzheimer disease.** *Radiology* 2013;269:671–91 CrossRef Medline
12. Liu Y, Paajanen T, Zhang Y, et al; Addneuromed Consortium. **Analysis of regional MRI volumes and thicknesses as predictors of conversion from mild cognitive impairment to Alzheimer's disease.** *Neurobiol Aging* 2010;31:1375–85 CrossRef Medline
13. Ross DE, Ochs AL, Seabaugh JM, et al; Alzheimer's Disease Neuroimaging Initiative. **Man versus machine: comparison of radiologists' interpretations and NeuroQuant® volumetric analyses of brain MRIs in patients with traumatic brain injury.** *J Neuropsychiatry Clin Neurosci* 2013;25:32–39 CrossRef Medline
14. Davatzikos C, Fan Y, Wu X, et al. **Detection of prodromal Alzheimer's disease via pattern classification of magnetic resonance imaging.** *Neurobiol Aging* 2008;29:514–23 CrossRef Medline
15. Misra C, Fan Y, Davatzikos C. **Baseline and longitudinal patterns of brain atrophy in MCI patients, and their use in prediction of short-term conversion to AD: results from ADNI.** *Neuroimage* 2009;44:1415–22 CrossRef Medline
16. Davatzikos C, Bhatt P, Shaw LM, et al. **Prediction of MCI to AD conversion, via MRI, CSF biomarkers, and pattern classification.** *Neurobiol Aging* 2011;32::2322.e19–27 CrossRef Medline
17. Vemuri P, Wiste HJ, Weigand SD, et al; Alzheimer's Disease Neuroimaging Initiative. **MRI and CSF biomarkers in normal, MCI, and AD subjects: predicting future clinical change.** *Neurology* 2009;73:294–301 CrossRef Medline
18. Plant C, Teipel SJ, Oswald A, et al. **Automated detection of brain atrophy patterns based on MRI for the prediction of Alzheimer's disease.** *Neuroimage* 2010;50:162–74 CrossRef Medline
19. Fennema-Notestine C, McEvoy LK, Hagler DJ Jr; The Alzheimer's Disease Neuroimaging Initiative. **Structural neuroimaging in the detection and prognosis of pre-clinical and early AD.** *Behav Neurol* 2009;21:3–12 CrossRef Medline
20. Moradi E, Pepe A, Gaser C, et al; Alzheimer's Disease Neuroimaging Initiative. **Machine learning framework for early MRI-based Alzheimer's conversion prediction in MCI subjects.** *Neuroimage* 2015;104:398–412 CrossRef Medline
21. Zhan Y, Chen K, Wu X, et al; Alzheimer's Disease Neuroimaging Initiative. **Identification of conversion from normal elderly cognition to Alzheimer's disease using multimodal support vector machine.** *J Alzheimers Dis* 2015;47:1057–67 CrossRef Medline
22. Adaszewski S, Dukart J, Kherif F, et al; Alzheimer's Disease Neuroimaging Initiative. **How early can we predict Alzheimer's disease using computational anatomy?** *Neurobiol Aging* 2013;34:2815–26 CrossRef Medline
23. Ahdidan J, Raji CA, DeYoe EA, et al. **Quantitative neuroimaging software for clinical assessment of hippocampal volumes on MRI.** *J Alzheimers Dis* 2015;49:723–32 CrossRef Medline
24. Brewer JB, Magda S, Airriess C, et al. **Fully-automated quantification of regional brain volumes for improved detection of focal atrophy in Alzheimer disease.** *AJNR Am J Neuroradiol* 2009;30:578–80 CrossRef Medline
25. Ahdidan J, Hviid LB, Chakravarty MM, et al. **Longitudinal MR study of brain structure and hippocampus volume in major depressive disorder.** *Acta Psychiatr Scand* 2011;123:211–19 CrossRef Medline
26. DeLong ER, DeLong DM, Clarke-Pearson DL. **Comparing the areas under two or more correlated receiver operating characteristic curves: a nonparametric approach.** *Biometrics* 1988;44:837–45 CrossRef Medline
27. Breiman L. **Random forests.** *Machine Learning* 2001;45:5–32 CrossRef
28. Heister D, Brewer JB, Magda S, et al; Alzheimer's Disease Neuroimaging Initiative. **Predicting MCI outcome with clinically available MRI and CSF biomarkers.** *Neurology* 2011;77:1619–28 CrossRef Medline
29. Risacher SL, Saykin AJ, West JD, et al; Alzheimer's Disease Neuroimaging Initiative (ADNI). **Baseline MRI predictors of conversion from MCI to probable AD in the ADNI cohort.** *Curr Alzheimer Res* 2009;6:347–61 CrossRef Medline
30. Yi HA, Moller C, Dieleman N, et al. **Relation between subcortical grey matter atrophy and conversion from mild cognitive impairment to Alzheimer's disease.** *J Neurol Neurosurg Psychiatry* 2016;87:425–32 CrossRef Medline
31. Macdonald KE, Bartlett JW, Leung KK, et al; ADNI investigators. **The**

value of hippocampal and temporal horn volumes and rates of change in predicting future conversion to AD. *Alzheimer Dis Assoc Disord* 2013;27:168–73 CrossRef Medline

32. Karas G, Sluimer J, Goekoop R, et al. **Amnestic mild cognitive impairment: structural MR imaging findings predictive of conversion to Alzheimer disease.** *AJNR Am J Neuroradiol* 2008;29:944–49 CrossRef Medline
33. Wyman BT, Harvey DJ, Crawford K, et al; Alzheimer's Disease Neuroimaging Initiative. **Standardization of analysis sets for reporting results from ADNI MRI data.** *Alzheimers Dement* 2013;9:332–37 CrossRef Medline
34. Hill DL, Schwarz AJ, Isaac M, et al. **Coalition Against Major Diseases/European Medicines Agency biomarker qualification of hippocampal volume for enrichment of clinical trials in predementia stages of Alzheimer's disease.** *Alzheimers Dement* 2014;10:21–9.e3 CrossRef Medline
35. Hawkins DM. **The problem of overfitting.** *J Chem Inf Comput Sci* 2004;44:1–12 CrossRef Medline
36. Gomar JJ, Bobes-Bascaran MT, Conejero-Goldberg C, et al; Alzheimer's Disease Neuroimaging Initiative. **Utility of combinations of biomarkers, cognitive markers, and risk factors to predict conversion from mild cognitive impairment to Alzheimer disease in patients in the Alzheimer's Disease Neuroimaging Initiative.** *Arch Gen Psychiatry* 2011;68:961–69 CrossRef Medline

Cortical Thickness of Native Tibetans in the Qinghai-Tibetan Plateau

W. Wei, X. Wang, Q. Gong, M. Fan, and J. Zhang

ABSTRACT

BACKGROUND AND PURPOSE: High-altitude environmental factors and genetic variants together could have exerted their effects on the human brain. The present study was designed to investigate the cerebral morphology in high-altitude native Tibetans.

MATERIALS AND METHODS: T1-weighted brain images were obtained from 77 Tibetan adolescents on the Qinghai-Tibetan Plateau (altitude, 2300–5300 m) and 80 matched Han controls living at sea level. Cortical thickness, curvature, and sulcus were analyzed by using FreeSurfer.

RESULTS: Cortical thickness was significantly decreased in the left posterior cingulate cortex, lingual gyrus, superior parietal cortex, precuneus, and rostral middle frontal cortex and the right medial orbitofrontal cortex, lateral occipital cortex, precuneus, and paracentral lobule. Curvature was significantly decreased in the left superior parietal cortex and right superior marginal gyrus; the depth of the sulcus was significantly increased in the left inferior temporal gyrus and significantly decreased in the right superior marginal gyrus, superior temporal gyrus, and insular cortex. Moreover, cortical thickness was negatively correlated with altitude in the left superior and middle temporal gyri, rostral middle frontal cortex, insular cortex, posterior cingulate cortex, precuneus, lingual gyrus, and the right superior temporal gyrus. Curvature was positively correlated with altitude in the left rostral middle frontal cortex, insular cortex, and middle temporal gyrus. The depth of the sulcus was negatively correlated with altitude in the left lingual gyrus and right medial orbitofrontal cortex.

CONCLUSIONS: Differences in cortical morphometry in native Tibetans may reflect adaptations related to high altitude.

ABBREVIATIONS: DMN = default mode network; HA = high altitude; PCC = posterior cingulate cortex; *PPARA* = peroxisome proliferator-activated receptor α

The Qinghai-Tibetan Plateau is one of the most extreme environments inhabited by humans. High-altitude (HA) natives have developed distinctive biologic characteristics in respiratory and circulatory functions,[1,2] hemoglobin concentration,[3] arterial oxygen saturation,[4] energy metabolism,[5] and genes[6] to offset the stresses of HA environmental factors. Previous studies have revealed the adaptation of the cerebral glucose metabolic rate[7] in HA Quechua natives and the adaptation of cerebral autoregulation in HA Himalayan natives[8] and Ethiopian natives.[9] However, existing studies provided no assessments of the cerebral structures in HA natives.

The brain is one of the organs in the body with the highest oxygen consumption and thus is particularly vulnerable to hypoxia.[10] In contrast, cold weather at a HA may result in hypothermia, which has been shown to have a neuroprotective effect against hypoxic damage.[11,12] Hypobaria at a HA could also be a factor contributing to brain lesions because it has been proved to induce white matter and cortical thickness impairment.[13-15] Environmental ultraviolet rays can cause neuronal damage in the visual system and brain.[16-18] Therefore, these HA environmental factors together could have exerted their effect on brain development.

Many present day native Tibetans on the Qinghai-Tibetan Plateau are the descendants of colonizers who arrived, at most, 25,000 years ago.[19] Genetic adaptations at HA have been found in

Received August 2, 2016; accepted after revision October 24.

From the MRI Center (W.W.), First Affiliated Hospital of Xiamen University, Xiamen, China; Institute of Brain Disease and Cognition (W.W., J.Z.), Medical College of Xiamen University, Xiamen, China; Department of Neurology (X.W.), Affiliated Hospital of Hangzhou Normal University, Hangzhou, China; Huaxi Magnetic Resonance Research Center (Q.G.), West China Hospital, Sichuan University, Chengdu, China; and Department of Cognitive Sciences (M.F.), Institute of Basic Medical Sciences, Beijing, China.

This work was supported by National Science Foundation of China (grant numbers: 81171324 and 81471630) and the National Key Project (2012CB518200).

Please address correspondence to Jiaxing Zhang, MD, Department of Physiology, Medical College of Xiamen University, Xiamen, 361005, China; e-mail: zhangjiaxing@xmu.edu.cn

http://dx.doi.org/10.3174/ajnr.A5050

the native Tibetans. Unique to Tibetans are the variants of genes within the hypoxia-inducible factor pathway, including Egl 9 homolog 1 (*EGLN1*), endothelial PAS domain protein 1 (*EPAS1*), and peroxisome proliferator-activated receptor α (*PPARA*), key genes in the oxygen homeostasis system at all altitudes.[20] Among these genes, *PPARA* is involved in neuronal proliferation, differentiation, and apoptosis[21] and neuroprotection against oxidative stress.[22] Genetic variants may also play a role in brain development at a HA.

In previous studies, we have investigated the brain acclimatization to HA in the Han immigrant descendants on the Qinghai-Tibetan Plateau[23] and in the lowlanders immigrating to the Qinghai-Tibetan Plateau for several days to several years.[24,25] We found that HA acclimatization was associated with brain structural and functional modifications. Therefore, we hypothesized that native Tibetans could have developed brain adaptations to HA under the combined actions of both environmental factors and genetic variants. To test this hypothesis, we investigated the cerebral morphology of 77 healthy Tibetan adolescents living at different altitudes, with 80 sea-level Han adolescents as controls.

MATERIALS AND METHODS

Subjects

Seventy-seven healthy native Tibetans (34 males and 43 females, 14–18 years of age) living in the southeast Tibet Autonomous Region (southeast Nagqu, Xigaze, Lasa, Nyingchi, and Chamdo) (altitude, 2300–5300 m) were recruited. Their ancestors were all native Tibetans living on the Qinghai-Tibetan Plateau. They were without any prior descent to the lowlands or ascent to higher altitudes. All had a normal body mass index. They were all 10th grade students and had been enrolled in a high school at Chengdu (altitude, <400 m) for half a month. The control subjects were 80 (34 males and 46 females, 14–18 years of age) adolescents living at sea level (altitude, <50 m), matched with the native Tibetans by sex, age, and education. Subjects were excluded if they had a history of mountain sickness, neurologic disorder, or head injury. The experimental protocol was approved by the Research Ethics Review Board of Xiamen University. Procedures were fully explained, and all subjects provided written informed consent before participating in the study.

MR Imaging Data Acquisition

Brain images were obtained on the same model 3T Signa Excite MR imaging system (GE Healthcare, Milwaukee, Wisconsin) at the Huaxi Magnetic Resonance Research Center, West China Hospital, Chengdu, China, and at the MR Imaging Center, First Affiliated Hospital of Xiamen University, Xiamen, China. Parameters for the T1-weighted MPRAGE sequences were the following: TR/TE = 1900/2.48 ms, FOV = 25 × 25 cm^2, NEX = 1, matrix = 512 × 256, section thickness = 1.0 mm. Conventional 2D T1 and T2 images were also obtained and examined for any incidental findings. Data analyses were conducted by 2 researchers who were blinded to the status of subjects.

FreeSurfer Analysis

FreeSurfer (Version 5.1.0; http://surfer.nmr.mgh.harvard.edu) was used for cortical thickness, curvature, and sulcus analyses. The process consisted of the removal of nonbrain tissue, mapping to Talairach-like space, and segmentation of the gray/white matter and pial boundaries. These maps of measurements were obtained by reconstructing representations of the GM/white matter boundary and the white matter boundary to the GM/CSF boundary and then calculating the closest distance from those surfaces at each vertex on the tessellated surfaces. All subject data were resampled to the FreeSurfer default common surface template by using a high-resolution surface-based averaging technique that aligned cortical folding patterns. Finally, the surface data were spatial smoothed by using a Gaussian kernel of 10-mm full width at half maximum. Regional variations of the cortical thickness, curvature, and sulcus were compared by using an independent samples *t* test, with age, sex, and education as covariates. The statistical parametric map was generated at $P < .05$ (false discovery rate–corrected for multiple comparisons).

Correlation Analysis

The correlations of cerebral structural measurements with altitude were analyzed, with age and sex as covariates. The false discovery rate of $P < .05$ was applied to correct for multiple comparisons.

RESULTS

Cortical Thickness, Curvature, and Depth of the Sulcus

Compared with controls, the significant changes of cerebral structural measurements in native Tibetans are shown in Fig 1. Cortical thickness was significantly decreased in the left posterior cingulate cortex (PCC), lingual gyrus, superior parietal cortex, precuneus, and rostral middle frontal cortex and the right medial orbitofrontal cortex, lateral occipital cortex, precuneus, and paracentral lobule (Table 1. Furthermore, curvature was significantly decreased in the left superior parietal cortex and right superior marginal gyrus. Finally, the depth of the sulcus was significantly increased in the left inferior temporal gyrus and significantly decreased in the right superior marginal gyrus, superior temporal gyrus, and insular cortex.

Correlations

The significant correlations of cerebral structural measurements with altitude in native Tibetans are shown in Fig 2. Cortical thickness was negatively correlated with altitude in the left superior and middle temporal gyri, rostral middle frontal cortex, PCC, precuneus, lingual gyrus, insular cortex, and right superior temporal gyrus (Table 2). Curvature was positively correlated with altitude in the left rostral middle frontal cortex, insular cortex, and middle temporal gyrus. The depth of the sulcus was negatively correlated with altitude in the left lingual gyrus and right medial orbitofrontal cortex.

Figure 3 indicates the overlaps of brain between the regions showing decreases of cortical thickness and those showing correlation between cortical thickness and altitude. These regions included the left PCC, precuneus, lingual gyrus, and rostral middle frontal cortex.

DISCUSSION

Our study is the first to reveal the cerebral characteristics of native Tibetans living on the Qinghai-Tibetan Plateau. Adaptations of Tibetans to HA were associated with structural modifications in

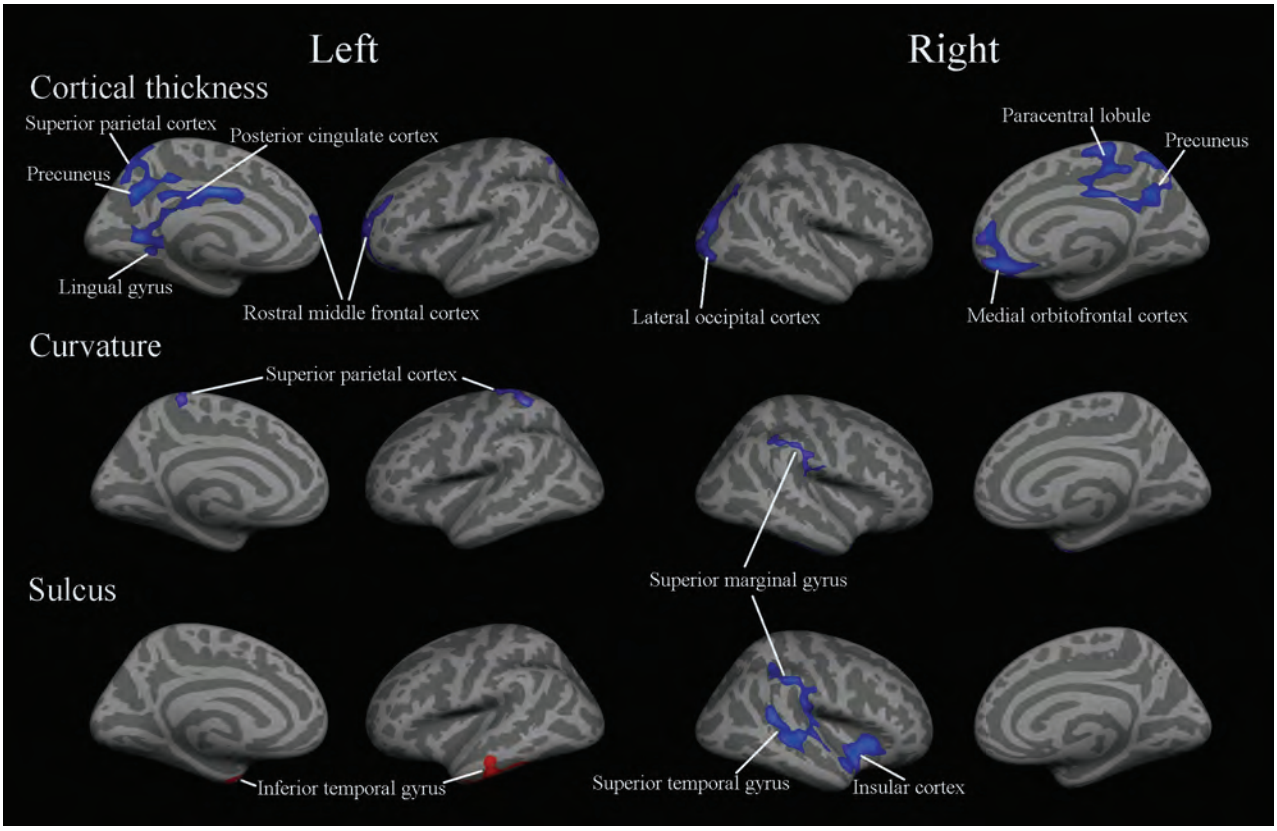

FIG 1. Regions showing changes of cortical measurements in native Tibetans compared with the sea-level Han controls ($P < .05$, false discovery rate–corrected for multiple comparisons). Blue indicates a decrease; red, an increase.

Table 1: Regional information of changed cortical thickness in native Tibetans

Areas	Volume (mm^3)	MNI Coordinate			*P* (Peak)
		x	y	z	
Left					
Posterior cingulate cortex/lingual gyrus	1467	−3.7	−8.5	33.8	3.651
Superior parietal cortex/precuneus	1815	−8.6	−68.1	56.0	2.571
Rostral middle frontal cortex	1575	−31.2	36.9	22.6	1.878
Right					
Lateral occipital cortex	2149	26.4	−83.9	14.4	3.081
Precuneus/paracentral lobule	2200	7.7	−61.8	58.2	2.583
Medial orbitofrontal cortex	1366	8.4	47.6	−13.8	3.296

Note:— MNI indicates Montreal Neurological Institute.

cortical thicknesses, curvature, and the sulcus. Mainly in the left hemisphere, the cortical structures were significantly correlated with altitude; moreover, with increasing altitude, native Tibetans had a decrease of regional cortical thickness, while they had an increase of cortical folding in terms of curvature. The regions showing decreases of cortical thickness and those showing correlations between cortical thickness and altitude overlapped in the left PCC, precuneus, lingual gyrus, and rostral middle frontal cortex.

The changed brain regions in the native Tibetans were in agreement with those found in our previous studies on Han immigrants living on the Qinghai-Tibetan Plateau. For example, Han immigrant descendants at HA showed decreases of GM volume in the cingulate cortex, rostral middle frontal cortex, lingual gyrus, and anterior insular cortex.[23] Adult immigrants who lived at a HA for 2 years showed decreases of cortical thickness in the paracentral lobule, PCC, and precuneus and increases of cortical thickness in the orbitofrontal cortex, superior parietal cortex, inferior temporal gyrus, and lingual gyrus.[25] Moreover, compared with Tibetan adolescents who had lived at sea level for 4 years, the Tibetan adolescents who lived at a HA all the time showed decreases of GM volume in the superior parietal cortex and insular cortex.[26]

Effects of Environmental Factors on Brain Structural Development

In native Tibetans, there were significant correlations between regional cortical measurements and altitude, suggesting that HA environmental factors influence brain development. The effects of HA environmental factors on brain development have been detected in Tibetan adolescents who were born and raised on the Qinghai-Tibetan Plateau compared with Tibetan adolescents who had lived at sea level during the past 4 years.[26]

Cortical changes may be induced by hypoxia. For example, cerebral edema was found after acute exposure to normobaric hypoxia.[27] In agreement with the present findings, damage of GM in the cingulate cortex, temporal gyrus, and insular cortex has been detected in patients with hypoxia with chronic obstructive pulmonary disease.[28] The changed cerebral circulation may be attributed to temporal and posterior brain structural alterations shown in the present study. The vertebral artery supplies blood to

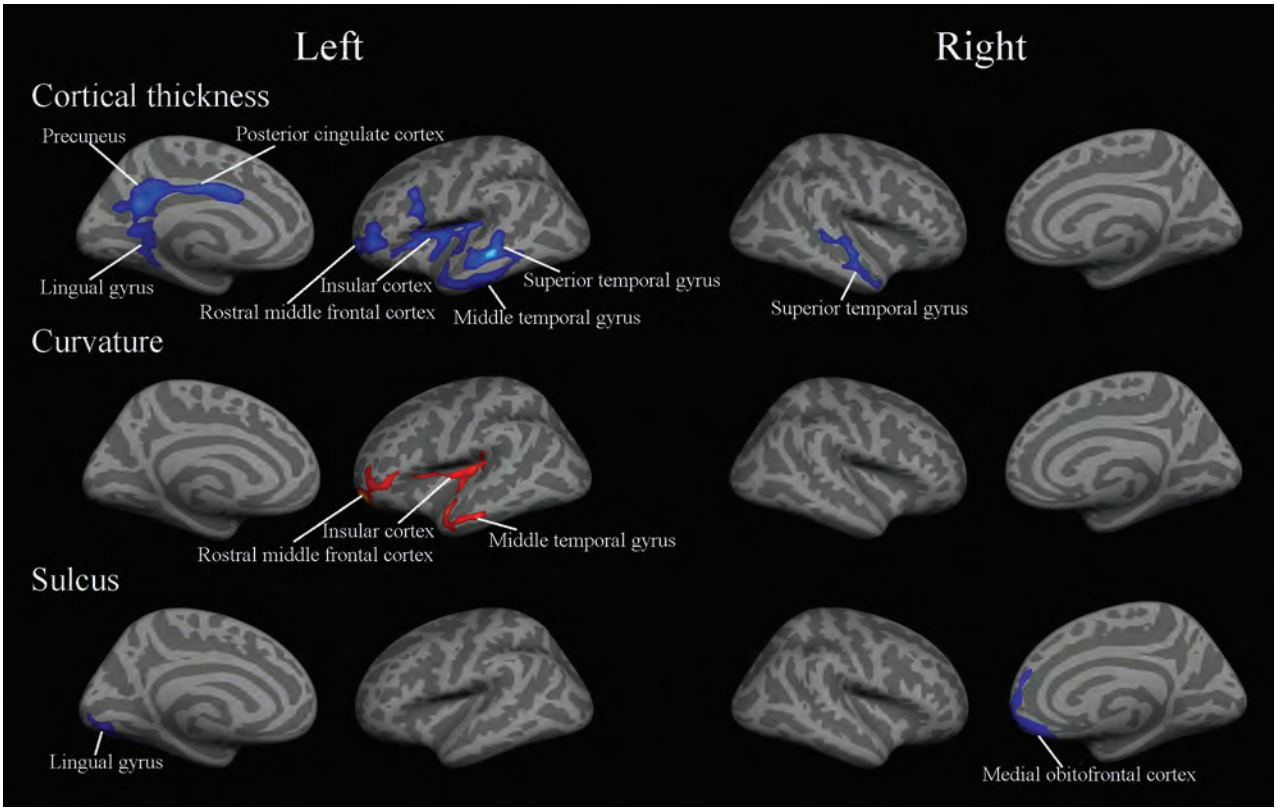

FIG 2. Regions in which the cortical measurements in native Tibetans showed significant correlations with altitude ($P < .05$, false discovery rate–corrected for multiple comparisons). Blue indicates a negative correlation; red, a positive correlation.

Table 2: Information of regions in which cortical thickness showed correlation with altitude in Tibetans

Areas	Volume (mm^2)	MNI Coordinate			*P* (Peak)
		x	y	z	
Left					
Superior/middle temporal gyrus	3150	−49.0	−32.6	−9.2	4.949
Precuneus/posterior cingulate cortex/lingual gyrus	2510	−9.4	−55.9	22.5	3.519
Rostral middle frontal cortex	1431	−23.8	51.8	−4.9	3.426
Insular cortex	2543	−27.8	24.3	5.7	2.445
Right					
Superior temporal gyrus	1174	56.6	−13.1	−4.7	2.134

Note:—MNI indicates Montreal Neurological Institute.

these 2 parts of the brain. Willie et al[29] found that with hypoxia, the relative increase in vertebral artery blood flow was 50% greater than in the other vessels. Ogoh et al[30] found that the internal carotid artery blood flow was unchanged, while the vertebral artery blood flow was significantly increased during acute hypoxia. Feddersen et al[31] found that in mountaineers during ascent to 5050 m, the cerebral blood flow velocity was decreased in the posterior cerebral arteries. Moreover, hypoxia-induced alteration of cerebral blood flow patterns was found in the posterior brain in patients with hypoxia and obstructive sleep apnea, which included the lingual gyrus, parietal lobule, precuneus, temporal cortex, and insular cortex.[32] Recently, Lawley et al[33] found that 2 hours of hypoxia caused an expected increase in frontal cortical gray matter perfusion but unexpected perfusion decreases predominantly in the PCC. After 10 hours in hypoxia, the decreased blood flow became more pronounced and widespread. They further confirmed that these reductions in cerebral blood flow from hypoxia were related to vasoconstrictions.

Hypobaria at HA could be another important factor contributing to brain alterations. Acute mountain sickness scores were higher,[34] and visual sensitivities were lower[35] in hypobaric than in normobaric hypoxia. Studies on U-2 pilots showed that hypobaria was associated with a change of white matter hyperintensity[14,36] and with the reduction of cortical thickness.[15] Moreover, exposure to hypobaria after traumatic brain injury worsened brain function.[37]

Cold ambient temperature at a HA may result in hypothermia. Mild hypothermia is associated with decreased ventricular function, oxygen extraction, and microvascular flow.[38] During hypoxia, hypothermia has been shown to have a neuroprotective effect against hypoxic encephalopathy.[12] Moreover, hypothermia treatment in an animal stroke model reduced infarct size and improved neurologic behavior.[11]

The decrease of visual cortical thickness in the present study may be an outcome of ultraviolet radiation at HA. Ultraviolet light has been shown to alter neuronal activity in the cortical structures involved in visual processing.[39] Environmental doses of ultraviolet rays can induce apoptosis in the retina and lamina ganglionaris within the visual system and in the brains of invertebrate crustaceans.[16-18]

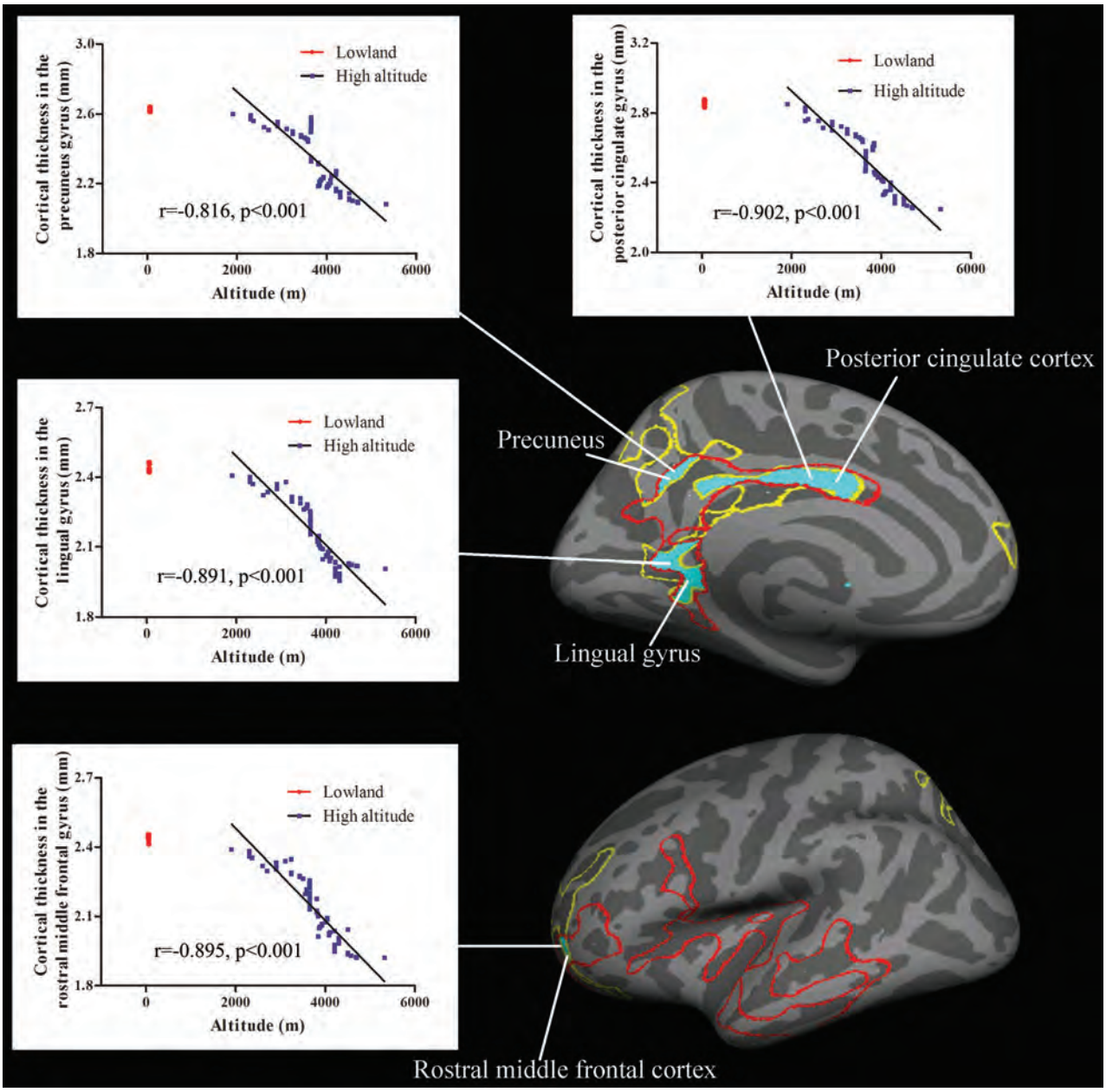

FIG 3. Tibetan brain overlaps (*blue areas*) between the regions showing significant decreases of cortical thickness (*yellow line*) and those showing correlations between cortical thickness and altitude (*red line*). For each correlation diagram, 80 overlapped *red dots* indicate the cortical thickness values in the sea-level controls. *Blue dots* indicate that the cortical thickness values in 77 Tibetans were significantly correlated with altitude.

Effects of Genes on Brain Structural Development

The results of the present study obtained from native Tibetans showed some differences from those found in the Han immigrant descendants,[23] which suggest that genes may play a role in Tibetan brain development. A recent study discovered genetic selection on the *PPARA* in HA native Tibetans on the Qinghai-Tibetan Plateau through comparing them with Chinese and Japanese lowland populations.[20] *PPARA* is expressed in the brain.[21,40] It is involved in neuronal proliferation, differentiation, and apoptosis.[21,41] *PPARA* encodes the fatty acid–activated transcription factors and fatty acid oxidation regulators; thus, it may affect brain structure through control of energy homeostasis.[42,43] *PPARA* is also involved in angiogenesis,[44] which may contribute to the GM change. Moreover, during hypoxia, *PPARA* supports a role in neuroprotection against oxidative stress.[22]

Gene or Environment: Which One Determines Brain Structure?

Reduced psychomotor speed has been tested in the subjects (6–16 years of age) of mixed-ethnic background (including Native American, European, or African ancestries who immigrated to HA during different periods) who were born and raised at HAs.[45] For the proportion of Native Americans, Europeans, and Africans, genetic admixture with reduced psychomotor speed was comparable across altitude groups; therefore, chronic hypoxic exposure rather than genetic inheritance appears to affect brain

function development at HA. However, pulmonary function (forced expiratory volume and forced vital capacity) measures were greater in the HA natives compared with the lowland natives born and raised at HAs; this finding suggests a genetic effect.[46] In contrast, these 2 pulmonary measures were similar in HA natives and sea-level natives at lowland; this finding suggests that the genetic potential for larger lung volumes at HA depended on the developmental exposure to HA. In summary, results from these studies emphasized the importance of developmental adaptations to HA.

Implications for the Changes in Cortical Structural Measurements

In our study, decreases of cortical thickness in the medial orbitofrontal cortex, PCC, lingual gyrus, and precuneus; a decrease of curvature in the superior parietal cortex; and a decrease of the depth of the sulcus in the temporal cortices were detected. These regions are core areas of the resting-state brain default mode network (DMN) in humans.[47,48] The impairment of GM structures may contribute to reduced neuronal activity. Previous multimodal neuroimaging studies have shed light on this function-structure association, underlining cognition, aging, disease, and behavior.[49] The changed activity within the DMN in response to chronic stress exposure has been found in humans[50] and animals.[51] The impairment of cortical structures in HA Tibetans is likely to reflect the stress-induced atrophic effects in cortical regions. Cortical atrophy within the DMN may reduce the brain response to HA environmental stress. Because regions within the DMN exert forebrain modulation over visceral responses mediated via the hypothalamus and brain stem, structural and functional changes within these circuits may contribute to modulations in autonomic and neuroendocrine functions associated with HA adaptations.

Tibetan college students were found to have higher levels of negative emotional expressivities such as fear, sadness, and anger in comparison with Han, Uighur, Hui, and Mongolian students.[52] The Cattell 16 Personality Factor Questionnaire revealed that Tibetan adolescents had lower stability, persistence, independence, and self-discipline and higher extroversion and excitability than Han adolescents.[53,54] The findings of the Eysenck Personality Questionnaire and Trait Coping Style Questionnaire suggested that Tibetan adolescents had higher neuroticism, introversion, and psychoticism and lower concealment than Han adolescents.[55] In humans, the DMN is thought to support a variety of self-referential functions and mind-wandering.[56] Anxiety disorders and high trait anxiety are associated with decreased functioning of the DMN.[57] The precuneus is implicated in social and emotional functions, especially among individuals with neuroticism.[58] The left posterior and middle cingulate cortices and precuneus were found to be negatively correlated with neuroticism.[59] The ventral medial prefrontal (orbitofrontal) cortex of the DMN functions as a sensory-visceromotor link concerned with social behavior, mood control, and motivational drive, all of which are important components of an individual's personality.[48] Therefore, a changed DMN may explain why Tibetan adolescents had personality traits distinct from those of the Han adolescents.

The decreases of cortical thickness in the PCC and lingual gyrus may be related to visual deficits at HA. The poor visual performances were consistent and prominent problems in the HA immigrants, such as the sea-level college students after 7 months of study at moderate altitudes,[60] and in the HA Han immigrant descendants.[61] The PCC and lingual gyrus have direct anatomic connectivities with the visual striate cortices.[62] The PCC lies at the parietomedial temporal visual stream pathway.[63] It is activated by visual perception, attention, and motion.[64-66] The lesions of the PCC produce an impairment in visual discrimination learning[67] and a decrease of resting-state functional connectivity in the PCC, which is indicated by severe myopia.[68] The lingual gyrus is a part of the occipitotemporal pathway that engages in object drawing[69] and is activated by visuospatial navigation[70] and angle discrimination tasks.[71] GM volume in the right lingual cortex has been proved to have a positive correlation with visual reproduction,[72] while GM atrophy in this area was associated with visual hallucinations.[73]

The decreased depth of the anterior insular sulcus and damage to the ventral medial prefrontal cortex in the present study support the hypothesis that these 2 regions are needed to process the perturbation of the homeostatic balance in extreme environments.[48,74] Because the lesions in the insular cortex have been proved to disrupt representation of internal states that underpin motivation,[75] the changes of the anterior insular cortex may also be related to the blunted hypoxic ventilatory response in HA residents.[76]

Limitations

There are several limitations to our study. First, brain images were obtained by using 2 MR imaging scanners. However, several studies have confirmed that the MR imaging scanner field strength, manufacturer, machine upgrade, and pulse sequence[77] and the different postprocessing algorithms applied to the images acquired from different MR imaging systems[78] have little effect on the reliability of cortical thickness measurements.

Second, the Tibetan subjects had moved to the lowlands for 1–15 days, which would have an influence on cerebral blood flow. However, given the previous investigations, this effect may be slight after residing at sea level for such a short time. For example, when HA adult natives descended to sea level for several weeks, their cardiac functions remained unchanged.[79,80]

Third, the interethnic difference of brain structure can be large. Brain morphologic differences between populations of different origins have been found in whole-brain and region-specific volume.[81] Future study should compare the interethnic difference of brain structures between Tibetans and Han populations at lowland.

Fourth, Tibetans have been living on the Qinghai-Tibetan Plateau and have developed a unique culture and language. The lifestyle of the Tibetans was different from that in the lowlands, for example, in the absence of crowds, which could have affected the subjects' emotional well-being. Moreover, diet was likely to be an important factor for the observed brain changes.

CONCLUSIONS

Native Tibetans have developed brain structural adaptations that enable their successful existence in the HA environment. The al-

terations of cortical structure in native Tibetans were mainly located in the resting-state brain DMN and were in agreement with those found in the Han immigrants on the Qinghai-Tibetan Plateau. Brain structural modifications may be derived from the interaction between genetic and environmental factors. Future study is need to test the personality traits, body homeostasis, and cognition and clarify the neuronal mechanisms of the Tibetans.

Disclosures: Ming Fan—*RELATED*: *Grant*: National Key Project, *Comments*: grant number 2012CB518200. Jiaxing Zhang—*RELATED*: *Grant*: National Science Foundation of China and National Key Project, *Comments*: grant Nos. 81171324 and 81471630.

REFERENCES

1. Houston CS, Riley RL. **Respiratory and circulatory changes during acclimatization to high altitude.** *Am J Physiol* 1947;149:565–88 Medline
2. Lahiri S, DeLaney RG, Brody JS, et al. **Relative role of environmental and genetic factors in respiratory adaptation to high altitude.** *Nature* 1976;261:133–35 CrossRef Medline
3. Beall CM, Reichsman AB. **Hemoglobin levels in a Himalayan high altitude population.** *Am J Phys Anthropol* 1984;63:301–06 CrossRef Medline
4. Niermeyer S, Yang P, Shanmina, et al. **Arterial oxygen saturation in Tibetan and Han infants born in Lhasa, Tibet.** *N Engl J Med* 1995; 333:1248–52 CrossRef Medline
5. Murray AJ. **Energy metabolism and the high-altitude environment.** *Exp Physiol* 2016;101:23–27 CrossRef Medline
6. Yi X, Liang Y, Huerta-Sanchez E, et al. **Sequencing of 50 human exomes reveals adaptation to high altitude.** *Science* 2010;329:75–78 CrossRef Medline
7. Hochachka PW, Clark CM, Brown WD, et al. **The brain at high altitude: hypometabolism as a defense against chronic hypoxia?** *J Cereb Blood Flow Metab* 1994;14:671–79 CrossRef Medline
8. Jansen GF, Krins A, Basnyat B, et al. **Role of the altitude level on cerebral autoregulation in man resident at high altitude.** *J Appl Physiol (1985)* 2007;103:518–23 Medline
9. Claydon VE, Gulli G, Slessarev M, et al. **Cerebrovascular responses to hypoxia and hypocapnia in Ethiopian high altitude dwellers.** *Stroke* 2008;39:336–42 CrossRef Medline
10. Hadanny A, Efrati S. **Oxygen: a limiting factor for brain recovery.** *Crit Care* 2015;19:307 CrossRef Medline
11. Gao XY, Huang JO, Hu YF, et al. **Combination of mild hypothermia with neuroprotectants has greater neuroprotective effects during oxygen-glucose deprivation and reoxygenation-mediated neuronal injury.** *Sci Rep* 2014;4:7091 CrossRef Medline
12. Kvistad CE, Thomassen L, Waje-Andreassen U, et al. **Body temperature and major neurological improvement in tPA-treated stroke patients.** *Acta Neurol Scand* 2014;129:325–29 Medline
13. Coppel J, Hennis P, Gilbert-Kawai E, et al. **The physiological effects of hypobaric hypoxia versus normobaric hypoxia: a systematic review of crossover trials.** *Extrem Physiol Med* 2015;4:2 CrossRef Medline
14. McGuire SA, Sherman PM, Wijtenburg SA, et al. **White matter hyperintensities and hypobaric exposure.** *Ann Neurol* 2014;76:719–26 CrossRef Medline
15. Simmons D, Bursaw A, Sherman P, et al. **Repeated exposure to hypobaria in U2 pilots is associated with reduced aggregate cortical thickness.** *Neurology* 2015;84(suppl):P4.161
16. Hollmann G, Linden R, Giangrande A, et al. **Increased p53 and decreased p21 accompany apoptosis induced by ultraviolet radiation in the nervous system of a crustacean.** *Aquati Toxicol* 2016;173:1–8 CrossRef Medline
17. Miguel NC, Meyer-Rochow VB, Allodi S. **Ultrastructural study of first and second order neurons in the visual system of the crab Ucides cordatus following exposure to ultraviolet radiation.** *Micron* 2002;33:627–37 Medline
18. Miguel NC, Wajsenzon IJ, Takiya CM, et al. **Catalase: Bax and p53 expression in the visual system of the crab Ucides cordatus following exposure to ultraviolet radiation.** *Cell Tissue Res* 2007;329: 159–68 CrossRef Medline
19. Aldenderfer MS. **Moving up in the world.** *American Scientist* 2003; 91:542–49
20. Simonson TS, Yang Y, Huff CD, et al. **Genetic evidence for high-altitude adaptation in Tibet.** *Science* 2010;329:72–75 CrossRef Medline
21. Cimini AM, Cerù MP. **Emerging roles of peroxisome proliferator-activated receptors (PPARs) in the regulation of neural stem cells proliferation and differentiation.** *Stem Cell Rev* 2008;4:293–303 CrossRef Medline
22. Fidaleo M, Fanelli F, Ceru MP, et al. **Neuroprotective properties of peroxisome proliferator-activated receptor alpha (PPARα) and its lipid ligands.** *Curr Med Chem* 2014;21:2803–21 CrossRef Medline
23. Zhang J, Yan X, Shi J, et al. **Structural modifications of the brain in acclimatization to high-altitude.** *PLoS One* 2010;5:e11449 CrossRef Medline
24. Zhang H, Lin J, Sun Y, et al. **Compromised white matter microstructural integrity after mountain climbing: evidence from diffusion tensor imaging.** *High Alt Med Biol* 2012;13:118–25 CrossRef Medline
25. Zhang J, Zhang H, Li J, et al. **Adaptive modulation of adult brain gray and white matter to high altitude: structural MRI studies.** *PLoS One* 2013;8:e68621 CrossRef Medline
26. Zhang J, Zhang H, Chen J, et al. **Structural modulation of brain development by oxygen: evidence on adolescents migrating from high altitude to sea level environment.** *PLoS One* 2013;8:e67803 CrossRef Medline
27. Kallenberg K, Bailey DM, Christ S, et al. **Magnetic resonance imaging evidence of cytotoxic cerebral edema in acute mountain sickness.** *J Cereb Blood Flow Metab* 2007;27:1064–71 Medline
28. Zhang H, Wang X, Lin J, et al. **Grey and white matter abnormalities in chronic obstructive pulmonary disease: a case-control study.** *BMJ Open* 2012;2:e000844 CrossRef Medline
29. Willie CK, Macleod DB, Shaw AD, et al. **Regional brain blood flow in man during acute changes in arterial blood gases.** *J Physiol* 2012;590: 3261–75 CrossRef Medline
30. Ogoh S, Sato K, Nakahara H, et al. **Effect of acute hypoxia on blood flow in vertebral and internal carotid arteries.** *Exp Physiol* 2013;98: 692–98 CrossRef Medline
31. Feddersen B, Neupane P, Thanbichler F, et al. **Regional differences in the cerebral blood flow velocity response to hypobaric hypoxia at high altitudes.** *J Cereb Blood Flow Metab* 2015;35:1846–51 CrossRef Medline
32. Baril AA, Gagnon K, Arbour C, et al. **Regional cerebral blood flow during wakeful rest in older subjects with mild to severe obstructive sleep apnea.** *Sleep* 2015;38:1439–49 CrossRef Medline
33. Lawley JS, Macdonald JH, Oliver SJ, et al. **Unexpected reductions in regional cerebral perfusion during prolonged hypoxia.** *J Physiol* 2016 Aug 9. [Epub ahead of print] CrossRef Medline
34. DiPasquale DM, Strangman GE, Harris NS, et al. **Hypoxia, hypobaria, and exercise duration affect acute mountain sickness.** *Aerosp Med Hum Perform* 2015;86:614–19 CrossRef Medline
35. Degache F, Larghi G, Faiss R, et al. **Hypobaric versus normobaric hypoxia: same effects on postural stability?** *High Alt Med Biol* 2012; 13:40–45 CrossRef Medline
36. McGuire S, Sherman P, Profenna L, et al. **White matter hyperintensities on MRI in high-altitude U-2 pilots.** *Neurology* 2013;81:729–35 CrossRef Medline
37. Skovira JW, Kabadi SV, Wu J, et al. **Simulated aeromedical evacuation exacerbates experimental brain injury.** *J Neurotrauma* 2016;33: 1292–302 CrossRef Medline
38. He X, Su F, Taccone FS, et al. **Cardiovascular and microvascular responses to mild hypothermia in an ovine model.** *Resuscitation* 2012;83:760–66 CrossRef Medline
39. Amir S, Robinson B. **Fos expression in rat visual cortex induced by**

ocular input of ultraviolet light. *Brain Res* 1996;716:213–18 CrossRef Medline
40. Gofflot F, Chartoire N, Vasseur L, et al. **Systematic gene expression mapping clusters nuclear receptors according to their function in the brain.** *Cell* 2007;131:405–18 CrossRef Medline
41. Pérez-Martín M, Rivera P, Blanco E, et al. **Environmental enrichment, age, and PPARα interact to regulate proliferation in neurogenic niches.** *Front Neurosci* 2016;10:89 CrossRef Medline
42. Knauf C, Rieusset J, Foretz M, et al. **Peroxisome proliferator-activated receptor-alpha-null mice have increased white adipose tissue glucose utilization, GLUT4, and fat mass: role in liver and brain.** *Endocrinology* 2006;147:4067–78 CrossRef Medline
43. Chakravarthy MV, Zhu Y, López M, et al. **Brain fatty acid synthase activates PPARalpha to maintain energy homeostasis.** *J Clin Invest* 2007;117:2539–52 CrossRef Medline
44. Rizvi YQ, Mehta CS, Oyekan A. **Interactions of PPAR-alpha and adenosine receptors in hypoxia-induced angiogenesis.** *Vascul Pharmacol* 2013;59:144–51 CrossRef Medline
45. Hogan AM, Virues-Ortega J, Botti AB, et al. **Development of aptitude at altitude.** *Dev Sci* 2010;13:533–44 CrossRef Medline
46. Brutsaert TD, Soria R, Caceres E, et al. **Effect of developmental and ancestral high altitude exposure on chest morphology and pulmonary function in Andean and European/North American natives.** *Am J Hum Biol* 1999;1:383–95 Medline
47. Li W, Mai X, Liu C. **The default mode network and social understanding of others: what do brain connectivity studies tell us.** *Front Hum Neurosci* 2014;8:74 CrossRef Medline
48. Raichle ME. **The brain's default mode network.** *Annu Rev Neurosci* 2015;38:433–47 CrossRef Medline
49. Sui J, Huster R, Yu Q, et al. **Function-structure associations of the brain: evidence from multimodal connectivity and covariance studies.** *Neuroimage* 2014;102:11–23 CrossRef Medline
50. Soares JM, Sampaio A, Ferreira LM, et al. **Stress impact on resting state brain networks.** *PLoS One* 2013;8:e66500 CrossRef Medline
51. Henckens MJ, van der Marel K, van der Toorn A, et al. **Stress-induced alterations in large-scale functional networks of the rodent brain.** *Neuroimage* 2015;105:312–22 CrossRef Medline
52. Lu W, Wang Z. **Emotional expressivity, emotion regulation, and mood in college students: a cross-ethnic study.** *Social Behavior and Personality: An International Journal* 2012;40:319–30 CrossRef
53. Jin D. **Mental health problems and personal characters in Tibetan school children.** *Chinese Mental Health Journal* 1989;3:257–58
54. Kang YW, Kang XW, Xie SJ. **Analysis on Tibetan undergraduates' personality in inland.** *Chinese Journal of School Health* 2012;33:1176–79
55. Chang XD, Shi JH, Dan-Ying MA. **Correlation between personality traits and coping styles for junior high school students from Tibetan in Shanghai.** *Medical Journal of Chinese Peoples Health* 2013;25:94–97
56. Mason MF, Norton MI, Van Horn JD, et al. **Wandering minds: the default network and stimulus-independent thought.** *Science* 2007;315:393–95 CrossRef Medline
57. Sylvester CM, Corbetta M, Raichle ME, et al. **Functional network dysfunction in anxiety and anxiety disorders.** *Trends Neurosci* 2012;35:527–35 CrossRef Medline
58. Adelstein JS, Shehzad Z, Mennes M, et al. **Personality is reflected in the brain's intrinsic functional architecture.** *PLoS One* 2011;6:e27633 CrossRef Medline
59. Servaas MN, van der Velde J, Costafreda SG, et al. **Neuroticism and the brain: a quantitative meta-analysis of neuroimaging studies investigating emotion processing.** *Neurosci Biobehav Rev* 2013;37:1518–29 CrossRef Medline
60. Zhang J, Liu H, Yan X, et al. **Minimal effects on human memory following long-term living at moderate altitude.** *High Alt Med Biol* 2011;12:37–43 CrossRef Medline
61. Yan X, Zhang J, Gong Q, et al. **Cerebrovascular reactivity among native-raised high altitude residents: an fMRI study.** *BMC Neurosci* 2011;12:94 CrossRef Medline
62. Whittingstall K, Bernier M, Houde JC, et al. **Structural network underlying visuospatial imagery in humans.** *Cortex* 2014;56:85–98 CrossRef Medline
63. Kravitz DJ, Saleem KS, Baker CI, et al**. A new neural framework for visuospatial processing.** *Nat Rev Neurosci* 2011;12:217–30 CrossRef Medline
64. Antal A, Baudewig J, Paulus W, et al. **The posterior cingulate cortex and planum temporale/parietal operculum are activated by coherent visual motion.** *Vis Neurosci* 2008;25:17–26 CrossRef Medline
65. Fischer E, Bülthoff HH, Logothetis NK, et al. **Visual motion responses in the posterior cingulate sulcus: a comparison to V5/MT and MST.** *Cereb Cortex* 2012;22:865–76 CrossRef Medline
66. Leech R, Sharp DJ. **The role of the posterior cingulate cortex in cognition and disease.** *Brain* 2014;137:12–32 CrossRef Medline
67. Bussey TJ, Muir JL, Everitt BJ, et al. **Dissociable effects of anterior and posterior cingulate cortex lesions on the acquisition of a conditional visual discrimination: facilitation of early learning vs. impairment of late learning.** *Behav Brain Res* 1996;82:45–56 CrossRef Medline
68. Zhai L, Li Q, Wang T, et al. **Altered functional connectivity density in high myopia.** *Behav Brain Res* 2016;303:85–92 CrossRef Medline
69. Ogawa K, Inui T. **The role of the posterior parietal cortex in drawing by copying.** *Neuropsychologia* 2009;47:1013–22 CrossRef Medline
70. Grön G, Wunderlich AP, Spitzer M, et al. **Brain activation during human navigation: gender-different neural networks as substrate of performance.** *Nat Neurosci* 2000;3:404–08 CrossRef Medline
71. Prvulovic D, Hubl D, Sack AT, et al. **Functional imaging of visuospatial processing in Alzheimer's disease.** *Neuroimage* 2002;17:1403–14 CrossRef Medline
72. Chee MW, Chen KH, Zheng H, et al. **Cognitive function and brain structure correlations in healthy elderly East Asians.** *Neuroimage* 2009;46:257–69 CrossRef Medline
73. Goldman JG, Stebbins GT, Dinh V, et al. **Visuoperceptive region atrophy independent of cognitive status in patients with Parkinson's disease with hallucinations.** *Brain* 2014;137:849–59 CrossRef Medline
74. Paulus MP, Potterat EG, Taylor MK, et al. **A neuroscience approach to optimizing brain resources for human performance in extreme environments.** *Neurosci Biobehav Rev* 2009;33:1080–88 CrossRef Medline
75. Dani JA, Montague PR. **Disrupting addiction through the loss of drug associated internal states.** *Nat Neurosci* 2007;10:403–04 CrossRef Medline
76. Frisancho AR. **Functional adaptation to high altitude hypoxia**. *Science* 1975;187:313–19 CrossRef Medline
77. Han X, Jovicich J, Salat D, et al. **Reliability of MRI-derived measurements of human cerebral cortical thickness: the effects of field strength, scanner upgrade and manufacturer.** *Neuroimage* 2006;32:180–94 CrossRef Medline
78. Durand-Dubief F, Belaroussi B, Armspach JP, et al. **Reliability of longitudinal brain volume loss measurements between 2 sites in patients with multiple sclerosis: comparison of 7 quantification techniques.** *AJNR Am J Neuroradiol* 2012;33:1918–24 CrossRef Medline
79. McKenzie DC, Goodman LS, Nath C, et al. **Cardiovascular adaptations in Andean natives after 6 wk of exposure to sea level.** *J Appl Physiol (1985)* 1991;70:2650–55 Medline
80. Sime F, Peñaloza D, Ruiz L. **Bradycardia, increased cardiac output, and reversal of pulmonary hypertension in altitude natives living at sea level.** *Br Heart J* 1971;33:647–57 CrossRef Medline
81. Bai J, Abdul-Rahman MF, Rifkin-Graboi A, et al. **Population differences in brain morphology and microstructure among Chinese, Malay, and Indian neonates.** *PLoS One* 2012;7:e47816 CrossRef Medline

Feasibility and Safety of Repeat Instant Endovascular Interventions in Patients with Refractory Cerebral Vasospasms

L. Andereggen, J. Beck, W.J. Z'Graggen, G. Schroth, R.H. Andres, M. Murek, M. Haenggi, M. Reinert, A. Raabe, and J. Gralla

ABSTRACT

BACKGROUND AND PURPOSE: For patients with cerebral vasospasm refractory to medical and hemodynamic therapies, endovascular therapies often remain the last resort. Data from studies in large cohorts on the efficacy and safety of multiple immediate endovascular interventions are sparse. Our aim was to assess the feasibility and safety of multiple repeat instant endovascular interventions in patients with cerebral vasospasm refractory to medical, hemodynamic, and initial endovascular interventions.

MATERIALS AND METHODS: This was a single-center retrospective study of prospectively collected data on patients with cerebral vasospasm refractory to therapies requiring ≥3 endovascular interventions during the course of treatment following aneurysmal subarachnoid hemorrhage. The primary end point was functional outcome at last follow-up (mRS ≤2). The secondary end point was angiographic response to endovascular therapies and the appearance of cerebral infarctions.

RESULTS: During a 4-year period, 365 patients with aneurysmal subarachnoid hemorrhage were treated at our institution. Thirty-one (8.5%) met the inclusion criteria. In 52 (14%) patients, ≤2 endovascular interventions were performed as rescue therapy for refractory cerebral vasospasm. At last follow-up, a good outcome was noted in 18 (58%) patients with ≥3 interventions compared with 31 (61%) of those with ≤2 interventions ($P = .82$). The initial Hunt and Hess score of ≤2 was a significant independent predictor of good outcome (OR, 4.7; 95% CI, 1.2–18.5; $P = .03$), whereas infarcts in eloquent brain areas were significantly associated with a poor outcome (mRS 3–6; OR, 13.5; 95% CI, 2.3–81.2; $P = .004$).

CONCLUSIONS: Repeat instant endovascular intervention is an aggressive but feasible last resort treatment strategy with a favorable outcome in two-thirds of patients with refractory cerebral vasospasm and in whom endovascular treatment has already been initiated.

ABBREVIATIONS: CVS = cerebrovascular vasospasm; GCS = Glasgow Coma Scale; HH = Hunt and Hess; IAN = intra-arterial nimodipine; PTA = percutaneous transluminal balloon angioplasty; RCVS = refractory CVS

Cerebral vasospasm (CVS) after aneurysmal subarachnoid hemorrhage remains a major cause of delayed cerebral ischemia and related morbidity and mortality.[1,2] Standard treatment consists of hyperdynamic/hypertensive therapy and orally administered nimodipine to prevent ischemic events.[3,4] Nevertheless, 20%–30% of patients develop refractory CVS with cerebral infarction causing permanent neurologic deficits or death.[5] In cases of severe CVS and threatened ischemia despite hemodynamic and medical treatment, no commonly accepted treatment guidelines exist.[6] Although endovascular methods offer some last resort treatment options, their use is generally not extended throughout the entire CVS course and application is limited to 1 or 2 or, at most, 3 interventions, resulting in an ambiguous functional outcome with most patients unable to resume work post-SAH.[7-10]

In this single-center audit of practice, we evaluated repeat immediate endovascular therapies in a subgroup of symptomatic patients with the most severe, refractory CVS during the vasospasm period.

MATERIALS AND METHODS

Patient Inclusion Criteria and Study End Points

To comply with the inclusion criteria, patients with proved aneurysmal subarachnoid hemorrhage had to fulfill the requirement of medically and hemodynamic refractory CVS (rCVS) necessitating ≥3 endovascular interventions during

Received April 21, 2016; accepted after revision October 11.

From the Department of Neurosurgery (L.A., J.B., W.J.Z., R.H.A., M.M., M.R., A.R.), Institute for Diagnostic and Interventional Neuroradiology (L.A., G.S., J.G.), Departments of Neurology (W.J.Z.), and Intensive Care Medicine (M.H.), Inselspital, Bern University Hospital, University of Bern, Switzerland.

The authors declare no conflict of interest. This study was approved by the Ethics Committee of the Canton of Bern, Switzerland (Kantonale Ethikkommission Bern, KEK, 177/14).

Paper previously presented in part at: Vasospasm 2013: The 13th International Conference on Neurovascular Events after Subarachnoid Hemorrhage, Lucerne, Switzerland; July 10–12, 2013.

Please address correspondence to Jan Gralla, MD, Director and Chairman, Institute of Diagnostic and Interventional Neuroradiology, Inselspital, Bern University Hospital, Freiburgstr 10, 3010 Bern, Switzerland; e-mail: jan.gralla@insel.ch

Indicates article with supplemental on-line tables.

http://dx.doi.org/10.3174/ajnr.A5024

the CVS period. These patients were compared with a cohort of patients with aneurysmal subarachnoid hemorrhage necessitating 1–2 endovascular interventions during the refractory CVS period. Patients with mycotic aneurysms were excluded from the study. The primary end point was functional outcome at last follow-up (modified Rankin Scale ≤2). The secondary end point was angiographic response to endovascular therapies and the appearance of cerebral infarctions.

Management of CVS

After early aneurysm treatment (≤24 hours with either clip or coil embolization), patients were continuously monitored in the intensive care unit and kept normovolemic with blood pressure at normal high levels. A daily check was made of electrolytes (ie, sodium), and an assessment with transcranial Doppler was performed. Medical therapy consisted of nimodipine administered by the enteral route (60 mg every 4 hours for 21 days). In conscious patients, immediate endovascular therapy was indicated in cases of symptomatic rCVS, defined as the appearance of a new neurologic deficit despite medical and hemodynamic treatment (ie, hyperdynamic/hypertensive therapy) or a decline in consciousness not resulting from hydrocephalus (ie, an NIHSS score increase of ≥2 and/or a Glasgow Coma Scale [GCS] score decrease of ≥2). In unconscious patients, rising transcranial Doppler mean velocities of ≥150 cm/s or increased flow velocity of ≥50 cm/s during 24 hours was considered an indication for endovascular treatment in cases in which the CT perfusion scan or MR imaging showed a mean transit time of >5.9 seconds.[11] Other indications for endovascular rescue therapies included patients with marked changes in brain-tissue oxygen pressure values (<15 mm Hg, Licox Brain Oxygen Monitoring System [Integra LifeSciences, Saint Priest, France]) who were not responding to medical and hemodynamic therapies when the MR imaging showed a diffusion-perfusion mismatch.[12,13]

Endovascular Interventions

Intra-arterial nimodipine (IAN) with continuous infusion was delivered locally through a 0.18-inch microcatheter (Renegade Hi-Flo; Boston Scientific, Natick, Massachusetts) into the most affected intracranial vessel segments. A dose of 2.5 mg of nimodipine was administered at the most proximal site of each spastic artery (12 mL in 38-mL saline, administered at 20–30 mL per hour for 30 minutes). Repeat angiography was performed 30 minutes after IAN to evaluate the response of the spastic vessels. In cases of poor response to IAN, percutaneous transluminal balloon angioplasty (PTA) was performed by using intracranial balloon catheters (Gateway; Stryker, Kalamazoo, Michigan). Balloon diameter and inflation pressure were chosen according to the target vessel diameter before vasospasm. "Angiographic CVS" was defined as narrowing of the arterial diameter by ≥30% from the baseline diameter, as assessed by 2 experienced interventional neuroradiologists (G.S., J.G.).

Neurologic Outcome

The immediate response to IAN and/or PTA was evaluated by neurosurgeons and critical care physicians. In those patients who did not respond, MR imaging was performed. In cases of confirmed multiple ischemic areas without any salvageable penumbra, therapy was suspended.[14,15] Complications resulting from SAH, obliteration procedures, and multiple interventions were recorded separately according to the clinical protocol. Neurologic outcome was assessed by mRS, the GCS, and Glasgow Outcome Scale at discharge and at the last follow-up.[5] For patients who lacked long-term follow-up data, the mRS was assessed via telephone interview.[16] The patients' morbidity and reintegration into the workplace at last follow-up were documented.

Assessment of Stroke

Radiologic ischemia was documented with CT or MR imaging.[17] Twenty-four hours following radiologic or surgical aneurysm obliteration, a cerebral CT scan was obtained in all patients to look for treatment-related ischemia. CT scans or MR imaging at the time of patient discharge allowed the visualization of new stroke areas resulting from CVS during the clinical course. Associated functional deficits were registered.

Statistical Methods

Data were analyzed by using SPSS statistical software, Version 21.0 (IBM, Armonk, New York). Clinical outcome was dichotomized into favorable (mRS ≤2) and poor outcome (mRS ≥3). Data are given as mean ± SD unless otherwise stated. For comparisons of means between the 2 analysis groups (ie, <2 interventions versus ≥3 interventions), the Student *t* test was used for normally distributed data (comparing patient age and follow-up time), and the Mann-Whitney *U* test, for skewed or non-normal data (comparing the number of treatments, vessel segments treated, and vascular territories). The other categoric variables were compared between the 2 analysis groups by using the Pearson χ^2 test or the Fisher exact test, as appropriate (Tables 1 and 2). To identify predictors of good functional outcome (mRS ≤2), we performed multivariable analysis with a binary logistic regression model, including the following variables: patient age, sex, Hunt and Hess (HH) grade after SAH, the number of treatments, the number of vessels treated, the number of vascular territories, aneurysm location, further aneurysms, aneurysm obliteration, necessity for PTA, cerebral infarcts, and length of follow-up. Odds ratios and 95% CI were calculated. *P* values ≤ .05 were considered statistically significant.

RESULTS

Patient Demographics

During the 4-year study period, 365 patients with aneurysmal SAH were admitted to our institution. Thirty-one (8.5%) met the inclusion criteria with ≥3 endovascular interventions during the CVS period. In 52 patients with aneurysmal SAH, 1–2 endovascular interventions were performed during the CVS period. Patient characteristics did not differ significantly between the 2 cohorts and are summarized in Table 1 (see also On-line Table 1). Mean age was 54 years (range, 24–77 years), and 66 (80%) were women. Forty-five (54%) patients presented with a Hunt and Hess grade of ≥3.[18] At admission, a mild GCS score of 14–15 was noted in 42% of patients; a moderate score (GCS, 9–13), in 21%; and a severe score (GCS, 3–8), in 38%. Most patients (92%) presented with a Fisher grade 3[19] at clinical onset. Patients with aneurysms not suitable for coil embolization were treated with clip

Table 1: Characteristics of patients with cerebral vasospasm treated with ≥3 interventions compared with those treated with ≤2 interventions

Characteristics	Group I: 1 or 2 Interventions	Group II: 3–6 Interventions	All Patients	*P* Value
Cases (No.) (%)	52 (63)	31 (37)	83 (100)	
Age (mean) (range) (yr)	55.5 ± 11.3, 24–75	52.1 ± 8.6, 34–77	54.2 ± 10.5, 24–77	.158
Women (No.) (%)	42 (81)	24 (77)	66 (80)	.782
Hunt and Hess grade (No.) (%)				
HH scale ≤2	27 (52)	11 (36)	38 (46)	.176
HH scale ≥3	25 (48)	20 (64)	45 (54)	.176
Fisher grade 3 (No.) (%)	46 (89)	30 (97)	76 (92)	.248
GCS at admission				
Mild	21 (41)	13 (42)	34 (42)	.999
Moderate	8 (16)	9 (29)	17 (21)	.162
Severe	22 (43)	9 (29)	31 (38)	.245
Aneurysms location (No.) (%)				
Anterior	33 (64)	21 (68)	54 (65)	.813
Posterior	19 (36)	10 (32)	29 (35)	.813
Multiple aneurysms	17 (33)	13 (42)	30 (36)	.481
Aneurysm obliteration				
Clipping	19 (36)	5 (16)	24 (29)	.078
Coiling	33 (64)	26 (84)	59 (71)	.078
Intracerebral hemorrhage	7 (14)	9 (29)	16 (20)	.15
Intra-arterial spasmolysis				
No. of treatments (mean) (range)	78 (1.5 ± 0.5, 1–2)	132 (4.3 ± 1.6, 3–10)	210 (2.5 ± 1.7, 1–10)	<.001
No. of vessel segments treated (mean) (range)	152 (2.9 ± 1.5, 1–6)	298 (9.6 ± 6.6, 4–40)	450 (5.4 ± 5.3, 1–40)	<.001
No. of vascular territories (mean) (range)	85 (1.6 ± 0.7, 1–3)	72 (2.3 ± 0.8, 1–3)	157 (1.9 ± 0.8, 1–3)	<.001
PTA (No.) (%)	9 (17)	17 (55)	26 (31)	.001
Vessel dissections (No.) (%)	1 (2)	5 (16)	6 (7)	.03
Follow-up (mean) (median) (range) (mo)	12 ± 8.7, 10, 1–24	10 ± 6.3, 9, 2–22	11 ± 7.9, 10, 1–24	.316

Table 2: Primary and secondary outcome measurements following multiple interventions

Outcome	Group I: 1 or 2 Interventions	Group II: 3–6 Interventions	All Patients	*P* Value
mRS ≤2 at discharge (No.) (%)	16 (31)	5 (16)	21 (25)	.193
mRS ≤2 (good outcome) at last FU (No.) (%)	31 (61)	18 (58)	49 (60)	.821
mRS 3–5 (poor outcome) at last FU (No.) (%)	13 (26)	4 (13)	17 (21)	.262
Persistent disabilities requiring constant nursing care (mRS 4 and 5) (No.) (%)	4 (8)	3 (10)	7 (9)	.999
Mortality (No.) (%)	7 (14)	9 (29)	16 (20)	.149
Infarcts in eloquent brain areas (No.) (%)	18 (37)	17 (55)	35 (44)	.165
Brain infarcts (No.) (%)	26 (52)	23 (74)	49 (61)	.062

Note:—FU indicates follow-up.

reconstruction (29% of patients) based on interdisciplinary review. Thirty-six percent of patients presented with multiple aneurysms. In 65% of patients, the ruptured aneurysm was located in the anterior, and in 35%, in the posterior circulation. In 51 patients (63%), an external ventricular drain was inserted due to acute hydrocephalus.

Endovascular Interventions

The number of treatments, vessel segments treated, and vascular territories and the requirement for PTA were significantly higher in patients with ≥3 interventions than in patients with ≤2 interventions (Table 1). Endovascular treatment for CVS was performed between 3 and 15 days after the initial ictus (mean, 6 days). The mean clinical course of vasospasm lasted for 4.8 ± 2.8 days (range, 1–14 days); in 15 patients (48%), it lasted for >5 days. A total of 210 (mean, 2.5 ± 1.7 per patient) endovascular interventions were performed (mean, 4.3 ± 1.6 in patients with ≥3 interventions, versus mean, 1.5 ± 0.5 in patients with ≤2 interventions; $P <$ .001), resulting in the treatment of 450 vessel segments (mean, 5.4 ± 5.3 per patient; range, 1–40 segments; mean, 9.6 ± 6.6 in patients with ≥3 interventions, versus mean, 2.9 ± 1.5 in patients with ≤2 interventions; $P <$ .001), and 157 vascular territories (mean, 1.9 ± 0.8 per patient; range, 1–3; mean, 2.3 ± 0.8 in patients with ≥3 interventions, versus mean, 1.6 ± 0.7 in patients with ≤2 interventions; $P <$ .001). A moderate immediate angiographic effect (arterial dilation <30%) was observed after IAN in 26 (31%) interventions, and consecutive transluminal PTA was applied in these cases, namely in 9 (17%) patients with ≤2 interventions versus 17 (55%) patients with ≥3 interventions ($P = .001$). In the cohort of patients with ≥3 interventions, 13 (42%) underwent 3 treatment sessions, 8 (26%) underwent 4 sessions, 4 (13%) underwent 5 sessions, and 4 (13%) underwent 6 sessions (Fig 1). One patient had a total of 7 treatment sessions, and another, 10 sessions during the CVS course. Of the 52 patients with ≤2 interventions, 26 (50%) underwent 1 treatment session and 26 (50%), 2 sessions.

Functional Outcome

Functional outcome was recorded at discharge (mean, 3 weeks; range, 2–6 weeks) and after a median follow-up at 10 months

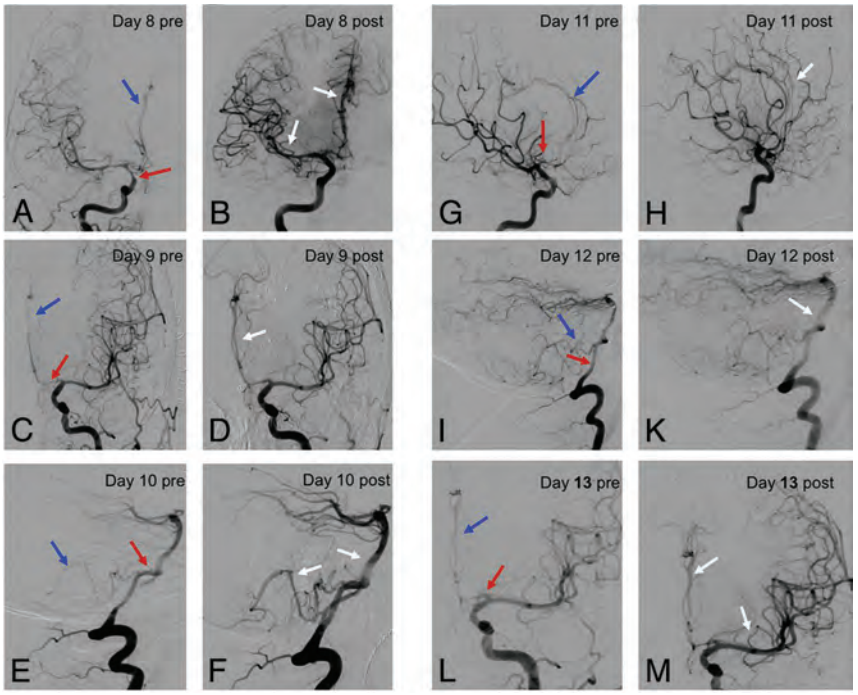

FIG 1. Repeat angiograms in refractory cerebral vasospasms. Repeat angiograms (*red arrows*: proximal spastic vessels; *blue arrows*: distal spastic vessels) in a 41-year-old woman with a ruptured anterior communicating artery aneurysm initially treated with coil embolization. On day 8 after the ictus, the patient presented with hemiparesis on the left side. *A*, ICA angiogram, anteroposterior view, shows vasospasm of the right-sided M1 and A1/A2 segments. *B*, ICA angiogram of the same patient after nimodipine infusion demonstrates reduced vasospasm of the M1 and A1/A2 segments, with improved perfusion of both the proximal and distal arteries. *C–M*, Corresponding angiograms of the anterior circulation (*C, D, G, H, L, M*) and posterior circulation (*E, F, I, K*) in the same patient during the CVS period from day 9 to day 13. Images on the right side show the effect after IAN. Note the effect of nimodipine infusion on the vessel diameter (*white arrows*).

(range, 1–24 months; Table 2 and On-line Table 2). A good functional outcome (median mRS ≤2) at last follow-up was recorded in 49 patients (60%); a poor outcome (median mRS 3–6), in 33 patients (40%), with no statistically significant difference between the 2 cohorts ($P = .82$). Persistent disabilities requiring constant nursing care (mRS 4–5) were noted in 4 patients (8%) with ≤2 interventions and in 3 (10%) of those with ≥3 interventions. Overall mortality (mRS 6) was 20%, with no differences between the 2 cohorts ($P = .31$).

Sixty-one percent of patients rated headache/fatigue and 39%, a persisting neurologic deficit as the most disturbing long-term effect. In patients with ≥3 interventions, none of the working-age patients were able to work full-time at long-term follow-up, 42% worked part-time either in the same or another profession, 23% had no employment, and early retirement was taken by 3%. In contrast, in patients with ≤2 interventions, 5 (6%) of the working-age patients were able to work full-time, whereas 6 (13%) worked part-time either in the same or another profession. Sixteen (33%) patients had no employment at last follow-up.

The following variable was associated with a good functional outcome (median mRS 0–2) at last follow-up (Table 3): Hunt and Hess scale of ≤2 (OR, 7.6; 95% CI, 2.7–22.3; $P < .001$), whereas new cerebral infarctions (OR, 14.8; 95% CI, 3.9–55.3; $P < .001$) and infarction in eloquent areas (OR, 26.0; 95% CI, 7.7–88.2; $P < .001$) were associated with a poor outcome (median mRS >2). Multivariable analysis revealed the HH scale score of ≤2 (OR, 4.7; 95% CI, 1.2–18.5; $P = .03$) as an independent predictor of favorable functional outcome (mRS ≤2) and infarcts in eloquent areas (OR, 13.5; 95% CI, 2.3–81.2; $P = .004$) as an independent risk factor for poor outcome (mRS 3–6) at last follow-up.

Cerebral Infarctions

Assessments of new infarcted areas and infarcts in eloquent regions are shown in Table 2 and On-line Table 2. New infarcted areas at discharge were registered in 23 (74%) patients with ≥3 interventions compared with 26 (52%) patients with ≤2 interventions ($P = .06$). There was no difference between the 2 cohorts regarding infarcts located in eloquent brain areas, which were observed in 17 (55%) patients with ≥3 interventions versus 18 (37%) patients with ≤2 interventions ($P = .17$). We identified the following risk factors associated with infarction at discharge (Table 4): number of treatments (OR, 1.4; 95% CI, 1.0–1.9; $P = .05$), number of vessels treated (OR, 1.2; 95% CI, 1.0–1.4; $P = .03$), and requirement for PTA (OR, 2.7; 95% CI, 1.0–7.9; $P = .06$). Multivariable analysis revealed the HH scale score of ≥3 (OR, 3.4; 95% CI, 1.2–9.3; $P = .02$) and the number of vascular territories treated (OR, 3.1; 95% CI, 1.3–7.3; $P = .01$) as independent predictors of infarcts at discharge.

Treatment-Related Morbidity and Mortality

There was no treatment-related mortality. Complications resulting from aneurysm obliteration procedures consisted of 2 (2%) patients with thrombosis of the parent vessel during coil embolization, which dissolved following intra-arterial thrombolytic therapy. In 1 patient (1%), aneurysm rerupture during coil embolization occurred but did not result in a clinical decline.

Complications resulting from spasmolysis therapies consisted of dissection in the access vessel of the ICA in 1 (2%) patient with ≤2 interventions versus 5 (16%) patients with ≥3 interventions ($P = .03$), requiring stent placement for persistent high-grade stenosis in 1 patient. Another patient (1%) developed a pseudoaneurysm at the puncture side of the femoral artery.

DISCUSSION

IAN offers some last resort treatment strategies, yet application generally remains limited to 1 or 2 or, at most, 3 interventions.[20-23] Cases of patients undergoing >3 endovascular interventions in response to persistent, recurrent, or worsening CVS have seldom been described, and results on functional outcome remain ambiguous.[24] Jun et al[25] reported a subgroup of patients

Table 3: Factors associated with good functional outcome (mRS ≤2) at last follow-up

Predictors for Good Outcome (mRS <2)	Univariable Analyses (OR) (95% CI)	*P* Value	Multivariable Analyses (OR) (95% CI)	*P* Value
No. of treatments	0.995 (0.77–1.29)	.969		
Male sex	1.816 (0.57–5.75)	.31		
Age (yr)	0.961 (0.92–1.01)	.084		
Aneurysm, anterior location	0.749 (0.29–1.92)	.547		
Further aneurysms	1.161 (0.46–2.94)	.752		
Aneurysm obliteration, clip	0.568 (0.22–1.49)	.249		
HH scale ≤2	7.75 (2.69–22.33)	<.001	4.72 (1.21–18.48)	.026
Infarcts in eloquent areas	0.038 (0.01–0.13)	<.001	0.074 (0.012–0.443)	.004
No. of vessels treated	0.965 (0.89–1.05)	.421		
No. of vascular territories	0.594 (0.33–1.07)	.082		
PTA	0.7 (0.27–1.79)	.458		
Brain infarcts	0.069 (0.02–0.25)	<.001	0.359 (0.04–3.08)	.35
Age younger than 50 yr	1.66 (0.62–4.47)	.316		
Length of FU (mo)	1.01 (0.95–1.07)	.72		

Note:—FU indicates follow-up.

Table 4: Risk factors associated with infarction at discharge

Risk Factors for Infarcts at Discharge	Univariable Analyses (OR) (95% CI)	*P* Value	Multivariable Analyses (OR) (95% CI)	*P* Value
Age (yr)	0.99 (0.95–1.0)	.646		
Female sex	1.23 (0.41–3.77)	.699		
Aneurysm, anterior location	1.76 (0.70–4.45)	.23		
Further aneurysms	0.97 (0.39–2.43)	.944		
Aneurysm obliteration, clip	1.73 (0.62–4.85)	.296		
HH scale ≥3	3.14 (1.24–7.92)	.016	3.35 (1.21–9.30)	.02
No. of treatments	1.39 (1.00–1.94)	.049	1.28 (0.66–2.46)	.469
No. of vessels treated	1.17 (1.01–1.36)	.034	0.93 (0.73–1.19)	.561
No. of vascular territories	2.91 (1.49–5.64)	.002	3.08 (1.30–7.30)	.011
PTA	2.74 (0.95–7.90)	.061		
Age younger than 50 yr	0.81 (0.30–2.14)	.807		

(6%, 12 of 189) with rCVS who underwent ≥3 endovascular interventions, and Pandey et al, [26] a subgroup of 7% of patients (2 of 27); but no functional outcome was reported in this subgroup of patients. Most interesting, in the study by Pandey et al, nicardipine was infused through a cervical catheter, with selective catheterization and angioplasty reserved for refractory cases, thereby reducing the risk related to microcatheterization itself.[26] In their series, no complications attributed to the angiographic interventions were described. Given that the rate of cervical artery dissections was higher than that recorded in other studies,[25,27] less aggressive approaches might be considered in selected cases.

Due to the transient vasodilatory effects of IAN,[23,28-31] Albanese et al[7] reported prevention of new ischemic events in 9 of 12 patients with prolonged intra-arterial infusion of verapamil. However, catheterization over an extended period might increase the risk of thrombus formation and subsequent embolisms.[29] Additionally, it generally involves different personnel in the intensive care unit, thereby increasing the risk of air embolism by manipulating the perfusion system. Indeed, repeat endovascular procedures via microcatheterization had greater risks for related complications but also allowed immediate initiation of endovascular therapies, which has been shown to markedly improve outcome compared with patients whose treatment was delayed.[32]

Depending on the location and severity of the CVS, either PTA or IAN can be used in the clinical setting. Balloon angioplasty is indeed effective in treating proximal artery vasospasms and results in more durable clinical improvement.[25,33,34] However, in smaller and more distal vessels, this technique is limited by the possibility of vessel rupture.[27] For more distal or diffuse vasospasms with reduced parenchymal perfusion, several superselective intra-arterial agents have been shown to be effective though transient.[35] A number of clinical studies regarding the effect of intra-arterial nimodipine in patients with severe refractory CVS exist[8,9,36]; however, some controversy remains as to the effectiveness of IAN.[37] Furthermore, these reports comprise mostly small, retrospective case series.[38]

While we noted a good clinical outcome in 61% of patients with ≤2 interventions versus 58% with ≥3 interventions ($P = .82$) after a median follow-up of 10 ± 8 months, 70% of patients recruited for the Barrow Ruptured Aneurysm Trial (BRAT) showed good functional outcome after 1 year,[39] 67% after 3 years,[40] and 62% after 6 years following SAH.[41]

In patients recruited for the International Subarachnoid Aneurysm Trial (ISAT), an mRS of ≤2 after 1 year was reported in 72.8% of them and in 70.2% 8 years later.[42-44] However, the BRAT and ISAT trials represent the full range of patients, including those with a good-grade SAH,[45] thus not reflecting the subpopulation at highest risk for refractory CVS with subsequent infarction and poor quality of life.[46]

Most important, a poor neurologic outcome (mRS 4 or 5) with persistent disabilities requiring constant nursing care could be prevented in most patients. Pegoli et al[46] noted an excellent outcome (mRS 0–1) in 63% of patients with aneurysmal SAH; however, symptomatic CVS and consecutive infarctions were risk factors for poor outcome.[46,47]

As many as 91% of patients with poor quality of life following SAH failed to return to full-time work.[48] Aneurysmal SAH is a cerebrovascular disease particularly affecting the younger working-age population, thereby increasing the economic burden for numerous patients, their families, and society as a whole.[49,50] At last follow-up, only 6% of patients worked full-time, 24% of patients worked part-time, and 29% were unemployed. Our results are in line with these earlier findings. Indeed, vasospasm-related delayed ischemic neurologic deficits and cerebral infarction are strongly associated with unfavorable outcomes following SAH.[15,51,52] While cerebral or angiographic vasospasm is a treatable condition, the effectiveness of nimodipine, hemodynamic therapy, and endovascular interventions, including angioplasty, in preventing neurologic deficits remains controversial.[53-55]

In summary, our approach of immediate repeat endovascular interventions in patients with the most severe CVS refractory to

traditional therapies resulted in a favorable outcome in about two-thirds of patients and prevented severe disability in most of them. However, it remains difficult to assess whether immediate endovascular treatments ultimately result in a better neurologic outcome because vasospasm is not the only cause of delayed ischemic complications.[56]

Nevertheless, rescue therapies to reduce the impact of rCVS following SAH might be beneficial in devastating cases. On the basis of the current data and from the experience we gained from performing these procedures in this subpopulation of patients at highest risk for refractory CVS, we think that it is important to continue the effort to treat even those patients who are refractory to 1 or 2 endovascular interventions, even when little or no effect and ongoing cerebral vasospasm are evident. Large multicenter, prospective, randomized controlled studies are, however, needed to prove the effectiveness of repeat instant endovascular interventions in patients with refractory cerebral vasospasms—not an easy undertaking given the ethical problems of withholding therapeutic interventions, even if the effect of the therapy remains ambiguous. At present, treatment of rCVS with immediate multiple endovascular interventions is feasible and safe and may be warranted until the significance of these interventions becomes better understood.

Study Limitations

Assessment of cerebral infarctions by CT in 36% of all patients may actually lower the true rate of radiographically detected cerebral infarctions, given the higher sensitivity of MR imaging in detecting vasospasm-related infarction.[17] In addition, a median follow-up of 10 ± 7.0 months may under-represent the true rate of poor outcome, considering longer term outcome studies that showed a steady increase in patients with poor outcome across time.[39,41]

CONCLUSIONS

The use of immediate repeat endovascular interventions is an aggressive but feasible last resort treatment strategy effective for a selected subgroup of patients who fail to respond to traditional CVS therapies and endovascular interventions.

ACKNOWLEDGMENTS

The assistance of Ms Susan Kaplan in preparing this manuscript is acknowledged. We wish to thank Dr Corrado Bernasconi for statistical advice.

Disclosures: Lukas Andereggen—*UNRELATED: Grants/Grants Pending*: Swiss National Science Foundation. Werner Z'Graggen—*UNRELATED*: *Employment*: Bern University Hospital. Gerhard Schroth—*UNRELATED*: *Employment*: Bern University Hospital, *Comments*: normal salary as a 50% senior consultant of the University Institute for Diagnostic and Interventional Neuroradiology of Bern University Hospital Inselspital; *Grants/Grants Pending*: Swiss National Science Foundation, *Comments*: grant for neuropsychological investigations before and after carotid stenting*; *Payment for Lectures including Service on Speakers Bureaus*: European Stroke Organisation, Master Course at the Danube University in Krems, Austria, *Comments*: lectures and hands-on workshops; money paid exclusively to the Inselspital. Michael Reinert—*UNRELATED*: *Consultancy*: Brainlab, DePuys Synthes*; *Employment*: Ente Ospedaliero Cantonale Ticino; *Grants/Grants Pending*: Lega Ticinesi contro il Cancro*; *Payment for Lectures including Service on Speakers Bureaus*: Brainlab.* Jan Gralla—*UNRELATED*: *Consultancy*: Covidien, *Comments*: former Global Principal Investigator for the Star Study on thrombectomy in acute stroke, consultant for Covidien.* *Money paid to the institution.

REFERENCES

1. Naidech AM, Drescher J, Tamul P, et al. **Acute physiological derangement is associated with early radiographic cerebral infarction after subarachnoid haemorrhage.** *J Neurol Neurosurg Psychiatry* 2006;77:1340–44 CrossRef Medline
2. van Gijn J, Kerr RS, Rinkel GJ. **Subarachnoid haemorrhage.** *Lancet* 2007;369:306–18 CrossRef Medline
3. Kassell NF, Sasaki T, Colohan AR, et al. **Cerebral vasospasm following aneurysmal subarachnoid hemorrhage.** *Stroke* 1985;16:562–72 CrossRef Medline
4. Platz J, Guresir E, Vatter H, et al. **Unsecured intracranial aneurysms and induced hypertension in cerebral vasospasm: is induced hypertension safe?** *Neurocrit Care* 2011;14:168–75 CrossRef Medline
5. Frontera JA, Fernandez A, Schmidt JM, et al. **Defining vasospasm after subarachnoid hemorrhage: what is the most clinically relevant definition?** *Stroke* 2009;40:1963–68 CrossRef Medline
6. Kimball MM, Velat GJ, Hoh BL. **Critical care guidelines on the endovascular management of cerebral vasospasm.** *Neurocrit Care* 2011;15:336–41 CrossRef Medline
7. Albanese E, Russo A, Quiroga M, et al. **Ultrahigh-dose intraarterial infusion of verapamil through an indwelling microcatheter for medically refractory severe vasospasm: initial experience—clinical article.** *J Neurosurg* 2010;113:913–22 CrossRef Medline
8. Biondi A, Ricciardi GK, Puybasset L, et al. **Intra-arterial nimodipine for the treatment of symptomatic cerebral vasospasm after aneurysmal subarachnoid hemorrhage: preliminary results.** *AJNR Am J Neuroradiol* 2004;25:1067–76 Medline
9. Hängg D, Turowski B, Beseoglu K, et al. **Intra-arterial nimodipine for severe cerebral vasospasm after aneurysmal subarachnoid hemorrhage: influence on clinical course and cerebral perfusion.** *AJNR Am J Neuroradiol* 2008;29:1053–60 CrossRef Medline
10. Komotar RJ, Zacharia BE, Otten ML, et al. **Controversies in the endovascular management of cerebral vasospasm after intracranial aneurysm rupture and future directions for therapeutic approaches.** *Neurosurgery* 2008;62:897–905; discussion 905–897 CrossRef Medline
11. Dankbaar JW, de Rooij NK, Rijsdijk M, et al. **Diagnostic threshold values of cerebral perfusion measured with computed tomography for delayed cerebral ischemia after aneurysmal subarachnoid hemorrhage.** *Stroke* 2010;41:1927–32 CrossRef Medline
12. Beck J, Raabe A, Lanfermann H, et al. **Tissue at risk concept for endovascular treatment of severe vasospasm after aneurysmal subarachnoid haemorrhage.** *J Neurol Neurosurg Psychiatry* 2004;75:1779–81 CrossRef Medline
13. Beck J, Raabe A, Lanfermann H, et al. **Effects of balloon angioplasty on perfusion- and diffusion-weighted magnetic resonance imaging results and outcome in patients with cerebral vasospasm.** *J Neurosurg* 2006;105:220–27 CrossRef Medline
14. Vatter H, Güresir E, Berkefeld J, et al. **Perfusion-diffusion mismatch in MRI to indicate endovascular treatment of cerebral vasospasm after subarachnoid haemorrhage.** *J Neurol Neurosurg Psychiatry* 2011;82:876–83 CrossRef Medline
15. Vergouwen MD, Ilodigwe D, Macdonald RL. **Cerebral infarction after subarachnoid hemorrhage contributes to poor outcome by vasospasm-dependent and -independent effects.** *Stroke* 2011;42:924–29 CrossRef Medline
16. Janssen PM, Visser NA, Dorhout Mees SM, et al. **Comparison of telephone and face-to-face assessment of the modified Rankin Scale.** *Cerebrovasc Dis* 2010;29:137–39 CrossRef Medline
17. Shimoda M, Takeuchi M, Tominaga J, et al. **Asymptomatic versus symptomatic infarcts from vasospasm in patients with subarachnoid hemorrhage: serial magnetic resonance imaging.** *Neurosurgery* 2001;49:1341–48; discussion 1348–50 CrossRef Medline
18. Hunt WE, Hess RM. **Surgical risk as related to time of intervention in the repair of intracranial aneurysms.** *J Neurosurg* 1968;28:14–20 CrossRef Medline
19. Fisher CM, Kistler JP, Davis JM. **Relation of cerebral vasospasm to subarachnoid hemorrhage visualized by computerized tomographic scanning.** *Neurosurgery* 1980;6:1–9 CrossRef Medline

20. Aburto-Murrieta Y, Marquez-Romero JM, Bonifacio-Delgadillo D, et al. **Endovascular treatment: balloon angioplasty versus nimodipine intra-arterial for medically refractory cerebral vasospasm following aneurysmal subarachnoid hemorrhage.** *Vasc Endovasc Surg* 2012;46:460–65 CrossRef Medline
21. John S, Spiotta AM, Turner RM, et al. **Initial experience with the coaxial dual-lumen Scepter C balloon catheter for endovascular management of cerebral vasospasm from subarachnoid hemorrhage.** *J Neurointerv Surg* 2014;6:125–28 CrossRef Medline
22. Santillan A, Knopman J, Zink W, et al. **Transluminal balloon angioplasty for symptomatic distal vasospasm refractory to medical therapy in patients with aneurysmal subarachnoid hemorrhage.** *Neurosurgery* 2011;69:95–101; discussion 102 CrossRef Medline
23. Wolf S, Martin H, Landscheidt JF, et al. **Continuous selective intraarterial infusion of nimodipine for therapy of refractory cerebral vasospasm.** *Neurocrit Care* 2010;12:346–51 CrossRef Medline
24. Mortimer AM, Steinfort B, Faulder K, et al. **Institution of sustained endovascular treatment prior to clinical deterioration in patients with severe angiographic vasospasm: A retrospective observational study of clinico-radiological outcomes.** *J Neuroradiol* 2015;42:176–83 CrossRef Medline
25. Jun P, Ko NU, English JD, et al. **Endovascular treatment of medically refractory cerebral vasospasm following aneurysmal subarachnoid hemorrhage.** *AJNR Am J Neuroradiol* 2010;31:1911–16 CrossRef Medline
26. Pandey P, Steinberg GK, Dodd R, et al. **A simplified method for administration of intra-arterial nicardipine for vasospasm with cervical catheter infusion.** *Neurosurgery* 2012;71(1 suppl operative):77–85 CrossRef Medline
27. Zwienenberg-Lee M, Hartman J, Rudisill N, et al; Balloon Prophylaxis for Aneurysmal Vasospasm (BPAV) Study Group. **Effect of prophylactic transluminal balloon angioplasty on cerebral vasospasm and outcome in patients with Fisher grade III subarachnoid hemorrhage: results of a phase II multicenter, randomized, clinical trial.** *Stroke* 2008;39:1759–65 CrossRef Medline
28. Doukas A, Petridis AK, Barth H, et al. **Resistant vasospasm in subarachnoid hemorrhage treated with continuous intraarterial nimodipine infusion.** *Acta Neurochir Suppl* 2011;112:93–96 CrossRef Medline
29. Musahl C, Henkes H, Vajda Z, et al. **Continuous local intra-arterial nimodipine administration in severe symptomatic vasospasm after subarachnoid hemorrhage.** *Neurosurgery* 2011;68:1541–47; discussion 1547 CrossRef Medline
30. Feng L, Fitzsimmons BF, Young WL, et al. **Intraarterially administered verapamil as adjunct therapy for cerebral vasospasm: safety and 2-year experience.** *AJNR Am J Neuroradiol* 2002;23:1284–90 Medline
31. Keuskamp J, Murali R, Chao KH. **High-dose intraarterial verapamil in the treatment of cerebral vasospasm after aneurysmal subarachnoid hemorrhage.** *J Neurosurg* 2008;108:458–63 CrossRef Medline
32. Rosenwasser RH, Armonda RA, Thomas JE, et al. **Therapeutic modalities for the management of cerebral vasospasm: timing of endovascular options.** *Neurosurgery* 1999;44:975–79; discussion 979–80 CrossRef Medline
33. Khatri R, Memon MZ, Zacharatos H, et al. **Impact of percutaneous transluminal angioplasty for treatment of cerebral vasospasm on subarachnoid hemorrhage patient outcomes.** *Neurocrit Care* 2011;15:28–33 CrossRef Medline
34. Pandey AS, Elias AE, Chaudhary N, et al. **Endovascular treatment of cerebral vasospasm: vasodilators and angioplasty.** *Neuroimaging Clin N Am* 2013;23:593–604 CrossRef Medline
35. Rahme R, Jimenez L, Pyne-Geithman GJ, et al. **Endovascular management of posthemorrhagic cerebral vasospasm: indications, technical nuances, and results.** *Acta Neurochir Suppl* 2013;115:107–12 CrossRef Medline
36. Hui C, Lau KP. **Efficacy of intra-arterial nimodipine in the treatment of cerebral vasospasm complicating subarachnoid haemorrhage.** *Clin Radiol* 2005;60:1030–36 CrossRef Medline
37. Firat MM, Gelebek V, Orer HS, et al. **Selective intraarterial nimodipine treatment in an experimental subarachnoid hemorrhage model.** *AJNR Am J Neuroradiol* 2005;26:1357–62 Medline
38. Hoh BL, Ogilvy CS. **Endovascular treatment of cerebral vasospasm: transluminal balloon angioplasty, intra-arterial papaverine, and intra-arterial nicardipine.** *Neurosurg Clin N Am* 2005;16:501–16, vi Medline
39. McDougall CG, Spetzler RF, Zabramski JM, et al. **The Barrow Ruptured Aneurysm Trial.** *J Neurosurg* 2012;116:135–44 CrossRef Medline
40. Spetzler RF, McDougall CG, Albuquerque FC, et al. **The Barrow Ruptured Aneurysm Trial: 3-year results.** *J Neurosurg* 2013;119:146–57 CrossRef Medline
41. Spetzler RF, McDougall CG, Zabramski JM, et al. **The Barrow Ruptured Aneurysm Trial: 6-year results.** *J Neurosurg* 2015;123:609–17 CrossRef Medline
42. Molyneux A, Kerr R, Stratton I, et al; International Subarachnoid Aneurysm Trial (ISAT) Collaborative Group. **International Subarachnoid Aneurysm Trial (ISAT) of neurosurgical clipping versus endovascular coiling in 2143 patients with ruptured intracranial aneurysms: a randomised trial.** *Lancet* 2002;360:1267–74 CrossRef Medline
43. Molyneux AJ, Kerr RS, Birks J, et al; ISAT Collaborators. **Risk of recurrent subarachnoid haemorrhage, death, or dependence and standardised mortality ratios after clipping or coiling of an intracranial aneurysm in the International Subarachnoid Aneurysm Trial (ISAT): long-term follow-up.** *Lancet Neurol* 2009;8:427–33 CrossRef Medline
44. Molyneux AJ, Kerr RS, Yu LM, et al; International Subarachnoid Aneurysm Trial (ISAT) Collaborative Group. **International subarachnoid aneurysm trial (ISAT) of neurosurgical clipping versus endovascular coiling in 2143 patients with ruptured intracranial aneurysms: a randomised comparison of effects on survival, dependency, seizures, rebleeding, subgroups, and aneurysm occlusion.** *Lancet* 2005;366:809–17 CrossRef Medline
45. Darsaut TE, Jack AS, Kerr RS, et al. **International Subarachnoid Aneurysm Trial-ISAT, Part II: study protocol for a randomized controlled trial.** *Trials* 2013;14:156 CrossRef Medline
46. Pegoli M, Mandrekar J, Rabinstein AA, et al. **Predictors of excellent functional outcome in aneurysmal subarachnoid hemorrhage.** *J Neurosurg* 2015;122:414–18 CrossRef Medline
47. Hänggi D, Etminan N, Macdonald RL, et al. **NEWTON: Nimodipine Microparticles to Enhance Recovery While Reducing Toxicity After Subarachnoid Hemorrhage.** *Neurocrit Care* 2015;23:274–84 CrossRef Medline
48. Taufique Z, May T, Meyers E, et al. **Predictors of poor quality of life 1 year after subarachnoid hemorrhage.** *Neurosurgery* 2016;78:256–56 CrossRef Medline
49. Dodel R, Winter Y, Ringel F, et al. **Cost of illness in subarachnoid hemorrhage: a German longitudinal study.** *Stroke* 2010;41:2918–23 CrossRef Medline
50. Sehba FA, Hou J, Pluta RM, et al. **The importance of early brain injury after subarachnoid hemorrhage.** *Prog Neurobiol* 2012;97:14–37 CrossRef Medline
51. Fergusen S, Macdonald RL. **Predictors of cerebral infarction in patients with aneurysmal subarachnoid hemorrhage.** *Neurosurgery* 2007;60:658–67; discussion 667 Medline
52. Rosengart AJ, Huo JD, Tolentino J, et al. **Outcome in patients with subarachnoid hemorrhage treated with antiepileptic drugs.** *J Neurosurg* 2007;107:253–60 CrossRef Medline
53. Bederson JB, Connolly ES Jr, Batjer HH, et al; American Heart Association. **Guidelines for the management of aneurysmal subarachnoid hemorrhage: a statement for healthcare professionals from a special writing group of the Stroke Council, American Heart Association.** *Stroke* 2009;40:994–1025 CrossRef Medline
54. Dorhout Mees SM, Rinkel GJ, Feigin VL, et al. **Calcium antagonists for aneurysmal subarachnoid haemorrhage.** *Cochrane Database Syst Rev* 2007:CD000277 Medline
55. Rabinstein AA, Lanzino G, Wijdicks EF. **Multidisciplinary management and emerging therapeutic strategies in aneurysmal subarachnoid haemorrhage.** *Lancet Neurol* 2010;9:504–19 CrossRef Medline
56. Budohoski KP, Czosnyka M, Kirkpatrick PJ, et al. **Clinical relevance of cerebral autoregulation following subarachnoid haemorrhage.** *Nat Rev Neurol* 2013;9:152–63 CrossRef Medline

Endovascular Rescue Therapy for Refractory Vasospasm: When and How?

Symptomatic vasospasm after subarachnoid hemorrhage is a common observation, with a considerable number of patients eventually failing conservative treatment (prophylactic nimodipine, induced hypertension). This subgroup of patients with refractory vasospasm remains particularly challenging[1] because critical hypoperfusion frequently culminates in delayed cerebral ischemia, cerebral infarction, and ultimately worsening of outcome. Consequently, clinical and experimental research effort focuses on timely detection of critical misery perfusion and identification of effective means to increase cerebral blood flow; on both issues, consensus is sparse and indications and technique of treatment remain a matter of individual experience and opinion.

The authors[2] present a retrospective analysis of 83 patients in whom endovascular rescue therapy (ERT) was initiated for refractory vasospasm in cases of neurologic or functional worsening (transcranial Doppler increase and MR/CT perfusion mismatch) despite maximal conservative treatment. ERT consisted of repeat, superselective bolus application of intra-arterial nimodipine (IAN) with or without concomitant percutaneous transarterial angioplasty (PTA). Patients were dichotomized according to the number of interventions performed (<3 interventions, ≥ 3 interventions); the central objective was a comparative analysis of safety and efficacy. The number of treatments, the number of vessels treated, and the need for PTA were associated with a higher risk of developing cerebral infarction. The risk of arterial dissection was significantly higher in patients requiring ≥ 3 ERTs. The complication rate for all other parameters, however, was comparable, and favorable functional outcome was observed in more than half of all patients, with no significant difference between the 2 treatment groups.

The study addresses an important aspect in the management of severely affected patients with SAH in whom conservative effort has been exhausted. Endovascular rescue therapies such as PTA or IAN represent treatment measures of last resort for refractory cerebral vasospasm[3]; in this context, recent studies were able to document improvement of cerebral oxygenation and metabolism after ERT.[4-7] Unfortunately, a positive influence on outcome can only be assumed but not proved due to the vast heterogeneity of patients with SAH and the lack of a comparable control group in which ERT is withheld. In view of this limitation but acknowledging the plausible hypothesis that functional improvement of oxygenation and metabolism is likely to contribute to better outcome, it is paramount to review and adhere to strict indications for ERT and to ensure a low periprocedural risk profile.

A detailed decision tree and escalating treatment—as implemented and followed by the authors—must be in place to identify and select those patients most likely to benefit from ERT. Angiographic narrowing of major cerebral vessels alone has been the basis for invasive spasmolytic treatment in the past, but the true hemodynamic relevance of angiographic findings within that compartment remains elusive. Without microcirculatory hypoperfusion, recently identified as a major contributor to territorial mismatch,[8-10] treatment may not always be indicated and should not encourage possible accusations of overtreatment in patients who would have fared well regardless of any adjuvant treatment. Quantification of actual cerebral function, with CT or MR perfusion or continuous assessment of CBF, oxygenation (brain tissue oxygen), metabolism (lactate to pyruvate ratio on microdialysis), or electroencephalography/near-infrared spectroscopy are prerequisites for a selective, even restrictive but, at the same time, more substantiated implementation of ERT. Quantification of cerebral function should enable both timely detection of critical hypoperfusion and monitoring of treatment efficacy as a necessary next step to validate ERT and individually titrate the dose and duration of treatment.

The authors are commended for their expert performance and low overall complication rate. Indiscriminate application of ERT, no matter how expertly performed, inevitably increases the number of complications, possibly even negating any potential benefit on outcome. Even in the context of the refined treatment algorithm presented in this study, the rate of arterial dissection (16% in patients requiring ≥ 3 ERTs, clinically without relevant sequelae) is a sharp reminder of the causal relationship between the frequency of treatment and the complication rate.

On a different note, continuous intra-arterial infusion may provide additional advantages compared with repeat bolus application.[11] The need for daily, oftentimes hazardous transportation[12] into the radiology department is substantially reduced in

patients who, at that time, are at their most critical and are vulnerable to many (cardiopulmonary) complications. In view of the average number of ERTs required (2.5 for all patients, 4.3 for patients with ≥3 ERTs, selected patients with up to 7–10 ERTs) and the short duration of treatment (usually <6–12 hours),[13] continuous IAN can be an alternative. Limiting the number of repeat catheterizations may also reduce the incidence of arterial dissection.[5,11] However, local experience, particularly in view of the immobilization of patients, handling of continuous anticoagulation, and invasive neuromonitoring are essential. It is our own observation that with continuous IAN, the complication profile can be reduced dramatically, with regard to both thrombosis or periprocedural hemorrhage, on an intensified anticoagulation regimen and dissection from an indwelling microcatheter (Weiss et al, unpublished data).

The authors are commended for adding valuable evidence for the feasibility of vigorous endovascular therapy; the present study convincingly demonstrates that when necessary, ERT can be escalated and that good outcome can be achieved, even in prolonged cases of refractory vasospasm.

The conclusion perfectly summarizes the raison d'être for ERT as an aggressive but effective last resort strategy to support patients when everything else has failed. Future studies will need to identify those patients most likely to benefit from ERT and to tailor treatment to the lowest possible risk with the highest efficacy.

REFERENCES

1. Francoeur CL, Mayer SA. **Management of delayed cerebral ischemia after subarachnoid hemorrhage.** *Crit Care* 2016;20:277 CrossRef Medline
2. Adereggen L, Beck J, Z'Graggen WJ, et al. **Feasibility and safety of repeated instant endovascular interventions in patients suffering from refractory cerebral vasospasms.** *AJNR Am J Neuroradiol* 2016 Dec 15. [Epub ahead of print] CrossRef Medline
3. Durrant JC, Hinson HE. **Rescue therapy for refractory vasospasm after subarachnoid hemorrhage.** *Curr Neurol Neurosci Rep* 2015;15:521 CrossRef Medline
4. Pierot L, Aggour M, Moret J. **Vasospasm after aneurysmal subarachnoid hemorrhage: recent advances in endovascular management.** *Curr Opin Crit Care* 2010;16:110–16 CrossRef Medline
5. Bele S, Proescholdt MA, Hochreiter A, et al. **Continuous intra-arterial nimodipine infusion in patients with severe refractory cerebral vasospasm after aneurysmal subarachnoid hemorrhage: a feasibility study and outcome results.** *Acta Neurochir (Wien)* 2015;157:2041–50 CrossRef Medline
6. Jestaedt L, Pham M, Bartsch AJ, et al. **The impact of balloon angioplasty on the evolution of vasospasm-related infarction after aneurysmal subarachnoid hemorrhage.** *Neurosurgery* 2008;62:610–17; discussion 610–17 CrossRef Medline
7. Albanna W, Weiss M, Mueller M, et al. **Endovascular rescue therapies for refractory vasospasm after subarachnoid hemorrhage: a prospective evaluation study using multimodal, continuous event neuromonitoring.** *Neurosurgery.* In press
8. Terpolilli NA, Brem C, Bühler D, et al. **Are we barking up the wrong vessels? Cerebral microcirculation after subarachnoid hemorrhage.** *Stroke* 2015;46:3014–19 CrossRef Medline
9. Wagner M, Steinbeis P, Güresir E, et al. **Beyond delayed cerebral vasospasm: infarct patterns in patients with subarachnoid hemorrhage.** *Clin Neuroradiol* 2013;23:87–95 CrossRef Medline
10. Schubert GA, Seiz M, Hegewald AA. et al. **Acute hypoperfusion immediately after subarachnoid hemorrhage: a xenon contrast-enhanced CT study.** *J Neurotrauma* 2009;26:2225–31 CrossRef Medline
11. Musahl C, Henkes H, Vajda Z, et al. **Continuous local intra-arterial nimodipine administration in severe symptomatic vasospasm after subarachnoid hemorrhage.** *Neurosurgery* 2011;68:1541–47; discussion 1547 CrossRef Medline
12. Papson JP, Russell KL, Taylor DM. **Unexpected events during the intrahospital transport of critically ill patients.** *Acad Emerg Med* 2007;14:574–77 CrossRef Medline
13. Liu JK, Couldwell WT. **Intra-arterial papaverine infusions for the treatment of cerebral vasospasm induced by aneurysmal subarachnoid hemorrhage.** *Neurocrit Care* 2005;2:124–32 CrossRef Medline

M. Weiss
G.A. Schubert
Cerebrovascular Section, Department of Neurosurgery
RWTH Aachen University
Aachen, Germany

http://dx.doi.org/10.3174/ajnr.A5082

Differences in Hemodynamics and Rupture Rate of Aneurysms at the Bifurcation of the Basilar and Internal Carotid Arteries

R. Doddasomayajula, B. Chung, F. Hamzei-Sichani, C.M. Putman, and J.R. Cebral

ABSTRACT

BACKGROUND AND PURPOSE: Cerebral aneurysms in the posterior circulation are known to have a higher rupture risk than those in the anterior circulation. We sought to test the hypothesis that differences in hemodynamics can explain the difference in rupture rates.

MATERIALS AND METHODS: A total of 117 aneurysms, 63 at the tip of the basilar artery (27 ruptured, 36 unruptured, rupture rate = 43%) and 54 at the bifurcation of the internal carotid artery (11 ruptured, 43 unruptured, rupture rate = 20%) were analyzed with image-based computational fluid dynamics. Several hemodynamic variables were compared among aneurysms at each location and between ruptured and unruptured aneurysms at each location.

RESULTS: On average, aneurysms at the basilar tip had more concentrated inflow ($P < .001$), a larger inflow rate ($P < .001$), a larger maximum oscillatory shear index ($P = .003$), more complex flows ($P = .033$), and smaller areas under low wall shear stress ($P < .001$) than aneurysms at the bifurcation of the internal carotid artery. In general, ruptured aneurysms had larger inflow concentration ($P = .02$), larger shear concentration ($P = .02$), more complex flows ($P < .001$), and smaller minimum wall shear stress ($P = .003$) than unruptured aneurysms.

CONCLUSIONS: High flow conditions, characterized by large and concentrated inflow jets, complex and oscillatory flow patterns, and wall shear stress distributions with focalized regions of high shear and large regions of low shear, are associated with aneurysm rupture, especially for basilar tip aneurysms. The higher flow conditions in basilar tip aneurysms could explain their increased rupture risk compared with internal carotid bifurcation aneurysms.

ABBREVIATIONS: BAtip = basilar artery tip; corelen = core-line length; ICAbif = internal carotid artery bifurcation; ICI = inflow concentration index; LSA = areas under low wall shear stress; max = maximum; min = minimum; OSI = oscillatory shear index; Q = flow rate; SCI = shear concentration index; VE = mean velocity; WSS = wall shear stress

Intracranial aneurysms are balloon-like pathologic dilations of the cerebral blood vessel walls. An estimated 2%–5% of the general population is affected by intracranial aneurysms.[1] Rupture of intracranial aneurysms is an event associated with high mortality and disability rates; consequently, many physicians often preventively treat incidentally discovered aneurysms. However, the treatment risk can exceed the low natural risk of rupture of incidental aneurysms.[2,3] Therefore, it is important to precisely distinguish high-risk aneurysms for immediate treatment from low-risk aneurysms, which could be conservatively followed.

Several patient, demographic, and behavioral characteristics have been investigated as possible risk factors, including sex, age, family history, smoking, hypertension, and ethnicity. Past studies have indicated that in addition to the size of the aneurysm, location is an important risk factor for intracranial aneurysm rupture.[4] In particular, aneurysms in the posterior circulation have been shown to have an overall higher rupture risk than aneurysms in the anterior circulation. The cause of this difference in rupture risk is largely unknown.[5] Because aneurysm evolution is thought to be governed by a progressive degradation and weakening of the vessel wall in response to abnormal flow conditions,[6] it is logical to ask whether differences in aneurysm hemodynamics, induced by diverse configurations and geometries of vessels of the anterior and posterior circulations, could help explain the various rupture rates.

The purpose of this study was to test whether intrasaccular flow characteristics are different between aneurysms at the basilar

Received May 11, 2016; accepted after revision October 11.

From the Bioengineering Department (R.D., B.C., J.R.C.), Volgenau School of Engineering, George Mason University, Fairfax, Virginia; Department of Neurosurgery (F.H.-S.), Icahn School of Medicine at Mount Sinai, New York, New York; and Interventional Neuroradiology (C.M.P.), Inova Fairfax Hospital, Falls Church, Virginia.

Please address correspondence to Juan R. Cebral, PhD, Bioengineering Department, Volgenau School of Engineering, George Mason University, 4400 University Dr, MSN 2A1, Fairfax, VA 22030; e-mail: jcebral@gmu.edu

Indicates article with supplemental on-line tables.

Indicates article with supplemental on-line photos.

http://dx.doi.org/10.3174/ajnr.A5088

Hemodynamic and geometric variables used in the study and the aspect of the aneurysm they characterize

Variables	Metrics	Characterizes
Hemodynamics		
Q, ICI	Inflow rate, inflow concentration index	Inflow jet
VE, KE	Mean velocity, kinetic energy	Flow speed in aneurysm
VO, SR, VD	Vorticity, shear rate, viscous dissipation	Flow rotation deformation/dissipation in aneurysm
<WSS>, WSSmin, WSSmax, SCI, LSA	Mean, min, and max WSS, shear concentration index, area under low WSS	WSS distribution
<OSI>, OSImax	Mean, max oscillatory shear index	Oscillatory flow/WSS
Corelen	Length of vortex core lines	Flow complexity
Podent, podenum	POD entropy and number of modes	Flow stability
Geometry		
Aneurysym size, volume, area, SizeR	Aneurysm diameter, volume, area, size ratio	Aneurysm size
Neck size, area	Neck diameter, area	Neck size
Depth, aspect ratio	Aneurysm depth, aspect ratio	Aneurysm shape elongation
Artery, branch1, branch2	Diameter parent and branch arteries	Artery sizes
Symmetry	Ratio of branch diameters	Bifurcation symmetry
<Taper>, taper1, taper2	Mean taper, branch taper	Artery tapering

Note:—POD indicates proper orthogonal decomposition; SizeR, size ratio.

artery tip (BAtip) in the posterior circulation and the internal carotid artery bifurcation (ICAbif) in the anterior circulation, as well as between ruptured and unruptured aneurysms at these locations. These locations were selected because the BAtip is the most common location of intracranial aneurysm rupture in the posterior circulation[7] and is anatomically similar to the ICAbif in that they are both terminal bifurcations of a major feeding artery. The information generated in this study is useful for understanding what hemodynamic conditions predispose aneurysms to rupture and which mechanobiologic processes could be involved in aneurysm weakening and eventual rupture.

MATERIALS AND METHODS

Image and Patient Data

We have developed a data base of intracranial aneurysms imaged with 3D rotational angiography. This data base contains 3D rotational angiography images and anonymized clinical information, including rupture status, size, and location and patient sex and age of approximately 1800 intracranial aneurysms. All aneurysms from our data base located at either the BAtip or ICAbif were included in the study. A total of 117 aneurysms were studied, with the distribution of locations as follows: 63 BAtip aneurysms consisting of 27 ruptured and 36 unruptured with a rupture rate of 43%, and 54 ICAbif aneurysms, among which 11 were ruptured and 43 were unruptured, with a rupture rate of 20%. Among the 117 patients studied, there were 94 (80%) women and 23 (20%) men. There was no statistical difference between sexes in the BAtip and ICAbif aneurysms ($P = .8163$). The mean age of the ICAbif group was slightly younger (52 years) than that of the BAtip group (57 years) ($P = .0284$).

Vascular and Flow Modeling

Computational fluid dynamics models of all 117 aneurysms were constructed from the corresponding 3D rotational angiography images, by using a methodology previously developed.[8] Briefly, the 3D rotational angiography images were filtered to reduce noise and the vascular geometry was reconstructed with an isosurface-deformable model.[9] These vascular models were subsequently smoothed, and the vessel branches were truncated at planes orthogonal to their axes. The ICAbif models extended proximally to the cavernous ICA, and the BAtip, at least to the origin of the basilar artery; the models included both vertebral arteries if they were adequately depicted in the 3D rotational angiography images.

Numeric simulations based on 3D incompressible Navier-Stokes equations were performed on the 117 patient-specific aneurysm geometries by using pulsatile flow conditions. Because patient-specific flow information was unavailable, typical flow boundary conditions for a healthy subject derived from phase-contrast MR imaging (On-line Fig 1) were scaled with the inlet cross-sectional areas to achieve a mean wall shear stress (WSS) of 15 dynes/cm^2 prescribed at the inlets for all the models. Fully developed velocity profiles were prescribed at the inlets by using the Womersley solution.[10] Outflow boundary conditions were selected to produce flow divisions consistent with the Murray law to avoid unrealistic jumps in the wall shear stress from parent to daughter branches. Assumptions included Newtonian viscosity for blood and rigid vessel walls. The simulations had a minimum mesh resolution of 200 μm and a time resolution of 10 ms and were run for 2 cardiac cycles by using an in-house fully implicit finite-element solver.[11,12]

Flow variables such as the flow rate (Q), maximum wall shear stress (WSSmax), inflow concentration index (ICI), and the shear concentration index (SCI) were computed from the results of the second cycle to characterize the flow conditions within the aneurysms.[13,14] Geometric variables such as aneurysm size (Asize) and aspect ratio (AR) were computed from the 3D anatomic models. The definitions of vessel geometric variables are presented in On-line Fig 2. The Table presents a list of all the hemodynamic and geometric variables analyzed.

Data Analysis

The hemodynamic parameters listed in the Table were used to test the following: 1) whether aneurysms at the BAtip have different hemodynamic environments than those at the ICAbif, and 2) whether ruptured and unruptured aneurysms have different flow environments at each of these 2 locations. Two-sided Wilcoxon

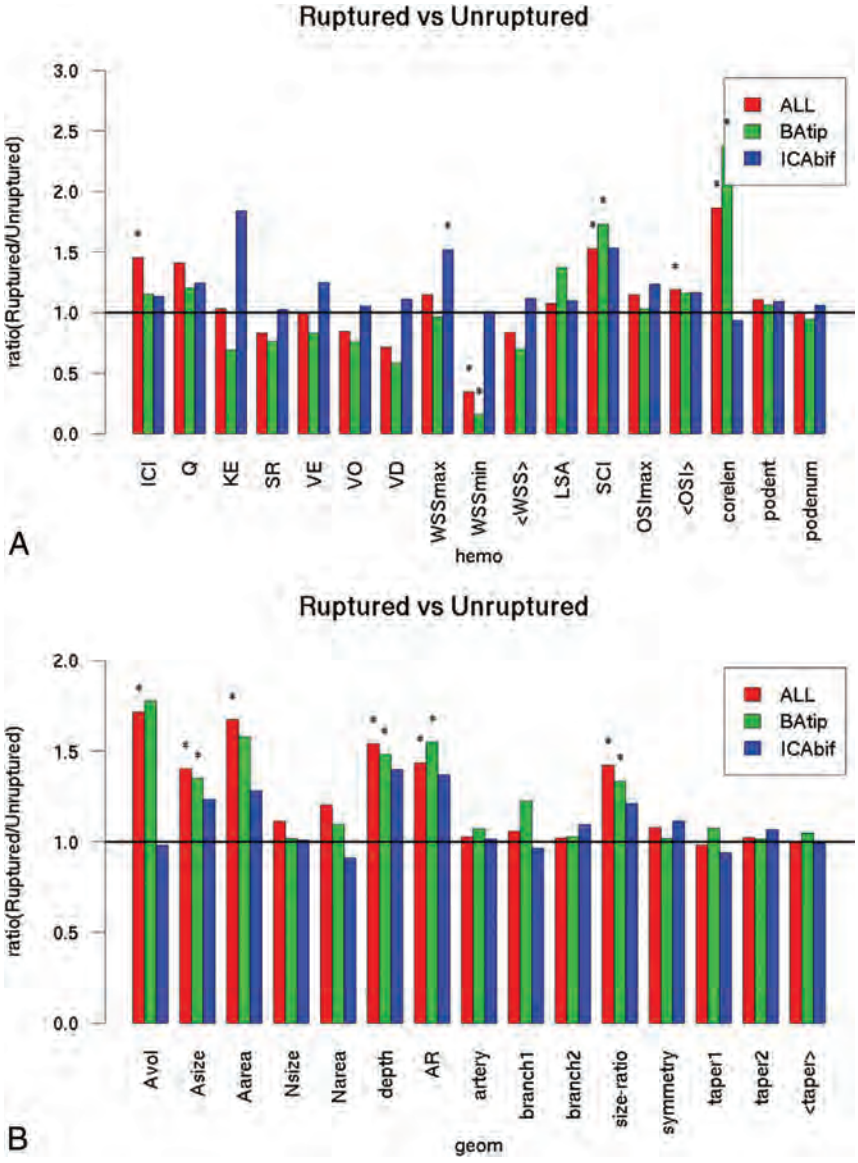

FIG 1. Ruptured-versus-unruptured aneurysms. Ratio of mean hemodynamic (*A*) and geometric (*B*) variables of ruptured over unruptured aneurysms for all aneurysms (*red bars*) and by location (*green bars*, BAtip; *blue bars*, ICAbif). *Asterisks* indicate statistically significant differences. Hemo indicates hemodynamic; geom indicates geometric; <taper>, mean taper; KE, kinetic energy; SR, shear rate; VO, vorticity; VD, viscous dissipation; <WSS>, mean WSS; podent, POD entropy; podenum, POD number of modes; <OSI>, mean OSI; A, aneurysm; N, neck; AR, aspect ratio.

rank sum tests were used to compare continuous variables between these groups. Differences were considered statistically significant with $P < .05$ (95% confidence level). To test for correlations or statistical dependence between the geometric and hemodynamic variables, we performed a Spearman rank correlation test among all the variables. A size-based comparison was then performed to assess any size-specific differences in ruptured and unruptured aneurysms at both locations. For this purpose, aneurysms were subdivided into 3 size groups: 1) large, >13 mm; 2) medium, 7–13 mm; and 3, small, <7 mm. Then the statistical analysis was repeated.[2]

RESULTS

The rupture rate among BAtip aneurysms was 43% compared with a 20% rupture rate in ICAbif aneurysms. A 2 × 2 contingency table analysis based on the Fisher exact test confirmed a statistically significant association between the aneurysm location (BAtip or ICAbif) and rupture rate ($P = .0107$).

A comparison of hemodynamic and geometric variables between ruptured and unruptured aneurysms at both locations (red bars), along with similar comparisons for aneurysms at the BAtip (green bars) and at the ICAbif (blue bars), is shown in Fig 1 (data is provided in On-line Tables 1–3 as means and SDs for ruptured and unruptured aneurysms for all aneurysms and by location). The bars in these graphs indicate the ratio of mean values of the corresponding variables of ruptured aneurysms over the mean values of the unruptured aneurysms. Variables that are significantly different between these groups are marked by an asterisk.

In general, irrespective of the location, ruptured aneurysms had more concentrated inflow jets (ICI, $P = .02$), more concentrated WSS distributions (SCI, $P = .02$), more complex flow patterns (characterized by a longer vortex core-line length [corelen], $P < .0001$), and lower minimum WSS (WSSmin, $P = .003$) than unruptured aneurysms, as indicated in Fig 1*A*. Geometrically, ruptured aneurysms were larger (aneurysm volume, $P = .006$; aneurysm size, $P = .002$; aneurysm area, $P = .005$; size ratio, $P = .003$) and had more elongated shapes (depth, $P < .001$; aspect ratio, $P = .001$) than unruptured aneurysms (red bars in Fig 1*B*).

Similar associations were found for aneurysms located at the BAtip (green bars in Fig 1*A*). Specifically, ruptured BAtip aneurysms had higher WSS concentration (SCI, $P = .02$), more complex flow patterns (corelen, $P < .0001$), and lower minimum WSS ($P = .02$) than unruptured aneurysms at this location. Ruptured BAtip aneurysms were also larger (aneurysm size, $P = .02$; size ratio, $P = .03$) and more elongated (depth, $P = .01$; aspect ratio, $P = .001$) than unruptured BAtip aneurysms (green bars in Fig 1*B*). In contrast, ruptured ICAbif aneurysms had larger maximum WSS ($P = .03$) than unruptured ICAbif aneurysms (blue bars in Fig 1). All other hemodynamic or geometric variables did not reach statistical significance.

Hemodynamic and geometric characteristics of aneurysms (including both ruptured and unruptured aneurysms) located at the BAtip and the ICAbif are shown in Fig 2. In general, BAtip aneurysms had more concentrated inflow jets (ICI, $P < .001$), larger

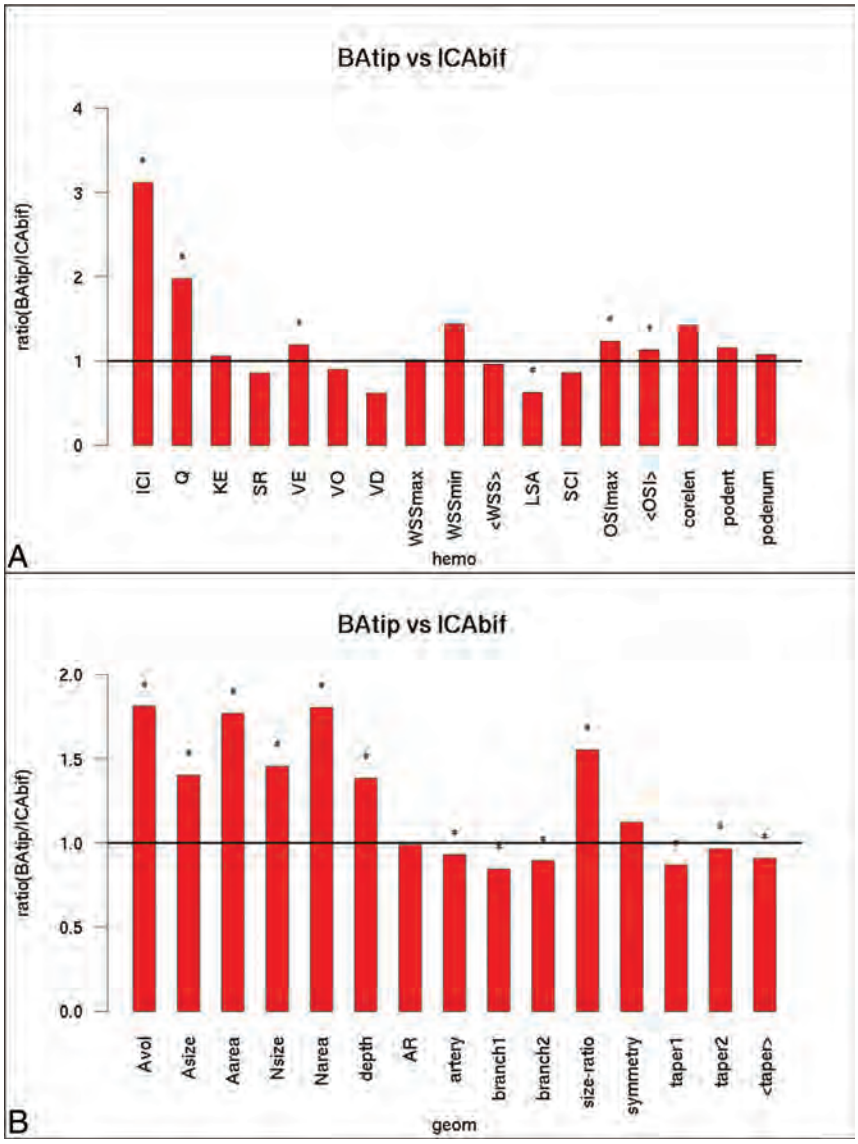

FIG 2. BAtip-versus-ICAbif aneurysms. Ratio of mean hemodynamic (*A*) and geometric (*B*) variables of BAtip aneurysms over ICAbif aneurysms. *Asterisks* indicate statistically significant differences. KE indicates kinetic energy; SR, shear rate; VO, vorticity; VD, viscous dissipation; <WSS>, mean WSS; podent, POD entropy; podenum, POD number of modes; <OSI>, mean OSI; hemo, hemodynamic; geom, geometric; <taper>, mean taper; A, aneurysm; N, neck; AR, aspect ratio.

inflow rates ($P < .001$; mean velocity [VE], $P = .04$), more oscillatory flows (maximum oscillatory shear index [OSImax], $P = .005$; mean OSI, $P = .04$), and smaller areas under low WSS (LSA, $P < .0001$) compared with ICAbif aneurysms. Additionally, BAtip aneurysms were larger (aneurysm volume, $P = .0005$; aneurysm size, $P = .0004$; Area, $P = .0006$; size ratio, $P < .001$) and had deeper domes (depth, $P = .01$) and wider necks (neck size, $P < .0001$; neck area, $P < .0001$) than ICAbif aneurysms. Most interesting, both parent and branch arteries were of a smaller caliber in the BAtip group (artery, $P = .003$; branch1, $P < .001$; branch2, $P = .006$) and had lower tapering (taper1, $P < .001$; taper2, $P = .04$; mean taper, $P = .0004$) compared with the ICAbif group.

The differences between BAtip and ICAbif hemodynamic environments were further analyzed by subdividing the aneurysms into groups based on their size (Fig 3). For large aneurysms (red bars), there were no significant differences in the hemodynamic variables. However, medium-sized BAtip aneurysms (green bars) had more concentrated inflow jets and higher inflow rates (ICI, $P < .001$; Q, $P = .003$), more oscillatory flows (OSImax, $P = .03$), and larger areas under low WSS ($P = .001$) compared with medium-sized ICAbif aneurysms. Similarly, small BAtip aneurysms had higher flow conditions characterized by larger inflow rates, more concentrated inflow jets, and larger intrasaccular velocity (ICI, $P < .001$; Q, $P = .01$; VE, $P = .04$) as well as larger areas under low WSS ($P < .001$) compared with small ICAbif aneurysms.

Illustrative examples of ruptured and unruptured aneurysms at the BAtip and ICAbif are shown in Figs 4 and 5, respectively. These figures show visualizations at peak systole of the WSS distribution, the inflow jets, the streamline patterns, and the flow structure by using vortex center lines. In both examples, the flow in the ruptured aneurysm (upper row) is characterized by a strong inflow jet impacting a concentrated area of the dome and producing a complex flow pattern within the aneurysm. In contrast, the unruptured aneurysms (lower row) exhibit a more uniform WSS distribution associated with a more diffuse inflow jet and simpler flow pattern.

DISCUSSION

Posterior circulation intracranial aneurysms are known to have higher rupture rates compared with anterior circulation intracranial aneurysms[15]; considering that there are 2 ICAs for every 1 basilar artery in a complete circle of Willis, the reported differences in rupture risk are probably even more substantial.[5] The results in our series showing a rupture rate of 43% among BAtip aneurysms compared with 20% among ICAbif aneurysms ($P = .0107$) are consistent with those published in previous studies.[5,15]

The exact reasons for these differences in rupture risks or the rupture mechanisms are still relatively unknown.[16] Thus, several previous studies have sought to determine the effects of morphometric features and hemodynamic forces on the mechanobiology of the vessel wall and on the rupture risk of intracranial aneurysms.[17-19] Some studies have suggested that aneurysms located at bifurcations are at the highest risk of rupture, attributing it to the increased hemodynamic stress at the tip of the bifurcation.[5,20] We sought to further understand the differences between these 2 locations by evaluating the intra-aneurysmal hemodynamics and

morphometric features of analogous bifurcations representing both systems.

Can et al[21] suggested that the larger P1-P1 angle of the BAtip bifurcation causes greater flow divergence into the daughter posterior cerebral arteries, thus causing lower WSS and leading to aneurysmal initiation. Our results do not seem to support the idea that this same mechanism results in aneurysm progression and rupture. Irrespective of whether the aneurysms were located at the BAtip or at the ICAbif, ruptured aneurysms in our series had more concentrated inflow jets, more concentrated WSS distributions, and longer vortex core-line lengths and, at the same time, had lower WSSmin. Although not confirmed in the ICAbif location, the BAtip location has significantly "higher flow conditions" associated with ruptured aneurysms compared with the unruptured ones. The longer vortex core-line lengths are an indicator of more complex flows and are consistent with the findings in several previously reported studies comparing ruptured and unruptured aneurysms.[14,22] Morphologically, ruptured aneurysms in our study were larger and more elongated than unruptured aneurysms as identified in multiple prior studies.[23,24]

Similarly, higher flow conditions were observed in general when comparing all BAtip and ICAbif aneurysms irrespective of rupture status. The differences observed between aneurysms at these locations were significant for small and medium-sized aneurysms, but not for large ones. This finding may be due to increased inertia effects associated with larger aneurysms.

Understanding the differences in the intra-aneurysmal hemodynamics requires attention to both the aneurysmal morphology and the geometric characteristics of the associated arterial vascular system. The BAtip aneurysms in our series were larger and had deeper domes and wider necks than ICAbif aneurysms. Larger neck sizes lead to higher intra-aneurysmal flow rates and, in combination with the greater depth and volume, have the possibility of greater flow complexity and instability. Why basilar tip aneurysms have larger sizes than ICA aneurysms is unclear. Better understanding of the mechanisms and mechanobiology of aneurysmal growth may prove helpful; however, the perianeurysmal environment may also play an important role in aneurysmal growth because contact with extravascular structures can constrain or influence the aneurysm evolution. Further studies are needed to elucidate the specific contribution of each of these factors and their combined effect on aneurysm progression.

Extending the arguments related to high flow mechanisms contributing to the initiation and progression of cerebral aneurysms can yield insight when applied to the 2 circulations discussed in this study. We chose to compare the ICA bifurcation with the basilar bifurcation because of their analogous anatomy of a T-type bifurcation. Yet, these aneurysms have very different hemodynamics, and

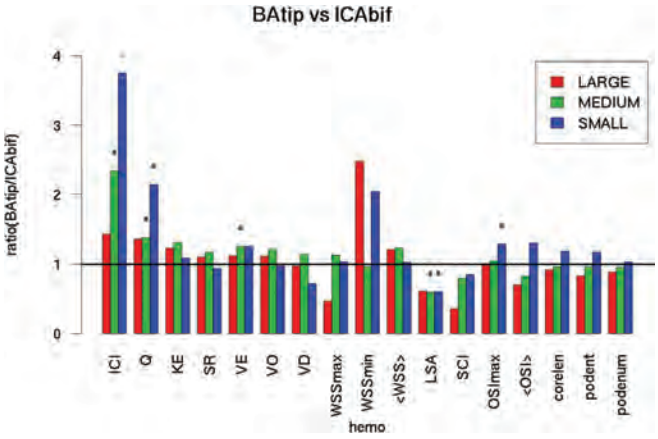

FIG 3. Comparison of hemodynamic variables across BAtip and ICAbif aneurysms grouped according to their sizes as small, medium, and large. KE indicates kinetic energy; SR, shear rate; VO, vorticitiy; VD, viscous dissipation; <WSS>, mean WSS; podent, POD entropy; podenum, POD number of modes; hemo, hemodynamic.

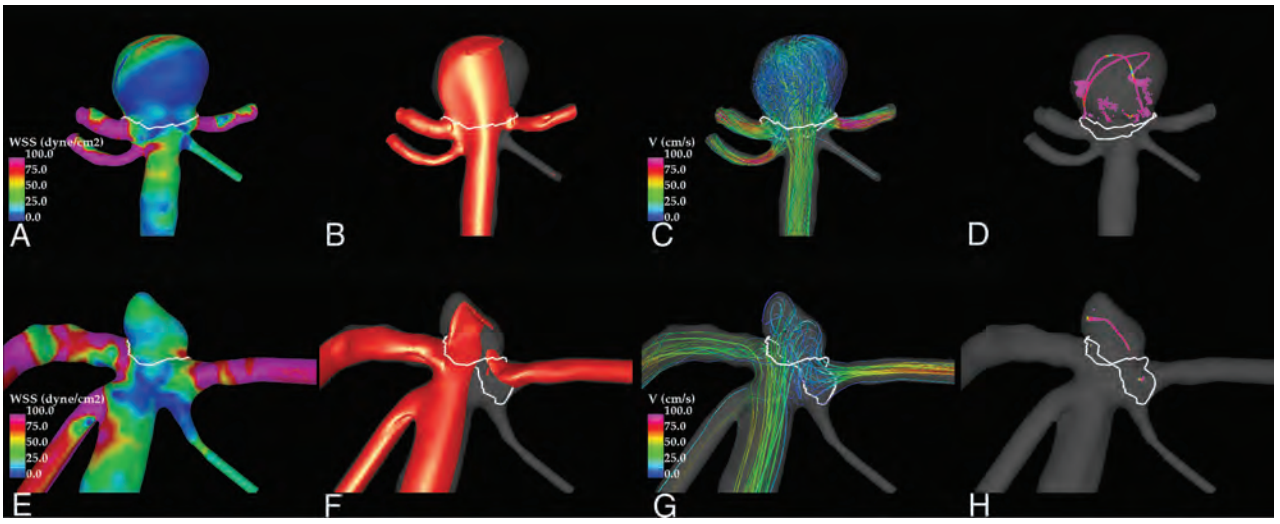

FIG 4. Examples of a ruptured (upper row) and an unruptured (lower row) BAtip aneurysm. Peak systole flow visualizations show the following: wall shear stress distribution (*A* and *E*), inflow jet (*B* and *F*), flow pattern (*C* and *G*), and vortex core lines (*D* and *H*). *White lines* indicate the aneurysm necks.

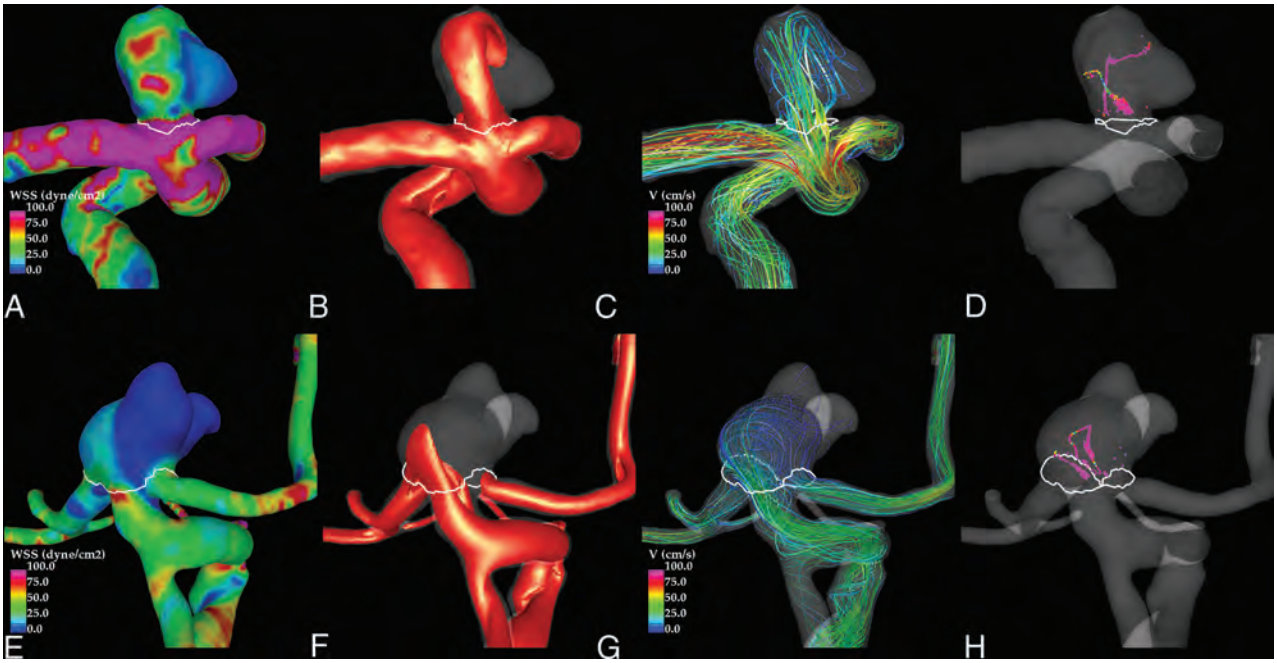

FIG 5. Examples of a ruptured (upper row) and an unruptured (lower row) ICAbif aneurysm. Peak systole flow visualizations show the following: wall shear stress distribution (*A* and *E*), inflow jet (*B* and *F*), flow pattern (*C* and *G*), and vortex core lines (*D* and *H*). *White lines* indicate the aneurysm necks.

a detailed assessment of the parent artery geometry reveals several distinct differences. The artery sizes (both parent and branch arteries) were significantly smaller in the BAtip group along with lower artery tapering compared with the ICAbif group. For a given flow rate, tapering can lead to faster flow velocities and larger pressure drops through an arterial segment, leading to increased WSS within that segment. If this effect occurs proximal to the site of aneurysm formation, then fewer kinetic forces are available for the impaction zone of the flow division where aneurysms are typically located. The tapering of the ICA proximal to the terminus, therefore, may act to reduce the shear at the region of the terminus compared with the basilar artery. Curvature of the proximal ICA can also influence the environment of the terminus. The carotid siphon may cause a consistent deflection of the main flow stream into an impaction in the posterior wall of the supraclinoid ICA, a region of high propensity to aneurysm formation. The curvature of the ICA distal to the posterior communicating artery origin often directs most of the flow stream within the M1 segment, avoiding a direct impaction on the terminus/origin of the A1 segment. In the basilar terminus, this outcome is less often the case with a near-perpendicular impaction and a more equally divided flow stream. Thus, the basilar artery geometry could more often lead to a much higher flow impaction and associated elevated WSS compared with the ICA. Variability of the bifurcation asymmetry and bifurcation angles can lead to further differences in the hemodynamic environments in an individual case. In this sense, ICAbif aneurysms seem to behave more like sidewall aneurysms, while BAtip aneurysms behave more like true bifurcation aneurysms.

Although a number of results reaching statistical significance were identified in this study, some limitations should be considered. The sample size is small when extending into the various subgroups, this could interfere with identifying significant differences. The study was taken from a data base of all aneurysms that had undergone angiography or embolization during a 10-year period. Selection bias related to referral patterns and the indications for treatment may lead to exclusion of an important subset of aneurysms. A number of assumptions were made during the modeling process, including the approximations of the vascular geometry, the inflow conditions, the Newtonian approximation, and the rigid wall assumption.

CONCLUSIONS

High flow conditions, characterized by large and concentrated inflow jets, complex and oscillatory intrasaccular flow patterns, and wall shear stress distributions with focalized regions of high WSS and large regions of low WSS are associated with aneurysm rupture in general and in basilar tip aneurysms in particular. The higher flow conditions in BAtip aneurysms could explain their increased rupture risk compared with ICAbif aneurysms. In ICAbif aneurysms, only trends toward high flow conditions were associated with aneurysm rupture, and these trends were observed in only smaller ICAbif aneurysms. Further studies with larger sample sizes will be needed to determine whether these trends are statistically significant.

ACKNOWLEDGMENTS

We thank Ms Alicia Suchi (George Mason University) for assistance in measuring vessel sizes.

Disclosures: Ravi Doddasomayajula—*UNRELATED*: *Grants/Grants Pending*: National Institutes of Health, *Comments*: research grant.* Christopher M. Putman—*UNRELATED*: *Consultancy*: Codman Neurovascular; *Payment for Lectures Including Service on Speakers Bureaus*: Penumbra. Juan R. Cebral—*UNRELATED*: *Grants/*

Grants Pending: National Institutes of Health, Philips Healthcare, *Comments*: research grants.* *Money paid to the institution.

REFERENCES

1. Rinkel GJ, Djibuti M, Algra A, et al. **Prevalence and risk of rupture of intracranial aneurysms: a systematic review.** *Stroke* 1998;29:251–56 CrossRef Medline
2. Wiebers DO, Whisnant JP, Huston J 3rd, et al; International Study of Unruptured Intracranial Aneurysms Investigators. **Unruptured intracranial aneurysms: natural history, clinical outcome, and risks of surgical and endovascular treatment.** *Lancet* 2003;362:103–10 Medline
3. Weibers DO, Piepgras DG, Meyer FB, et al. **Pathogenesis, natural history, and treatment of unruptured intracranial aneurysms.** *Mayo Clinic Proc* 2004;79:1572–83 CrossRef Medline
4. Clarke M. **Systematic review of reviews of risk factors for intracranial aneurysms.** *Neuroradiology* 2008;50:653–64 CrossRef Medline
5. van der Kolk NM, Algra A, Rinkel GJ. **Risk of aneurysm rupture at intracranial arterial bifurcations.** *Cerebrovasc Dis* 2010;30:29–35 CrossRef Medline
6. Sforza DM, Putman CM, Cebral JR. **Hemodynamics of cerebral aneurysms.** *Annu Rev Fluid Mech* 2009;41:91–107 CrossRef Medline
7. Higa T, Ujiie H, Kato K, et al. **Basilar artery trunk saccular aneurysms: morphological characteristics and management.** *Neurosurg Rev* 2009;32:181–91; discussion 191 CrossRef Medline
8. Cebral JR, Mut F, Weir J, et al. **Quantitative characterization of the hemodynamic environment in ruptured and unruptured brain aneurysms.** *AJNR Am J Neuroradiol* 2011;32:145–51 CrossRef Medline
9. Yim PJ, Vasbinder GB, Ho VB, et al. **Isosurfaces as deformable models for magnetic resonance angiography.** *IEEE Trans Med Imaging* 2003;22:875–81 CrossRef Medline
10. Taylor CA, Hughes T Jr, Zarins CK. **Finite element modeling of blood flow in arteries.** *Computer Methods in Applied Mechanics and Engineering* 1998;158:155–96 CrossRef
11. Cebral JR, Castro MA, Appanaboyina S, et al. **Efficient pipeline for image-based patient-specific analysis of cerebral aneurysm hemodynamics: technique and sensitivity.** *IEEE Trans Med Imaging* 2005;24:457–67 CrossRef Medline
12. Mut F, Aubry R, Löhner R, et al. **Fast numerical solutions of patient-specific blood flows in 3D arterial systems.** *Int J Numer Method Biomed Eng* 2010;26:73–85 CrossRef Medline
13. Mut F, Löhner R, Chien A, et al. **Computational hemodynamics framework for the analysis of cerebral aneurysms.** *Int J Numer Method Biomed Eng* 2011;27:822–39 CrossRef Medline
14. Byrne G, Mut F, Cebral JR. **Quantifying the large-scale hemodynamics of intracanial aneurysms.** *AJNR Am J Neuroradiol* 2014;35:333–38 CrossRef Medline
15. Tykocki T, Kostkiewicz B. **Aneurysms of the anterior and posterior cerebral circulation: comparison of the morphometric features.** *Acta Neurochir (Wien)* 2014;156:1647–54 CrossRef Medline
16. Wermer MJ, van der Schaaf IC, Algra A, et al. **Risk of rupture of unruptured intracranial aneurysms in relation to patient and aneurysm characteristics: an updated meta-analysis.** *Stroke* 2007;38:1404–10 CrossRef Medline
17. Chien A, Castro MA, Tateshima S, et al. **Quantitative hemodynamic analysis of brain aneurysms at different locations.** *AJNR Am J Neuroradiol* 2009;30:1507–12 CrossRef Medline
18. Robertson AM, Duan X, Aziz KM, et al. **Diversity in the strength and structure of unruptured cerebral aneurysms.** *Ann Biomed Eng* 2015;43:1502–15 CrossRef Medline
19. Cebral JR, Raschi M. **Suggested connections between risk factors of intracranial aneurysms: a review.** *Ann Biomed Eng* 2013;41:1366–83 CrossRef Medline
20. Meng H, Tutino VM, Xiang J, et al. **High WSS or low WSS? Complex interactions of hemodynamics with intracranial aneurysm initiation, growth, and rupture: toward a unifying hypothesis.** *AJNR Am J Neuroradiol* 2014;35:1254–62 CrossRef Medline
21. Can A, Mouminah A, Ho AL, et al. **Effect of vascular anatomy on the formation of basilar tip aneurysms.** *Neurosurgery* 2015;76:62–66; discussion 66 CrossRef Medline
22. Cebral JR, Mut F, Weir J, et al. **Association of hemodynamic characteristics and cerebral aneurysm rupture.** *AJNR Am J Neuroradiol* 2011;32:264–270 CrossRef Medline
23. Dhar S, Tremmel M, Mocco J, et al. **Morphology parameters for intracranial aneurysm rupture risk assessment.** *Neurosurgery* 2008;63:185–197; discussion 196–97 CrossRef Medline
24. Fan J, Wang Y, Liu J, et al. **Morphological-hemodynamic characteristics of intracranial bifurcation mirror aneurysms.** *World Neurosurg* 2015;84:114–20.e2 CrossRef Medline

Usefulness of Non–Contrast-Enhanced MR Angiography Using a Silent Scan for Follow-Up after Y-Configuration Stent-Assisted Coil Embolization for Basilar Tip Aneurysms

N. Takano, M. Suzuki, R. Irie, M. Yamamoto, N. Hamasaki, K. Kamagata, K.K. Kumamaru, M. Hori, H. Oishi, and S. Aoki

ABSTRACT

BACKGROUND AND PURPOSE: Y-configuration stent-assisted coil embolization is used for treating wide-neck aneurysms. Noninvasive alternatives to x-ray DSA for follow-up after Y-configuration stent-assisted coil embolization treatment are required. This study aimed to assess the usefulness of non–contrast-enhanced MRA by using a Silent Scan (silent MRA) for follow-up after Y-configuration stent-assisted coil embolization for basilar tip aneurysms.

MATERIALS AND METHODS: Seven patients treated with Y-configuration stent-assisted coil embolization for basilar tip aneurysms underwent silent MRA, 3D TOF-MRA, and DSA. Silent MRA and 3D TOF-MRA images were obtained during the same scan session on a 3T MR imaging system. Two neuroradiologists independently reviewed both types of MRA images and subjectively scored the flow in the stents on a scale of 1 (not visible) to 5 (nearly equal to DSA) by referring to the latest DSA image as a criterion standard. Furthermore, we evaluated the visualization of the neck remnant.

RESULTS: In all patients, the 2 observers gave a higher score for the flow in the stents on silent MRA than on 3D TOF-MRA. The average score ± standard deviation was 4.07 ± 0.70 for silent MRA and 1.93 ± 0.80 ($P < .05$) for 3D TOF-MRA. Neck remnants were depicted by DSA in 5 patients. In silent MRA, neck remnants were depicted in 5 patients, and visualization was similar to DSA; however, in 3D TOF-MRA, neck remnants were depicted in only 1 patient.

CONCLUSIONS: Silent MRA might be useful for follow-up after Y-configuration stent-assisted coil embolization.

ABBREVIATIONS: BA = basilar artery; CE-MRA = contrast-enhanced MRA; PCA = posterior cerebral artery; UTE = ultrashort echo time

In recent years, intracranial stents have been used for the treatment of wide-neck aneurysms. The Y-configuration stent-assisted coil embolization technique has been generally used for wide-neck bifurcation aneurysms such as those at the tip of the basilar artery (BA).[1-6] The Y stent deploys 2 stents from the BA to the bilateral posterior cerebral artery (PCA). The 2 stents overlap in the distal BA trunk, with 1 stent penetrating the mesh of the other. The use of 2 stents in a "Y" configuration to assist with coil embolization for bifurcation aneurysms has been accepted for broad-neck aneurysms.

X-ray DSA is the standard technique used for follow-up after an intracranial stent. However, DSA is an invasive technique that carries a risk of neurologic complications, contrast materials, and x-ray radiation.[7-10]

On the other hand, 3D TOF-MRA is widely used as a noninvasive substitute for DSA for the follow-up of coiled aneurysms.[11-14] Although there have been reports of 3D TOF-MRA being used after stent-assisted coil embolization,[12,13] it remains difficult to visualize flow in an intracranial stent when using this method because of magnetic susceptibility and radiofrequency shielding. Therefore, contrast-enhanced MRA (CE-MRA) is used for follow-up after stent-assisted coil embolization. However, the use of contrast materials in CE-MRA is associated with nephrogenic systemic fibrosis and anaphylactic shock; therefore, this

Received June 29, 2016; accepted after revision October 12.

From the Department of Radiology (N.T., M.S., K. Kamagata, K.K. Kumamaru, M.H., S.A.), Graduate School of Medicine, Juntendo University, Tokyo, Japan; Department of Radiology (N.T., M.S., R.I., N.H., K. Kamagata, K.K. Kumamaru, M.H., S.A.), Juntendo University Hospital, Tokyo, Japan; and Departments of Neurosurgery (M.Y., H.O.) and Neuroendovascular Therapy (H.O.), Juntendo University School of Medicine, Tokyo, Japan.

This work was supported in part by the ImPACT Program of Council for Science, Technology and Innovation (Cabinet Office, Government of Japan) and by a Grant-in-Aid for Scientific Research on Innovative Areas (ABiS) from the Ministry of Education, Culture, Sports, Science and Technology of Japan.

Paper previously presented as an electronic poster at: European Congress of Radiology, March 2–6, 2016; Vienna, Austria. doi:10.1594/ecr2016/C-1028.

Please address correspondence to Nao Takano, MMSc, Department of Radiology, Graduate School of Medicine, Juntendo University, 2-1-1 Hongo, Bunkyo-ku, Tokyo 113-8421, Japan; e-mail: ntakano@juntendo.ac.jp

Indicates open access to non-subscribers at www.ajnr.org

Indicates article with supplemental on-line table.

http://dx.doi.org/10.3174/ajnr.A5033

technique might not be appropriate for repeated examinations.[15-17] Furthermore, it has been reported that gadolinium-based contrast material accumulates in the dentate nucleus and globus pallidus.[18]

Silent MRA uses a Silenz pulse sequence (GE Healthcare, Milwaukee, Wisconsin) containing an ultrashort echo time (UTE) combined with arterial spin-labeling. Data acquisition is based on 3D radial sampling, and the arterial spin-labeling technique is used as a preparation pulse for visualization of the blood flow.[19,20] It is a non–contrast-enhanced MRA technique; therefore, it is better for the patient and suitable for repeated follow-ups.

UTE of silent MRA minimizes phase dispersion of the labeled blood flow signal and decreases magnetic susceptibility to coils and stents. Thus, silent MRA can evaluate the blood flow in an intracranial stent.[20]

To the best of our knowledge, there have been no studies of the use of non–contrast-enhanced MRA for follow-up after Y-configuration stent-assisted coil embolization for basilar tip aneurysms. Therefore, in the present study, we evaluated the usefulness of silent MRA compared with 3D TOF-MRA for follow-up after Y-configuration stent-assisted coil embolization for basilar tip aneurysms.

MATERIALS AND METHODS

Between October 2014 and September 2015, 7 aneurysm cases treated with Y-configuration stent-assisted coil embolization were retrospectively examined. Written informed consent was not required because of the retrospective nature of this study. All patients had incidentally found unruptured aneurysms and were followed-up with silent MRA, 3D TOF-MRA, and DSA. The average interval between the latest DSA and both MRAs was 27 days (range, 1–180 days). The average interval between the aneurysm treatment and both MRAs was 187.9 days (range, 1–395 days).

The DSA of catheter-based intraarterial cerebral angiography was performed with the following biplane angiographic systems: the AXIOM Artis dTA (Siemens, Erlangen, Germany) until February 2014 and the Artis Q BA Twin (Siemens) from March 2014 to present.

The intracranial stents used were the Enterprise stent (Codman & Shurtleff, Raynham, Massachusetts), Neuroform stent (Stryker Neurovascular, Kalamazoo, Michigan), and LVIS (Low-profile Visualized Intraluminal Support) Jr stent (MicroVention, Tustin, California).

Silent MRA and 3D TOF-MRA were performed during the same scan session on a 3T MR imaging system (Discovery MR750w; GE Healthcare) with a 12-channel head-neck coil. The scan parameters of silent MRA were as follows: TR, 1116.4 ms; TE, 0.016 ms; flip angle, 5°; FOV, 180 × 180 mm; matrix, 150 × 150; section thickness, 1.2 mm; NEX, 1.5; bandwidth, ±20 kHz; and acquisition time, 7 minutes, 40 seconds. The scan parameters of 3D TOF-MRA were as follows: TR, 19 ms; TE, 2.9 ms; flip angle, 15°; FOV, 200 × 200 mm; matrix, 416 × 192; section thickness, 1.2 mm; NEX, 1; bandwidth, ±41.7 kHz; and acquisition time, 3 minutes, 31 seconds (3 slabs, overlap between a slab: 10 sections, 1 slab: 32 sections)

Visualization of the parent artery with silent MRA and 3D TOF-MRA was compared with that of the DSA images. The latest DSA images were used as a criterion standard. Silent MRA and 3D TOF-MRA images were processed to MIP in the same manner as the DSA images. We evaluated DSA images and 2 types of MRA images. The 2 types of MRA images were independently assessed to minimize bias from the knowledge of the results of the other MRA image. Two experienced neuroradiologists (M.S., R.I.) independently reviewed silent MRA and 3D TOF-MRA and rated the conditions of visualization of the flow in each stent subjectively on a 5-point scale as follows: 1, not visible (almost no signal in the stent); 2, poor (structures are slightly visible, but with substantial blurring or artifacts); 3, acceptable (acceptable quality diagnostic information with medium blurring or artifacts); 4, good (good quality diagnostic information with minimum blurring or artifacts); or 5, excellent (the depiction is almost equal to DSA). This scale is used to assess the image quality. Furthermore, we evaluated the visualization of the neck remnants of silent MRA and 3D TOF-MRA in patients in whom DSA indicated neck remnants. The scores given by the 2 observers were averaged, and a Wilcoxon signed rank test was performed in the statistical analysis of the subjective scores for the flow in the stents. $P < .05$ was considered statistically significant.

RESULTS

Patient data and the scores given by the 2 observers are shown in the On-line Table. Both observers gave silent MRA a higher score than 3D TOF-MRA in all cases. The average score ± standard deviation was 4.07 ± 0.70 for silent MRA and 1.93 ± 0.80 for 3D TOF-MRA ($P < .05$). Neck remnants were depicted by DSA in 5 cases (case number 1, 3, 4, 5, and 7). In silent MRA, neck remnants were depicted in all of these 5 cases, and visualization was similar to DSA; however, in 3D TOF-MRA, neck remnants were depicted in only 1 case. Figs 1–3 show the silent MRA, 3D TOF-MRA, and DSA images for each case.

DISCUSSION

The Y-configuration stent-assisted coil embolization technique has been used for wide-neck bifurcation aneurysms such as those of the tip of the BA. In the present study, we evaluated the usefulness of silent MRA compared with that of 3D TOF-MRA for follow-up after Y-configuration stent-assisted coil embolization for basilar tip aneurysms. It has been reported that 3D TOF-MRA and CE-MRA have been used after single stent–assisted coil embolization.[12,13,15-17] Irie et al[20] reported follow-up after stent-assisted coil embolization by using silent MRA, and Cho et al[12] reported that the degree of agreement and correlation between 3D TOF-MRA and 3D rotational angiography was high. With respect to the status of neck remnants, the sensitivity was 80% (4/5 cases). It is thought that magnetic susceptibility artifacts and radiofrequency shielding were decreased because of the very small voxel size (reconstructed voxel size, 0.24/0.24/0.7 mm). Cho et al[13] reported comparisons between the 3D TOF-MRA and conventional angiography, showing that the MIP plus source images had almost perfect agreement ($\kappa = 0.892$), with better agreement than with the MIP images alone ($\kappa = 0.598$). It is difficult, through the evaluation of source images, to assess the residual flow that is protruding in the direction of the body axis after stent-assisted coil embolization. To confirm the residual flow, MPR with an

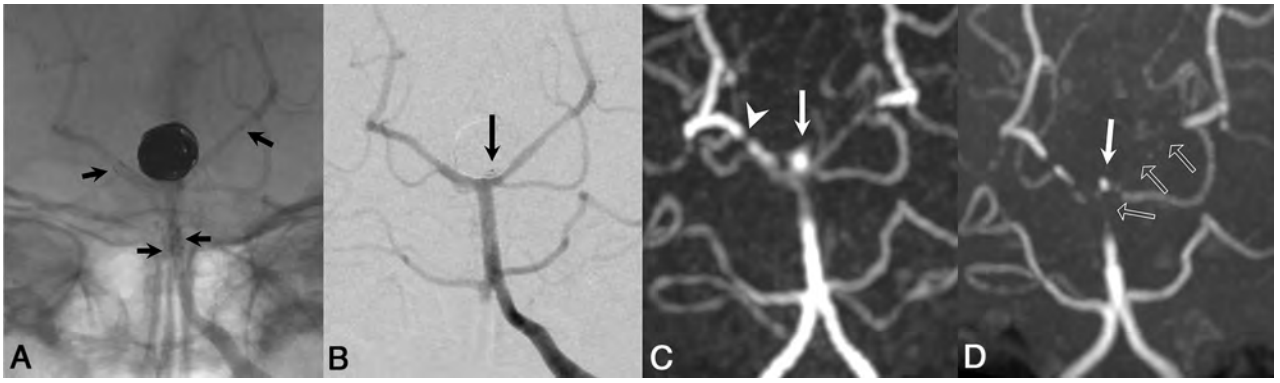

FIG 1. Patient number 1: 53-year-old woman. *A*, Y-configuration stent-assisted coil embolization is performed with Neuroform (right PCA) and Enterprise stent (left PCA). *Short arrows* are stent edges. *B*, X-ray DSA shows neck remnant (*long arrow*). *C*, Silent MRA demonstrates minimal signal loss at stented segments; right PCA stent edge segment demonstrates strong signal loss (*arrowhead*). Neck remnant is depicted (*long arrow*). *D*, 3D TOF-MRA on same day shows strong signal loss at BA, and left PCA segment demonstrates complete signal loss (*outlined arrows*). Neck remnant is depicted (*long arrow*).

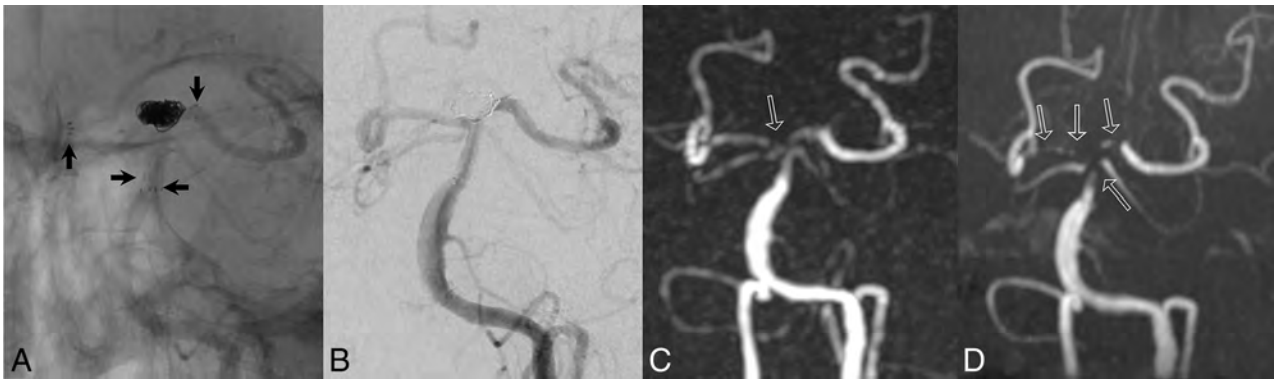

FIG 2. Patient number 2: 75-year-old woman. *A*, Y-configuration stent-assisted coil embolization is performed with Neuroform (right PCA) and Enterprise stent (left PCA). *Short arrows* are stent edges. *B*, X-ray DSA shows complete occlusion. *C*, Silent MRA demonstrates mild signal loss at right PCA segment. Silent MRA shows complete occlusion. *D*, 3D TOF-MRA on same day shows mild signal loss at BA, and bilateral PCA segments demonstrates complete signal loss (*outlined arrows*).

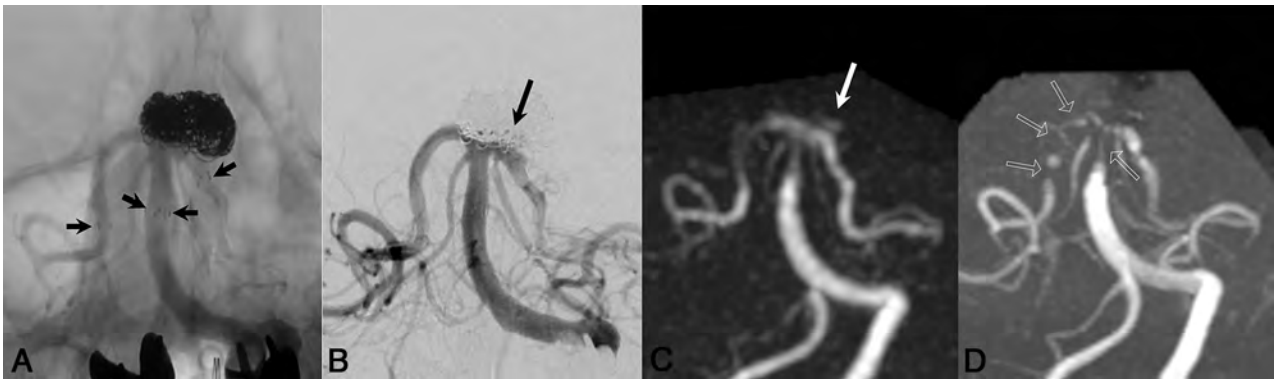

FIG 3. Patient number 3: 66-year-old woman. *A*, Y-configuration stent-assisted coil embolization is performed with Neuroform (left PCA) and Enterprise stent (right PCA). *Short arrows* are stent edges. *B*, X-ray DSA immediately after stent-assisted coil embolization shows neck remnant (*long arrow*). *C*, Silent MRA demonstrates minimal signal loss at stented segment and visualizes neck remnant (*long arrow*). *D*, 3D TOF-MRA on same day shows mild signal loss at BA, and right PCA segment demonstrates almost complete signal loss (*outlined arrows*).

accurate image angle should be obtained. Irie et al[20] showed the usefulness of the silent MRA for stent-assisted coil embolization rather than a comparison between silent MRA and 3D TOF-MRA. Moreover, the visualization of neck remnants was good.

CE-MRA has a better depiction of the flow in a stent than 3D TOF-MRA, and it is reported that CE-MRA has a visualization ability similar to DSA.[15] Previous reports have examined 3D TOF-MRA and CE-MRA for stent-assisted coil embolization by using 1 stent; however, a Y-configuration stent-assisted coil embolization case was not examined. Moreover, there have been no studies on the use of MRA for follow-up after Y-configuration stent-assisted coil embolization. The Y stent has a strong influence on magnetic susceptibility artifacts and radiofrequency shielding effects, particularly at the cross point of the 2 stents. It is thought

that the depiction of the flow in Y stents is difficult in 3D TOF-MRA.

On the other hand, CE-MRA has certain problems such as nephrogenic systemic fibrosis, gadolinium accumulation, and anaphylactic shock, and it is not necessarily suitable for repeated examination. Therefore, we examined the usefulness of silent MRA in the present study. Silent MRA is a non–contrast-enhanced MRA technique as is 3D TOF-MRA. In the present study, the visualization ability of silent MRA was higher than that of 3D TOF-MRA for Y-configuration stent-assisted coil embolization. The reason silent MRA is superior in the depiction of the flow in a stent is the data acquisition by UTE. The TE of silent MRA was 0.016 ms and that of 3D TOF-MRA was 2.9 ms. Gönner et al[21] reported that 3D TOF-MRA using UTE reduced the artifacts after coil or stent placement; however, a TE of 2.4 ms was used in that study. In addition, Yamada et al[22] reported that a TE of 1.54–1.60 ms was used in their 3D TOF-MRA study. In silent MRA, UTE can minimize the phase dispersion of the labeled blood flow signal in the voxel and decrease magnetic susceptibility artifacts, and accordingly, the artifacts from stents or coils are decreased.

The Y stent deploys 2 stents from the BA to the bilateral PCA. Moreover, the PCA is positioned almost perpendicular to the BA by stent deployment. Therefore, the PCA has weak inflow effect parallel to a section direction. The visualization ability of the PCA decreased because 3D TOF-MRA was used inflow effect. The limitation of 3D TOF-MRA is spin dephasing by slow flow, turbulent flow, and horizontal directional flow. Moreover, the visualization ability of the BA trunk is worse because of the susceptibility artifacts with 2 stents.

On the other hand, the visualization ability of the BA and PCA is good in silent MRA. The arterial spin-labeling technique is used as a preparation pulse for the visualization of the blood flow. Therefore, visualization of the blood flow does not depend on the flow direction, such as with 3D TOF-MRA in the silent MRA.

In the series, we experienced an interesting case (Fig 1) that used both a Neuroform and Enterprise stent. The Neuroform stent was deployed from the BA trunk to the right PCA, and the Enterprise stent was deployed from the BA trunk to the left PCA. The stent sizes were 3.0 × 20 mm and 4.5 × 22 mm, respectively. In this particular case, the depiction of the distal stent edge of the right PCA showed strong signal loss in both MRAs. Neuroform and Enterprise stents are nitinol stents.[12,16,17,23] The Neuroform stent has an open-cell design (ie, stent-strut is not interconnected). On the other hand, the Enterprise stent has a closed-cell design (ie, stent-strut is interconnected). Open cell–design stents have lower susceptibility artifacts than closed-cell designs.[16,17,23] Therefore, the Neuroform stent has a better visualization ability compared with the Enterprise stent.

The marker of Neuroform comprises stainless steel and platinum.[15,23] On the other hand, the marker of Enterprise comprises tantalum.[12,16] Agid et al[15] reported a "marker band effect" that appeared in small arteries with a diameter of 2 mm or less and markers of different alloy than the rest of the stent (usually made of platinum), which creates a stronger local susceptibility artifact.[15] The markers of Neuroform stents are made of platinum, which creates a strong magnetic susceptibility artifact.[15]

In our study, this effect appeared in the right PCA, where the Neuroform stent (marker made of stainless steel and platinum) with a 3-mm diameter (the smallest diameter in our 7 cases) was deployed. This phenomenon corresponded with that in the report by Agid et al[15]; it is thought that a similar phenomenon is caused in the silent MRA.

Case number 3 (Fig 3) also used both a Neuroform and Enterprise stent. The left PCA segment was depicted more clearly than the right PCA segment. The Enterprise stent was deployed in the right PCA. Choi et al[23] reported that the open-cell design and thinner strut of the Neuroform stent provide better image quality than the Enterprise stent when using 3D TOF-MRA. In the present study, silent MRA more clearly depicted the Neuroform stent than the Enterprise stent, similar to the previous study. The cell design and thickness of the stent strut are important factors in both silent MRA and 3D TOF-MRA.

The depiction of the neck remnants in silent MRA was similar to that of DSA in the present study. Cho et al[13] and Agid et al[15] reported good depiction of the neck remnants in 3D TOF-MRA and CE-MRA in a case of single stent–assisted coil embolization. In the present study, 3D TOF-MRA had poor image quality compared with that reported in previous studies.[12,13] With respect to Y-configuration stent-assisted coil embolization, the aneurysm is sandwiched between 2 stents.

Therefore, the influence of 2 stents on the susceptibility artifact was stronger. On the other hand, silent MRA uses UTE and the arterial spin-labeling technique, decreasing susceptibility artifacts and depicting the neck remnants in comparison with 3D TOF-MRA.

As a similar sequence to silent MRA, Iryo et al[24] reported the contrast inherent inflow-enhanced multiphase angiography, or CINEMA, sequence. The CINEMA sequence is a non–contrast-enhanced MRA using arterial spin-labeling, such as silent MRA. This is a 4D MRA sequence. They evaluated patients with AVF. It is thought that the reduction of the susceptibility artifacts can possibly decrease if we shorten TE by this sequence. However, TE of silent MRA is 0.016 ms. TE of CINEMA cannot use UTE, such as silent MRA. They reported that a TE of 2.2 ms was used. Therefore, it is thought that silent MRA has a higher visualization ability of the artery treated with intracranial stenting compared with the CINEMA sequence. On the other hand, CINEMA has high temporal resolution; as a result, it is useful for a patient needing temporal resolution, such as one with shunt lesions.

On the other hand, Koktzoglou et al[25] reported the pointwise encoding time reduction with radial acquisition, or PETRA, sequence. PETRA uses the UTE sequence.[26] They evaluated carotid stenosis by using a vascular phantom. They reported that arterial spin-labeling MRA could improve the display of hemodynamically significant carotid arterial stenosis. Silent MRA and PETRA MRA are arterial spin-labeling with a UTE MRA sequence. If we use the PETRA MRA sequence, a result similar to that of our examination may be provided.

A major limitation of the present study is the small sample size. The examination of more cases and a variety of stents, lengths, and diameters is required. In the future, we should evaluate stent-specific visualization. There is a report that CE-MRA is useful,[15] and comparative evaluations with CE-MRA are also required. It is important to elucidate whether silent MRA is not inferior to CE-

MRA; however, patients in the current study did not undergo CE-MRA. In the current study, silent MRA picked up all neck remnants, with 1 false-positive test result. Thus, we postulate that silent MRA is noninferior to CE-MRA, which needs to be confirmed in future studies.

CONCLUSIONS

Silent MRA could visualize flow in the stent more clearly than 3D TOF-MRA at the Y-configuration stent-assisted coil embolization for basilar tip aneurysms. Moreover, it is not necessary to use contrast materials. Silent MRA might be useful for follow-up after Y-configuration stent-assisted coil embolization for basilar tip aneurysms.

ACKNOWLEDGMENTS

The authors thank Shuji Sato, Hideo Kawasaki, and Haruyoshi Hoshito (Radiologic Technologist of the Department of Radiology) for technical advice.

Disclosures: Nao Takano—*RELATED*: *Grant*: Cabinet Office of the Government of Japan,* The Ministry of Education, Culture, Sports, Science and Technology of Japan,* *Comments*: this work was funded by ImPACT Program of Council for Science, Technology and Innovation (Cabinet Office, Government of Japan). This work is supported by a Grant-in-Aid for Scientific Research on Innovative Areas (ABiS) from the Ministry of Education, Culture, Sports, Science and Technology of Japan*; *UNRELATED*: *Payment for Lectures (including service on Speakers Bureaus)*: GE Healthcare Japan, *Comments*: 42nd Japanese Society of Radiological Technology Autumn Scientific Congress, October 9–11, 2014; Sapporo, Hokkaido, Japan and luncheon seminar ["Experience of MR angiography (Silent MRA) using Silenz sequence"]. Shigeki Aoki—*UNRELATED*: *Payment for Lectures (including service on Speakers Bureaus)*: GE Healthcare Japan, *Comments*: luncheon seminar. *Money paid to the institution.

REFERENCES

1. Conrad MD, Brasiliense LB, Richie AN, et al. **Y stenting assisted coiling using a new low profile visible intraluminal support device for wide necked basilar tip aneurysms: a technical report.** *J Neurointerv Surg* 2014;6:296–300 CrossRef Medline
2. Spiotta AM, Lena J, Chaudry MI, et al. **Y-stenting for bifurcation aneurysm coil embolization: what is the risk?** *Stroke Res Treat* 2014; 2014:762389 CrossRef Medline
3. Jeon P, Kim BM, Kim DJ, et al. **Y-configuration double-stent-assisted coiling using two closed-cell stents for wide-neck basilar tip aneurysms.** *Acta Neurochir (Wien)* 2014;156:1677–86 CrossRef Medline
4. Kono K, Shintani A, Terada T. **Retreatment of recanalized aneurysms after Y-stent-assisted coil embolization with double Enterprise stents: case report and systematic review of the literature.** *Turk Neurosurg* 2014;24:593–97 CrossRef Medline
5. Fargen KM, Mocco J, Neal D, et al. **A multicenter study of stent-assisted coiling of cerebral aneurysms with a Y configuration.** *Neurosurgery* 2013;73:466–72 CrossRef Medline
6. Spiotta AM, Gupta R, Fiorella D, et al. **Mid-term results of endovascular coiling of wide-necked aneurysms using double stents in a Y configuration.** *Neurosurgery* 2011;69:421–29 CrossRef Medline
7. Ferns SP, Sprengers ME, van Rooij WJ, et al. **Coiling of intracranial aneurysms: a systematic review on initial occlusion and reopening and retreatment rates.** *Stroke* 2009;40:e523–29 CrossRef Medline
8. Kanaan H, Jankowitz B, Aleu A, et al. **In-stent thrombosis and stenosis after neck-remodeling device-assisted coil embolization of intracranial aneurysms.** *Neurosurgery* 2010;67:1523–32; discussion 1532–33 CrossRef Medline
9. Mocco J, Fargen KM, Albuquerque FC, et al. **Delayed thrombosis or stenosis following Enterprise-assisted stent-coiling: is it safe? Mid-term results of the interstate collaboration of Enterprise stent coiling.** *Neurosurgery* 2011;69:908–13; discussion 913–14 CrossRef Medline
10. Kaufmann, TJ Huston J 3rd, Mandrekar JN, et al. **Complications of diagnostic cerebral angiography: evaluation of 19,826 consecutive patients.** *Radiology* 2007;243:812–19 CrossRef Medline
11. Lavoie P, Gariépy JL, Milot G, et al. **Residual flow after cerebral aneurysm coil occlusion: diagnostic accuracy of MR angiography.** *Stroke* 2012;43:740–46 CrossRef Medline
12. Cho WS, Kim SS, Lee SJ, et al. **The effectiveness of 3T time-of-flight magnetic resonance angiography for follow-up evaluations after the stent-assisted coil embolization of cerebral aneurysms.** *Acta Radiol* 2014;55:604–13 CrossRef Medline
13. Cho YD, Kim KM, Lee WJ, et al. **Time-of-flight magnetic resonance angiography for follow-up of coil embolization with Enterprise stent for intracranial aneurysm: usefulness of source images.** *Korean J Radiol* 2014;15:161–68 CrossRef Medline
14. Schaafsma JD, Velthuis BK, Majoie CB, et al. **Intracranial aneurysms treated with coil placement: test characteristics of follow-up MR angiography—multicenter study 1.** *Radiology* 2010;256:209–18 CrossRef Medline
15. Agid R, Schaaf M, Farb R. **CE-MRA for follow-up of aneurysms post stent-assisted coiling.** *Interv Neuroradiol* 2012;18:275–83 Medline
16. Takayama K, Taoka T, Nakagawa H, et al. **Usefulness of contrast-enhanced magnetic resonance angiography for follow-up of coil embolization with the Enterprise stent for cerebral aneurysms.** *J Comput Assist Tomogr* 2011;35:568–72 CrossRef Medline
17. Choi JW, Roh HG, Moon WJ, et al. **Time-resolved 3D contrast-enhanced MRA on 3.0T: a non-invasive follow-up technique after stent-assisted coil embolization of the intracranial aneurysm.** *Korean J Radiol* 2011;12:662–70 CrossRef Medline
18. Kanda T, Ishii K, Kawaguchi H, et al. **High signal intensity in the dentate nucleus and globus pallidus on unenhanced T1-weighted MR images: relationship with increasing cumulative dose of a gadolinium-based contrast material.** *Radiology* 2014;270:834–41 CrossRef Medline
19. Alibek S, Vogel M, Sun W, et al. **Acoustic noise reduction in MRI using Silent Scan: an initial experience.** *Diagn Interv Radiol* 2014;20: 360–63 CrossRef Medline
20. Irie R, Suzuki M, Yamamoto M, et al. **Assessing blood flow in an intracranial stent: a feasibility study of MR angiography using a silent scan after stent-assisted coil embolization for anterior circulation aneurysms.** *AJNR Am J Neuroradiol* 2015;36:967–70 CrossRef Medline
21. Gönner F, Heid O, Remonda L, et al. **MR angiography with ultrashort echo time in cerebral aneurysms treated with Guglielmi detachable coils.** *AJNR Am J Neuroradiol* 1998;19:1324–28 Medline
22. Yamada N, Hayashi K, Murao K, et al. **Time-of-flight MR angiography targeted to coiled intracranial aneurysms is more sensitive to residual flow than is digital subtraction angiography.** *AJNR Am J Neuroradiol* 2004;25:1154–57 Medline
23. Choi JW, Roh HG, Moon WJ, et al. **Optimization of MR parameters of 3D TOF-MRA for various intracranial stents at 3.0T MRI.** *Neurointervention* 2011;6:71–77 CrossRef Medline
24. Iryo Y, Hirai T, Kai Y, et al. **Intracranial dural arteriovenous fistulas: evaluation with 3-T four-dimensional MR angiography using arterial spin labeling.** *Radiology* 2014;271:193–99 CrossRef Medline
25. Koktzoglou I, Giri S, Piccini D, et al. **Arterial spin labeled carotid MR angiography: a phantom study examining the impact of technical and hemodynamic factors.** *Magn Reson Med* 2016;75:295–301 CrossRef Medline
26. Grodzki DM, Jakob PM, Heismann B. **Ultrashort echo time imaging using pointwise encoding time reduction with radial acquisition (PETRA).** *Magn Reson Med* 2012;67:510–18 CrossRef Medline

Surpass Flow Diverter for Treatment of Posterior Circulation Aneurysms

C.A. Taschner, S. Vedantham, J. de Vries, A. Biondi, J. Boogaarts, N. Sakai, P. Lylyk, I. Szikora, S. Meckel, H. Urbach, P. Kan, R. Siekmann, J. Bernardy, M.J. Gounis, and A.K. Wakhloo

ABSTRACT

BACKGROUND AND PURPOSE: Flow diverters for the treatment of posterior circulation aneurysms remain controversial. We aimed to identify factors contributing to outcome measures in patients treated with the Surpass flow diverter for aneurysms in this location.

MATERIALS AND METHODS: We conducted an observational study of 53 patients who underwent flow-diverter treatment for posterior circulation aneurysms at 15 centers. Key outcome measures were mortality, complete aneurysm occlusion, and modified Rankin Scale score at follow-up.

RESULTS: At follow-up (median, 11.3 months; interquartile range, 5.9–12.7 months), 9 patients had died, resulting in an all-cause mortality rate of 17.3% (95% CI, 7%–27.6%); 7 deaths (14%) were directly related to the procedure and none occurred in patients with a baseline mRS score of zero. After adjusting for covariates, a baseline mRS of 3–5 was more significantly ($P = .003$) associated with a higher hazard ratio for death than a baseline mRS of 0–2 (hazard ratio, 17.11; 95% CI, 2.69–109.02). After adjusting for follow-up duration, a 1-point increase in the baseline mRS was significantly ($P < .001$) associated with higher values of mRS at follow-up (odds ratio, 2.93; 95% CI, 1.79–4.79). Follow-up angiography in 44 patients (median, 11.3 months; interquartile range, 5.9–12.7 months) showed complete aneurysm occlusion in 29 (66%; 95% CI, 50.1%–79.5%).

CONCLUSIONS: Clinical results of flow-diverter treatment of posterior circulation aneurysms depend very much on patient selection. In this study, poorer outcomes were related to the treatment of aneurysms in patients with higher baseline mRS scores. Angiographic results showed a high occlusion rate for this subset of complex aneurysms.

ABBREVATIONS: BT = basilar trunk; FD = flow diverter; HR = hazard ratio; KWANOVA = Kruskal-Wallis analysis of variance; PCA = posterior cerebral artery; Q1–Q3 = quartiles 1–3; VB = vertebrobasilar

Flow diverters (FDs) have proved to be reliable tools for the treatment of complex aneurysms,[1] but their use for aneurysms in the posterior circulation remains controversial.[2-4] The large number of perforating and branching arteries of the posterior circulation potentially increases the risk in flow diversion, exposing patients to thromboembolic complications and brain stem stroke. FD treatment of giant, fusiform aneurysms of the vertebrobasilar (VB) junction or basilar trunk (BT) has been associated with high morbidity and mortality of up to 71%.[2-4]

A recent meta-analysis identified 14 studies, which reported on 225 posterior circulation aneurysms treated with FDs in 220 patients.[5] The procedure-related good outcome rate was 79% (95% confidence interval, 72%–84%), and the procedure-related mortality rate was 15% (95% CI, 10%–21%). Most studies in-

Received August 3, 2016; accepted after revision October 11.

From the Department of Neuroradiology (C.A.T., S.M., H.U., J.B.), Medical Centre–University of Freiburg, Freiburg, Germany; Department of Radiology (S.V.), New England Center for Stroke Research (M.J.G.), and Division of Neuroimaging and Intervention (A.K.W.), Departments of Radiology, Neurology, and Neurosurgery, University of Massachusetts Medical School, Worcester, Massachusetts; Department of Neurosurgery (J.d.V., J.B.), Radboud University Nijmegen Medical Center, Nijmegen, the Netherlands; Department of Neuroradiology and Endovascular Therapy (A.B.), University of Besançon, Besançon, France; Department of Neurosurgery (N.S.), Kobe City Medical Center General Hospital, Kobe, Japan; Department of Neurosurgery (P.L.), Equipo de Neurocirugía Endovascular Radiología Intervencionista, Buenos Aires, Argentina; National Institute of Neurosciences (I.S.), Budapest, Hungary; Department of Neurosurgery (P.K.), Baylor College of Medicine, Houston, Texas; and Department of Neuroradiology (R.S.), Klinikum Kassel, Kassel, Germany.

We obtained a travel grant for monitoring visits from Stryker Neurovascular ($1100).

Trial Registration: http://www.germanctr.de. Unique identifier: DRKS00006881.

Preliminary data from this study were presented at: Anatomy, Biology, Clinical Correlations - Working Group in Interventional Neuroradiology (ABC-WIN) Seminar, January 18–23, 2015; Val d'Isère, France; the American Society of Neuroradiology Annual Meeting and the Foundtion of the ASNR Symposium, April 25–30, 2015; Chicago, Illinois; and the Annual Meeting of the German Society of Neuroradiology, October 15–17, 2015; Cologne, Germany.

Please address correspondence to Christian A. Taschner, MD, Department of Neuroradiology; Medical Center–University of Freiburg, Breisacherstr 64, D-79106 Freiburg, Germany; e-mail: christian.taschner@uniklinik-freiburg.de

Indicates open access to non-subscribers at www.ajnr.org

Indicates article with supplemental on-line tables.

http://dx.doi.org/10.3174/ajnr.A5029

cluded only a small number of patients (median, 9.5; range, 5–55), and most of these patients (155/220) were treated with the Pipeline Embolization Device (Covidien, Irvine, California).

The Surpass FD (Stryker Neurovascular, Fremont, California) has various features that seem to predetermine its use in the posterior circulation: 1) The maximum length of 50 mm allows aneurysm treatment with a single device, thus avoiding telescoping; 2) due to the rhomboid shape of the FD cells, the flow-diverting effect remains constant in tapered vessels. The rhomboid shape allows a consistent cell shape across a wide range of vessel diameters. Specifically, this feature enables consistent porosity and pore density along the length of the implant in a tapering vessel. These are known variables that contribute to flow diversion and thrombosis of the aneurysm.

On the other hand, the Surpass FD has a particularly high mesh density compared with the Pipeline Embolization Device, potentially increasing the risk of perforator strokes.[6] The purpose of this study was to identify factors contributing to outcome measures in patients treated with the Surpass FD for aneurysms located in the posterior circulation.

MATERIALS AND METHODS

Study Design and Participants

This multicenter, retrospective, observational study was approved by the appropriate ethics committee of the lead institution (Faculty of Medicine, University of Freiburg) and was registered in the German Clinical Trials Register (DRKS-ID: DRKS00006881). In Europe, patients were treated with the Surpass FD after it received approval for distribution by the Notified Body (CE Mark); outside Europe, patients were treated under a compassionate use protocol. Patients were entered prospectively into a data base if they had a posterior circulation aneurysm for which treatment was attempted with the Surpass FD. The design and technical specifications of the Surpass FD have been detailed elsewhere.[7] Interventional procedures with the Surpass FD were performed in accordance with local institutional guidelines at each participating center. Before the procedure, each patient was given dual antiplatelet therapy. When possible, this consisted of clopidogrel, 75 mg, and aspirin, 325 mg, for 5 days. In the acute setting, patients were routinely given a loading dose of clopidogrel, 600 mg, and aspirin, 325 mg, the night before the operation.

Patient demographics and aneurysm characteristics were obtained from medical charts. Technical success, complications, clinical outcome, and imaging follow-up were determined.

Data Collection

Collected data included age, sex, modified Rankin Scale score at baseline, aneurysm location, aneurysm size (height, width, and depth) and morphology, neck diameter (in fusiform aneurysms, the length of the affected vessel segment was considered the aneurysm neck), previous treatment attempts, rupture status, number of FDs, additional coiling, procedural complications, new neurologic deficits 24 hours posttreatment, mRS score at discharge, mRS score at last clinical follow-up, duration of clinical follow-up (months), angiographic evaluation of aneurysm occlusion by using Kamran or Raymond scores, time point of angiographic follow-up, and date of death (if applicable). Aneurysm location was defined as a categoric variable representing the VB junction, BT, V4, and posterior cerebral artery (PCA).

Data were missing for age and sex in 1 patient; aneurysm size, in another patient; and neck diameter, in 4 patients. Two patients died before discharge, and 2 died after discharge (mRS scores at discharge: 1 and 5) and before the first follow-up. Of the remaining 48 patients, angiographic follow-up was available for 44.

Outcomes

Clinical outcomes were graded according to the mRS at baseline (presentation), discharge, and follow-up.[8] The primary safety and effectiveness measures were mortality and angiographic evidence of complete occlusion at the median follow-up of approximately 12 months, respectively. The secondary outcome measures were procedural complications, new neurologic deficits at 24 hours following the procedure, mRS score at hospital discharge, and morbidity defined as an mRS score of 3–5 at clinical follow-up.

Statistical Methods

Outcome Measures. The analyzed outcome measures listed in temporal order of assessment were procedural complications (binary), new neurologic deficit at 24 hours posttreatment (binary), mRS at discharge (ordinal), complete angiographic occlusion at last angiographic follow-up (binary), mRS at last clinical follow-up (ordinal), mortality (binary), and morbidity (binary) at last follow-up.

Data Preparation. Complete angiographic occlusion (binary) was defined as a Kamran score of 4 or a Raymond score of 1. If mortality occurred and the date of death was known, it was specified as the last follow-up date along with mRS = 6. For the 2 patients who died after hospital discharge but before follow-up, the date of death could not be determined; hence, the date of last clinical contact was pragmatically assigned as date of death along with mRS = 6.

All analyses were performed by using statistical software (SAS 9.3; SAS Institute, Cary, North Carolina). For all final analyses, effects associated with $P < .05$ were considered statistically significant. Correlations (Spearman ρ) between all variables were assessed. When appropriate, the Sidak multiple comparisons adjustment was performed. Associations between procedural factors (number of FDs, additional coiling) and patient characteristics at baseline were assessed by using appropriate nonparametric tests. Binary outcome measures at fixed time points (procedural complications, new deficits at 24 hours posttreatment) were analyzed by using logistic regression models using the Firth bias correction. Variables that were significantly correlated with each binary outcome or variables that had $P < .2$ in univariate logistic regression were included in the corresponding multivariable logistic regression model that used stepwise selection. In multivariable models, interaction among predictors was evaluated and is reported only if significant. Hosmer-Lemeshow goodness-of-fit tests were performed.

Ordinal outcomes (mRS at discharge, mRS at last clinical follow-up) were initially modeled by using ordered logistic regression, and if the proportional odds assumption could not be satisfied, generalized linear models were fit by specifying a multinomial distribution and cumulative logit-link function. Variables that were statistically correlated with the outcome measure were

included in the initial model, which was refined by sequentially excluding the variable with the highest P value, provided that the P value was $>.05$. The goodness-of-fit of the model was assessed by using the Pearson χ^2 test.

Kaplan-Meier survival analysis and the Cox proportional hazards model were used to analyze the binary outcomes (complete occlusion, mortality, and morbidity) assessed at varying time points. For continuous covariates, survival analysis was performed by categorizing at the quartiles of each variable. All covariates that exhibited $P < .1$ in Kaplan-Meier analysis were included in the Cox proportional hazards model that used stepwise selection. For Cox proportional hazards models, cumulative Martingale residuals to check the functional form for the continuous variables and a standardized score process to check the proportional hazards assumptions were performed. Kolmogorov-type supremum tests were computed with 500 simulated patterns.

RESULTS

From July 2010 through March 2015, data from 53 consecutive patients with 53 acutely ruptured or unruptured aneurysms in the posterior circulation treated with Surpass FDs at 15 centers in 8 countries were entered into the data base. In 1 patient with a saccular vertebral artery aneurysm, tortuosity of major vessels prevented FD placement. Treatment with a different FD failed, and the aneurysm was treated with stent-assisted coiling. This patient was excluded from this cohort analysis, resulting in a final dataset of 52 patients.

Baseline Characteristics

Patient demographics, clinical presentations, and aneurysm characteristics are summarized in Table 1. Of 52 patients, 20 (38%) were mRS 0, 18 (35%) were mRS 1 or 2, and 14 (27%) were mRS 3–5 at presentation. Of 52 aneurysms treated with the Surpass FD, 40 (77%) were fusiform or dissecting. Seventeen aneurysms (33%) were >20 mm. Seven patients presented with acutely ruptured aneurysms.

Figures 1 and 2 show case examples, and Fig 3 summarizes the results of the statistical analysis. The detailed results of the statistical analysis are available in On-line Tables 1–4.

Procedures

Technical success was achieved in 52/53 patients (98%); coverage of the target aneurysm consisted of 1 ($n = 35$; 67%), 2 ($n = 12$; 23%), or 3 ($n = 5$; 10%) FDs. In 15 patients (29%), aneurysms were additionally coiled. The associations between procedural factors (number of FDs, additional coiling) and patient/aneurysm characteristics are summarized in On-line Table 1. More than 1 FD was used in patients presenting with a higher baseline mRS score ($P = .013$), large aneurysm neck and size ($P < .001$), and aneurysms located at the BT or VB ($P < .001$). Additional coiling was performed in patients presenting with a larger aneurysm neck and size ($P < .002$), and the aneurysms were often located at the BT or VB ($P = .001$).

Outcome Measures

On-line Table 2 summarizes the correlations (Spearman ρ) between the outcome measures and the explanatory variables. For clarity, analyses of the outcome measures are listed in the temporal order of assessment.

Table 1: Patient data and characteristics of aneurysms treated with FD

Characteristics	
Patients (No.)	52
Aneurysms (No.)	52
Women (%)	21/52 (41%)
Mean age (range) (yr)	54 (16–79)
Presentation/indications for treatment (No.) (%)	
Incidental finding/headaches	20 (38%)
Recurrent after coiling/coiling and stenting/failed clipping	16 (31%)
Cranial nerve deficit/mass effect	14 (27%)
Stroke/transient ischemic attack	7 (13%)
Acute SAH	7 (13%)
Baseline mRS (No.)	
mRS 0	20 (38%)
mRS 1–2	18 (35%)
mRS 3–5	14 (27%)
Aneurysm size ($n = 51$) (%)	
<5 mm	4 (8%)
5–9.9 mm	13 (25%)
10–20 mm	17 (33%)
>20 mm	17 (33%)
Aneurysm neck size (mm)	
Mean (range)	17.5 ± 17.7 (2–90)
Location (No.) (%)	
V4 segment of vertebral artery	20 (38%)
VB junction	11 (21%)
BT	15 (29%)
PCA	6 (12%)
Morphology (No.) (%)	
Wide-neck saccular	12 (23%)
Fusiform/dissecting	40 (77%)
Treatment	
No. of flow diverters	1.4 ± 0.7 (range, 1–3)
No. of additional coiling	15 (29%)

Procedural Complications

Technical problems and procedural complications were encountered in 9 (17%) of 52 patients (95% CI, 8.2%–30.3%). Technical problems were the following: breakage of the pusher wire of the Surpass FD in 1 and damage of Surpass FD during positioning in 1. Procedural complications were the following: dissections along the arterial access in 3 (6%), procedural thrombus formation along the parent vessel in 2 (4%), rupture of the target aneurysm during FD placement in 1 (2%), and infarction of the medulla oblongata related to takedown of the contralateral vertebral artery in a large VB junction aneurysm in 1 (2%) (case example 2, Fig 2). Five of these patients remained clinically stable during follow-up. One patient worsened clinically (mRS 1–3, case example 1), and 3 patients died during follow-up. As seen in On-line Table 2, procedural complications were correlated with age. Procedural complications did not differ with aneurysm location ($P = .304$, Kruskal-Wallis analysis of variance [KWANOVA]). Univariate logistic regression did not identify any significant predictor ($P > .085$). Age, baseline mRS, and number of FDs were eligible for inclusion ($P < .2$) in the multivariable model (On-line Table 3). The multivariable logistic regression model did not identify any significant predictor.

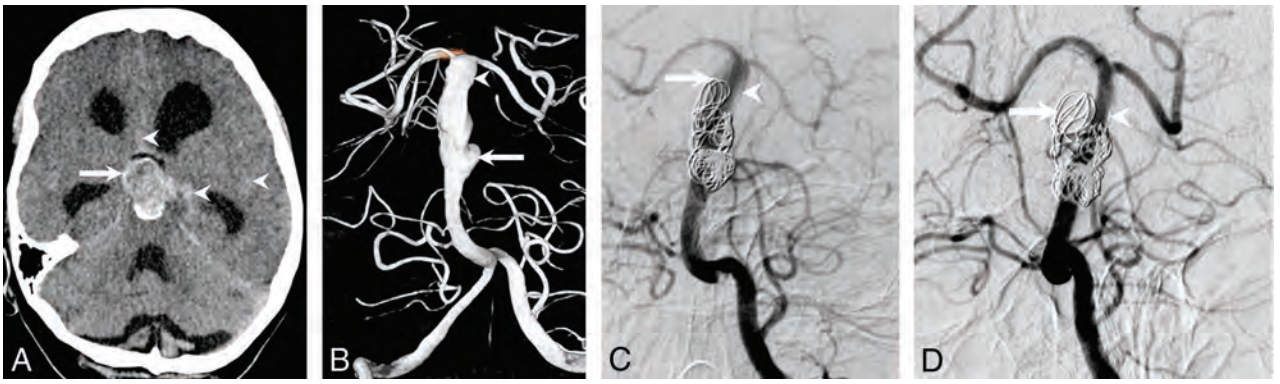

FIG 1. A 51-year-old woman presenting with Hunt and Hess grade 4 subarachnoid hemorrhage from a previously diagnosed fusiform aneurysm of the basilar trunk. *A,* Unenhanced CT scan shows diffuse SAH (*arrowheads*). The *arrow* indicates the partially thrombosed, fusiform aneurysm. *B,* The 3D reconstruction image shows a fusiform aneurysm (*arrowhead*) of the basilar artery with saccular components (*arrow*). *C,* Angiogram after placement of a Surpass FD (*arrowhead*) from the P1 segment of the right PCA to the midbasilar level. Additional coils were implanted. Note filling of the aneurysm (*arrow*). *D,* The 6-month follow-up angiogram shows complete occlusion of the aneurysm (*arrow*) and some intimal hyperplasia along the flow diverter (*arrowhead*). The mRS had changed from 2 before the SAH to 4 during follow-up. The clinical deterioration was most likely related to the SAH. No new infarcts occurred in the posterior circulation after implantation of the flow diverter.

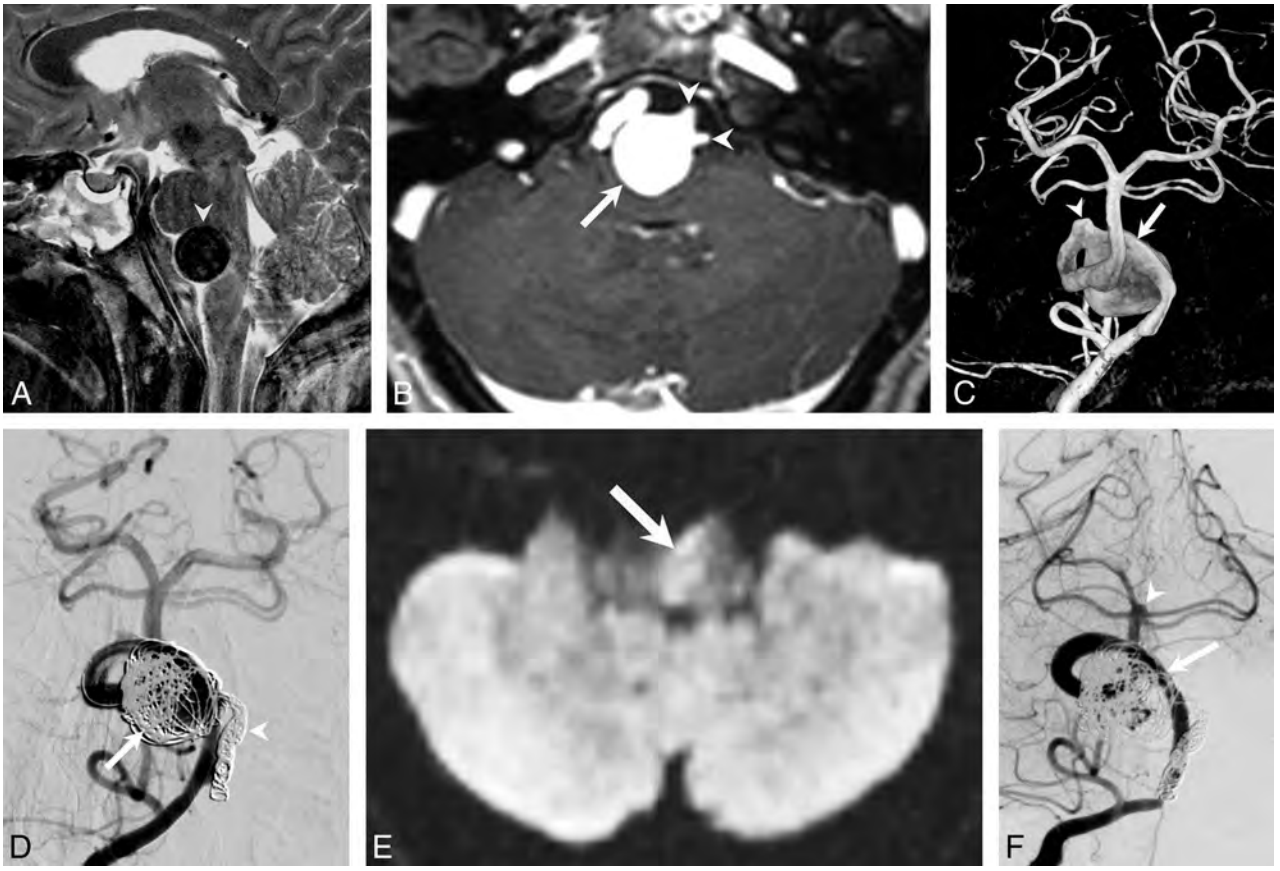

FIG 2. A 29-year-old man presenting with headaches and mild ataxia (mRS 1). *A,* Sagittal T2-weighted image shows a 32-mm vertebrobasilar junction aneurysm (*arrowhead*) compressing the medulla. *B,* Axial T1-weighted image with contrast shows the saccular aneurysm (*arrow*) and the 2 vertebral arteries (*arrowheads*) joining the aneurysm. *C,* The 3D reconstruction image shows a wide-neck (*arrow*) vertebrobasilar aneurysm with additional dysplastic segments (*arrowhead*) along the course of the basilar artery. *D,* Angiogram after placement of 2 Surpass FDs from the midbasilar level to the right vertebral artery. Additional coils were implanted (*arrow*). The distal segment of the left vertebral artery is occluded with coils (*arrowhead*). The patient was extubated 2 hours after the treatment and presented with paraplegia and respiratory insufficiency. *E,* Axial diffusion-weighted MR image (b=1000) reveals a medullar infarct (*arrow*) within the vascular territory of the left anteromedial group of medullary arteries, most likely related to the voluntary occlusion of the left vertebral artery. *F,* The 6-month follow-up angiogram shows complete occlusion of the aneurysm (*arrow*). The left posterior cerebral artery is occluded (*arrowhead*). The time-of-flight MR angiography shows good collateral filling of the left posterior cerebral artery via the left posterior communicating artery (not shown). Clinically, the patient has improved. He now presents with a mild hemiparesis, slightly slurred speech, and ataxia (mRS 3).

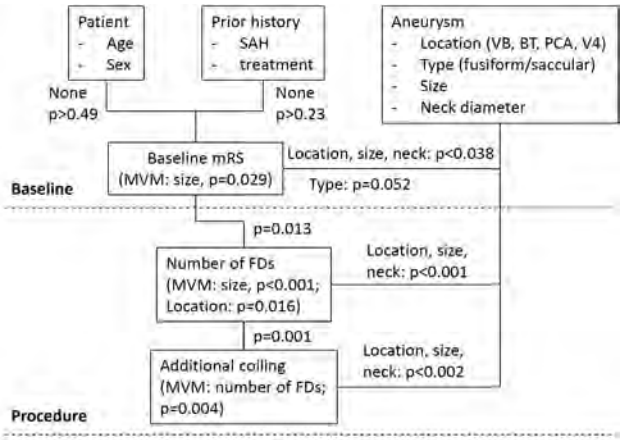

Outcomes (variables that were significant in univariate and multivariable models)

Outcomes	Univariate models	Multivariable model
Complications	None	None
New deficits at 24 hours	Aneurysm size, neck, location and baseline mRS	Baseline mRS
mRS at hospital discharge	Aneurysm size, neck, location, baseline mRS, and number of FDs	Baseline mRS and number of FDs
Complete occlusion at follow-up	None	None
mRS at clinical follow-up	Aneurysm size, neck, location, baseline mRS, and number of FDs	Baseline mRS
Mortality	Age, aneurysm size, neck, location, number of FDs, dichotomized baseline mRS (0-2 vs. 3-5)	Dichotomized baseline mRS, neck and age (marginal)

FIG 3. Summary of statistical analysis. Univariate model results are along the connecting lines; multivariate model (MVM) results are within the box.

Twenty-Four Hours Posttreatment

Fourteen (27%) of 52 patients (95% CI, 15.6%–41%) experienced new neurologic symptoms, including the aforementioned patient with intraprocedural aneurysm rupture who died. For the remaining 13 patients, new neurologic symptoms ranged from minor cranial nerve deficits to tetraparesis. In 4 patients, new neurologic symptoms were related to procedural complications. Two patients with new neurologic symptoms 24 hours posttreatment had worsened mRS scores at follow-up (1–3 and 2–4), and 7 patients from this group died during follow-up. The mRS for the remaining 5 patients was either stable or improved. No symptomatic intracranial hemorrhage was observed immediately posttreatment. New neurologic deficits were positively correlated (On-line Table 2) with baseline mRS, BT location, aneurysm size, neck diameter, and the number of FDs, and they were negatively correlated with V4 location. All of the aforementioned variables were significant ($P < .036$) in univariate logistic regression (On-line Table 3). Multivariable logistic regression identified only baseline mRS as a significant predictor ($P = .002$, On-line Table 3). The model satisfied the Hosmer-Lemeshow goodness-of-fit test ($P = .801$). A unit (1-point) increase in baseline mRS was associated with a higher likelihood for new neurologic deficits at 24 hours posttreatment (OR, 2.28; 95% CI, 1.60–3.82).

Hospitalization and Discharge

During hospitalization, another patient died following a medullary infarct. Four patients were discharged with deterioration of their clinical statuses, of which 3 were related to ischemic stroke. Another patient with a ruptured aneurysm and subarachnoid hemorrhage (Hunt and Hess grade 3) presented with clinical worsening associated with severe vasospasm. The remaining patients were either clinically stable (39/50, 78%) or had improved neurologically (7/50, 14%). The mRS score at discharge was positively correlated with baseline mRS, VB location, aneurysm size, neck diameter, and number of FDs, and it was negatively correlated with V4 location (On-line Table 2). Because the proportional odds assumption ($P < .001$) could not be satisfied, generalized linear models were used for analysis (On-line Table 4). The final model included baseline mRS ($P < .001$) and number of FDs (2 versus 1, adjusted $P = .008$) as significant predictors. The model satisfied the goodness-of-fit criterion ($P = .551$). After we adjusted for the number of FDs, a unit (1-point) increase in baseline mRS was associated with higher values of mRS at discharge (OR, 7.59; 95% CI, 3.6–15.98).

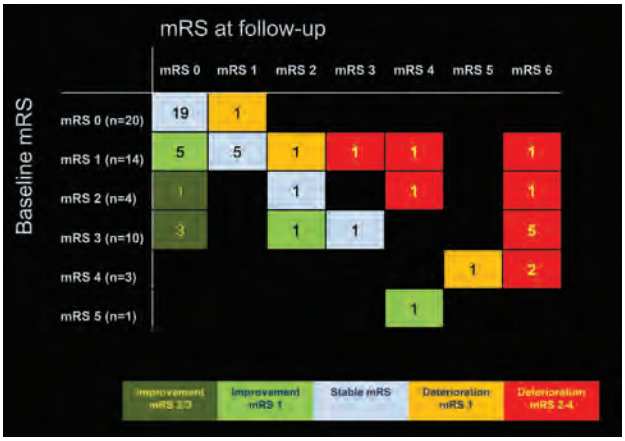

FIG 4. Shift from baseline mRS to mRS at follow-up ($n = 52$).

Complete Occlusion

Angiographic follow-up was available for 44 (92%) of 48 surviving patients; the median (quartiles 1–3, [Q1–Q3]) follow-up duration was 11.3 months (5.9–12.7 months). Complete occlusion was observed in 29 (66%; 95% CI, 50.1%–79.5%) of 44 patients and was positively correlated with prior SAH (On-line Table 2). Complete aneurysm occlusion differed with neither aneurysm location ($P = .768$, KWANOVA) nor baseline mRS ($P = .075$, KWANOVA). Neither univariate logistic regression ($P > .144$) nor Kaplan-Meier analysis ($P > .194$) identified any significant predictor.

mRS at Clinical Follow-Up

The median (Q1–Q3) follow-up duration was 11.3 months (5.9–12.7 months). Figure 4 shows the shift in mRS from baseline to follow-up. The mRS at follow-up was positively correlated with baseline mRS, VB location, aneurysm size, neck diameter, and number of FDs, and it was negatively correlated with V4 location and follow-up duration (On-line Table 2). The mRS at follow-up ($P < .009$, KWANOVA) and the difference in mRS between follow-up and baseline ($P = .008$, KWANOVA) varied with aneurysm location. Because the proportional odds assumption ($P = .001$) could not be satisfied, generalized linear models were used

Table 2: Patients with fatal outcomes[a]

Sex	Age (yr)	Baseline mRS	Location	Type	Size (mm)	No. of FDs	Cause of Death	Survival Time (days)
M	60	3	BT	Fusiform	10	1	Ischemic stroke 48 hr after FD treatment	2
M	58	4	BT	Fusiform	55	1	Rupture during placement of the FD	7
M	64	2	VB junction	Fusiform	90	1	Medullary infarct	15
M	55	3	BT	Fusiform	39	3	Stable mRS at discharge; acute brain stem infarct	50
M	57	3	VB junction	Fusiform	40	3	Stable mRS at discharge; acute gastrointestinal bleed; clopidogrel was stopped; died of urosepsis	170
M	59	4	VB junction	Saccular	55	3	Improved mRS at discharge (mRS 3); follow-up DSA at 7 months; aneurysm patent (>50%); at 8 mo, sudden clinical impairment	242
M	74	3	BT	Fusiform	28	2	Stable mRS at discharge; died of pneumonia	388
F	75	3	VB junction	Fusiform	30	2	mRS 5 at discharge to a tertiary care facility; died of pneumonia	Unknown
F	65	1	Vertebral artery	Fusiform	8	1	Stable mRS at discharge; died from complications related to brain tumor treatment	Unknown

[a] All patients had presented with unruptured aneurysms.

for analysis. The final model (On-line Table 4) included baseline mRS ($P < .001$) and follow-up duration ($P = .005$) as significant predictors and satisfied the goodness-of-fit criterion ($P = .182$). After we adjusted for follow-up duration, a unit (1-point) increase in baseline mRS was associated with higher values of mRS at follow-up (OR, 2.93; 95% CI, 1.79–4.79). If we restricted the analysis to surviving patients ($n = 43$), the baseline mRS was the only significant predictor of mRS at follow-up ($P = .002$) and a unit (1-point) increase in baseline mRS was associated with higher values of mRS at follow-up (OR, 2.53; 95% CI, 1.42–4.51). Of 7 patients with SAH, 2 had an improved mRS (1–0, 3–0), 4 had a stable mRS (0 in 3, 3 in 1), and 1 had a deteriorated mRS (2–4).

Mortality and Morbidity

The overall morbidity and mortality rate in our series was 14 of 52 (27%). Nine of 52 patients died, resulting in an all-cause mortality rate of 17% (95% CI, 7%–27.6%). Their clinical course is summarized in Table 2; the baseline mRS scores were 1 ($n = 1$), 2 ($n = 1$), 3 ($n = 5$), and 4 ($n = 2$). More important, asymptomatic patients had 5% morbidity and 0% mortality, while symptomatic patients had morbidity and mortality rates of 44% and 28%, respectively.

Mortality was positively correlated with baseline mRS, age, VB location, aneurysm size, neck diameter, and number of FDs and was negatively correlated with follow-up duration (On-line Table 2). The baseline mRS was dichotomized at 2 (inclusive) because there were no deaths in patients with baseline mRS scores of 0 and 5. Kaplan-Meier univariate analysis indicated age ($P = .018$), aneurysm size ($P = .01$), number of FDs ($P = .001$), dichotomized baseline mRS ($P = .001$), and aneurysm location ($P = .02$) as significant, with neck diameter being marginal ($P = .06$). All of the aforementioned variables were included in the Cox proportional hazards model with stepwise selection, which identified dichotomized baseline mRS ($P = .003$) and neck diameter ($P = .004$) as significant, with age being marginal ($P = .072$). Supremum tests for the functional form ($P > .358$) and the proportional hazards assumption ($P = .444$) were satisfied. After we adjusted for age and neck diameter, a baseline mRS of 3–5 was significantly ($P = .003$) associated with a higher hazard ratio (HR) for death, compared with a baseline mRS of 0–2 (HR, 17.11; 95% CI, 2.69–109.02). During a median (Q1–Q3) follow-up of 11.6 months (5.9–13.3 months), 2 (5.3%) of 38 patients with baseline mRS scores of 0–2 and 7 (50%) of 14 patients with baseline mRS of 3–5 died. Among the surviving patients, the median (Q1–Q3) follow-up durations were 11.7 months (8.5–12 months) and 11.9 months (8.6–14.6 months) for baseline mRS scores of 3–5 and 0–2, respectively. Longer follow-up of patients in this cohort is needed to estimate survival times. Among the 43 patients surviving at the last follow-up, 6 had mRS ≥ 3, resulting in a morbidity rate of 14% (95% CI, 3.6%–24.3%). Of the 6 surviving subjects with mRS 3–5 at follow-up, 3 worsened from the baseline mRS (1→3, 1→4, and 2→4), 2 were stable (3→3 and 4→4), and 1 subject showed improvement (5→3). None of the subjects with a baseline mRS of zero had mRS 3–5 at follow-up. Of the 38 subjects with a baseline mRS of <3 and excluding the 2 mortality events, the morbidity rate was 8.3% (3/36). Of the 14 subjects with baseline mRS scores of 3–5, there were 7 deaths and 3/7 (43%) surviving subjects had mRS scores of 3–5 at follow-up. Because only 6 patients had mRS ≥3 at follow-up, statistical analysis was not pursued.

DISCUSSION

To the best of our knowledge, this is the largest study to date to report exclusively on FD treatment of posterior circulation aneurysms.

The overall morbidity and mortality rate in our series was 27%. Most important, asymptomatic patients had 5% morbidity and 0% mortality, while symptomatic patients had morbidity and mortality rates of 44% and 28%, respectively. A recent meta-analysis on flow-diverter treatment of posterior circulation aneurysms, including 220 patients with 225 posterior circulation aneurysms, reported morbidity and mortality rates of 6% and 15%, respectively.[5] The morbidity and mortality rates reported in the underlying studies ranged from 0% to 71% and 0% to 57%, respectively. The variability in outcomes clearly reflects the heterogeneity of the underlying pathology.

Most posterior circulation aneurysms treated in our series were fusiform or saccular sidewall aneurysms and most likely dissecting aneurysms. Mizutani et al[9] proposed a comprehensive classification of dissecting aneurysms. Type 1 corresponds to classic acute dissecting aneurysms, the pathogenesis of which is char-

acterized by acute widespread disruption of the internal elastic lamina without intimal thickening. These aneurysms often have an ominous course with SAH. Type 2 aneurysms are segmental ectasias that have an extended or fragmented internal elastic lamina with intimal thickening. The luminal surface of the thickened intima is smooth without thrombus formation, and these aneurysms most often are located within the distal vertebral artery. Type 3 aneurysms are dolichoectatic dissecting aneurysms, pathologically characterized by fragmentation of the internal elastic lamina, multiple dissections of thickened intima, and organized thrombus in the lumen. Most of these lesions are symptomatic and progressively enlarge with time.[9]

For treatment of acutely ruptured type 1 aneurysms of the posterior circulation, stent-assisted coiling has become the treatment of choice.[10] There is sparse literature on the use of FDs in this clinical setting. In our study, FDs alone and FDs in combination with coils resulted in acceptable clinical outcomes.

Patients with type 2 aneurysms are often asymptomatic at presentation. In our series, we observed no stroke-related symptoms related to FD treatment in this subset of patients, though a large number of perforating arteries were covered by the Surpass FD—a device with the highest mesh density available on the market.[6] The clinical outcome was comparable with that of FD treatment of aneurysms in the anterior circulation.[1] The notion that an increased risk of perforator occlusion in the posterior circulation may warrant caution in the use of FDs is not supported in this particular indication. In those cases in which perforators are directly covered by FD stents, those perforators most likely remain open. FDs seem to be a reasonably safe and effective treatment for type 2 aneurysms. There is some evidence that acute intervention is not always required, and close follow-up with antithrombotic therapy is a reasonable option.[11-13] Yet, we lack greater knowledge on the clinical course of these potentially benign vascular lesions; this issue complicates any meaningful risk-benefit analysis of FD treatment in this clinical setting.

The high morbidity and mortality rates in our series were related to the treatment of patients with symptomatic type 3 aneurysms. These aneurysms are typically located at the level of the VB junction or the basilar trunk. In these large fusiform aneurysms that often present with a mural hematoma, perforators are displaced laterally and are at a distance from the FD device; this scenario results in eventual perforator occlusion. In addition, multiple overlapping devices may have a detrimental effect on incidentally covered small perforators.[2] The results of our study and the review of the scarce literature illustrate the challenge of FD treatment of posterior circulation aneurysms. Type 3 aneurysms in the posterior circulation commonly are symptomatic due to ischemic strokes or may be diagnosed due to cranial nerve palsy, brain stem compression, obstructive hydrocephalus, SAH, or hemorrhages into the vessel wall. If left untreated, the natural history of these aneurysms is poor, with mortality rates between 23% and 35% in 5 years.[14,15] Mortality increases significantly to 80% for untreated giant aneurysms in the posterior circulation.[16] FD treatment in this setting, however, has a high risk of permanent morbidity and mortality, as our study demonstrates. It remains debatable whether intervention with an FD offers an improvement over the natural history of these lesions.[17] In a small subset of patients with asymptomatic type 3 aneurysms (fusiform, located at the VB junction or basilar trunk, ± the presence of an intramural hematoma) clinical results were surprisingly good.

It has been common practice to refrain from treating patients with large, fusiform, or partially thrombosed aneurysms in the posterior circulation as long as they are asymptomatic. Patients are often told to return for treatment only when they become symptomatic. Our analysis indicates that it may be safer to offer these particular patients early treatment. When treating these lesions, FD systems with longer single implants may be more advantageous than using multiple telescoping devices. In univariate analyses, our study showed that an increasing number of FDs was associated with poorer outcomes, including new neurologic deficits at 24 hours, higher mRS at follow-up, and mortality, but not in multivariable analyses. Patients treated with an increasing number of FDs presented with a higher baseline mRS score and larger aneurysm dimensions (On-line Table 1), and these baseline patient and aneurysm characteristics were contributors to poorer outcomes in multivariable analyses. Also, additional coiling was performed in patients presenting with larger aneurysm dimensions, and they were treated with >1 FD (On-line Table 1). These factors contribute to the observed results in multivariable analyses. Finally, the importance of adequate and long-term dual antiplatelet therapy has already been discussed in previous publications and cannot be emphasized enough.[2,17]

The angiographic complete occlusion rate in our series of 66% (29/44 cases; 95% CI, 50.1%–79.5%) had overlapping 95% confidence intervals with the meta-analysis of Wang et al[5] (84%; 95% CI, 68%–94%). Any differences might be explained by the higher rates of giant and fusiform aneurysms in our patient cohort, with 33% versus 23% and 77% versus 66%, respectively.[5]

Our study has various inherent limitations. It was designed as an international multicenter study in which patient selection was heterogeneous. Monitoring the dual antiplatelet therapy response was not standard procedure in all of the participating centers. Clinical and angiographic end points were self-reported by the institutions. In mRS at follow-up, we might have missed ischemic events related to FD treatment that did not lead to a deterioration of mRS score.

CONCLUSIONS

The mortality rate was comparable with that in prior studies, and angiographic results showed a high occlusion rate for this subset of complex aneurysms. Clinical results of FD treatment depend very much on patient selection, with poorer outcomes related to the treatment of aneurysms in patients with higher baseline mRS scores.

ACKNOWLEDGMENTS

The authors thank Mrs Dagmar Schnau for her invaluable assistance in editing and reviewing this manuscript.

Disclosures: Christian A. Taschner—*RELATED*: *Consulting Fee or Honorarium*: Stryker; *UNRELATED*: *Consultancy*: Acandis, Neuravi; *Grants/Grants Pending*: MicroVention, Acandis.* Joost de Vries—*UNRELATED*: *Consultancy*: Stryker Neurovascular; *Grants/Grants Pending*: Stryker Neurovascular; *Payment for Development of Educational Presentations*: Stryker Neurovascular; *Travel/Accommodations/Meeting Expenses Unrelated to Activities Listed*: Stryker Neurovascular. Nobuyuki Sakai—*UNRELATED*: *Grants/Grants Pending*: Terumo, *Comments*: modest*; *Pay-*

ment for Lectures including Service on Speakers Bureaus: Achieve, BioMedical Solutions, Codman Neuro, Medtronic, MicroVention/Terumo, Penumbra, Stryker Neurovascular, *Comments*: modest. Pedro Lylyk—*UNRELATED*: *Travel/Accommodations/Meeting Expenses Unrelated to Activities Listed*: Surpass, Covidien, phenox, Cardiatis. Istvan Szikora—*UNRELATED*: *Consultancy*: Stryker Neurovascular, Codman Neuro, Medtronic, Sequent Medical. Stephan Meckel—*UNRELATED*: *Board Membership*: Acandis, *Comments*: consultancy and honoraria as member of the Scientific Advisory Board; *Travel/Accommodations/Meeting Expenses Unrelated to Activities Listed*: Covidien/Medtronic, MicroVention, Stryker Neurovascular, Acandis. Peter Kan—*UNRELATED*: *Consultancy*: consultant for Stryker Neurovascular. Matthew J. Gounis—*RELATED*: *Grant*: Stryker Neurovascular*; *Consulting Fee or Honorarium*: Stryker Neurovascular; *UNRELATED*: *Consultancy*: Codman Neuro; *Expert Testimony*: Harris Beach PLLC; *Grants/Grants Pending*: National Institutes of Health, Asahi, Blockade Medical, CereVasc LLC, Codman Neuro, Cook Medical, Gentuity LLC, Fraunhofer Society, InNeuroCo Inc, Lazarus Effect, Medtronic Neurovascular, MicroVention/Terumo, Neuravi, Philips Healthcare, Stryker Neurovascular, Wyss Institute*; *Stock/Stock Options*: InNeuroCo. *Money paid to the institution.

REFERENCES

1. Brinjikji W, Murad MH, Lanzino G, et al. **Endovascular treatment of intracranial aneurysms with flow diverters: a meta-analysis.** *Stroke* 2013;44:442–47 CrossRef Medline
2. Siddiqui AH, Abla AA, Kan P, et al. **Panacea or problem: flow diverters in the treatment of symptomatic large or giant fusiform vertebrobasilar aneurysms.** *J Neurosurg* 2012;116:1258–66 CrossRef Medline
3. Meckel S, McAuliffe W, Fiorella D, et al. **Endovascular treatment of complex aneurysms at the vertebrobasilar junction with flow-diverting stents: initial experience.** *Neurosurgery* 2013;73:386–94 CrossRef Medline
4. Ertl L, Holtmannspötter M, Patzig M, et al. **Use of flow-diverting devices in fusiform vertebrobasilar giant aneurysms: a report on periprocedural course and long-term follow-up.** *AJNR Am J Neuroradiol* 2014;35:1346–52 CrossRef Medline
5. Wang CB, Shi WW, Zhang GX, et al. **Flow diverter treatment of posterior circulation aneurysms: a meta-analysis.** *Neuroradiology* 2016;58:391–400 CrossRef Medline
6. Lieber BB, Sadasivan C. **Endoluminal scaffolds for vascular reconstruction and exclusion of aneurysms from the cerebral circulation.** *Stroke* 2010;41(10 suppl):S21–25 CrossRef Medline
7. Wakhloo AK, Lylyk P, de Vries J, et al; Surpass Study Group. **Surpass flow diverter in the treatment of intracranial aneurysms: a prospective multicenter study.** *AJNR Am J Neuroradiol* 2015;36:98–107 CrossRef Medline
8. Bonita R, Beaglehole R. **Recovery of motor function after stroke.** *Stroke* 1988;19:1497–500 CrossRef Medline
9. Mizutani T, Miki Y, Kojima H, Suzuki H. **Proposed classification of nonatherosclerotic cerebral fusiform and dissecting aneurysms.** *Neurosurgery* 1999;45:253–59; discussion 259–60 CrossRef Medline
10. Nam KH, Ko JK, Cha SH, et al. **Endovascular treatment of acute intracranial vertebral artery dissection: long-term follow-up results of internal trapping and reconstructive treatment using coils and stents.** *J Neurointerv Surg* 2015;7:829–34 CrossRef Medline
11. Kai Y, Nishi T, Watanabe M, et al. **Strategy for treating unruptured vertebral artery dissecting aneurysms.** *Neurosurgery* 2011;69:1085–91; discussion 1091–92 CrossRef
12. Shapiro M, Becske T, Riina HA, et al. **Non-saccular vertebrobasilar aneurysms and dolichoectasia: a systematic literature review.** *J Neurointerv Surg* 2014;6:389–93 CrossRef Medline
13. Kobayashi N, Murayama Y, Yuki I, et al. **Natural course of dissecting vertebrobasilar artery aneurysms without stroke.** *AJNR Am J Neuroradiol* 2014;35:1371–75 CrossRef Medline
14. Echiverri HC, Rubino FA, Gupta SR, et al. **Fusiform aneurysm of the vertebrobasilar arterial system.** *Stroke* 1989;20:1741–47 CrossRef Medline
15. Flemming KD, Wiebers DO, Brown RD Jr, et al. **The natural history of radiographically defined vertebrobasilar nonsaccular intracranial aneurysms.** *Cerebrovasc Dis* 2005;20:270–79 CrossRef Medline
16. Steinberg GK, Drake CG, Peerless SJ. **Deliberate basilar or vertebral artery occlusion in the treatment of intracranial aneurysms: immediate results and long-term outcome in 201 patients.** *J Neurosurg* 1993;79:161–73 CrossRef Medline
17. Toth G, Bain M, Hussain MS, et al. **Posterior circulation flow diversion: a single-center experience and literature review.** *J Neurointerv Surg* 2015;7:574–83 CrossRef Medline

Flow Diversion in Ruptured Intracranial Aneurysms: A Meta-Analysis

T.P. Madaelil, C.J. Moran, D.T. Cross III, and A.P. Kansagra

ABSTRACT

BACKGROUND: Flow diversion is now an established technique to treat unruptured intracranial aneurysms not readily amenable to endovascular coil embolization or open microsurgical occlusion. The role of flow-diverting devices in treating ruptured aneurysms is less clear.

PURPOSE: To estimate rates of angiographic occlusion and good clinical outcome in patients with ruptured intracranial aneurysms treated with flow-diverting devices.

DATA SOURCES: Systematic review of Ovid MEDLINE, PubMed, Cochrane databases, and EMBASE from inception to December 2015 for articles that included ruptured aneurysms treated with flow diversion.

STUDY SELECTION: One hundred seventy-two records were screened, of which 20 articles contained sufficient patient and outcome data for inclusion.

DATA ANALYSIS: Clinical and radiologic characteristics, procedural details, and outcomes were extracted from these reports. Aggregated occlusion rates and clinical outcomes were analyzed by using the Fisher exact test (statistical significance, $\alpha = .05$).

DATA SYNTHESIS: Complete occlusion of the aneurysm was achieved in 90% of patients, and favorable clinical outcome was attained in 81%. Aneurysm size greater than 7 mm was associated with less favorable clinical outcomes ($P = .027$). Aneurysm size greater than 2 cm was associated with a greater risk of rerupture after treatment ($P < .001$).

LIMITATIONS: Observational studies and case reports may be affected by reporting bias.

CONCLUSIONS: Although not recommended as a first-line treatment, the use of flow diverters to treat ruptured intracranial aneurysms may allow high rates of angiographic occlusion and good clinical outcome in carefully selected patients. Aneurysm size contributes to treatment risk because the rerupture rate following treatment is higher for aneurysms larger than 2 cm.

ABBREVIATIONS: FD = flow diverter; GOS = Glasgow Outcome Scale

Endovascular treatment of intracranial aneurysms with detachable coils was first described in 1991[1] and has since become an established method of aneurysm treatment. The International Study of Unruptured Intracranial Aneurysms[2] and Analysis of Treatment by Endovascular Approach of Nonruptured Aneurysms (ATENA)[3] demonstrated the effectiveness and relative safety of endovascular coiling for unruptured aneurysms. Similarly, the International Subarachnoid Aneurysm Trial (ISAT), the Barrow Ruptured Aneurysm Trial, and other trials[4-7] have demonstrated the effectiveness and relative safety of endovascular coiling in ruptured aneurysms.

In recent years, flow diverters (FDs) have emerged as a new endovascular treatment option for intracranial aneurysms. FDs are a reconstructive treatment in which altered flow within an aneurysm induces gradual remodeling and eventual thrombosis of the aneurysm. Several studies have demonstrated good safety and efficacy of FDs for the treatment of unruptured intracranial aneurysms,[8-17] though the safe use of these devices requires the use of dual antiplatelet therapy.[18-20]

Understandably, the need for antiplatelet medications and the delayed nature of aneurysm thrombosis have tempered en-

Received August 11, 2016; accepted after revision October 11.

From the Mallinckrodt Institute of Radiology (T.P.M., C.J.M., D.T.C., A.P.K.) and Department of Neurosurgery (C.J.M., D.T.C., A.P.K.), Washington University School of Medicine, St. Louis, Missouri.

Please address correspondence to Thomas P. Madaelil, MD, Mallinckrodt Institute of Radiology, Washington University School of Medicine, 510 South Kingshighway Blvd, St. Louis, MO 63110; e-mail: madaelilt@mir.wustl.edu; @AkashKansagra

Indicates article with supplemental on-line table.

http://dx.doi.org/10.3174/ajnr.A5030

thusiasm for using FDs for ruptured aneurysms. Nevertheless, several reports have described the use of FDs to treat recently ruptured aneurysms, particularly those that are difficult to treat by other endovascular or open microsurgical techniques.

In this meta-analysis, we review the outcomes associated with the use of FDs for the treatment of ruptured intracranial aneurysms. Specifically, we review aneurysm characteristics and endovascular treatment strategies in relation to the rates of angiographic occlusion and good clinical outcome, with the overall goal of guiding FD use in ruptured aneurysms when other treatment options are not viable.

MATERIALS AND METHODS

Literature Search

Systematic review of Ovid Medline, PubMed, the Cochrane Central Register of Controlled Trials, the Cochrane Database of Systemic Reviews, and EMBASE from inception to December 2015 was performed by using the terms "rupture" and "aneurysm" in all permutations with "pipeline embolization," "flow diversion," or "flow diverting stent." The search was restricted to human studies in English. Bibliographies of all studies were also reviewed to identify additional relevant studies.

Eligibility Criteria

All titles and abstracts were screened for eligibility. Studies that provided patient-level information regarding clinical presentation of subarachnoid hemorrhage, aneurysm characteristics, procedural details, periprocedural complications, occlusion status, and clinical status at last follow-up were deemed eligible. If studies included treatment of both ruptured and unruptured aneurysms, only the information from ruptured aneurysms was included.

Data Synthesis and Analysis

Following eligibility verification, data were extracted from the manuscript text, patient demographic tables and on-line tables, and figures. These data were entered into a predefined digitized form according to the Preferred Reporting Items for Systematic Reviews and Meta-Analyses: The PRISMA Statement. These data points included patient characteristics of age, sex, and clinical status at admission (Hunt and Hess scale/World Federation of Neurosurgical Societies score, and the Fisher scale); aneurysm characteristics, including type, size, and location; procedural details such as time to treatment and devices used, including the type of FD and adjunctive devices (eg, coils) used before or during FD placement; and outcomes, including periprocedural complications, aneurysmal occlusion status, clinical outcome, and duration of both clinical and angiographic follow-up. Time to treatment was classified as acute if FD placement occurred within 15 days of initial SAH and delayed otherwise. The clinical score at presentation was classified as good for Hunt and Hess/World Federation of Neurosurgical Societies scores of 1–3 and poor for scores of 4–5.[21] Clinical outcome was classified by the Glasgow Outcome Scale (GOS) or mRS at last clinical follow-up. Favorable clinical outcome was defined as GOS = 4–5 or mRS = 0–2, and unfavorable clinical outcomes corresponded to GOS = 1–3 or mRS = 3–6.

Data for each patient were analyzed as if all patients belonged to a single cohort.[22] The association among demographic and clinical risk factors, periprocedural complication rate, occlusion rate based on device selection, and favorable outcome was evaluated by using the Fisher exact and 2-tailed t tests for categorical and continuous variables, respectively. Data are reported as simple proportions. The threshold of statistical significance was $\alpha = .05$. All statistical analyses were performed by using SPSS, Version 22 (IBM, Armonk, New York) and Excel 2007 (Microsoft, Redmond, Washington).

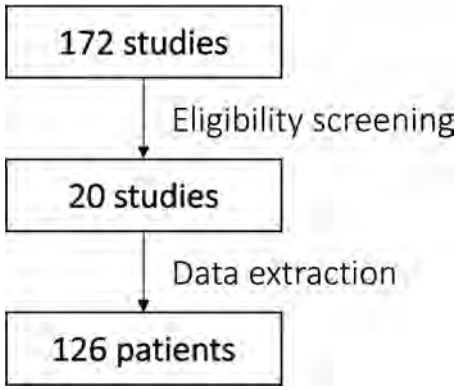

FIG 1. Simplified flowchart of literature search strategy.

RESULTS

Studies and Aneurysm Characteristics

The initial electronic search yielded 172 records (Fig 1). Large observational studies that shared institutional data bases with smaller reported case series were excluded to prevent case duplication. Studies that did not report individual patient data points were also excluded. Ultimately, 20 observational studies and case reports representing 126 distinct cases met the inclusion criteria (Online Table).

Median age was 51 years (interquartile range, 45–60 years), and 71% of patients were women. The median Hunt Hess/World Federation of Neurosurgical Societies grading scale at presentation was 2 (interquartile range, 1–3). The median aneurysm size was 3.5 mm (interquartile range, 2.3–10 mm). Five distinct aneurysm morphologies were present, including dissecting (28%, 35/125), fusiform (10%, 12/125), giant (3%, 4/125), blister (38%, 47/125), and saccular (22%, 27/125) types. Treated aneurysms were located in the anterior circulation in 64% (81/126) of cases, and 36% (45/126) were in the posterior circulation.

Treatment

In total, 67% of cases (84/126) specified the timing of treatment, with an average time to treatment of 9.6 days (range, 0–60 days); 74% (62/84) were treated in the acute phase, and 26% (22/84), in a delayed fashion. The Pipeline Embolization Device (Covidien, Irvine, California) was used for FD-based treatment in 96% (121/126) of cases, while the Silk flow diverter (Balt Extrusion, Montmorency, France) was used in the remaining 4% (5/126) of cases. Seventy-three percent (92/126) of aneurysms were treated with FD placement only, while 27% (34/126) were treated with a combination of an FD and adjunctive coils. These included 4 cases in which FD-based treatment was implemented after initial unsuccessful treatment with microsurgical clipping or stent-assisted

Table 1: Angiographic outcomes following flow diversion in ruptured intracranial aneurysms[a]

Angiographic Occlusion	FD		FD and Coils		Total	
	Complete	Incomplete	Complete	Incomplete	Complete	Incomplete
Overall	74	4	23	7	97	11
Size						
Aneurysm <7 mm	44	3	10	1	54	4
Aneurysm >7 mm	10	1	12	5	22	6
Treatment timing						
Acute treatment	38	3	11	1	49	4
Delayed treatment	5	0	10	5	15	5
Clinical score						
Good clinical score	47	2	19	5	66	7
Poor clinical score	8	1	5	1	13	2
Location						
Anterior circulation	33	2	16	1	49	3
Posterior circulation	25	2	7	5	32	7
Type						
Dissecting	18	2	8	1	26	3
Fusiform	5	0	3	2	8	2
Blister	27	1	7	1	34	2
Saccular	7	1	7	3	14	4
Giant	1	0	0	0	1	0

[a] Data are numbers.

coiling.[23-25] An FD and coils were placed in a single session in 56% (19/34) of cases. The average size of aneurysms treated with an FD alone was 5.6 ± 6.4 mm, which was significantly smaller than the 10.6 ± 6.4 mm average size of aneurysms treated with an FD and adjunctive coiling ($P = .001$).

Complications

Aneurysm rerupture occurred following FD placement in 5% (6/126) of aneurysms, with 67% (4/6) of these reruptures occurring in aneurysms measuring >2 cm.[24-28] The rate of rerupture following FD placement in aneurysms of >2 cm was 57% (4/7), which was significantly greater than the 2% (2/94) rate of rerupture in aneurysms of <2 cm ($P < .001$). The rate of aneurysm rerupture with an FD alone was 6% (5/80), which was comparable with the 3% (1/32) rate following FD and adjunctive coiling ($P = .672$). Among reruptured aneurysms of >2 cm, 75% (3/4) were treated with an FD and adjunctive coiling, while 25% (1/4) were treated with an FD alone. Among all aneurysms that reruptured, 67% (4/6) occurred during or within the first 24 hours of treatment. No aneurysms reruptured at >1week after treatment.

Hemorrhagic complications not related to aneurysm rerupture occurred in 4% (5/126) of patients. One was an asymptomatic cerebellar hemorrhage,[25] and 2 were related to external ventricular drain placement.[26,29] Two fatal hemorrhagic complications occurred, including 1 after intra-arterial tPA instillation through a microcatheter for intraprocedural thrombosis of the FD and 1 related to postprocedural hemorrhage distant from the treated aneurysm.[26,29] Ischemic complications occurred in 5% (5/111) of patients, of whom 4% (4/111) were symptomatic, including 1 case with fatal brain stem ischemia.[26]

Overall, the composite rate of hemorrhagic or ischemic complications was 12% (15/126) because 2 complications occurred in 1 patient.[25] This rate was 16% (10/62) in patients treated in the acute phase, compared with 0% (0/22) in patients treated in a delayed fashion ($P = .057$).

Angiographic Outcomes

Complete occlusion of the aneurysm was achieved in 90% (97/108) of patients on follow-up imaging (Table 1), with a median angiographic follow-up of 6 months (interquartile range, 5–6 months). Patients with a good clinical score on presentation had an occlusion rate of 90% (66/73), compared with patients with a poor presenting clinical score, with an occlusion rate of 87% (13/15) ($P = .647$). Aneurysms in the anterior circulation demonstrated complete occlusion in 94% (49/52) of cases, which was comparable with the 82% (32/39) rate for aneurysms in the posterior circulation ($P = .092$). Aneurysms treated acutely demonstrated complete occlusion in 92% (49/53) of cases, compared with 75% (15/20) for aneurysms treated in a delayed fashion ($P = .103$).

Complete occlusion was achieved in 93% (54/58) of aneurysms of <7 mm, compared with 79% (22/28) for aneurysms of >7 mm ($P = .072$). In aneurysms of <7 mm, treatment with an FD alone resulted in complete occlusion of 94% (44/47) of aneurysms, compared with 91% (10/11) when treated with an FD and adjunctive coiling ($P = 1.000$). In aneurysms of >7 mm, treatment with an FD alone resulted in complete occlusion of 91% (10/11) of aneurysms, compared with 71% (12/17) when treated with FD and adjunctive coiling ($P = .355$).

Clinical Outcomes

At last clinical follow-up, there was a favorable clinical outcome in 81% (101/124) of treated patients and an unfavorable clinical outcome in 19% (23/124) (Table 2), with a median clinical follow-up of 6 months (interquartile range, 5–10 months). In patients with a good presenting clinical score, favorable clinical outcome was 84% (70/83), compared with a 67% (10/15) rate of favorable clinical outcome in patients with poor presenting clinical scores ($P = .143$). Favorable clinical outcome was observed in 79% (49/62) of patients treated in the acute phase, compared with 88% (15/17) of patients treated in a delayed fashion ($P = .503$). Favorable clinical

Table 2: Clinical outcomes following flow diversion in ruptured intracranial aneurysms[a]

Clinical Outcome	FD		FD and Coils		Total	
	Favorable	Unfavorable	Favorable	Unfavorable	Favorable	Unfavorable
Overall	77	14	24	9	101	23
Size						
Aneurysm <7 mm	51	5	8	3	59	8
Aneurysm >7 mm	8	7	14	3	22	10
Treatment timing						
Acute treatment	41	9	8	4	49	13
Delayed treatment	5	0	10	2	15	2
Clinical score						
Good clinical score	51	9	19	4	70	13
Poor clinical score	7	3	3	2	10	5
Location						
Anterior circulation	39	7	14	3	53	10
Posterior circulation	23	5	8	4	31	9
Type						
Dissecting	18	2	6	2	24	4
Fusiform	4	3	4	1	8	4
Blister	28	3	4	3	32	6
Saccular	11	3	9	2	20	5
Giant	1	1	0	1	1	2

[a] Data are numbers.

outcome was achieved in 88% (59/67) of patients with treated aneurysms of <7 mm, compared with 69% (22/32) in patients with aneurysms of >7 mm ($P = .027$). The use of an FD alone was associated with an 85% (77/91) rate of favorable clinical outcome, compared with 73% (24/33) for aneurysms treated with an FD and adjunctive coiling ($P = .189$). In aneurysms of <7 mm, treatment with an FD alone resulted in favorable outcome in 91% (51/56) of cases, compared with 73% (8/11) when treated with an FD and adjunctive coiling ($P = .117$). In aneurysms of >7 mm, treatment with an FD alone resulted in favorable outcome in 53% (8/15) of cases, compared with 82% (14/17) when treated with an FD and adjunctive coiling ($P = .128$). Favorable clinical outcome was achieved in 84% (53/63) of patients with aneurysms in the anterior circulation, compared with 78% (31/40) of patients with aneurysms in the posterior circulation ($P = .441$).

DISCUSSION

Endovascular coil embolization and open microsurgical clipping are the traditional methods for treatment of ruptured intracranial aneurysms. Recently, newer endovascular devices such as FDs have also been used to treat ruptured intracranial aneurysms. In this meta-analysis of case series and reports, we found that 81% of patients with ruptured aneurysms treated with FDs had favorable clinical outcomes, which is comparable with the number of patients with similar outcomes in large trials such as ISAT.[4] Thus, FDs may present a viable treatment option for ruptured intracranial aneurysms that are not readily amenable to first-line treatments such as coil embolization or clipping.

Nevertheless, the use of FDs for ruptured intracranial aneurysms is controversial because dual antiplatelet therapy and the delayed nature of aneurysm thrombosis may both increase the likelihood and severity of hemorrhagic complications during and after treatment. Indeed, our meta-analysis identified a 9% composite rate of intracranial hemorrhagic complications, including 5% from aneurysm rerupture and 4% from other causes. Complication-induced neurologic morbidity is not well-defined,[30] however, because some of these complications did not produce new symptoms. Notably, hemorrhagic complications following other procedures (eg, tracheostomy, extraventricular drainage,[26,29] and ventriculoperitoneal shunt placement) are included in the 4% of patients with nonaneurysmal hemorrhagic complications. In addition to hemorrhagic complications, there was a 4% rate of symptomatic ischemic complications, though the rate of asymptomatic or undetected ischemic events is likely higher.[24-26,29,31]

At least part of the risk of hemorrhagic complications appears to be related to aneurysm size. It has been proposed that reduction of local vascular compliance after FD placement may exaggerate the "Windkessel effect"[32] and result in increased vessel flow distal to the aneurysm, which may lead to intraparenchymal hemorrhage after flow diversion.[33,34] This phenomenon may be amplified in giant aneurysms[33] because increased distal vessel wall shear stress and increased intra-aneurysmal pressure[35] heighten the risk of aneurysm rerupture after flow diversion. Indeed, in this meta-analysis, aneurysms of >2 cm were significantly more likely than smaller aneurysms to rerupture after treatment, even though the natural rate of aneurysm rerupture in giant aneurysms is similar to that in smaller lesions.[36] These results, along with overall improved angiographic and clinical outcomes in aneurysms of <7 mm, suggest that FD-based treatment is more effective for small aneurysms. If larger aneurysms must be treated with FDs, then adjunctive coiling is likely worthwhile.[25,37,38] Alternatively, a staged treatment strategy of initial coiling followed by later FD placement may be appropriate in this setting because rebleeding has not been observed between procedures.[39] In these cases, loose packing of the aneurysm dome may be sufficient to accelerate aneurysm thrombosis[26,38] without producing a mass effect on the FD that could result in device thrombosis.[40]

In general, ruptured aneurysms in the posterior circulation carry an overall poorer prognosis than those in the anterior circulation.[41] Furthermore, FD placement in the posterior circula-

tion is associated with a higher rate of ischemic complications.[42] In this meta-analysis, however, there was no appreciable difference in the rate of complete angiographic occlusion or good clinical outcome between aneurysms in the anterior circulation and those in the posterior circulation.

Despite the importance of antiplatelet therapy on the success of FD-based interventions, there is wide variability in antiplatelet management surrounding the use of FDs in aneurysmal subarachnoid hemorrhage. For example, some authors reported performing invasive procedures (eg, extraventricular drain or central line placement) 12 hours before FD placement or dual antiplatelet inhibition, administering a loading dose of aspirin and clopidogrel before FD placement and continuing dual antiplatelet therapy for at least 3 months.[26] Other authors avoided preprocedural antiplatelet therapy altogether, instead administering aspirin, clopidogrel, and a glycoprotein IIb/IIIa inhibitor during FD placement, followed by a 12-hour maintenance infusion of a glycoprotein IIb/IIIa inhibitor and postprocedural dual antiplatelet therapy for 6 months.[27]

This study has several limitations. First, the lack of independent clinical and angiographic assessment and the potential for reporting bias in the included studies may affect the estimated rates of angiographic occlusion and favorable clinical outcome. Second, reporting of procedural details, aneurysm characteristics, angiographic follow-up, and outcome data was not uniform across all studies. As a result, we used composite measures (eg, good clinical outcome instead of specific mRS scores) that may partially obscure underlying details. Third, details describing the administration and monitoring of antiplatelet therapy during the periprocedural period was variable and infrequently specified. Finally, despite an overall large number of cases represented in this meta-analysis, the smaller number of cases in some subgroups (particularly those for which FD-based treatment is unlikely to be strongly considered, such as very large aneurysms) may not provide sufficient power to discriminate small effect sizes. We suspect that this effect may account for the inability to demonstrate a statistically significant difference in the rate of occlusion between small and large aneurysms or between aneurysms treated with an FD alone and those treated with an FD and adjunctive coiling.

CONCLUSIONS

Endovascular coil embolization and microsurgical clipping are likely to remain the first-line treatment of ruptured intracranial aneurysms, but when these options are not feasible, the use of FDs and appropriate dual antiplatelet therapy can allow a high rate of angiographic occlusion and a reasonable likelihood of good clinical outcome. However, one must be cognizant of the possibility that FDs may not be protective against rerupture in aneurysms of >2 cm. Clinical outcomes associated with FD treatment of ruptured aneurysms appear most favorable for aneurysms of <7 mm.

Disclosures: Christopher J. Moran—*UNRELATED*: *Consultancy*: Medtronic; *Grants/Grants Pending*: Medtronic*; *Payment for Lectures including Service on Speakers Bureaus*: Medtronic; *Payment for Development of Educational Presentations*: Medtronic. **Money paid to the institution.*

REFERENCES

1. Guglielmi G, Viñuela F, Dion J, et al. **Electrothrombosis of saccular aneurysms via endovascular approach, Part 2: preliminary clinical experience.** *J Neurosurg* 1991;75:8–14 Medline
2. Wiebers DO, Whisnant JP, Huston J 3rd, International Study of Unruptured Intracranial Aneurysms Investigators. **Unruptured intracranial aneurysms: natural history, clinical outcome, and risks of surgical and endovascular treatment.** *Lancet* 2003;362:103–10 CrossRef Medline
3. Pierot L, Spelle L, Vitry F, et al; ATENA Investigators. **Immediate clinical outcome of patients harboring unruptured intracranial aneurysms treated by endovascular approach: results of the ATENA study.** *Stroke* 2008;39:2497–504 CrossRef Medline
4. Molyneux A, Kerr R, Stratton I; International Subarachnoid Aneurysm Trial (ISAT) Collaborative Group. **International Subarachnoid Aneurysm Trial (ISAT) of neurosurgical clipping versus endovascular coiling in 2143 patients with ruptured intracranial aneurysms: a randomised trial.** *Lancet* 2002;360:1267–74 CrossRef Medline
5. McDougall CG, Spetzler RF, Zabramski JM, et al. **The Barrow Ruptured Aneurysm Trial.** *J Neurosurg* 2012;116:135–44 CrossRef Medline
6. Brilstra EH, Rinkel GJ, Algra A, et al. **Rebleeding, secondary ischemia, and timing of operation in patients with subarachnoid hemorrhage.** *Neurology* 2000;55:1656–60 CrossRef Medline
7. Koivisto T, Vanninen R, Hurskainen H, et al. **Outcomes of early endovascular versus surgical treatment of ruptured cerebral aneurysms: a prospective randomized study.** *Stroke* 2000;31:2369–77 CrossRef Medline
8. Yu SC, Kwok CK, Cheng PW, et al. **Intracranial aneurysms: midterm outcome of Pipeline embolization device—a prospective study in 143 patients with 178 aneurysms.** *Radiology* 2012;265:893–901 CrossRef Medline
9. Zhu Y, Pan J, Shen J, et al. **Clinical and radiological outcomes after treatment of unruptured paraophthalmic internal carotid artery aneurysms: a comparative and pooled analysis of single-center experiences.** *World Neurosurg* 2015;84:1726–38 CrossRef Medline
10. Becske T, Kallmes DF, Saatci I, et al. **Pipeline for uncoilable or failed aneurysms: results from a multicenter clinical trial.** *Radiology* 2013;267:858–68 CrossRef Medline
11. Petr O, Brinjikji W, Cloft H, et al. **Current trends and results of endovascular treatment of unruptured intracranial aneurysms at a single institution in the flow-diverter era.** *AJNR Am J Neuroradiol* 2016;37:1106–13 CrossRef Medline
12. Di Maria F, Pistocchi S Clarençon F, et al. **Flow diversion versus standard endovascular techniques for the treatment of unruptured carotid-ophthalmic aneurysms.** *AJNR Am J Neuroradiol* 2015;36:2325–30 CrossRef Medline
13. Kühn AL, Hou SY, Perras M, et al. **Flow diverter stents for unruptured saccular anterior circulation perforating artery aneurysms: safety, efficacy, and short-term follow-up.** *J Neurointerv Surg* 2015;7:634–40 CrossRef Medline
14. Tanweer O, Raz E, Brunswick A, et al. **Cavernous carotid aneurysms in the era of flow diversion: a need to revisit treatment paradigms.** *AJNR Am J Neuroradiol* 2014;35:2334–40 CrossRef Medline
15. Chalouhi N, Starke RM, Yang S, et al. **Extending the indications of flow diversion to small, unruptured, saccular aneurysms of the anterior circulation.** *Stroke* 2014;45:54–58 CrossRef Medline
16. Chalouhi N, Tjoumakaris S, Starke RM, et al. **Comparison of flow diversion and coiling in large unruptured intracranial saccular aneurysms.** *Stroke* 2013;44:2150–54 CrossRef Medline
17. Kallmes DF, Hanel R, Lopes D, et al. **International retrospective study of the Pipeline embolization device: a multicenter aneurysm treatment study.** *AJNR Am J Neuroradiol* 2015;36:108–15 CrossRef Medline
18. Fiorella D, Hsu D, Woo HH, et al. **Very late thrombosis of a Pipeline embolization device construct: case report.** *Neurosurgery* 2010;67(3 suppl operative):onsE313–14; discussion onsE314 CrossRef Medline

19. Saatci I, Yavuz K, Ozer C, et al. **Treatment of intracranial aneurysms using the Pipeline flow-diverter embolization device: a single-center experience with long-term follow-up results.** *AJNR Am J Neuroradiol* 2012;33:1436–46 CrossRef Medline
20. Fischer S, Vajda Z, Aguilar Perez M, et al. **Pipeline embolization device (PED) for neurovascular reconstruction: initial experience in the treatment of 101 intracranial aneurysms and dissections.** *Neuroradiology* 2012;54:369–82 CrossRef Medline
21. Proust F, Hannequin D, Langlois O, et al. **Causes of morbidity and mortality after ruptured aneurysm surgery in a series of 230 patients: the importance of control angiography.** *Stroke* 1995;26:1553–57 CrossRef Medline
22. Riley RD, Lambert PC, Abo-Zaid G. **Meta-analysis of individual participant data: rationale, conduct, and reporting.** *BMJ* 2010;340:c221 CrossRef Medline
23. Çinar C, Oran İ, Bozkaya H, et al. **Endovascular treatment of ruptured blister-like aneurysms with special reference to the flow-diverting strategy.** *Neuroradiology* 2013;55:441–47 CrossRef Medline
24. Cruz JP, O'Kelly C, Kelly M, et al. **Pipeline embolization device in aneurysmal subarachnoid hemorrhage.** *AJNR Am J Neuroradiol* 2013;34:271–76 CrossRef Medline
25. McAuliffe W, Wenderoth JD. **Immediate and midterm results following treatment of recently ruptured intracranial aneurysms with the Pipeline embolization device.** *AJNR Am J Neuroradiol* 2012;33:487–93 CrossRef Medline
26. Lin N, Brouillard AM, Keigher KM, et al. **Utilization of Pipeline embolization device for treatment of ruptured intracranial aneurysms: US multicenter experience.** *J Neurointerv Surg* 2015;7:808–15 CrossRef Medline
27. Chalouhi N, Zanaty M, Whiting A, et al. **Treatment of ruptured intracranial aneurysms with the Pipeline embolization device.** *Neurosurgery* 2015;76:165–72; discussion 172 CrossRef Medline
28. Nerva JD, Morton RP, Levitt MR, et al. **Pipeline embolization device as primary treatment for blister aneurysms and iatrogenic pseudoaneurysms of the internal carotid artery.** *J Neurointerv Surg* 2015;7:210–16 CrossRef Medline
29. Yoon JW, Siddiqui AH, Dumont TM, et al; Endovascular Neurosurgery Research Group. **Feasibility and safety of Pipeline embolization device in patients with ruptured carotid blister aneurysms.** *Neurosurgery* 2014;75:419–29; discussion 429 CrossRef Medline
30. Mahaney KB, Chalouhi N, Viljoen S, et al. **Risk of hemorrhagic complication associated with ventriculoperitoneal shunt placement in aneurysmal subarachnoid hemorrhage patients on dual antiplatelet therapy.** *J Neurosurg* 2013;119:937–42 CrossRef Medline
31. Brasiliense LB, Stanley MA, Grewal SS, et al. **Silent ischemic events after Pipeline embolization device: a prospective evaluation with MR diffusion-weighted imaging.** *J Neurointerv Surg* 2016;8:1136–1139 CrossRef Medline
32. Chiu AHY, Wenderoth J. **Cerebral hyperperfusion after flow diversion of large intracranial aneurysms.** *J Neurointerv Surg* 2013;5:e48 CrossRef Medline
33. Velat GJ, Fargen KM, Lawson MF, et al. **Delayed intraparenchymal hemorrhage following Pipeline embolization device treatment for a giant recanalized ophthalmic aneurysm.** *J Neurointerv Surg* 2012;4:e24 CrossRef Medline
34. Cruz J, Chow M, O'Kelly C, et al. **Delayed ipsilateral parenchymal hemorrhage following flow diversion for the treatment of anterior circulation aneurysms.** *AJNR Am J Neuroradiol* 2012;33:603–08 CrossRef Medline
35. Cebral J, Mut F, Raschi M, et al. **Aneurysm rupture following treatment with flow-diverting stents: computational hemodynamics analysis of treatment.** *AJNR Am J Neuroradiol* 2011;32:27–33 CrossRef Medline
36. Khurana VG, Piepgras DG, Whisnant JP. **Ruptured giant intracranial aneurysms, Part I: a study of rebleeding.** *J Neurosurg* 1998;88:425–29 CrossRef Medline
37. Park MS, Kilburg C, Taussky P, et al. **Pipeline embolization device with or without adjunctive coil embolization: analysis of complications from the IntrePED Registry.** *AJNR Am J Neuroradiol* 2016;37:1127–31 CrossRef Medline
38. Lin N, Brouillard AM, Krishna C, et al. **Use of coils in conjunction with the Pipeline embolization device for treatment of intracranial aneurysms.** *Neurosurgery* 2015;76:142–49 CrossRef Medline
39. Brinjikji W, Piano M, Fang S, et al. **Treatment of ruptured complex and large/giant ruptured cerebral aneurysms by acute coiling followed by staged flow diversion.** *J Neurosurg* 2016;125:120–27 CrossRef Medline
40. Siddiqui AH, Kan P, Abla AA, et al. **Complications after treatment with Pipeline embolization for giant distal intracranial aneurysms with or without coil embolization.** *Neurosurgery* 2012;71:E509–13; discussion E513 CrossRef Medline
41. Schievink WI, Wijdicks EF, Piepgras DG, et al. **The poor prognosis of ruptured intracranial aneurysms of the posterior circulation.** *J Neurosurg* 1995;82:791–95 CrossRef Medline
42. Brinjikji W, Murad MH, Lanzino G, et al. **Endovascular treatment of intracranial aneurysms with flow diverters a meta-analysis.** *Stroke* 2013;44:442–47 CrossRef Medline

FRED Flow Diverter: A Study on Safety and Efficacy in a Consecutive Group of 50 Patients

H. Luecking, T. Engelhorn, S. Lang, P. Goelitz, S. Kloska, K. Roessler, and A. Doerfler

ABSTRACT

BACKGROUND AND PURPOSE: Endovascular flow diverters are increasingly used for the treatment of cerebral aneurysms. We assessed the safety and efficacy of the Flow-Redirection Endoluminal Device (FRED) in a consecutive series of 50 patients.

MATERIALS AND METHODS: Inclusion criteria were wide-neck, blister-like, or fusiform/dissecting aneurysms independent of size, treated with the FRED between February 2014 and May 2015. Assessment criteria were aneurysm occlusion, manifest ischemic stroke, bleeding, or death. The occlusion rate was assessed at 3 months with flat panel CT and at 6 months with DSA by using the Raymond classification and the O'Kelly-Marotta grading scale.

RESULTS: Fifty patients with 52 aneurysms were treated with 54 FREDs; 20 patients were treated with the FRED and coils. Aneurysm size ranged from 2.0 to 18.5 mm. Deployment of the FRED was successful in all cases. There were no device-associated complications. One patient developed mild stroke symptoms that fully receded within days. There have been no late-term complications so far and no treatment-related mortality. Initial follow-up at 3 months showed complete occlusion in 72.3% of the overall study group, Six-month follow-up showed total and remnant-neck occlusion in 87.2% of patients, distributed over 81.5% of the FRED-only cases and 95.0% of the cases with combined treatment.

CONCLUSIONS: The FRED flow diverter is a safe device for the treatment of cerebral aneurysms of various types. Our data reveal high occlusion rates at 3 and 6 months, comparable with those in other flow diverters. Long-term occlusion rates are expected.

ABBREVIATIONS: FPCT = flat panel CT; FRED = Flow-Redirection Endoluminal Device; RROC = Raymond-Roy occlusion classification

Endovascular treatment has become the therapy of choice for intracranial aneurysms.[1-3] In addition to the well-established embolization with coils, supported by balloons or stents,[4-6] flow-modulating stents are increasingly used for dedicated aneurysms.[7]

Flow diverters can cause intra-aneurysmal thrombosis and thus occlusion.[8-19] This outcome is achieved by a narrowly braided stent wall, which, on the other hand, allows the blood to pass through to perforator arteries or major branches where the pressure gradient is high enough.

The Flow-Redirection Endoluminal Device (FRED; MicroVention, Tustin, California) uses a new principle because it combines an outer, self-expanding and dimensionally stable open-pored stent with an inner, narrowly braided stent. It is intended to combine easy deployment with flow-redirecting properties. The ends of the outer layer ("flared ends") exceed the inner layer on each side by approximately 3 mm where there is little or no flow-diverting effect.[12,20]

We report our results for safety and efficacy in a consecutive series of 50 patients treated with the FRED flow diverter with incidental cerebral aneurysms or those who were retreated after initial coiling in SAH.

MATERIALS AND METHODS

Inclusion Criteria

The inclusion period was from February 2014 through May 2015. All patients treated with a FRED flow diverter for ≥1 aneurysm were included. In the otherwise consecutive series, only 2 patients were excluded, being treated for carotid-cavernous fistulas with 2 FREDs each (stent-in-stent). The FRED was not used exclusively during this period but as an alternative to other flow diverters when it seemed appropriate.

The decision about whether to perform open surgery or intravascular therapy is made in a clinical conference with a neurosur-

Received August 18, 2016; accepted after revision October 23.

From the Departments of Neuroradiology (H.L., T.E., S.L., P.G., S.K., A.D.) and Neurosurgery (K.R.), University of Erlangen-Nuremberg, Erlangen, Germany.

Please address correspondence to Hannes Luecking, MD, University Hospital of Erlangen, Department of Neuroradiology, Schwabachanlage 6, 91054 Erlangen, Germany; e-mail: hannes.luecking@uk-erlangen.de

http://dx.doi.org/10.3174/ajnr.A5052

geon and neurologist. Accessibility and form (especially the neck and the neck/dome visual ratio) of the aneurysm, age, clinical condition, and the patient's wishes influence the decision. The selection of the particular device and the choice of whether to use additional coils are made by 2 senior neuroradiologists. In general, in our department flow diverters are used for all blister-like aneurysms or those with a wide neck where coil dislocation is expected or where a proper reconstruction of the base seems unlikely with a balloon only, leading to an assumed higher risk of reperfusion. Although there is no sharp cutoff in aneurysm size for additional coiling, we attempt to use coils in aneurysms of >5 mm when safe catheterization is possible. If so, there is an attempt at dense packing to reduce the rate of reperfusion[21] and post-flow-diverting hemorrhage.[22] In the aneurysms treated in this cohort with a flow diverter and coils, the flow diverter was necessary for remodeling the aneurysm base. Solitary coil embolization was not a proper option in those cases.

The FRED is preferred compared with other flow diverters if major branches are in the vicinity (eg, the anterior choroid artery) because one can achieve proper coverage of the aneurysm neck combined with stable positioning while the major branch is only covered by the open-pored part of the flow diverter.

In patients with acute SAH, flow diversion was used only when there was no other intravascular or surgical option available. Administration of aspirin and clopidogrel hours before placement of the stent has not seemed appropriate to us in light of a possible re-SAH, though new regimens with short loading intervals using adjunctive tirofiban have a low complication profile.[23] Furthermore, platelet suppression might severely affect further surgical options such as placing a CSF drain.

Preinterventional Diagnostic Imaging

Both diagnostic angiography and intervention were performed by using an Axiom Artis dBA biplane system (Siemens, Erlangen, Germany).

All patients underwent diagnostic angiography before the intervention for planning of endovascular therapy. For each patient, 3D imaging of the aneurysm (with multiplane and volume rendering technique reconstructions) was acquired combined with targeted series, depicting the aneurysm neck and parent vessel.

Patient Preparation

Before the intervention, all patients provided informed consent for the procedure. Forty-eight patients were prepared with 75 mg of clopidogrel and 100 mg of aspirin 7 days before the intervention. Of the 2 other patients, one was pretreated with 500 mg of ticlopidine, and one, with 150 mg of clopidogrel due to aspirin intolerance. Sufficient platelet suppression was observed by using a Multiplate analyzer (Roche, Basel, Switzerland) 1 day before the intervention. The Multiplate analyzer indicates proper response to aspirin and clopidogrel/ticlopidine when ASPItest and ADPtest values are beneath standard range. Because there were no nonresponders in our study group for either of the drugs, no action was taken.

Intervention

Standard transfemoral access was obtained by using an 80-/90-cm 6F sheath placed in the common carotid artery or a 65-cm 6F sheath placed in the subclavian artery, respectively. We placed 6F Envoy guiding catheters (Codman & Shurtleff, Raynham, Massachusetts) with or without a soft tip (distal access type) in the C1 section of the internal carotid artery or the proximal V3 segment of the vertebral artery, as appropriate. At the start of the intervention, standard posterior-anterior and lateral series were acquired for later comparison. Coil positioning and deployment of the flow diverter were surveilled under road-mapping/fluoroscopy. After the procedure, posterior-anterior and lateral series of the vascular territory were acquired to rule out distal embolisms. Hemorrhage was ruled out by flat panel CT (FPCT, Dyna CT; Siemens) following the intervention.

Materials

FRED is approved in Europe and several other countries. There is no FDA approval so far.

The FRED is available from 3.5 to 5.5 mm in diameter, in increments of 0.5 mm and from 13/7 to 32/25 mm in length: The first number gives the total length, and the second number denotes the working (flow-diverting) length. It is delivered via a 2-tip microcatheter (Headway 27 microcatheter; MicroVention; distal: 2.6F/proximal: 3.1F). The FRED size was based on the diameter of the parent vessel or slightly overdimensioned. An example case is given in Fig 1 illustrating shape and visualization of the FRED.

For additional coiling bioactive (Cerecyte coils; Codman & Shurtleff) or Hydrogel coils (MicroVention) were used according to the aneurysm size. The microcatheter was placed in the aneurysm before deployment of the FRED ("jailing").

Follow-Up

Follow-up imaging included MR imaging with TOF MRA and contrast-enhanced MRA and flat panel CT[24] with intravenous contrast application during the hospital stay and at 3 months after the intervention; DSA, MR imaging, and FPCT were performed 6 months after the intervention. Clopidogrel was stopped 3 months after the intervention if no pathologic findings occurred.

Assessment Criteria

Safety. Patients were examined by a neurologist for neurologic deficits at admission, after the intervention, and at discharge. Assessment criteria were the following: manifest ischemic stroke, flow diverter–associated hemorrhage, or death. Procedural safety (deployment, visibility) was assessed by 2 experienced interventionists.

Efficacy. Occlusion rates were assessed by 2 interventionists in a consensus reading. The O'Kelly-Marotta grading scale[25] for flow diversion (A, total filling; B, subtotal filling; C, entry remnant; D, no filling; 1, immediate washout; 2, stasis until the capillary phase; 3, stasis until the venous phase) was used in time-resolved DSA imaging immediately and 6 months after the intervention. The Raymond-Roy occlusion classification (RROC; 1, complete oc-

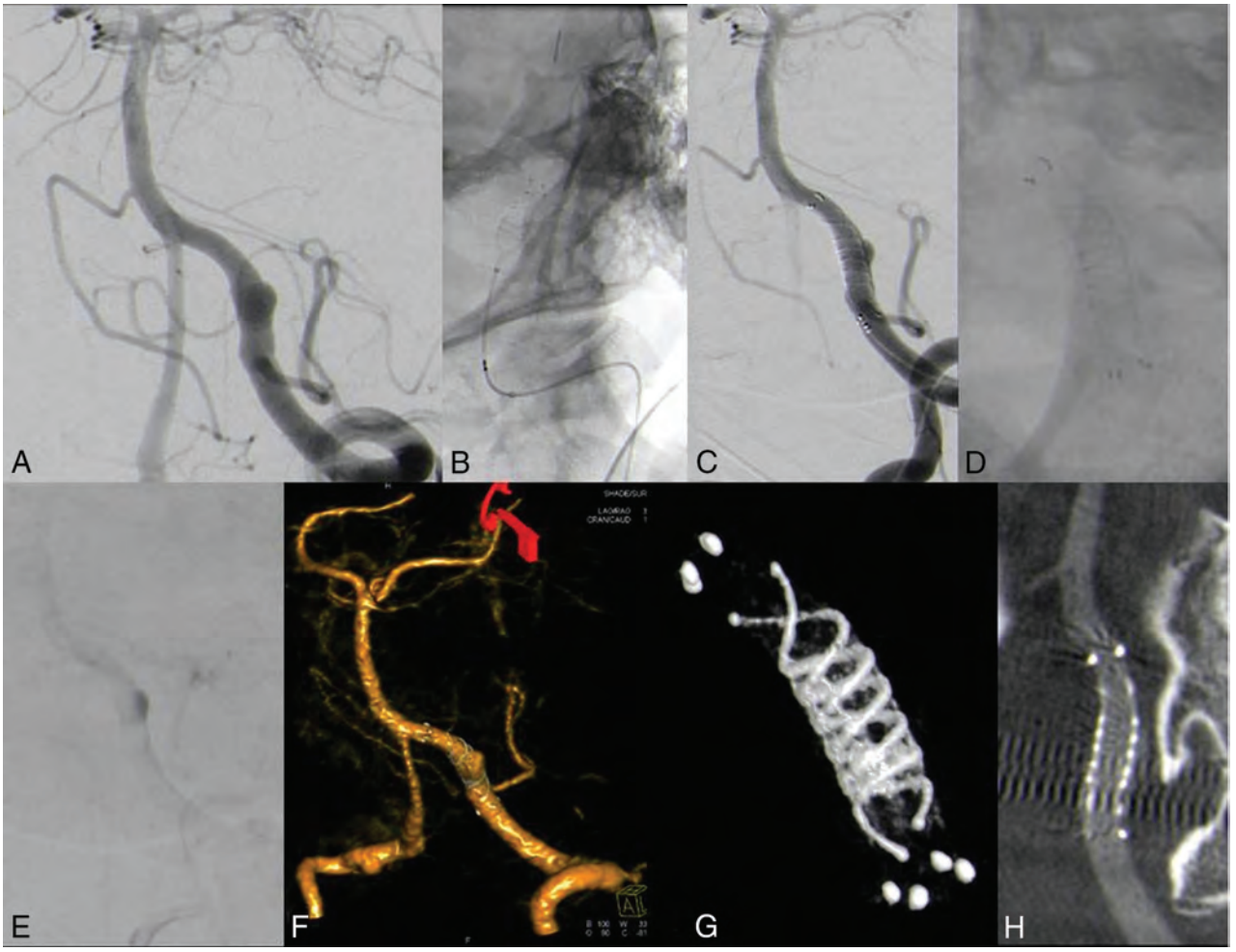

FIG 1. Sidewall aneurysm of the left vertebral artery (*A*). Gradual deployment of the FRED device (*B* and *C*). Note delayed washout of contrast right after deployment (*E*) and good visualization of the flow diverter on 2D and 3D imaging (*D*, *F–H*) (3D imaging acquired with flat panel CT). *D* and *G*, The overall (4 markers at each end) and working length (radiopaque "*double helix*") are illustrated.

clusion; 2, remnant neck/dog ear; 3, remnant aneurysm) was used in steady-state angiography (FPCT, MRA) during the hospital stay and at 3 and 6 months.

RESULTS

Fifty patients (39 women, 11 men; 55.4 ± 11.9 years of age; range, 25–77 years) with 52 aneurysms were treated.

In our series, we used FRED implant sizes from 3.5 × 13/7 mm to 5.5 × 32/25 mm.

Forty-four (88%) aneurysms were located at the ICA and carotid bifurcation, including the posterior communicating artery origin (2 patients had 2 aneurysms in the same segment covered with 1 flow diverter); 1 (2%), at the MCA; 3 (6%), at the intracranial part of the vertebral artery; and 1 each, at the PICA origin and basilar tip. Forty-two aneurysms (84%) were incidental findings. Fourteen patients (28%) were retreated with the FRED for recurrence of a previously coiled aneurysm. Four of the retreated patients had an SAH from the targeted aneurysm before the first treatment. Prior treatment included stent placement ($n = 2$), stent-protected coiling ($n = 2$), implantation of a different flow diverter ($n = 2$), prior clipping ($n = 1$), flow-diverter-protected coiling ($n = 1$), and prior coiling ($n = 6$). Another 4 (8%) patients had SAH originating from another aneurysm.

Thirty (60%) patients were treated exclusively with a FRED device (group A) in the current intervention. In 4 patients (8%), 2 overlapping flow diverters (stent-in-stent) were used because no safe catheterization of the aneurysm was possible ($n = 2$) or the aneurysm was at the origin of the ophthalmic artery ($n = 2$). The former showed no relevant stasis of contrast after deployment of the first FRED and they were thus treated with a second flow diverter. The latter was thought unlikely to occlude because a high-pressure gradient from the ophthalmic artery was present. Twenty (40%) patients underwent additional coiling (group B), as explained in the "Materials and Methods" section.

Aneurysm sizes ranged from 2.0 to 18.5 mm, resulting in a mean diameter of 5.4 ± 4.5 mm in the overall group. Aneurysm sizes ranged from 2.0 to 13.0 mm (mean, 3.6 ± 2.7 mm) in group A and from 2.5 to 18.5 mm (mean, 8.0 ± 5.2 mm) in group B. Thirty-nine saccular, 8 blister-like, and 3 fusiform/dissecting aneurysms were treated, with mean sizes of 5.8 ± 4.6 mm (range, 1.5–18.5 mm), 2.1 ± 0.6 mm (range, 1.5–3 mm), and 8.3 ± 3.3 mm (range, 5.5–13 mm), respectively.

Table 1: Initial occlusion rates using OKMGS

	Overall Study Group		Group A		Group B	
OKMGS	*n* = 50	%	*n* = 30	%	*n* = 20	%
A1	10	20	10	33.3	0	0
A2	6	12	5	16.7	1	5.0
A3	11	22	11	36.7	0	0
B1	3	6	2	6.7	1	5.0
B2	0	0	0	0	0	0
B3	1	2	0	0	1	5.0
C1	4	8	0	0	4	20.0
C2	2	4	1	3.3	1	5.0
C3	4	8	1	3.3	3	15.0
D	9	18	0	0	9	45.0

Note:—OKMGS indicates O'Kelly-Marotta grading scale for flow diversion.

Safety

Thirty-nine patients (78%) had neither clinical complications nor pathologic imaging findings. Nine patients (18%) showed punctual subcortical ischemic lesions on postprocedural MR imaging without neurologic deficits. One patient had mild contralateral hemiparesis right after the intervention but recovered completely during the hospital stay. In 1 patient in group B treated with additional bioactive coils, the early MR imaging showed several punctual contrast-enhancing lesions on the ipsilateral hemisphere; this patient had moderate temporary headache but no focal deficits. Hence, no intervention-related mortality was observed.

In 1 patient with a primarily successful deployment and complete wall adaptation of the FRED, there was a shift in configuration on initial follow-up, showing a concentric narrowing of the distal end with 2 of 4 markers sticking together ("fish mouth" configuration), resulting in a mild delay of time-to-peak and mean transit time on perfusion-weighted imaging. This finding remained stable at 3 months but showed complete resolution at the routine DSA follow-up at 6 months.

At 6-month follow-up, we found endothelial hyperplasia without hemodynamic effects in MR perfusion in 1 patient and concentric narrowing of the flow diverter and parent vessel in 2 patients, one of whom had delayed time-to-peak perfusion on MR imaging.

As a consequence, patients with fish-mouthing or endothelial hyperplasia received extended dual platelet inhibition until 6 months after the intervention. In an additional follow-up with FPCT 3 months later, the findings remained stable and clopidogrel was stopped again.

Efficacy

Immediate complete occlusion occurred in group B in 9 patients (18%); there was no case of immediate complete occlusion in group A. Detailed immediate postinterventional occlusion rates are given in Table 1.

Three-month FPCT and MR imaging were available in 47 cases. One FPCT dataset was not evaluable because of hardening artifacts from the coil package; therefore, only MR imaging was used for occlusion rate assessment.[26,27] Three patients were lost to follow-up: One patient died of a heart attack in the meantime; in 2 patients, the 3-month follow-up was not performed because they refused to undergo further imaging.

Table 2: Three-month occlusion rates using the RROC

	Overall Study Group		Group A		Group B	
RROC	*n* = 47	%	*n* = 28	%	*n* = 19	%
3	5	10.6	5	17.9	0	0
2	8	17.0	4	14.3	4	21.1
1	34	72.3	19	67.9	15	79.0

Table 3: Six-month occlusion rates using OKMGS

	Overall Study Group		Group A		Group B	
OKMGS	*n* = 43	%	*n* = 24	%	*n* = 19	%
A1	0	0	0	0	0	0
A2	0	0	0	0	0	0
A3	0	0	0	0	0	0
B1	1	2.3	1	4.2	0	0
B2	2	4.7	2	8.3	0	0
B3	2	4.7	1	4.2	1	5.3
C1	1	2.3	0	0	1	5.3
C2	3	7.0	2	8.3	1	5.3
C3	1	2.3	0	0	1	5.3
D	33	76.7	18	75.0	15	78.9

Table 4: Six-month occlusion rates including DSA and alternative follow-up with RROC

	Overall Study Group		Group A		Group B	
RROC	*n* = 47	%	*n* = 27	%	*n* = 20	%
3	6	12.8	5	18.5	1	5.0
2	5	10.6	2	7.4	3	15.0
1	36	76.6	20	74.1	16	80.0

In the overall group, we observed complete aneurysm occlusion in 34 of 47 patients (72.3%). Another 8 patients (17.0%) showed functional occlusion with only a remaining "dog ear," resulting in 89.3% complete or subtotal occlusion. Occlusion rates after 3 months in the particular treatment groups are given in Table 2. Reperfusion occurred in 2 patients (4%) in group B (aneurysm sizes, 18 and 18.5 mm) who changed from RROC grade 1 in the postprocedural scan to RROC grade 2 at the 3-month follow-up, remaining unchanged after 6 months.

Six-month DSA follow-up (particular occlusion rates given in Table 3) was available in 43 patients. In addition to the 1 patient who died in the first 3-month period, 6 patients (12%) refused to have another diagnostic angiography because of anxiety or unknown reasons. For those patients, MR imaging ($n = 3$) or FPCT (patient = 1) was available in 4 as an alternative imaging method. The results of all patients, including DSA and FPCT or MRA, are shown in Table 4 with RROC because there was no dynamic information available throughout the overall group. The additional patient with RROC grade 3 in group B did not have a recurrence but did not undergo follow-up at 3 months for medical reasons (severe impairment after SAH with prolonged rehabilitation) and thus was not considered in Table 3. Occlusion rates for the different subtypes of aneurysms are given in Table 5.

Adding RROC 1 and 2 results, we achieved an occlusion rate of

Table 5: Six-month occlusion rates for the particular forms of aneurysms[a]

	Overall Study Group				Group A				Group B			
		RROC				RROC				RROC		
Form	No.	1	2	3	No.	1	2	3	No.	1	2	3
Saccular	37	28 (76)	5 (14)	4 (11)	18	13 (72)	2 (11)	3 (17)	19	15 (79)	3 (16)	1 (5)
Blister	7	6 (86)	0	1 (14)	7	6 (86)	0	1 (14)		0	0	0
Fusiform	3	2 (67)	0	1 (33)	2	1 (50)	0	1 (50)	1	1 (100)	0	0

[a] Numbers in parentheses are percentages.

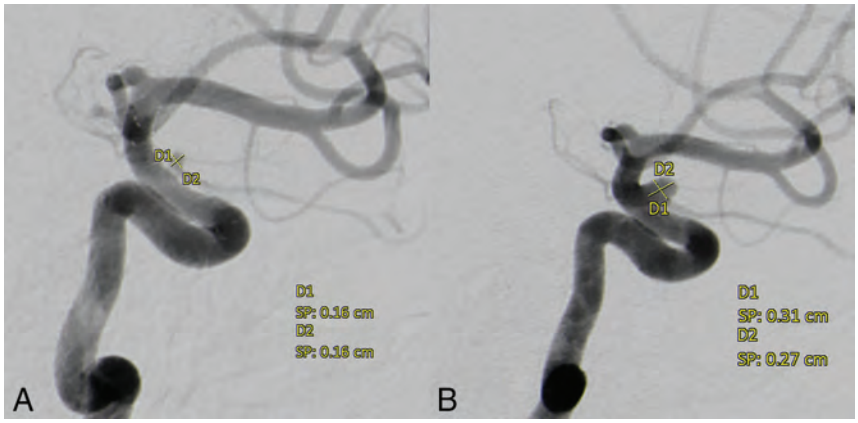

FIG 2. Paraophthalmic aneurysm 6 months after (*A*) and before (*B*) implantation of 2 FREDs. Note the "white collar" between the parent vessel and the aneurysm, suggesting endothelialization of the stents.

81.5% in group A, 95.0% in group B, and 87.2 % in the overall study group.

DISCUSSION

In this single-center prospective study, we examined the FRED flow diverter, a device designed to combine easy deployment with flow-diversion properties and a safety profile similar to that of other flow diverters on the market.

Six-month follow-up revealed an overall complete occlusion rate of 76.6%, with a recognizable lower rate of 74.1% in group A (FRED exclusively) than the group B (FRED and coils) rate of 80.0%. Given that most aneurysms were incidental findings in which a small remnant neck might be acceptable, there was subtotal occlusion (complete occlusion or small remnant neck) of 87.2% in the overall group (81.5% group A, 95.0% group B). The occlusion rates were stable during the time observed in all except 2 patients in group B in whom large aneurysms of 18.0 and 18.5 mm showed reperfusion after 3 months.

The occlusion rate in group A was almost identical to the results of the meta-analysis of Brinjikji et al,[28] which showed total occlusion in 76% (95% confidence interval, 70%–81%) of 1654 cases with various flow diverters. It was also similar to the data of Möhlenbruch et al[12] and Kocer et al,[20] who assessed the FRED in particular, with 73% and 80% complete occlusion, respectively. Results for the Pipeline Embolization Device (PED; Covidien, Irvine, California) indicated that occlusion rates might increase during long-term follow-up of up to 2 years.[29] Patients in group B had larger aneurysms with a mean diameter of 8.1 mm compared with those of group A, who had a mean size of 3.7 mm, indicating a tendency to use coils in larger aneurysms, mainly for easier probing and an expected higher rate of occlusion. After adjusting for aneurysm size, we achieved complete occlusion in 33/38 patients (86.8%) with aneurysms of up 10 mm. An occlusion rate of 12/12 (100%) in group B with aneurysms of up to 10 mm indicates that additional coiling likely results in better immediate and long-term occlusion; thus, it can prevent hemorrhage that is reported to happen after flow diversion due to mechanical and inflammatory changes within the aneurysm wall.[22,30,31]

Four patients (8%) were treated with 2 flow diverters as stent-in-stent over the same aneurysm, 2 of whom had an aneurysm of ophthalmic artery origin. In the latter, considerable shrinkage could be achieved (Fig 2). Shrinking aneurysms at the origin of smaller arteries where a relevant blood pressure gradient is present are described for the PED as well.[29] In the other 2 patients, there was complete occlusion of the aneurysm at 6 months after treatment with 2 FREDs.

Only low occlusion rates (1/6 complete occlusions, another 3/6 remnant necks) were achieved in aneurysms of >10 mm. Because this study included a very small number of patients and rather short follow-up, our results are probably insufficient for reliable assessment of the efficacy in large aneurysms. On the other hand, we could achieve a reduction in size and thus mass effect in two-thirds of large aneurysms. We also expect advancing occlusion of the larger aneurysms during further follow-up.

While 78% of all patients had neither clinical deficits nor pathologic imaging findings after the intervention, manifest stroke was observed in 1 patient. This patient had mild stroke symptoms that receded during the hospital stay. Postprocedural MR imaging revealed subclinical pointed DWI lesions in another 9 patients (18%). These punctual lesions did not cause neurologic symptoms or prolonged hospitalization; there were no noticeable periprocedural abnormalities in those cases (eg, prolonged duration of the intervention). All these patients had proper suppression of platelet function. A rate of 18% asymptomatic minor lesions is well below that seen in prior studies, which found microembolism in up to 37% of patients treated with flow-diverter stents for embolization of intracranial aneurysms.[32]

In 1 patient, contrast-enhancing lesions were found on postprocedural MR imaging. The only clinical symptom was moderate headache for several days. As a precaution, cortisone was administered orally for 2 weeks; clinical symptoms dissipated within days after administration. We do not assume that these findings are associated with the FRED or its delivery catheter in particular. The exact cause of this phenomenon is not fully under-

stood, though an inflammatory reaction, probably due to scraped-off hydrophilic coating, is suspected and has been reported for different microcatheters.[33]

There was no acute or subacute in-stent thrombosis. One patient had mild endothelial hyperplasia at 6-month follow-up with only a minor effect on time-to-peak maps in perfusion-weighted MR imaging. Two FRED flow diverters showed a concentric narrowing of the distal end of the stent or the distal end of the flow-diverting segment, respectively, including the parent vessel. This kind of alteration has been observed in other stents and flow diverters as well. The geometry of the stent and the parent vessel, vessel size, and healing reactions have been discussed as potential causes of this phenomenon[20,34]; however, there is no accepted explanation. In all 3 cases of endothelial hyperplasia or change in stent configuration, dual antiplatelet therapy was extended until 6 months after the intervention. While further deterioration was not seen in any of these patients, in 1 patient, the fish-mouth configuration spontaneously resolved almost completely between the 3- and 6-month follow-up. All the alterations mentioned were noticed on FPCT with intravenous contrast application; thus, we are encouraged to use this method to obtain high-quality information on the shape and perfused lumen of the flow diverter and the hemodynamics downstream of the stent for interim follow-up or in patients in whom DSA is not an option.[35]

CONCLUSIONS

The FRED flow diverter is a technically safe device with a low rate of complications. It has occlusion rates similar to those of other flow diverters. It is our experience that its higher radial force allows easier deployment in certain cases. Long-term follow-up is needed to prove stable occlusion, especially in larger aneurysms and those with no additional coiling.

REFERENCES

1. Brinjikji W, Rabinstein AA, Nasr DM, et al. **Better outcomes with treatment by coiling relative to clipping of unruptured intracranial aneurysms in the United States, 2001–2008.** *AJNR Am J Neuroradiol* 2011;32:1071–75 CrossRef Medline
2. Alshekhlee A, Mehta S, Edgell RC, et al. **Hospital mortality and complications of electively clipped or coiled unruptured intracranial aneurysm.** *Stroke* 2010;41:1471–76 CrossRef Medline
3. Molyneux A, Kerr R, Stratton I, et al; International Subarachnoid Aneurysm Trial (ISAT) Collaborative Group. **International Subarachnoid Aneurysm Trial (ISAT) of neurosurgical clipping versus endovascular coiling in 2143 patients with ruptured intracranial aneurysms: a randomised trial.** *Lancet* 2002;360:1267–74 CrossRef Medline
4. Consoli A, Vignoli C, Renieri L, et al. **Assisted coiling of saccular wide-necked unruptured intracranial aneurysms: stent versus balloon.** *J Neurointerv Surg* 2016;8:52–57 CrossRef Medline
5. Moret J, Cognard C, Weill A, et al. **The "Remodelling Technique" in the treatment of wide neck intracranial aneurysms: angiographic results and clinical follow-up in 56 cases.** *Interv Neuroradiol* 1997;3:21–35 Medline
6. Shapiro M, Becske T, Sahlein D, et al. **Stent-supported aneurysm coiling: a literature survey of treatment and follow-up.** *AJNR Am J Neuroradiol* 2012;33:159–63 CrossRef Medline
7. Briganti F, Leone G, Marseglia M, et al. **Endovascular treatment of cerebral aneurysms using flow-diverter devices: a systematic review.** *Neuroradiol J* 2015;28:365–75 CrossRef Medline
8. Zanaty M, Chalouhi N, Tjoumakaris SI, et al. **Flow-diversion panacea or poison?** *Front Neurol* 2014;5:21 CrossRef Medline
9. Lylyk P, Miranda C, Ceratto R, et al. **Curative endovascular reconstruction of cerebral aneurysms with the Pipeline embolization device: the Buenos Aires experience.** *Neurosurgery* 2009;64:632–42; discussion 642–43; quiz N6 CrossRef Medline
10. De Vries J, Boogaarts J, Van Norden A, et al. **New generation of flow diverter (Surpass) for unruptured intracranial aneurysms: a prospective single-center study in 37 patients.** *Stroke* 2013;44:1567–77 CrossRef Medline
11. McAuliffe W, Wycoco V, Rice H, et al. **Immediate and midterm results following treatment of unruptured intracranial aneurysms with the Pipeline embolization device.** *AJNR Am J Neuroradiol* 2012;33:164–70 CrossRef Medline
12. Möhlenbruch MA, Herweh C, Jestaedt L, et al. **The FRED flow-diverter stent for intracranial aneurysms: clinical study to assess safety and efficacy.** *AJNR Am J Neuroradiol* 2015;36:1155–61 CrossRef Medline
13. Byrne JV, Beltechi R, Yarnold JA, et al. **Early experience in the treatment of intra-cranial aneurysms by endovascular flow diversion: a multicentre prospective study.** *PLoS One* 2010;5:pii: e12492 CrossRef Medline
14. Phillips TJ, Wenderoth JD, Phatouros CC, et al. **Safety of the Pipeline embolization device in treatment of posterior circulation aneurysms.** *AJNR Am J Neuroradiol* 2012;33:1225–31 CrossRef Medline
15. Becske T, Kallmes DF, Saatci I, et al. **Pipeline for uncoilable or failed aneurysms: results from a multicenter clinical trial.** *Radiology* 2013;267:858–68 CrossRef Medline
16. Nelson PK, Lylyk P, Szikora I, et al. **The Pipeline embolization device for the intracranial treatment of aneurysms trial.** *AJNR Am J Neuroradiol* 2011;32:34–40 CrossRef Medline
17. Pistocchi S, Blanc R, Bartolini B, et al. **Flow diverters at and beyond the level of the circle of Willis for the treatment of intracranial aneurysms.** *Stroke* 2012;43:1032–38 CrossRef Medline
18. Yu SC, Kwok CK, Cheng PW, et al. **Intracranial aneurysms: midterm outcome of Pipeline embolization device—a prospective study in 143 patients with 178 aneurysms.** *Radiology* 2012;265:893–901 CrossRef Medline
19. D'Urso PI, Lanzino G, Cloft HJ, et al. **Flow diversion for intracranial aneurysms: a review.** *Stroke* 2011; 42:2363–88 CrossRef Medline
20. Kocer N, Islak C, Kizilkilic O, et al. **Flow Re-direction Endoluminal Device in treatment of cerebral aneurysms: initial experience with short-term follow-up results.** *J Neurosurg* 2014;120:1158–71 CrossRef Medline
21. Mpotsaris A, Skalej M, Beuing O, et al. **Long-term occlusion results with SILK flow diversion in 28 aneurysms: do recanalizations occur during follow-up?** *Interv Neuroradiol* 2015;21:300–10 CrossRef Medline
22. Kulcsár Z, Houdart E, Bonafé A, et al. **Intra-aneurysmal thrombosis as a possible cause of delayed aneurysm rupture after flow-diversion treatment.** *AJNR Am J Neuroradiol* 2011;32:20–25 CrossRef Medline
23. Chalouhi N, Jabbour P, Daou B, et al. **A new protocol for anticoagulation with tirofiban during flow diversion.** *Neurosurgery* 2016;78:670–74 CrossRef Medline
24. Struffert T, Saake M, Ott S, et al. **Intravenous flat detector CT angiography for non-invasive visualisation of intracranial flow diverter: technical feasibility.** *Eur Radiol* 2011;21:1797–801 CrossRef Medline
25. O'Kelly CJ, Krings T, Fiorella D, et al. **A novel grading scale for the angiographic assessment of intracranial aneurysms treated using flow diverting stents.** *Interv Neuroradiol* 2010;16:133–37 Medline
26. Lubicz B, Levivier M, Sadeghi N, et al. **Immediate intracranial aneurysm occlusion after embolization with detachable coils: a comparison between MR angiography and intra-arterial digital subtraction angiography.** *J Neuroradiol* 2007;34:190–07 CrossRef Medline
27. Attali J, Benaissa A, Soize S, et al. **Follow-up of intracranial aneurysms treated by flow diverter: comparison of three-dimensional time-of-flight MR angiography (3D-TOF-MRA) and contrast-enhanced MR angiography (CE-MRA) sequences with digital subtraction angiography as the gold standard.** *J Neurointerv Surg* 2016;8:81–86 CrossRef Medline

28. Brinjikji W, Murad MH, Lanzino G, et al. **Endovascular treatment of intracranial aneurysms with flow diverters: a meta-analysis.** *Stroke* 2013;44:442–47 CrossRef Medline
29. Chiu AH, Cheung AK, Wenderoth JD, et al. **Long-term follow-up results following elective treatment of unruptured intracranial aneurysms with the Pipeline Embolization Device.** *AJNR Am J Neuroradiol* 2015;36:1728–34 CrossRef Medline
30. Kim M, Levy EI, Meng H, et al. **Quantification of hemodynamic changes induced by virtual placement of multiple stents across a wide-necked basilar trunk aneurysm.** *Neurosurgery* 2007;61:1305–12; discussion 1312–13 CrossRef Medline
31. Fox B, Humphries WE, Doss VT, et al. **Rupture of giant vertebrobasilar aneurysm following flow diversion: mechanical stretch as a potential mechanism for early aneurysm rupture.** *J Neurointerv Surg* 2015; 7:e37 CrossRef Medline
32. Park JC, Lee DH, Kim JK, et al. **Microembolism after endovascular coiling of unruptured cerebral aneurysms: incidence and risk factors.** *J Neurosurg* 2016;124:777–83 CrossRef Medline
33. Cruz JP, Marotta T, O'Kelly C, et al. **Enhancing brain lesions after endovascular treatment of aneurysms.** *AJNR Am J Neuroradiol* 2014; 35:1954–58 CrossRef Medline
34. Valdivia y Alvarado M, Ebrahimi N, Benndorf G. **Study of conformability of the new Leo Plus stent to a curved vascular model using flat-panel detector computed tomography (DynaCT).** *Neurosurgery* 2009; 64(3 suppl):ons130–34; discussion ons134 CrossRef Medline
35. Richter G, Engelhorn T, Struffert T, et al. **Flat panel detector angiographic CT for stent-assisted coil embolization of broad-based cerebral aneurysms.** *AJNR Am J Neuroradiol* 2007;28:1902–08 CrossRef Medline

Compacting a Single Flow Diverter versus Overlapping Flow Diverters for Intracranial Aneurysms: A Computational Study

R.J. Damiano, V.M. Tutino, N. Paliwal, D. Ma, J.M. Davies, A.H. Siddiqui, and H. Meng

ABSTRACT

BACKGROUND AND PURPOSE: Locally compacting the mesh of a flow diverter by a dynamic push-pull technique can accelerate intracranial aneurysm healing. We asked how this deployment strategy compares with overlapping 2 flow diverters for aneurysmal flow reduction.

MATERIALS AND METHODS: Using a high-fidelity virtual stent placement method, we simulated 3 flow-diverter strategies (single noncompacted, 2 overlapped, and single compacted) in 3 aneurysms (fusiform, large saccular, and medium saccular). Computational fluid dynamics analysis provided posttreatment hemodynamic parameters, including time-averaged inflow rate, aneurysm-averaged velocity, wall shear stress, total absolute circulation, and turnover time. We examined the relationship between the achieved degree of compaction and aneurysm orifice area.

RESULTS: Flow-diverter compaction resulted in a compaction coverage of 57%, 47%, and 22% over the orifice of the fusiform, large, and medium saccular aneurysm, respectively. Compaction coverage increased linearly with orifice area. In the fusiform aneurysm, the single compacted flow diverter accomplished more aneurysmal flow reduction than the other 2 strategies, as indicated by all 5 hemodynamic parameters. In the 2 saccular aneurysms, the overlapped flow diverters achieved the most flow reduction, followed by the single compacted and the noncompacted flow diverter.

CONCLUSIONS: Compacting a single flow diverter can outperform overlapping 2 flow diverters in aneurysmal flow reduction, provided that the compaction produces a mesh denser than 2 overlapped flow diverters and this denser mesh covers a sufficient portion of the aneurysm orifice area, for which we suggest a minimum of 50%. This strategy is most effective for aneurysms with large orifices, especially fusiform aneurysms.

ABBREVIATIONS: CC = compaction coverage; CFD = computational fluid dynamics; DPPT = dynamic push-pull technique; FD = flow diverter; HiFiVS = high-fidelity virtual stent placement; IA = intracranial aneurysm

Flow diversion is a minimally invasive, endovascular therapy for treating intracranial aneurysms (IAs). Flow diverters (FDs) are self-expandable, densely braided metallic stents that are deployed across the IA neck. Their low-porosity mesh redirects blood flow back into the parent vessel, decreasing flow into the aneurysm and thereby encouraging parent vessel reconstruction and aneurysm embolization.[1] However, embolization does not occur immediately, leaving treated IAs at risk of rupture before complete occlusion is achieved.[2] Treatment strategies aimed at reducing aneurysmal flow beyond that achievable by conventional FD deployment can decrease the time to occlusion and reduce rupture risk.[3]

One of these strategies is to overlap multiple FDs to increase mesh coverage over the aneurysm neck to accelerate IA occlusion. The strategy of overlapping FDs was used in 2 large clinical trials testing the safety and efficacy of the Pipeline Embolization Device (Covidien, Irvine, California) in treating unruptured aneurysms: the Pipeline Embolization Device for the Intracranial Treatment of Aneurysms[4] and Pipeline for Uncoilable or Failed Aneurysms.[5] Additional overlapping FDs were deployed to treat aneurysms at

Received May 23, 2016; accepted after revision October 27.

From the Department of Mechanical and Aerospace Engineering (R.J.D., N.P., D.M., H.M.), Toshiba Stroke and Vascular Research Center (R.J.D., V.M.T., N.P., D.M., J.M.D., A.H.S., H.M.), Department of Biomedical Engineering (V.M.T., H.M.), and Department of Neurosurgery (J.M.D., A.H.S., H.M.), University at Buffalo, State University of New York, Buffalo, New York.

This study was supported by the National Institutes of Health (R01 NS 091075) and Covidien (VTGCC053012–009).

Please address correspondence to Hui Meng, PhD, Department of Mechanical and Aerospace Engineering, University at Buffalo, State University of New York, Buffalo, NY 14260; e-mail: huimeng@buffalo.edu

Indicates open access to non-subscribers at www.ajnr.org

Indicates article with supplemental on-line appendix.

Indicates article with supplemental on-line photo.

http://dx.doi.org/10.3174/ajnr.A5062

the discretion of the neurointerventionalists, and an analysis of treatments at the conclusions of the trials showed that the average number of FDs used per case was 1.52 and 3.1, respectively. These trials demonstrated 6-month occlusion rates of 93% and 73.6%, respectively, supporting the efficacy of using overlapping FDs to treat IAs. Computational studies of sequentially overlapping stents for treating IAs have supported this concept, showing increased flow reduction with the increases in mesh coverage over the IA orifice.[6] More recently, we simulated realistic deployment of the Pipeline Embolization Device and demonstrated that overlapping 2 devices reduced aneurysmal flow velocity 30% more than deploying 1 device.[7]

However, negative clinical consequences of overlapping FDs have also been reported, including in-stent thrombosis, stenosis, and perforator occlusion.[8,9] These complications are likely due to the increased metal surface area and lowered porosity due to additional FDs.[8] It would be desirable to deploy a single FD but to achieve as much aneurysmal flow reduction as overlapping multiple FDs, to reduce the risk of these complications.

Most interesting, because its individual wires can slide over one another, an FD can generate spatially varying mesh density when deployed. This ability was demonstrated by several benchtop experiments that showed that when longitudinally compressed during deployment, an FD expands radially and its wires compact into a localized zone of higher mesh density.[10,11] To use this property, we recently developed a novel deployment strategy to achieve local FD compaction for patient-specific IAs: the dynamic push-pull technique (DPPT).[12] With this strategy, the mesh density of an FD can be increased over the IA orifice during deployment through synergistic push-and-pull maneuvers between the microcatheter and delivery wire. We demonstrated the use of the DPPT for patient-specific IAs in vitro by physically deploying FDs and compacting their meshes in several IA flow phantoms.[13] We also showed that an FD compacted by using the DPPT reduced aneurysmal flow velocity 38% more than a noncompacted, uniformly deployed FD.[14] A recent in vivo study of canine aneurysm models also found that compacted FDs resulted in more frequent occlusion than noncompacted FDs.[15] We hypothesized that a single compacted FD could realize the benefits of overlapping multiple FDs without associated complications.

This study tested numerically whether compacting a single FD could be as effective as 2 overlapped FDs in aneurysmal flow reduction. To this end, we used a finite element method–based modeling technique—the high-fidelity virtual stenting (HiFiVS)[12] method—to simulate various FD deployment strategies, including single noncompacted, 2 overlapped, and single compacted. Applying these modeling strategies, we virtually "treated" 3 representative patient-specific IAs: a fusiform, a large saccular, and a medium saccular aneurysm. We then performed computational fluid dynamics (CFD) analysis to assess hemodynamic modifications in each scenario and compared the resulting flow modifications by using 5 hemodynamic parameters.

MATERIALS AND METHODS

Creation of IA Models

For this computational study, we chose 3 representative patient-specific IAs as test cases: a medium 9-mm fusiform basilar trunk IA, a large 18-mm saccular internal carotid artery IA, and a medium 9.5-mm saccular internal carotid artery IA. They were all treated by FDs at Gates Vascular Institute (Buffalo, New York), and their pretreatment angiographic images were obtained at the time of treatment under institutional review board approval. Although all 3 cases were treated by FDs, the FD strategies tested in the current numeric study answered the question of the effectiveness of different competing treatment strategies and did not correspond to the actual treatments received by these patients.

To create the 3D IA models, we segmented their angiographic images by using the level set and marching cube methods in The Vascular Modeling Toolkit (www.vmtk.org).[16] To make the FD deployment simulations computationally tractable, we assumed that the IA models were rigid. This assumption was reasonable because FDs exhibit lower radial forces[1] than closed-pore stents and thus have less effect on vessel morphology.

FD Size Selection

We selected the FD size for each IA by following standard clinical procedures.[17] The nominal diameter of an FD was chosen to approximate the size of the recipient parent vessel in each IA, and the nominal length was chosen to be at least 6 mm longer than the length of the IA neck. This process gave rise to 3 FD specifications for each IA: FDs measuring at least 5 × 13, 4.25 × 12, and 3.25 × 10 mm in the fusiform, large, and medium IAs, respectively.

Modeling the Deployment Strategies of Noncompacting and Overlapping FDs with HiFiVS

The HiFiVS[12] method was used to virtually deploy FDs in this study. As previously described, HiFiVS is a finite element method–based FD simulation technique that models several components of the FD delivery system, including the crimper, microcatheter, distal coil, and proximal pusher. All deployment mechanics and critical steps that affect the final configurations of FDs were simulated, including crimping, delivery, release, and expansion.

The HiFiVS method was rigorously validated in our previous experimental studies.[12,13] Side-by-side comparisons between experimental deployment of FDs in transparent IA phantoms and in silico deployment in identical IA models showed excellent agreement, as demonstrated in Fig 6 of Ma et al (2013).[12] Local mesh characteristics of compacted FDs deployed by HiFiVS matched those deployed experimentally by the DPPT, as demonstrated in Fig 2 of Ma et al (2014).[13]

In the current study, we modeled the FDs after the Pipeline Embolization Device. The wire braiding pattern for each FD was generated in Matlab (MathWorks, Natick, Massachusetts) on the basis of mathematic description.[18] The FD deployment procedure was simulated by using the finite element solver Abaqus/Explicit 6.13 (SIMULIA; 3DS, Waltham, Massachusetts).

To virtually deploy an FD without compaction, we retracted the microcatheter proximally while holding the distal coil still to produce uniform mesh density over the IA orifice. To simulate the deployment of 2 overlapped FDs, we ran 2 independent HiFiVS simulations consecutively.[7] Following the deployment of the first FD in each IA (5 × 20, 4.5 × 20, and 3.25 × 14 mm for the fusiform, large, and medium IAs, respectively), a second FD mea-

suring 5 × 20, 4.5 × 14, and 3.25 × 12 mm was coaxially deployed in the fusiform, large, and medium IAs, respectively.

Modeling the Deployment Strategy of Compacting a Single FD with HiFiVS

The previously described modeling technique of emulating the DPPT[12,13] was used in the current study to compact a single FD. This consisted of retracting the microcatheter proximally as in regular noncompacting deployment to unsheathe the FD, while advancing the proximal pusher distally to generate dense FD mesh over the IA orifice.

To generate the most flow diversion in each IA, we maximized the FD compaction during deployment by maneuvering the movement of the microcatheter and proximal pusher. The simulation procedure was stopped if the FD started to migrate distally or the wires of the FD began to unwind or tangle. Using this procedure, we maximally compacted FDs measuring 5 × 20, 4.5 × 20, and 3.25 × 14 mm in the fusiform, large, and medium IAs, respectively.

Quantification of FD Mesh Characteristics

The amount of aneurysmal flow reduction achievable by an FD in a patient-specific IA is affected by its mesh porosity and pore density in its fully deployed state.[1] An ideal FD has low porosity and high pore density to maximize flow diversion[1]: Porosity represents the amount of empty space created by the mesh pores of the FD, and pore density, the number of pores per unit area.[19] We quantified these parameters near the IA orifice along the length of a deployed FD in 5 consecutive zones: proximal vessel, proximal transition, middle, distal transition, and distal vessel, as defined previously on the basis of an FD compacted via the DPPT.[13] The proximal/distal vessel zones were the portions of the FD constrained in the parent vessel. The FD mesh in the middle zone (ie, over the IA orifice) was compacted because the goal of the DPPT is to increase mesh density over the IA orifice.[13] The remainder of the IA orifice not covered by the middle zone was covered by the proximal/distal transition zones. Even though FDs deployed without compaction presented more or less uniform meshes, to compare porosity and pore density between different strategies, we analyzed all FDs in these 5 zones.

Quantification of FD Mesh Compaction

When an FD is axially compressed, 2 things happen simultaneously: The woven wires of the FD compact together and the FD construct expands radially. With FD deployment via the DPPT, the aim is to create local mesh compaction over the IA orifice to block flow into the IA.[13] While the FD wires compact together, the IA orifice provides space to allow the FD construct to expand during compaction. Clearly the size of the orifice limits the degree to which an FD can be compacted and thus the effectiveness of the FD compaction strategy at improving aneurysmal flow reduction. Therefore, we investigated the relationship between the IA orifice area and the achievable compaction. This information could help clinicians determine the types of IA geometry for which the FD compaction strategy is most effective.

To that end, we measured IA orifices on the plane that separates the IA sac from the parent vessel for the saccular IAs and on the plane that separates the largest bulge from the parent vessel for the fusiform IA. Once the orifice was identified, we quantified the degree of achievable FD compaction by a new parameter, the compaction coverage (CC), as defined in Equation 1. Here, compaction coverage represents the percentage of the IA orifice covered by the middle zone of the compacted FD.

$$\text{CC}\ (\%) = \frac{\text{Compaction Zone Area}}{\text{IA Orifice Area}} \quad (1)$$

CFD Simulations

Pre- and posttreatment hemodynamics in all IA models were simulated by using CFD in Star-CCM+ v.10 (CD-adapco, Melville, New York). Blood flow was assumed to be pulsatile, laminar, incompressible, and Newtonian (density = 1056 kg/m^3, dynamic viscosity = 3.5 cP). A patient-specific, pulsatile velocity waveform was prescribed at each inlet, having a mean velocity matching typical flow rates at each IA location. A traction-free boundary condition was specified at each outlet.[7] To solve for the aneurysmal flow fields, we spatially discretized each IA into unstructured grids by using polyhedral cells.[7] Additional details of the CFD meshing parameters and the results of a mesh independence study are included in the On-line Appendix. Three cardiac cycles were simulated to ensure numeric stability of the flow solutions in all IA models. All hemodynamic parameters presented were time averages over the third cycle.

To compare aneurysmal flow modifications by the 3 FD strategies, we assessed posttreatment changes of 5 hemodynamic parameters: inflow rate, aneurysm-averaged velocity, wall shear stress, total absolute circulation, and turnover time. Previous studies reported that FDs reduced inflow rate, velocity, and wall shear stress and increased turnover time and that the amount of change correlated with IA occlusion rates.[20,21] In addition, we also examined posttreatment changes in the total absolute hydrodynamic circulation. This new parameter is a modified version of hydrodynamic circulation that was used previously to compare aneurysmal flow changes by several custom-designed FDs.[19] By definition, hydrodynamic circulation is an integration of vorticity flux over a region. Because the positive and negative vortex subregions could cancel out and give zero or small total circulation in this region, the use of hydrodynamic circulation could mask the true amount of rotational flow activity in this region. To capture the total amount of rotational flow activity of both positive and negative vortices in an aneurysm, we defined the total absolute circulation (Γ_A) as the integration of the absolute value of vorticity flux over the IA midplane as shown in Equation 2:

$$\Gamma_A = \int\int |\vec{\omega} \cdot \hat{n}|\, dA \quad (2)$$

where $\vec{\omega}$ is the local time-averaged vorticity, $\vec{\omega} \cdot \hat{n}$ is its component normal to the IA midplane, and the integration is over the entire midplane. The IA midplane is formed by 2 vectors: 1) the vector pointing from the centroid of the IA orifice to the centroid of the IA sac, and 2) the vector pointing from the centroid of the cross-section of the parent vessel immediately proximal to the IA to the centroid of the parent vessel cross-section immediately distal. We

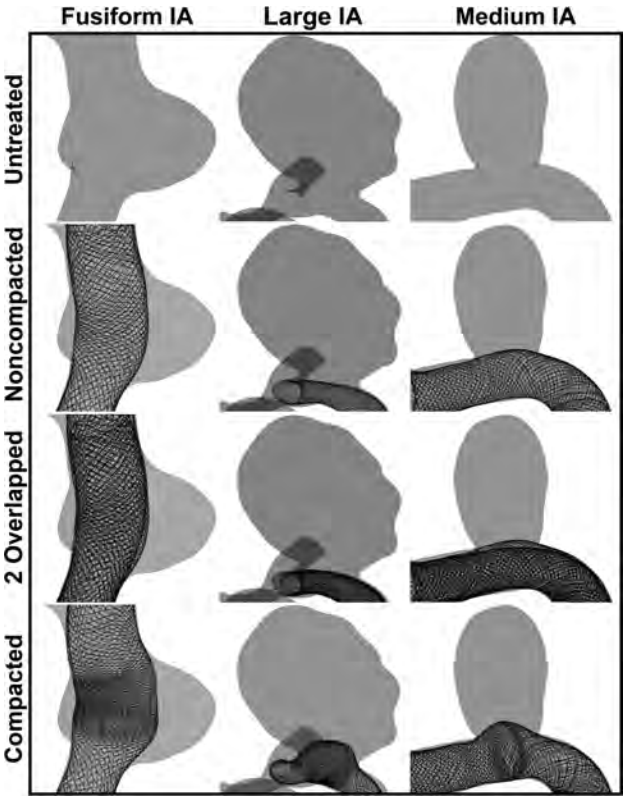

FIG 1. FD deployment results in all 3 IAs.

define the IA sac as the volume enclosed by the wall of the IA and the IA orifice.

RESULTS

Compacting a Single FD Achieved Similar Porosity and Pore Density as Overlapping FDs

Figure 1 shows the geometry of the 3 IA models and the FDs virtually deployed by the 3 FD treatment strategies in each IA. The fusiform IA (on the basilar artery) involves the entire circumference of the parent vessel, with the largest bulge protruding to the right (left column of Fig 1). The 2 saccular IAs both occur sidewall on the internal carotid artery. After treatment, the mesh density appears rather uniform in all 3 IA models for the noncompacted FD and overlapped FDs. The compacted FD, on the other hand, shows highly variable mesh density in all 3 cases, bulging into the IA sac and compacting in a distinct zone of higher mesh density. The middle zone is largest in the fusiform IA and decreases in the large and medium IAs. The remaining zones of the compacted FD are less dense in comparison with the middle zone in all 3 IAs.

Figure 2 shows the quantification of mesh variations in terms of porosity and pore density of all virtually deployed FDs. The 5 mesh zones for calculating these quantities are illustrated in Fig 2*A*, with the fusiform IA as an example, wherein the middle zone (M) of the compacted FD has much higher mesh density over other zones. Figure 2*B*, -*C* shows porosity and pore density, respectively, plotted over the consecutive mesh zones for all FD strategies. Overall, the single noncompacted FDs have the highest porosity and lowest pore density, while the overlapped FDs have the lowest porosity and highest pore density. The compacted FDs show large variations in both porosity and pore density along their lengths. They are generally similar to those in the single noncompacted FDs, but in the middle zone, they have a large jump, approaching or exceeding the overlapped FDs, except for 2 cases.

Compaction Coverage Increased Linearly with IA Orifice Area

To explore the relationship between the maximally achievable FD compaction and IA geometry, we quantified the IA orifice area, the area of compaction, and the compaction coverage. Figure 3 shows the FD mesh at the orifices of the 3 IAs and the CC plotted against the orifice area. The fusiform IA orifice had the largest coverage by the middle zone (ie, the compacted portion), and the medium IA orifice had the smallest (Fig 3*A*). Conversely, the medium IA orifice had the largest coverage by the transition zones (ie, the noncompacted portions), and the fusiform IA orifice had the smallest. The orifice areas for the fusiform, large, and medium IAs were 34.5, 30.0, and 14.7 mm^2, respectively, while the corresponding CCs were 57%, 47%, and 22%, respectively. Figure 3*B* demonstrates a strong linear correlation between the CC and IA orifice area ($R^2 = 0.9965$). In both saccular IAs, CC was below 50%, meaning less than half of the IA orifice was covered by the middle zone.

Compacting a Single FD Outperformed Overlapping 2 FDs in Aneurysmal Flow Reduction in the Fusiform IA

We performed CFD simulations for all 12 IA models shown in Fig 1, including the 3 untreated IAs, and posttreatment hemodynamics by using all 3 treatment strategies in each IA. Figure 4 shows the volume-rendered time-averaged velocity magnitude in all 12 IA models. In addition to the velocity magnitude (rendered in color), streamlines (rendered in black) are plotted to visualize the flow modifications by each FD strategy. In the fusiform IA, a strong vortex was formed in the large bulge, and it was diminished by the FDs to various extents, with the compacted FD delivering the most reduction. In the large and medium saccular IAs, an inflow jet entered the IA sac distally and circulated throughout the IA sac before exiting proximally. In the large IA, the size and velocity of the inflow jet was reduced most by the compacted FD, followed by the overlapped FDs and then the noncompacted FD. On the other hand, in the medium IA, the overlapped FDs reduced the size and velocity of the inflow jet the most. The compacted FD appeared to disrupt the inflow jet as much as, but no more than, the noncompacted FD in the medium IA.

To quantify the different effects of flow reduction by the 3 FD strategies, we calculated posttreatment modifications in the time-averaged inflow rate, aneurysm-averaged velocity, wall shear stress, total absolute circulation, and turnover time, all shown in Fig 5. Regardless of the deployment strategy, FDs reduced intraaneurysmal flow in all 3 IAs, as evidenced by the decrease in inflow rate, aneurysm-averaged velocity, wall shear stress, and total absolute circulation and an increase in turnover time from the untreated IAs. In the fusiform IA, the compacted FD outperformed the overlapped FDs in all 5 hemodynamic parameters. In contrast, the overlapped FDs outperformed the compacted FD in the large and medium IAs, except for total absolute circulation in the large IA, where the compacted FD performed best.

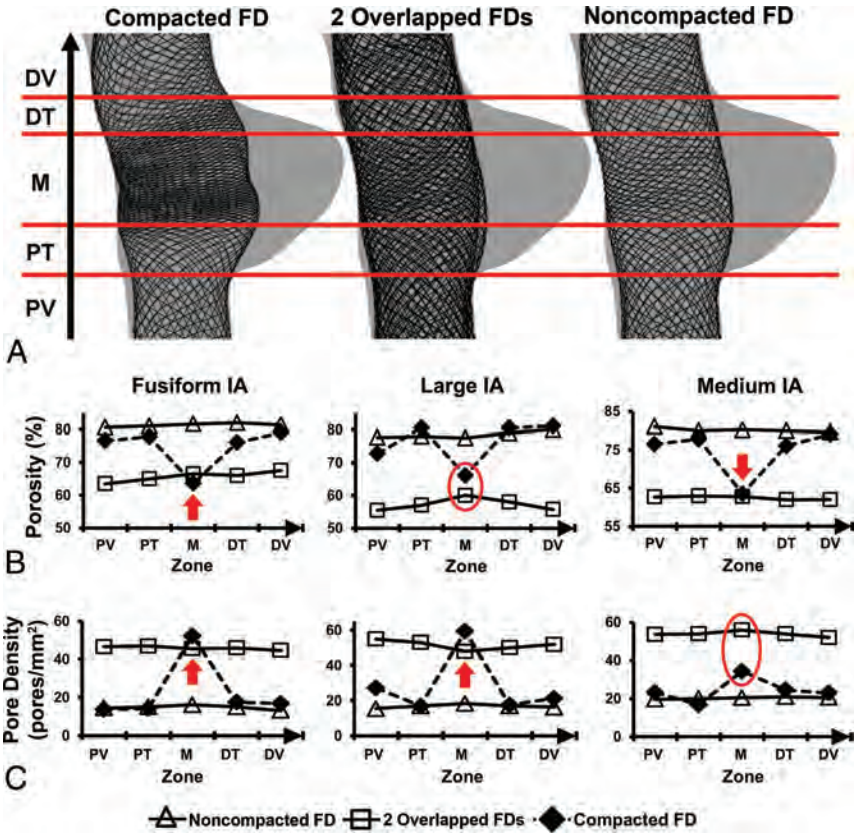

FIG 2. Porosity and pore density distributions of deployed FDs resulting from all 3 deployment methods in the 3 IAs. *A*, Deployed FD meshes in the fusiform IA and demarcations of FD zones used for porosity and pore density calculations: proximal vessel (PV), proximal transition (PT), middle (M), distal transition (DT), and distal vessel (DV). These zones are defined on the basis of the compacted FD but applied to all 3 deployment strategies for calculation of porosity and pore density. *B*, Porosity distribution. *C*, Pore density distribution. The *arrows* indicate middle zones in which the compacted FD has lower porosity or higher pore density than the overlapped FDs, whereas the *ovals* indicate middle zones in which it does not.

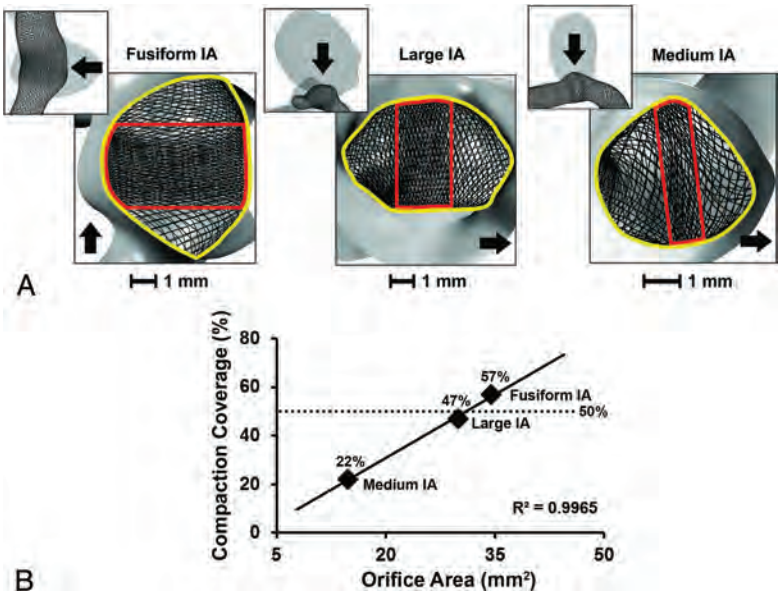

FIG 3. FD mesh compaction achieved in the 3 IAs. *A*, Compacted meshes at the IA orifice. Orifice areas are highlighted by the *circular regions*, and the compaction zones, by the *rectangular regions*. The *arrows* in the smaller schematics of each IA indicate viewing directions at each IA orifice. The *arrows* in the larger schematics of each IA orifice indicate the flow direction. *Scale bars* below each IA orifice indicate distances of 1 mm. *B*, Plot of compaction coverage (percentage) versus IA orifice area, showing a strong linear relationship.

DISCUSSION

In this computational study, we tested whether a single compacted FD could outperform 2 overlapped FDs in IA flow reduction. Our results suggest that this goal is achievable provided that the compaction of the single FD can achieve 2 conditions: 1) It produces a compacted mesh in the middle zone that is denser than 2 overlapped FDs, as judged by both porosity and pore density; and 2) this denser mesh covers a sufficient portion of the IA orifice area, of which we suggest a minimum of 50%.

In the fusiform IA model, compacting a single FD achieved both of these conditions. Not surprising, the compacted FD outperformed the 2 overlapped FDs in all 5 hemodynamic parameters. In the 2 saccular IAs, however, compacting a single FD did not achieve both compaction conditions above. In the large saccular IA, the porosity did not get down to the level of the 2 overlapped FDs (Fig 2*B*), while in the medium saccular IA, the pore density did not reach that of the overlapped FDs (Fig 2*C*) and neither IA allowed CC of >50%. We believe that this inadequate compaction was responsible for the flow simulation results in the 2 saccular IAs—that is, the compacted FD did not outperform the overlapped FDs in aneurysmal flow reduction. We further found that the degree to which an FD can be compacted and thus the ability to achieve both mesh conditions when compacting an FD are linearly related to the area of the aneurysm orifice. An FD can be compacted to a larger degree over an IA with a larger orifice because a large orifice provides more space for the FD to expand. This radial expansion occurs to accommodate the compaction of the woven wires of the FD as the FD is axially compressed. Therefore, the salient finding of this study is that compacting a single FD can outperform overlapping 2 FDs in aneurysms with large orifices, especially fusiform IAs.

We believe that compacting a single FD could be a superior strategy to overlapping multiple FDs, from both a biologic and economic standpoint. One concern with overlapping multiple FDs is that it increases the mesh density in the parent vessel, thereby increasing the

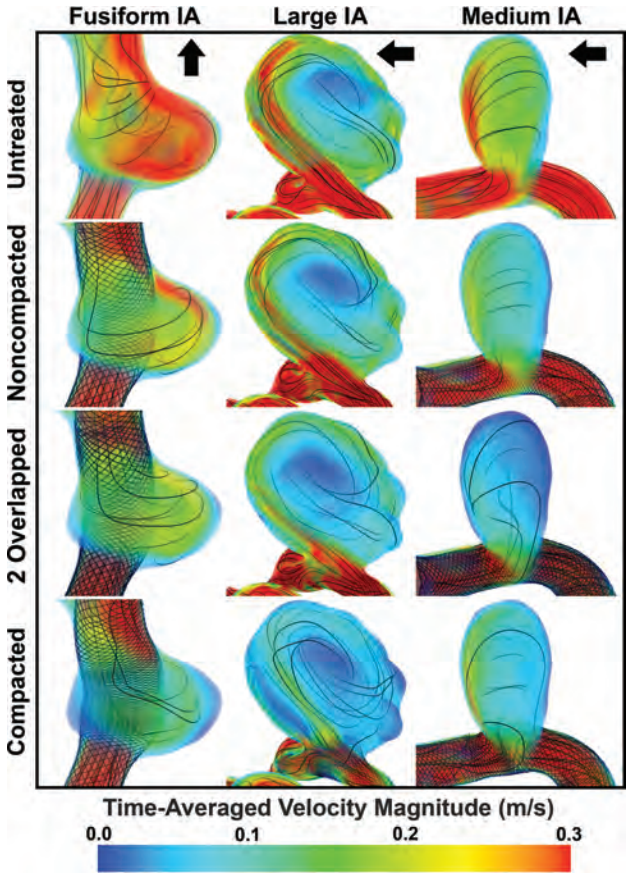

FIG 4. Time-averaged, volume-rendered velocity magnitude in all 3 IAs for each FD strategy. Streamlines are plotted to enhance visualization of flow modifications due to each FD strategy. The *arrows* indicate the flow direction for each untreated IA.

chance of perforator occlusion.[8] Overlapping multiple metal devices also increases the risk for in-stent thrombosis and stenosis.[9] In contrast, the strategy of compacting a single FD increases the mesh density only over the IA orifice, but not in the parent vessel, thereby minimizing the risk of occluding nearby perforators. In addition, this strategy uses a single device, thereby minimizing the amount of thrombogenic metal and eliminating the costs and procedural risks associated with additional devices.

The goal of compacting an FD is to increase mesh density over the IA orifice beyond that achievable by not compacting an FD, in the hope of accelerating IA occlusion. However, failing to achieve adequate mesh compaction may render the compacted FD no more effective at aneurysmal flow reduction than a noncompacted FD. This result is because the less area of an FD that is compacted over the IA orifice, the more area of the orifice that is left at a lower mesh density. In other words, the smaller the middle zone, the larger is the transition zones. Benchtop experiments have shown that mesh transition zones are unavoidable when compacting an FD.[10] In addition, the experiments showed that the transition zones were always less dense than the middle zone; this feature could compromise the ability of the FD mesh to divert aneurysm inflow. Our study supports this observation. We found that the mesh transition zones of the compacted FDs were approximately as dense as those of the noncompacted FDs in all 3 IAs (Fig 2*B*, -*C*). The implications of this result in our study were

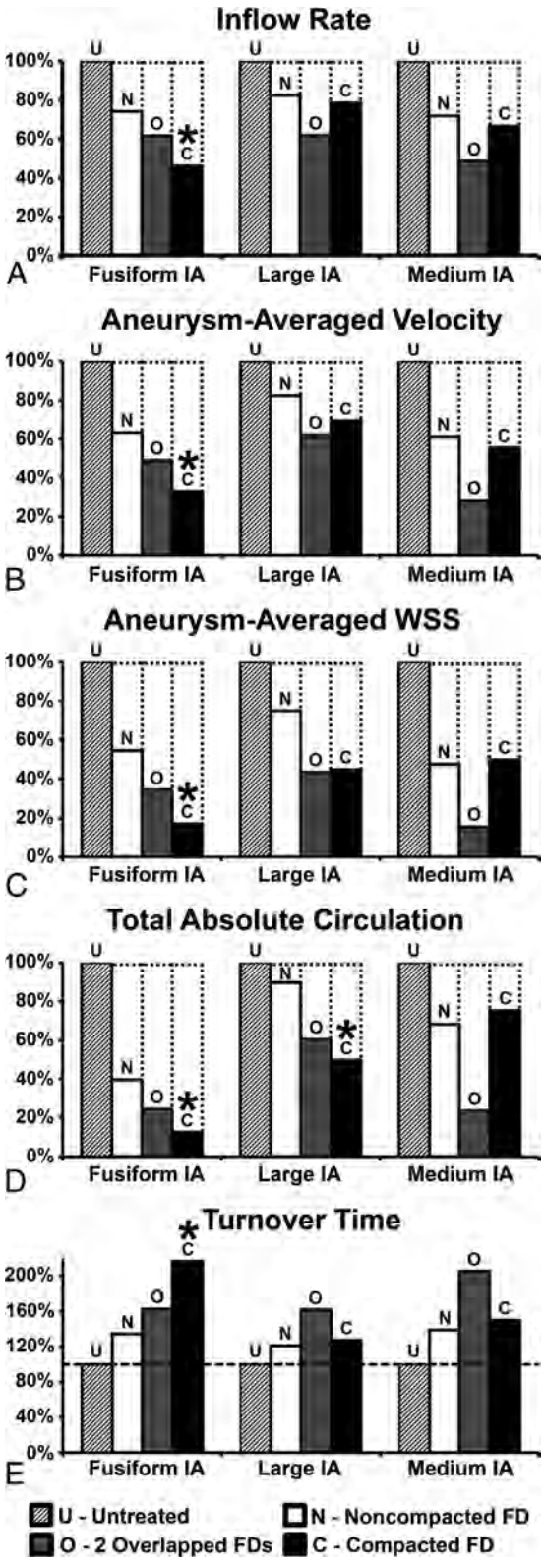

FIG 5. Changes in time-averaged hemodynamic parameters by FDs in each IA, relative to the untreated IAs. *A*, Inflow rate at the IA orifice. *B*, Aneurysm-averaged velocity in the IA sac. *C*, Aneurysm-averaged wall shear stress on the wall of the IA sac. *D*, Total absolute circulation at the IA midplane. *E*, Turnover time in the IA sac. Changes in hemodynamic parameters by FDs are reported as percentages of the values in the untreated IAs. The *asterisks* indicate instances in which the compacted FD outperformed the overlapped FDs.

most revealing when considering the medium IA, which has the smallest orifice area of the 3 IA cases. In this aneurysm, the compacted FD disrupted the IA inflow jet as much as but no more than the noncompacted FD, and the jet passed through the distal transition zone of the FD (Fig 4). We could not further compact the FD due to the small orifice (<50% CC). Consequently, most of the orifice was covered by the lower mesh density transition zones. Thus, inadequate compaction of an FD leaves the orifice covered by lower density mesh, thereby delaying or preventing thrombosis due to insufficient flow diversion. On the basis of our results, we suggest ensuring that at least 50% of the IA orifice is covered by the higher density middle zone when compacting an FD.

On the other hand, excessive compaction of an FD could also cause complications, for example, causing the FD to prolapse into the aneurysm or migrate along the parent vessel. Gentric et al,[15] in an attempt to treat several canine aneurysm models by compacting single FDs in vivo, experienced excessive compaction, which caused 4 FDs to prolapse into the aneurysm sac during deployment and 1 to migrate distally along the parent vessel following deployment. In the current in silico study, we also saw that if too much force was applied to the proximal pusher during compaction, the FD would migrate along the parent vessel. Consequently, we had to rerun the simulation with less force applied to ensure that the FD was anchored properly in the parent vessel. In the clinical setting, however, it would be extremely hard to salvage a prolapsed or migrated FD after deployment. Therefore, extra precaution is required to avoid excessively compacting an FD and causing FD prolapse or migration during the intervention.

Our study shows that no FD deployment strategy, including compacting FDs, is optimal for all IAs. We believe that IA geometry is the most important determining factor for the success of any flow-diversion strategy. Other factors also come into play as well. For example, the type and dimensions of the FD devices will determine the deployment process and the resulting mesh characteristics (eg, porosity and pore density). These, in turn, will determine the flow-diversion effect of the FD strategy (as demonstrated by Mut et al[22]). Furthermore, the success of the FD treatment also depends on the experience level of the neurointerventionalist. A steep learning curve is well-recognized in performing FD deployments, and the deployment procedure requires substantial technical ability,[23] especially for complex deployment techniques such as compacting or overlapping FDs.

CONCLUSIONS

We investigated whether compacting a single FD could outperform overlapping 2 FDs in aneurysmal flow reduction in 3 patient-specific IAs. We found that compacting a single FD can be as effective as overlapping 2 FDs in aneurysmal flow reduction, provided that the compaction of the single FD can produce a dense mesh in the middle zone that is denser than 2 overlapped FDs and this denser mesh covers a sufficient portion of the IA orifice area, of which we suggest a minimum of 50%. FD compaction is most suitable for IAs with large orifice areas, especially fusiform IAs.

ACKNOWLEDGMENTS

The authors thank the Center for Computational Research at the University at Buffalo for providing computational resources.

Disclosures: Adnan H. Siddiqui—*UNRELATED*: *Board Membership*: Intersocietal Accreditation Committee; *Consultancy*: Codman & Shurtleff, Medtronic, GuidePoint Global Consulting, Penumbra, Stryker, MicroVention, W.L. Gore & Associates, Three Rivers Medical Center, Corindus Vascular Robotics, Amnis Therapeutics, CereVasc, Pulsar Vascular, The Stroke Project, Cerebrotech Medical Systems, Rapid Medical, Lazarus (acquired by Medtronic), Medina Medical (acquired by Medtronic), Reverse Medical (acquired by Medtronic), Covidien (acquired by Medtronic), Neuroavi, Silk Road Medical, Rebound Medical; *Consulting Fee or Honorarium*: Medtronic, MicroVention; *Stock/Stock Options*: StimSox, Valor Medical, Neuro Technology Investors, Cardinal Health, Medina Medical, Buffalo Technology Partners, International Medical Distribution Partners; *Other*: Principal Investigators/National Steering Committees for various trials, *Comments*: the Penumbra 3D Separator Trial, the Covidien (Now Medtronic) Solitaire With the Intention For Thrombectomy as PRIMary Endovascular Treatment Trial and SWIFT DIRECT Trials, the MicroVention FRED Trial and CONFIDENCE Study, the LARGE Trial, POSITIVE Trial, Penumbra COMPASS Trial, and Penumbra INVEST Trial. Hui Meng—*RELATED*: *Grant*: National Institutes of Health*; *UNRELATED*: *Consultancy*: National Institutes of Health study sections*; *Grants/Grants Pending*: Brain Aneurysm Foundation*; *Payment for Lectures Including Service on Speakers Bureaus*: University of California, San Francisco*; *Patents (Planned, Pending, or Issued)*: University at Buffalo.* *Money paid to the institution.

REFERENCES

1. Sadasivan C, Cesar L, Seong J, et al. **An original flow diversion device for the treatment of intracranial aneurysms: evaluation in the rabbit elastase-induced model.** *Stroke* 2009;40:952–58 CrossRef Medline
2. Kulcsár Z, Houdart E, Bonafé A, et al. **Intra-aneurysmal thrombosis as a possible cause of delayed aneurysm rupture after flow-diversion treatment.** *AJNR Am J Neuroradiol* 2011;32:20–25 CrossRef Medline
3. Szikora I, Berentei Z, Kulcsar Z, et al. **Treatment of intracranial aneurysms by functional reconstruction of the parent artery: the Budapest experience with the Pipeline Embolization Device.** *AJNR Am J Neuroradiol* 2010;31:1139–47 CrossRef Medline
4. Nelson PK, Lylyk P, Szikora I, et al. **The Pipeline embolization device for the intracranial treatment of aneurysms trial.** *AJNR Am J Neuroradiol* 2011;32:34–40 CrossRef Medline
5. Becske T, Kallmes DF, Saatci I, et al. **Pipeline for uncoilable or failed aneurysms: results from a multicenter clinical trial.** *Radiology* 2013;267:858–68 CrossRef Medline
6. Kim M, Levy EI, Meng H, et al. **Quantification of hemodynamic changes induced by virtual placement of multiple stents across a wide-necked basilar trunk aneurysm.** *Neurosurgery* 2007;61:1305–12; discussion 1312–13 CrossRef Medline
7. Damiano RJ, Ma D, Xiang J, et al. **Finite element modeling of endovascular coiling and flow diversion enables hemodynamic prediction of complex treatment strategies for intracranial aneurysm.** *J Biomech* 2015;48:3332–40 CrossRef Medline
8. Tan LA, Keigher KM, Munich SA, et al. **Thromboembolic complications with Pipeline Embolization Device placement: impact of procedure time, number of stents and pre-procedure P2Y12 reaction unit (PRU) value.** *J Neurointerv Surg* 2015;7:217–21 CrossRef Medline
9. Tse MM, Yan B, Dowling RJ, et al. **Current status of Pipeline embolization device in the treatment of intracranial aneurysms: a review.** *World Neurosurg* 2013;80:829–35 CrossRef Medline
10. Makoyeva A, Bing F, Darsaut TE, et al. **The varying porosity of braided self-expanding stents and flow diverters: an experimental study.** *AJNR Am J Neuroradiol* 2013;34:596–602 CrossRef Medline
11. Shapiro M, Raz E, Becske T, et al. **Variable porosity of the Pipeline embolization device in straight and curved vessels: a guide for optimal deployment strategy.** *AJNR Am J Neuroradiol* 2014;35:727–33 CrossRef Medline
12. Ma D, Dumont TM, Kosukegawa H, et al. **High fidelity virtual stent-**

ing (HiFiVS) for intracranial aneurysm flow diversion: in vitro and in silico. *Ann Biomed Eng* 2013;41:2143–56 CrossRef Medline
13. Ma D, Xiang J, Choi H, et al. **Enhanced aneurysmal flow diversion using a dynamic push-pull technique: an experimental and modeling study.** *AJNR Am J Neuroradiol* 2014;35:1779–85 CrossRef Medline
14. Xiang J, Ma D, Snyder KV, et al. **Increasing flow diversion for cerebral aneurysm treatment using a single flow diverter.** *Neurosurgery* 2014;75:286–94; discussion 294 CrossRef Medline
15. Gentric JC, Salazkin I, Gevry G, et al. **Compaction of flow diverters improves occlusion of experimental wide-necked aneurysms.** *J Neurointerv Surg* 2016;8:1072–77 CrossRef Medline
16. Antiga L, Piccinelli M, Botti L, et al. **An image-based modeling framework for patient-specific computational hemodynamics.** *Med Biol Eng Comput* 2008;46:1097–112 CrossRef Medline
17. Eller JL, Dumont TM, Sorkin GC, et al. **The Pipeline embolization device for treatment of intracranial aneurysms.** *Expert Rev Med Devices* 2014;11:137–50 CrossRef Medline
18. Ma D, Dargush GF, Natarajan SK, et al. **Computer modeling of deployment and mechanical expansion of neurovascular flow diverter in patient-specific intracranial aneurysms.** *J Biomech* 2012; 45:2256–63 CrossRef Medline
19. Lieber BB, Sadasivan C. **Endoluminal scaffolds for vascular reconstruction and exclusion of aneurysms from the cerebral circulation.** *Stroke* 2010;41:S21–25 CrossRef Medline
20. Xiang J, Damiano RJ, Lin N, et al. **High-fidelity virtual stenting: modeling of flow diverter deployment for hemodynamic characterization of complex intracranial aneurysms.** *J Neurosurg* 2015;123: 832–40 CrossRef Medline
21. Mut F, Raschi M, Scrivano E, et al. **Association between hemodynamic conditions and occlusion times after flow diversion in cerebral aneurysms.** *J Neurointerv Surg* 2015;7:286–90 CrossRef Medline
22. Mut F, Cebral JR. **Effects of flow-diverting device oversizing on hemodynamics alteration in cerebral aneurysms.** *AJNR Am J Neuroradiol* 2012;33:2010–16 CrossRef Medline
23. Jabbour P, Chalouhi N, Tjoumakaris S, et al. **The Pipeline Embolization Device: learning curve and predictors of complications and aneurysm obliteration.** *Neurosurgery* 2013;73:113–20; discussion 120 CrossRef Medline

Differential Interstrain Susceptibility to Vertebrobasilar Dolichoectasia in a Mouse Model

Y.-Q. Zhu, H. Xing, D. Dai, D.F. Kallmes, and R. Kadirvel

ABSTRACT

BACKGROUND AND PURPOSE: Vetebrobasilar dolichoectasia is characterized by arterial elongation, dilation, and tortuosity and leads to high risks of ischemic stroke. Our aim was to investigate the differential susceptibility to elastase-induced vertebrobasilar dolichoectasia induction in 2 different mouse strains.

MATERIALS AND METHODS: Elastase (25 mU) was injected into the cisterna magna in C57BL/6J ($n = 36$) and 129/SvEv (SV129) ($n = 36$) mice. Control animals were injected with heat-inactivated elastase ($n = 12$ for each strain). At 3, 7, 14, and 28 days after elastase injection, MICROFIL polymer perfusion was performed. The arterial tortuosity index and the percentage increase in diameter were calculated for the basilar artery. Arterial samples were processed for conventional histologic examination, immunostaining, and matrix metalloproteinase expression. A ≥50% increase in diameter and a tortuosity index of ≥10 for the basilar artery were used to indicate success in achieving vertebrobasilar dolichoectasia.

RESULTS: Successful vertebrobasilar dolichoectasia induction was noted in 67% (18 of 27) of the C57BL/6J strain versus 0% (0 of 19) of the SV129 strain ($P < .001$). Vertebrobasilar dolichoectasia was not observed in sham-operated controls. Both the tortuosity index and diameter increase for the basilar artery were greater in the C57BL/6J strain compared with the SV129 strain (56.3% ± 16.4% versus 21.1% ± 21.6% for diameter, $P < .001$; 17.4 ± 7.6 versus 10.4 ± 3.8 for tortuosity index, $P < .001$). Expression of pro-matrix metalloproteinase-2 and pro- and active matrix metalloproteinase-9 was increased in elastase-injected C57BL/6J animals compared with elastase-injected SV129 animals ($P = .029$, 0.029, and 0.029, respectively). Inflammation scores were significantly higher in C57BL/6J animals versus SV129 animals ($P < .001$). C57BL/6J subjects demonstrated arterial wall dilation and elongation characterized by internal elastic lamina disruption, muscular layer discontinuity, inflammatory cell infiltration, and high matrix metalloproteinase expression in the media.

CONCLUSIONS: C57BL/6J mice demonstrated greater susceptibility to vertebrobasilar dolichoectasia induction than SV129 mice.

ABBREVIATIONS: BA = basilar artery; MMP = matrix metalloproteinase; TI = tortuosity index; VBD = vertebrobasilar dolichoectasia

Intracranial arterial dolichoectasia is an arteriopathy characterized by elongation, dilation, and tortuosity of the intracranial vasculature, with the posterior circulation and basilar artery (BA) most frequently affected.[1,2] Development of vertebrobasilar dolichoectasia (VBD) portends a high risk of subsequent neurologic decline, resulting from ischemic stroke, perforator infarction, and compression of critical posterior fossa structures. Recent, large clinical studies have shown that VBD may be found in up to 12% of patients presenting with stroke.[3] Current understanding has focused on the role of the internal elastic lamina, the disruption of which, along with medial smooth-muscle atrophy, has been suggested as critical in the progression of the disease. However, the exact pathophysiology of this disorder is poorly understood,[4,5] and therapeutic options remain limited. Indeed, at present, there is no medical, surgical, or interventional therapy shown to mitigate the progression of VBD. Improved understanding of molecular and genetic features may allow improved treatment paradigms for this often-devastating disorder.

Notwithstanding widely acknowledged limitations of small-animal models in human disease, aneurysmal disease represents a focused area in which murine models have shown promise. Previous studies of experimental abdominal aortic aneurysms have used numerous lines of research, including assessment of differential susceptibility to aneurysm formation in different mouse strains, to probe the underlying pathophysiology of this disorder. We recently reported a preclinical model, in C57BL/6J mice, of

Received April 29, 2016; accepted after revision October 11.

From the Department of Radiology (Y.-Q.Z., H.X., D.D., D.F.K., R.K.), Mayo Clinic, Rochester, Minnesota; Department of Radiology (Y.-Q.Z.), Shanghai Jiao Tong University Affiliated Sixth People's Hospital, Shanghai, China; and Department of Pathology (H.X.), Shanghai East Hospital, Medical School of Shanghai Tongji University, Shanghai, China.

Please address correspondence to Ramanathan Kadirvel, PhD, Mayo Clinic, 200 First St SW, Rochester, MN 55905; e-mail: kadir@mayo.edu

http://dx.doi.org/10.3174/ajnr.A5028

VBD induced via microsurgical injection of porcine elastase into the cisterna magna to induce morphologic changes similar to human VBD.[6] The aims of the current study were to elucidate the morphologic and molecular differences in VBD between C57BL/6J and 129/SvEv (SV129) mouse strains.

MATERIALS AND METHODS

Elastase Injection Procedure

C57BL/6J ($n = 48$) and SV129 ($n = 48$) female mice (6–8 weeks of age) (Charles River Laboratories, Wilmington, Massachusetts) were used in the current study and were divided into a test group ($n = 36$ for each strain) and a control group ($n = 12$ for each strain). The use of animals and procedures was reviewed and approved by the Institutional Animal Care and Use Committee in Mayo Clinic.

The mouse model of VBD was induced as previously described.[6] Using a 10-μL micro NanoFil syringe (World Precision Instruments, Sarasota, Florida) with a 36-ga beveled needle, we injected 25 mU of porcine elastase (Worthington Biochemical, Lakewood, New Jersey) in 2.5 μL of phosphate-buffered saline (10 mU/μL) into the cisterna magna under a dissection microscope. Control mice were injected with inactivated elastase.

MICROFIL Perfusion and Tissue Harvest

Animals in the test group of each strain were randomly assigned to 4 subgroups ($n = 8$ at each time point) and were sacrificed at 3, 7, 14, and 28 days after elastase injection. Control mice ($n = 8$ for each strain) were sacrificed at 28 days. The MICROFIL (Flow-Tech, Cockeysville, Maryland) perfusion was performed at follow-up as described previously.[6] After MICROFIL perfusion, the whole brain along with the cerebral vascular trees was harvested and fixed in 10% buffered formalin at room temperature at least 24 hours before imaging. Animals designated for zymography analysis were perfused with saline; the basilar artery was harvested at 14 days and snap frozen in liquid nitrogen ($n = 8$ for each strain; $n = 4$ for each control and test group).

Morphometric Analysis

Under the dissecting microscope, visual inspection of the arteries at the skull base was performed to determine the presence of tortuosity and enlargement compared with the control samples. The vascular trees were then photographed by using the Micro-Publisher 5.0 RTV camera (QImaging; http://www.qimaging.com/) attached to the dissection microscope; Q-Capture Pro 7 software (QImaging) with inner calibration was used to capture the images. Morphometric analysis was performed for the BA. We selected the area of maximal dilation for diameter measurements (exterior side to exterior side) from the MICROFIL-perfused gross images by using Image-Pro Plus software (Media Cybernetics, Bethesda, Maryland). The percentage increase in arterial diameter ([individual measured diameter − average diameter of control samples] ÷ average diameter of control samples) was determined. The previously validated tortuosity index (TI)[7] was applied to calculate the TI for the current study. TI was defined as the following: [(actual length of the vessel / straight-line length of same vessel − 1) × 100]. Successful VBD induction was defined as a TI ≥ 10 and a ≥50% increase in BA diameter compared with control samples.

Histologic Examination

Harvested samples were fixed in 10% neutral-buffered formalin for >48 hours, dehydrated by using a graded ethanol series (70%–100%), and embedded in paraffin. Transverse sections containing the BA were taken at 4-μm thickness and stained with hematoxylin-eosin and elastic fiber stains (Verhoeff-van-Gieson) to assess internal elastic lamina disruption in the media. Serial cross-sections of the BA were used to evaluate inflammation reaction on the basis of inflammation scores.[8] The score was defined as follows: 0 = no inflammatory cell infiltration; 1 = minimal or mild: scant, scattered inflammatory cell infiltration; 2 = patchy but localized or limited inflammatory cells; 3 = marked, attenuated, diffuse inflammatory cell infiltration. Samples were also immunostained by using the rabbit polyclonal smooth-muscle α-actin antibody (1:200; Abcam, Cambridge, Massachusetts), rabbit polyclonal CD45 antibody (leukocyte common antigen; 1:200; Abcam), mouse monoclonal antimacrophage antibody (clone MAC387; 1:200; Thermo Fisher Scientific, Waltham, Massachusetts), rabbit polyclonal matrix metalloproteinase (MMP)-9 antibody (1:100; Abcam), and rabbit monoclonal MMP-12 antibody (clone EP1261Y; 1:200; Abcam) by using the immunofluorescent technique. Double immunofluorescent staining was performed by using anti-CD45 (leukocytes) and antimacrophages to assess whether macrophages were included in leukocytes. Negative controls were performed by omitting primary antibodies. Statistical analysis of the histopathologic images was performed with Image-Pro Plus software in at least 5 randomly selected high-power (×400) tubulointerstitial fields from each section. Two pathologists assessed every pathologic index in each section and reached agreement by consensus in a blinded manner.

Gelatin Zymography for MMPs

Soluble proteins were extracted from the BA of elastase-injected ($n = 4$ for each strain) and heat-inactivated elastase-injected ($n = 4$ for each strain) groups at 14-day follow-up. Protein samples (20 μg per lane) were separated by 10% zymogram gel (Bio-Rad Laboratories, Hercules, California). Gels were washed with renaturation buffer (Bio-Rad) for 1 hour and then incubated for 48 hours at 37°C in development buffer (Bio-Rad). The gels were stained with 0.5% Coomassie blue R-250 (Thermo Fisher Scientific). The gelatinolytic bands, representing the activities of MMPs, were scanned and analyzed densitometrically by using ImageJ software (National Institutes of Health, Bethesda, Maryland).

Data Analysis and Statistical Methods

Animals that had neurologic complications or did not survive for specified follow-up time points were excluded from the analysis, as were the MICROFIL-perfused samples that did not show proper casting as indicated by air bubbles or partial filling in the cast.

Effect of follow-up time and strain on percentage BA increase and TI were assessed with robust analysis of variance by using the Huber M-estimator. Variables were then dichotomized into successful or unsuccessful injections for percentage BA increase and

Table 1: Success of VBD formation in C57BL/6J and SV129 mouse strains[a]

Follow-Up Time Point (Days)	C57BL/6J			SV129			
	Total No.	No. Successful	Success Rate (95% CI)	Total No.	No. Successful	Success Rate (95% CI)	*P* Value
3	7	4	0.57 (0.18–0.90)	5	0	0.00 (0.00–0.52)	
7	8	6	0.75 (0.35–0.97)	3	0	0.00 (0.00–0.71)	
14	7	4	0.57 (0.18–0.90)	6	0	0.00 (0.00–0.46)	
28	5	4	0.80 (0.28–1.0)	5	0	0.00 (0.00–0.52)	
Total No.	27	18	0.67 (0.46–0.84)	19	0	0.00 (0.00–0.18)	<.001

[a] Successful VBD was defined as the percentage increase in basilar artery diameter of ≥50% and a tortuosity index of ≥10. The number and proportion of mice showing successful VBD for each strain and time point are displayed. Ninety-five percent Clopper-Pearson CIs are displayed for each estimate. Proportion of successes was compared between strains using the Fisher exact test.

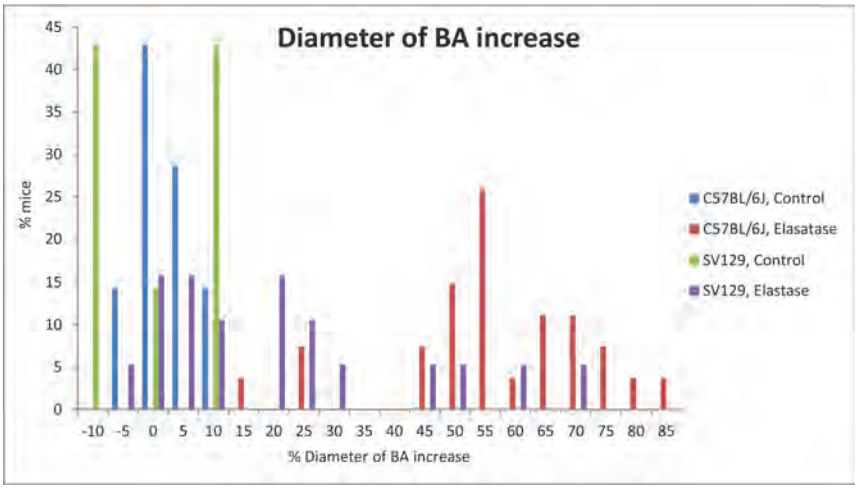

FIG 1. Extent of basilar artery dilation in increased distribution in C57BL/6J and SV129 mouse strains after elastase injection.

TI (with success being defined for BA as a percentage BA increase of ≥50 or for TI as a TI increase of ≥10). Results were pooled across time points within strains before between-strain comparisons were performed. The overall proportion of successful VBD (both percentage BA increase of ≥50 and TI of ≥10), proportion of BA increase of ≥50%, and the proportion of TI of ≥10 in treated mice were compared by using the Fisher exact test. MMP expression and inflammation scores between strains were compared by using Wilcoxon rank sum tests. Kruskal-Wallis tests were performed to test for the effect of the date of sacrifice on the inflammation score in treated mice, and subsequent pair-wise comparisons were performed by using the Dunn test with a Bonferroni correction. Significance was defined as $P < .05$. Analyses of variance were performed by using SAS (Version 9.3; SAS Institute, Cary, North Carolina). All other analyses were performed by using R statistical and computing software (Version 3.1.1; http://www.r-project.org/).

RESULTS

Mortality and Exclusion

Mortality rates after injection of elastase in C57BL/6J and SV129 mice were 4.2% (2 of 48) and 2.1% (1 of 48), respectively ($P = 1.00$). Two C57BL/6J mice and 1 SV129 mouse had injection-related neurologic complications, including muscle weakness of the left hind leg in 1 and dysequilibrium in 2. No deaths or neurologic complications were observed in the control groups. Three animals in the test group of the C57BL/6J strain and 12 animals in the test group of the SV129 strain did not show proper MICROFIL polymerization in the BA and were excluded from the analysis.

Macroscopic Examination

VBD was present in 18 (67%; 95% CI, 46.0%–83.5%) of 27 subjects in the C57BL/6J group and none (0%; 95% CI, 0%–17.6%) of 19 subjects in the SV129 group ($P < .001$) (Table 1). VBD was absent in sham-operated control animals of both strains ($n = 8$ for each strain).

Both TI and diameter increases for BA were greater in the C57BL/6J strain compared with the SV129 strain (56.3% ± 16.4% versus 21.1% ± 21.6% for diameter; 17.4 ± 7.6 versus 10.4 ± 3.8 for TI). There was a significant effect of strain on the percentage BA increase and TI ($P < .001$) and no significant effect of time on the percentage BA increase or TI increase ($P = .69$ and $P = .55$, respectively).

Results were pooled across time points, and the proportion of successful injections was assessed between strains. The proportion of animals with BA increase of ≥50% was significantly higher in C57BL/6J mice at 81% (22 of 27; 95% CI, 61.9%–93.7%) compared with 16% (3 of 19; 95% CI, 3.4%–39.6%) in the SV129 strain (Fig 1; $P < .001$). The C57BL/6J strain exhibited TI of ≥10 in 81% of cases (22 of 27; 95% CI, 61.9%–93.7%) compared with 58% of cases (11 of 19; 95% CI, 33.5%–79.7%) in the SV129 strain (Fig 2; $P = .1$). The basilar artery diameter increase and TI categorized by time points are presented in Table 2.

Within strain, the Fisher exact tests showed no significant effect of day of sacrifice on the proportion of successful VBD formation in treated mice of either strain ($P = .98$ and $P = 1$).

Histologic Examination

Histologic examination showed marked luminal dilation of the BA characterized by internal elastic lamina disruption and a disconnection of the elastic layer in the C57BL/6J strain at each time point. CD45-positive cells (monocyte/macrophage) were found in the extravascular space, with some inflammatory cells attached or even infiltrated into the media of the arterial wall. Macrophage staining showed a distribution similar to that of leukocytes. Furthermore, double staining with anti-CD45 and anti-MAC387 revealed that some of the infiltrated inflammatory cells in this model were macrophages (Fig 3). At 14 days, both MMP-9–positive and MMP-12–positive cells were found in the media of the arterial wall in VBD models; MMP-9–positive staining was also found in the infiltrated inflammatory cells (Fig 4).

In the SV129 strain, the internal elastic lamina of the BA appeared to be discontinued, fragmented, and/or it had disappeared

in the elastase-injected group as that in the C57BL/6J at all follow-up time points. Acute and/or chronic inflammatory cell infiltration was found surrounding and/or within the vessel walls in samples taken at days 3, 7, and 14, but not at day 28 or in control samples. We did not observe positive staining for MMP-9, MMP-12, CD45, or MAC387 at any time point.

Inflammation scores in C57BL/6J mice were 2.2 ± 0.84, 1.67 ± 0.58, 3.0 ± 0.0, and 1.5 ± 0.58 at 3, 7, 14, and 28 days, respectively; in SV129 mice, they were 1.0 ± 0.82, 0.5 ± 1.0, 1 ± 1.41, and 0.0 ± 0.0 at 3, 7, 14, and 28 days, respectively. Inflammation scores were significantly different between strains at all time points ($P < .001$). Within-strain comparisons showed a difference between the dates of sacrifice for the C57BL/6J strain, but not for the SV129 strain ($P = .03$ and $P = .38$, respectively).

Gelatin Zymography

Gelatin zymography analysis showed that the activities of pro- and active MMP-2 and MMP-9 were dramatically increased in the VBD samples in C57BL/6J mice compared with sham-operated controls and elastase-injected SV129 mice at 14 days after elastase injection. The activities of pro-MMP-2, active MMP-2, pro-MMP-9, and active MMP-9 were higher in elastase-injected C57BL/6J groups compared with elastase-injected SV129 mice and sham-operated C57BL/6J and SV129 groups (Fig 5). Samples from both test and control SV129 mice did not show the activities of either MMP. Wilcoxon rank sum test results were significant for pro-MMP-2 and pro- and active MMP-9 ($P = .03$, 0.03, and 0.03, respectively), but not active MMP-2 ($P = .07$).

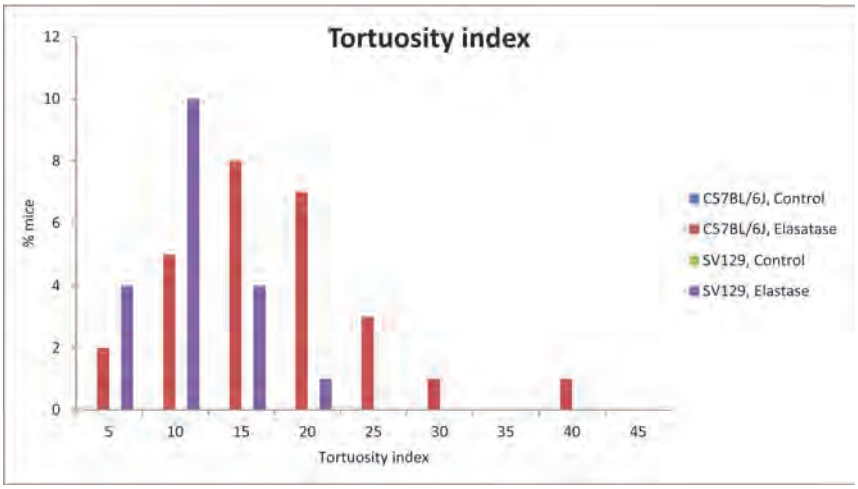

FIG 2. Extent of tortuosity index distribution in C57BL/6J and SV129 mouse strains after elastase injection.

Table 2: Basilar artery diameter increase and tortuosity index in C57BL/6J and SV129 strains categorized by follow-up time points

	BA Diameter Increase				Tortuosity Index			
	<50%		>50%		<10		>10	
	C57BL/6J	SV129	C57BL/6J	SV129	C57BL/6J	SV129	C57BL/6J	SV129
Control	7	7			7	7		
3 Days	1	5	6			3	5	2
7 Days		3	8				6	3
14 Days	3	4	4	2	2	4	7	2
28 Days	1	5	4			1	4	4

DISCUSSION

In the current study, we demonstrated that C57BL/6J mice are markedly more susceptible to VBD induction than SV129 mice. While both mouse strains demonstrated some manifestations of the elongation, dilation, and tortuosity of the intracranial arteries around the circle of Willis, most C57BL/6J mice achieved our prespecified threshold for VBD induction but none of the SV129 mice reached that threshold. In addition, high levels of inflammatory cells and MMPs were observed in the C57BL/6J strain compared with the SV129 strain. Our findings suggest that the inflammatory cascade may be important in the development of VBD and that susceptibility to VBD formation

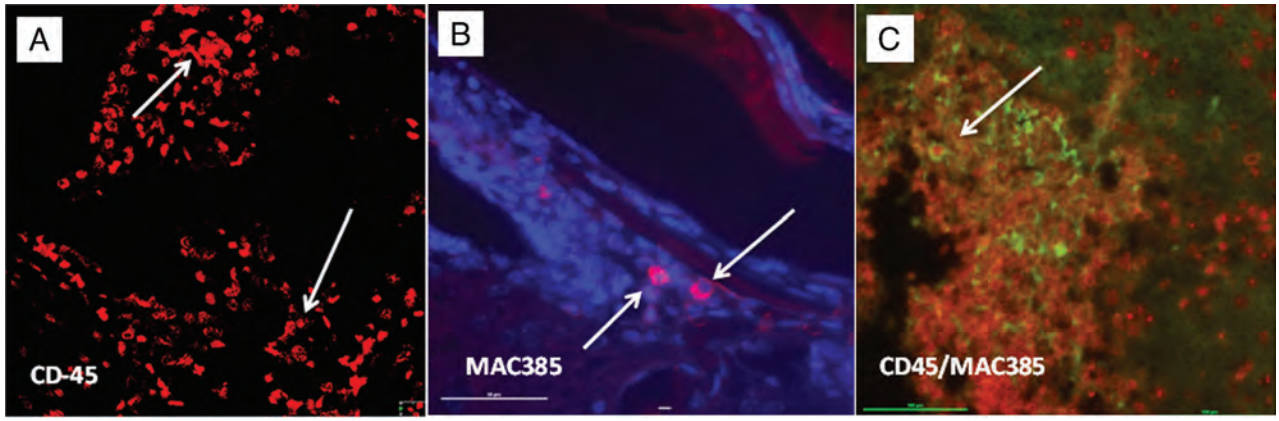

FIG 3. Immunostaining of inflammatory cells in the C57BL/6J mouse strain (×40 magnification). Single immunofluorescence staining showing infiltrating CD45+ cells (*A*, *arrows*) and macrophages (*B*, *arrows*). Double immunostaining of infiltrating cells (CD45+/MAC387+) revealed that the infiltrated inflammatory cells were macrophages (*C*).

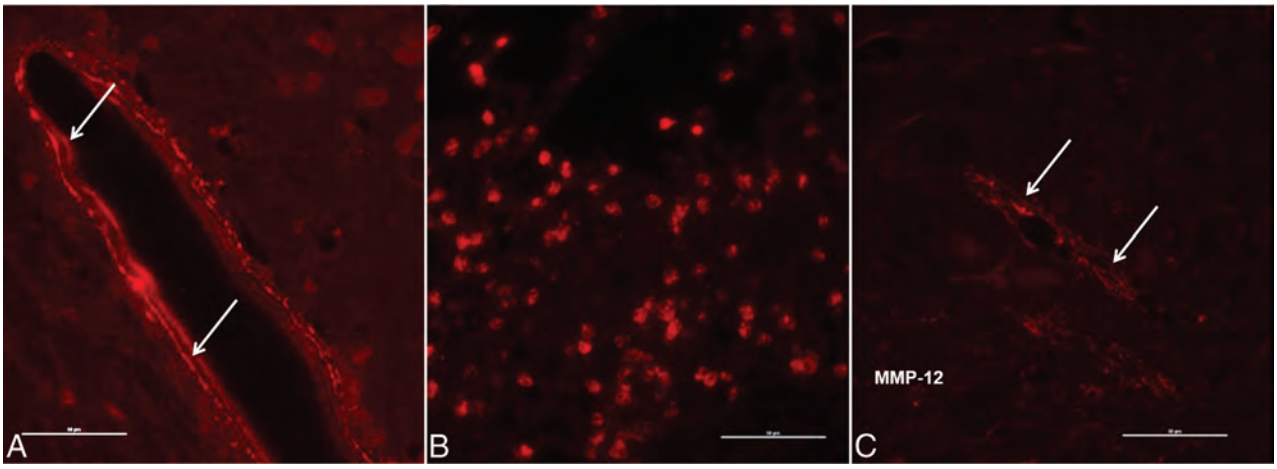

FIG 4. Immunostaining of matrix metalloproteinases in C57BL/6J mouse strain (×40 magnification). MMP-9 (*A*) and MMP-12 (*C*) were highly expressed in the arterial wall after elastase injection. Elevated expression of MMP-9 was also detected in the infiltrated inflammatory cells (*B*).

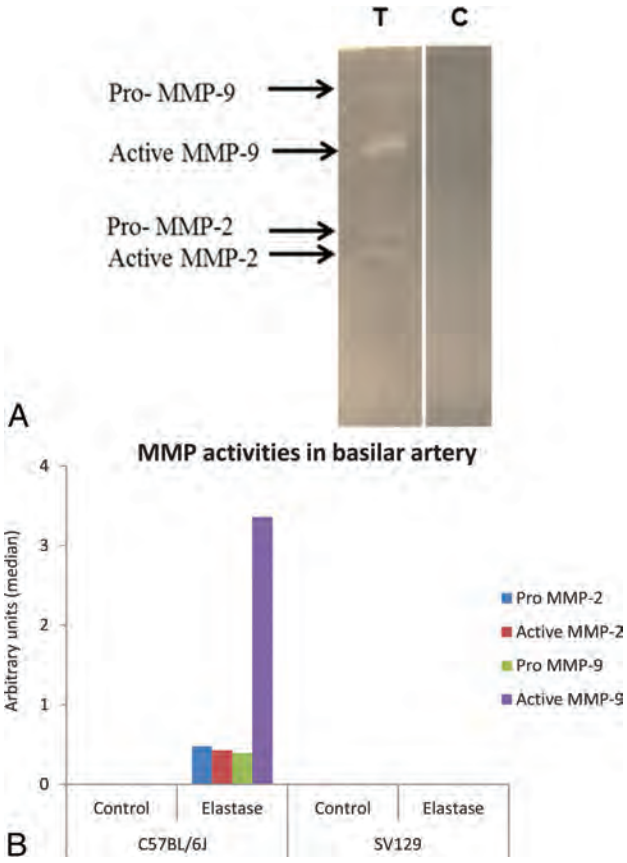

FIG 5. *A*, Gelatin zymography showing expression of matrix metalloproteinases MMP-2 and MMP-9 in the basilar artery of elastase-injected (T) and heat-inactivated elastase-injected (C) C57BL/6J mice. *B*, Densitometric analysis of MMP activities in the basilar artery.

after elastase infusion is associated, at least in part, with genetically determined inherited traits. These current findings are important not only in identifying key elements relevant to the development of VBD but also in providing a potential pathway for future discovery of genetic determinants of VBD susceptibility, possibly through linkage analysis of different strains.

The relationship among inflammation, MMPs, and aneurysms has been widely reported in aneurysm models and clinical cases.[9-14] The disruption of the internal elastic lamina by elastase injection could be the initial factor for induction of VBD. Subsequent infiltration of macrophages and inflammatory cells in the medial layer with secretion of both MMP-9 (collagenase) and MMP-12 (macrophage elastase) followed by degradation of extracellular matrix and elastic lamellae could be leading to the progression of VBD in the C57BL/6J strain. The low level of inflammatory cells and undetectable activities of MMPs in SV129 mice could be associated with less BA dilation and elongation compared with the C57BL/6J strain.

A prospective clinical trial focused on MMP activities, and polymorphism in intracranial arterial dolichoectasia revealed that plasma levels of MMP-2 and MMP-9 were not associated with dolichoectasia.[15] Furthermore, dolichoectasia was strongly connected to lower levels of MMP-3 and 5A/6A polymorphism of the promoter region of MMP-3. This study was in contradiction to our findings; however, we did not measure MMP levels in plasma. It is possible that specific genetic factors may lead to VBD.

Similar to our own findings, Fujii et al[16] revealed that a wide divergence in susceptibility to aneurysmal dilation occurred between C57BL/6J and SV129 mice in an elastase-induced abdominal aortic aneurysm (AAA) model. In particular, C57BL/6J mice were termed "AAA susceptible," and SV129 mice, "AAA resistant." Following elastase perfusion, the SV129 mice had an extent of dilation of 100.0%, whereas the C57BL/6J mice demonstrated an extent of dilation of 156%. The outcross strain between 129/SvEv and C57BL/6J (ie, B6xSvEv F1 heterozygotes) showed an overall extent of dilation of 150.0%, in between the 2 parent strains. These observations suggest that the susceptibility to form abdominal aortic aneurysms following elastase perfusion is associated, at least in part, with genetically determined inherited traits. It is expected that future investigations based on this information will help define the inherited genetic elements that might influence aneurysmal dilation. Meanwhile, other studies showed differences between these mouse strains in susceptibility to ischemic injury and insulin resistance.[16,17]

Our study has several limitations. In the previous study, the success of achieving the intracranial dolichoectasia was defined as the

arterial diameter increase of ≥25% compared with controls.[6] In this article, we applied high stringent and clinically relevant criteria in defining the VBD formation and thus changed the arterial diameter increase from ≥25% to ≥50% on the basis of the criteria of Smoker et al.[18] The arterial dilation and tortuosity index were calculated by using 2D images; however, we believed that 2D images could well reflect its 3D tortuosity because we had found that the vertebrobasilar artery mainly goes on the pons and its tortuosity occurred parallel to the surface of pons and in 1 plane. In addition, the pressure perfusion was not performed for MICROFILL polymer injections; instead, manual perfusion was performed. However, extreme care was taken to avoid the variations in the perfusion fixation among animals. In this study, we used a referred dosage for the C57BL/6J strain, which might not be the optimal dosage for the 129/SvEv strain and could be a partial reason for differences. We performed neither bone marrow transplant experiments nor quantitative loci trait analysis to characterize VBD susceptibility between strains. We did not use any inflammation or MMP inhibitors or gene knockout animals to identify the roles of inflammation and MMPs in the pathogenesis of VBD. We did not observe any MMP expression in the SV129 strain, which could be related to the lower quantity (20 μg) of total protein used for zymography experiments. A robust longitudinal study is critical in elucidating the mechanisms of VBD pathobiology.

CONCLUSIONS

C57BL/6J mice demonstrated greater susceptibility to VBD induction than SV129 mice.

ACKNOWLEDGMENTS

We express our gratitude to Tina Gunderson, MS, Department of Biomedical Statistics and Informatics, Mayo Clinic, for her generous help with the study.

Disclosures: David F. Kallmes—*UNRELATED*: *Consultancy*: Medtronic, *Comments*: clinical trial planning*; *Grants/Grants Pending*: MicroVention, Sequent Medical, Surmodics, NeuroSigma, Codman Neuro, Medtronic, *Comments*: preclinical research and clinical trials*; *Travel/Accommodations/Meeting Expenses Unrelated to Activities Listed:* Medtronic, *Comments*: FDA panel meeting presentation.* *Money paid to the institution.

REFERENCES

1. Pico F, Labreuche J, Touboul PJ, et al. **Intracranial arterial dolichoectasia and small-vessel disease in stroke patients.** *Ann Neurol* 2005; 57:472–79 CrossRef Medline
2. Wolters FJ, Rinkel GJ, Vergouwen MD. **Clinical course and treatment of vertebrobasilar dolichoectasia: a systematic review of the literature.** *Neurol Res* 2013;35:131–37 CrossRef Medline
3. Lou M, Caplan LR. **Vertebrobasilar dilatative arteriopathy (dolichoectasia).** *Ann N Y Acad Sci* 2010;1184:121–33 CrossRef Medline
4. Read D, Esiri MM. **Fusiform basilar artery aneurysm in a child.** *Neurology* 1979;29:1045–49 CrossRef Medline
5. Sudhir K, Ports TA, Amidon TM, et al. **Increased prevalence of coronary ectasia in heterozygous familial hypercholesterolemia.** *Circulation* 1995;91:1375–80 CrossRef Medline
6. Dai D, Kadirvel R, Rezek I, et al. **Elastase-induced intracranial dolichoectasia model in mice.** *Neurosurgery* 2015;76:337–43; discussion 343 CrossRef Medline
7. Morris SA, Orbach DB, Geva T, et al. **Increased vertebral artery tortuosity index is associated with adverse outcomes in children and young adults with connective tissue disorders.** *Circulation* 2011;124: 388–96 CrossRef Medline
8. Fan XJ, Zhao HD, Yu G, et al. **Role of inflammatory responses in the pathogenesis of human cerebral aneurysm.** *Genet Mol Res* 2015;14: 9062–70 CrossRef Medline
9. Tulamo R, Frosen J, Hernesniemi J, et al. **Inflammatory changes in the aneurysm wall: a review.** *J Neurointerv Surg* 2010;2:120–30 CrossRef Medline
10. Yoshimura K, Nagasawa A, Kudo J, et al. **Inhibitory effect of statins on inflammation-related pathways in human abdominal aortic aneurysm tissue.** *Int J Mol Sci* 2015;16:11213–28 CrossRef Medline
11. Ishibashi R, Aoki T, Nishimura M, et al. **Contribution of mast cells to cerebral aneurysm formation.** *Curr Neurovasc Res* 2010;7:113–24 CrossRef Medline
12. Kanematsu Y, Kanematsu M, Kurihara C, et al. **Critical roles of macrophages in the formation of intracranial aneurysm.** *Stroke* 2011;42: 173–78 CrossRef Medline
13. Aoki T, Kataoka H, Moriwaki T, et al. **Role of TIMP-1 and TIMP-2 in the progression of cerebral aneurysms.** *Stroke* 2007;38:2337–45 CrossRef Medline
14. Nuki Y, Tsou TL, Kurihara C, et al. **Elastase-induced intracranial aneurysms in hypertensive mice.** *Hypertension* 2009;54:1337–44 CrossRef Medline
15. Pico F, Jacob MP, Labreuche J, et al. **Matrix metalloproteinase-3 and intracranial arterial dolichoectasia.** *Ann Neurol* 2010;67:508–15 CrossRef Medline
16. Fujii M, Hara H, Meng W, et al. **Strain-related differences in susceptibility to transient forebrain ischemia in SV-129 and C57black/6 mice.** *Stroke* 1997;28:1805–10; discussion 1811 CrossRef Medline
17. Almind K, Kahn CR. **Genetic determinants of energy expenditure and insulin resistance in diet-induced obesity in mice.** *Diabetes* 2004;53:3274–85 CrossRef Medline
18. Smoker WR, Corbett JJ, Gentry LR, et al. **High-resolution computed tomography of the basilar artery, 2: vertebrobasilar dolichoectasia: clinical-pathologic correlation and review.** *AJNR Am J Neuroradiol* 1986;7:61–72 Medline

White Matter Microstructural Abnormalities in Type 2 Diabetes Mellitus: A Diffusional Kurtosis Imaging Analysis

Y. Xie, Y. Zhang, W. Qin, S. Lu, C. Ni, and Q. Zhang

ABSTRACT

BACKGROUND AND PURPOSE: Increasing DTI studies have demonstrated that white matter microstructural abnormalities play an important role in type 2 diabetes mellitus–related cognitive impairment. In this study, the diffusional kurtosis imaging method was used to investigate WM microstructural alterations in patients with type 2 diabetes mellitus and to detect associations between diffusional kurtosis imaging metrics and clinical/cognitive measurements.

MATERIALS AND METHODS: Diffusional kurtosis imaging and cognitive assessments were performed on 58 patients with type 2 diabetes mellitus and 58 controls. Voxel-based intergroup comparisons of diffusional kurtosis imaging metrics were conducted, and ROI-based intergroup comparisons were further performed. Correlations between the diffusional kurtosis imaging metrics and cognitive/clinical measurements were assessed after controlling for age, sex, and education in both patients and controls.

RESULTS: Altered diffusion metrics were observed in the corpus callosum, the bilateral frontal WM, the right superior temporal WM, the left external capsule, and the pons in patients with type 2 diabetes mellitus compared with controls. The splenium of the corpus callosum and the pons had abnormal kurtosis metrics in patients with type 2 diabetes mellitus. Additionally, altered diffusion metrics in the right prefrontal WM were significantly correlated with disease duration and attention task performance in patients with type 2 diabetes mellitus.

CONCLUSIONS: With both conventional diffusion and additional kurtosis metrics, diffusional kurtosis imaging can provide additional information on WM microstructural abnormalities in patients with type 2 diabetes mellitus. Our results indicate that WM microstructural abnormalities occur before cognitive decline and may be used as neuroimaging markers for predicting the early cognitive impairment in patients with type 2 diabetes mellitus.

ABBREVIATIONS: AD = axial diffusivity; AK = axial kurtosis; CC = corpus callosum; DKI = diffusional kurtosis imaging; FA = fractional anisotropy; HbA1c = glycosylated hemoglobin; lEC = left external capsule; MD = mean diffusivity; MK = mean kurtosis; RD = radial diffusivity; rPF_WM = right prefrontal white matter; RK = radial kurtosis; RT of ANT = reaction time of Attention Network Test; T2DM = type 2 diabetes mellitus

Type 2 diabetes mellitus (T2DM) is a common metabolic disorder with an increasing worldwide prevalence,[1] and is widely accepted as a risk factor associated with mild cognitive impairment and dementia.[2,3] A number of neuroimaging studies have demonstrated that GM structural abnormalities[4-6] might account for cognitive deficits in patients with T2DM. By contrast, studies on white matter structures, which play a vital role in transferring information between GM regions, are relatively rare. A few studies using the DTI method identified microstructural changes of WM in patients with T2DM,[7-13] and alterations of local and global network properties were also observed in patients with T2DM with the tractography method.[14] In addition, the association between the WM microstructural abnormalities and cognitive performance was also revealed in patients with T2DM.[7,10,12-14]

However, information provided by DTI was limited, partly because diffusion metrics obtained from DTI are calculated on the basis of the assumption of Gaussian diffusion of water molecules.[15] However, non-Gaussian diffusion is known to be sub-

Received March 16, 2016; accepted after revision October 18.

From the Department of Radiology and Tianjin Key Laboratory of Functional Imaging (Y.X., Y.Z., W.Q., Q.Z.), Tianjin Medical University General Hospital, Tianjin, China; and Departments of Radiology (S.L.) and Cardiology (C.N.), Tianjin Medical University Metabolic Diseases Hospital, Tianjin, China.

Y. Xie and Y. Zhang contributed equally to this work.

Y.X., Y.Z., and Q.Z. designed the research; Y.X., Y.Z., and Q.Z. performed the research; C.N. and S.L. were involved in the clinical assessment; Y.X., Y.Z., W.Q., and Q.Z. analyzed the data; Y.X., Y.Z., and Q.Z. wrote the paper. Q.Z is the guarantor of this work and, as such, had full access to all the data in the study and takes responsibility for the integrity of the data and the accuracy of the data analysis.

No potential conflicts of interest relevant to this article were reported.

Please address correspondence to Quan Zhang, MD, Department of Radiology, Tianjin Medical University General Hospital, No. 154, Anshan Rd, Heping District, Tianjin 300052, China; e-mail: zhangquan0912@163.com

Indicates article with supplemental on-line tables.

http://dx.doi.org/10.3174/ajnr.A5042

stantial[16] and is believed to result from the diffusion barriers, such as cell membranes and organelles, as well as water compartments (eg, extracellular and intracellular) with altering diffusion properties. In this study, we sought to further characterize WM changes in patients with T2DM without cognitive impairment by using diffusional kurtosis imaging (DKI), which is a clinically feasible extension of DTI that enables the examination of additional non-Gaussian diffusion effects, providing both DTI-compatible diffusion metrics and additional kurtosis metrics.[17] Additionally, due to the inclusion of non-Gaussian effects, DKI-derived estimates of diffusion metrics are generally more accurate than those obtained with conventional DTI,[18] and the added kurtosis metrics can yield additional information about tissue microstructure beyond that provided by diffusion metrics.

The aims of this study were the following: 1) to assess the ability of DKI and DTI to identify microstructural abnormalities in patients with T2DM; 2) to investigate whether DKI-specific diffusion and kurtosis metrics could provide additional information about the WM microstructural changes; and 3) to investigate whether these microstructural abnormalities are related to clinical/cognitive variables in patients with T2DM without cognitive impairment.

MATERIALS AND METHODS

Subjects

Fifty-eight right-handed patients with T2DM who met the guideline criteria of the American Diabetes Association "Diagnosis and Classification of Diabetes Mellitus"[19] and did not have T2DM-related complications (retinopathy, peripheral neuropathy, and nephropathy) were enrolled. The presence of retinopathy was ascertained by using direct ophthalmoscopy, peripheral neuropathy by clinical examination, and nephropathy by a laboratory test of microalbuminuria. Exclusion criteria included a Mini-Mental State Examination score of <27, any psychiatric or neurologic disorders that could influence cognitive function, cerebrovascular accidents (screened by history and MR imaging), a self-reported history of alcohol or substance abuse, and a family history of dementia, hypertension, or hyperlipidemia. Additionally, all patients self-reported no experience of hypoglycemia during the past 2 years. Twenty-nine of the 58 patients with T2DM controlled blood glucose by using oral hypoglycemic agents, 9 patients were under treatment with insulin, 14 patients were treated with both insulin and oral hypoglycemic agents, and 6 patients were exclusively treated with moderate exercise and diet therapy (On-line Table 1). Fifty-eight euglycemic participants were recruited as healthy controls; the age, sex, and years of education of these controls were well-matched with those of patients with T2DM. Exclusion criteria for controls were the same as those for patients with T2DM.

In the morning of the day when the participants underwent MR imaging, fasting blood glucose, glycosylated hemoglobin (HbA1c), total cholesterol, triglyceride, high-density lipoprotein, and low-density lipoprotein levels were measured by standard laboratory tests after an overnight fast of at least 10 hours. Blood pressure was measured while sitting, at 3 different time points during the day, and averaged.

The protocol of this study was approved by the Ethical Committee of Tianjin Medical University General Hospital, and all participants provided written informed consent according to institutional guidelines.

Cognitive Testing

A battery of neuropsychological tests was performed to assess participants' general mental status and cognitive domains. Possible dementia was assessed by the Mini-Mental State Examination.[20] Anxiety and depression were evaluated with the Self-Rating Anxiety Scale[21] and Self-Rating Depressive Scale,[22] respectively. Short- and long-term memory was tested by using the Auditory Verbal Learning Test.[23] Working memory was assessed with the forward and backward Digit Span tests.[24] Executive function was evaluated with the Wisconsin Card Sorting Test.[25] A modified version[26] of the Attention Network Test described by Fan et al[27] was used to evaluate attention. Information-processing speed was tested with Trail-Making Test A.[28]

MR Imaging Data Acquisition

MR imaging data were obtained with a 3T MR imaging system (Discovery MR750; GE Healthcare, Milwaukee, Wisconsin). DKI data were acquired by using a spin-echo single-shot EPI sequence with the following parameters: TR = 5800 ms, TE = 77 ms, matrix = 128 × 128, FOV = 256 × 256 mm, in-plane resolution = 2 × 2 mm, section thickness = 3 mm without a gap, 48 axial sections, 25 encoding diffusion directions with 2 b-values (b=1000 and 2000 s/mm^2) for each direction and 10 non-diffusion-weighted images (b=0 s/mm^2). The total acquisition time for DKI was 5 minutes 54 seconds. Sagittal 3D T1WI was acquired by a brain volume sequence with the following parameters: TR = 8.2 ms, TE = 3.2 ms, TI = 450 ms, flip angle = 12°, FOV = 256 × 256 mm, matrix = 256 × 256, section thickness = 1 mm, no gap, and 188 sagittal sections.

Calculation of Kurtosis and Diffusion Metrics

Before the preprocessing of the diffusion data, we visually inspected all images to ensure that only volumes without visible artifacts in each subject were included in the subsequent analyses (On-line Table 2). Then, eddy current–induced distortion and motion artifacts in the DKI dataset were corrected by using affine alignment of each diffusion-weighted image to the b=0 image by using the FMRIB Diffusion Toolbox (FSL 4.0; http://fsl.fmrib.ox.ac.uk/fsl/fslwiki/FDT). After skull-stripping, the Diffusional Kurtosis Estimator (http://www.nitrc.org/projects/dke) was implemented to calculate the kurtosis and diffusion tensors by using the constrained linear least squares–quadratic programming algorithm as described previously.[17] All data (b=0, 1000, 2000 s/mm^2) were used for DKI fitting because DKI metrics (mean kurtosis [MK], axial kurtosis [AK], radial kurtosis [RK], fractional anisotropy [FA], mean diffusivity [MD], axial diffusivity [AD], and radial diffusivity [RD]) can only be estimated on the basis of at least 2 nonzero b-values in >15 independent directions.[29]

To compare the efficiency in detection of T2DM-induced changes between the DKI and classic DTI models, we additionally calculated the diffusion indices by using the classic DTI algorithm based on the monoexponential decay model and a single-tensor least squares solution with images of b=0 and 1000 s/mm^2 as input.

Preprocessing of Kurtosis and Diffusion Parametric Images

The preprocessing was performed by using Statistical Parametric Mapping (SPM8; http://www.fil.ion.ucl.ac.uk/spm). First, all of the subjects' T1-weighted structural images were segmented into GM, WM, and CSF. Second, a high-dimensional Diffeomorphic Anatomical Registration Through Exponentiated Lie Algebra (DARTEL) algorithm was used to normalize these components into Montreal Neurological Institute space. Third, individual skull-stripped B0 images of DKI were affinely coregistered to the patient's skull-stripped native T1-weighted structural images and were written into the Montreal Neurological Institute space by using the deformation matrix generated by DARTEL. Then, all the parametric images (MK, AK, RK, FA, MD, AD, and RD) of each subject were transformed into the Montreal Neurological Institute space by using the deformation matrix generated by both of these registration steps and were resectioned into a voxel size of $2 \times 2 \times 2$ mm. Finally, the images were smoothed with a Gaussian kernel of $6 \times 6 \times 6$ mm at full width at half maximum by using SPM8. The preprocessing of DTI data was the same as that of DKI.

Statistical Analysis

Demographic and Clinical Characteristic Analyses. The demographic and clinical data were analyzed by using the Statistical Package for the Social Sciences, Version 19.0 (SPSS; IBM, Armonk, New York). Before data analysis, we evaluated the normality of continuous variables by using the Kolmogorov-Smirnov test. Normally distributed variables were evaluated by using a 2-tailed independent samples *t* tests. For those variables that were non-normally distributed, the Mann-Whitney *U* test was used. A χ^2 test was used to test the intergroup difference in sex. The significance level was set as $P < .05$.

Intergroup Comparisons of DKI Metrics. To detect the intergroup differences in primary DKI metrics (FA, MD, and MK), we conducted the voxelwise General Linear Model embedded in SPM8 with group (T2DM versus controls) as the main effect and age, sex, and years of education as the nuisance regressors. The a priori WM template embedded in SPM8 binarized with a threshold of >0.5 was used as a mask to confine intergroup comparisons within WM regions. A correction for multiple comparisons was performed by using a Monte Carlo simulation (AlphaSim [http://afni.nimh.nih.gov/pub/dist/doc/program_help/AlphaSim.html] program in REST software [http://www.restfmri.net]). Parameters were the following: single-voxel $P = .001$; 5000 simulations; estimated full width at half maximum (FWHMx,y,z) of FA = 9.707, 10.839, 10.177 mm; FWHMx,y,z of MD = 14.156, 15.150, 15.346; FWHMx,y,z of MK = 11.629, 12.185, 12.228; cluster connection radius $r = 3$ mm within the WM mask with a resolution of $2 \times 2 \times 2$ mm. The clusters with 54, 72, and 68 contiguous voxels for intergroup comparisons of FA, MD, and MK, respectively, would achieve an effective threshold of $P < .05$.

To further inspect the reason for the primarily altered DKI parameters (FA, MD, and MK), we drew a sphere (9 mm in diameter) centering at the peak coordinate of each cluster with a significant intergroup difference by voxelwise comparison and defined the overlapping voxels of each cluster and corresponding sphere as the ROI. Then, the average values of AD, RD, AK, and RK within corresponding ROIs were extracted, and ROI-based intergroup comparisons were further performed by using a General Linear Model after controlling for the effects of age, sex, and years of education to reveal the intergroup differences in the AD and RD values (the reason for the altered FA and MD values) and AK and RK values (the reason for the altered MK values).

Correlation Analysis. The correlations between DKI metrics within all of the ROIs and clinical (disease duration and HbA1c)/cognitive variables in patients with T2DM and controls were analyzed by using the partial correlations after controlling for age, sex, and years of education with SPSS 19.0. The significant level was set as $P < .05$.

Subgroup Comparison between Patients with T2DM Treated with and without Insulin. Considering that some of the patients were treated with insulin, we further compared the DKI metrics (ROI-based FA, MD, and MK) and the clinical/cognitive variables between 2 subgroups, which were classified according to the application of insulin, by using the General Linear Model after controlling for the effects of age, sex, and years of education with SPSS 19.0. The significant level was set as $P < .05$.

Comparison of DKI and DTI. The intergroup comparisons of DTI metrics were also conducted by using voxel-based analysis, which is the same as the statistical analysis used for the DKI metrics. To verify the ability of DKI and DTI in identifying microstructural abnormalities in patients with T2DM, we overlapped the results of both DKI and DTI for observation.

RESULTS

Demographic and Clinical Characteristic of Subjects

The demographic information and cognitive and clinical data of the 2 groups are provided in Tables 1 and 2. No significant intergroup differences were observed in terms of age, sex, years of education, and cognitive performance. Compared with the controls, patients with T2DM had increased fasting blood glucose ($P < .001$) and HbA1c ($P < .001$) levels and reduced high-density lipoprotein levels ($P < .05$).

Diffusion Metrics from DKI

Patients with T2DM had significantly reduced FA values in the right prefrontal WM (rPF_WM) and the splenium of the corpus callosum (CC) compared with the controls ($P < .05$, AlphaSim correction) (Fig 1 and Table 3). Moreover, ROI-based intergroup comparisons showed that the RD values within the rPF_WM significantly increased in patients with T2DM compared with controls ($P < .05$) (Table 4); this result leads to decreased FA in patients with T2DM. However, there was no significant intergroup difference in the AD values within the rPF_WM ($P > .05$). The AD and RD values within the splenium of the CC significantly increased in patients with T2DM compared with controls ($P < .05$) (Table 4); this result leads to decreased FA in patients with T2DM.

Compared with controls, patients with T2DM had significantly increased MD values in the rPF_WM (including 3 clusters defined as superior, middle, and inferior rPF_WM according to their coordinates at the z-axis), the right superior temporal WM, the left prefrontal WM, the left external capsule (lEC), the sp-

Table 1: Demographic and clinical information[a]

	T2DM (n = 58)	Healthy Controls (n = 58)	Statistics	P
Demographics				
Age (yr)	56.09 ± 8.16	54.66 ± 7.03	t = 1.012	.314
Sex (M/F)	34:24	35:23	χ^2 = 0.036	.850
Education level (yr)	11.72 ± 3.31	11.07 ± 2.64	t = 1.178	.241
Clinical information				
Disease duration (mo)	91.25 ± 69.81	–	–	–
BMI (kg/m^2)	25.57 ± 2.19	24.64 ± 2.99	t = 1.915	.058
Systolic BP (mm Hg)	130 (110–170)	122.5 (100–170)	z = −1.713	.087
Diastolic BP (mm Hg)	80 (60–100)	80 (60–100)	z = −1.015	.310
FBG (mmol/L)	8.06 ± 2.81	5.13 ± 0.65	t = 7.717	<.001
HbA1c (%)	8.35 ± 2.10	5.56 ± 0.33	t = 10.020	<.001
HbA1c (mmol/mol)	67.76 ± 22.87	37.31 ± 3.62	t = 10.013	<.001
Total cholesterol (mmol/L)	5.06 ± 1.35	5.39 ± 0.91	t = −1.541	.126
Triglycerides (mmol/L)	1.66 (0.49–8.03)	1.24 (0.46–7.35)	z = −1.698	.090
HDL (mmol/L)	1.15 ± 0.27	1.27 ± 0.31	t = −2.167	.032
LDL (mmol/L)	3.17 ± 0.93	3.47 ± 0.85	t = −1.799	.075

Note:—FBG indicates fasting blood glucose; HDL, high-density lipoprotein; LDL, low-density lipoprotein; BP, blood pressure; BMI, body mass index.

[a] Data distributed normally or non-normally are presented as mean ± SD or median (range).

Table 2: Cognitive information[a]

	T2DM (n = 58)	Healthy Controls (n = 58)	Statistics	P
MMSE score	29.21 ± 0.89	29.50 ± 0.94	t = −1.720	.088
RT of ANT (ms)	536.53 ± 71.31	566.51 ± 92.09	t = −1.911	.059
ACC of ANT (%)	98.65 ± 1.83	97.89 ± 4.49	t = 1.157	.250
RPEP (%)	0.07 ± 0.02	0.08 ± 0.02	t = −1.908	.059
SAS	32.19 ± 6.16	30.71 ± 5.24	t = 1.397	.165
SDS	34.09 ± 7.79	31.64 ± 7.07	t = 1.772	.079
Long-term memory	10.75 ± 2.65	11.04 ± 2.85	t = −0.555	.580
Short-term memory	47.14 ± 9.25	48.69 ± 9.29	t = −0.879	.381
Forward Digit Span	8.25 ± 1.50	8.18 ± 1.26	t = 0.258	.797
Backward Digit Span	5.07 ± 1.45	5.13 ± 1.07	t = −0.230	.818
TMT-A (s)	61.65 ± 25.54	58.15 ± 27.60	t = 0.686	.494

Note:—ACC of ANT indicates the accuracy rate of Attention Network Test; RPEP, the percentage of the preservative response error; SAS, Self-Rating Anxiety Scale; SDS, Self-Rating Depressive Scale; TMT-A, Trail Making Test A; MMSE, Mini-Mental State Examination.

[a] Data are presented as mean ± SD.

lenium of the CC, and the pons (P < .05, AlphaSim correction) (Fig 1 and Table 3). The intergroup differences in MD were driven by increased AD and RD within corresponding ROIs in patients with T2DM (P < .05) (Table 5).

Kurtosis Metrics from DKI

In the voxel-based analysis, patients with T2DM showed significantly decreased MK values in the splenium of the CC and the pons compared with controls (P < .05, AlphaSim correction) (Fig 1 and Table 3). In addition, ROI-based intergroup comparisons showed that the AK and RK values within the splenium of the CC and the pons significantly decreased in patients with T2DM compared with controls (P < .05) (Table 6); this decrease drives the decreased MK within corresponding ROIs in patients with T2DM.

Correlation Analyses with Clinical and Cognitive Variables

By using the partial correlation analyses, we found a negative correlation between the FA values of the rPF_WM and the reaction time of the Attention Network Test (RT of ANT) (r = −0.280, P = .047) and a positive correlation between the RD values of rPF_WM and the RT of ANT (r = 0.322, P = .021) (Fig 2) in patients with T2DM. Moreover, positive correlations were demonstrated between disease duration and MD values (r = 0.273, P = .044), AD values (r = 0.269, P = .047), and RD values (r = 0.270, P = .046) of the superior rPF_WM in patients with T2DM (Fig 2).

However, there were no significant correlations between the kurtosis metrics and cognitive/clinical variables in patients with T2DM and the controls (P > .05).

Analyses of the Subgroup Comparison between Patients with T2DM with and without Insulin

No significant intergroup differences were observed in terms of age, sex, years of education, and cognitive performance between the insulin-injection group and the non-insulin-injection group (P > .05) (On-line Table 3).

In the ROI-based analysis, no significant intergroup differences in FA, MD, and MK values were found between the 2 subgroups (P > .05) (On-line Tables 4 and 5).

Comparison of Diffusion Metrics from DTI and DKI

On the basis of the voxel-based analysis of DTI metrics, deceased FA in the splenium of the CC and increased MD in the superior and inferior rPF_WM and lEC were noted in patients with T2DM compared with healthy controls (Fig 3). The overlapping map of the DKI and DTI results showed that intergroup differences detected by DTI mostly overlapped those revealed by DKI. Some additional intergroup differences could only be identified by using DKI, including increased MD in the middle rPF_WM, left prefrontal white matter, and right superior temporal white matter and increased MD and decreased MK in the splenium of the CC and the pons (Fig 3).

DISCUSSION

In the present study, the DKI method was used to explore WM microstructural alterations in patients with T2DM without cognitive impairment. Compared with DTI, DKI can provide both diffusion and kurtosis metrics for identifying WM microstructural changes and can provide additional information of WM microstructural abnormalities in patients with T2DM. Furthermore, patients with T2DM had decreased FA in the rPF_WM and the splenium of the CC; increased MD in the bilateral prefrontal and right temporal WM, lEC, splenium of the CC, and pons; and decreased MK in the splenium of the CC and the pons. In addition, significant correlations were detected between the altered diffusion metrics and disease duration and the RT of ANT.

Comparison between DTI and DKI

In our study, the intergroup differences detected by DTI mostly overlapped those revealed by DKI, and increased MD in rPF_WM, left prefrontal white matter, and right superior temporal white matter and both increased MD and decreased MK in the splenium of the CC and the pons could only be detected by using DKI (Fig 3). Moreover, our results were partially consistent with those in the previous DTI studies on T2DM in which decreased FA and/or increased MD of the prefrontal WM,[7-9] the temporal WM,[7] the CC,[10,12] and the lEC[12] were observed in patients with T2DM compared with controls. Our patients with T2DM also had decreased MK and increased MD values in the pons, which were not reported in previous DTI studies.[7-13] These results demonstrated that DKI is reliable for identifying T2DM-related WM microstructural abnormalities and can provide additional information on WM microstructural abnormalities. DKI is superior to DTI because diffusion metrics obtained from DTI are calculated on the basis of the assumption of Gaussian diffusion of water molecules,[15] whereas non-Gaussian diffusion is known to be substantial.[16] Due to the inclusion of non-Gaussian effects, the DKI-derived estimates of the diffusion metrics are generally more accurate than those obtained with conventional DTI.[18] In addition to the differences in imaging methods, the variation of subjects enrolled in the studies may also lead to the inconsistency of the results. The patients with T2DM in our study did not have T2DM-related complications (retinopathy, peripheral neuropathy, or nephropathy) and showed no significant intergroup difference in cognitive performance relative to the healthy controls. In contrast, patients with T2DM enrolled in several previous studies[10,12,13] had slightly or significantly worse cognitive functions, which may contribute to the results of more global differences in their studies compared with ours.

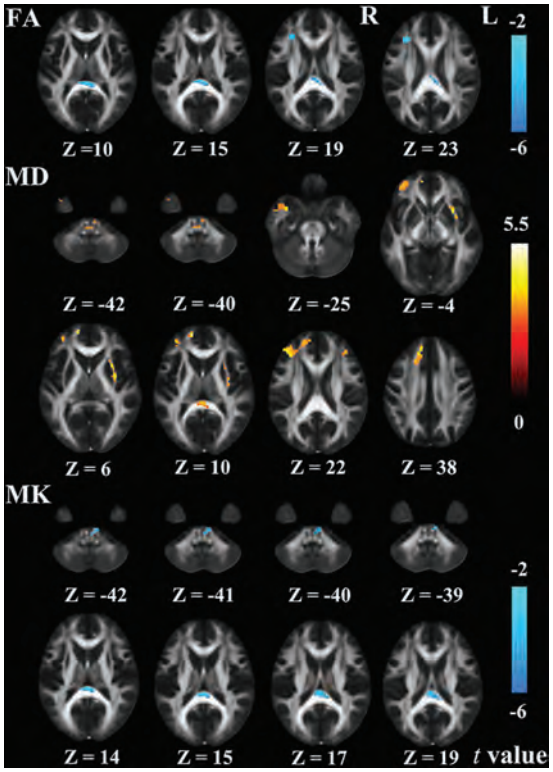

FIG 1. WM regions showed significant differences in DKI metrics between patients with T2DM and controls. The regions with decreased FA (*upper row*), increased MD (*middle row*), and decreased MK (*lower row*) in patients with T2DM were overlapped on the FA template. Color bars represent the *t* values of intergroup comparisons.

Table 3: Brain regions showing significant voxel-based intergroup differences in DKI metrics

Structure Name	Metrics	Cluster Voxel No.	Peak *t* Value	MNI Coordinates		
				X	Y	Z
Splenium of CC	FA	184	−4.679	−2	−34	8
rPF_WM	FA	78	−4.483	30	26	20
Superior rPF_WM	MD	204	5.094	10	36	36
Middle rPF_WM	MD	521	5.077	14	52	10
Inferior rPF_WM	MD	90	3.900	38	42	−2
lPF_WM	MD	80	4.372	−46	32	26
rST_WM	MD	189	4.608	34	0	−22
Splenium of CC	MD	75	3.882	−2	−38	8
lEC	MD	261	5.068	−32	12	−2
Pons	MD	133	4.487	−6	−28	−42
Splenium of CC	MK	172	−4.427	0	−32	14
Pons	MK	150	−4.659	−6	−28	−42

Note:—lPF_WM indicates left prefrontal white matter; MNI, Montreal Neurological Institute; rST_WM, right superior temporal white matter.

Altered Diffusion and Kurtosis Metrics in Patients with T2DM

FA and MD are the primary diffusion metrics that reflect overall WM health, maturation, and organization.[30] In addition to these primary diffusion metrics, AD (reflecting axon integrity) and RD (reflecting myelin sheath integrity) are of great importance in understanding the underlying physiology.[31] Decreased FA values are presumably based on predominantly increased RD[8,13] or both increased RD and AD.[10] Thus, our finding of decreased FA was most probably driven by a significantly increased RD, indicating that the impairment of WM integrity was possibly a result of demyelination according to the study of Song et al.[32] In addition, the increased MD values driven by the increased AD and RD, which are partly consistent with results in a previous DTI study,[10] may reflect the expansion of extracellular space due to the degeneration of fibers or edema.[33] Additionally, the decreased MK was attributed to both the decrease in RK and AK in patients with T2DM compared with controls. Kurtosis values quantify the degree of diffusion restriction or tissue complexity,[34] and the reduced MK value may indicate reduced tissue heterogeneity, which could be attributed to microstructural impairment such as the thinner packing of axons and fiber bundles, lower axonal membrane permeability (reflected as reduced RK), decreased microstructural complexity, or cell structure deficits along the axial direction of WM fibers (reflected as reduced AK).

On the basis of the voxel-based analysis, we observed decreased FA in the rPF_WM and the splenium of the CC and increased MD in bilateral prefrontal WM, the right superior temporal white matter, the lEC, the splenium of the CC, and the pons in patients with T2DM. Additionally, decreased MK, RK, and

Table 4: Intergroup differences of the AD and RD values that contributed to the altered FA values[a]

	T2DM (*n* = 58)	Healthy Controls (*n* = 58)	*F*	*P*
rPF_WM				
AD, $\times 10^{-5}$ mm^2/s	111.10 ± 4.83	111.79 ± 4.63	0.967	.328
RD, $\times 10^{-5}$ mm^2/s	82.06 ± 5.48	78.84 ± 4.71	12.095	.001
Splenium of CC				
AD, $\times 10^{-5}$ mm^2/s	288.14 ± 26.33	270.95 ± 33.14	8.490	.004
RD, $\times 10^{-5}$ mm^2/s	179.24 ± 36.37	151.55 ± 41.77	13.321	<.001

[a] Data are presented as mean ± SD. The intergroup comparisons were performed with ANCOVA adjusted for age, sex, and years of education.

Table 5: Intergroup differences of the AD and RD values that contributed to the altered MD values[a]

	T2DM (*n* = 58)	Healthy Controls (*n* = 58)	*F*	*P*
Superior rPF_WM				
AD, $\times 10^{-5}$ mm^2/s	111.06 ± 6.52	105.23 ± 4.25	31.431	<.001
RD, $\times 10^{-5}$ mm^2/s	93.28 ± 6.41	87.75 ± 4.49	28.488	<.001
Middle rPF_WM				
AD, $\times 10^{-5}$ mm^2/s	113.59 ± 6.04	108.52 ± 3.48	31.472	<.001
RD, $\times 10^{-5}$ mm^2/s	90.12 ± 6.39	85.27 ± 3.53	27.982	<.001
Inferior rPF_WM				
AD, $\times 10^{-5}$ mm^2/s	116.85 ± 5.98	112.19 ± 5.53	18.548	<.001
RD, $\times 10^{-5}$ mm^2/s	84.53 ± 5.95	81.24 ± 4.38	10.752	.001
lPF_WM				
AD, $\times 10^{-5}$ mm^2/s	121.75 ± 10.54	114.50 ± 6.62	19.725	<.001
RD, $\times 10^{-5}$ mm^2/s	107.47 ± 11.40	98.84 ± 7.44	23.252	<.001
rST_WM				
AD, $\times 10^{-5}$ mm^2/s	127.10 ± 10.59	119.03 ± 6.38	22.413	<.001
RD, $\times 10^{-5}$ mm^2/s	102.70 ± 10.25	94.47 ± 5.85	25.394	<.001
Splenium of CC				
AD, $\times 10^{-5}$ mm^2/s	269.21 ± 20.44	255.20 ± 24.27	9.865	.002
RD, $\times 10^{-5}$ mm^2/s	152.25 ± 32.11	127.36 ± 32.84	15.805	<.001
lEC				
AD, $\times 10^{-5}$ mm^2/s	122.54 ± 7.42	117.14 ± 4.84	21.495	<.001
RD, $\times 10^{-5}$ mm^2/s	92.85 ± 8.70	86.36 ± 6.14	22.007	<.001
Pons				
AD, $\times 10^{-5}$ mm^2/s	222.11 ± 27.07	201.58 ± 26.15	18.416	<.001
RD, $\times 10^{-5}$ mm^2/s	177.25 ± 27.60	157.84 ± 24.38	17.237	<.001

Note:—lPF_WM indicates left prefrontal white matter; rST_WM, right superior temporal white matter.
[a] Data are presented as mean ± SD. The intergroup comparisons were performed with ANCOVA adjusted for age, sex, and years of education.

Table 6: Intergroup differences of the AK and RK values that contributed to the altered MK values[a]

	T2DM (*n* = 58)	Healthy Controls (*n* = 58)	*F*	*P*
Splenium of CC				
AK, $\times 10^{-5}$ mm^2/s	46.10 ± 2.39	47.90 ± 3.16	11.249	.001
RK, $\times 10^{-5}$ mm^2/s	112.35 ± 22.24	131.37 ± 26.62	16.883	<.001
Pons				
AK, $\times 10^{-5}$ mm^2/s	66.02 ± 6.19	71.75 ± 8.09	18.289	<.001
RK, $\times 10^{-5}$ mm^2/s	83.59 ± 8.98	90.75 ± 8.84	17.912	<.001

[a] Data are presented as mean ± SD. The intergroup comparisons were performed with ANCOVA adjusted for age, sex, and years of education.

AK values were also detected in the splenium of the CC and the pons of patients with T2DM compared with controls. To date, several studies have suggested various WM impairments in patients with T2DM. For example, Yau et al[7] suggested that patients with T2DM had significantly lower FA in the frontal and temporal WM compared with controls. A remarkable decrease in FA and an increase in MD were also mainly located in the frontal cortex.[8,9] Compelling evidence acquired from a variety of structural and functional MR imaging studies demonstrated that the prefrontal cortex has an important role in increased cognitive function.[35] Given the important role of the prefrontal WM in transferring information between the prefrontal cortex and other brain regions, the microstructural changes in the prefrontal WM may lead to cognitive impairment.

The CC plays an important role in interhemispheric functional integration. The loss of WM connectivity and regionally specific atrophy of the CC are observed in patients with Alzheimer disease and mild cognitive impairment,[36] indicating that CC abnormalities may be related to the cognitive deficits. The external capsule is a route for cholinergic fibers from the basal forebrain to the temporal cortex, transmitting auditory and polymodal sensory information. As reported, the external capsule is crucial for cognition, including memory and executive function.[37] All of these results demonstrate that T2DM impacts WM integrity. Moreover, the disease duration rather than HbA1c is related to the MD, AD, and RD values of the superior rPF_WM in patients with T2DM, which may indicate that T2DM may have a cumulative effect on the WM microstructural damage. This positive correlation between disease duration and diffusion metrics in patients with T2DM was also reported in a previous DTI study.[8]

Recently, disease duration was also cited as an important contributing factor for developing diabetic peripheral neuropathy or cardiovascular autonomic neuropathy in patients with T2DM.[38,39] Additionally, there were significant correlations between the FA/RD of the superior rPF_WM and the RT of ANT, indicating that patients with T2DM with lower WM integrity have worse behavioral performance. Although no abnormal cognitive functions were detected in our patients with T2DM compared with healthy controls, these findings make it plausible to postulate that the T2DM-related cognitive decline would occur with an increase in disease duration. In addition, it is possible that the neuropsychological tests used in our study were not sensitive enough to detect subtle cognitive impairment. In our study, there were no significant correlations between the diffusion/kurtosis metrics and HbA1c in patients with T2DM, which is consistent with findings in previous DTI studies.[8] Among these studies,[7-14] only 2 reported a significant[11] or trend correlation[10] between the altered diffusion metrics and HbA1c. Although the patients included in the studies of Reijmer et al[10] and Hoogenboom et al[11] and our study were all free from any T2DM-related complications, the duration of the T2DM group is

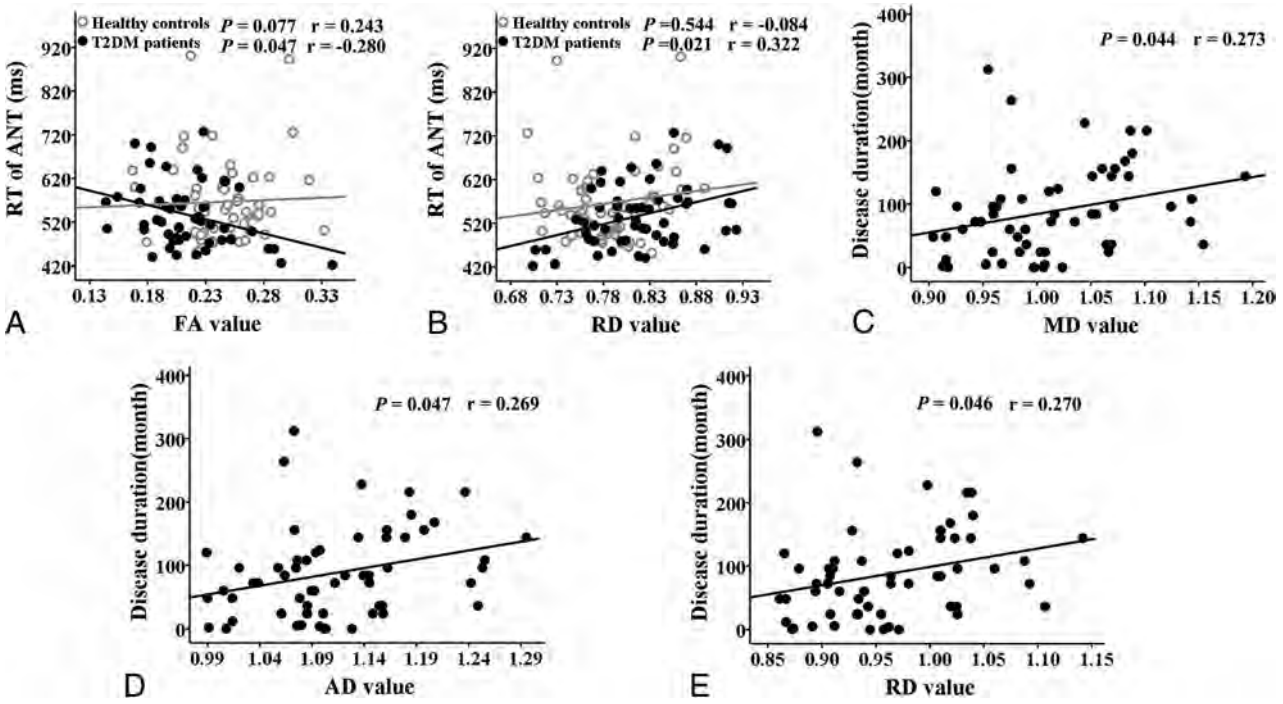

FIG 2. Correlations between DKI parameters and clinical/cognitive variables in the patients with T2DM and controls. *A*, Correlation between decreased FA in the rPF_WM and RT of ANT. *B*, Correlation between increased RD in rPF_WM and RT of ANT. *C*, Correlation between increased MD in the superior rPF_WM and disease duration. *D*, Correlation between increased AD in the superior rPF_WM and disease duration. *E*, Correlation between increased RD in the superior rPF_WM and disease duration.

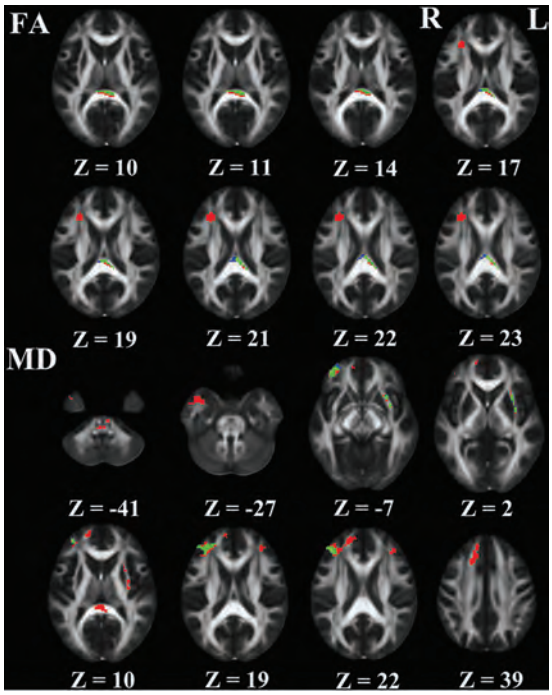

FIG 3. WM regions that showed significant differences in DKI metrics (red) and DTI metrics (blue) between patients with T2DM and controls were overlapped on the FA template. Green represents the overlapped region of the results of the DKI and the DTI between patients with T2DM and controls.

longer in the studies of Reijmer et al and Hoogenboom et al compared with our study, which may be an indirect factor contributing to correlations between the altered diffusion metrics and HbA1c. Thus, the current HbA1c may not be the best predictor of brain health. Additional studies are needed to investigate the effects of long-term glucose control on the diffusion/kurtosis metrics.

Altered WM integrity of the pons was detected in our patients with T2DM, which was not reported in previous DTI studies.[7-12] The locus coeruleus is located in the pons[40] and is related to numerous functions via its widespread projections to cortical and subcortical regions.[41] Previously, Clewett et al[42] provided human evidence that functional connectivity exists between the locus coeruleus and the dorsolateral prefrontal cortex. In the current study, patients with T2DM had decreased MK (driven by decreased AK and RK) and increased MD (driven by increased AD and RD) in the pons, which reflected reduced tissue heterogeneity in this area. Our results suggest that DKI-based metrics may be more sensitive to the change in complex WM microstructures of the pons and that the clinical significance of WM microstructure change in the pons in patients with T2DM is worthy of further study.

With the ROI-based analysis, we observed no significant differences in both primary DKI parameter values (FA, MD, and MK) and cognitive assessments between the patients with T2DM with and without insulin injection, which may, to some extent, reflect the use of insulin having no effect on our reported results. In addition, there is no knowledge of how oral antidiabetic drugs may affect the DTI/DKI indices to date[7-13]; thus, the medication-related impact on the results should be a focus of future studies.

Limitations

Several limitations should be acknowledged. First, our study is limited by its cross-sectional design, and further longitudinal studies are of great importance in investigating the clinical values

of DKI for predicting longitudinal cognitive decline. Second, although we attempted to maintain sample consistency by controlling for complications and hypoglycemia, variations in disease duration and treatment methods remained; these variations should be noted as a limitation.

CONCLUSIONS

To the best of our knowledge, this is the first DKI study on patients with T2DM. With both diffusion and kurtosis metrics, DKI can provide additional information about WM microstructural abnormalities in patients with T2DM. Our results demonstrated that WM microstructural abnormalities occur before cognitive decline in patients with T2DM; the correlations between the FA/RD of the rPF_WM and the RT of ANT have suggested that WM microstructural alterations may be used as a neuroimaging marker for predicting the early cognitive impairment in patients with T2DM.

REFERENCES

1. Zimmet P, Alberti KG, Shaw J. **Global and societal implications of the diabetes epidemic.** *Nature* 2001;414:782–87 CrossRef Medline
2. Biessels GJ, Staekenborg S, Brunner E, et al. **Risk of dementia in diabetes mellitus: a systematic review.** *Lancet Neurol* 2006;5:64–74 CrossRef Medline
3. Biessels GJ, Deary IJ, Ryan CM. **Cognition and diabetes: a lifespan perspective.** *Lancet Neurol* 2008:7:184–90 Medline
4. Brundel M, van den Heuvel M, de Bresser J, et al; Utrecht Diabetic Encephalopathy Study Group. **Cerebral cortical thickness in patients with type 2 diabetes.** *J Neurol Sci* 2010;299:126–30 CrossRef Medline
5. Knopman DS, Penman AD, Catellier DJ, et al. **Vascular risk factors and longitudinal changes on brain MRI: the ARIC study.** *Neurology* 2011;76:1879–85 CrossRef Medline
6. Moran C, Phan TG, Chen J, et al. **Brain atrophy in type 2 diabetes: regional distribution and influence on cognition.** *Diabetes Care* 2013;36:4036–42 CrossRef Medline
7. Yau PL, Javier D, Tsui W, et al. **Emotional and neutral declarative memory impairments and associated white matter microstructural abnormalities in adults with type 2 diabetes.** *Psychiatry Res* 2009; 174:223–30 CrossRef Medline
8. Hsu JL, Chen YL, Leu JG, et al. **Microstructural white matter abnormalities in type 2 diabetes mellitus: a diffusion tensor imaging study.** *Neuroimage* 2012;59:1098–105 CrossRef Medline
9. Falvey CM, Rosano C, Simonsick EM, et al; Health ABC Study. **Macro- and microstructural magnetic resonance imaging indices associated with diabetes among community-dwelling older adults.** *Diabetes Care* 2013;36:677–82 CrossRef Medline
10. Reijmer YD, Brundel M, de Bresser J, et al; Utrecht Vascular Cognitive Impairment Study Group. **Microstructural white matter abnormalities and cognitive functioning in type 2 diabetes: a diffusion tensor imaging study.** *Diabetes Care* 2013;36:137–44 CrossRef Medline
11. Hoogenboom WS, Marder TJ, Flores VL, et al. **Cerebral white matter integrity and resting-state functional connectivity in middle-aged patients with type 2 diabetes.** *Diabetes* 2014;63:728–38 CrossRef Medline
12. Zhang J, Wang Y, Wang J, et al. **White matter integrity disruptions associated with cognitive impairments in type 2 diabetic patients.** *Diabetes* 2014;63:3596–605 CrossRef Medline
13. Xiong Y, Sui Y, Xu Z, et al. **A diffusion tensor imaging study on white matter abnormalities in patients with type 2 diabetes using tract-based spatial statistics.** *AJNR Am J Neuroradiol* 2016;37:1462–69 CrossRef Medline
14. Reijmer YD, Leemans A, Brundel M, et al; Utrecht Vascular Cognitive Impairment Study Group. **Disruption of the cerebral white matter network is related to slowing of information processing speed in patients with type 2 diabetes.** *Diabetes* 2013;62:2112–15 CrossRef Medline
15. Alexander DC. **Multiple-fiber reconstruction algorithms for diffusion MRI.** *Ann N Y Acad Sci* 2005;1064:113–33 CrossRef Medline
16. Le Bihan D. **Molecular diffusion, tissue microdynamics and microstructure.** *NMR Biomed* 1995;8:375–86 CrossRef Medline
17. Tabesh A, Jensen JH, Ardekani BA, et al. **Estimation of tensors and tensor-derived measures in diffusional kurtosis imaging.** *Magn Reson Med* 2011;65:823–36 CrossRef Medline
18. Veraart J, Poot DH, Van Hecke W, et al. **More accurate estimation of diffusion tensor parameters using diffusion kurtosis imaging.** *Magn Reson Med* 2011;65:138–45 CrossRef Medline
19. American Diabetes Association. **Diagnosis and classification of diabetes mellitus.** *Diabetes Care* 2010;33(suppl 1):S62–69 CrossRef Medline
20. Folstein MF, Folstein SE, McHugh PR. **"Mini-mental state": a practical method for grading the cognitive state of patients for the clinician.** *J Psychiatric Res* 1975;12:189–98 CrossRef Medline
21. Zung WW. **A rating instrument for anxiety disorders.** *Psychosomatics* 1971;12:371–79 CrossRef Medline
22. Zung WW. **A self-rating depression scale.** *Arch Gen Psychiatry* 1965; 12:63–70 CrossRef Medline
23. Rosenberg SJ, Ryan JJ, Prifitera A. **Rey Auditory-Verbal Learning Test performance of patients with and without memory impairment.** *J Clin Psychol* 1984;40:785–87 Medline
24. Powell DH, Hiatt MD. **Auditory and visual recall of forward and backward digit spans.** *Percept Mot Skills* 1996;82:1099–103 CrossRef Medline
25. Grant DA, Berg EA. **A behavioral analysis of degree of reinforcement and ease of shifting to new responses in a Weigl-type card-sorting problem.** *J Exp Psychol* 1948;38:404–11 CrossRef Medline
26. Zhang Y, Du G, Yang Y, et al. **Higher integrity of the motor and visual pathways in long-term video game players.** *Front Hum Neurosci* 2015;9:98 CrossRef Medline
27. Fan J, McCandliss BD, Sommer T, et al. **Testing the efficiency and independence of attentional networks.** *J Cog Neurosci* 2002;14: 340–47 CrossRef Medline
28. Reitan R. **Validity of the Trail Making Test as an indicator of organic brain damage.** *Percept Mot Skills* 1958;8:271–76 CrossRef
29. Hui ES, Cheung MM, Qi L, et al. **Towards better MR characterization of neural tissues using directional diffusion kurtosis analysis.** *Neuroimage* 2008;42:122–34 CrossRef Medline
30. Basser PJ, Mattiello J, LeBihan D. **MR diffusion tensor spectroscopy and imaging.** *Biophys J* 1994;66:259–67 CrossRef Medline
31. Budde MD, Kim JH, Liang HF, et al. **Toward accurate diagnosis of white matter pathology using diffusion tensor imaging.** *Magn Reson Med* 2007;57:688–95 CrossRef Medline
32. Song SK, Sun SW, Ju WK, et al. **Diffusion tensor imaging detects and differentiates axon and myelin degeneration in mouse optic nerve after retinal ischemia.** *Neuroimage* 2003;20:1714–22 CrossRef Medline
33. Nilsson D, Go C, Rutka JT, et al. **Bilateral diffusion tensor abnormalities of temporal lobe and cingulate gyrus white matter in children with temporal lobe epilepsy.** *Epilepsy Res* 2008;81:128–35 CrossRef Medline
34. Wu EX, Cheung MM. **MR diffusion kurtosis imaging for neural tissue characterization.** *NMR Biomed* 2010;23:836–48 CrossRef Medline
35. Miller EK, Cohen JD. **An integrative theory of prefrontal cortex function.** *Annu Rev Neurosci* 2001;24:167–202 CrossRef Medline
36. Di Paola M, Spalletta G, Caltagirone C. **In vivo structural neuroanatomy of corpus callosum in Alzheimer's disease and mild cognitive impairment using different MRI techniques: a review.** *J Alzheimer Dis* 2010;20:67–95 CrossRef Medline
37. Jung RE, Chavez RS, Flores RA, et al. **White matter correlates of neuropsychological dysfunction in systemic lupus erythematosus.** *PLoS One* 2012;7:e28373 CrossRef Medline

38. Chen HT, Lin HD, Won JG, et al. **Cardiovascular autonomic neuropathy, autonomic symptoms and diabetic complications in 674 type 2 diabetes.** *Diabetes Res Clin Pract* 2008;82:282–90 CrossRef Medline
39. Hsu WC, Chiu YH, Chen WH, et al. **Simplified electrodiagnostic criteria of diabetic polyneuropathy in field study (KCIS No. 14).** *Neuroepidemiology* 2007;28:50–55 CrossRef Medline
40. Keren NI, Lozar CT, Harris KC, et al. **In vivo mapping of the human locus coeruleus.** *Neuroimage* 2009;47:1261–67 CrossRef Medline
41. Sara SJ, Bouret S. **Orienting and reorienting: the locus coeruleus mediates cognition through arousal.** *Neuron* 2012;76:130–41 CrossRef Medline
42. Clewett D, Schoeke A, Mather M. **Locus coeruleus neuromodulation of memories encoded during negative or unexpected action outcomes.** *Neurobiol Learn Mem* 2014;111:65–70 CrossRef Medline

Hippocampal Atrophy Is Associated with Altered Hippocampus–Posterior Cingulate Cortex Connectivity in Mesial Temporal Lobe Epilepsy with Hippocampal Sclerosis

Y.C. Shih, C.E. Tseng, F.-H. Lin, H.H. Liou, and W.Y.I. Tseng

ABSTRACT

BACKGROUND AND PURPOSE: Unilateral mesial temporal lobe epilepsy and hippocampal sclerosis have structural and functional abnormalities in the mesial temporal regions. To gain insight into the pathophysiology of the epileptic network in mesial temporal lobe epilepsy with hippocampal sclerosis, we aimed to clarify the relationships between hippocampal atrophy and the altered connection between the hippocampus and the posterior cingulate cortex in patients with mesial temporal lobe epilepsy with hippocampal sclerosis.

MATERIALS AND METHODS: Fifteen patients with left mesial temporal lobe epilepsy with hippocampal sclerosis and 15 healthy controls were included in the study. Multicontrast MR imaging, including high-resolution T1WI, diffusion spectrum imaging, and resting-state fMRI, was performed to measure the hippocampal volume, structural connectivity of the inferior cingulum bundle, and intrinsic functional connectivity between the hippocampus and the posterior cingulate cortex, respectively.

RESULTS: Compared with controls, patients had decreased left hippocampal volume (volume ratio of the hippocampus and controls, 0.366% ± 0.029%; patients, 0.277% ± 0.063%, corrected $P = .002$), structural connectivity of the bilateral inferior cingulum bundle (generalized fractional anisotropy, left: controls, 0.234 ± 0.020; patients, 0.193 ± 0.022, corrected $P = .0001$, right: controls, 0.226 ± 0.022; patients, 0.208 ± 0.017, corrected $P = .047$), and intrinsic functional connectivity between the left hippocampus and the left posterior cingulate cortex (averaged z-value: controls, 0.314 ± 0.152; patients, 0.166 ± 0.062). The left hippocampal volume correlated with structural connectivity positively (standardized $\beta = 0.864$, $P = .001$), but it had little correlation with intrinsic functional connectivity (standardized $\beta = -0.329$, $P = .113$). On the contralesional side, the hippocampal volume did not show any significant correlation with structural connectivity or intrinsic functional connectivity ($F_{2,12} = 0.284$, $P = .757$, $R^2 = 0.045$).

CONCLUSIONS: In left mesial temporal lobe epilepsy with hippocampal sclerosis, the left inferior cingulum bundle undergoes degeneration in tandem with the left hippocampal volume, whereas intrinsic functional connectivity seems to react by compensating the loss of connectivity. Such insight might be helpful in understanding the development of the epileptic network in left mesial temporal lobe epilepsy with hippocampal sclerosis.

ABBREVIATIONS: DSI = diffusion spectrum imaging; GFA = generalized fractional anisotropy; HS = hippocampal sclerosis; HV = hippocampal volume; iCB = inferior cingulum bundle; iFC = intrinsic functional connectivity; MTLE = mesial temporal lobe epilepsy; PCC = posterior cingulate cortex; SC = structural connectivity

Unilateral mesial temporal lobe epilepsy (MTLE) is a common type of refractory focal epilepsy in which hippocampal sclerosis (HS) is the most frequent pathologic finding. Gray matter atrophy associated with MTLE and HS (MTLE+HS) involves the hippocampus and brain regions outside the mesial temporal lobe.[1,2] The atrophied GM constitutes a network of regions that are structurally and functionally connected to the epileptogenic mesial temporal region.[3] Evidence has indicated that an epileptic network consists of both atrophied GM regions[2-4] and epileptic

Received June 2, 2016; accepted after revision October 17.

From the Institute of Biomedical Engineering (Y.C.S., F.-H.L.) and Molecular Imaging Center (W.Y.I.T.), National Taiwan University, Taipei, Taiwan; and Institute of Medical Device and Imaging (Y.C.S., C.E.T., W.Y.I.T.), Graduate Institute of Brain and Mind Sciences (H.H.L., W.Y.I.T.), and Departments of Neurology (H.H.L) and Medical Imaging (W.Y.I.T.), College of Medicine, National Taiwan University, Taipei, Taiwan.

This work was supported by the Ministry of Science and Technology, Taiwan; grant No. MOST104-2325-B-002-040 and MOST 103-2314-B-002-063-MY3; and the Ministry of Economic Affairs, Taiwan; grant No. 101-EC-17-A-19-S1-175.

Results previously presented in part at: Scientific Meeting and Exhibition of the International Society for Magnetic Resonance in Medicine, May 5–11, 2012; Melbourne, Australia; and April 20–26, 2013; Salt Lake City, Utah.

Please address correspondence to W.Y.I. Tseng, MD, PhD, Institute of Medical Device and Imaging, National Taiwan University College of Medicine, No. 1, Section 1, Jen-Ai Rd, Taipei 10051, Taiwan; e-mail: wytseng@ntu.edu.tw; H.H. Liou, MD, PhD, Department of Neurology, National Taiwan University Hospital and College of Medicine, No. 7, Chung-Shan South Rd, Taipei 10002, Taiwan; e-mail: hhl@ntu.edu.tw

Indicates open access to non-subscribers at www.ajnr.org

Indicates article with supplemental on-line appendix and table.

Indicates article with supplemental on-line photo.

http://dx.doi.org/10.3174/ajnr.A5039

seizure-spreading pathways.[1] Elucidation of altered structural and functional pathways with respect to atrophied GM can provide insight into the pathophysiology of epileptic network development, which might help in identifying biomarkers for the clinical diagnosis and treatment of unilateral MTLE+HS.[5]

The connection between the hippocampus or parahippocampus and the posterior cingulate cortex (PCC) is an afferent pathway of the hippocampus in the Papez circuit, which is altered in MTLE.[6] Kubota et al[7] used corticocortical-evoked potentials to investigate the connectivity between the hippocampus and the PCC in unilateral MTLE. They reported that prominent corticocortical-evoked potential responses were elicited in the hippocampus under PCC stimulation and suggested that electrical stimulation was directly transmitted from the PCC to the hippocampus through a white matter tract.[7] The inferior cingulum bundle (iCB) is a WM tract projecting from the PCC to the hippocampus or parahippocampus and the entorhinal cortex.[8] A DTI study reported decreased structural connectivity (SC) of the iCB in patients with unilateral MTLE+HS.[8] These and the findings of Kubota et al indicated that the iCB might be a structural pathway transmitting epileptiform discharges into the epileptic network.

Intrinsic functional connectivity (iFC) between brain regions represents the synchronization of blood oxygenation level–dependent signal fluctuations in MR imaging during the resting state.[9] The resting-state fMRI studies have shown decreased iFC between the epileptogenic hippocampus and the PCC in patients with unilateral MTLE+HS, suggesting that this functional metric represents an altered functional pathway of the epileptic network.[10,11] Taken together, hippocampus-PCC connectivity (both structural and functional) is a potential pathway of the epileptic network in unilateral MTLE+HS.

Bernasconi et al[12] reported that volume loss in the hippocampus was related to epilepsy duration in patients with unilateral MTLE+HS.[12] Moreover, on the basis of previous human[13] and animal studies,[14] they speculated that the progression of hippocampal atrophy leads to the development of an epileptogenic network and aggravates repeated seizures. Therefore, the elucidation of altered structural and functional pathways with respect to hippocampal atrophy can provide insight into the pathophysiology of the epileptic network in MTLE+HS. However, to date, few studies have investigated this relationship.

Therefore, in the present study, we investigated the relationship between hippocampal atrophy and hippocampus-PCC connectivity in unilateral MTLE+HS. We hypothesized that SC and iFC are altered in patients with unilateral MTLE+HS and that the altered connectivity is associated with hippocampal atrophy, which reflects the pathophysiology of the epileptic network. We used multicontrast MR imaging examinations, including high-resolution T1WI, diffusion spectrum imaging (DSI), and resting-state fMRI to measure the hippocampal volume (HV), SC of the iCB, and iFC between the hippocampus and the PCC, respectively.

MATERIALS AND METHODS

Participants

Fifteen patients (mean age, 36.87 ± 8.79 years) with left MTLE+HS and 15 healthy controls (mean age, 36.33 ± 8.73 years) were recruited for the study. The study was approved by the National Taiwan University Hospital research ethics committee, and all participants provided informed consent before entering the study. The demographics of the participants and detailed criteria for participant recruitment are listed in the Table and the On-line Appendix, respectively.

Demographic data of patients with left MTLE+HS and healthy controls

	Left MTLE+HS (n = 15)	Controls (n = 15)
Age (mean) (yr)	36.87 ± 8.79	36.33 ± 8.73
Sex (male/female)	9:6	8:7
Handedness (left/right)	0/15	0/15
Epilepsy duration (mean) (yr)	23.47 ± 10.58	–
Onset age (mean) (yr)	13.4 ± 7.11	–
Seizure type: (No.)		–
SPS	1	
CPS	13	
CPS with secondary generalization	1	

Note:—CPS indicates complex partial seizure; SPS, simple partial seizure.

Data Acquisition

All participants underwent MR imaging examinations on a 3T MR imaging system (Tim Trio; Siemens, Erlangen, Germany) with a 32-channel phased array head coil. The MR imaging examinations included T1WI, DSI, and resting-state fMRI. T1WI was performed by using a 3D magnetization-prepared rapid acquisition of gradient echo sequence with the following parameters: TR/TE = 2000/3 ms, flip angle = 9°, FOV = 256 × 192 × 208 mm^3, and acquisition matrix = 256 × 192 × 208. DSI was performed by using a pulsed gradient spin-echo diffusion EPI sequence with a twice-refocused balanced echo and the following parameters: TR/TE = 9600/130 ms, flip angle = 90°, FOV = 200 × 200 mm^2, acquisition matrix = 80 × 80 × 56, and section thickness = 2.5 mm. A total of 102 diffusion-encoding gradients were applied by using the maximum diffusion sensitivity of 4000 s/mm^2. These encoding gradients corresponded to grid points filled within the half sphere of the q-space with a radius of 3 units.[15] We performed resting-state fMRI by using 2D gradient-echo EPI with the following parameters: TR/TE = 2000/24 ms, flip angle = 90°, FOV = 256 × 256 mm^2, acquisition matrix = 64 × 64 × 34, section thickness = 3 mm, and 180 volumes per run.

Data Analysis

The MR imaging procedures and statistical analyses are presented in Fig 1. The volume ratio of the hippocampus (HV/whole-brain volume) was calculated to evaluate the degree of hippocampal atrophy. The whole-brain volume and HV calculations were performed by using FreeSurfer 5.0 software (http://surfer.nmr.mgh.harvard.edu). The details of the analysis procedures have been described elsewhere.[16] Neuroanatomic labels were automatically assigned to each voxel on the basis of probabilistic information estimated from a manually labeled training set. The HV was obtained in each hemisphere.

We used DSI to evaluate accurate tractography of the iCB because of its ability to resolve crossing fibers,[17] and we used tract-specific analysis to measure the microstructural integrity along the iCB to index SC. Within each voxel, the 102 samples within the

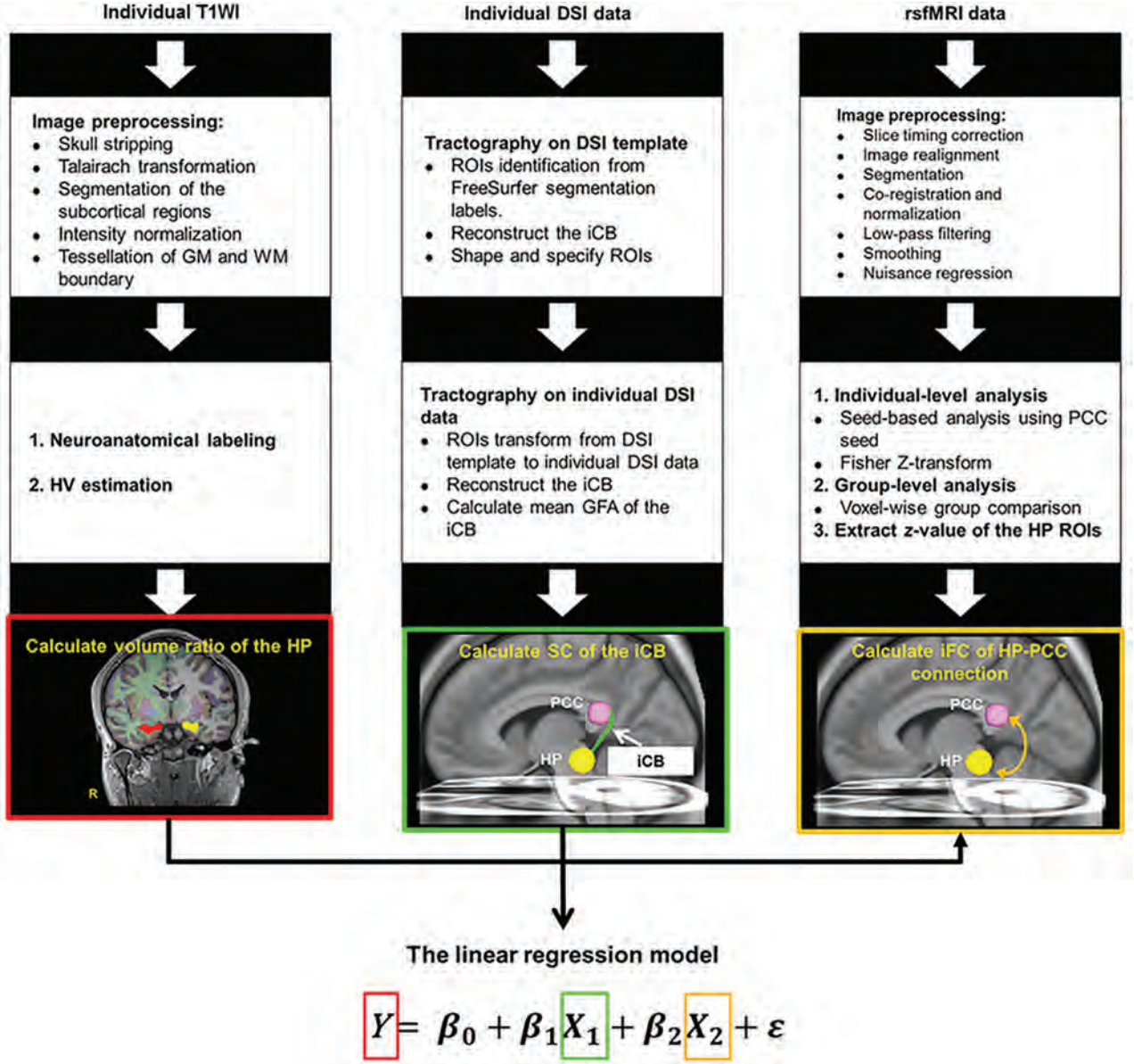

FIG 1. The pipeline of MR imaging and statistical analyses. Multicontrast MR imaging examinations including T1WI, DSI, and resting-state fMRI were performed to measure HV and SC of the iCB and iFC between the hippocampus and the PCC, respectively. A linear regression model was used to evaluate the correlation of HV with SC and iFC indices, where Y is the volume ratio of the hippocampus and X_1 and X_2 are the SC and iFC of the HP-PCC connection, respectively. HP indicates hippocampus; rsfMR, resting-state fMRI.

half sphere of the q-space were projected to fill the other half sphere, and 8 corners outside the sphere were filled with zeros. Fourier transform was performed on the q-space signal to obtain the diffusion probability density function.[17] The orientation distribution function was obtained by computing the second moment of the probability density function along each of the 362 radial directions in 6-fold tessellated icosahedrons. To quantify the microstructural integrity, we computed generalized fractional anisotropy (GFA), an index equivalent to fractional anisotropy in DTI,[18,19] for each voxel by using the following formula: (SD of the Orientation Distribution Function)/(Root Mean Square of the Orientation Distribution Function).[20] The decomposition of the orientation distribution function was performed to determine local tract directions in each voxel,[21] which were then used for the diffusion tractography of the iCB. The mean GFA of the left or right iCB was calculated to indicate SC between the hippocampus and the PCC. We performed a template-based tract-specific analysis based on the local tract direction and GFA maps derived from DSI data by using DSI Studio (http://dsi-studio.labsolver.org/). The detailed procedure of tracking the iCB is described in the On-line Figure.

The Data Processing Assistant for Resting-State fMRI (DPARSF; http://www.rfmri.org/DPARSF) was used to analyze resting-state fMRI data.[22] The detailed procedures of data preprocessing have been described elsewhere.[22] The preprocessed data were then filtered by using a bandpass filter (0.01–0.08 Hz). Finally, nuisance regression was performed to correct the polynomial trend, 6 rigid-body parameters, head-motion scrubbing (power of framewise displacement), and WM and CSF mean signals. We performed seed-based analysis to obtain whole-brain iFC maps by placing a

spheric seed ($r = 6$ mm) covering the bilateral PCC.[23] We computed iFC maps by using voxelwise Pearson correlation coefficients between the time course of each voxel and the averaged time course of the predefined PCC seed. Furthermore, iFC maps were transformed into *Z*-maps by using Fisher *Z*-transform. We used 2-sample *t* tests to conduct voxelwise group comparison with *Z*-maps between patients with left MTLE+HS and healthy controls. Moreover, we used the spheric ROIs with the radius of 8 mm centered at peak coordinates to extract z-values. The averaged z-values of the spheric ROIs in the hippocampus indicated the iFC between the hippocampus and the PCC.

Statistical analyses were performed by using SPSS, Version 20 (IBM, Armonk, New York). A Mann-Whitney *U* test was used for comparing age, volume ratio of the hippocampus, and SC between the hippocampus and the PCC (mean GFA of the iCB) between groups. In addition, we performed a Benjamini-Hochberg correction to address the issue of multiple testing. A linear regression model was used to investigate the relationship between the HV and SC and the iFC indices between the hippocampus and the PCC in patients.

RESULTS

Comparison between Groups

Healthy controls and patients were well-matched in age ($t(28) = 0.167$, $P = .869$), sex, and handedness (Table). Compared with healthy controls, patients had a significant decrease in the volume ratio of the left hippocampus (controls, 0.366% ± 0.029%; patients, 0.277% ± 0.063%; Benjamini-Hochberg–corrected $P = .002$) and no significant difference in the volume ratio of the right hippocampus (controls, 0.387% ± 0.041%; patients, 0.389% ± 0.039%; $P = .775$). In both the left and right iCBs, the mean GFA was significantly lower in patients than in healthy controls (left iCB: controls, 0.234 ± 0.020; patients, 0.193 ± 0.022; Benjamini-Hochberg–corrected $P = .0001$; right iCB: controls, 0.226 ± 0.022; patients, 0.208 ± 0.017; Benjamini-Hochberg–corrected $P = .047$).

The group comparison of iFC maps (*Z*-maps) revealed 2 peak coordinates in the left hippocampus, indicating decreased iFC between the left hippocampus and the PCC (On-line Table); this was defined by a higher contrast in healthy controls than in patients (peak 1: $T = 2.84$, small-volume–corrected[24] $P = .004$; peak 2: $T = 2.39$, small-volume–corrected $P = .012$). Moreover, 2 peak coordinates were observed in the right hippocampus, indicating increased iFC between the right hippocampus and the PCC; this was defined by a higher contrast in patients than in healthy controls (peak 3: $T = 2.01$, small-volume–corrected $P = .027$; peak 4: $T = 1.91$, small-volume–corrected $P = .028$). The averaged z-values of the spheric ROIs in the left hippocampus were 0.314 ± 0.152 and 0.166 ± 0.062 in healthy controls and patients, respectively, whereas those in the right were 0.200 ± 0.130 and 0.291 ± 0.091 in healthy controls and patients, respectively.

Relationship between the HV and Hippocampus-PCC SC and iFC Indices in Patients

In patients' left hemispheres, the overall regression model was significant ($F_{2,12} = 12.656$, $P = .001$, $R^2 = 0.678$). The regression model revealed that 62.6% (adjusted $R^2 = 0.626$) of the volume ratio of the left hippocampus was explained by the mean GFA of the left iCB and the averaged z-value of the left hippocampus. As presented in Fig 2*A*, the mean GFA of the left iCB positively correlated with the volume ratio of the left hippocampus ($\beta = 0.025$, standardized $\beta = 0.840$, $P = .0004$). The averaged z-value of the left hippocampus negatively correlated with the volume ratio of the left hippocampus ($\beta = -0.005$, standardized $\beta = -0.509$, $P = .013$, Fig 2*B*). In patients' right hemispheres, the regression model was not significant ($F_{2,12} = 0.284$, $P = .757$, $R^2 = 0.045$). Both the mean GFA of the right iCB and averaged z-value of the right hippocampus did not significantly correlate with the volume ratio of the right hippocampus (Fig 2*C*, -*D*). We found a potential outlier in 1 patient whose averaged z-value of the left hippocampus was larger than 2.5 times the SD. After we removed the outlier, the overall regression model was still significant in the left hemisphere ($F_{2,12} = 10.212$, $P = .003$, $R^2 = 0.650$, adjusted $R^2 = 0.586$). The correlation was significant between the mean GFA of the left iCB and the volume ratio of the left hippocampus ($\beta = 0.024$, standardized $\beta = 0.864$, $P = .001$); however, the correlation was no longer significant between the averaged z-value and the volume ratio of the left hippocampus ($\beta = -0.004$, standardized $\beta = -0.329$, $P = .113$).

DISCUSSION

To the best of our knowledge, this is the first study elucidating the relationship between hippocampal atrophy and structural and functional connectivity in patients with left MTLE+HS. We observed that the regression model used was highly significant, even though a potential outlier of data was removed from the model estimation. Specifically, left HV positively correlated with the mean GFA of the left iCB, but it did not correlate with the left iFC. Compared with controls, the HV, SC, and iFC indices were significantly decreased on the lesion side of patients. As discussed below, the association between the HV and its connection to the PCC allowed us to explore the pathophysiology of the epileptic network in unilateral MTLE+HS.

We observed a significant positive correlation between the left HV and the mean GFA of the left iCB in patients with left MTLE+HS (Fig 2*A*). Two mechanisms could explain this relationship: First, the iCB may be disrupted because of the excitotoxic effect caused by the spreading of epileptogenic activity through the Papez circuit.[25,26] The sclerotic hippocampus may generate epileptic activity and spread it through the Papez circuit to multiple epileptogenic regions, such as the mammillary body, thalamus, entorhinal cortex, and cingulate gyrus. The iCB is assumed to receive antegrade epileptic activity from secondary epileptogenic regions and to propagate it back to the hippocampus. Using DTI, Scanlon et al[27] demonstrated a positive correlation between the HV and fractional anisotropy in the middle cingulum bundle in patients with unilateral MTLE+HS. Our study further confirmed the correlation in the iCB on the lesion side. Another possible mechanism is that hippocampal cellular death caused by HS may affect the extrahippocampal WM, resulting in the axonal degeneration of the iCB.[28] This interpretation is based on an assumption that the iCB directly connects to the hippocampus. Kubota et al[7] used corticocortical-evoked poten-

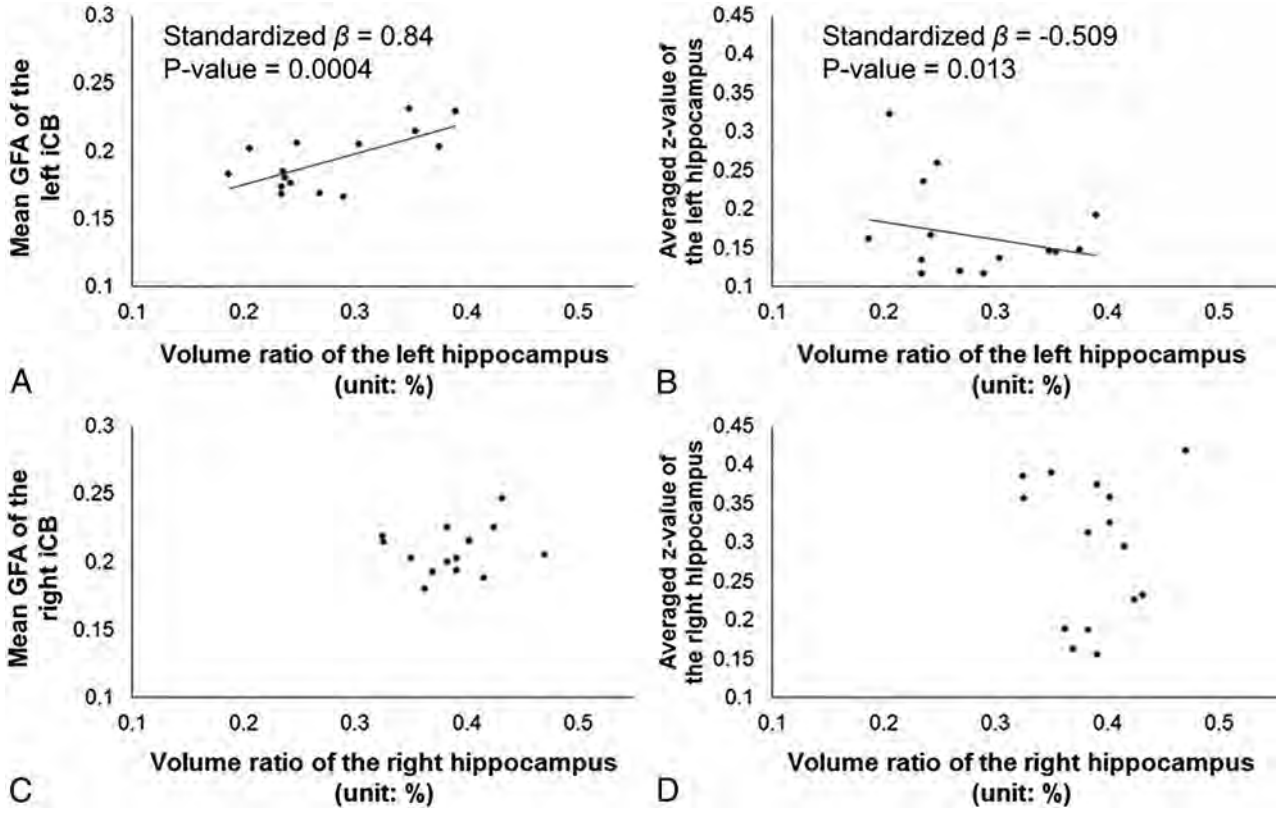

FIG 2. Relationships between HV and hippocampus-PCC SC and iFC indices in patients. We found a significant relationship between the volume ratio of the hippocampus (x-axis) and the mean GFA of the iCB (y-axis) (*A*) and between the volume ratio of the hippocampus (x-axis) and averaged z-value of the hippocampus (y-axis) (*B*) in the left hemisphere in patients with left MTLE+HS, whereas there were no correlations in the right hemisphere (*C* and *D*).

tials for electrical stimulation studies and reported that hippocampal stimulation induced a prominent response in the PCC and, conversely, that the hippocampus was elicited by PCC stimulation in patients with unilateral MTLE. Moreover, on the basis of corticocortical-evoked potentials, they speculated strong functional connectivity between the hippocampus and the PCC through the iCB. Therefore, hippocampal cellular death caused by HS following epileptogenesis might directly degrade the SC of the iCB.

Recent DTI studies have reported inconsistent results on the relationship between GM atrophy and impaired hippocampal WM structure in patients with unilateral MTLE+HS.[3,29] Ellmore et al[29] reported that the number of hippocampal fibers derived from probabilistic tractography positively correlated with the HV. Bonilha et al[3] investigated the relationship between the mean fractional anisotropy or mean diffusivity of perihippocampal fibers and the GM density of several brain regions in unilateral MTLE+HS; they did not find correlations between the HV and diffusion properties (fractional anisotropy and mean diffusivity) of perihippocampal fibers. With the advantage of DSI in resolving crossing fibers, we used tract-specific analysis to calculate the SC of the iCB and observed strong coupling with hippocampal atrophy in left MTLE+HS.

We observed decreased mean GFA of the left iCB in patients with left MTLE+HS. Our finding is similar to that of a previous DTI study on unilateral MTLE+HS.[8] In addition to the left iCB, decreased fractional anisotropy was observed in the right iCB in patients with left MTLE+HS,[8] which is consistent with our results. Their findings and ours support the idea that the SC of the bilateral iCB is altered in unilateral MTLE+HS; this alteration suggests that unilateral MTLE+HS is an extensive network disease.[30] Moreover, we did not observe a significant relationship between the right HV and mean GFA of the right iCB. According to our results, the right HV of patients was comparable with that of controls. Therefore, the mean GFA of the right iCB might be decreased in patients because of the excitotoxic injury caused by seizure spread.[25,26]

We found decreased iFC between the left hippocampus and the left PCC in patients with left MTLE+HS (On-line Table). Our results are consistent with those of previous studies that reported decreased iFC between the PCC and the epileptogenic hippocampus or mesial temporal lobe in patients with left MTLE+HS.[10,31] In addition, we observed increased iFC on the right side in the same group of patients (On-line Table). Bettus et al[32] investigated iFC between the hippocampus and other limbic structures on the healthy side in a group of patients with unilateral MTLE[32]; they reported increased iFC between the right hippocampus and the right temporal pole and right amygdala in patients with left MTLE. Their and our results suggest that increased iFC of the contralesional hippocampus is a compensatory response to decreased hippocampal connectivity on the lesion side.

Unlike strong coupling between the left HV and the mean GFA of the left iCB found in patients, the left HV showed little correlation with left iFC, especially after removal of an outlier (Fig 2*B*).

A study hypothesized that increased hippocampal activation or connectivity in patients with hippocampal injury might be a compensatory response relying on brain plasticity or an abnormal brain function reflecting pathologic changes.[33] In the same vein, our negative findings may imply dynamic changes of iFC in response to hippocampal atrophy or iCB degeneration. The left iFC in patients being generally decreased implies a decompensated, rather than compensated, status of iFC.

This study has some limitations. First, although we investigated the relationship between hippocampal atrophy and impaired hippocampus-PCC connectivity, the cross-sectional study design precludes us from determining a causal relationship. Second, the sample size in this study was relatively small. We included a small cohort of patients with unilateral MTLE who had only a left atrophic hippocampus. to reduce the influence of the heterogeneity within the populations of patients with MTLE+HS.[34,35] The strict inclusion criteria of subject selection limited our sample size. Nonetheless, our findings still remained significant after adjusting for multiple tests. Third, considering differences in the epileptogenic and neurophysiologic processes between left and right MTLE+HS,[36] our results might not be applicable to right, bilateral, or other subtypes of MTLE+HS.

CONCLUSIONS

We performed multicontrast MR imaging examinations and demonstrated that patients with left MTLE+HS had decreased HV, SC, and iFC indices on the lesion side. The left HV was positively correlated with SC, but not iFC. Such findings reflect the development of a degenerative fiber pathway with functional reactivity in an epileptic network. Such insight might be helpful in understanding the pathophysiology of the epileptic network.

ACKNOWLEDGMENTS

We thank all participants who joined this study and research assistants who helped collect and archive the data.

Disclosures: Fa-Hsuan Lin—*RELATED*: *Grant*: Ministry of Science and Technology, Taiwan, *Comments*: MOST 104-2314-B-002-238, MOST 103-2628-B-002-002-MY3.* *Money paid to the institution.

REFERENCES

1. Chan S, Erickson JK, Yoon SS. **Limbic system abnormalities associated with mesial temporal sclerosis: a model of chronic cerebral changes due to seizures.** *Radiographics* 1997;17:1095–110 CrossRef Medline
2. Riederer F, Lanzenberger R, Kaya M, et al. **Network atrophy in temporal lobe epilepsy: a voxel-based morphometry study.** *Neurology* 2008;71:419–25 CrossRef Medline
3. Bonilha L, Edwards JC, Kinsman SL, et al. **Extrahippocampal gray matter loss and hippocampal deafferentation in patients with temporal lobe epilepsy.** *Epilepsia* 2010;51:519–28 CrossRef Medline
4. Spencer SS. **Neural networks in human epilepsy: evidence of and implications for treatment.** *Epilepsia* 2002;43:219–27 CrossRef Medline
5. Gleichgerrcht E, Kocher M, Bonilha L. **Connectomics and graph theory analyses: novel insights into network abnormalities in epilepsy.** *Epilepsia* 2015;56:1660–68 CrossRef Medline
6. McDonald CR, Ahmadi ME, Hagler DJ, et al. **Diffusion tensor imaging correlates of memory and language impairments in temporal lobe epilepsy.** *Neurology* 2008;71:1869–76 CrossRef Medline
7. Kubota Y, Enatsu R, Gonzalez-Martinez J, et al. **In vivo human hippocampal cingulate connectivity: a corticocortical evoked potentials (CCEPs) study.** *Clin Neurophysiol* 2013;124:1547–56 CrossRef Medline
8. Liacu D, Idy-Peretti I, Ducreux D, et al. **Diffusion tensor imaging tractography parameters of limbic system bundles in temporal lobe epilepsy patients.** *J Magn Reson Imaging* 2012;36:561–68 CrossRef Medline
9. Fox MD, Raichle ME. **Spontaneous fluctuations in brain activity observed with functional magnetic resonance imaging.** *Nat Rev Neurosci* 2007;8:700–11 CrossRef Medline
10. McCormick C, Quraan M, Cohn M, et al. **Default mode network connectivity indicates episodic memory capacity in mesial temporal lobe epilepsy.** *Epilepsia* 2013;54:809–18 CrossRef Medline
11. James GA, Tripathi SP, Ojemann JG, et al. **Diminished default mode network recruitment of the hippocampus and parahippocampus in temporal lobe epilepsy.** *J Neurosurg* 2013;119:288–300 CrossRef Medline
12. Bernasconi N, Natsume J, Bernasconi A. **Progression in temporal lobe epilepsy: differential atrophy in mesial temporal structures.** *Neurology* 2005;65:223–28 CrossRef Medline
13. Bragin A, Wilson CL, Engel J Jr. **Chronic epileptogenesis requires development of a network of pathologically interconnected neuron clusters: a hypothesis.** *Epilepsia* 2000;41(suppl 6):S144–52 CrossRef Medline
14. Roch C, Leroy C, Nehlig A, et al. **Magnetic resonance imaging in the study of the lithium-pilocarpine model of temporal lobe epilepsy in adult rats.** *Epilepsia* 2002;43:325–35 CrossRef Medline
15. Kuo LW, Chiang WY, Yeh FC, et al. **Diffusion spectrum MRI using body-centered-cubic and half-sphere sampling schemes.** *J Neurosci Methods* 2013;212:143–55 CrossRef Medline
16. Fischl B, van der Kouwe A, Destrieux C, et al. **Automatically parcellating the human cerebral cortex.** *Cereb Cortex* 2004;14:11–22 CrossRef Medline
17. Wedeen VJ, Hagmann P, Tseng WY, et al. **Mapping complex tissue architecture with diffusion spectrum magnetic resonance imaging.** *Magn Reson Med* 2005;54:1377–86 CrossRef Medline
18. Fritzsche KH, Laun FB, Meinzer HP, et al. **Opportunities and pitfalls in the quantification of fiber integrity: what can we gain from Q-ball imaging?** *Neuroimage* 2010;51:242–51 CrossRef Medline
19. Takagi T, Nakamura M, Yamada M, et al. **Visualization of peripheral nerve degeneration and regeneration: monitoring with diffusion tensor tractography.** *Neuroimage* 2009;44:884–92 CrossRef Medline
20. Tuch DS. **Q-ball imaging.** *Magn Reson Med* 2004;52:1358–72 CrossRef Medline
21. Yeh FC, Tseng WY. **Sparse solution of fiber orientation distribution function by diffusion decomposition.** *PLoS One* 2013;8:e75747 CrossRef Medline
22. Chao-Gan Y, Yu-Feng Z. **DPARSF: A MATLAB toolbox for "pipeline" data analysis of resting-state fMRI.** *Front Syst Neurosci* 2010;4:13 CrossRef Medline
23. Fox MD, Snyder AZ, Vincent JL, et al. **The human brain is intrinsically organized into dynamic, anticorrelated functional networks.** *Proc Natl Acad Sci U S A* 2005;102:9673–78 CrossRef Medline
24. Worsley KJ, Marrett S, Neelin P, et al. **A unified statistical approach for determining significant signals in images of cerebral activation.** *Hum Brain Mapp* 1996;4:58–73 Medline
25. de Lanerolle NC, Lee TS. **New facets of the neuropathology and molecular profile of human temporal lobe epilepsy.** *Epilepsy Behav* 2005;7:190–203 CrossRef Medline
26. Williamson A, Spencer SS, Spencer DD. **Depth electrode studies and intracellular dentate granule cell recordings in temporal lobe epilepsy.** *Ann Neurol* 1995;38:778–87 CrossRef Medline
27. Scanlon C, Mueller SG, Cheong I, et al. **Grey and white matter abnormalities in temporal lobe epilepsy with and without mesial temporal sclerosis.** *J Neurol* 2013;260:2320–29 CrossRef Medline
28. De Vos KJ, Grierson AJ, Ackerley S, et al. **Role of axonal transport in**

neurodegenerative diseases. *Ann Rev Neurosci* 2008;31:151–73 CrossRef Medline
29. Ellmore TM, Pieters TA, Tandon N. **Dissociation between diffusion MR tractography density and strength in epilepsy patients with hippocampal sclerosis.** *Epilepsy Res* 2011;93:197–203 CrossRef Medline
30. Concha L, Beaulieu C, Gross DW. **Bilateral limbic diffusion abnormalities in unilateral temporal lobe epilepsy.** *Ann Neurol* 2005;57:188–96 CrossRef Medline
31. Doucet G, Osipowicz K, Sharan A, et al. **Extratemporal functional connectivity impairments at rest are related to memory performance in mesial temporal epilepsy.** *Hum Brain Mapp* 2013;34:2202–16 CrossRef Medline
32. Bettus G, Guedj E, Joyeux F, et al. **Decreased basal fMRI functional connectivity in epileptogenic networks and contralateral compensatory mechanisms.** *Hum Brain Mapp* 2009;30:1580–91 CrossRef Medline
33. La Joie R. **Toward a better understanding of the injured hippocampus: multimodal imaging in functionally relevant substructures.** *J Neurosci* 2014;34:10793–94 CrossRef Medline
34. Bonilha L, Martz GU, Glazier SS, et al. **Subtypes of medial temporal lobe epilepsy: influence on temporal lobectomy outcomes?** *Epilepsia* 2012;53:1–6 CrossRef Medline
35. Thom M, Mathern GW, Cross JH, et al. **Mesial temporal lobe epilepsy: how do we improve surgical outcome?** *Ann Neurol* 2010;68:424–34 CrossRef Medline
36. Zhang Z, Lu G, Zhong Y, et al. **Altered spontaneous neuronal activity of the default-mode network in mesial temporal lobe epilepsy.** *Brain Res* 2010;1323:152–60 CrossRef Medline

Arterial Spin-Labeling to Discriminate Pediatric Cervicofacial Soft-Tissue Vascular Anomalies

G. Boulouis, V. Dangouloff-Ros, O. Boccara, N. Garabedian, V. Soupre, A. Picard, V. Couloigner, N. Boddaert, O. Naggara, and F. Brunelle

ABSTRACT

BACKGROUND AND PURPOSE: Differentiating major subtypes of cervicofacial vascular lesions is crucial for appropriate management. The aim of our study was to evaluate the performance of an MR imaging arterial spin-labeling perfusion sequence in discriminating pediatric cervicofacial soft-tissue vascular anomalies.

MATERIALS AND METHODS: We conducted a retrospective analysis of data from a prospectively maintained registry including pediatric patients at a tertiary pediatric center between January 2012 and January 2014. We included pediatric patients with a final diagnosis of soft-tissue vascular anomalies and an MR imaging, including an arterial spin-labeling sequence at presentation. We performed an analysis of lesion perfusion, blinded to clinical data, by using concurrent spiral 3D pseudocontinuous arterial spin-labeling (1.5T magnet; spiral matrix, 512 × 8 mm; postlabeling delay, 1025 ms). Lesional flow was recorded with calibrated intralesional ROIs. Perfusion characteristics were compared among lesion subtypes with the Mood Median test.

RESULTS: Among 840 patients screened, 46 matched the inclusion criteria and were included (median age, 1.45 years; interquartile range, 0.4–5.1 years; 27 females). Hemangiomas, including infantile hemangiomas ($n = 18$ patients) and noninvoluting ($n = 2$) and rapidly involuting ($n = 1$) congenital types, demonstrated marked hyperperfusion (median flow, 436 mL/min/100 g; interquartile range, 212.5–603 mL/min/100 g), significantly higher than that of lymphatic malformations (median, 22.5 mL/min/100 g; interquartile range, 16–60 mL/min/100 g; $P < .001$) or venous malformations (median, 25 mL/min/100 g; interquartile range, 15–66.5 mL/min/100 g; $P = .003$).

CONCLUSIONS: MR imaging arterial spin-labeling is a valuable tool for the assessment of soft-tissue vascular anomaly hemodynamics and for the classification of major lesion subtypes.

ABBREVIATIONS: ASL = arterial spin-labeling; HI = infantile hemangioma; IQR = interquartile range; NICH = noninvoluting congenital hemangioma; RICH = rapidly involuting congenital hemangioma; STVA = soft-tissue vascular anomaly

Soft-tissue vascular anomalies (STVAs) include vascular tumors and vascular malformations; they can involve any part of the body and can be responsible for non negligible morbidity.[1] Vascular lesions represent the first cause of soft-tissue tumors and pseudotumors in children.[2] The International Society for the Study of Vascular Anomalies has classified these lesions in a framework of consistent nomenclature, last updated in April 2014.[3] This nomenclature is based on a body of clinical, biologic, pathologic, genetic, and imaging data. In this classification, perfusion characteristics play a central role in lesion definition[3]; therefore, any technique allowing local blood perfusion measurement is of critical importance for the diagnostic work-up.[4,5] In this behavior-based lesion classification, vascular anomalies are divided into vascular tumors, which include hemangiomas (benign tumor subgroup) and vascular malformations, which include lymphatic and venous lesions (locally aggressive or borderline subgroup). Differentiating these major subtypes of vascular lesions is crucial for appropriate management.

The sonographic appearance and flow pattern on Doppler examinations are the most commonly available diagnostic tests to classify STVAs in most centers; however, their use for cervicofacial STVAs can be challenging. Intracranial extensions are obvi-

Received July 20, 2016; accepted after revision October 18.

From the Department of Pediatric Radiology (G.B., V.D.-R., N.B., O.N., F.B.), Institut National de la Santé et de la Recherche Médicale U1000 (V.D.-R., N.B., F.B.), and Institut National de la Santé et de la Recherche Médicale U894 (G.B., O.N.), Descartes University, Paris, France; Departments of Pediatric Dermatology (O.B.), Pediatric Oto-Rhino-Laryngology (O.B., N.G., V.C.), and Pediatric Maxillo-Facial and Plastic Surgery (O.B., V.S., A.P., O.N.), Necker Children's Hospital, Descartes University, Paris, France; Centre de Référence des Malformations Rares de la Face de la Cavite Buccale (O.B., V.S., A.P.), Maxillofacial Malformation Reference Center, Paris, France; Faculté de Médecine Paris-Descartes (O.B., N.G., V.S., A.P., V.C., N.B., F.B.), Université Paris 5, Paris, France; Department of Neuroradiology (G.B., O.N.), Centre Hospitalier Sainte Anne, Paris, France; and Unite Mixte de Recherche 1163 (N.B., F.B.), Institut Imagine, Paris, France.

Please address correspondence to Gregoire Boulouis, MD, MSc, Stroke Research Center, 175 Cambridge St, Suite 300, Boston, MA 02114; e-mail: gregoireboulouis@gmail.com; @gboulouis

http://dx.doi.org/10.3174/ajnr.A5065

ously out of reach when the fontanels are closed, and the extent of the lesions can be underestimated when assessed solely by ultrasound, especially when they are embedded or hidden by bony structures.[5]

MR imaging has emerged as a key complementary examination for these complex or deep vascular lesions[2,5,6] or when examination of the brain is mandated by potential lesion associations.[2,6,7] In such situations, contrast medium injection may be required to assess the enhancement pattern of the lesion.[8] However, besides needing a venous access, contrast enhancement is not a direct reflection of STVA perfusion and only captures contrast medium leakage in the extravascular space.[9] Conversely, arterial spin-labeling (ASL) is an MR imaging technique that allows quantitative measurement of tissue perfusion by using magnetically labeled blood, therefore without any contrast medium injection.[10] Accumulating evidence has demonstrated the reliability of ASL in evaluating regional perfusion and its utility in the diagnostic work-up of vascular anomalies.[10-13] Of particular interest in pediatric patients, waiving the need for contrast injection, ASL is an interesting asset for the diagnosis of STVAs in this population.

The aim of our study was to retrospectively assess the potential value of the ASL sequence for the characterization of cervicofacial soft-tissue vascular anomalies in children.

MATERIALS AND METHODS

Study Population

The study population was derived from a prospective longitudinal cohort of consecutive children referred to Necker Children's Hospital, a tertiary care pediatric hospital, between January 2012 and January 2014. Our STVA registry is a prospectively implemented data base collecting demographic, clinical, imaging, and treatment data of consecutive patients with STVAs admitted at our institution. The initial clinical examination was performed by experienced pediatric dermatologists, and all cases were discussed at a pediatric multidisciplinary meeting, including head and neck surgeons, pediatric radiologists, and interventional neuroradiologists.

This data base was retrospectively queried to identify patients matching the following inclusion criteria: 1) children between birth and 18 years of age; 2) those with cervicofacial STVAs (defined by clinical examination, ultrasound examination, CT angiography, or venography); and 3) patients who had undergone an MR imaging ASL sequence during their initial diagnostic work-up before any treatment or biopsy.

Final diagnosis was obtained prospectively for each patient from the conclusions of our multidisciplinary symposium, which included pediatric dermatologists, radiologists, and surgeons, on the basis of the clinical-imaging features and evolution of the lesion and the pathologic examination findings, when available.

Test Method

MR Imaging Acquisition. An ASL perfusion sequence was acquired by using a 1.5T MR imaging scanner (Signa HDxt; GE Healthcare, Milwaukee, Wisconsin) and consisted of a concurrent spiral 3D pseudocontinuous ASL (12-channel head coil; 3D volume with a 4-mm section thickness; number of excitations, 3; axial partitions, 80; FOV, 240 × 240; acquisition matrix, 4 mm^3; spiral arms in each 3D partition, 8; points per arm, 512; TE, 10.5 ms; TR, 4428 ms; postlabeling delay, 1025 ms; flip angle, 155°). All patients underwent a routine MR imaging examination, including T1 and T2 sequences (including fat saturation when needed); additional sequences were performed at the discretion of the attending radiologist (contrast medium injection, dynamic injection).

MR Imaging Analysis. Regional flow measurements (in milliliters/100 g/minute) were obtained by using an optimized dedicated in-house postprocessing software on Advantage Windows workstations (GE Healthcare), as previously described.[14] Quantitative measurements were performed in consensus by 2 trained pediatric radiologists (F.B., V.D.-R.), blinded to clinical data. Lesional flow was measured in spheric calibrated ROIs of variable sizes according to the STVA size (mean, 50 mm^2), positioned in the center of the lesion, with care being taken to avoid partial volume averaging from adjacent tissues.

A third reader (O.N.) performed quantitative measurements independently to allow the calculation of interrater agreement statistics.

Ethics

The study conformed to generally accepted scientific principles and to ethical standards of research and was approved by an advisory opinion of the Ethics Committee (Comité de Protection des Personnes Ile de France III, AC051) at Necker Children's Hospital. The manuscript was prepared in accordance with Strengthening the Reporting of Observational Studies in Epidemiology

Table 1: Population characteristics[a]

Variable	Value
Age at diagnosis (yr)	1.45 (0.4–5.1)
Age categories (yr)	
0–1	17 (37%)
1–5	18 (39.1%)
Older than 5	11 (23.9%)
Female sex	27 (58.7%)
Localization	
Head	41 (89.1%)
Neck	5 (10.9%)
Precise location	
Cheek	5 (10.9%)
Submental region	5 (10.9%)
Eyelid	4 (8.7%)
Parotid gland	4 (8.7%)
Scalp	4 (8.7%)
Lip	3 (6.5%)
Multiple	3 (6.5%)
Other	7 (15.2%)
ISSVA subtypes	
Hemangioma	21 (45%)
Infantile hemangioma	18 (39.1%)
NICH	2 (4.3%)
RICH	1 (2.2%)
Lymphatic malformation	10 (21.7%)
Common venous malformation	9 (19.6%)
Other (hamartoma, AVF, AVM)	3 (6.7%)
Total No. of patients in study	46

Note:—ISSVA indicates International Society for the Study of Vascular Anomalies.
[a] Values are expressed as absolute number (percentage of total) or median (IQR).

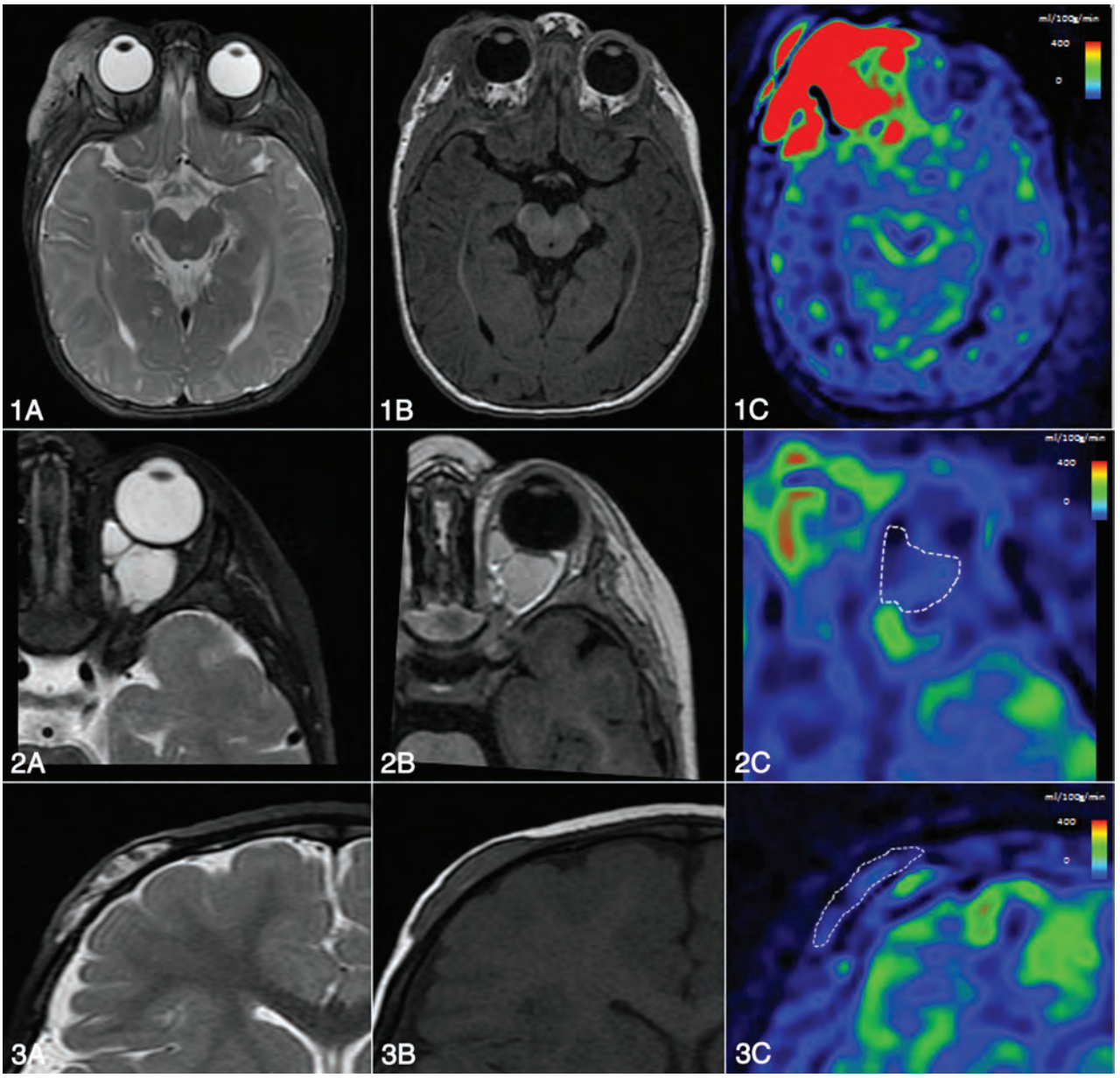

FIG 1. Illustrative cases of blood flow differences in major subtypes of STVA. Blood flow measured with ASL helps distinguish vascular anomalies. *A–C*, T2, T1, and ASL sequence blood flow maps. 1) Right intra- and periorbital hemangioma in a 6-month-old boy. ASL flow map demonstrates major lesional hyperperfusion (blood flow = 477 mL/100 g/min). 2) Intraorbital venous malformation of a 14-month-old boy with low blood flow (67 mL/min/100 g). 3) Intraosseous cystic lymphangioma of a 13-month-old girl with a low blood flow (45 mL/min/100 g).

guidelines (http://www.equator-network.org/reporting-guidelines/strobe/).

Statistical Methods

Values are expressed as mean ± SD or median/interquartile range (IQR), as appropriate. For the comparison of flow measurements, the Mood Median test was used due to the unequal variance of samples.

We performed interrater measures by using pair-wise correlations (Pearson product-moment correlation of each pair), comparing mean ASL values of the initial consensus reading with those performed independently by a third reader.

RESULTS

Among 840 pediatric patients screened for eligibility, 75 in the registry had undergone an ASL sequence at presentation, 49 of whom had a final diagnosis of cervicofacial STVA. Among these 49 patients, the ASL sequence was not interpretable in 3 cases due to kinetic artifacts. The remaining 46 patients were included in the study. Demographic and clinical characteristics of the study population are described in Table 1. The ASL perfusion characteristics in milliliters/100 g/minute of the 3 most frequent lesional subtypes of STVA are summarized in Fig 1 and Table 2.

Interobserver agreement was excellent for the measurement of ASL perfusion (pair-wise correlation, 0.94; 95% CI, 0.90–0.97).

Hemangiomas

Lesion characteristics are detailed in Table 2.

Infantile Hemangioma. For infantile hemangiomas (HIs), the median age was 2.9 months; there were 11 girls and 7 boys. Seven

Table 2: Summary of baseline clinical and imaging characteristics by diagnostic category in major lesion subtypes[a]

Variable	Hemangiomas (*n* = 21)	Common Venous Malformations (*n* = 9)	Common Lymphatic Malformations (*n* = 10)
Age (yr)	1.46 (0.1–8.2)	4.6 (1.2–11)	2.65 (0.7–11.5)
Female sex	12 (57)	7 (78)	5 (50)
Median ASL flow	477 (212–603)	25 (15–66.5)	22.5 (16–60)
T1 signal	Iso: 15 (88)	Iso: 9 (100)	Iso: 6 (75)
T2 signal	Hyper: 19 (95)	Hyper: 9 (100)	Hyper: 10 (100)

Note:—Iso indicates isointense; Hyper, hyperintense.

[a] Values are expressed as absolute number (percentage of column total) or as mean (range) or median (25th–75th percentiles).

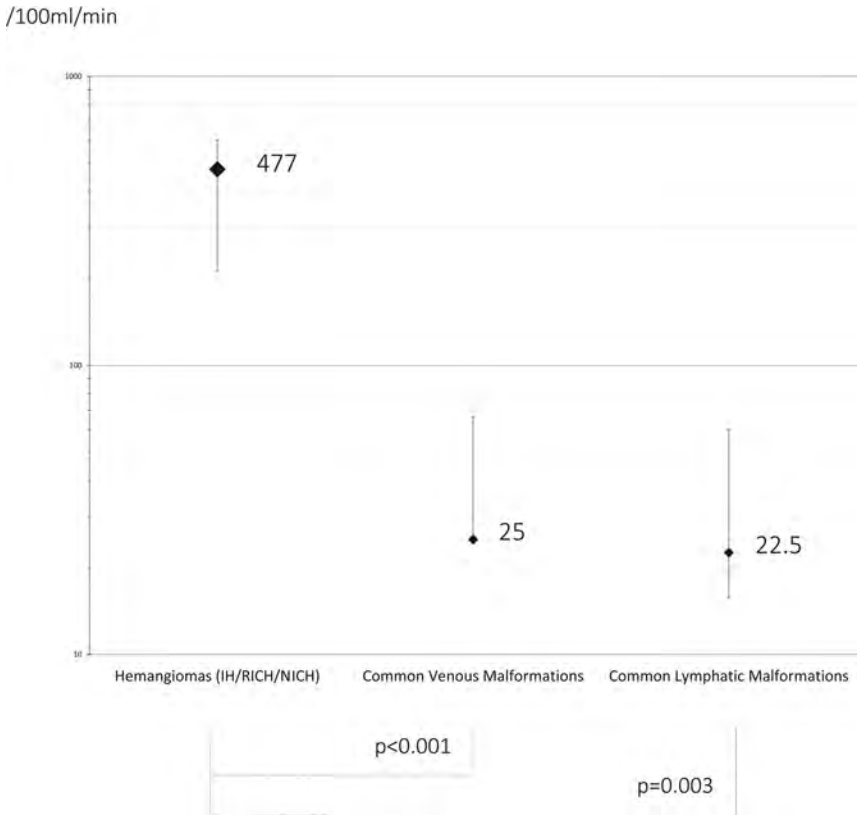

FIG 2. Comparison of major STVA subtypes by using ASL blood flow maps. ASL blood flow values are plotted and labeled median on a 0- to 1000-mL/100 g/min base 10 logarithmic scale; error bars represent interquartile range. IH indicates infantile hemagioma; RICH and NICH indicate rapidly and noninvoluting congenital hemangioma.

HIs (39%) were located in the orbital region. In all cases in which gadolinium injection was performed, the hemangiomas were massively and homogeneously enhanced. All HIs presented with an increased ASL tissue flow. The median perfusion value was 491 mL/100 g/min (IQR, 290–622 mL/100 g/min) with a range between 100 and 880 mL/100 g/min.

Rapidly and Noninvoluting Congenital Hemangioma. Two patients (6.1 and 8.2 years of age, respectively) had noninvoluting congenital hemangioma (NICH), and 1 patient (0 years) had rapidly involuting congenital hemangioma (RICH). After contrast injection, all 3 lesions enhanced massively. They presented with increased ASL-measured flow (median, 196 mL/100 g/min; IQR, 126–424 mL/100 g/min).

Overall, ASL showed a marked perfusion increase in all hemangiomas (HI, NICH, and RICH), with a median perfusion value of 477 mL/100 g/min (IQR, 212.5–603 mL/100 g/min).

Venous Malformations

For venous malformations, the median age was 4.6 years (range, 1.2–11years). There were 7 girls and 2 boys. All venous malformations presented with typical MR imaging features: isointense on T1 and moderately hyperintense on T2 fat-saturated sequences, with multiple small hypointense nodules representing focal nodular thromboses, precursors of phleboliths (uncalcified or soft phleboliths). The median flow was very low in all lesions (25 mL/min/100 g; IQR, 15–66.5 mL/min/100 g).

Lymphatic Malformations

For lymphatic malformations, the median age was 2.65 years (range, 8 months to 11.5 years). There were 5 girls and 5 boys. One patient (10%) presented with a fluid/fluid level. None of the lesions presented with enhanced perfusion (median flow, 22.5 mL/100 g/min; IQR, 16–60 mL/min/100 g).

Other Lesion Subtypes

Both AVMs and AVFs demonstrated increased intralesional perfusion (respectively, 779 and 451 mL/100 g/min), and none of the remaining lesions (namely, 1 hamartoma and 2 capillary lymphatic malformations) showed measurable increased perfusion (data not shown).

Lesion Subtype Comparisons

Hemangiomas, including NICH and RICH, presented with significantly higher flows than lymphatic ($P < .0001$) or venous malformations ($P = .003$). There was no significant difference between lymphatic and venous malformations (Fig 2).

DISCUSSION

We demonstrated that the ASL sequence, through its ability to quantitatively measure lesional flow, helps discriminate major subtypes of STVAs. In addition to providing increased lesion conspicuity, the ASL sequence is an excellent tool for refining the diagnosis. In our cohort, ASL was able to characterize an increased perfusion in all hemodynamically active lesions (HI, RICH, NICH, AVM, and AVF) and the absence of any measurable increase of perfusion in the others (lymphatic malformation, venous malformation, and hamartoma) and thus provided decisive help in making the diagnosis. This difference reached statistical significance when we compared the most frequent lesion subtypes (infantile hemangioma, lymphatic malformation, and venous malformation).

These findings provide strong support for the use of the ASL sequence in pediatric patients with STVAs. To date, the role of ASL in the diagnostic work-up of cervicofacial regions has been

examined in only a handful of studies.[15-17] Our systematic approach sheds light on the diagnostic possibilities of ASL in pediatric cervicofacial soft-tissue lesions.

Whereas vascular anomalies in children are commonly diagnosed by a combination of clinical examination and ultrasound Doppler findings, CT or MR imaging is often used to solve ambiguous cases or when an extended work-up is needed before treatment (nonexhaustively for osseous, complex, or intracranial lesions). MR imaging, in particular, has emerged as a key complementary tool in this setting.[5] Several studies have reported the use of dynamic contrast-enhanced sequences to characterize soft-tissue vascular anomalies,[8,18-20] emphasizing the paramount importance of the analysis of the hemodynamics of these lesions.[21] The present exploratory pilot study demonstrates the ability of the ASL sequence to discriminate infantile hemangiomas from venous and lymphatic malformations. Moreover, in view of its ability to quantitatively measure perfusion changes, the ASL sequence also has potential implications for patient follow-up during or after treatment. The blood flow response during or after treatment could easily be assessed by using ASL, but further longitudinal studies will be needed to examine its usefulness in this context.

Caution is needed regarding the interpretation of our results and those of future studies. ASL measures tissue perfusion—that is, the volume of blood that crosses the sample per minute per 100 g of tissue weight. On the other hand, gadolinium contrast accumulation in the extravascular space and intravascular signal change are responsible for enhancement; hence, the "enhancement" that is seen in structural T1-weighted MR imaging after gadolinium infusion is distinct from tissue perfusion characteristics captured by the ASL sequence. Thus, the terms "hyperperfused" and "enhancing" must not be considered interchangeable. Additionally, the presence of arteriovenous shunts might induce a bias in the perfusion measure because blood is diverted from tissue into the venous side and the diverted labeled blood is not taken into account for the flow measurement. The effect of this technical caveat most certainly accounts for the unexpected—albeit not significant and derived from a very small number of observations—relatively lower perfusion of AVM in our sample compared with HIs. This limitation could be addressed in the future by using multidelay pseudocontinuous ASL, which allows the characterization of blood pools with variable speeds.[22]

Our study has some limitations. The first is its retrospective design and the associated biases. Also, given the absence of normalized atlas values for soft-tissue lesion flow alteration measurements, we chose to compare the most frequent lesions and could not assess the relative perfusion with adjacent healthy soft tissues. Given the wide variety of STVAs, it was not possible to establish a control group for flow comparison. Finally, even if STVAs were classified in our sample by using a careful and systematic diagnostic approach, our criterion standard for the final diagnosis was based on the conclusions of a multidisciplinary symposium (and not a biopsy in most cases). Thus, we did not compare the diagnostic capacities of ASL with those of conventional noncontrast sequences (T1- and T2-weighted) because the final diagnosis was not made on those sequences alone but on a body of clinical-imaging data. Furthermore, a degree of bias in the classification cannot be ruled out because ASL (qualitatively high or low) may, in some instances, have been used as an additional argument for lesion classification.

CONCLUSIONS

This study of 46 children with a cervicofacial vascular anomaly demonstrates the potential role of ASL in discriminating major vascular lesion subtypes and assessing the hemodynamics of STVAs. In view of its ability to quantitatively measure lesional flow, ASL could be a useful tool for the follow-up of patients with hemodynamically active STVAs who are under treatment. Further studies will be needed to test this hypothesis.

Disclosures: Olivia Boccara—*UNRELATED*: *Consultancy*: Fabre Dermatology; *Payment for Lectures Including Service on Speakers Bureaus*: Pierre Fabre Dermatology; *Travel/Accommodations/Meeting Expenses Unrelated to Activities Listed*: Pierre Fabre Dermatology.

REFERENCES

1. Esterly NB. **Kasabach-Merritt syndrome in infants.** *J Am Acad Dermatol* 1983;8:504–13 CrossRef Medline
2. Navarro OM, Laffan EE, Ngan BY. **Pediatric soft-tissue tumors and pseudo-tumors: MR imaging features with pathologic correlation, part 1: imaging approach, pseudotumors, vascular lesions, and adipocytic tumors.** *Radiographics* 2009;29:887–906 CrossRef Medline
3. Wassef M, Blei F, Adams D, et al; ISSVA Board and Scientific Committee. **Vascular anomalies classification: recommendations from The International Society for the Study of Vascular Anomalies.** *Pediatrics* 2015;136:e203–14 CrossRef Medline
4. Trop I, Dubois J, Guibaud L, et al. **Soft-tissue venous malformations in pediatric and young adult patients: diagnosis with Doppler US.** *Radiology* 1999;212:841–45 CrossRef Medline
5. Flors L, Leiva-Salinas C, Maged IM, et al. **MR imaging of soft-tissue vascular malformations: diagnosis, classification, and therapy follow-up.** *Radiographics* 2011;31:1321–40; discussion 1340–41 CrossRef Medline
6. Flors L, Leiva-Salinas C, Norton PT, et al. **Ten frequently asked questions about MRI evaluation of soft-tissue vascular anomalies.** *Am J Roentgenol* 2013;201:W554–62 CrossRef Medline
7. Laffan EE, Ngan BY, Navarro OM. **Pediatric soft-tissue tumors and pseudotumors: MR imaging features with pathologic correlation, part 2: tumors of fibroblastic/myofibroblastic, so-called fibrohistiocytic, muscular, lymphomatous, neurogenic, hair matrix, and uncertain origin.** *Radiographics* 2009;29:e36 CrossRef Medline
8. Ohgiya Y, Hashimoto T, Gokan T, et al. **Dynamic MRI for distinguishing high-flow from low-flow peripheral vascular malformations.** *AJR Am J Roentgenol* 2005;185:1131–37 CrossRef Medline
9. Sharafuddin MJ, Sundaram M. **The role of magnetic resonance imaging in the diagnosis of soft tissue lesions.** *Crit Rev Diagn Imaging* 1994;35:379–483 Medline
10. Petersen ET, Zimine I, Ho YC, et al. **Non-invasive measurement of perfusion: a critical review of arterial spin labelling techniques.** *Br J Radiol* 2006;79:688–701 CrossRef Medline
11. Heijtel DF, Mutsaerts HJ, Bakker E, et al. **Accuracy and precision of pseudo-continuous arterial spin labeling perfusion during baseline and hypercapnia: a head-to-head comparison with ^{15}O H_2O positron emission tomography.** *Neuroimage* 2014;92:182–92 CrossRef Medline
12. Kistner I, Ott C, Jumar A, et al. **1D.09: Applicability of measurement of renal perfusion using 1.5 Tesla MRI arterial spin labelling.** *J Hypertens* 2015;33(suppl 1):e17 CrossRef Medline
13. Iv M, Fischbein NJ, Zaharchuk G. **Association of developmental venous anomalies with perfusion abnormalities on arterial spin-labeling and bolus perfusion-weighted imaging.** *J Neuroimaging* 2015;25:243–50 CrossRef Medline
14. Blauwblomme T, Naggara O, Brunelle F, et al. **Arterial spin labeling magnetic resonance imaging: toward noninvasive diagnosis and**

follow-up of pediatric brain arteriovenous malformations. *J Neurosurg Pediatr* 2015;15:451–58 CrossRef Medline
15. Pollock JM, Tan H, Kraft RA, et al. **Arterial spin-labeled MRI perfusion imaging: clinical applications.** *Magn Reson Imaging Clin N Am* 2009;17:315–38 CrossRef Medline
16. Pollock J, Kraft R, Tan H, et al. **Arterial spin labeled perfusion imaging of the orbit: initial experience.** In: *Proceedings of the Annual Meeting of the American Society of Head and Neck Radiology*, Toronto, Ontario, Canada. September 10–14, 2008
17. Mamlouk MD, Hess CP. **Arterial spin-labeled perfusion for vascular anomalies in the pediatric head and neck.** *Clin Imaging* 2016;40:1040–46 CrossRef Medline
18. Thawait SK, Puttgen K, Carrino JA, et al. **MR imaging characteristics of soft tissue vascular anomalies in children.** *Eur J Pediatr* 2013;172:591–600 CrossRef Medline
19. Lidsky ME, Spritzer CE, Shortell CK. **The role of dynamic contrast-enhanced magnetic resonance imaging in the diagnosis and management of patients with vascular malformations.** *J Vasc Surg* 2012;56:757–64.e1 CrossRef Medline
20. Masand P. **Radiographic findings associated with vascular anomalies.** *Semin Plast Surg* 2014;28:69–78 CrossRef Medline
21. Wang J, Licht DJ, Jahng GH, et al. **Pediatric perfusion imaging using pulsed arterial spin labeling.** *J Magn Reson Imaging* 2003;18:404–13 CrossRef Medline
22. Qiu D, Straka M, Zun Z, et al. **CBF measurements using multidelay pseudocontinuous and velocity-selective arterial spin labeling in patients with long arterial transit delays: comparison with xenon CT CBF.** *J Magn Reson Imaging* 2012;36:110–19 CrossRef Medline

Structural Connectivity Analysis in Children with Segmental Callosal Agenesis

M. Severino, D. Tortora, B. Toselli, S. Uccella, M. Traverso, G. Morana, V. Capra, E. Veneselli, M.M. Fato, and A. Rossi

ABSTRACT

BACKGROUND AND PURPOSE: Segmental callosal agenesis is characterized by the absence of the intermediate callosal portion. We aimed to evaluate the structural connectivity of segmental callosal agenesis by using constrained spherical deconvolution tractography and connectome analysis.

MATERIALS AND METHODS: We reviewed the clinical-radiologic features of 8 patients (5 males; mean age, 3.9 years). Spherical deconvolution and probabilistic tractography were performed on diffusion data. Structural connectivity analysis, including summary network metrics, modularity analysis, and network consistency measures, was applied in 5 patients and 10 age-/sex-matched controls.

RESULTS: We identified 3 subtypes based on the position of the hippocampal commissure: beneath the anterior callosal remnant in 3 patients (type I), beneath the posterior callosal remnant in 3 patients (type II), and between the anterior and posterior callosal remnants in 2 patients (type III). In all patients, the agenetic segment corresponded to fibers projecting to the parietal lobe, and segmental Probst bundles were found at that level. Ectopic callosal bundles were identified in 3 patients. Topology analysis revealed reduced global connectivity in patients compared with controls. The network topology of segmental callosal agenesis was more variable across patients than that of the control connectomes. Modularity analysis revealed disruption of the structural core organization in the patients.

CONCLUSIONS: Three malformative subtypes of segmental callosal agenesis were identified. Even the absence of a small callosal segment may impact global brain connectivity and modularity organization. The presence of ectopic callosal bundles may explain the greater interindividual variation in the connectomes of patients with segmental callosal agenesis.

ABBREVIATIONS: ACC = agenesis of the corpus callosum; HC = hippocampal commissure; PVC = partial virtual callosotomy; segACC = segmental agenesis of the corpus callosum

Segmental agenesis of the corpus callosum (segACC) is a peculiar form of partial callosal agenesis (ACC) characterized by the absence of the central portion of the corpus callosum with disconnection between the anterior corpus callosum and the splenium.[1,2] On conventional imaging, the anterior and posterior segments appear, respectively, as genual and splenial remnants, while the intermediate segment is a thin lamina, usually corresponding to the hippocampal commissure.[2] These features were traditionally considered the result of an early destructive insult during central nervous system development. Indeed, for many years, the prevailing theory held that the corpus callosum developed in an anterior-to-posterior direction, starting with the genu, followed by the body, splenium, and finally the rostrum.[3] According to this model, segACC can only be explained by an acquired disruptive event occurring after corpus callosum development has been completed. On the other hand, segACC has been described in siblings and in patients with no evidence of cerebral lesions, suggesting a malformative rather than acquired origin.[1] Moreover, new theories on the bicentric origin of the corpus callosum have further supported the malformative hypothesis.[2] Nevertheless, little is still known about the structural connectivity pattern and clinical-genetic phenotypes associated with this rare callosal malformation.

In past years, there has been increasing interest in the application of advanced diffusion MR imaging techniques for in vivo

Received August 9, 2016; accepted after revision October 18.

From the Neuroradiology Unit (M.S., D.T., G.M., A.R.), Neuropsychiatry Unit (S.U., M.T., E.V.), and Genetic Unit of the Department of Neurosurgery (V.C.), Istituto Giannina Gaslini, Genoa, Italy; and Department of Informatics, Bioengineering, Robotics and System Engineering (B.T., M.M.F.), Università degli Studi di Genova Scuola Politecnica, Genoa, Italy.

Please address correspondence to Mariasavina Severino, MD, Neuroradiology Unit, Istituto Giannina Gaslini, via Gaslini 5, Genoa 16147, Italy; e-mail: mariasavinaseverino@gaslini.org

Indicates article with supplemental on-line tables.

Indicates article with supplemental on-line photos.

http://dx.doi.org/10.3174/ajnr.A5043

investigation of callosal malformations. In particular, diffusion tensor imaging has offered the first clues about structural white matter organization in patients with ACC, showing the connectivity pattern of Probst bundles and revealing the presence of aberrant heterotopic callosal tracts in partial ACC.[4,5] High-angular-resolution DWI and probabilistic tractography, taking into account multiple fiber orientations in the same voxel, have then improved the reconstruction of WM bundles, demonstrating the wide variability of callosal connections in partial ACC.[6] More recently, a further step in DWI postprocessing associated with the application of graph analysis techniques, the so-called "structural connectome," has enabled exploring the connectivity of WM networks of the human brain.[7,8] This approach models the brain as a graph represented by a collection of nodes, corresponding to cortical and subcortical regions and their WM connections (edges). Several topologic metrics and properties may be defined to characterize the global and regional organization of brain networks.[7,8] The structural connectivity framework has greatly improved the characterization of WM abnormalities in patients with ACC, revealing different patterns of global and local connectivity and greater interindividual variation of brain network organization compared with healthy subjects.[9-11]

In this study, we aimed to characterize the structural features of segACC by using constrained spherical deconvolution and probabilistic tractography and to describe the associated clinical and genetic phenotypes in 8 children with this rare malformation. Moreover, to determine the impact of segACC on large-scale brain networks, we compared network topologic properties related to integration and segregation among children with this malformation relative to healthy controls, and we applied network-based statistics to quantify connectivity differences. In particular, we hypothesized that the absence of the central callosal portion reduces the long-range global connectivity and increases the short-range local connectivity in patients with segACC. Second, we expected to find increased variability of node degree spatial distribution and correlation strengths in patients with segACC compared with controls. Finally, we postulated that the modular organization of the segACC brain is different compared with healthy controls.

MATERIALS AND METHODS

Subjects

This was a single-center retrospective case-control study, performed with Gaslini Institute review board approval and parental written informed consent. We reviewed the MR imaging studies, clinical information, and genetic data of 8 children consecutively diagnosed with segACC between 2010 and 2015 (5 males; mean age at MR imaging, 3.9 years; range, 22 days to 5.11 years). Connectome analysis was performed in the 5 patients with segACC older than 2 years of age, because no major reorganization of structural modules is usually observed after this age.[12] We selected 10 age-/sex-matched controls who underwent brain MR imaging with DTI for transient febrile convulsion, minor trauma, or headaches; all had normal brain anatomy, psychomotor development, and neurologic examination.

Imaging Acquisition

MR imaging was performed on a 1.5T scanner with an 8-channel head coil and included 3-mm-thick axial T2WI, FLAIR, and DWI; 3-mm-thick coronal T2WI; sagittal 0.6-mm-thick 3D driven equilibrium; and 3D turbo field echo T1WI. DWI data were collected along 34 noncollinear directions by using an axial single-shot spin-echo echo-planar sequence, with b-values of 0 and 1000s/mm^2, TR = 9203 ms, TE = 71 ms, section thickness = 2 mm, FOV = 240 × 240 mm, matrix size = 128 × 128. Uncooperative patients were sedated during the examinations.

Data Preprocessing

The FMRIB Diffusion Toolbox 3.0 (http://fsl.fmrib.ox.ac.uk/fsl/fslwiki/FDT) was used to correct DWI raw data for motion artifacts and eddy current distortion and to calculate the tensor and DTI metrics maps. Subsequently, we used the FMRIB Linear Image Registration Tool (FLIRT; http://www.fmrib.ox.ac.uk/) to perform linear registration between the reference B0 images and 3D-T1WI. Nonbrain tissue was removed by using the MRtrix3 package (https://github.com/MRtrix3/mrtrix3).

Probabilistic Tractography

Constrained spherical deconvolution and probabilistic tractography were performed on the preprocessed diffusion-weighted images by using the MRtrix3 package.[13] For each subject, a whole-brain tractography consisting of 3 million streamlines was generated, by using the anatomically constrained tractography framework.[14] The seeds used for generating streamlines were distributed uniformly in the gray/white matter interface. The tractograms were filtered by using the spherical deconvolution–informed filtering of tractograms, and the final result consisted of 1.5 million streamlines for each subject.[15]

Fiber segmentation was performed by using TrackVis 0.5.1 (www.trackvis.org) with a manually drawn multi-ROI approach, following the callosal fiber segmentation method described by Wahl et al[6] (On-line Fig 1). Qualitative analysis was performed by 2 pediatric neuroradiologists with 20 and 8 years of experience, respectively, who evaluated the anatomic course of reconstructed tracts on superimposed 3D-T1WI and the presence of other brain anomalies.

Cortical Parcellation and Connectivity Matrix Construction

The 3D-T1WI was automatically segmented by using FreeSurfer 5.1.0 (http://surfer.nmr.mgh.harvard.edu/) in 84 regions (68 cortical and 16 subcortical), representing the network nodes used as seeds for connectome construction.[16] To compare the structural connectivity studies of patients and controls, we modified the virtual callosotomy approach used by Owen et al,[9] simulating the segACC in each matched control (partial virtual callosotomy [PVC]). In particular, in MRtrix3, we placed a manually drawn exclusion mask on the midsagittal plane over the exact callosal segment corresponding to the patient's agenetic callosum portion. The size and shape of the mask varied for each pair of matched controls on the basis of the specific type of segACC, effectively removing only the streamlines passing through the corresponding agenetic callosal segment.

The connectome edges were calculated by using probabilistic tractography performed with MRtrix3. The tracking results of each of the seeds were masked by each of the other 83 regions, referred to as targets, to obtain a connection strength between each seed and target pair, with the total number of streamlines connecting 2 regions as the connection strength. The 84 × 84 connection matrices were symmetric about the diagonal, and the matrix diagonal was set to zero. The connection strength was then divided by the sum of voxels in the seed and target regions to account for differences in volumes between various cortical and subcortical regions.

Individual and consensus connectomes were created for the 3 groups of subjects: patients with segACC, controls with PVC, and controls without PVC. In particular, we thresholded each individual connectome to remove the weakest connections, setting to zero all connection strengths that were <0.5% of the maximum strength.[9] The individual connectomes were then binarized setting to 1 all the nonzero connections. For each group, a consensus connectome was obtained by averaging the thresholded matrices of all subjects in the group; subsequently, all connections that were present in <75% of the subjects in the group were removed from the group's consensus matrix. The consensus matrices were then binarized by setting to 1 all the nonzero connections.

Network Analysis

For topology analysis, we calculated measures of structural segregation (clustering coefficient, transitivity, local efficiency, and modularity) and integration (mean degree, characteristic path length, mean normalized betweenness, global efficiency, and cost) for the binarized individual and consensus connectomes of subjects with segACC and PVC and controls, with the Brain Connectivity Toolbox (https://sites.google.com/site/bctnet).

In each group, hub nodes were separately identified for individual and consensus connectomes. A node in a single network (individual or consensus) was marked as a hub if its degree was 1 SD higher than the mean degree of its network. To test the hypothesis that the segACC brain has higher within-group variability compared with controls, we assessed the spatial distribution of node degree by transforming the degrees of the 84 nodes in each connectome into a vector and by using the correlation coefficient in a pair-wise fashion between all individuals in each group.[9] To measure network similarity, we calculated the connection strength correlation coefficient between each individual connectome and its group consensus connectome, as well as between every pair of individual connectomes in each group.[9]

Modularity and mean participation coefficient (quantifying the diversity of intermodular connections) were calculated for each partitioning of the consensus and individual connectome.[8] To evaluate the stability of modular assignment, we computed the mean Hubert-Rand Index for each of the 3 groups: 1) between the modular assignment for each of the individual connectomes and the assignment for the consensus connectome, and 2) pair-wise between the modular assignments for the individual connectomes (Matlab R2015b; MathWorks, Natick, Massachusetts).[9] The Hubert-Rand index is an adjustment of the Rand index (measuring the similarity of 2 partitions of a dataset) that takes into account the probability of both agreement and disagreement between partitions.[17]

To subdivide the networks into nonoverlapping modules, we applied the Louvain community detection algorithm with an iterative fine-tuning method by using the function provided by the Brain Connectivity Toolbox. The iterations were stopped when the modularity value did not change between steps.

Network-based statistics was performed to evaluate the differences in subnetworks between patients and PVC controls.[18] The statistical model included a design matrix of 5 patients and 10 controls. We used a contrast vector (1, −1) to test for an increase of subnetwork connectivity in controls compared with patients, and a contrast vector (−1, 1) to test for the opposite hypothesis. A t test was applied to assess the statistical significance of between-group comparisons of the network metrics. For each metric, the data labels were randomly reassigned between the 2 groups and t values were computed for each relabeling. A total of 5000 permutations were performed to estimate the null distribution, and associations with $t > 3$ were analyzed by network-based statistics. A family-wise error rate–corrected significance level of $P \leq .01$ was used.

Statistics

To assess the statistical significance of between-group comparisons of the network metrics and the measures of connectome variability, we used a nonparametric permutation testing procedure. For each metric, the data labels were randomly reassigned between the 2 groups and t values were computed for each relabeling, for a total of 5000 permutations. P values were calculated on the basis of the distribution of t values obtained from the permutations and were adjusted for multiple comparisons with a false-discovery rate correction. Statistical significance was set at $P < .05$. Data were analyzed by using SPSS Statistics for Mac 21.0 (IBM, Armonk, New York).

RESULTS

Clinical, genetic, and neuroradiologic characteristics of patients with segACC are described in On-line Table 1. On conventional imaging, in most patients (7/8; 87.5%), the agenetic segment corresponded to the posterior callosal body and the splenium was hypoplastic. In 1 patient (1/8; 12.5%), the anterior callosal body was additionally involved. Probst bundles were noted in all patients (8/8; 100%) at the level of the agenetic callosal segment on coronal images. The anterior commissure was hypoplastic in 4 cases (4/8; 50%). A colpocephalic appearance of the lateral ventricle was evident in 3 patients (3/8, 34.5%).

On constrained spherical deconvolution tractography, no callosal fiber tracts were detectable at the level of the thin lamina corresponding to the agenetic segment. Three malformative subtypes were identified on the basis of the relationship of the hippocampal commissure (HC) with the callosal remnants (Fig 1 and On-line Fig 2): The HC lay beneath the anterior callosal remnant in 3 patients (segACC type I), while in 3 other patients, it was attached to the posterior callosal remnant (segACC type II). Finally, in 2 patients, the intermediate segment of the commissural plate was made of green-coded longitudinal bundles corresponding to the fornices joined in the midline, forming the HC (segACC type III).

According to the projection areas, the intermediate agenetic

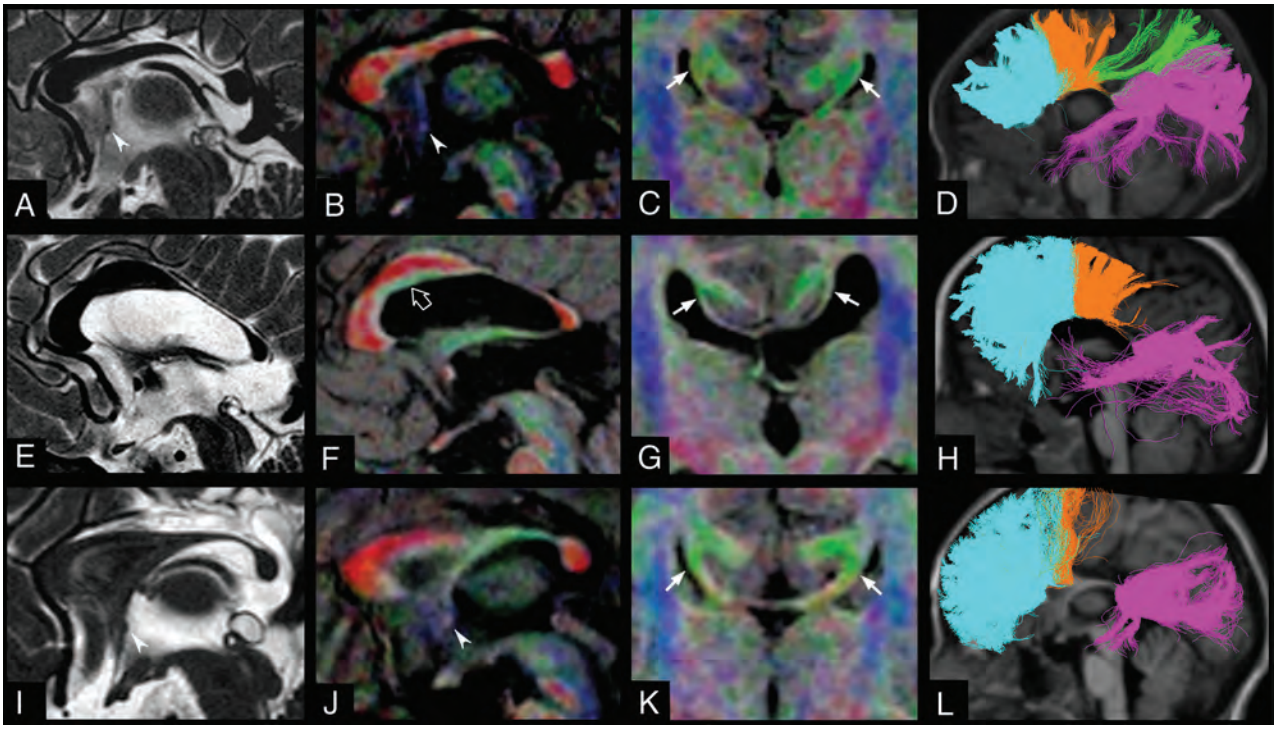

FIG 1. The 3 subtypes of segmental agenesis of the corpus callosum: SegACC type I in a 2-year-old girl (patient 3, *A–D*), segACC type II in a 5.4-year-old boy with Klippel-Feil syndrome (patient 5, *E–H*), and segACC type III in a 5.7-year-old boy with septo-optic dysplasia (patient 6, *I–L*). Midline sagittal T2WI driven equilibrium (*A*, *E*, and *I*) and corresponding fractional anisotropy color directional maps fused with 3D-T1WI (*B*, *F*, and *J*) reveal the focal absence of the posterior part of the callosal body in all patients. Hypoplasia of the anterior commissure may be associated, as shown in patient 3 (*A* and *B*, *arrowhead*) and patient 6 (*I* and *J*, *arrowhead*). Note the presence of a green-coded longitudinal bundle located in the inferior part of the anterior callosal segment, corresponding to an ectopic callosal bundle in patient 5 (*F*, *empty arrow*). Coronal fractional anisotropy color directional maps fused with 3D-T1WI (*C*, *G*, and *K*) demonstrate Probst bundles, with variable thickness, at the level of agenetic callosal segments in the 3 patients (*arrows*). Tractographic reconstructions of callosal fibers overlaid on T1WI (*D*, *H*, and *L*) show the homotopic callosal connections in the 3 patients. *D*, In segACC type I, the anterior callosal remnant contains fibers connecting the anterior frontal, posterior frontal, and parietal lobes, while the posterior callosal segment contains fibers connecting the parieto-occipitotemporal lobes. In segACC types II (*H*) and III (*L*), the anterior callosal segments exclusively contain frontal callosal fibers, while the posterior callosal remnants contain fibers connecting the parieto-occipitotemporal lobes. In segACC type III (*L*), the intermediate segment of the commissural plate is made of green-coded bundles, corresponding to the fornices joined in the midline, forming the hippocampal commissure. The callosal fibers are colored according to their projections to specific lobar areas (ie, light blue for anterior frontal callosal fibers, orange for posterior frontal callosal fibers, green for parietal callosal fibers, and violet for occipitotemporal callosal fibers).

Table 1: Network metrics of consensus and individual connectomes

	Consensus Connectomes			Individual Connectomes (Mean) (SD)			*P* Values	
	Control	PVC	SegACC	Control	PVC	SegACC	SegACC vs Control	SegACC vs PVC
Assortativity	0.03	−0.02	0.02	−0.02 (0.03)	−0.05 (0.03)	−0.02 (0.04)	.815	.379
Global efficiency	0.45	0.42	0.38	0.54 (0.02)	0.52 (0.02)	0.48 (0.03)	.005[a]	.024[a]
Mean local efficiency	0.69	0.70	0.71	0.77 (0.02)	0.77 (0.02)	0.75 (0.04)	.553	.597
Mean normalized betweenness	0.02	0.02	0.03	0.01 (0.00)	0.02 (0.00)	0.02 (0.00)	.001[a]	.031[a]
Characteristic path length	2.63	2.83	3.36	2.13 (0.09)	2.24 (0.13)	2.42 (0.12)	.002[a]	.021[a]
Transitivity	0.38	0.40	0.40	0.45 (0.02)	0.46 (0.02)	0.46 (0.04)	.555	.904
Mean clustering coefficient	0.49	0.51	0.53	0.56 (0.03)	0.57 (0.03)	0.57 (0.04)	.905	.929
Mean degree	8.64	8.17	7.31	14.71 (1.27)	13.66 (1.33)	12.02 (1.62)	.005[a]	.054
Cost	0.21	0.20	0.18	0.35 (0.03)	0.33 (0.03)	0.29 (0.04)	.005[a]	.054

[a] Significant.

segment corresponded to fibers projecting to the parietal lobe in all patients with segACC and healthy controls after PVC. The hypoplastic posterior callosal remnants consistently connected the occipitotemporal lobes, while the anterior remnants always connected the frontal lobes, including the frontal associative regions and, in all except 1 case, the motor areas. In the 3 patients with segACC-type I, the anterior callosal remnants also contained splenial fibers connecting the occipitoparietal lobes. Segmental Probst bundles corresponding to the agenetic callosal segment were confirmed in all patients. These bundles merged anteriorly with the ventral callosal remnant and extended posteriorly to the parietal lobes. Callosal ectopic bundles were identified in 3 patients.

Network Analysis

Table 1 reports the topology metrics of consensus and individual connectomes. Patients with SegACC had less integrated structural connectivity compared with those with PVC and controls. No

Table 2: Modularity metrics of individual connectomes

	Control (Mean) (SD)	PVC (Mean) (SD)	SegACC (Mean) (SD)	*P* Values	
				SegACC vs Control	SegACC vs PVC
Modularity	0.38 (0.02)	0.41 (0.03)	0.44 (0.03)	.002[a]	.151
Mean participation coefficient	0.39 (0.05)	0.31 (0.07)	0.28 (0.04)	.003[a]	.335
Mean Hubert-Rand Index (vs consensus)	0.53 (0.05)	0.54 (0.08)	0.58 (0.09)	.311	.394
Mean Hubert-Rand Index (vs individual)	0.63 (0.03)	0.61 (0.06)	0.68 (0.02)	.009[a]	.017[a]

[a] Significant.

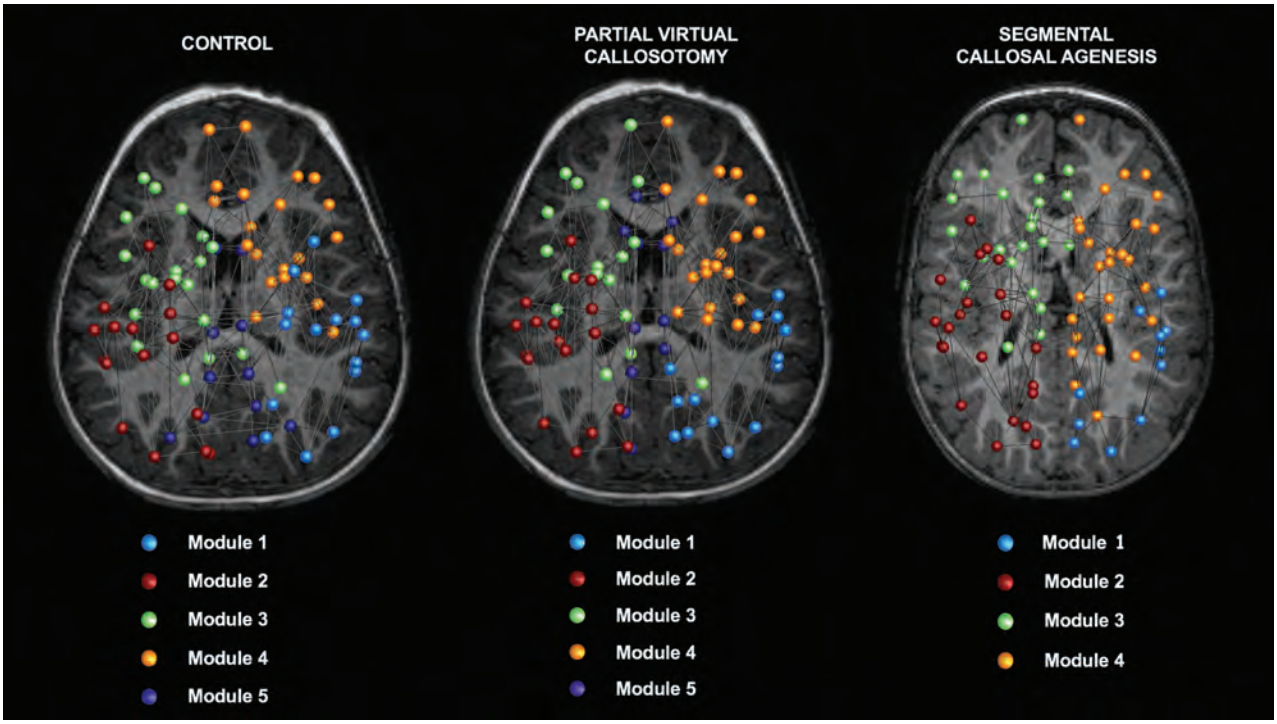

FIG 2. Module assignments for the consensus connectomes. Topology analysis of network modules reveals 5 modules for the control and partial virtual callosotomy groups and 4 modules for patients with segACC. Modules 3 and 4 largely consist of frontal nodes, while modules 1 and 2 are more posterior. Note that module 5, corresponding to the "structural core" of the network, is not present in the segACC consensus connectome. The 82 nodes are plotted with a *circle* colored according to the community to which it was assigned (see the legend). For the complete list of the regions included in each module, refer to On-line Tables 3–5.

significant differences in the segregation metrics were found among patients with segACC and PVC and controls.

On-line Figs 3 and 4 show the hubs found respectively for the consensus and individual connectomes. The analysis of within-group variability revealed that the spatial distribution of node degrees was significantly more variable in segACC, as demonstrated by a lower mean correlation coefficient ($r = 0.634 \pm 0.089$), compared with both controls ($r = 0.735 \pm 0.052$) and subjects with PVC ($r = 0.729 \pm 0.066$) at $P < .05$.

There were no differences in the connection strength correlation coefficients between the consensus network and each individual network, indicating that the consensus connectomes represented individuals in their group to approximately the same extent. Conversely, the interindividual variability of the segACC connectome was greater than that of the control and PVC connectomes, as shown by a significantly lower consistency between individual networks ($P < .05$, On-line Table 2).

The mean and SD of modularity-related metrics are provided in Table 2. Six modules were identified in the consensus network of controls and those with PVC, while only 5 were found in patients with segACC, due to disruption of the module corresponding to the structural core (Fig 2 and On-line Tables 3–5).

Network-based statistics identified 3 subnetworks of decreased connectivity in patients compared with controls (Fig 3 and Table 3).

DISCUSSION

ACC is a highly heterogeneous condition that may result from disruption of several developmental stages, from early midline telencephalic patterning to neuronal specification and axonal pathfinding.[2,19] This study further supports the hypothesis that segACC is a malformation rather than an acquired condition.[1,2] Indeed, in the cases here described, no signs of congenital or acquired conditions preventing commissuration, such as encephalomalacia, interhemispheric cysts, or lipomas, were noted. Moreover, although we did not identify a specific genetic phenotype associated with segACC, 2 patients had chromosomal aberrations traditionally related to callosal malformations, such as 1p36 deletion and 8p duplication.[19] In addition, clinical-radiologic features

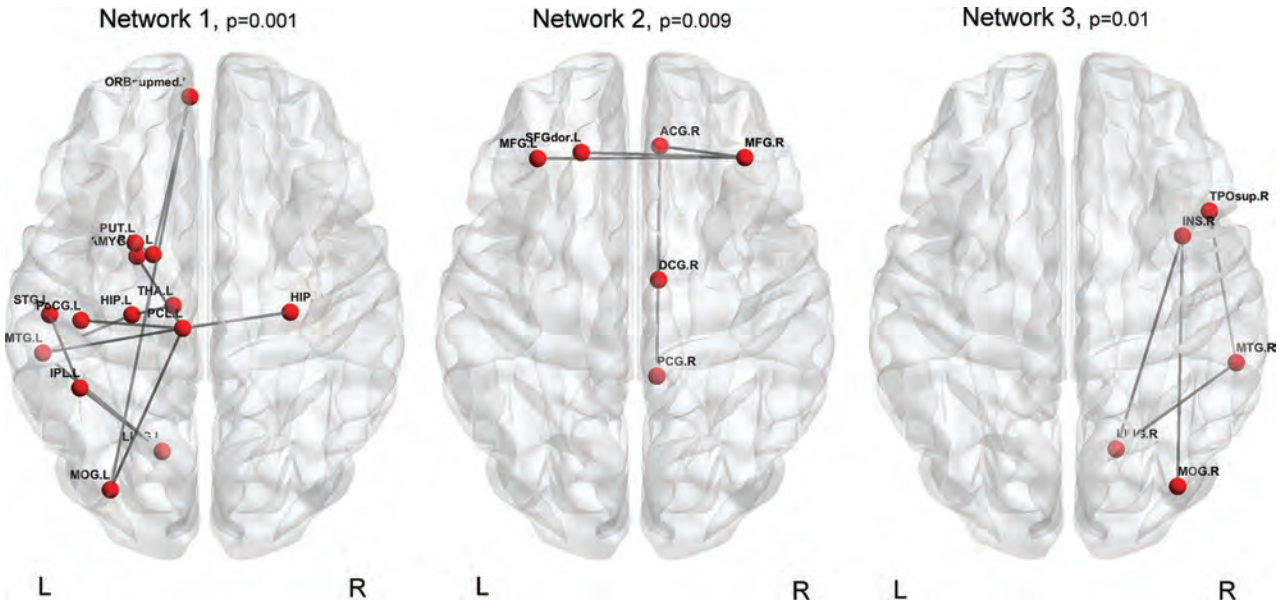

FIG 3. Subnetworks with decreased connectivity in patients with SegACC compared with controls with partial virtual callosotomy. Networks 1 and 3 are prevalently intrahemispheric and involve the temporoinsular and nuclear regions, while network 2 is interhemispheric and connects the frontal lobes and right cingulum.

Table 3: Subnetworks with decreased connectivity in patients with SegACC compared with controls with partial virtual callosotomy

Node 1	Node 2	*t* Test Value	*P* Value
Network 1			
L inferoparietal	L lingual	6.24	.001
L lingual	L middle temporal	5.89	
L paracentral	L postcentral	5.89	
L hippocampus	L middle temporal	4.16	
L paracentral	L amygdala	3.61	
L inferoparietal	L postcentral	3.61	
L paracentral	L middle temporal	3.53	
L pallidum	L medio-orbitofrontal	3.53	
L paracentral	R hippocampus	3.53	
L hippocampus	L thalamus proper	3.53	
L middle occipital	L medio-orbitofrontal	3.53	
L putamen	L pallidum	3.18	
L paracentral	L medio-orbitofrontal	3.18	
Network 2			
L superior frontal	R rostral middle frontal	3.53	.009
R posterior cingulate	R rostral anterior cingulate	3.53	
R isthmus cingulate	R rostral anterior cingulate	3.53	
L rostral middle frontal	R rostral middle frontal	3.18	
R rostral anterior cingulate	R rostral middle frontal	3.18	
Network 3			
R lingual	R insula	3.61	.01
R middle temporal	R lingual	3.61	
R middle temporal	R temporal pole	3.53	
R middle occipital	R insula	3.18	

Note:—R indicates right; L, left.

of septo-optic dysplasia and Klippel-Feil syndrome were noted in 2 other patients.

Notably, the constrained spherical deconvolution tractography data on the interhemispheric connections of these patients provided further insight into the embryogenesis of segACC. Recent data on callosal formation have suggested that at about gestational weeks 12–13, the first pioneer axons from the cingulate cortex cross the commissural plate in 2 separate loci, corresponding to the anterior commissure and HC, and then fuse to form the complete corpus callosum.[20-25] This complex process is guided by 3 specialized glial structures at the corticoseptal boundary: the glial sling forming a bridge between the hemispheres and guiding the anterior callosal fibers across the midline, associated with the indusium griseum glia above and the glial wedge below.[23,25] Moreover, several guidance factors (both attractive and repulsive), cell adhesion molecules, growth factors, intracellular signaling molecules, and transcription factors, are involved in this delicate developmental phase.[22] Failure in any one of these steps might explain complete agenesis or incomplete formation of the corpus callosum. Hence, at least hypotheses may be formulated regarding the origin of segACC: 1) The callosal projecting neurons corresponding to the agenetic segment did not develop; 2) all callosal projecting neurons are preserved as well as the corresponding homotopic interhemispheric connections, and the malformation results from an isolated defect of fusion of the 2 callosal segments; or 3) the callosal projecting neurons corresponding to the intermediate agenetic segment are preserved, but there is an additional axonal guidance defect rerouting these callosal fibers in other directions with loss of homotopic interhemispheric connections. In this study, we found that the agenetic segment most commonly corresponded to the posterior part of the callosal body, resulting in a loss of homotopic interhemispheric fibers projecting to the parietal lobes. At this level, we consistently identified segmental Probst bundles rerout-

ing the parietal projecting fibers. Moreover, we also noted heterotopic commissural tracts in 3 patients. These findings lend support to the third hypothesis: Axonal guidance defects likely play a role in this malformation.

Most interesting, we identified 3 types of segACC, characterized by different positions of the HC and connectivity patterns of the anterior remnants. In particular, when the HC lay at the level of the intermediate agenetic segment (segACC type III) or beneath the posterior callosal remnant (segACC type II), the defect of fusion between the callosal segments lay anterior to the HC and the anterior callosal segments exclusively connected the frontal lobes. On the other hand, when the HC lay beneath the anterior callosal remnant (segACC type I), the defect of fusion was located posterior to the HC and the anterior callosal remnant also contained splenial fibers connecting the parieto-occipital lobes. These findings confirm the close embryologic relationship of the splenium with the HC, as shown by studies on mouse embryos revealing that pioneer splenial axons cross the midline, fasciculating along and between the hippocampal axons at the dorsal edge of the HC.[23] However, on the basis of current embryologic theories, we could not explain why the agenetic segment was located posterior to the HC in patients with segACC type I. In fact, the fusion between the anterior, sling-derived callosum and the HC-associated splenium has been hypothesized to occur just anterior to the HC[24]; however, this theory remains to be proved[2] and might indeed represent an oversimplification of a more complex mechanism in which other as-yet-unidentified factors could play a role, generating variability in the mode and location of fusion between the 2 callosal segments and thereby justifying the different patterns in our series. Future genetic studies and mouse models of segACC are needed to provide further insight regarding this unsolved question.

Finally, we used a structural connectome framework to assess WM connectivity in patients with segACC. In particular, we hypothesized that the absence of a relatively small portion of the corpus callosum, corresponding to parietal commissural fibers, could have an impact on the global and local connectivity of these patients. Indeed, recent works on structural connectivity in adults and children with ACC have shown that the absence of long-range interhemispheric callosal fibers results in a reduction of information transmission and integration between the cerebral hemispheres.[9-11] Additionally, an increase of local connectivity, indicating a more segregated network organization, has been observed in these subjects,[9,10] likely reflecting the profound rearrangement of cortical and subcortical connectivity within the cerebral hemispheres due to the formation of pre- and postnatal structural compensatory mechanisms, such as the Probst bundles.[9,11] The topology analysis in our study partially confirmed this hypothesis even in patients with segACC, showing a less integrated structural connectivity, with reduced global efficiency, and increased path length and mean normalized betweenness.

On the other hand, no significant differences in the segregation metrics were found among segACC patients and controls, differently from the high-functioning adults with ACC studied by Owen et al,[9] suggesting that local connectivity is not increased. Taken together, these findings may indicate that loss of parietal commissural fibers in segACC results in a reduction of interhemispheric information integration, but the compensatory WM rewiring mechanisms, represented by segmental Probst bundles and heterotopic callosal connections, are insufficient to circumvent the absence of direct interhemispheric callosal connections. In other words, while the integration decreases in segACC, a potentially compensatory increase of segregation, supporting higher order cognition and specialized processing within densely interconnected brain sub-networks,[7,8] does not occur. This interpretation is supported by the results of the network-based statistics analysis in patients with segACC showing decreased connectivity in 3 subnetworks mostly related to cognitive, language, and memory functions and by the presence of psychomotor delay in all our patients. Indeed, even if deficits in higher order cognition and social skills have been described in subjects with isolated ACC, their global intelligence quotient may fall within normal limits.[25] Conversely, patients with partial ACC more often present a greater degree of developmental delay or cognitive impairment, with a worse neurologic prognosis.[25] Therefore, we hypothesize that a distinct anatomic connectivity substrate may contribute to the different neurocognitive profiles and neurologic prognosis of patients with partial ACC compared with neurotypical individuals with complete ACC. However, because the small sample size of this study is underpowered to detect subtler effects on the segregation metrics, larger scale investigations are needed to draw firm conclusions regarding the potential role of these connectome patterns as endophenotypes in patients with complete and partial ACC.

The second step of our analysis demonstrated that the structural connectivity of segACC subjects was also different from that of normally developing controls based on local changes in brain regions that normally serve as connectional hubs.[12] In particular, both in the consensus and individual analyses, the cortical and subcortical hubs demoted or promoted from their statuses were different in the segACC group compared with the PVC group, indicating that network topology reorganization in segACC may not be explained by only the exclusion of callosal fibers from the normal brain.[9] Moreover, as recently described both in adults and fetuses with ACC,[9,11] we found an increased connectome variability in segACC, with increased variability in the spatial distribution of node degree and in correlation strengths in patients compared with controls. There are several anatomic substrates for this increased variability, including transient aberrant WM connections during fetal life,[11] the connection variability of Probst bundles,[5] the thickening of phylogenetically older commissures,[2] the alternative tracts through the ventral forebrain and the dorsal midbrain midline,[26] and the heterotopic interhemispheric tracts.[5]

Most interesting, in this study, we identified aberrant commissural tracts in 3 patients with segACC. The first aberrant tracts connecting heterotopic cortical regions in subjects with partial ACC, the "sigmoid aberrant bundles," were described by Tovar-Moll et al in 2007.[5] These S-shaped fascicles typically connected 1 frontal lobe with the contralateral parietal lobe. Later, Wahl et al[6] demonstrated the wide variability and complexity of heterotopic callosal connections in partial ACC. The functional role of these miswired fibers, however, is a matter for speculation because a direct approach to their functional performance is not available. These heterotopic callosal connections being found in patients

with developmental delay and cognitive impairment,[5] as in the present study, seems to point to a maladaptive rather than compensatory function.

The last part of our analysis focused on the modular organization of segACC consensus networks. Indeed, different modules have been described in patients with ACC compared with healthy controls.[9,10] Accordingly, we found a lower number of modules and a higher Hubert-Rand Index in patients with segACC compared with those with PVC and controls. These findings suggest that neural plasticity in segACC reorganizes structural connectivity in a more stereotyped manner, with loss of a distinct posterior medial module corresponding to the network structural core. The structural core of the human brain comprises regions of the cortex that are highly connected and highly central.[27] In particular, portions of posterior medial cortex, such as the posterior cingulate cortex, the precuneus, and the lateral and medial parietal cortex, are key core components known to be highly activated at rest in the default mode network. Therefore, it has been suggested that the structural core may have a central role in integrating information across functionally segregated brain regions.[27] Owen et al[9] demonstrated a weakened structural core in adults with ACC associated with reduced connectivity between regions of the cingulate cortex. Most interesting, the focal absence of callosal fibers connecting the parietal lobes in segACC may also lead to disruption of the structural core, therefore contributing to the impairment of large-scale brain dynamics in these patients.

The present study has several limitations, including the small sample size and the suboptimal DWI data acquired on a 1.5T scanner with diffusion gradients along 34 noncollinear directions and a b-value of 1000 s/mm^2. Indeed, for constrained spherical deconvolution approaches, higher b-values and more diffusion gradient directions are suggested.[28] On the other hand, our results are consistent with those in previous structural connectivity studies on ACC.[9-11] Moreover, the feasibility of both constrained spherical deconvolution tractography and the structural connectome based on suboptimal DWI raw data has been recently demonstrated.[10,11,29] Finally, the relatively high interindividual variation of the interhemispheric connections due to the presence of ectopic callosal bundles in the patient group may have hampered the quantitative comparison of topologic metrics between graphs. However, to address this problem, we created consensus connectomes, in which all connections present in <75% of subjects are removed from the group's consensus matrix; this step smoothed out individual variation and allowed comparison of graph metrics. Future larger scale investigations performed with better DWI acquisition schemes on 3T scanners are awaited to confirm our observations.

CONCLUSIONS

We have further characterized the imaging and clinical phenotypes of segACC, describing 3 malformation subtypes and providing further insight on commissural development in these patients. Moreover, we demonstrated that even the absence of a small callosal segment may impact global brain connectivity and modularity organization of brain networks. Additionally, the presence of ectopic callosal bundles may explain the greater interindividual variation of segACC connectomes. Although direct structural connectivity does not appear to be a strict determinant of functional connectivity in healthy brains, disruption of large-scale network organization may be the anatomic substrate of neurocognitive dysfunction in children with segACC.

Disclosures: Mariasavina Severino—*UNRELATED*: *Employment*: Istituto Giannina Gaslini, *Comments*: neuroradiology consultant; *Travel/Accommodations/Meeting Expenses Unrelated to Activities Listed*: European Society of Neuroradiology, *Comments*: invited speaker, European Course in Neuroradiology, Diagnostic and Interventional, 14th Cycle, Module 1 (October 2016).* Andrea Rossi—*UNRELATED*: *Consultancy*: Bracco Imaging S.r.l. *Money paid to the institution.

REFERENCES

1. Raybaud C, Girard N. **Anatomic MRI study of commissural agenesis and dysplasia of the telencephalon (agenesis of the corpus callosum and related anomalies): clinical correlations and morphogenetic interpretation** [in French]. *Neurochirurgie* 1998;44(suppl 1):38–60 Medline
2. Raybaud C. **The corpus callosum, the other great forebrain commissures, and the septum pellucidum: anatomy, development, and malformation.** *Neuroradiology* 2010;52:447–77 CrossRef Medline
3. Barkovich AJ, Kjos BO. **Normal postnatal development of the corpus callosum as demonstrated by MR imaging.** *AJNR Am J Neuroradiol* 1988;9:487–91 Medline
4. Lee SK, Mori S, Kim DJ, et al. **Diffusion tensor MR imaging visualizes the altered hemispheric fiber connection in callosal dysgenesis.** *AJNR Am J Neuroradiol* 2004;25:25–28 Medline
5. Tovar-Moll F, Moll J, de Oliveira-Souza R, et al. **Neuroplasticity in human callosal dysgenesis: a diffusion tensor imaging study.** *Cereb Cortex* 2007;17:531–41 Medline
6. Wahl M, Strominger Z, Jeremy RJ, et al. **Variability of homotopic and heterotopic callosal connectivity in partial agenesis of the corpus callosum: a 3T diffusion tensor imaging and Q-ball tractography study.** *AJNR Am J Neuroradiol* 2009;30:282–89 Medline
7. Sporns O, Tononi G, Kötter R. **The human connectome: a structural description of the human brain.** *PLoS Comput Biol* 2005;1:e42 CrossRef Medline
8. Rubinov M, Sporns O. **Complex network measures of brain connectivity: uses and interpretations.** *Neuroimage* 2010;52:1059–69 CrossRef Medline
9. Owen JP, Li YO, Ziv E, et al. **The structural connectome of the human brain in agenesis of the corpus callosum.** *Neuroimage* 2013;70:340–55 CrossRef Medline
10. Meoded A, Katipally R, Bosemani T, et al. **Structural connectivity analysis reveals abnormal brain connections in agenesis of the corpus callosum in children.** *Eur Radiol* 2015;25:1471–78 CrossRef Medline
11. Jakab A, Kasprian G, Schwartz E, et al. **Disrupted developmental organization of the structural connectome in fetuses with corpus callosum agenesis.** *Neuroimage* 2015;111:277–88 CrossRef Medline
12. Hagmann P, Sporns O, Madan N, et al. **White matter maturation reshapes structural connectivity in the late developing human brain.** *Proc Natl Acad Sci U S A* 2010;107:19067–72 CrossRef Medline
13. Tournier JD, Calamante F, Gadian DG, et al. **Direct estimation of the fiber orientation density function from diffusion-weighted MRI data using spherical deconvolution.** *Neuroimage* 2004;23:1176–85 CrossRef Medline
14. Smith RE, Tournier JD, Calamante F, et al. **Anatomically-constrained tractography: improved diffusion MRI streamlines tractography through effective use of anatomical information.** *Neuroimage* 2012;62:1924–38 CrossRef Medline
15. Smith RE, Tournier JD, Calamante F, et al. **SIFT: spherical-deconvolution informed filtering of tractograms.** *Neuroimage* 2013;67:298–312 CrossRef Medline
16. Fischl B, Salat DH, van der Kouwe AJ, et al. **Sequence-independent segmentation of magnetic resonance images.** *Neuroimage* 2004;23:S69–84 Medline

17. Hubert LJ, Baker FB. **Comparisons and fitting of given classification schemes.** *Journal of Mathematical Psychology* 1977;16:233–53 CrossRef
18. Zalesky A, Fornito A, Bullmore ET. **Network-based statistic: identifying differences in brain networks.** *Neuroimage* 2010;53:1197–207 CrossRef Medline
19. Edwards TJ, Sherr EH, Barkovich AJ, et al. **Clinical, genetic and imaging findings identify new causes for corpus callosum development syndromes.** *Brain* 2014;137:1579–613 CrossRef Medline
20. Rakic P, Yakovlev PI. **Development of the corpus callosum and cavum septi in man.** *J Comp Neurol* 1968;132:45–72 CrossRef Medline
21. Lindwall C, Fothergill T, Richards L. **Commissure formation in the mammalian forebrain.** *Curr Opin Neurobiol* 2007;17:3–14 CrossRef Medline
22. Richards LJ, Plachez C, Ren T. **Mechanisms regulating the development of the corpus callosum and its agenesis in mouse and human.** *Clin Genet* 2004;66:276–89 CrossRef Medline
23. Rash BG, Richards LJ. **A role for cingulate pioneering axons in the development of the corpus callosum.** *J Comp Neurol* 2001;434:147–57 CrossRef Medline
24. Livy DJ, Wahlsten D. **Retarded formation of the hippocampal commissure in embryos from mouse strains lacking a corpus callosum.** *Hippocampus* 1997;7:2–14 Medline
25. Paul LK, Brown WS, Adolphs R, et al. **Agenesis of the corpus callosum: genetic, developmental and functional aspects of connectivity.** *Nat Rev Neurosci* 2007;8:287–99 CrossRef Medline
26. Tovar-Moll F, Monteiro M, Andrade J, et al. **Structural and functional brain rewiring clarifies preserved interhemispheric transfer in humans born without the corpus callosum.** *Proc Natl Acad Sci U S A* 2014;111:7843–48 CrossRef Medline
27. Hagmann P, Cammoun L, Gigandet X, et al. **Mapping the structural core of human cerebral cortex.** *PLoS Biol* 2008;6:e159 CrossRef Medline
28. Tournier JD, Calamante F, Connelly A. **Determination of the appropriate b-value and number of gradient directions for high-angular-resolution diffusion-weighted imaging.** *NMR Biomed* 2013;26:1775–86 CrossRef Medline
29. Fiori S, Poretti A, Pannek K, et al. **Diffusion tractography biomarkers of pediatric cerebellar hypoplasia/atrophy: preliminary results using constrained spherical deconvolution.** *AJNR Am J Neuroradiol* 2016;37:917–23 CrossRef Medline

Multivariate Analysis of MRI Biomarkers for Predicting Neurologic Impairment in Cervical Spinal Cord Injury

J. Haefeli, M.C. Mabray, W.D. Whetstone, S.S. Dhall, J.Z. Pan, P. Upadhyayula, G.T. Manley, J.C. Bresnahan, M.S. Beattie, A.R. Ferguson, and J.F. Talbott

ABSTRACT

BACKGROUND AND PURPOSE: Acute markers of spinal cord injury are essential for both diagnostic and prognostic purposes. The goal of this study was to assess the relationship between early MR imaging biomarkers after acute cervical spinal cord injury and to evaluate their predictive validity of neurologic impairment.

MATERIALS AND METHODS: We performed a retrospective cohort study of 95 patients with acute spinal cord injury and preoperative MR imaging within 24 hours of injury. The American Spinal Injury Association Impairment Scale was used as our primary outcome measure to define neurologic impairment. We assessed several MR imaging features of injury, including axial grade (Brain and Spinal Injury Center score), sagittal grade, length of injury, maximum canal compromise, and maximum spinal cord compression. Data-driven nonlinear principal component analysis was followed by correlation and optimal-scaled multiple variable regression to predict neurologic impairment.

RESULTS: Nonlinear principal component analysis identified 2 clusters of MR imaging variables related to 1) measures of intrinsic cord signal abnormality and 2) measures of extrinsic cord compression. Neurologic impairment was best accounted for by MR imaging measures of intrinsic cord signal abnormality, with axial grade representing the most accurate predictor of short-term impairment, even when correcting for surgical decompression and degree of cord compression.

CONCLUSIONS: This study demonstrates the utility of applying nonlinear principal component analysis for defining the relationship between MR imaging biomarkers in a complex clinical syndrome of cervical spinal cord injury. Of the assessed imaging biomarkers, the intrinsic measures of cord signal abnormality were most predictive of neurologic impairment in acute spinal cord injury, highlighting the value of axial T2 MR imaging.

ABBREVIATIONS: AIS = American Spinal Injury Association Impairment Scale; BASIC = Brain and Spinal Injury Center; MCC = maximum canal compromise; MSCC = maximum spinal cord compression; NL-PCA = nonlinear principal component analysis; PC = principal component; SCI = spinal cord injury

Early biomarkers of spinal cord injury (SCI) are essential during the acute phase of injury, a time when crucial management decisions are made and a period of great prognostic anxiety for patients and families.[1-3] As emerging experimental therapies translate to the clinic, early biomarkers will also be important for patient selection and monitoring in clinical trials. Multiple potential MR imaging biomarkers exist to evaluate acute SCI.[1,4-20] These measures primarily focus on the sagittal imaging plane, examining factors such as length of T2-hyperintense signal within the cord, whether abnormal signal is confined or spans multiple vertebral levels, presence of hemorrhage, and secondary markers of cord injury such as spinal cord compression and spinal canal compromise.[1,5-22] The internal structure of the spinal cord, with predominantly longitudinally oriented WM tracts, suggests that the axial injury extent and WM sparing should also be strong predictors of outcome. This concept has been demonstrated in preclinical studies and recently in human studies introduc-

Received August 1, 2016; accepted after revision October 4.

From the Departments of Neurological Surgery (J.H., S.S.D., P.U., G.T.M., J.C.B., M.S.B., A.R.F.), Radiology and Biomedical Imaging (M.C.M., J.F.T.), Emergency Medicine (W.D.W.), and Anesthesia and Perioperative Care (J.Z.P.), University of California San Francisco and Zuckerberg San Francisco General Hospital, San Francisco, California; Weill Institute for Neurosciences, Brain and Spinal Injury Center (J.H., W.D.W., S.S.D., J.Z.P., P.U., G.T.M., J.C.B., M.S.B., A.R.F., J.F.T.), San Francisco VA Medical Center (A.R.F.), San Francisco, California.

This work was supported by R01NS067092 (A.R.F.), R01NS088475 (A.R.F.), the Craig H. Neilsen Foundation (A.R.F., J.C.B.), Wings for Life Foundation (A.R.F.), and Department of Defense grant SC120259 (M.S.B., J.C.B.). M.C.M. was supported by a National Institutes of Health T32 Fellowship, 5T32EB001631-10. J.H. was supported by a Craig H. Neilsen Foundation fellowship (313739).

M.C.M. and J.H. contributed equally to this research and to the manuscript and are considered co–first authors.

Please address correspondence to Adam R. Ferguson, PhD, Department of Neurological Surgery, Zuckerberg San Francisco General Hospital, Building 1, Room 101, San Francisco, CA 94110; e-mail: adam.ferguson@ucsf.edu

Indicates open access to non-subscribers at www.ajnr.org
Indicates article with supplemental on-line tables.
Indicates article with supplemental on-line photo.

http://dx.doi.org/10.3174/ajnr.A5021

ing an axial scoring system known as the Brain and Spinal Injury Center (BASIC) score.[4,23-30] However, until now, it has been unclear how the axial grading relates to other imaging biomarkers of the sagittal plane and extrinsic compression measures.

The various MR imaging–based metrics have been shown to be reproducible, and all have some individual degree of predictive validity for clinical outcome.[1,4-20] Here, we evaluated the relationships of these MR imaging metrics to each other and to neurologic impairment. We applied a data-driven tool, nonlinear principal component analysis (NL-PCA), to understand the relationship between different MR imaging biomarkers and assess their ability to predict neurologic impairment. NL-PCA detects statistical patterns, incorporating multiple variables independent of their scale and decomposing them into a smaller set representing multidimensional clusters of variables (principal components [PCs]) that covary.[31,32] We then used nonlinear regression approaches to benchmark different MR imaging assessments against each other for predicting neurologic impairment at discharge. We hypothesized that MR imaging measures of acute cervical SCI would group together as a coherent multivariate PC ensemble and that distinct PCs (PC1, PC2, etc) would predict neurologic impairment. We intended 1) to provide insight into relationships between early MR imaging biomarkers after acute cervical SCI and 2) to provide an evaluation of the predictive validity of each individual measure of neurologic impairment.

MATERIALS AND METHODS

Study Cohort

This study was HIPAA and institutional review board compliant. We performed a retrospective cohort study of patients with acute blunt cervical SCI evaluated at a Level I trauma center (Zuckerberg San Francisco General Hospital) from 2005 to 2014. Inclusion criteria were 1) blunt acute cervical SCI, 2) age ≥18 years, 3) presurgical cervical spine MR imaging performed within 24 hours after injury, and 4) documented American Spinal Injury Association Impairment Scale (AIS) at both admission and discharge. Exclusion criteria were 1) penetrating SCI, 2) surgical decompression and/or fusion before MR imaging, 3) MR imaging that was too degraded by motion or other artifact such that images were nondiagnostic, and 4) preexisting surgical hardware. Of 212 patients initially identified, 95 patients met all inclusion and exclusion criteria and were included in the study. The data collected included sex and age, AIS at admission and discharge (as documented in the chart and performed by appropriately trained physiatrists and neurosurgeons), hours to MR imaging from time of injury, days to discharge, and whether surgical decompression of the cervical spine was performed before discharge. Fifty-two of the 95 patients included in this study were included in a cohort of patients as part of a previously published study.[4] This prior, smaller study involved initial development and interrater reliability testing of the BASIC score, whereas the current study tests multiple MR imaging grading schemes against each other, and against neurologic outcome, by using multivariate statistical analysis.

MR Imaging

All MR imaging examinations were acquired on the same 1.5T Genesis Signa scanner (GE Healthcare, Milwaukee, Wisconsin). We assessed sagittal T2 FSE, sagittal T1, and axial T2 FSE sequences performed as part of our routine imaging protocol, with these sequences not substantially changing over the study interval. Additional sequences performed as part of our trauma imaging protocol were not evaluated. Sequences were performed with the following parameters (presented as mean ± standard deviation from 10 randomly selected examinations): 1) for axial T2 FSE through the entire cervical spine: TR, 3798 ms ± 586 ms; TE, 102 ms ± 6 ms; section thickness, 3 ms; echo-train length, 17 ± 3.4; in-plane FOV, = 160 × 160 mm with a 512 × 512 matrix for nominal in-plane resolution of 0.31 mm^2; 2) for sagittal T2 FSE: TR, 3585 ms ± 563 ms; TE, 105 ms ± 5 ms; section thickness, 3 mm; echo-train length, 17.1 ± 3; in-plane FOV, 200 × 200 mm; and 3) for sagittal T1: TR, 528 ms ± 103 ms; TE, 16 ms ± 1.3 ms; section thickness, 3 mm; echo-train length, 2.6 ± 0.8; and in-plane FOV, 200 × 200 mm with a 512 × 512 matrix for nominal in-plane resolution of 0.39 mm^2.

Image Analysis

A neuroradiology fellow (M.C.M.) and attending physician (J.F.T.) performed consensus MR imaging ratings for all metrics while blinded to clinical outcome. The interrater reliability and BASIC axial MR imaging grading have been previously described as follows[4,30]: grade 0, no cord signal abnormality; grade 1, T2 hyperintensity confined to GM; grade 2, intramedullary T2 hyperintensity extends beyond expected gray matter margins to involve spinal white matter, but does not involve entire transverse extent of the spinal cord; grade 3, T2 hyperintensity involving GM and some but not all of WM; grade 4, T2 hyperintensity involving the entire axial plane of the spinal cord; grade 5, grade 3 injury with the addition of foci of T2 hypointensity consistent with hemorrhage. Sagittal grading was assigned as previously described: grade 1, no spinal cord signal abnormality; grade 2, single-level T2 hyperintensity; grade 3, >1 vertebral level T2 signal hyperintensity; grade 4, T2 signal hyperintensity with areas of hypointensity representing hemorrhage.[1,19] The greatest length (mm) of injury on sagittal T2 was measured as described in the National Institutes of Health/National Institute of Neurologic Disorders and Stroke SCI common data elements version 1.0.[3] Maximum canal compromise (MCC) and maximum spinal cord compression (MSCC) assessed midsagittal images by dividing the anteroposterior diameter of the canal (on sagittal T1 for MCC) and the anteroposterior diameter of spinal cord (on sagittal T2 for MSCC) by the average of the canal or spinal cord above and below as previously described.[8,15,16,22]

Multidimensional Analysis Workflow and Statistical Analysis

NL-PCA assessed the relationship among MR imaging measures by incorporating pattern detection with optimal-scaling transformations to accommodate nonparametric, ordinal, and nonlinear relationships that are common in clinical assessment tools such as MR imaging scoring by a radiologist.[33,34] Established decision rules defined the final dimensionality: Kaiser rule criterion of eigenvalue >1 and Cattell rule (ie, scree plot).[33-36] Validity of MR imaging and PC scores for predicting AIS at discharge involved linear mixed model, Spearman rank correlation, and an optimal-scaled regression.

Receiver operating characteristic curves assessed sensitivity and specificity of MR imaging measures for predicting AIS at

discharge by using a sliding scale (ie, AIS A versus B, C, D, E; AIS A, B versus C, D, E; AIS A, B, C versus D, E; and AIS A, B, C, D versus E), resulting in 4 separate receiver operating characteristic curves. In addition, we completed a supplementary analysis where we compared adjacent groups. Because of the low number of patients in the AIS B subgroup ($n = 3$), AIS A and B were grouped together as a motor complete group. We compared the areas under the curve of the different MR imaging biomarkers.

In a next step, we used discriminant function analysis to assess within the BASIC measure the optimal combination of scores to discriminate the different AIS groups. BASIC score was recoded as: 1) a simple lesion/no lesion score (BASIC 0 = no lesion, and BASIC 1–4 = any lesion) and 2) into a 3-point scale merging BASIC score subcategories 1–3 into 1 category. All MR imaging variables and the 2 recoded BASIC score variables were fed into a discriminant function analysis test for discrimination of AIS at discharge. Statistical significance for all tests was set at $\alpha = .05$. All statistical analyses were performed in SPSS v.23 (IBM, Armonk, New York). Syndromic plots for the PC loadings were generated in custom-designed software in R (http://www.r-project.org/).[37]

Table 1: Patient characteristics[a]

Age	57.91 ± 18.15
Sex (M, F)	67, 28
AIS at admission	A = 26, B = 9, C = 18, D = 42
AIS at discharge	A = 17, B = 3, C = 15, D = 41, E = 19
Time to MRI (hours)	6.97 ± 5.15
Time to discharge (days)	25.15 ± 35.31
Surgical decompression	Yes = 63, No = 32

[a] Values expressed as *N* or mean ± SD.

Table 2: MRI scoring schemes

BASIC	Ordinal	0–4: 0 = normal; 1 = GM only; 2 = some WM; 3 = all WM in plane; 4 = with hemorrhage
Sagittal grade	Ordinal	1–4: 1 = normal; 2 = less than a VB; 3 = longer than 1 VB; 4 = with hemorrhage
Longitudinal extent of T2 signal abnormality	Numeric	[mm]
MCC	Numeric	MCC % = $1 - \{D_i/[(D_a + D_b)/2]\} \times 100\%$; D = canal width[a]
MSCC	Numeric	MSCC % = $1 - \{d_i/[(d_a + d_b)/2]\} \times 100\%$; d = spinal cord width[a]

Note:—VB indicates vertebral body.
[a] See Fig 1 for further description.

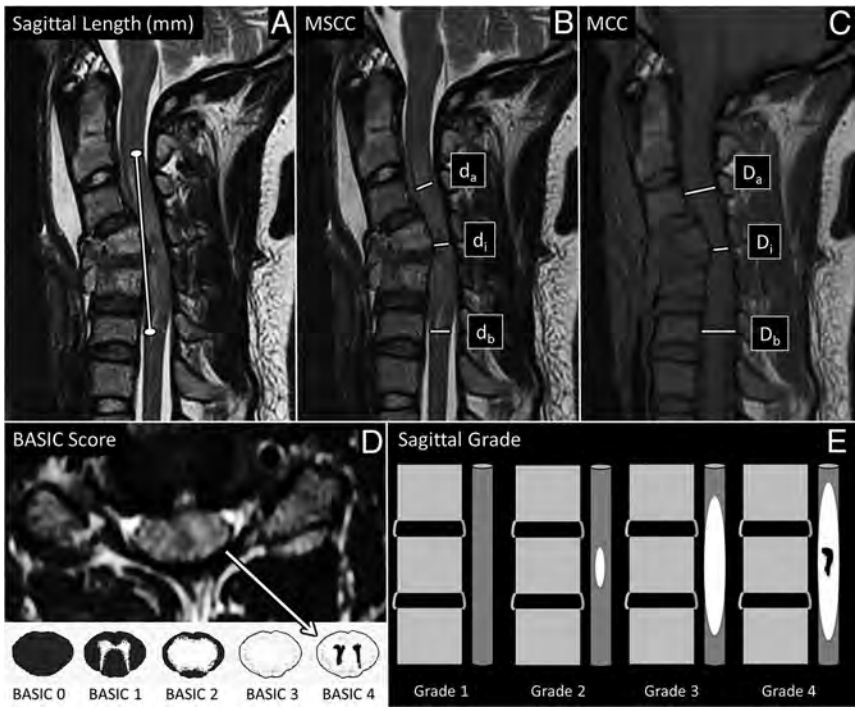

FIG 1. MR imaging-based metrics. *A* and *B*, Sagittal T2-weighted MR imagings of the cervical spine of patients with acute SCI were used to measure the length of T2 signal hyperintensity in mm (*A*, *white line*) and to calculate MSCC (*B*, $1 - \{d_i/[(d_a + d_b)/2]\} \times 100\%$). d_i indicates distance of the spinal cord at the injury site; d_b, one segment below the injury site; d_a, one segment above the injury site. *C*, Sagittal T1-weighted image of the cervical spine demonstrating how we used this sequence to measure MCC ($1 - \{D_i/[(D_a + D_b)/2]\} \times 100\%$). D_i indicates distance of the spinal canal at the injury site; D_b, one segment below the injury site; D_a, one segment above the injury site. *D*, The axial T2-weighted MR imaging of the cervical spine at the level of the epicenter of injury was used to define the BASIC score. Areas of macroscopic T2-hypointense hemorrhage are surrounded by hyperintense edema with no normal cord signal, consistent with BASIC grade 4. BASIC axial grade cartoons are depicted in the *lower panel*. *E*, Shows cartoons of the sagittal grading system. Sag indicates sagittal.

RESULTS

Patient characteristics are listed in Table 1. MR imaging measurements are outlined in Table 2 and Fig 1. The relationships between the BASIC score and AIS at discharge are listed in Table 3. NL-PCA demonstrated all imaging parameters loaded highly on PC1. PC2 discriminated MR imaging measures, with only MSCC and MCC showing high loadings (On-line Fig 1*A*). Statistical decision rules pruned the initial 5-dimensional NL-PCA solution to 2 dimensions (On-line Fig 1*B*). The optimal-scaled transformation matrix revealed a high correlation between the lesion length, sagittal grade, and the BASIC score and, to a lesser extent, between the compression variables (MSCC and MCC) (Fig 2*A*). The loading patterns of the 2-dimensional NL-PCA solution are displayed in Fig 2*B*. PC1–2 accounted for 88.6% of the total variance in the dataset (PC1, 58.6%; PC2, 30%). All imaging variables loaded highly on PC1. Variance explained by PC1 represents convergence across all MR imaging variables. In contrast, PC2 mainly captures compression variables MSCC and MCC, representing divergence of the MR imaging variables of intrinsic cord signal abnormality.

In Fig 2*C*, individual PC scores are projected into PC1 and PC2 space, with each patient color-coded by AIS change and by AIS grade at discharge. Patients with higher scores on the PC1 axes have worse AIS at discharge. Confirming this,

a linear mixed model revealed that PC1, but not PC2, significantly predicted AIS at discharge (PC1: $F = 33.79$, $P < .001$; PC2: $F = 2.11$, $P = .086$).

To compare predictive validity of PC1 and PC2 versus univariate MR imaging measures, we applied univariate nonparametric Spearman rank correlations for prediction of AIS at discharge (Table 4 and Fig 3). Based on Spearman rank correlation, variables of intrinsic cord signal abnormality (lesion length, sagittal grade, BASIC score) and both PC1 and PC2 predicted AIS at discharge. Neither MSCC nor MCC significantly correlated with AIS at discharge. Lesion length ($\rho = -0.66$), sagittal grade ($\rho = -0.70$), BASIC score ($\rho = -0.85$), and PC1 ($\rho = -0.69$) all negatively correlated with AIS at discharge, whereas PC2 showed a weak positive correlation with AIS at discharge ($\rho = 0.22$).

Table 3: BASIC score in relation to AIS at discharge[a]

	AIS A	AIS B	AIS C	AIS D	AIS E	Total Patients
BASIC 0				1 (7.7)	12 (92.3)	13
BASIC 1				12 (70.6)	5 (29.4)	17
BASIC 2		1 (2.6)	10 (25.6)	26 (66.7)	2 (5.1)	39
BASIC 3	7 (43.8)	2 (12.5)	5 (31.3)	2 (12.5)		16
BASIC 4	10 (100)					10

[a] Data presented as no. of patients (%).

We used optimal-scaled regression to benchmark the predictive validity of MR imaging measures against each other. An advantage of the optimal-scaled regression is that it takes into account different analysis levels (ordinal versus continuous) in a single model. PC scores were not included in this analysis because of multicollinearity. BASIC was the only significant predictor of AIS at discharge ($P < .01$).

We next benchmarked how individual MR imaging measures perform in predicting AIS at discharge compared with AIS at admission. Not surprisingly, AIS at admission showed a strong positive correlation with AIS at discharge by Spearman rank correlation ($\rho = 0.82$, $P < .01$). Optimal-scaling regression revealed that BASIC score and AIS at admission were the only significant predictors of AIS at discharge (both $P < .01$) (On-line Table 1).

We were concerned that BASIC prediction of AIS at discharge may be confounded by the decision to perform surgical decompression, which could also influence outcome. To test this, we performed 2 additional waves of analysis. First, we tested whether BASIC score significantly predicted the decision to perform surgical decompression by using a generalized linear model. BASIC score significantly predicted surgical decompression decision-making (Wald $\chi^2 = 9.00$, $P = .003$). To test whether this confounded BASIC's predictive validity for AIS at discharge, we reran the generalized linear model with an interaction term, testing whether BASIC and surgical decompression were statistically entangled. This analysis maintained the significant predictive main effect of BASIC on AIS (Wald $\chi^2 = 34.92$, $P < .001$). Furthermore, undergoing decompression surgery was not a significant predictor of AIS at discharge (Wald $\chi^2 = 0.17$, $P = .68$), nor was there a significant interaction between BASIC and decompression surgery (Wald $\chi^2 = 1.58$, $P = .66$). Similarly, we wanted to assess if BASIC significantly predicts AIS at discharge after correcting for MSCC. Using the same analysis tools, the predictive validity of BASIC was maintained ($F = 30.69$, $P < .001$), and there was no interaction effect between AIS at discharge and MSCC ($F = 0.79$, $P = .53$).

The sensitivity and specificity (receiver operating characteristic and area under the curve) of the MR imaging

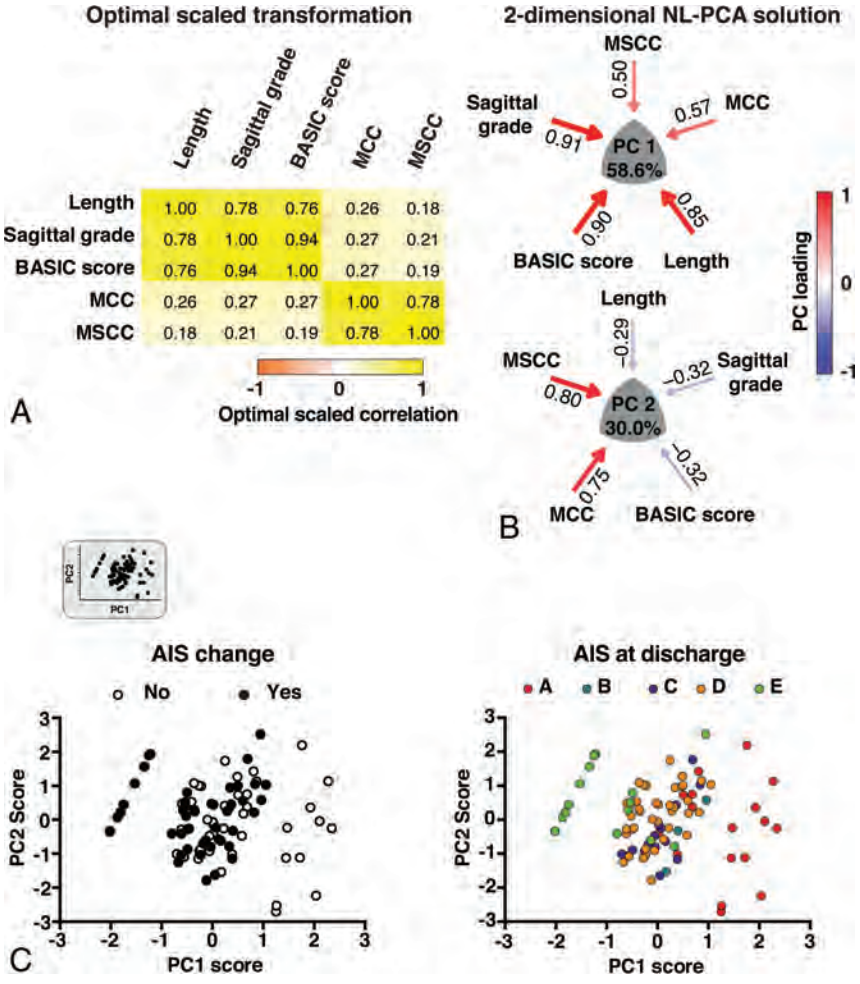

FIG 2. Results of the 2-dimensional NL-PCA. *A*, Heat map of the optimal-scaled transformation matrix of all MR imaging measures included in the NL-PCA. The matrix indicates all bivariate cross-correlations: *yellow* indicates a positive relationship and *orange* indicates a negative relationship. *B*, 2-dimensional NL-PCA solution. PCs reflect the clustered variance shared by the MR imaging measures and are represented by a *convex triangle*. The *arrow gauge* and the intensity of the color (*red* indicates a positive relationship and *blue* indicates a negative relationship) show the magnitude (ie, loading weights) of the correlation between each MR imaging measure and the PC. *C*, Bi-plots of individual patients ($n = 95$) in the 2-dimensional space described by PC1 and PC2. In the *top left corner*, the extracted bi-plot is displayed. In the *left graph*, the same bi-plot is color-coded by AIS change (ie, AIS change from admission to discharge) and is color-coded in the *right graph* by AIS at discharge. PCA indicates principal component analysis.

Table 4: Predicting AIS at discharge—Spearman rank correlation and optimal scaling regression results

	Spearman Correlation			Optimal Scaling Regression			
	ρ	ρ^2	*P* Value	Zero-Order	Partial	Part	*P* Value
Length	−0.66	0.44	<.01	−0.65	−0.11	−0.05	.50
Sagittal grade	−0.70	0.49	<.01	−0.69	0.36	0.18	.10
BASIC score	−0.85	0.72	<.01	−0.87	−0.75	−0.50	<.01
MCC	−0.20	0.04	.05	−0.24	0.02	0.01	.90
MSCC	−0.14	0.02	.18	−0.20	−0.08	−0.04	.62
PC1	−0.69	0.48	<.01				
PC2	0.22	0.05	.03				

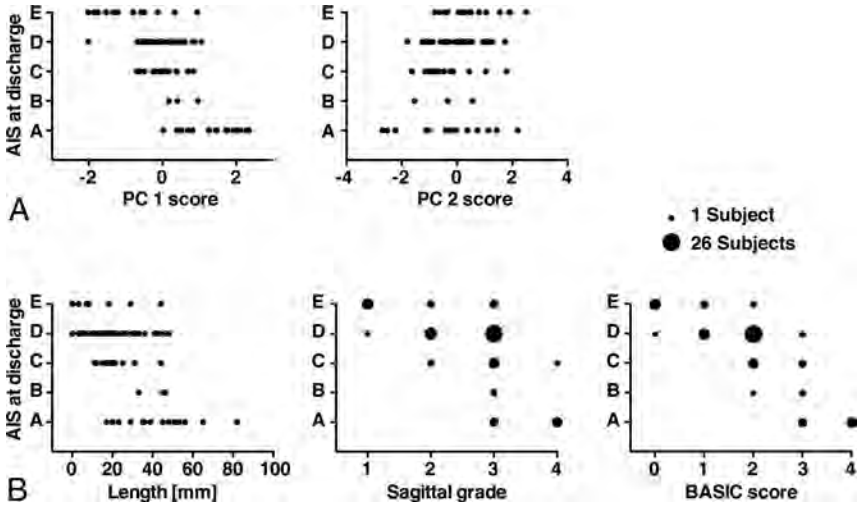

FIG 3. Multivariate (PCs) and univariate prediction of AIS at discharge. *A*, PC1 was negatively correlated with AIS at discharge, and PC2 showed a weak positive correlation. *B*, The length of the lesion, the sagittal grade, and the BASIC score showed a negative correlation with AIS at discharge. Note that because of the ordinal scale of the BASIC score and the sagittal grade, some subjects coincide on the same value. The number of subjects within each sphere is represented by the size of the spheres. Only scatterplots of the statistically significant correlations between the MR imaging measures and AIS at discharge are displayed.

measures in predicting AIS at discharge are shown in Fig 4 (AIS sliding scale). Supporting previous analysis, the length, sagittal grade, and BASIC score predicted AIS at discharge, with their areas under the curve statistically superior to random guessing (Table 5). BASIC consistently had the highest area under the curve in comparison with the other MR imaging measures. In a supplementary analysis, we tested how well the MR imaging measures can discern adjacent AIS categories. The results are shown in On-line Table 2. Similar to the sliding scale results, BASIC consistently had the highest area under the curve for distinguishing both severe and mild AIS categories in comparison with the other MR imaging measures.

Finally, to assess discriminative value score subcategories, we applied a linear discriminant function analysis. This supervised pattern detection approach discovers the optimal combination of scores to discriminate the different AIS groups. The full BASIC score had the largest absolute correlation with the canonical discriminant function for AIS, suggesting that the full 5-point BASIC score performs better than truncated scoring schemes (0.962). The full BASIC score outperformed both the simple dichotomous score (lesion versus no lesion, with BASIC 0 = no lesion and BASIC 1–4 = any lesion; 0.388) and a 3-point scale merging BASIC score subcategories 1–3 into 1 category (BASIC 0 = no lesion, BASIC 1–3 = nonhemorrhagic lesion, BASIC 4 = hemorrhagic lesion; 0.639). A second discriminant function analysis included only patients with a BASIC score of 1–3 (ie, those patients with nonhemorrhagic intramedullary T2 signal abnormality) to define the prognostic value of BASIC in this specific subpopulation. BASIC had the largest absolute correlation with the discriminative function (0.991), followed by the length of the lesion (0.416).

DISCUSSION

We applied data-driven multivariate analytic techniques to evaluate how multiple MR imaging–derived metrics relate to each other and to short-term impairment when applied to a group of 95 patients with acute blunt cervical SCI. We identified 2 principal components (PC1 and PC2) that explained 88.6% of the total variance in the dataset. Measures of intrinsic spinal cord signal abnormality had the highest positive loading on PC1, whereas measures of extrinsic cord compression had more modest positive loading. Both the BASIC score and sagittal grade had greater correlation with outcome than PC1, whereas BASIC score was the only univariate MR imaging measure to correlate with outcome when correcting for differences in data measurement scales. The present results support the prognostic relevance of the BASIC score compared with other MR imaging measures of SCI.

Although all imaging variables loaded positively on PC1, PC2 was more discriminatory in nature, segregating structural measures of compression from variables reflecting intrinsic cord signal abnormality. PC2 had a weakly positive correlation with AIS ($\rho = 0.22$, $P = .03$), whereas measures of extrinsic compression had no significant correlation with outcome. These findings demonstrate the discriminant validity of NL-PCA and highlight the split between MR imaging measures of intrinsic cord signal abnormality and structural measures of compression.[30] Structural measures of compression thus have a complex relationship with outcome. The present data do not necessarily conflict with prior work examining the predictive validity of MSCC in acute SCI.[8,15,16,21,22] Miyanji and colleagues[8] showed that MSCC was a key predictor of neurologic recovery after traumatic SCI. In that study, outcome for patients with SCI was dichotomized into complete and incomplete categories, whereas we have used the more granular 5-point AIS grading scale. In addition, after correcting for baseline neurologic status, only intrinsic measures of SCI significantly correlated with neurologic recovery, findings consistent with the present results.[8]

Receiver operating characteristic analysis confirmed that of the imaging variables examined, the BASIC score was the most accurate for predicting short-term impairment. We were con-

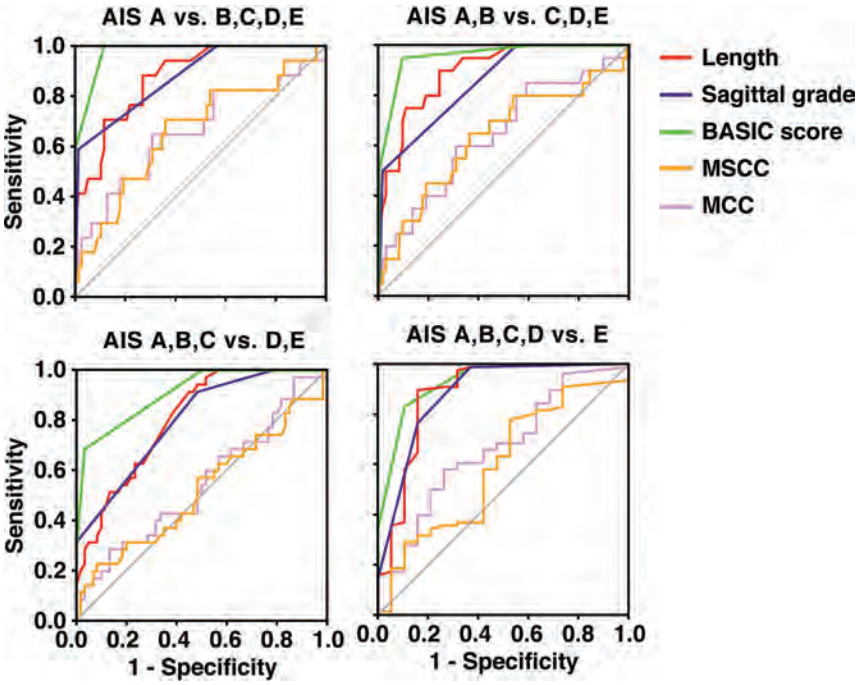

FIG 4. Receiver operating characteristic curves for the different MR imaging measures. The curves show the sensitivity and specificity of the different measures to predict AIS at discharge. AIS at discharge was dichotomized by using a sliding scale, resulting in 4 separate receiver operating characteristic curves (AIS A versus B, C, D, E; AIS A, B versus C, D, E; AIS A, B, C versus D, E; and AIS A, B, C, D versus E). The *diagonal gray line* represents a reference line that corresponds to random guessing. The further the receiver operating characteristic curves are located to the *top left corner*, the higher is the sensitivity and specificity of the measure in predicting the dichotomized AIS at discharge.

Table 5: Receiver operating characteristic analysis results

	AUC	*P* Value	95% CI
AIS A vs. B, C, D, E			
Length	0.88	<.01	0.80–0.96
Sagittal grade	0.88	<.01	0.79–0.97
BASIC score	0.98	<.01	0.95–1.00
MCC	0.66	.039	0.50–0.82
MSCC	0.66	.036	0.51–0.81
AIS A, B vs. C, D, E			
Length	0.90	<.01	0.83–0.97
Sagittal grade	0.86	<.01	0.77–0.94
BASIC score	0.96	<.01	0.92–1.00
MCC	0.65	.05	0.50–0.79
MSCC	0.64	.06	0.49–0.79
AIS A, B, C vs. D, E			
Length	0.81	<.01	0.72–0.89
Sagittal grade	0.80	<.01	0.71–0.89
BASIC score	0.91	<.01	0.85–0.97
MCC	0.55	.44	0.43–0.67
MSCC	0.52	.71	0.40–0.65
AIS A, B, C, D vs. E			
Length	0.88	<.01	0.77–0.99
Sagittal grade	0.88	<.01	0.79–0.98
BASIC score	0.93	<.01	0.86–0.99
MCC	0.66	.03	0.52–0.80
MSCC	0.59	.21	0.45–0.74

Note:—AUC indicates area under the curve.

cerned that other factors may confound the prognostic validity of the BASIC score. For example, the decision to perform surgical decompression may be influenced by the presence and pattern of signal abnormality in the spinal cord, which could influence outcome.[38-40] In addition, the extent of spinal cord compression with associated cord deformation may potentially confound BASIC grading. Our analysis confirms that the predictive validity of the BASIC score was maintained after correcting for potential interactions from surgical decompression and spinal cord compression.

Prior studies suggest MR imaging is most accurate at predicting outcomes when patients have evidence for very mild (normal cord signal) or very severe (intramedullary hemorrhage) injury.[1,6,7,10,13,14,20] In contrast, tremendous variability in clinical outcomes has been described in the setting of intermediate degrees of injury.[1] To specifically evaluate MR imaging measures and outcomes in this subgroup of patients from our cohort, we applied discriminant function analysis to patients with a BASIC score of 1–3 (patients with nonhemorrhagic intramedullary T2 signal hyperintensity; $n = 72$). Even in this subpopulation, the BASIC score had a very high absolute correlation with the discriminant function (0.991), followed by the length of the lesion (0.416). Therefore, the prognostic capabilities of the BASIC score are not simply attributable to the ease of prognosis at the ends of the injury severity spectrum.

Limitations of our study primarily relate to the retrospective, single-institution study design. We are actively pursuing this subject further in a prospective fashion with longer clinical follow-up at multiple time points and more detailed outcome measures. Our technique was designed to look at the relationships of the various imaging metrics to each other and to clinical outcome (AIS at discharge). Although we believe that the current study is adequate for investigating these relationships, we realize that there are changes in neurologic impairment expected over a longer time course. In addition, in a future prospective study, more detailed outcome measures need to be included to more comprehensively capture neurologic function.

CONCLUSIONS

This study demonstrates the utility of applying NL-PCA for defining the relationship between MR imaging biomarkers in a complex clinical syndrome of cervical SCI. Independent, prospective studies are needed to validate our conclusion that intrinsic measures of spinal cord pathology on acute MR imaging, particularly the BASIC score, best predict neurologic impairment in acute SCI compared with measures of extrinsic compression. This analytic pipeline is suited for future patient-level investigation and is amenable to inclusion of emerging potential biomarkers. Multidimensional approaches may also be useful for future prospective validation of imaging metrics

derived from advanced quantitative techniques such as DTI, which are under active investigation for spinal cord pathology.[26,41-43]

Disclosures: Jenny Haefeli—*RELATED*: *Grant*: Craig H. Neilsen Foundation, *Comments*: Craig H. Neilsen postdoctoral scholar*; *UNRELATED*: *Grants/Grants Pending*: Craig H. Neilsen Foundation, *Comments*: Craig H. Neilsen postdoctoral scholar. William Whetstone—*RELATED*: *Grant*: Department of Defense, *Comments*: grant 2013–2016.* Sanjay Dhall—*UNRELATED*: *Other*: DePuy Spine, Globus Spine, *Comments*: speaking honoraria. Pavan Upadhyayula—*RELATED*: *Grant*: National Institutes of Health.* Jacqueline Bresnahan—*RELATED*: *Grant*: Department of Defense*; *Support for Travel to Meetings for the Study or Other Purposes*: Department of Defense*; *UNRELATED*: *Grants/Grants Pending*: National Institutes of Health, Department of Defense, Craig H. Neilsen Foundation.* Michael Beattie—*RELATED*: *Grant*: Department of Defense Congressionally Directed Medical Research Programs - Spinal Cord Injury Research Program, *Comments*: grant SC120259, principal investigator.* Adam Ferguson—*RELATED*: *Grant*: National Institutes of Health/National Institute of Neurologic Disorders and Stroke, Wings for Life Foundation, Craig H. Neilsen Foundation, *Comments*: principal investigator on multiple grants cited in the paper that supported the work*; *UNRELATED*: *Grants/Grants Pending*: National Institutes of Health, Department of Defense, Veterans Affairs, Craig H. Neilsen Foundation, Wings for Life Foundation, *Comments*: principal investigator or co-investigator on many grants unrelated to the reported work.* Jason Talbott—*UNRELATED*: *Other*: StemCells, Inc, *Comments*: member of data monitoring committee for clinical trial which is now ended. *Money paid to the institution.

REFERENCES

1. Bozzo A, Marcoux J, Radhakrishna M, et al. **The role of magnetic resonance imaging in the management of acute spinal cord injury.** *J Neurotrauma* 2011;28:1401–11 CrossRef Medline
2. Reier PJ, Lane MA, Hall ED, et al. **Translational spinal cord injury research: preclinical guidelines and challenges.** *Handb Clin Neurol* 2012;109:411–33 CrossRef Medline
3. Biering-Sørensen F, Alai S, Anderson K, et al. **Common data elements for spinal cord injury clinical research: a National Institute for Neurological Disorders and Stroke project.** *Spinal Cord* 2015;53:265–77 CrossRef Medline
4. Talbott JF, Whetstone WD, Readdy WJ, et al. **The Brain and Spinal Injury Center score: a novel, simple, and reproducible method for assessing the severity of acute cervical spinal cord injury with axial T2-weighted MRI findings.** *J Neurosurg Spine* 2015;23:495–504 CrossRef Medline
5. Shimada K, Tokioka T. **Sequential MR studies of cervical cord injury: correlation with neurological damage and clinical outcome.** *Spinal Cord* 1999;37:410–15 CrossRef Medline
6. Schaefer DM, Flanders A, Northrup BE, et al. **Magnetic resonance imaging of acute cervical spine trauma. Correlation with severity of neurologic injury.** *Spine (Phila Pa 1976)* 1989;14:1090–95 CrossRef Medline
7. Ramón S, Domínguez R, Ramírez L, et al. **Clinical and magnetic resonance imaging correlation in acute spinal cord injury.** *Spinal Cord* 1997;35:664–73 CrossRef Medline
8. Miyanji F, Furlan JC, Aarabi B, et al. **Acute cervical traumatic spinal cord injury: MR imaging findings correlated with neurologic outcome–prospective study with 100 consecutive patients.** *Radiology* 2007;243:820–27 CrossRef Medline
9. Mihai G, Nout YS, Tovar CA, et al. **Longitudinal comparison of two severities of unilateral cervical spinal cord injury using magnetic resonance imaging in rats.** *J Neurotrauma* 2008;25:1–18 CrossRef Medline
10. Marciello MA, Flanders AE, Herbison GJ, et al. **Magnetic resonance imaging related to neurologic outcome in cervical spinal cord injury.** *Arch Phys Med Rehabil* 1993;74:940–46
11. Kulkarni MV, McArdle CB, Kopanicky D, et al. **Acute spinal cord injury: MR imaging at 1.5 T.** *Radiology* 1987;164:837–43 CrossRef Medline
12. Freund P, Weiskopf N, Ashburner J, et al. **MRI investigation of the sensorimotor cortex and the corticospinal tract after acute spinal cord injury: a prospective longitudinal study.** *Lancet Neurol* 2013;12:873–81 CrossRef Medline
13. Flanders AE, Spettell CM, Tartaglino LM, et al. **Forecasting motor recovery after cervical spinal cord injury: value of MR imaging.** *Radiology* 1996;201:649–55 CrossRef Medline
14. Flanders AE, Spettell CM, Friedman DP, et al. **The relationship between the functional abilities of patients with cervical spinal cord injury and the severity of damage revealed by MR imaging.** *AJNR Am J Neuroradiol* 1999;20:926–34 Medline
15. Fehlings MG, Rao SC, Tator CH, et al. **The optimal radiologic method for assessing spinal canal compromise and cord compression in patients with cervical spinal cord injury. Part II: Results of a multicenter study.** *Spine (Phila Pa 1976)* 1999;24:605–13 CrossRef Medline
16. Fehlings MG, Furlan JC, Massicotte EM, et al. **Interobserver and intraobserver reliability of maximum canal compromise and spinal cord compression for evaluation of acute traumatic cervical spinal cord injury.** *Spine (Phila Pa 1976)* 2006;31:1719–25 CrossRef Medline
17. Collignon F, Martin D, Lénelle J, et al. **Acute traumatic central cord syndrome: magnetic resonance imaging and clinical observations.** *J Neurosurg* 2002;96(1 Suppl):29–33 Medline
18. Chakeres DW, Flickinger F, Bresnahan JC, et al. **MR imaging of acute spinal cord trauma.** *AJNR Am J Neuroradiol* 1987;8:5–10 Medline
19. Bondurant FJ, Cotler HB, Kulkarni MV, et al. **Acute spinal cord injury. A study using physical examination and magnetic resonance imaging.** *Spine (Phila Pa 1976)* 1990;15:161–68 CrossRef Medline
20. Andreoli C, Colaiacomo MC, Rojas Beccaglia M, et al. **MRI in the acute phase of spinal cord traumatic lesions: Relationship between MRI findings and neurological outcome.** *Radiol Med* 2005;110:636–45 Medline
21. Rao SC, Fehlings MG. **The optimal radiologic method for assessing spinal canal compromise and cord compression in patients with cervical spinal cord injury. Part I: An evidence-based analysis of the published literature.** *Spine (Phila Pa 1976)* 1999;24:598–604 CrossRef Medline
22. Furlan JC, Fehlings MG, Massicotte EM, et al. **A quantitative and reproducible method to assess cord compression and canal stenosis after cervical spine trauma: a study of interrater and intrarater reliability.** *Spine (Phila Pa 1976)* 2007;32:2083–91 CrossRef Medline
23. Budde MD, Kim JH, Liang HF, et al. **Axonal injury detected by in vivo diffusion tensor imaging correlates with neurological disability in a mouse model of multiple sclerosis.** *NMR Biomed* 2008;21:589–97 CrossRef Medline
24. Bresnahan JC, Beattie MS, Stokes BT, et al. **Three-dimensional computer-assisted analysis of graded contusion lesions in the spinal cord of the rat.** *J Neurotrauma* 1991;8:91–101 CrossRef Medline
25. Tator CH, Koyanagi I. **Vascular mechanisms in the pathophysiology of human spinal cord injury.** *J Neurosurg* 1997;86:483–92 CrossRef Medline
26. Rao J-S, Zhao C, Yang ZY, et al. **Diffusion tensor tractography of residual fibers in traumatic spinal cord injury: a pilot study.** *J Neuroradiol* 2013;40:181–86 CrossRef Medline
27. Griffin JF, Davis MC, Ji JX, et al. **Quantitative magnetic resonance imaging in a naturally occurring canine model of spinal cord injury.** *Spinal Cord* 2015;53:278–84 CrossRef Medline
28. Kelley BJ, Harel NY, Kim CY, et al. **Diffusion tensor imaging as a predictor of locomotor function after experimental spinal cord injury and recovery.** *J Neurotrauma* 2014;31:1362–73 CrossRef Medline
29. Kim JH, Loy DN, Wang Q, et al. **Diffusion tensor imaging at 3 hours after traumatic spinal cord injury predicts long-term locomotor recovery.** *J Neurotrauma* 2010;27:587–98 CrossRef Medline
30. Mabray MC, Talbott JF, Whetstone WD, et al. **Multidimensional analysis of magnetic resonance imaging predicts early impairment in thoracic and thoracolumbar spinal cord injury.** *J Neurotrauma* 2016;33:954–62 CrossRef Medline
31. Ghodadra A, Alhilali L, Fakhran S. **Principal component analysis of diffusion tensor images to determine white matter injury patterns**

underlying postconcussive headache. *AJNR Am J Neuroradiol* 2016; 37:274–78 CrossRef Medline
32. Jolliffe IT, Cadima J. **Principal component analysis: a review and recent developments.** *Philos Trans A Math Phys Eng Sci* 2016;374: 20150202 CrossRef Medline
33. Linting M, Meulman JJ, Groenen PJ, et al. **Nonlinear principal components analysis: introduction and application.** *Psychol Methods* 2007;12:336–58 CrossRef Medline
34. Linting M, van der Kooij A. **Nonlinear principal components analysis with CATPCA: a tutorial.** *J Pers Assess* 2012;94:12–25 CrossRef Medline
35. Cattell RB. **The scree test for the number of factors.** *Multivariate Behav Res* 1966;1:245–76 CrossRef Medline
36. Kaiser HF. **The application of electronic computers to factor analysis.** *Educ Psychol Meas* 1960;20:141–51 CrossRef
37. SyndromicPlot: Loadings Plot Generator. https://zenodo.org/record/47079#.WB3iWzdGXMQ. Accessed March 7, 2016
38. Wilson JR, Singh A, Craven C, et al. **Early versus late surgery for traumatic spinal cord injury: the results of a prospective Canadian cohort study.** *Spinal Cord* 2012;50:840–43 CrossRef Medline
39. Fehlings MG, Vaccaro A, Wilson JR, et al. **Early versus delayed decompression for traumatic cervical spinal cord injury: results of the Surgical Timing in Acute Spinal Cord Injury Study (STASCIS).** *PloS One* 2012;7:e32037 CrossRef Medline
40. La Rosa G, Conti A, Cardali S, et al. **Does early decompression improve neurological outcome of spinal cord injured patients? Appraisal of the literature using a meta-analytical approach.** *Spinal Cord* 2004;42:503–12 CrossRef Medline
41. Wheeler-Kingshott CA, Hickman SJ, Parker GJ, et al. **Investigating cervical spinal cord structure using axial diffusion tensor imaging.** *Neuroimage* 2002;16:93–102 CrossRef Medline
42. Martin AR, Aleksanderek I, Cohen-Adad J, et al. **Translating state-of-the-art spinal cord MRI techniques to clinical use: a systematic review of clinical studies utilizing DTI, MT, MWF, MRS, and fMRI.** *Neuroimage Clin* 2016;10:192–238 CrossRef Medline
43. Talbott JF, Nout-Lomas YS, Wendland MF, et al. **Diffusion-weighted magnetic resonance imaging characterization of white matter injury produced by axon-sparing demyelination and severe contusion spinal cord injury in rats.** *J Neurotrauma* 2016;33:929–42 CrossRef Medline

Benchmarking Lumbar Puncture Fluoroscopy Time during Fellowship Training

H. Yang, K. Schaffer, L. Liu, M. Mahesh, and D.M. Yousem

ABSTRACT

SUMMARY: We sought to establish a guide for identifying fellowship competency in performing fluoroscopically guided lumbar punctures. With a linear mixed-effects model, we compared the fluoroscopy time between the first and last 3 months of neuroradiology training. During 7 years, 55 fellows performed 1142 and 861 lumbar punctures in the first and last quarters of training. A target fluoroscopy time of 0.26 minutes, the upper 95% confidence interval, can serve as a fellowship benchmark for successfully achieving competence in fluoroscopically guided lumbar punctures.

ABBREVIATIONS: FGLP = fluoroscopically guided lumbar puncture; FT = fluoroscopy time

Fluoroscopically guided lumbar puncture (FGLP) is often requested in radiology departments when "blind" attempts fail by clinicians. Under the guidance of fluoroscopy, one can visualize real-time bony anatomic landmarks and targets, leading to improved accuracy of needle placement for lumbar puncture in such difficult situations. However, both patients and operators are exposed to ionizing radiation during this procedure.[1] The risk from radiation exposure accumulates during one's lifetime.[2] A Sentinel Event Alert published by the Joint Commission in 2011 recommended that one attempt to reduce the radiation dose to "as low as reasonably achievable (ALARA)" without sacrificing patient care.[3]

Both the American Board of Radiology and the Accreditation Council for Graduate Medical Education have listed FGLP as an essential competency for radiology residents and neuroradiology fellows. The American College of Radiology encourages recording the fluoroscopy time (FT) during lumbar punctures and comparing it with benchmarks.[4] The Radiological Society of North America competency initiative encourages setting parameters for proficiency in procedures. To our knowledge, FT benchmarks have not been established for neuroradiology fellows performing FGLP. We conducted this retrospective study to establish FT benchmark data for proficiency assessment during a 1-year neuroradiology fellowship program.

MATERIALS AND METHODS

This study was performed with institutional review board approval and was Health Insurance Portability and Accountability Act compliant. We retrospectively identified first-year neuroradiology fellows who performed fluoroscopically guided lumbar punctures in the neuroradiology division of Johns Hopkins Medical Institution between 2009 and 2016. All lumbar punctures were performed on an Arcadis Orbic C-Arm fluoroscopic unit (Siemens, Erlangen, Germany) for guidance and were performed in the first year of the neuroradiology fellowship program.

Three lectures ("Radiation Safety," "Spine Procedures," and "Degenerative Spine Disease") on fluoroscopic techniques were given to the first-year fellows in the first 2 months of their fellowship. The fellows were scheduled on weekly rotations for spine procedures, including lumbar punctures and myelography; there were usually 8 first-year fellows per year. This meant that during their first rotation through the spine service, they likely had not completed all 3 educational presentations on lumbar puncture techniques.

Each procedure was monitored in the room by neuroradiology faculty who provided helpful hints and instructions on improving the procedure technique; fellows do not perform the procedures unattended. The fluoroscopy time at the end of the procedure was displayed on the screen of the C-arm system. No spot films were obtained for the lumbar punctures. One senior technologist recorded the fluoroscopy time for each procedure in a logbook. We collected the fluoroscopy time of each lumbar

Received September 3, 2016; accepted after revision October 8.

From the Division of Neuroradiology (H.Y., K.S., L.L., M.M., D.M.Y.), The Russell H. Morgan Department of Radiology and Radiological Science, Johns Hopkins Medical Institutions, Baltimore, Maryland; and Shandong Medical Imaging Research Institute (H.Y.), Shandong University, Jinan, Shandong, China.

Please address correspondence to David M. Yousem, MD, MBA, Johns Hopkins Medical Institutions, 600 N. Wolfe St, Phipps B100F, Baltimore, MD 21287; e-mail: dyousem1@jhu.edu

http://dx.doi.org/10.3174/ajnr.A5031

puncture in the first 3 months (July, August, and September of the first year of fellowship) and last 3 months of the fellowship (April, May, and June of the same academic year [July–June]) for each neuroradiology fellow. The fluoroscopy times had been recorded for all such procedures from July 2009 to June 2016, the time course for this retrospective study. The fluoroscopy times were not recorded before July 2009. No cervical C1–2 punctures were included.

The fluoroscopy time was analyzed as a continuous variable. The median with interquartile range and mean with 95% confidence interval were reported. A linear mixed-effects model was used to estimate the average fluoroscopy time at the first and the last quarters of fellowship adjusted for the year of ending the fellowship (2010–2016), the total number of cases performed by each fellow, and within-fellow variation. The distribution of fluoroscopy time was highly skewed; therefore, log-transformed values were used for statistical tests and modeling. The estimated mean and 95% CI then were converted to the original scale (in minutes) for presentation. Statistical significance was defined at $P < .05$. All analyses were performed by using STATA (StataCorp, College Station, Texas).

RESULTS

During the 7-year period, 55 neuroradiology fellows performed 1142 lumbar punctures in their first 3 months of fellowship and 861 procedures in their last 3 months of fellowship. Seven fellows did not have data for either the first or the last 3 months of fellowship, and 3 fellows had performed only 1 procedure in 1 timeframe. These 10 fellows were excluded from the comparison analyses. The variation between the quarters may reflect the influence of senior residents requesting neuroradiology rotations at the end of the academic year who also had week-long rotations on the spine service (but whose data were not included).

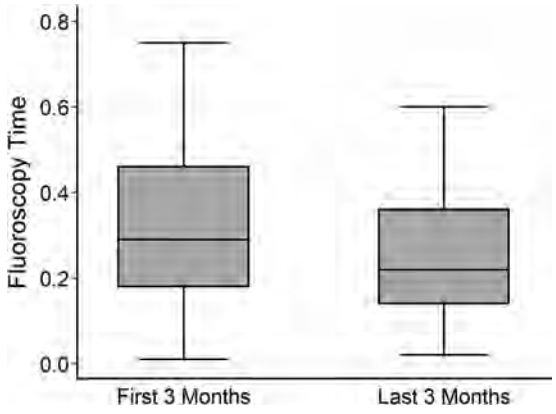

FIG 1. Comparison of fluoroscopy time for FGLP in the first and the last 3 months of the fellowship.

We surveyed the indications for 1 month of the study and found that 49/70 lumbar punctures were performed to instill chemotherapy and withdraw CSF; 8, for suspected high or low intracranial pressure; 5, to exclude meningitis; 4, for multiple sclerosis evaluation; 3, for afebrile change in mental status; and 1, for neuropathy.

The average number of procedures performed per fellow in the first and the last 3 months of the fellowship was 19 (median; interquartile range, 14–25) and 18 (median; interquartile range, 10–25), respectively. The median of fluoroscopy time was 0.29 minutes (interquartile range, 0.18–0.46 minutes) for the first 3 months of fellowship and 0.22 minutes (interquartile range, 0.14–0.36 minutes) for the last 3 months of fellowship (Fig 1).

The estimated overall mean fluoroscopy time was 0.31 minutes (95% CI, 0.28–0.33 minutes) at the beginning of training and 0.24 minutes (95% CI, 0.22–0.26 minutes) at the end of training. There was a 22.1% reduction in fluoroscopy time when comparing the first and last quarters of the fellowship ($P < .001$). The total number of cases performed by each fellow was not significantly associated with the fluoroscopy time reduction ($P = .088$), though the trend showed that the more cases performed, the shorter was the fluoroscopy time. Most (34 of 45, 75.6%) fellows showed a reduction in fluoroscopy time from the first 3 months to the last 3 months of the fellowship (Table).

DISCUSSION

This study provides benchmarks for neuroradiology trainees performing FGLP in programs that have similar volumes of cases. We believe that at the end of training, based on data we have from a large number of fellows during several years, a mean target of <0.26 minutes (16 seconds) of FT should be used to establish that the fellow has gained expertise in that technique. This value for the end of the fellows' practice, on average, represents the upper 95% confidence interval from our dataset. We acknowledge that on the basis of body habitus and the degree of spinal stenosis, any individual case may take longer or shorter time, but our FT value may be applied to the mean value of several FGLPs performed by a fellow, to assess competency.

Overall, our data show a 22.1% reduction in fluoroscopy time when comparing the first and last quarters of the fellowship for 7 years, indicating the improvement of the operators' expertise

Average level and reduction of FT in early and later fellowship, adjusting for the total number of cases performed by each fellow

Year	No. of Fellows	FT in Early Fellowship (Mean) (95% CI) (min)	FT in Late Fellowship (Mean) (95% CI) (min)	Reduction	Percentage of Reduction[a]	No. of Improved (%)
2009–10	6	0.40 (0.33–0.49)	0.31 (0.26–0.38)	0.09	28.8	4 (66.7)
2010–11	9	0.35 (0.29–0.44)	0.27 (0.21–0.34)	0.08	25.1	7 (77.8)
2011–12	5	0.27 (0.23–0.32)	0.21 (0.17–0.25)	0.06	19.9	3 (60.0)
2012–13	7	0.28 (0.23–0.33)	0.21 (0.18–0.26)	0.06	20.4	4 (57.1)
2013–14	6	0.39 (0.34–0.44)	0.30 (0.27–0.34)	0.09	27.8	6 (100.0)
2014–15	6	0.24 (0.19–0.29)	0.18 (0.15–0.22)	0.05	18.1	4 (66.7)
2015–16	6	0.25 (0.21–0.30)	0.19 (0.16–0.23)	0.06	18.7	6 (100.0)
Total	45	0.31 (0.28–0.33)	0.24 (0.22–0.26)[b]	0.07	22.1	34 (75.6)

[a] The percentage of reduction was based on the log-transformed value.
[b] There was a significant difference between early and late fellowship ($P < .05$).

through training and experience. The data also demonstrate a trend showing that the more cases performed, the shorter was the fluoroscopy time. Our model showed that for every 2 additional cases performed, there was a 0.01-minute reduction in fluoroscopy time ($P = .088$). This non-statistically significant association may be caused by a similar number of cases performed by each fellow during the 1-year fellowship.

The initial value of 0.33 minutes (20 seconds of FT) at the upper 95% confidence interval at the beginning of fellowship could represent what one might hope a graduating resident could achieve. The bias herein is that these are residents who are entering neuroradiology fellowships who may have more interest and proficiency in FGLP. This circumstance may explain why the initial FT of our fellows was substantively shorter than that reported by Boddu et al[5] for residents and fellows for a normal body mass index (mean, 0.48 minutes; 95% CI, 0.40–0.56 minutes). Boddu et al noted that the fluoroscopy time of fellows was significantly lower than that of residents ($P = .03$). This is the only other study that has looked at FT times for FGLP, to our knowledge.

Proper training of radiologists was reported to have effects on the reduction of fluoroscopy time in different procedures. Lim et al[6] reported that the fluoroscopy time for voiding cystourethrography of pediatric radiology fellows was shorter than that of senior radiology residents. A statistically significant training effect ($P < .05$) was demonstrated by Stuart et al[7]when performing uterine artery embolization during a 1-year radiology fellowship training. Some programs across the country have begun to emphasize the training of radiology residents in fluoroscopically guided lumbar puncture. A simulation-based fluoroscopically guided lumbar puncture curriculum, including a 1-hour lecture and hands-on training with a lumbar spine phantom, was reported to improve residents' procedure efficiency.[8] The mean fluoroscopy times for the retrospective resident group and the prospective group were 1.09 ± 0.65 minutes and 0.87 ± 0.68 minutes, respectively. These values are approximately 2.5 times higher than those at the beginning and end of fellowship training in our study, respectively.

Fluoroscopy time is one of the most widely reported as a dose metric for fluoroscopic procedures. For interventional procedures, fluoroscopy time alone is not a representative dose descriptor because these procedures often include digital runs (digital subtraction angiography) or spot films; however, for lumbar punctures, there are no spot films or digital runs performed. Thus, fluoroscopy time becomes the key dose metric. A number of dose-optimization strategies[9] can be applied to reduce the dose to patients and personnel: They include the use of pulse fluoroscopy and collimating the radiation field to the area of interest, and using the last image or last series hold features to avoid unnecessary exposure, especially in a teaching environment. In addition, education and training of fluoroscopists play a role in reducing the radiation dose to patients. Our study demonstrates the importance of training and experience, which leads to reducing the patient dose. For our study purpose, we only compared the fluoroscopy time as representative of the operator's experience.

The study is limited by the exclusion of data points from 10 fellows who did not perform sufficient lumbar punctures in the study periods examined. We do not know the patient characteristics that may influence the fluoroscopy time such as body habitus or significant degenerative changes. We did not record needle lengths or indications as part of our data. We believe the daily FGLP volume of our service is reflective of programs with large fellowships. Of 15 programs that responded to an e-mail survey on the topic, the averages (2.3 FGLPs per day) were slightly lower than our average of 3.8 per day but the range was between zero (CT-directed only) and 5.

CONCLUSIONS

We established a target mean FT value of 0.26 minutes as one of the criteria of proficiency for fellows for FGLP. Proper training of operators on fluoroscopically guided procedures will reduce the radiation exposure for personnel and patients.

Disclosures: David M. Yousem—*UNRELATED*: *Expert Testimony*: self; *Payment for Lectures including Service on Speakers Bureaus*: ACR Ed Center*; *Royalties*: Elsevier; *Payment for Development of Educational Presentations*: CMEInfo.com.* *Money paid to the institution.

REFERENCES

1. Cauley KA. **Fluoroscopically guided lumbar puncture.** *AJR Am J Roentgenol* 2015;205:W442–50 CrossRef Medline
2. Amis ES Jr, Butler PF; American College of Radiology. **ACR white paper on radiation dose in medicine: three years later.** *J Am Coll Radiol* 2010;7:865–70 CrossRef Medline
3. **Radiation risks of diagnostic imaging.** *Sentinel Event Alert* 2011;24:1–4 Medline
4. Amis ES Jr, Butler PF, Applegate KE, et al; American College of Radiology. **American College of Radiology white paper on radiation dose in medicine.** *J Am Coll Radiol* 2007;4:272–84 CrossRef Medline
5. Boddu SR, Corey A, Peterson R, et al. **Fluoroscopic-guided lumbar puncture: fluoroscopic time and implications of body mass index—a baseline study.** *AJNR Am J Neuroradiol* 2014;35:1475–80 CrossRef Medline
6. Lim R, Khawaja RD, Nimkin K, et al. **Relationship between radiologist training level and fluoroscopy time for voiding cystourethrography.** *AJR Am J Roentgenol* 2013;200:645–51 CrossRef Medline
7. Stuart S, Mayo JR, Ling A, et al. **Retrospective study of the impact of fellowship training on two quality and safety measures in uterine artery embolization.** *J Am Coll Radiol* 2014;11:471–76 CrossRef Medline
8. Faulkner AR, Bourgeois AC, Bradley YC, et al. **Simulation-based educational curriculum for fluoroscopically guided lumbar puncture improves operator confidence and reduces patient dose.** *Acad Radiol* 2015;22:668–73 CrossRef Medline
9. Mahesh M. **Fluoroscopy: patient radiation exposure issues.** *Radiographics* 2001;21:1033–45 CrossRef Medline

David O. Davis

David Oliver Davis, MD, Past President of the American Society of Neuroradiology (ASNR), died at his home in McLean, Virginia, on November 29, 2016, after a long battle with Parkinson disease. The son of Oliver and Marie (Collignon) Davis, he was born on June 25, 1933, in Danville, Illinois. As a teenager, he was an accomplished hunter, played on the football team, and graduated first in his class at Schlarman High School. He received his undergraduate education at the University of Illinois, Champaign-Urbana, graduating in 1954. Subsequently, he graduated from St. Louis University School of Medicine in 1958. He and his high school sweetheart, Agnes Layden, began a 61-year marriage in Hoopeston, Illinois, on December 26, 1955.

After an internship at the US Public Health Service Hospital in Staten Island and a radiology residency at Columbia Presbyterian Medical Center in New York, he then served a 2-year neuroradiology fellowship with Juan Taveras at the Neurological Institute and remained on the staff. In 1965, when Taveras assumed the Chairmanship of Radiology at the Edward Mallinckrodt Institute of Radiology at Washington University, he invited Davis to accompany him as Director of Neuroradiology. At Mallinckrodt, he established an excellent fellowship program, earned great respect from the Departments of Neurology and Neurosurgery, began significant investigations, and built friendships with neuroradiologists around the country, particularly with Hans Newton at the University of California, San Francisco.

Dave left St. Louis to join the Department of Radiology at the University of Utah and eventually moved to George Washington University, where he was Director of Neuroradiology and subsequently Professor and Chairman of the Department of Radiology. The Davis family lived in the Watergate Apartments for 22 years. His 5 daughters ran a wildly successful hot dog stand in front of the Watergate for 4 summers in the 1970s. Agnes launched a successful real estate enterprise, not only in the DC area but also on Captiva Island in Florida.

A wag once said, "The public memory is six weeks." For this reason, Dave's many contributions to the ASNR and to organized radiology certainly deserve recounting. While he was a Past President of ASNR, his most important service to the society was as a "senior statesman," representing the Society as it pursued some of its most important issues during the turbulent years from 1980 to 2000. Facing the Society in those years were competition from nonfellowship-trained radiologists and other physicians to interpret neuroradiology studies and the question of whether neuroradiologists should train non-neuroradiologists in the performance of cerebral angiography and interventional neuroradiology. These issues resulted in a push to create a Certificate of Added Qualification (CAQ) in neuroradiology. This met with considerable opposition within the ASNR, within organized radiology, within various specialty-certifying boards, and the American Hospital Association.

Dr Davis was a major activist in lobbying for the CAQ in neuroradiology. Time after time, he presented what was an unpopular argument before the Society, at the Radiology Summit, and before a hostile American Board of Radiology, but his diplomacy and personal integrity were major factors in achieving that goal. Despite his unpopular cause, he was elected to the Board of Chancellors of the American College of Radiology and was an effective voice for neuroradiology in that body. Being respected as a radiologist and being personally well-liked were major factors in the success of the ASNR in establishing a CAQ.

ASNR Founding President Juan M. Taveras (left) with David O. Davis.

The fledgling *American Journal of Neuroradiology* (*AJNR*) was originally owned and published by the American Roentgen Ray Society (ARRS). As a member of the Executive Council of the ARRS, he was an important liaison between the ARRS and the *AJNR*. As Chair of the ASNR Publications Committee, he handled the delicate negotiations between the ARRS and the ASNR, which resulted in the successful venture of the *AJNR* into self-publication. He also oversaw the subsequent development of the Journal with his wise fiscal and managerial expertise.

In my years on the Executive Committee and as Editor-in-Chief of *AJNR*, whenever a thorny issue of turf arose, the decision was usually to "let Dave handle it." He never refused a mandate, often accepting challenges in which he differed with the views of the Society, but which he pursued because he felt they would benefit the Society and improve patient care.

There is a devoted cadre of ASNR members who trained under Dave. They recall his devotion to developing our specialty in its early days with innovations such as the "Davis rake" and the "Davis needle." He was a stickler for impeccable radiographic technique and safe performance of invasive procedures. No matter where he practiced, clinicians sought his opinion above those of all others because of his astute observations and his innovative ideas and because he delivered them all with confidence and a fine sense of humor.

There were few members of ASNR with greater personal and professional respect than Dave. He would never seek an honor, and his curriculum vitae was pried from him with great resistance to nominate him for the ASNR Gold Medal, which was awarded to him in 2002. Beginning in 2000, illness crept up insidiously, and George Washington University awarded him emeritus status in 2010.

Devoted to his family, he instilled in his 5 daughters a love of travel. He treated them and their children to serious tennis lessons, skiing, and road trips throughout the Western United States and taught them to throw a football with a perfect spiral. Nineteen grandchildren arrived between 1987 and 2001. Many grandkids only knew that Grandpa was "ill" with what was eventually diag-

nosed as Parkinson disease. Nevertheless, he and Agnes took nearly the "whole pack" (27) on family vacations, touring Ireland in 2006 and Nicaragua in 2012, and annually hosted the family in Captiva at Christmas time.

In May 2015, Dave and Agnes moved into assisted living in McLean, Virginia, where Dr Davis died on November 29, 2016. A mass of Christian burial was celebrated at Holy Trinity Catholic Church in Georgetown, where 4 of his 5 daughters had been married. Before the mass, Dr Michael Newman, his friend and personal physician eulogized Dave as "A Midwesterner with a huge presence who … held himself to the highest of standards and expected no less from others…. He was smart, very smart and intuitive whether interviewing someone to recruit, mulling over a clinical problem, or designing a research project with a 'why not?' approach. He was a leader at George Washington Medical Center and a leader in professional societies and organizations of Radiology and Neuroradiology. His manner was direct, honest, and supportive often by using sardonic wit to make a point. He was always respectful and, when appropriate, critical in an instructive manner and never demeaning."

Neuroradiology has lost a leader whose impact on the specialty will be felt for many years. Those of us fortunate enough to have known him personally have lost a wonderful friend.

M. Huckman

http://dx.doi.org/10.3174/ajnr.A5114

Celebrating 35 Years of the AJNR

March 1982 edition

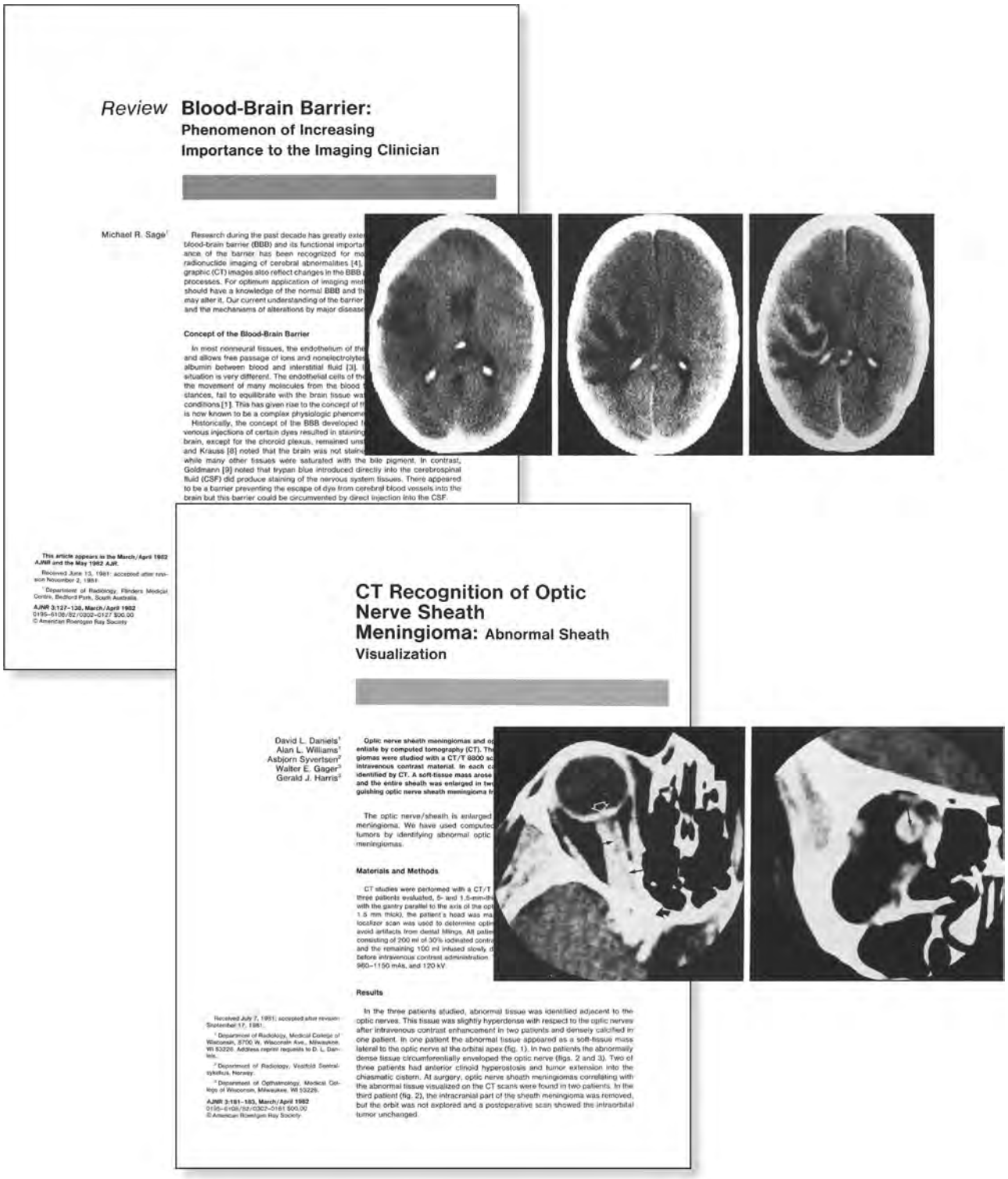

Review **Blood-Brain Barrier: Phenomenon of Increasing Importance to the Imaging Clinician**

Michael R. Sage[1]

Research during the past decade has greatly exte
blood-brain barrier (BBB) and its functional importa
ance of the barrier has been recognized for ma
radionuclide imaging of cerebral abnormalities [4],
graphic (CT) images also reflect changes in the BBB
processes. For optimum application of imaging mot
should have a knowledge of the normal BBB and th
may alter it. Our current understanding of the barrier
and the mechanisms of alterations by major disease

Concept of the Blood-Brain Barrier

In most nonneural tissues, the endothelium of the
and allows free passage of ions and nonelectrolytes
albumin between blood and interstitial fluid [3].
situation is very different. The endothelial cells of the
the movement of many molecules from the blood
stances, fail to equilibrate with the brain tissue wa
conditions [1]. This has given rise to the concept of t
is now known to be a complex physiologic phenome
Historically, the concept of the BBB developed f
venous injections of certain dyes resulted in staining
brain, except for the choroid plexus, remained uns
and Krauss [8] noted that the brain was not stain
while many other tissues were saturated with the bile pigment. In contrast,
Goldmann [9] noted that trypan blue introduced directly into the cerebrospinal
fluid (CSF) did produce staining of the nervous system tissues. There appeared
to be a barrier preventing the escape of dye from cerebral blood vessels into the
brain but this barrier could be circumvented by direct injection into the CSF.

This article appears in the March/April 1982 AJNR and the May 1982 AJR.

Received June 13, 1981; accepted after revision November 2, 1981.

[1] Department of Radiology, Flinders Medical Centre, Bedford Park, South Australia.

AJNR 3:127–130, March/April 1982
0195–6108/82/0302–0127 $00.00
© American Roentgen Ray Society

CT Recognition of Optic Nerve Sheath Meningioma: Abnormal Sheath Visualization

David L. Daniels[1]
Alan L. Williams[1]
Asbjorn Syvertsen[2]
Walter E. Gager[3]
Gerald J. Harris[1]

Optic nerve sheath meningiomas and o
entiate by computed tomography (CT). Th
giomas were studied with a CT/T 8800 sc
intravenous contrast material. In each c
identified by CT. A soft-tissue mass arose
and the entire sheath was enlarged in tw
guishing optic nerve sheath meningioma fr

The optic nerve/sheath is enlarged
meningioma. We have used computed
tumors by identifying abnormal optic
meningiomas.

Materials and Methods

CT studies were performed with a CT/T
three patients evaluated, 5- and 1.5-mm-th
with the gantry parallel to the axis of the opt
1.5 mm thick), the patient's head was ma
localizer scan was used to determine optim
avoid artifacts from dental fillings. All patie
consisting of 200 ml of 30% iodinated contra
and the remaining 100 ml infused slowly d
before intravenous contrast administration
960–1150 mAs, and 120 kV.

Results

In the three patients studied, abnormal tissue was identified adjacent to the optic nerves. This tissue was slightly hyperdense with respect to the optic nerves after intravenous contrast enhancement in two patients and densely calcified in one patient. In one patient the abnormal tissue appeared as a soft-tissue mass lateral to the optic nerve at the orbital apex (fig. 1). In two patients the abnormally dense tissue circumferentially enveloped the optic nerve (figs. 2 and 3). Two of three patients had anterior clinoid hyperostosis and tumor extension into the chiasmatic cistern. At surgery, optic nerve sheath meningiomas correlating with the abnormal tissue visualized on the CT scans were found in two patients. In the third patient (fig. 2), the intracranial part of the sheath meningioma was removed, but the orbit was not explored and a postoperative scan showed the intraorbital tumor unchanged.

Received July 7, 1981; accepted after revision September 17, 1981.

[1] Department of Radiology, Medical College of Wisconsin, 8700 W. Wisconsin Ave., Milwaukee, WI 53226. Address reprint requests to D. L. Daniels.

[2] Department of Radiology, Vestfold Sentralsykehus, Norway.

[3] Department of Opthalmology, Medical College of Wisconsin, Milwaukee, WI 53226.

AJNR 3:181–183, March/April 1982
0195–6108/82/0302–0181 $00.00
© American Roentgen Ray Society

Regarding "Computer-Extracted Texture Features to Distinguish Cerebral Radionecrosis from Recurrent Brain Tumors on Multiparametric MRI: A Feasibility Study"

We read with great interest the recently published article by Tiwari et al[1] regarding automated radiomic features for distinguishing radiation necrosis and recurrent tumor. Because our neuro-oncologists and neurosurgeons frequently ask us to make this distinction for clinical management, we find this subject deserving of attention.

However, we found that the authors' provided limitations in the "Discussion" did not acknowledge several important points that we believe should be addressed. First, the 2 neuroradiologists performed their interpretations without standard-of-care imaging; contrast-enhanced T1-weighted imaging was absent in 5/15 patients, and T2-weighted imaging was absent in 8/15 patients. Furthermore, other routine imaging sequences such as diffusion-weighted imaging, which can be helpful particularly with bevacizumab therapy, were not available to the radiologists. Second, the neuroradiologists were not allowed to view prior imaging, including pretreatment, postoperative, and the most recent prior images, which is also below the current standard of care. Third, no MR perfusion was performed. At both of our institutions with high-volume brain tumor centers and at many other academic centers, this is considered routine for differentiating tumor recurrence from treatment-related change. In our experience and in the literature,[2-5] dynamic contrast-enhanced MR perfusion is reliable, reproducible, and only adds a short time to the examination. No published data exist to support the authors' suggestion that including MR perfusion increases cost or diminishes cost-effectiveness. Finally, FDG-PET was not performed, which again is often used to confirm cases that remain equivocal by MR imaging.[6]

We were further surprised that the authors included mixed pathologies in their small test sample: Four of the 15 cases were metastases. It is known that T2 hyperintensity in metastases reflects vasogenic edema, whereas in gliomas, it may reflect a combination of nonenhancing tumor and treatment change. Because the computer algorithm and neuroradiologists were basing their interpretations primarily on the T2 FLAIR sequence, it is inappropriate for these 2 entities to be considered together.

Finally, we would be interested to hear the authors' basis for their suggestion that radiomics is more readily available than advanced imaging because it is our impression that the opposite is true by a wide margin when considering the availability of human (computer scientists, computational biologists, physicists), hardware (servers, workstations), and software (non-FDA-approved, nonstandardized analysis tools) resources.

We believe that the authors' conclusion that "radiomic features may provide complementary diagnostic information on routine MR imaging sequences," while probably correct, is not supported by their limited data, and further work is required to prove the utility of radiomics in addition to the current standard of care.

Unfortunately, social media outlets have taken the next step in reporting headings such as "Neuroradiologists Beaten by Computer at Making a Key Diagnostic Distinction on MR Imaging" (http://www.healthimaging.com/topics/advanced-visualization/neuroradiologists-beaten-computer-making-key-diagnostic-distinction-mri; HealthImaging link included in the American College of Radiology Daily News Scan). Furthermore, the Twitter statement of the American Society of Neuroradiology[7] that "computer program outperforms #neurorads at differentiating radiation necrosis from recurrent tumor on MR imaging" is unsubstantiated given the evidence and is counterproductive to the advancement of neuroradiology as a field. One of the concerns among bright medical students in choosing radiology versus another field is that the work radiologists do is threatened by computers, and such judgments erroneously support that narrative.

We agree with the authors that further study is needed to determine whether there is an MR imaging texture "signature" for radiation necrosis, and we applaud the authors' effort in pushing this research forward. We look forward to future research and discussion.

REFERENCES

1. Tiwari P, Prasanna P, Wolansky L, et al. **Computer-extracted texture features to distinguish cerebral radionecrosis from recurrent brain tumors on multiparametric MRI: a feasibility study.** *AJNR Am J Neuroradiol* 2016 Sep 15. [Epub ahead of print] CrossRef Medline
2. Yun TJ, Park CK, Kim TM, et al. **Glioblastoma treated with concurrent radiation therapy and temozolomide chemotherapy: differentiation of true progression from pseudoprogression with quantita-**

http://dx.doi.org/10.3174/ajnr.A5019

tive dynamic contrast-enhanced MR imaging. *Radiology* 2015;274:830–40 CrossRef Medline
3. Thomas AA, Arevalo-Perez J, Kaley T, et al. **Dynamic contrast enhanced T1 MRI perfusion differentiates pseudoprogression from recurrent glioblastoma.** *J Neurooncol* 2015;125:183–90 CrossRef Medline
4. Hatzoglou V, Yang TJ, Omuro A, et al. **A prospective trial of dynamic contrast-enhanced MRI perfusion and fluorine-18 FDG PET-CT in differentiating brain tumor progression from radiation injury after cranial irradiation.** *Neuro Oncol* 2016;18:873–80 CrossRef Medline
5. Patel P, Baradaran H, Delgado D, et al. **MR perfusion-weighted imaging in the evaluation of high-grade gliomas after treatment: a systematic review and meta-analysis.** *Neuro Oncol* 2016 Aug 8. [Epub ahead of print] Medline
6. Chiang GC, Galla N, Ferraro R, et al. **The added prognostic value of metabolic tumor size on FDG-PET at first suspected recurrence of glioblastoma multiforme.** *J Neuroimaging* 2016 Aug 12. [Epub ahead of print] CrossRef Medline
7. @TheASNR. https://twitter.com/TheASNR/status/777889433022558208. Posted September 19, 2016

A.D. Schweitzer
G.C. Chiang
Department of Radiology
Weill Cornell Medicine
New York, New York
J. Ivanidze
H. Baradaran
Department of Radiology
Weill Cornell Medicine
New York, New York
Department of Radiology
Memorial Sloan Kettering Cancer Center
New York, New York
R.J. Young
Department of Radiology
Memorial Sloan Kettering Cancer Center
New York, New York
R.D. Zimmerman
Department of Radiology
Weill Cornell Medicine
New York, New York

REPLY:

We thank Dr. Schweitzer and colleagues for their interest in our recent article, "Computer-Extracted Texture Features to Distinguish Cerebral Radionecrosis from Recurrent Brain Tumors on Multiparametric MRI: A Feasibility Study," and their feedback and also thank the editor for the opportunity to address the concerns raised.

First and foremost, we must clarify that the preliminary nature of the data is emphasized in the title itself, where the study is identified as "A Feasibility Study." The study was not meant to be a head-to-head comparison of "standard of care" neuroradiology versus machine performance. Our conclusions were limited to suggesting that radiomic features may provide complementary diagnostic information on routine MR imaging to distinguish radionecrosis from tumor recurrence.

We absolutely agree that the readings were not conducted as "standard of care." In most cases, research protocols differ from "standard of care." As an example, RECIST (Response Evaluation Criteria in Solid Tumors) 1.1,[1] the international reference standard of response assessment, limits the number of lesions to be tracked on serial scans to 5, even in patients with dozens of lesions. Similarly, in RANO (Response Assessment in Neuro-Oncology) criteria,[2] a single bidimensional measurement of the area of enhancement is the central feature tracked serially, with a 50% decrease in area constituting a partial response. When it comes to research, deviation from "standard of care" is indeed standard.

Just as the expert readers in our study were not provided access to prior imaging and a full complement of pulse sequences, the radiomics machine classifier was not provided this information.[3] Our experiments were designed to ensure a "fair" comparison between the radiomics classifier and the diagnostic reads by 2 expert readers. Our aim was to demonstrate that the radiomics classifier was able to pull out information from the posttreatment scans, features that may not be discernible or understood through visual analysis by readers. The higher accuracy suggests that the radiomics classifier can serve as a useful adjunct to the human reader in future machine-assisted decision-support studies for this problem.

Regarding the concern regarding mixed pathologies (both primary and metastatic cases), it should be noted that the disparity between accuracy was entirely related to the assessment of primary tumors. The addition of metastases to the study had no impact on the disparity between "man and machine."

We also agree with Dr. Schweitzer et al that advanced imaging has much to offer. In point of fact, in a pilot study of 28 cases evaluated with FDG-PET-MR imaging incorporating perfusion, both the sensitivity and specificity of PET-MR imaging was 100%.[4] The success of this pilot study notwithstanding, there are obvious advantages to maximizing the yield of existing scan data rather than carrying out additional imaging due to cost savings and better quality of life for the patient. There are several FDA-approved examples of decision-support solutions that use routine MR imaging scans, including products from Riverain, GE Healthcare, and iCAD, being used by radiologists in clinical decision-making for different oncology applications (eg, breast, prostate, and colon cancer). Further, contrary to the comments on difficulty in computation by using radiomics, our analysis did not require any advanced high-performance server or workstation and was run on a standard machine (Core i7 processor, 16 GB RAM) with off-the-shelf hardware. The computational analysis took less than a minute per study to render diagnosis.

Lastly, Dr. Schweitzer et al expressed concerns about bright medical students choosing other medical fields over radiology. It is indeed unfortunate that our paper has been used as the basis for sensationalist journalism. In the early days of MR imaging, because the technique did not depend on ionizing radiation, a background in radiation biology was not needed to administer it to patients. As a result, there was a fear among radiologists that they would lose control of the technique. The joke was that the acronym "NMR" stood for "No More Radiologists." A few years later, once "NMR" was replaced with the name "MR imaging," it was joked that the acronym stood for "More Radiologist Income." Joking aside, the key was that radiologists did not attempt to discredit the new technique, but mastered it instead.

In his recent commentary on our article[5] entitled "Am I about to Lose My Job?!", Dr. Andrei Holodny states, ". . . working with computers, rather than some apocalyptical struggle against them, will lead to optimal results for the patients we serve."

The era of "computer-assisted diagnosis" is upon us. Running and hiding from it would be the greatest disservice to young radiologists. The key to not being *replaced* by the machines is to be the one *using* the machines.

REFERENCES

1. Eisenhauer EA, Therasse P, Bogaerts J, et al. **New response evaluation criteria in solid tumours: revised RECIST guideline (version 1.1).** *Eur J Cancer* 2009;45:228–47 CrossRef Medline
2. Wen PY, Macdonald DR, Reardon DA, et al. **Updated response assessment criteria for high-grade gliomas: Response Assessment in Neuro-Oncology Working Group.** *J Clin Oncol* 2010;28:1963–72 CrossRef Medline
3. Tiwari P, Prasanna P, Wolansky L, et al. **Computer-extracted texture features to distinguish cerebral radionecrosis from recurrent brain tumors on multiparametric MRI: a feasibility study.** *AJNR Am J Neuroradiol* 2016 Sep 15. [Epub ahead of print]. CrossRef Medline
4. Hojjati M, Badve C, Garg V, et al. Diagnostic utility of quantitative ^{18}F-FDG-PET/MR imaging, DSC pMRI and ^{18}F-FDG-PET/CT in differentiating radiation necrosis from tumor recurrence in post therapy GBM. Presented at: 116th Annual ARRS Meeting; April 17–22, 2016; Los Angeles, California.
5. Holodny AI. **"Am I about to lose my job?!": a comment on "Computer-extracted texture features to distinguish cerebral radiation necrosis from recurrent brain tumors on multiparametric MRI: a feasibility study".** *AJNR Am J Neuroradiol* 2016 Oct 13. [Epub ahead of print] CrossRef Medline

P. Tiwari
Department of Biomedical Engineering
L. Wolansky
Department of Radiology
A. Nayate
Department of Radiology
A. Madabhushi
Department of Biomedical Engineering
Case Western Reserve University
Cleveland, Ohio

http://dx.doi.org/10.3174/ajnr.A5045

Comment on "Computer-Extracted Texture Features to Distinguish Cerebral Radionecrosis from Recurrent Brain Tumors on Multiparametric MRI: A Feasibility Study"

We have read with great interest the article published by Tiwari et al, "Computer-Extracted Texture Features to Distinguish Cerebral Radionecrosis from Recurrent Brain Tumors on Multiparametric MRI: A Feasibility Study."[1]

In their article, they refer to our work regarding brain metastasis differentiation from radionecrosis.[2] They mention that our results may have been affected by the classifier being contaminated by sections from the same patient being used in both the training and testing sets during classification.

As stated in our article, 115 lesions from 73 patients were analyzed.[2] There were more lesions than patients because some of the patients showed 2 or 3 lesions in different brain regions. For each lesion, only the MR imaging section depicting the most solid component was used for analysis. Therefore, only 1 section per lesion was used for classification and training, while testing sets were independent. These latter statements were probably misinterpreted by Tiwari et al[1] regarding our methodology.

REFERENCES

1. Tiwari P, Prasanna P, Wolansky L, et al. **Computer-extracted texture features to distinguish cerebral radionecrosis from recurrent brain tumors on multiparametric MRI: a feasibility study.** *AJNR Am J Neuroradiol* 2016;37:2231–36 CrossRef Medline
2. Larroza A, Moratal D, Paredes-Sánchez A, et al. **Support vector machine classification of brain metastasis and radiation necrosis based on texture analysis in MRI.** *J Magn Reson Imaging* 2015;42:1362–68 CrossRef Medline

http://dx.doi.org/10.3174/ajnr.A5071

A. Larroza
Department of Medicine
Universitat de València
Valencia, Spain
D. Moratal
A. Paredes-Sánchez
Center for Biomaterials and Tissue Engineering
Universitat Politècnica de València
Valencia, Spain
E. Soria-Olivas
Intelligent Data Analysis Laboratory
Electronic Engineering Department
Universitat de València
Valencia, Spain
M.L. Chust
L.A. Arribas
Department of Radiation Oncology
E. Arana
Department of Radiology
Fundación Instituto Valenciano de Oncología
Valencia, Spain

REPLY:

We thank Larroza and colleagues for their interest in our article "Computer-Extracted Texture Features to Distinguish Cerebral Radionecrosis from Recurrent Brain Tumors on Multiparametric MRI: A Feasibility Study."[1]

We are responding to the following comment by Larroza and colleagues in their letter: "Our results may have been affected by the classifier being contaminated by sections from the same patient being used in both the training and testing sets during classification."

Our understanding of the analysis in the article by Larroza et al[2] was that it was done on a lesion basis. The study comprised 115 lesions from 73 unique patient studies, with some patients having >1 lesion in different regions of the brain. Specifically, as mentioned in Larroza et al, the authors merged training and test sets and performed repeated training/test splits 100 times, holding 70% in training and then averaging the area under the curve values on test sets.

After we read the article by Larroza et al,[2] it was not clear whether lesions from the same patient appeared simultaneously in the training and test sets. This could bias analysis because adjacent MR imaging sections tend to be highly correlated; thus, the features extracted (albeit from 2 different lesions from the same patient) might also be correlated. Thus, for a patient, including features from one lesion in training and features from another lesion in the test set within the same iteration of cross-validation may lead to overfitting[3] and may yield unreliable results. It is not clear that patient-specific separation across lesions was ensured during their cross-validation analysis.

http://dx.doi.org/10.3174/ajnr.A5120

REFERENCES

1. Tiwari P, Prasanna P, Wolansky L, et al. **Computer-extracted texture features to distinguish cerebral radionecrosis from recurrent brain tumors on multiparametric MRI: a feasibility study.** *AJNR Am J Neuroradiol* 2016;37:2231–36 CrossRef Medline
2. Larroza A, Moratal D, Paredes-Sánchez A, et al. **Support vector machine classification of brain metastasis and radiation necrosis based on texture analysis in MRI.** *J Magn Reson Imaging* 2015;42:1362–68 CrossRef Medline
3. Hastie T, Tibishirani R, Friedman J. *The Elements of Statistical Learning*: *Data Mining, Inference, and Prediction*: *Springer Series in Statistics*. 2nd ed. New York: Springer-Verlag; 2009:chap 7

P. Tiwari
A. Madabhushi
Department of Biomedical Engineering
Case Western Reserve University
Cleveland, Ohio

Regarding "Uremic Encephalopathy: MR Imaging Findings and Clinical Correlation"

We thank Kim et al[1] for their article on the MR imaging of uremic encephalopathy (UE) in correlation with clinical findings. On a cursory read, the article presents a unique concept: When one reviews an MR imaging study and sees the lentiform fork sign (LFS), consider UE. However, more detailed analysis of the article questions the process used to reach this conclusion.

The LFS was initially described by Kumar and Goyal in 2010.[2] When they tried to identify an imaging finding specific to UE, a single patient was identified with LFS, uremia, and metabolic acidosis. A subsequently performed literature search found that patients with metabolic acidosis from multiple etiologies also exhibited this sign.

The conclusion of this article sought to shift this association between the LFS and metabolic acidosis to UE. Nine of the 10 patients examined demonstrated the LFS, only 1 of whom demonstrated metabolic acidosis via arterial blood gas. However, only 5 patients in the study had arterial blood gas data, and it is unclear whether the samples were obtained before or after dialysis. The timing of arterial blood gas testing in relation to the MR imaging would be critical for determining whether MR imaging findings had any correlation with metabolic acidosis.

Chronic renal failure (CRF) and metabolic acidosis are strongly associated.[3] Approximately 80% of patients with a glomerular filtration rate of <20 have metabolic acidosis, as well as most patients on dialysis. This finding suggests that most of the patients were, at some time, acidotic; Kumar and Goyal[2] reasoned that being acidotic might result in the LFS with normal blood pH. Although it is feasible that routine dialysis might mitigate the degree of metabolic acidosis, the markedly elevated creatinine levels suggest that the patients in this study had not been dialyzed recently. This suggestion, too, is confusing because the article stated that the patients with CRF "regularly received hemodialysis," which should preclude uremia and, therefore, uremic encephalopathy.

Other details briefly mentioned warrant further elaboration. The article states that 1 patient was "subsequently identified and added to the study." There is no discussion of why this patient was not identified initially. Of the 10 patients, 1 had acute renal failure. He may have been excluded if the first search was restricted to chronic renal failure, but the reasoning behind his eventual inclusion is unclear because he was the only patient not to demonstrate the LFS in the study.

In the "Materials and Methods," the sequences obtained on the 1.5T and 3T magnets are described. There is no mention of FLAIR or gradient recalled-echo/SWI sequences on the 1.5T magnet or which patient was scanned on which magnet. This omission has implications for the subsequent "Discussion": When the central variant posterior reversible encephalopathy syndrome (PRES) was mentioned, microhemorrhages on SWI were noted as one of a few key distinguishing features. Of note, the cited article describing central variant PRES found microhemorrhages in 2 of the 4 patients with SWI sequences available, a less strong association than the article implies.[4]

In the "Results," when describing the imaging findings of the 9 patients with chronic renal failure, the authors stated that increased signal on apparent diffusion coefficient maps in the basal ganglia was seen consistent with vasogenic edema. Four of 9 patients had increased signal intensity on diffusion-weighted imaging without restricted diffusion, 2 showed restricted diffusion, and 5 had normal signal on DWI, a total of 11 patients, 2 more than the study population. If all study patients showed the LFS, how could the DWI signal be normal in 5 patients? Could the authors clarify? Because only 4 of 10 patients had follow-up imaging after hemodialysis and the authors did not include the 2 patients with restricted diffusion on the initial study, any conclusion about the reversibility of imaging finding should be viewed with caution. The authors further stated that DWI changes did not correlate with serum creatinine levels between the 2 groups of 4 and 5 patients, but they did not specify what these 2 subgroups were, if restricted diffusion was only seen in 2 patients. Toward the end of the "Discussion," the authors stated that 3/9 patients who underwent DWI showed cytotoxic edema in the globus pallidus; this is very confusing for the readers because the numbers do not match.

If only 2/10 patients had cortical involvement on T2 and FLAIR images and these 2 patients were markedly hypertensive, it is unclear how one can conclude that cortical involvement is a distinct subset of findings in UE.

In the "Discussion," there is mention of diabetes possibly being implicated in the LFS in the presence of UE, a relationship that has been noted previously by Kumar and Goyal.[2] This article[1] stated that 7 of the 9 patients with the LFS had diabetes. However, diabetes is the most common cause of renal failure, and all the

http://dx.doi.org/10.3174/ajnr.A5058

patients with CRF, including 2 with hypertension, demonstrated the LFS. This finding would seem to suggest that all causes of CRF, not just diabetes, are associated.

The article concludes with the statement that the LFS is reliable in the early diagnosis of UE; this conclusion implies some degree of specificity. However, the sensitivity and specificity of the LFS for UE were not determined. It is also unclear how it helped in the "early" diagnosis. Until there is a better understanding of the pathophysiology underlying the imaging findings, it may be more prudent to use the LFS as originally described—to alert clinicians to potential metabolic acidosis.

REFERENCES

1. Kim DM, Lee IH, Song CJ. **Uremic encephalopathy: MR imaging findings and clinical correlation.** *AJNR Am J Neuroradiol* 2016;37:1604–09 CrossRef Medline
2. Kumar G, Goyal MK. **Lentiform fork sign: a unique MRI picture—is metabolic acidosis responsible?** *Clin Neurol Neurosurg* 2010;112:805–12 CrossRef Medline
3. Kraut JA, Kurtz I. **Metabolic acidosis of CKD: diagnosis, clinical characteristics, and treatment.** *Am J Kidney Dis* 2005;45:978–93 CrossRef Medline
4. McKinney AM, Jagadeesan BD, Truwit CL. **Central-variant posterior reversible encephalopathy syndrome: brainstem or basal ganglia involvement lacking cortical or subcortical cerebral edema.** *AJR Am J Roentgenol* 2013;201:631–38 CrossRef Medline

N. Das
Department of Radiology and Biomedical Imaging
Yale School of Medicine
X. Wu
Yale School of Medicine
A. Malhotra
Department of Radiology and Biomedical Imaging
Yale School of Medicine
New Haven, Connecticut

REPLY:

We thank Dr Das and colleagues for their interest in our article and their comments.

In our article,[1] we tried to evaluate the specific MR imaging findings in patients with clinically diagnosed uremic encephalopathy. Therefore, we enrolled 9 of 10 patients with chronic renal failure (CRF) and the lentiform fork sign (LFS) on brain MR imaging and 1 patient with acute renal failure (ARF) without the LFS. In 9 patients with CRF, despite regular hemodialysis (3 times a week in all patients), the various neurologic symptoms developed between regular hemodialysis sessions and the LFS was shown on brain MR imaging. Thus, they were included. One patient with ARF was first clinically diagnosed with uremic encephalopathy and then was included in the study, though there was no LFS on brain MR imaging. In our article, we suggested that the expansile T2 high signal intensity of the bilateral basal ganglia (LFS) may be a reliable finding of uremic encephalopathy.

Before brain MR imaging for a diagnosis and then additional intensive hemodialysis as a treatment for uremic encephalopathy, 6 of 10 patients underwent arterial blood gas analysis and only 2 of them showed metabolic acidosis (1 with CRF and 1 with ARF). As Dr Das and colleagues have suggested, there may be a relationship between the LFS and metabolic acidosis in patients with underlying CRF, but we did not find a specific one. In addition, regular hemodialysis may not always prevent various neurologic complications, including uremic encephalopathy from uremia.

Nine patients showed the LFS on T2WI or FLAIR. However, unfortunately, FLAIR was not available in 3/3 patients imaged with a 1.5T scanner and 2/7 patients imaged with a 3T scanner. In general, 9 patients with CRF and the LFS showed diffusely increased signal intensity ($n = 4$) and normal signal intensity ($n = 5$) in the basal ganglia on DWI, but 3 of 9 patients showed focal restricted diffusion in the globus pallidus or putamen—that is, various patterns of cytotoxic or vasogenic edema may be present in patients with uremic encephalopathy. Thus, the LFS on T2WI does not mean increased signal intensity on DWI in all patients.

Renal failure may be attributed to uremic encephalopathy and posterior reversible encephalopathy syndrome (PRES). In addition to the pathophysiologic findings such as vascular autoregulatory dysfunction,[2] imaging findings may overlap between PRES and uremic encephalopathy. Also, as PRES can be divided into 2 types, the cortical or subcortical type and the central variant type, uremic encephalopathy can be divided into 3 patterns according to the involved area: basal ganglia, cortical or subcoritcal area, and white matter. Considering the clinical condition and imaging findings, we classified the 2 patients showing cortical and basal ganglia involvement as having uremic encephalopathy. As Dr Das and colleagues have suggested, SWI is helpful for detecting microhemorrhage in some conditions such as PRES and is more sensitive than the gradient recalled-echo (GRE) sequence of 1.5T and 3T scanners. However, in our study only GRE sequence was available in 2/3 patients with a 1.5T scanner and 4/7 patients with a 3T scanner, and we did not find any microhemorrhages related to uremic encephalopathy.

Many various etiologies may play an important role in CRF, but diabetes mellitus–related CRF may be related to the LFS in the patients with uremic encephalopathy, especially Asian individuals, considering previous studies[3-7] as well as our study.

Once again, although we did not verify the sensitivity or specificity of the LFS due to the small number and selection bias in our study, it is important to consider the relationship between uremic encephalopathy and LFS in patients with CRF or ARF.

http://dx.doi.org/10.3174/ajnr.A5077

REFERENCES

1. Kim DM, Lee IH, Song CJ. **Uremic encephalopathy: MR imaging findings and clinical correlation.** *AJNR Am J Neuroradiol* 2016;37:1604–09 CrossRef Medline
2. Port JD, Beauchamp NJ Jr. **Reversible intracerebral pathologic entities mediated by vascular autoregulatory dysfunction.** *Radiographics* 1998;18:353–67 CrossRef Medline
3. Okada J, Yoshikawa K, Matsuo H, et al. **Reversible MRI and CT findings in uremic encephalopathy.** *Neuroradiology* 1991;33:524–26 CrossRef Medline
4. Wang HC, Cheng SJ. **The syndrome of acute bilateral basal ganglia lesions in diabetic uremic patients.** *J Neurol* 2003;250:948–55 CrossRef Medline
5. Lee EJ, Park JH, Ihn Y, et al. **Acute bilateral basal ganglia lesions in diabetic uraemia: diffusion-weighted MRI.** *Neuroradiology* 2007;49:1009–13 CrossRef Medline
6. Yoon CH, Seok JI, Lee DK, et al. **Bilateral basal ganglia and unilateral cortical involvement in a diabetic uremic patient.** *Clin Neurol Neurosurg* 2009;111:477–79 CrossRef Medline
7. Kang E, Jeon SJ, Choi SS. **Uremic encephalopathy with atypical magnetic resonance features on diffusion-weighted images.** *Korean J Radiol* 2012;13:808–11 CrossRef Medline

I.H. Lee
D.M. Kim
C.J. Song
Department of Radiology
Chungnam National University Hospital
Chungnam National University School of Medicine
Daejeon, South Korea